SAND2020-11539R

Process Model Development and Experimental Investigation for Spent Fuel Disposal in Crystalline Rocks: FY20 Report

Spent Fuel and Waste Disposition

Draft

Prepared for
US Department of Energy
Spent Fuel and Waste Science Technology
Y. Wang, Y. Xiong, T. Hadgu, E. Kalinina, M. M. Mills, A. C. Sanchez
Sandia National Laboratories
J. Jerden, S. Thomas, E. Lee, V. K. Gattu, W. Ebert
Argonne National Laboratory
H. Viswanathan, S. Chu, A. R. Hoinville, J. Hyman,
S. Karra, N. Makedonska, K. Telfeyan
Los Alamos National Laboratory
Y. Guglielmi, C. Chang, P. Cook, P. Dobson, F. Soom, S. Nakagawa,
C.-F, Tsang, S. Borglin, C. Doughty, L. Zheng,
Lawrence Berkeley National Laboratory
M. Zavarin, E. Balboni, C. Atkins-Duffin, W. Bourcier, S.F. Carle
K. Smith, C. Booth
Lawrence Livermore National Laboratory
July 15, 2020
M2SF-20SN010302051

Revision 6
10/7/2019

APPENDIX E
NFCSC DOCUMENT COVER SHEET[1]

Name/Title of Deliverable/Milestone/Revision No.	Process model development and experimental investigation for Spent fuel disposal in crystalline rocks (M2SF-20SN010302051)
Work Package Title and Number	Crystalline disposal R&D - SNL
Work Package WBS Number	SF-20SN010305
Responsible Work Package Manager	Yifeng Wang (Name/Signature)
Date Submitted	

Quality Rigor Level for Deliverable/Milestone[2]	☐ QRL-1 ☐ Nuclear Data	☐ QRL-2	☒ QRL-3	☐ QRL-4 Lab QA Program[3]

This deliverable was prepared in accordance with Sandia National Laboratories
(Participant/National Laboratory Name)

QA program which meets the requirements of
☒ DOE Order 414.1 ☐ NQA-1 ☐ Other

This Deliverable was subjected to:

☒ Technical Review ☐ Peer Review

Technical Review (TR)
Review Documentation Provided
☐ Signed TR Report or,
☐ Signed TR Concurrence Sheet or,
☒ Signature of TR Reviewer(s) below

Peer Review (PR)
Review Documentation Provided
☐ Signed PR Report or,
☐ Signed PR Concurrence Sheet or,
☐ Signature of PR Reviewer(s) below

Name and Signature of Reviewers

Carlos F. Jove-Colon 9/14/2020

NOTE 1: *Appendix E should be filled out and submitted with the deliverable. Or, if the PICS:NE system permits, completely enter all applicable information in the PICS:NE Deliverable Form. The requirement is to ensure that all applicable information is entered either in the PICS:NE system or by using the NFCSC Document Cover Sheet.*

- *In some cases there may be a milestone where an item is being fabricated, maintenance is being performed on a facility, or a document is being issued through a formal document control process where it specifically calls out a formal review of the document. In these cases, documentation (e.g., inspection report, maintenance request, work planning package documentation or the documented review of the issued document through the document control process) of the completion of the activity, along with the Document Cover Sheet, is sufficient to demonstrate achieving the milestone.*

NOTE 2: *If QRL 1, 2, or 3 is not assigned, then the QRL 4 box must be checked, and the work is understood to be performed using laboratory QA requirements. This includes any deliverable developed in conformance with the respective National Laboratory / Participant, DOE or NNSA-approved QA Program.*

NOTE 3: *If the lab has an NQA-1 program and the work to be conducted requires an NQA-1 program, then the QRL-1 box must be checked in the work Package and on the Appendix E cover sheet and the work must be performed in accordance with the Lab's NQA-1 program. The QRL-4 box should not be checked.*

This page left blank intentionally

EXCUTIVE SUMMARY

The U.S. Department of Energy Office of Spent Fuel Waste Disposition (SFWD) established in fiscal year 2010 (FY10) the Spent Fuel Waste Science & Technology (SFWST) Program (formerly the Used Fuel Disposition Campaign - UFDC) program to conduct the research and development (R&D) activities related to storage, transportation and disposal of used nuclear fuel and high level nuclear waste. The Mission of the SFWST is:

> *To identify alternatives and conduct scientific research and technology development to enable storage, transportation and disposal of used nuclear fuel and wastes generated by existing and future nuclear fuel cycles*.

The work package of Crystalline Disposal R&D directly supports the following SFWST objectives:

- Develop a fundamental understanding of disposal system performance in a range of environments for potential wastes that could arise from future nuclear fuel cycle alternatives through theory, simulation, testing, and experimentation.
- Develop a computational modeling capability for the performance of storage and disposal options for a range of fuel cycle alternatives, evolving from generic models to more robust models of performance assessment.

The objective of the Crystalline Disposal R&D work packages is to advance our understanding of long-term disposal of used fuel in crystalline rocks and to develop necessary experimental and computational capabilities to evaluate various disposal concepts in such media. Specifically, FY20 work aims to:

- Assist the geologic disposal safety assessment (GDSA) team to develop a robust repository performance assessment model.
- Provide the GDSA with a basic "minimal" set of process models and model feeds to support the GDSA near-term goal.
- Develop basis for process modeling that enables streamlined integration with system modeling resulting in feeds to GDSA.
- Consolidate model parameter data, especially thermodynamic data, to ensure more consistent usage of the data across the project.
- With the existence of different approaches taken by various researchers there is a need to understand how well the models are developed in terms of pedigree and rigor.
- Fully leverage international collaborations for data collection and model development and validation.
- Closely collaborate with other work packages, especially those on disposal in argillite and engineered barrier system design.

Significant progress has been made in FY20 in both experimental and modeling arenas in evaluation of used fuel disposal in crystalline rocks, especially in model demonstration using field data. The work covers a wide range of research topics identified in the R&D plan. The major accomplishments are summarized below:

- *Discrete Fracture Network Model Development:* Many model-based studies assume fractures to be smooth planes. However, real-world fractures are known to have rough surface asperities. We accounted for fracture roughness by assuming textures with different connectivity structure and investigate how this impacts transport behavior. We demonstrated that this type of fracture roughness could control important features of flow and waterborne mass transport. We also investigated the relative impact of advective transport compared to retention due to matrix diffusion. Flow and solute transport through low-permeability fractured media at short time scales

is generally determined by fractures and the interconnected networks that they form. However, at longer time scales, matrix diffusion, where solutes are exchanged between flowing regions (fractures) and non-flowing regions (matrix) via molecular diffusion, also influences solute transport. A long-standing question in this area of research is the relative impact of matrix diffusion on power-law scaling in the tails of the solute transport breakthrough curve, which are observed in field and laboratory experiments. While classical theory requires that matrix diffusion produces a decay rate of time $t^{-3/2}$, deviations have also been observed. We address this question through the development of a new theory that elucidates how interactions between two critical physical processes (advection and matrix diffusion) can produce either the classical -3/2 decay rate or alternative decay rates based on two dimensionless parameters. Our theoretical predictions were validated against particle tracking simulations using a high-fidelity three-dimensional discrete fracture network simulator.

- *Understanding bentonite swelling behaviors and colloid stability:* We addressed uncertainties related to bentonite behavior under disturbances, such as high temperature or swelling induced by changes in groundwater ionic strength and to understand the implications for colloid-facilitated transport of radionuclides. Column experiments were designed to test the effects of temperature on bentonite mineralogy and electrochemical properties. In the first experiment, bentonite spiked with ^{137}Cs was heated for 2 weeks at 200˚C prior to making a dilute colloid solution to inject through a series of analcime columns. Another experiment involved injecting a similar colloid solution through a granodiorite column heated in-situ to 200˚C. The results suggest that morphological and mineralogical changes to the bentonite occur, potentially increasing its sorption capacity. By contrast, elevated temperatures also reduce the repulsive force between colloids, lowering their stability. The colloid concentration of the solution eluting through the columns heated to 200˚C dropped by roughly half, indicating that colloids are less stable at high temperature. The zeta potential and average diameter of the colloids, however, showed minimal changes from the increased temperature. A new method was also developed to quantify the anisotropy of bentonite swelling in order to inform bentonite swelling and erosion models. Solutions of variable ionic strength were introduced to pressed bentonite pellets, and images were taken over time through a microscope. The swelling rate and circularity were quantified at set time steps to relate anisotropy to swelling rate as predicted by simulations.
- *Rock testing capability development:* We have developed a high pressure (up to 10,000 psi), high temperature (up to 200˚C) triaxial loading system to enable long-term (days to months) laboratory experiments of flow simultaneously on multiple core samples under temperature, mechanical, and chemically controlled conditions. We also used the system for permeability measurements of granite samples obtained from the Grimsel Underground Research Laboratory.
- *In-situ evaluation of transmissive fractures:* Lawrence Berkeley National Laboratory (LBNL) conducted in-situ transmissive fracture testing in collaboration with the Collisional Orogeny in the Scandinavian Caledonides (COSC) scientific team. The research activities were conducted using the COSC-1 borehole as a testbed to evaluate the hydrology of a crystalline basement environment. This research is aimed at providing insights on the problem of nuclear waste disposal in crystalline formations. In June of 2019, the LBNL team deployed a unique borehole monitoring tool, called Step-rate Injection Method for Fracture In-situ Properties (SIMFIP), to measure real-time 3D mechanical deformation of rock within three intervals of the COSC-1 borehole. The following field tests were carried out: pressure buildup tests, pressure falloff tests, and constant flow rate tests for each of the three intervals. Two approaches were used to evaluate the stress conditions: an inversion of the displacement data, and a fully coupled numerical simulation of fracture stimulation and fluid flow using the distinct element code 3DEC. These analyses provided insights into the stress state for the borehole intervals, as well as how the fractures responded to hydraulic stimulation. Laboratory and modeling investigations were conducted on COSC-1 core samples that correspond with the borehole intervals tested in the field.

- *Model validation for fluid flow and transport in fractured rocks:* Updated modeling analyses were conducted on DECOVALEX Task C inflow and recovery simulations. The inflow simulations included a study of boundary conditions related to domain size by comparing inflow results for the base case domain (200 m x 300 m x 200 m) with that of a much larger domain (1386 m x 1486 m x 806 m). The comparisons were done for all ten fracture realizations. Pressure distribution simulation results for one of the realizations show that the site-scale domain exhibited boundary effects while the larger domain had no such effects. As a result, the inflow results for the 10 realizations using the larger domain show significantly reduced values compared to the base case domain. Thus, the inflow is better predicted with the larger domain. Updated simulations were also conducted to model water-filling of the plugged CTD and resulting pressure recovery. For the analysis the base case domain with domain size of 200 m x 300 m x 200 m was used. The 10 upscaled fracture realizations were used to provide permeability and porosity distributions. Simulation results were compared with project experimental data. The results show that pressure predictions of many of the 10 realizations closely match the experimental data at the observation points in 12MI33. Reasonable results were also obtained for predictions of chloride concentrations at most of the observation points. For this study upscaling of DFN to a continuum grid was conducted using the Oda method. The Oda method is an efficient geometric method to calculate grid block permeability without the use of flow simulations. However, it relies on well-connected fracture networks and thus tends to over-predict grid block permeability. In this work the Oda method was used to study the effect of grid block size on flow and transport. Simulations have shown that results are highly dependent on grid lock size.
- *Fuel Matrix Degradation Model Parameterization:* Electrochemical experiments were conducted to quantify the corrosion rates of the four most abundant alloys that make up the internal components of a typical spent fuel waste package (316 stainless steel, carbon steel, and aluminum alloy and Zircaloy-4) at several pH values and chloride concentrations. These rates were used to determine the amount of hydrogen gas generated during anoxic corrosion and to parameterize a prototype in-package chemistry (IPC) model that has been integrated with the fuel matrix degradation (FMD) model. The combined model provides spent fuel degradation rates over a range of Eh, pH and chemical conditions relevant for argillite and crystalline rock repository environments. This combined model was developed by coupling the FMD model with the reactive transport code X1t, which is a module within the Geochemist's Workbench (GWB) software package. The reactive transport model was used to calculate the amount of H_2 produced and accumulated within a breached waste package due to the corrosion of stainless steel, carbon steel, aluminum alloys and Zircaloy based on the corrosion rates measured in the experiments. The environmental dependencies of in-package alloy corrosion rates must be taken into account in the FMD model to represent the range of conditions that can occur in a breached waste package. Instantaneous alloy corrosion rates and environmental dependencies (Eh, pH, Cl, T) are needed to calculate the spent fuel degradation rates used to define the radionuclide source term in a repository system performance assessment. The electrochemical measurements of alloy corrosion rates provide values and dependencies on T, Eh, pH, and Cl^- conditions that are needed for source term model parameterization and validation for carbon steel and aluminum alloy, which corrode actively, and for 316 stainless steel and Zircaly-4, which passivate.
- *Waste package material development:* Corrosion-resistant waste packages constitute a key component of a multiple barrier system for waste isolation. Metallic copper has been proposed as an outer layer material for a waste package. However, a concern has been raised regarding potential copper corrosion induced by hydrogen sulfides in a reducing disposal environment. We here demonstrate that lead/lead-alloy materials could be an excellent alternative material for waste package outer layers, owing to their corrosion resistance (especially to hydrogen sulfide attack) and radiation-shielding capability. Our long-term corrosion experiments show that lead is passivated

by its corrosion products, cerussite ($PbCO_3$) and tarnowitzite $(Ca,Pb)CO_3$, in carbonate-bearing groundwaters, because of the formation of a dense surface layer of corrosion products and the low solubility of the corrosion products. With its low solubility ($<10^{-6}$ mol kg^{-1}), cerussite is more favored to form over galena (PbS) in a typical disposal environment; thus, the issue of sulfide-induced metal corrosion as related to copper can be completely eliminated. If needed, the carbonate concentration in a repository can be conditioned with carbonate materials such as calcite or hydromagnesite to ensure cerussite precipitation. Furthermore, using lead/lead alloy will provide excellent radiation shielding for waste package transportation and repository operation.

- *Enhancement of bentonite thermal conductivity:* In high-level radioactive waste disposal, a heat-generating waste canister is generally encased with a layer of bentonite-based buffer material acting as an engineered barrier to limit water percolation and radionuclide release. The low thermal conductivity of bentonite (~ 0.5 W/mK) combined with a high thermal loading waste package may result in a high surface temperature on the package that can potentially impact the structural integrity of the package itself as well as the surrounding buffer material. We showed that the thermal conductivity of bentonite could be effectively enhanced by embedding copper meshes across the buffer layer to form fully connected high heat conduction pathways. A simple calculation based on Rayleigh's model indicates that a thermal conductivity value of 5 W/mK required for effective heat dissipation can be achieved simply by adding ~ 1 v % of copper meshes into bentonite. As a result, the peak surface temperature on a large waste package such as a dual-purpose canister can be reduced by up to 300 °C, thus significantly reducing the surface storage time for waste cooling and therefore the overall cost for direct disposal of such waste packages. Because of the ensured full thermal percolation across the buffer layer, copper meshes turn out to be much more effective than any other materials currently suggested (such as graphene or graphite) in enhancing thermal conductivity of buffer material. Furthermore, the embedded copper meshes will help reinforce the mechanical strength of the buffer material, thus preventing the material from a potential erosion by an intrusion of dilute groundwater.
- *Understanding radionuclide incorporation into corrosion products:* The incorporation of radionuclides into corrosion phases may limit the rate of radionuclide release by sequestering a portion of the radionuclide source term. We performed a literature review on Se and Tc interactions with various Fe minerals to identify the most critical radionuclides and data gaps associated with radionuclide interaction with corrosion products. We synthesized ferrihydrite with various amounts of Pu(IV) (3000, 1000 and 400 ppm) following either a coprecipitation or sorption process and then subsequently used this material to crystallize goethite. We performed extended x-ray absorption fine structure (EXAFS) spectroscopy, transmission electron microscopy (TEM) and acid leaching analysis to elucidate the nature of plutonium association with ferrihydrite and goethite. Our results show that variations in synthetic routes have impacts on the nature of Pu associated with both the ferrihydrite precursor and the ferrihydrite recrystallization product (goethite). When a Pu containing solution is added to a ferrihydrite mineral (sorption route), a fraction of the Pu precipitates as PuO_2 nanoparticles and the remaining Pu fraction forms a complex on the mineral surface. After hydrothermal alteration to goethite, the PuO_2-like nanoparticles are preserved while a fraction of Pu is still present as a surface adsorbed species on the goethite mineral surface. There is evidence that this adsorbed species is more weakly bound to goethite than to ferrihydrite, as evidenced by a decrease in the number of Pu-Fe scatters identified in the respective sample. This observation suggests that Pu adsorbed to ferrihydrite may be mobilized during the recrystallization processes. The analysis of the supernatant after hydrothermal alteration of ferrihydrite to goethite showed a small increase in Pu concentration confirming that some Pu re-mobilization occurs during the mineral recrystallization process. However, when ferrihydrite is precipitated directly from a solution containing Fe and Pu (coprecipitation route), no PuO_2-like nanoparticles are observed. Although it is difficult to identify the exact nature of Pu in the sample due to a high degree of disorder, there is evidence that Pu is strongly bound to the ferrihydrite solids through a combination of adsorption and/or coprecipitation as evidenced by the high number of Pu-Fe scatters. A fraction

of Pu could coprecipitate with ferrihydrite and/or form a polynuclear inner sphere complex. The EXAFS data show that the Pu binding site changes significantly during ferrihydrite recrystallization to goethite, indicating that Pu is mobilized during hydrothermal alteration. However, only a small fraction of Pu in the highest Pu concentration sample is remobilized to form PuO_2. In the lower concentration goethite samples Pu is strongly sorbed (either coprecipitated and/or adsorbed as inner sphere complex) to the goethite as evidenced by the high number of Pu-Fe scatters, and PuO_2 is not observed. The acid leaching results support this conclusion by showing that less Pu is accessible to leaching in goethite formed via coprecipitation process, compared to the goethite formed via the sorption process. These observations confirm that that the nature of Pu associated with the mineral will affects the leachability of Pu from the solids. In addition, Pu-doped magnetite was synthesized to study in an anaerobic glovebox to study the coprecipitation of magnetite with plutonium. Analysis of the supernatant after 30 days of oxidation experiments showed that less than 1% Pu is released to solution during 30-days oxidation, suggesting that Pu associates strongly to magnetite and is retained upon exposure to oxidative conditions.

- *Thermodynamic database development and international collaboration:* In FY20, we focused on our long-term commitment to engaging our partners in international nuclear waste repository research. This includes participation in the Nuclear Energy Agency Thermochemical Database Project, thermodynamic database collaborations, and surface complexation model international collaborations. Work is in progress to produce a software tool to add new species and to produce enhanced data files for reactive transport codes relevant to the SFWST Generic Disposal System Assessment (GDSA) efforts. The tool is built around the SUPCRT data base as amended by Chen Zhu and co-workers (SUPCRTBL). The code is meant to be used by someone wanting to add new data to SUPCRT and ensure that it is internally consistent with the existing data. The code will produce a new version of the data file needed to run any of several reactive transport codes. Currently we plan to produce files for PHREEQC, EQ3/6, and GWB. Additional file configurations can be readily added to support the GDSA efforts. Furthermore, our code can readily be modified to use data files other than SUCPRT as the starting database. In particular, this code will be applicable to the modified SUPCRT code under development in the Argillite work package and for use in the US SFWST Generic Disposal System Assessment (GDSA) efforts. A key goal is to facilitate the integration of US SFWST thermodynamic database development with international thermodynamic database compilations (e.g. the NEA-TDB radiochemical thermodynamic data).
- *Understanding smectite-to-illite transformation:* In order to predict how well a bentonite barrier will function over time at repository relevant temperatures for heat generating waste, it is important to understand thermal alteration effects on smectite, a main constituent of bentonite. One type of thermal alteration is the conversion of smectite to illite (illitization) when exposed to elevated temperatures and a sufficient amount of potassium ions, thereby weakening barrier functions. Laboratory studies have tried to reproduce the transformation under a wide variety of conditions. However, the conditions were based on efforts to replicate natural earth processes. To facilitate the conversion of smectite to illite, illitization experiments on less than 2 μm fractions of Na-rich and K-exchanged smectite clay were performed within hydrothermal reaction vessels over one-week, two-week, two-month, and four-month timescales. The clay was exposed to hydrothermal conditions with various liquid to solid ratios at 200°C. Multiple analysis techniques were used to characterize the altered clay and identify extent of conversion, including XRD, XRF, surface area, and morphology changes by SEM; this section reports findings solely provided by XRD. The pore-water chemistry was also analyzed by ICP-OES to detect any dissolved products such as silica content. Results suggest the conversion rate is relatively fast and is dependent not only on the amount of K, but also dissolved silica concentration related to total solid in solution (liquid to solid ratio).

In the next five years, the disposal research will continue to focus on process model development and model implementation in a GDSA framework for different generic reference cases. At the end of the five years, it is anticipated that a GDSA model developed will contain a sufficiently detailed representation of relevant process models and thus can be used for sensitivity analyses and programmatic prioritization.

The crystalline R&D thrust area has a significant focus on opportunities to improve model representations of the most significant processes to repository performance. Buffer erosion is a good example of an instance in which a new mechanistic representation can be developed, building on work that has already been done in Europe. Hydrologic properties of the EDZ represent another opportunity for improved representation. Flow and transport in fractures, including matrix diffusion, are an ongoing focus. Overall, modeling a repository in crystalline rocks involves more issues than other rock types, so there is a continued need for more crystalline R&D activities over the next five years.

Crystalline R&D thrust areas cover a wide range of topics. Primary among these is the continued development of a crystalline media model that can be input to the GDSA PA system framework. In the near-term, i.e. the next two years, model development associated with this activity will be aimed at providing a minimal set of process models and model feeds to the GDSA PA. Modeling of fluid flow and transport in fractured crystalline media will continue to be a thrust area in the next five years. We will continue to focus on model capability demonstrations using actual field data obtained from international collaborations. Systematic investigations of the potential effects of fracture geometry and distribution on fracture connectivity and hydrologic permeability will continue. Potential implications to site selection and characterization will be explored over the next five years.

The interaction between the crystalline host rock and the EBS has been an important research thrust in the crystalline area and will continue to be so in the coming five years. Engineered buffer materials in the EBS are an important component for waste isolation in a crystalline repository. The performance of various candidate buffer materials under a range of disposal conditions will be investigated over the next five years. The development of a new generation of buffer materials that can be tailored to various disposal environments for effective waste isolation is a significant thrust. Molecular modeling and experimental testing will be used to understand radionuclide interactions with newly developed buffer materials or corrosion products of EBS components. The aim of this modeling is the development of a continuum model used to simulate fluid flow and transport in the EBS as materials degrade. Such a model will be used to evaluate the efficacy of new buffer materials and EBS design options.

International collaborations have been, and will continue to be, a significant aspect of the crystalline research area over the next five years. These activities include continued participation in DECOVALEX as well as other international geologic disposal research programs. Collating and analyzing data from international URL's will be a continued activity in the crystalline area over the next five years.

CONTENTS

ACRONYMS

ANL	Argonne National Laboratory
CFT	Colloid-Facilitated Transport
COSC	Collisional Orogeny in the Scandinavian Caledonides Project
CTD	Closure Test Drift
CFM	Continuum fracture model
DECOVALEX	DEvelopment of COupled Models and their VALidation Against EXperiments
DFN	Discrete Fracture Network
EBS	Engineered Barrier System
EDS	Energy dispersive spectroscopy
EDZ	Excavation Damaged Zone
EXAFS	Extended X-Ray Absorption Fine Structure
FEBEX	Full-scale engineered barriers experiment
FMD	Fuel Matrix Degradation
FMDM	Fuel Matrix Degradation Model
GDSA	Geologic Disposal Safety Assessment
GREET	Groundwater Recovery Experiment in Tunnel
GWB	Geochemist's Workbench
HLW	High-Level Nuclear Waste (HLW)
JAEA	Japan Atomic Energy Agency
LANL	Los Alamos National Laboratory
LBNL	Lawrence Berkeley National Laboratory
LLNL	Lawrence Livermore National Laboratory
NEA	Nuclear Energy Agency
PA	Performance Assessment
R&D	Research and Development
SEM	Scanning electron microscopy
SFWD	Spent Fuel Waste Disposition

SFWST	Spent Fuel Waste Science & Technology
SIMFIP	Step-rate Injection Method for Fracture In-situ Properties
SNF	Spent Nuclear Fuel
URL	Underground Research Lab
XRD	X-ray diffraction
XRF	X-ray fluorescence

1. GOAL AND OUTLINE

The U.S. Department of Energy Office of Spent Fuel Waste Disposition (SFWD) established in fiscal year 2010 (FY10) the Spent Fuel Waste Science & Technology (SFWST) Program (formerly the Used Fuel Disposition Campaign) program to conduct the research and development (R&D) activities related to storage, transportation and disposal of used nuclear fuel and high level nuclear waste. The Mission of the SFWST is:

> *To identify alternatives and conduct scientific research and technology development to enable storage, transportation and disposal of used nuclear fuel and wastes generated by existing and future nuclear fuel cycles*.

The work package of Crystalline Disposal R&D directly supports the following SFWST objectives:

- Develop a fundamental understanding of disposal system performance in a range of environments for potential wastes that could arise from future nuclear fuel cycle alternatives through theory, simulation, testing, and experimentation.
- Develop a computational modeling capability for the performance of storage and disposal options for a range of fuel cycle alternatives, evolving from generic models to more robust models of performance assessment.

The objective of the Crystalline Disposal R&D control account is to advance our understanding of long-term disposal of used fuel in crystalline rocks and to develop necessary experimental and computational capabilities to evaluate various disposal concepts in such media. The main research topics identified for this control account are summarized in a research plan developed by Wang et al. (2014). FY20 work is aims to:

- Assist the geologic disposal safety assessment (GDSA) team to develop a robust repository performance assessment model.
- Provide the GDSA with a basic "minimal" set of process models and model feeds to support the GDSA near-term goal.
- Develop basis for process modeling that enables streamlined integration with system modeling resulting in feeds to GDSA.
- Consolidate model parameter data, especially thermodynamic data, to ensure more consistent usage of the data across the project.
- With the existence of different approaches taken by various researchers there is a need to understand how well the models are developed in terms of pedigree and rigor.
- Fully leverage international collaborations for data collection and model development and validation.
- Closely collaborate with other work packages, especially those on disposal in argillite and engineered barrier system design.

The FY20 work continues to focus on: (1) better characterization and understanding of fractured media and fluid flow and transport in such media, and (2) designing effective engineered barrier systems (EBS) for waste isolation.

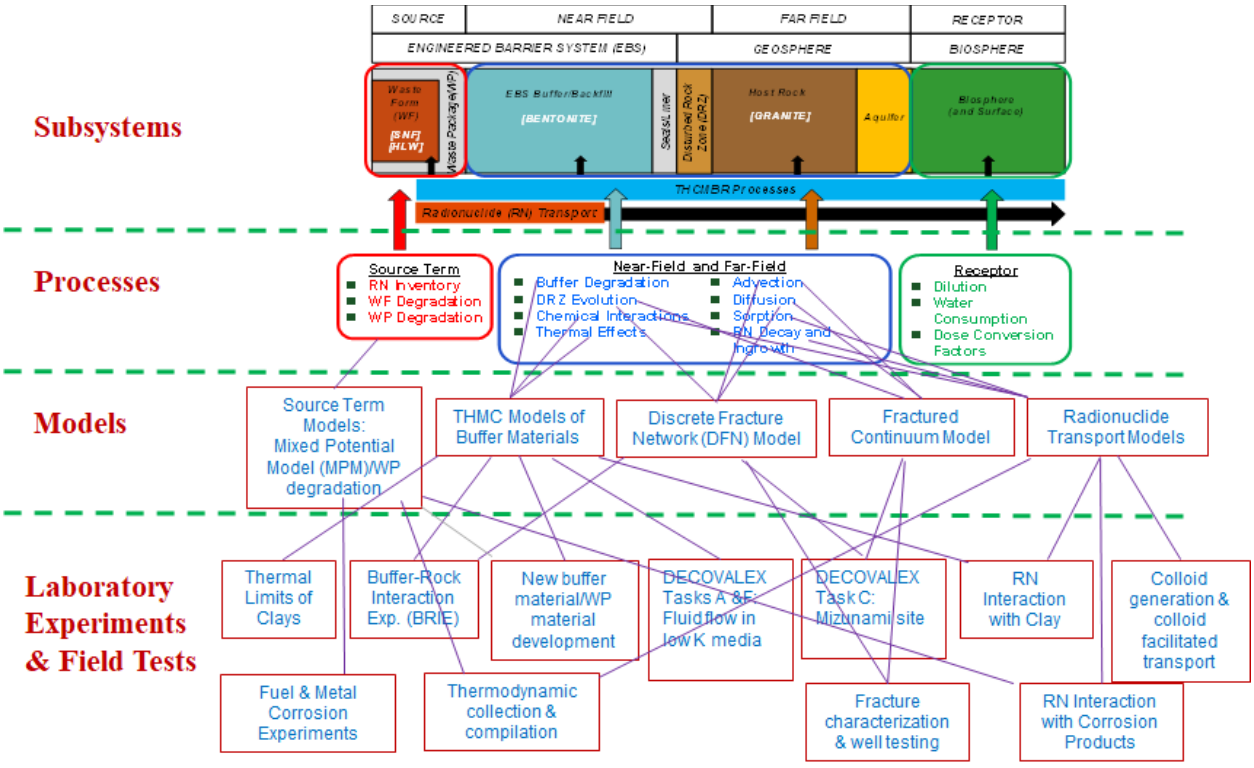

Figure 1.1. Integration of laboratory experiments, field tests and process model development to support a generic safety case analysis for deep geologic nuclear waste disposal in crystalline rocks.

The FY20 work for the Crystalline Disposal R&D work packages covers the following research topics:

- Parameterization of the fuel matrix degradation model (FMDM). Account for the effect of metal corrosion (jointed with argillite work package).
- Understand and quantify radionuclide interactions with corrosion products, especially Pu sorption and incorporation into magnetite and green rust.
- Understand and quantify bentonite erosion and colloid generation and their impact on radionuclide transport.
- Understand fluid flows in low-permeability media, e.g., gas migration in water-saturated compacted bentonite materials.
- Continue development of new-generation buffer materials/waste package materials; understand thermal limits of buffer materials
- Continue development of the discrete fracture network (DFN) model; especially develop a reduced order model for GDSA.
- Continue development and demonstration of a workflow for field data synthesis and flow modeling in fractured media.
- Develop geophysical and well-testing techniques and laboratory rock testing capabilities for characterizing fractures and inflows; reduce the uncertainties of key flow parameters in the excavation disturbed zone (EDZ).

This report summarizes work accomplished in FY19 for the Crystalline Disposal R&D control account. The report is outlined as follows, covering topics from near-field waste form degradation, to engineered barrier material performance, and finally to far-field flow and transport:

- Chapter 2 documents the development of long-term laboratory EDZ characterization testing capability (LBNL).
- Chapter 3 documents a borehole testing technique for in-situ characterization of transmissive fractures in crystalline rocks (LBNL).
- Chapter 4 presents a continued effort on discrete fracture network model development and applications (LANL).
- Chapter 5 focuses on clay swelling, alteration and stability in alkaline solutions at elevated temperatures (LANL).
- Chapter 6 updates the work of using a continuum fracture model (CFM) to simulate fluid flow and transport at Japanese Mizunami site (SNL).
- Chapter 7 focuses the parameterization of fuel matrix degradation model. The work documented is a jointed effort between the Crystalline and the Argillite Work Packages (ANL).
- Chapter 8 proposes a concept of using lead or lead alloys as an outer layer package material (SNL).
- Chapter 9 proposes a concept of using copper wires or meshes to enhance bentonite thermal conductivity (SNL).
- Chapter 10 documents the work on the incorporation of radionuclides into corrosion products (LLNL).
- Chapter 11 updates the on-going effort on thermodynamic database development (LLNL)
- Chapter 12 documents the experimental study of smectite-to-illite transformation (SNL).
- Chapter 13 provides an overall summary of FY20 accomplishment for Crystalline Disposal R&D control account.

The results documented in this report represents the major portion of the work conducted in FY20 for the Crystalline Disposal R&D work packages but not all the work. The work not reported includes the development of a new generation of buffer materials. Either being at an early stage of data synthesis or due to a concern with intellectual properties, the related work will be reported later as it becomes appropriate for public release.

1.1 References

Wang Y. et al., (2014) *Used Fuel Disposal in Crystalline Rocks: Status and FY14 Progress*, FCRD-UFD-2014-000060, SAND2014, Sandia National Laboratories, Albuquerque, NM.

2. LONG-TERM LABORATORY EDZ CHARACTERIZATION TESTING CAPABILITY DEVELOPMENT

2.1. Introduction

The strength and failure of rock is time dependent (Lajtai et al., 1991). The strength, geophysical, and hydrological properties of the rock surrounding the tunnel will change with time, affecting the evolution of Excavation Damaged Zone (EDZ), which may lead to a tunnel collapse (Bieniawski, 1989). After the emplacement of a bentonite backfill, the microcrack growth within EDZ is impacted by a number of factors including stress, temperature, water activity, capillary processes, chemistry, and mineralogy, which exhibit time-dependent, complex interaction. Understanding these processes and predicting the long-term performance of the rock surrounding a drift tunnel is critical for ensuring the safe storage of spent nuclear fuel and wastes.

In FY20, we have continued the development of a dedicated laboratory method to conduct long-term (days to months), temperature-controlled (up to ~200˚C) flow, mechanical, and chemical experiments simultaneously on multiple core-scale samples. Preliminary laboratory tests were used to characterize some fundamental properties (i.e., porosity and permeability) of granite core samples obtained from the Grimsel URL, Switzerland. Later in FY20, we will also conduct experiments to investigate (1) a time-dependent failure of rock subjected to a constant stress (i.e., static fatigue or creep experiment), and (2) a loading-rate dependent strength and its impact on the failure mode (i.e., ductile vs. brittle), both under the influence of elevated temperature, and, particularly, of the fluid chemistry. Additionally, we will conduct post-experiment characterization of the rock samples, which will include determination of the impact of long-term loading on changes in the acoustic (seismic) properties, and to evaluate the feasibility of using geophysical techniques to monitor *in-situ* rock property changes.

2.2 Designing and construction of a dual-sample triaxial rock testing system

In this section, we will describe the key components of the fabricated test system, including (1) the pressure vessels and a load frame, (2) hydraulic plumbing and a stress control system, (3) a temperature control system, and (4) strain measurement system.

2.2.1 Test system

The baseline characteristics of the developed test system are:

- Tested rock core size is 3.8 cm in diameter and up to 10 cm in length,
- Confining pressure is up to 10,000 psi (~70 MPa),
- Axial stress is up to ~29,000 psi (200 MPa),
- Temperature is up to 200˚C, and
- Two core samples can be tested simultaneously.

The schematic of the design of the test system is presented in Figure 2-1a. Figures 2-1c shows fabricated end plugs with a Viton jacket (TEMCO/CoreLab, OK) used for holding the core samples. A 3.8 cm diameter core with a maximum length of 10 cm is jacketed in a Viton sleeve, and the interfaces between the core plug and the top piston plug and also the bottom pedestal are sealed by the jacket. The core sample, jacket, top and bottom end plugs are housed in a cylindrical Grade-23 titanium hull (Figure 2-1b). A previously fabricated loading frame (Figure 2-1b) is used to apply and control the axial stress.

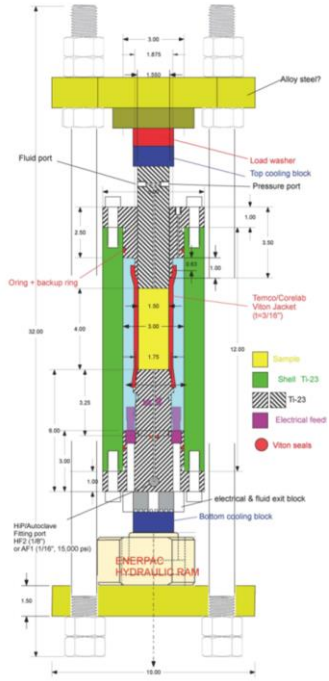

a. Design drawing

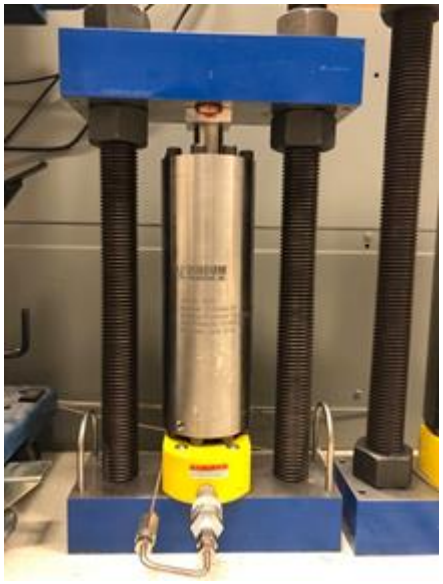

b. Single unit of assembled system

c. Top and bottom end plugs with jacketed cores

Figure 2-1. (a) A schematic of the high temperature triaxial test system. This system (excluding plumbing for axial and confining stress fluids and pore fluid flow) has the following main parts: a confining cell consisting of Grade-23 titanium hull (shell), flanges, end plugs, and an external loading frame. A hydraulic ram (jack) is used to apply axial stress to the sample in the vessel. (b) The photos of assembled single unit of the vessel along with the load frame and the hydraulic rams, and (c) the fabricated top and bottom end plugs held together with a Viton jacket holding a core sample.

2.2.2 Hydraulic plumbing and stress control

The confining stress and axial stress of each unit of the dual rock testing system are controlled independently by units of high-pressure (up to 12,000 psi [83 MPa]), and two-cylinder syringe pumps (Vindum Engineering VP-12K-SS) (Figure 2-2). The two cylinders of these pumps can be operated independently and can be refilled automatically with a minimal impact from pressure and volume perturbations during valve operation, which cannot be avoided for recharging fluids. Because we anticipate that the elastomeric (typically Viton) part of the heated sections of the test system degrades quickly when exposed to hot water at temperature above 150 °C, we plan to use silicone oil as the confining fluid, and hydraulic oil in the hydraulic ram. In order to avoid contamination of the syringe pumps with oils, we have installed a series of transfer cylinders so that the oil pressure and flow can be controlled using water in the syringe pumps.

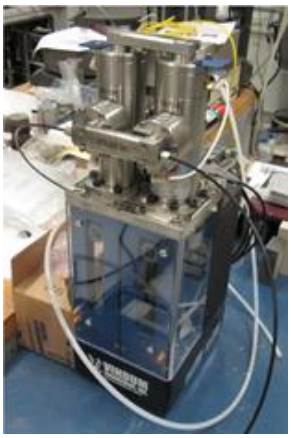

Figure 2-2. The high-pressure syringe pumps used for confining and axial stress control.

Figure 2-3a shows a schematic of the hydraulic plumbing, which includes (1) a control and data acquisition system, (2) a front fluid control panel, and (3) a load frame and pressure vessels. Using two dual-

cylinder Vindum pumps, the confining and axial stress for each unit can be controlled independently. After preparation, the pumps can be controlled and the pressure, volume and a pumping rate are monitored remotely through a PC using a designated software. The front fluid control panel was assembled using stainless steel tubing rated at 12,000 to 60,000 psi to satisfy the test pressure requirement. High-pressure valves and fittings were used at a rated pressure of 60,000 psi from High-Pressure Equipment (HiP) parts, which provide secure pressure connections minimizing leakage. The panel consists of four high-pressure transfer cylinders for using oils (silicone and hydraulic) to control confining and axial stress. The upstream of each cylinder is connected to a pressure relief value set at 9,500 psi in case of over pressurization. The downstream of each cylinder is connected to a fluid reservoir via a 3-way coupling with a valve, so that the fluid depleted during initial setup and during a loading test can be refilled. During the test, the valve is closed to disconnect the fluid reservoirs (ambient pressure) from the rest of the system. The downstream of each cylinder is also connected to either the hydraulic ram (for axial stress) or the pressure vessel (for confining stress), depending on its function. To prevent over pressurization, we also implemented four pressure relief values at the upstream of each hydraulic ram and pressure vessel. Figure 2-3b shows a photograph of the system.

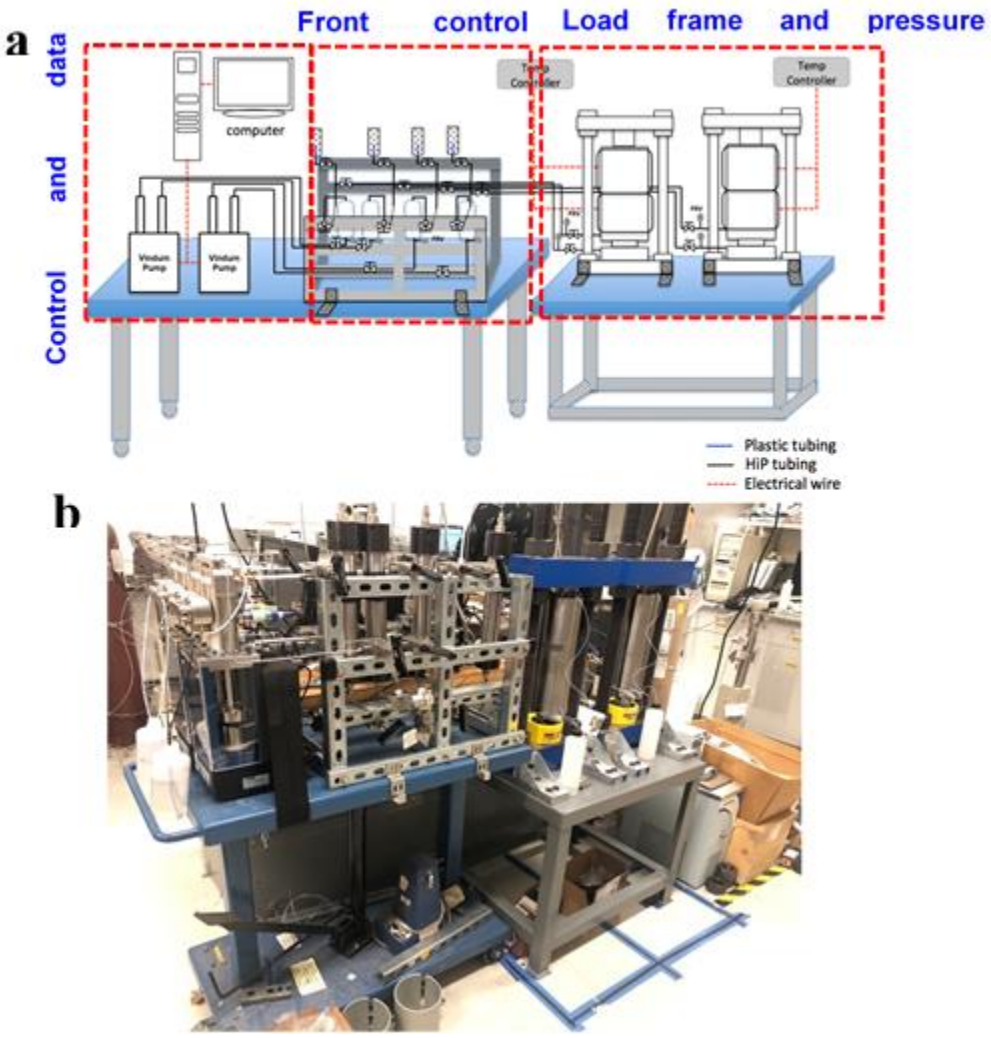

Figure 2-3. A schematic (a) and a photo (b) of the hydraulic plumbing system for the core-scale rock tests.

2.2.3 Temperature control

The temperature of the pressure vessels will be controlled using four rings of mica band heaters (Marathon/Western Thermal MISC 503-3) with fiberglass insulation. Both internal and external temperature of the pressure vessel will be monitored and controlled using temperature regulators. While the pressure vessel can be heated up to 200˚C through the mica band heater, the bottom hydraulic ram requires the temperature not exceeding 40˚C, because of possible seal damage. We adopted a cooling circulation bath with a U-shape cold plate to maintain a low surface temperature of the hydraulic ram. Figure 2-4 presents the temperature control system, both for heating the vessel and for cooling the bottom hydraulic ram (the yellow block). A proper heating insulation is required to maintain a high temperature difference, high mechanical strength, and to fit into the frame aperture without making the test assembly mechanically unstable.

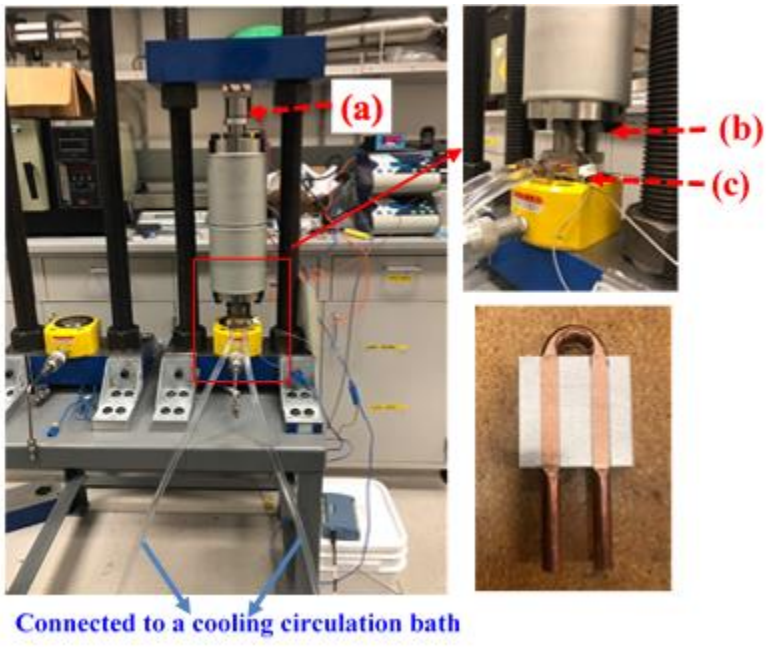

Figure 2-4. A temperature control system that includes two mica band heaters, U-shape cooling plates connected to a water circulation bath (chiller), a Grade-5 Titanium rod for thermal insulation between the vessel and the cooling plate. The symbols (a), (b) and (c) mark the locations of later-mentioned temperature measurement in which the heating band temperature was controlled at a range of temperatures up to 100°C.

After an extensive survey of the mechanic and thermal properties of different materials, we selected a high-strength Grade-5 Titanium rod (2’’diameter) for heat insulation. The grade 5 titanium has a high mechanical strength (120,000 psi yield strength), and a low thermal conductivity at 7.2 W/m·K. The thickness of the rod was designed based on the heat load and the thermal impedance of the cold plate + circulation system.

The heat load Q induced is calculated via

$$Q = k\Delta TA/H \qquad (2\text{-}1)$$

where k is the thermal conductivity (7.2 W/m·K), ΔT=160 K is the temperature difference, A=0.002 m^2 and H are the surface area and thickness of the insulation block, respectively. The thermal impedance is the sum of the thermal resistance of a material. For the cold plate, it was calculated by the following equation:

$$\theta = (T_{max} - T_{out}) * (A'/Q) \quad (2\text{-}2)$$

where T_{max}=40°C is the maximum desired surface temperature of the cold plate, A'=3.27×10^{-3} m^2 (5.0625 inch^2) is the surface area, and T_{out} is temperature of water leaving the cold plate, which is calculated as

$$T_{out} = T_{in} + \frac{Q}{\rho \upsilon C_p} \quad (2\text{-}3)$$

where T_{in} is the water temperature at the inlet of the cold plate, which will be marinated at 15° C by the fluid circulated by the cooling bath, ρ, υ and C_p are water density (1 g/cm^3), circulation rate (maximum at 350 mL/s) and specific heat (4.2 J/g·°C). Combining Eqs. (2-2) and (2-3), we were able to calculate the impedance (θ) and plot its relationship with the thickness (H) of the insulation block. Figures 2-5a and b show the calculated relationships of heat load and thermal impedance vs. block thickness.

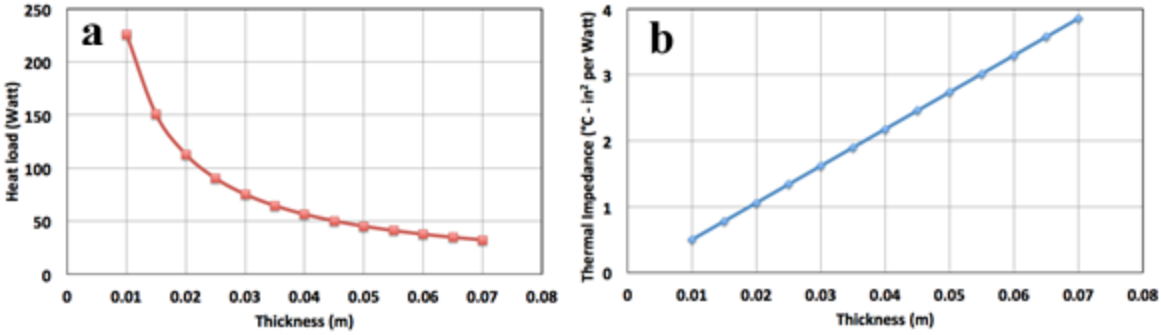

Figure 2-5. The relationship of heat load (a) and thermal impedance (b) vs. the insulation block thickness calculated from Eq. (2-1) and (2-2).

The calculated thermal impedance shown in Figure 2-5b can then be compared with the thermal impedance vs. water circulation rate for different cold plates shown in Figure 2-6. Any plate could be adopted only when its plots is below the thermal impedance required from Figure 2-5b. We selected the CP10 2-pass plate, which meets the performance requirement only when the thermal impedance in Figure 2-7b is higher than 2 °C· in^2/W, and the block thickness is >0.04 m. Note that our cooling bath has a maximum circulation rate of 5.5 gallons/min, which will ensure satisfying the performance requirement because the characteristic curve for CP10 2-PASS in Figure 2-6 decreases with increasing water circulation rate. After this analysis, a 0.05 m thick Grade-5 Ti block was used for thermal insulation between the heated high-pressure vessel and the cold plate.

To verify the performance of the actual system experimentally, we turned on the mica heater bands and maintained the temperature of the gap between the bands and vessel surface constant up to 100°C. Three thermocouple sensors were installed at different locations: (a) on the surface of the top piston plug, (b) at the bottom of the vessel, but above the insulation block, and (c) beneath the cold plate on the surface of the hydraulic ram. Figure 2-7 displays steady-state temperature measured by the three thermocouple sensors at a range of elevated temperatures. Note that the temperature on the hydraulic ram surface was successfully kept as low at 18°C, even when the heating temperature was increased to 100°C. We can reduce the temperature further if necessary by lowering the chiller temperature (e.g., from the current 15 to 4°C) to ensure the surface temperature of the hydraulic ram is maintained below 40°C when heating temperature is increased to 200°C. We will also adopt the same method for thermal insulation between the loading frame and the top piston plug, although the required insulation performance is not as strong as the bottom interface.

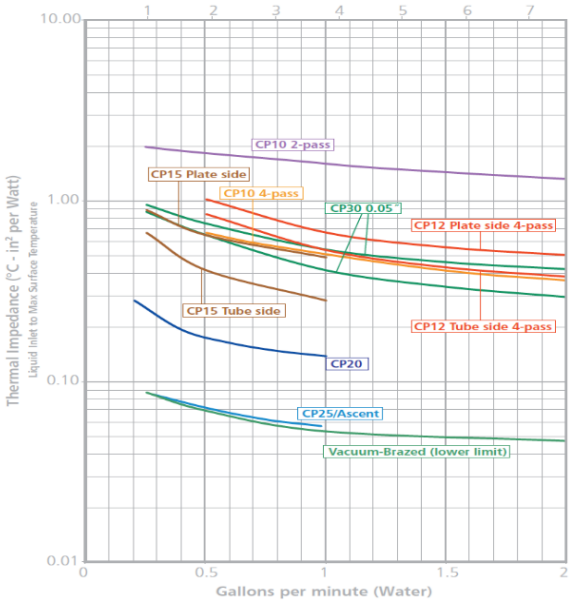

Figure 2-6. The diagram of thermal impedance vs. water circulation rate showing the capability of the cooling plate from https://www.boydcorp.com/thermal/liquid-cooling/liquid-cold-plates.html (Note we adopted the CP10 2-pass mode).

.

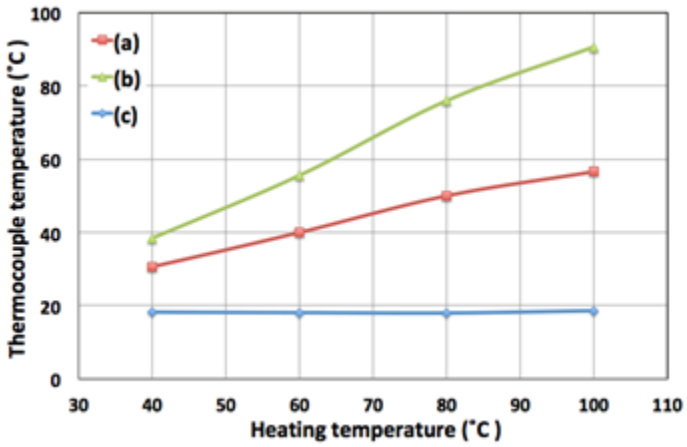

Figure 2-7. The temperature changes monitored at different locations of the vessel vs. the heating temperature. The locations of thermocouple senor (a), (b) and (c) are shown in Figure 2-4.

2.2.4 Strain measurements

The axial strain of the sample will be measured using a high-precision Linear Variable Differential Transformer (LVDT) sensor (RDP Electrosense, PA) at a resolution of 0.001% of the full scale (i.e., 0.1 micron over a +/-1 cm range) (Figure 2-8a). Note that each pressure vessel is also equipped with 20 electrical feedthroughs (five Kemlon 16-B-02924-00 4-pin PMS connectors) (Figure 2-8b) for internal sensor installment. For example, these sensors include temperature sensors and strain gages for circumferential strain measurement, giving extendable capability of the system if more monitoring is needed. All these sensors were connected to a data acquisition box (16 measurement channels and 2 analog

and record the measurements together with the pump volume and pressure data, using a software for operating the Vindum syringe pumps.

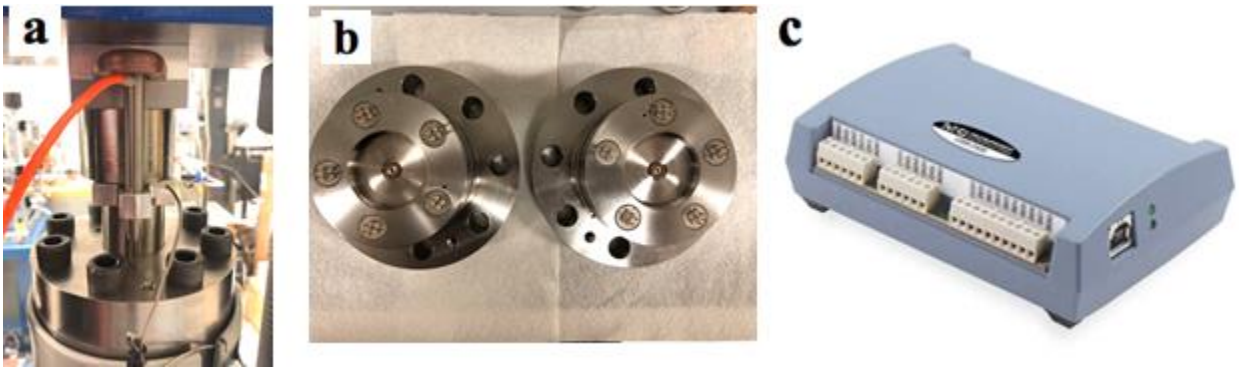

Figure 2-8. (a) The LVDT sensor emplaced on the top piston plug of the vessel for axial strain measurement. (b) The five feedthrough ports at the bottom pedestal that allow for maximum 20 electrical feedthroughs. The ports can be modified and fabricated for other sensing purpose. (c) The data accusation box for simultaneous external data monitoring along with Vindum pump control and monitoring.

2.3 Sample preparation

We obtained two large disk (slab) samples from the Grimsel URL. The sampling location, shown in Figure 2-9a, is BK cavern, where the formation rock is highly fractured (Bossart and Mazuret, 1991). The borehole (drill bit diameter of 300 mm) was drilled with a plunge azimuth of 178° (almost N-S trending) and was slightly upward plunging (Figure 2-9b). The provided two rock disks were cut from the original large core at drilling depths of 0 to 10 cm and 250 to 257 cm from the wall surface (Figure 2-9b). The rock showed strong foliation and coarse grains up to ~1 cm in size (Figure 2-9c).

Ten rock core samples (with a diameter of 3.8 cm and a maximum length of 10 cm) were extracted from one of the slabs, perpendicular to the borehole drilling direction, and the coring direction is parallel to the vertical, maximum principal stress (Figure 2-10). The end faces of eight cores were sawn flat, and grounded smooth along with the sides. The fresh cut surfaces present clear foliations that are parallel to the long axis of the cores. Extra caution was taken to ensure that the two end surfaces were perpendicular to the sides as closely as possible. The machined cores were characterized for bulk density, porosity, and permeability.

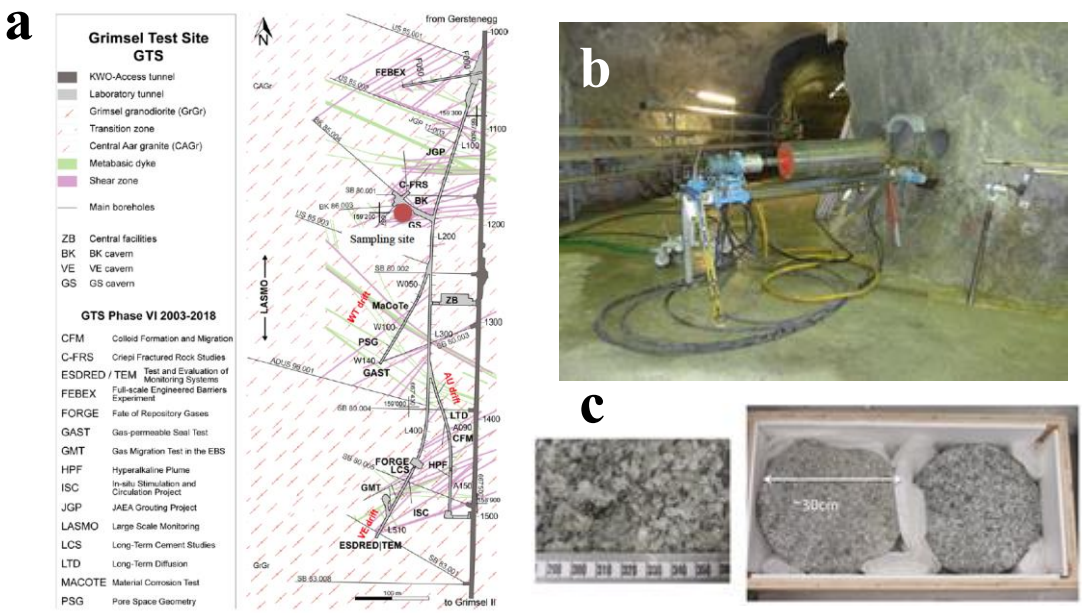

Figure 2-9. (a) The sampling site (marked by the red dot) at the Grimsel Test Site, (b) the photo of the drilling large rock blocks at the tunnel wall, and (c) photographs of large field cores (slabs) obtained from Grimsel URL (Courtesy of Kober Florian, NAGRA).

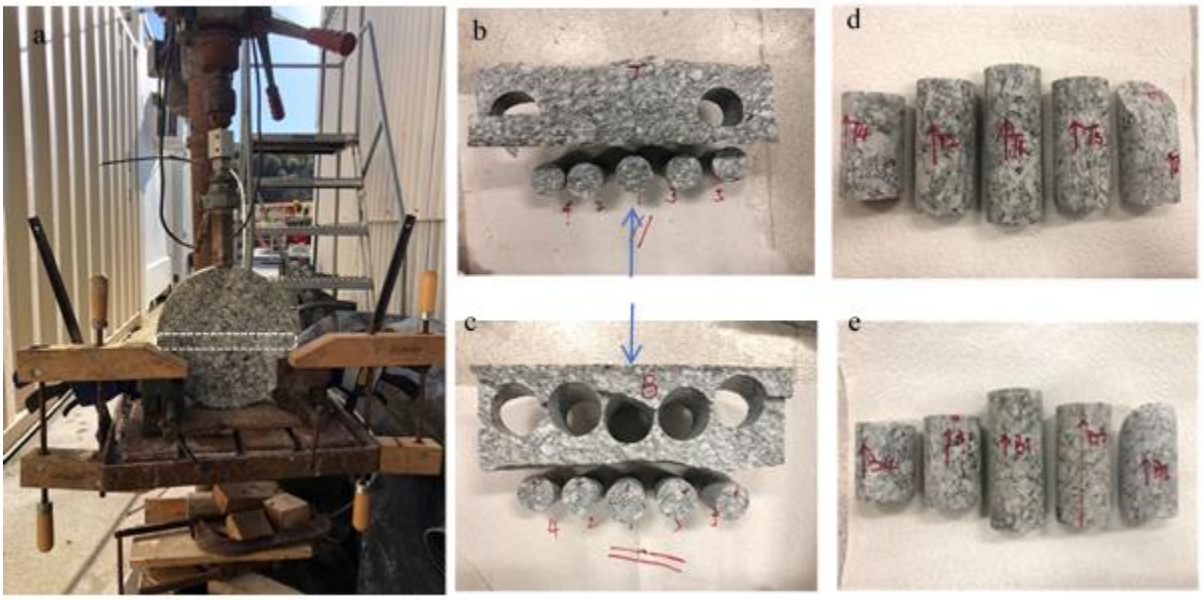

Figure 2-10. (a) Photograph of the coring operation of the rock slab from the side in the vertical direction. The slab was cut into two pieces (marked by T and B for top and bottom in (b) and (c)) along the white dotted box, leaving a rectangular piece in the middle. (b), (c) also show the clear foliations parallel to the long axis of the cores. (d) and (e) present the ten cores fabricated at 3.8 cm diameter and 5-10 cm long. The blue arrows in (b) and (c) mark the drilling direction at the field site.

2.4 Porosity and permeability measurements

The laboratory testing system was used to determine the porosity and permeability of the granite samples. The rock cores were first oven dried and weighed for dry mass, then submerged under water and connected to vacuum at -101 kPa. We vacuum-saturated the samples at different length of time, with an aim to fully saturate the samples by comparing the mass change vs. vacuum time. Figure 2-11 shows the porosity calculated from the volume of each core sample and mass change (by weighing) after vacuuming for 3 and 6 hours. Note the small variations of porosity measured from vacuuming of 3 and 6 hours (<0.021%). After 6 hours of vacuuming, the porosity of the eight core samples varies from 0.5% to 0.6%, similar to the measurements from Keusen et al. (1989).

Before the permeability tests, a series of leakage tests was conducted on the lab system. The system, excluding the pressure vessels, was filled by water in the hydraulic lines and presurized to 2,000 psi by the Vindum pumps, and the pressure was held constant for 3 days. The volume changes of the pumps were monitored to quantify any leakage of the system. Over the 3 days, the volumes of the four pump cylinders (two for confining stress control and two for axial stress control) fluctuated from -0.018 mL to 0.044 mL relative to the initial value, with no continuous decrease in volume observed. This indicates a good hydraulic sealing of the system and the small volume variations (especially for the negative changes) may due to room daily temperature changes. The high pressure vessels were pressure tested to check for leakage. This was conducted independently by the manufacturer/vendor (Vindum Engineering Inc.) before the vessels were delivered to the lab.

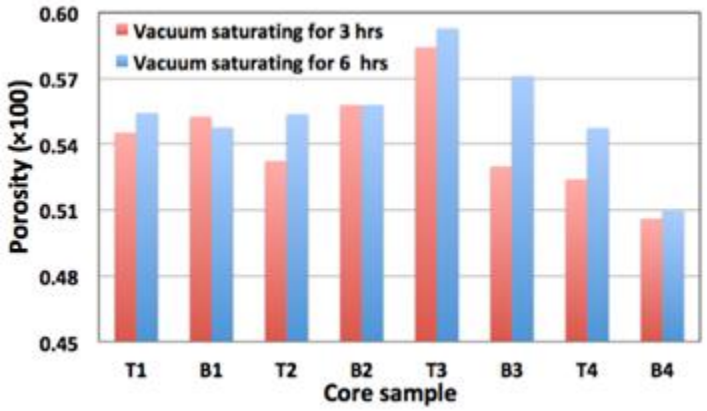

Figure 2-11. The porosity calculated for core samples based on the results of saturation under vacuum for 3 and 6 hours.

After the leakage test, the lab system was used to conduct permeability measurements on Samples T2 and T3 (with the same length of 8.4 cm) under room temperature and without axial loading (see Figure 2-3b). Water-saturated cores, jacketed with a Viton sleeve and assembled together with end plugs, were emplaced into vessel shells. The remaining space of the vessel chambers and the system pipelines was filled with the deionized (DI) water. Finally, the confining pressure for both vessels was increased to 900 psi and held constant. For Sample T2, stepwise constant flow rate water injection was performed, and the differential pressure was measured along the core. An ambient pressure was maintained at the outlet of the core thus the differential pressure equals to the injection pressure applied at the inlet. Figure 2-12 shows the measured confining pressure and the differential pressure vs. injected water volume (PV refers to the pore volume) at (a) 0.01 mL/min, (b) 0.0075 mL/min, (c) 0.005 ml/min, (d) 0.001 mL/min, and (e) 0.0005 mL/min. The average differential pressures at the steady states were computed and are plotted against applied differential pressure in Figure 2-14a. During the permeability tests (~1 week), the volume change was <0.1 mL in both pumps providing constant confining pressure.

For Sample T3, we first conducted the same constant-rate injection tests. However, the inlet pressure showed a quick increase, and it then exceeded the confining pressure before reaching a steady state. When the injection pressure exceeded the confining pressure, it could have created near-wall flow, leading to overestimated permeability. Thus, instead of using the constant-rate injections, we performed constant-pressure injection tests, and monitored the flow rate changes as a function of time. Figure 2-13 shows the flow rate changes as a function of time at applied differential pressure of (a) 150 psi, (b) 300 psi, (c) 375 psi, (d) 450 psi, (e) 560 psi, and (f) 675 psi. These injection pressures were maintained lower than the confining pressure to avoid any near-wall flow. The average flow rate at the steady state was also obtained and plotted against applied differential pressure in Figure 2-14b.

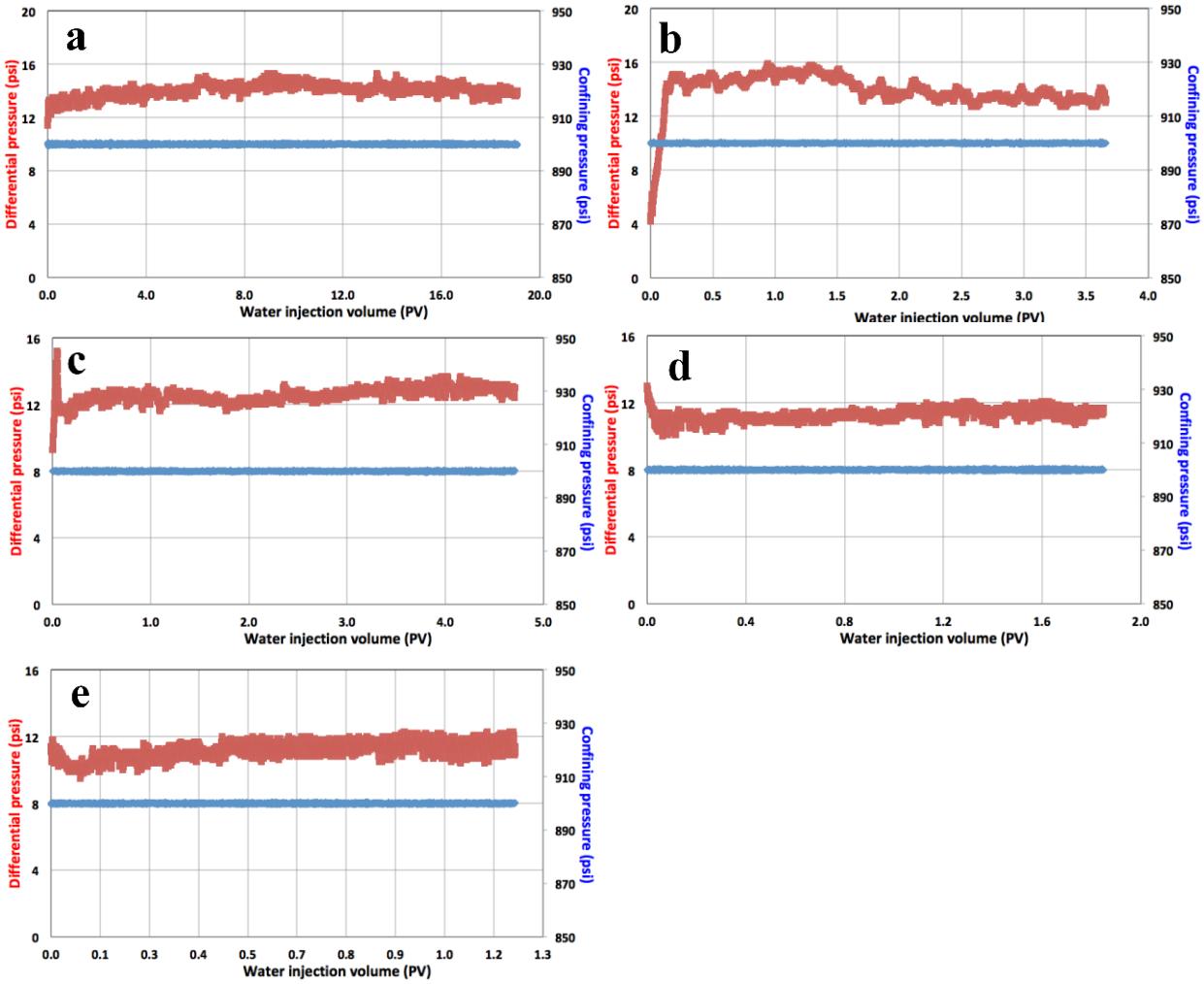

Figure 2-12. The confining pressure and differential pressure vs. injected water volume (PV refers to the pore volume) in Sample T2 at (a) 0.01 mL/min, (b) 0.0075 mL/min, (c) 0.005 ml/min, (d) 0.001 mL/min and (e) 0.0005 mL/min. The pressure data was recorded at every 5s. The confining pressure (marked by the blue lines) was maintained constant at 900 psi in each test.

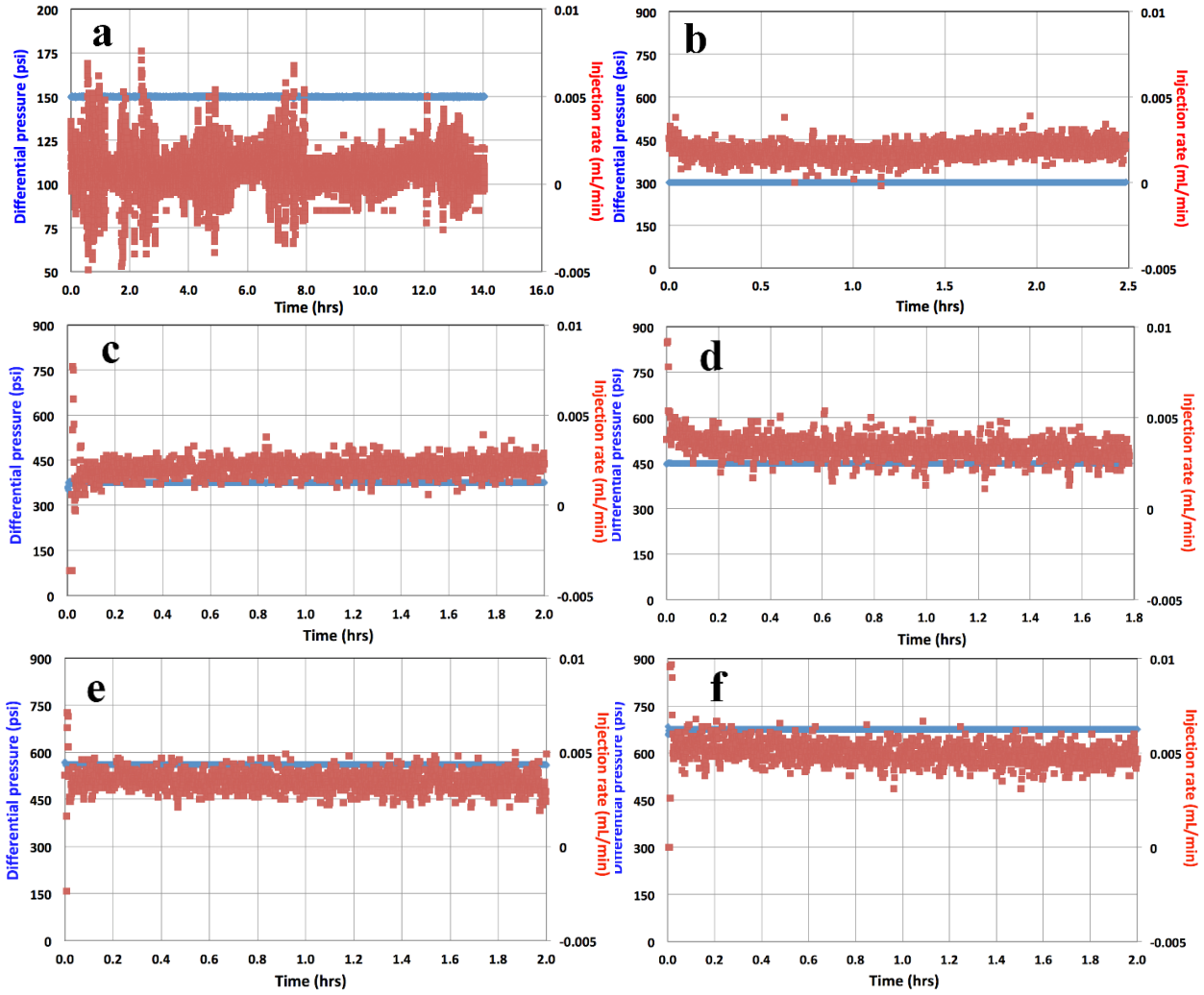

Figure 2-13. The injection rate variations as a function of time at applied differential pressure of (a) 150 psi, (b) 300 psi, (c) 375 psi, (d) 450 psi, (e) 560 psi and (f) 675 psi. Both pressure and injection rate were recorded at every 5s.

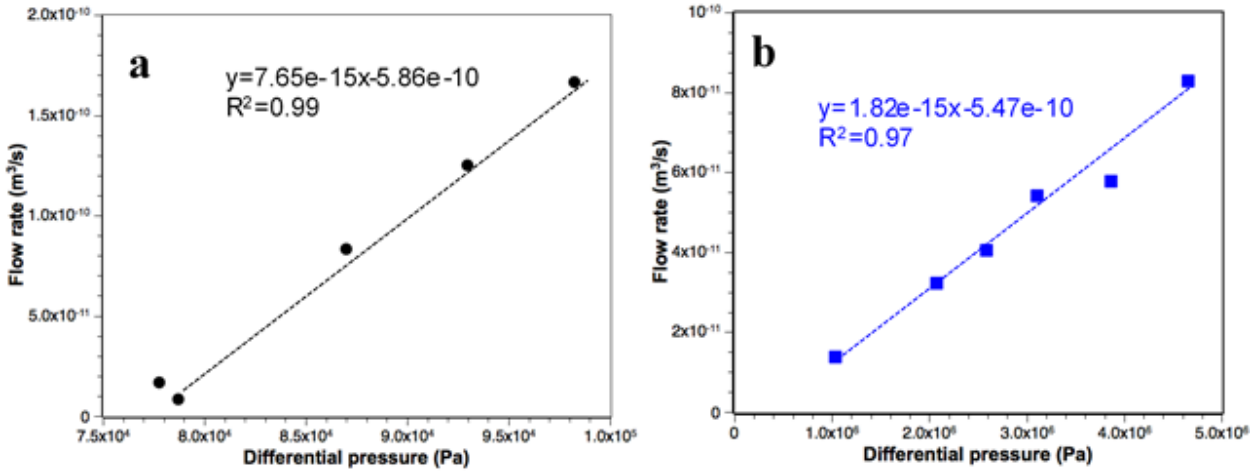

Figure 2-14. The relationships of flow rate vs. differential pressure at the core inlet and outlet for Samples T2 (a) and T3 (b). Note the pressure and flow rate data were converted to Pa and m^3/s to calculate permeability. Each data point was averaged over the stable different pressure and flow rate shown in Figures 2-12 and 2-13.

Based on the linear relationship between the flow rate and the differential pressure, shown in Figure 2-14, the flow process in cores can be described using Darcy's law given by

$$\frac{Q}{\Delta P} = k\frac{A}{\mu L} \tag{2-4}$$

where k is absolute permeability (m^2), A is the cross-section area of the core (m^2), μ and L refer to the water viscosity at room temperature at 25 ˚C (0.00089 Pa·s) and sample length (m), respectively.

The permeability values calculated using Eq. (2-4) are 504.3 and 1.2 μD for Samples T2 and T3, respectively. We compared our measurements with available data from K for Grimsel Granodiorite Benchmark (KG^2B) (David, 2018a, b), a collaborative benchmarking exercise for estimating the permeability of Grimsel granodiorite. In KG^2B, 24 laboratories were involved in measuring permeability of the rock under the same effective confining pressure (730 psi). The samples were obtained from a granite and granodiorite tunnel in the Central Aar Massif in Switzerland. Along the tunnel, major damage zones are located in meter-scale shear zones or widely spaced discontinuities caused by regional deformation. Two cores of Grimsel granodiorite, each about 1 m in length and 85 mm in diameter, were retrieved at a distance of 4–6 m from the tunnel wall of the Grimsel test site, far away from the EDZ. The cores were cut into small blocks at lengths requested by each participant (between 2 and 10 cm). These cores showed similar, visible grain shape and foliations parallel to the core axis (at an angle of about 20˚–30˚). From 35 independent measurements, an average permeability of 1.11 μD with a standard deviation of 0.57 μD was obtained. This result is similar to the permeability of Sample T2.

Note that we conducted tests of samples that were obtained within the EDZ (~2.5 m away from the tunnel wall). This may explain the unexpectedly high permeability measured for Sample T2. While both samples were obtained from the same large host rock block (~30 cm diameter), the two orders of magnitude difference in permeability indicates pronounced heterogeneity, and potential open cracks/fractures in Sample T2, which caused high permeability (although there is no visible crack/damage on the sample surface). Also note that during the experiments, water flow direction is parallel to the foliations of both samples (see Figure 2-10d) and the maximum principal stress, which would be the preferred orientation of

tensile microcracks and fractures. We will conduct anisotropic seismic velocity measurements independently to verify/compare any potential cracks/fractures in both samples. We will also produce thin sections of the rock and conduct detailed examination of the microstructures and foliations under the microscope. As an option, it may be informative to perform additional permeability tests and/or seismic velocity measurements using cores collected in directions perpendicular to the foliations to characterize the anisotropy.

2.5 Summary of the current status and plans for the remainder of FY20

We have developed a high pressure (up to 10,000 psi), high temperature (up to 200˚C) triaxial loading system to enable long-term (days to months) laboratory experiments of flow simultaneously on multiple core samples under temperature, mechanical, and chemically controlled conditions. We also used the system for permeability measurements of granite samples obtained from the Grimsel URL. We will conduct additional tests to better understand the mechanical, chemical and microstructural properties of the rock.

We will conduct rate-dependent strength and creep tests of the samples for relatively long time (up to weeks). Due to the COVID-19 pandemic and a shelter-in-place order, the originally planned creep tests have been delayed. We will resume the experiments as soon as the access to the laboratory is permitted.

2.6 References

See Section 3.10.

3. CHARACTERIZATION OF TRANSMISSIVE FRACTURES IN CRYSTALLINE ROCKS

3.1 Introduction

Crystalline rocks are one of several potential geologic environments that have been considered for long term disposal of nuclear waste due to their inherent low permeability (e.g., Witherspoon et al., 1981; Bredehoeft and Maini, 1981). One key challenge in evaluating the safety case for crystalline rocks is that fractures present within these rocks may serve as transmissive pathways for radionuclide transport (Cherry et al., 2014). The 2019 update to the SFWST R&D roadmap identified that improved site characterization techniques are needed for crystalline repository systems, especially to characterize fractures and their hydrogeologic properties; such data are needed to develop accurate discrete fracture network (DFN) models (e.g., Follin et al., 2014; Hadgu et al., 2017). Such DFN models have been also used to model fluid flow for enhanced geothermal systems (Makedonska et al., 2020) and evaluate the potential for leakage from geologic CO_2 sequestration sites (Chen et al., 2019).

Our team at LBNL has been collaborating with the Collisional Orogeny in the Scandinavian Caledonides (COSC) scientific team to use the COSC-1 borehole as a testbed to evaluate fracture transmissivity within a crystalline basement environment. This borehole, located in central Sweden, was drilled to a depth of 2.5 km, and encountered a sequence of high-grade metamorphic rocks, such as felsic gneisses, amphibolite gneisses, calc-silicate gneisses, amphibolite, migmatites, and garnet mica schists, with discrete zones of mylonite and microkarst (Lorenz et al., 2015). Our initial work focused on using Flowing Fluid Electrical Conductivity (FFEC) logging to identify hydrologically transmissive fractures (e.g., Tsang et al., 2016; Doughty et al., 2017) and to link these identified flow zones to potential correlative fractures observed in image logs and core samples. During the 2019 field campaign (Guglielmi et al., 2019), we deployed the Step-rate Injection Method for Fracture In-situ Properties (SIMFIP) tool (Guglielmi et al., 2013; 2015) to test a suite of selected fractures within the COSC-1 borehole.

During the 2019 field study, we evaluated three different intervals within the COSC-1 borehole (Figure 3-1): 1) a gently dipping transmissive fracture at a depth of ~505.9 m, which is subparallel to foliation; 2) a steeply dipping cemented fracture located at a depth of ~515.1 m; and 3) an unfractured interval located at a depth of 485.2 m. Our team was able to leverage previous detailed characterization of the core and borehole, and use gamma log mapping to precisely locate the SIMFIP tool relative to the features that our team selected for testing. The transmissive fracture is located in an interval that had been previously identified as permeable by FFEC logging at ~506 m – three distinct fluid entry zones (at 504.6, 504.8 and 505.9 m depths) were identified using an *in-situ* conductivity probe (see Section 3.2). The other two zones that were examined did not have measurable transmissivity based on previous FFEC logging runs. The goal was to better characterize two distinct types of fractures (steeply dipping features and shallow dipping, foliation parallel fractures) and to also determine fundamental rock properties, stress orientation, and Sh_{min} values by creating a hydrofracture within an intact section of the borehole and modeling the results of these field tests (Sections 3.3–3.6). Our team obtained core samples that correspond with the tested depths for more detailed characterization in the laboratory – the preliminary results of these tests are presented in Section 3.7. Additional core characterization is planned, along with borehole televiewer logging of the COSC-1 borehole in the tested intervals to obtain fracture orientation data from the stimulated features. This field test represents the deepest borehole deployment of the SIMFIP tool (by a factor of 10) to date.

Intact rock, 485.2 m

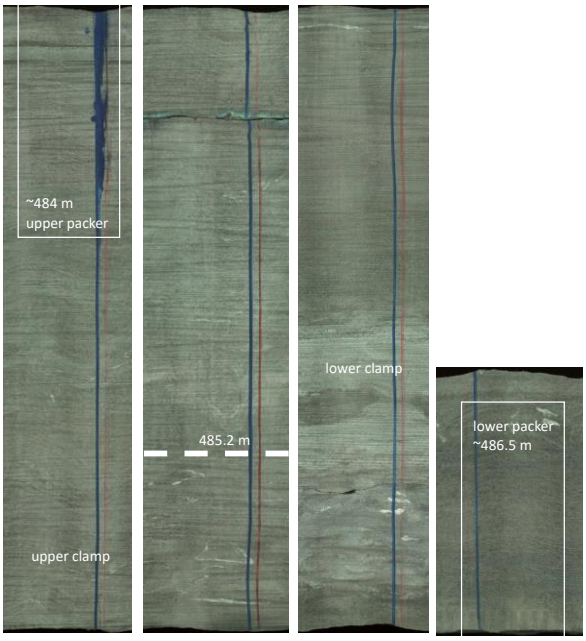

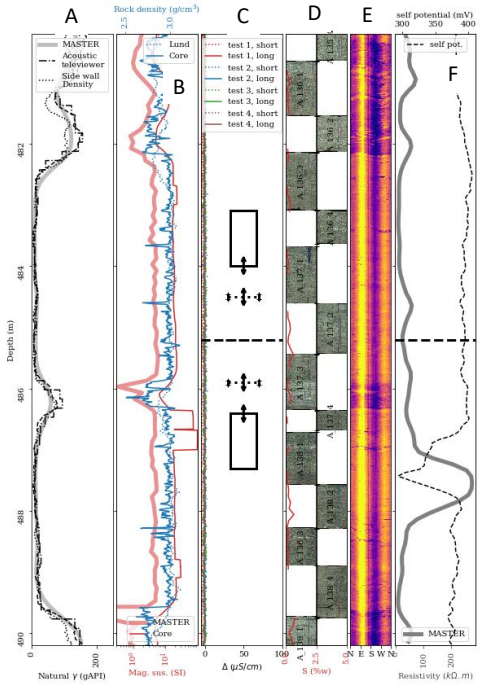

Flow zone 505.9 m

Two to three flowing fractures 504.6, 504.8 and 505.9 m

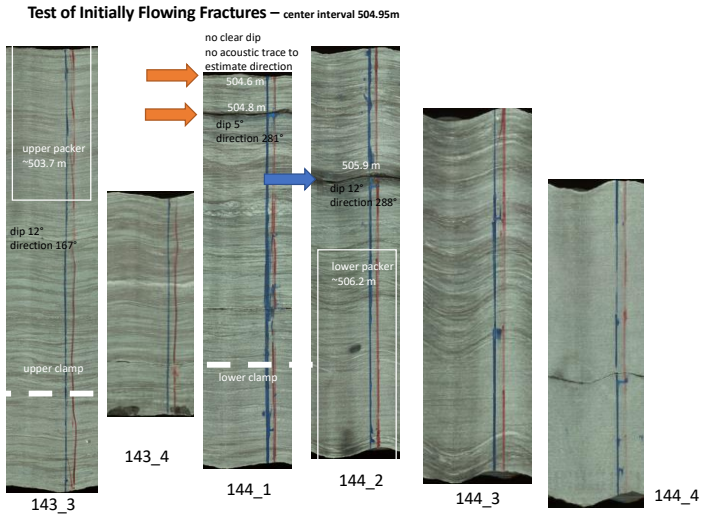

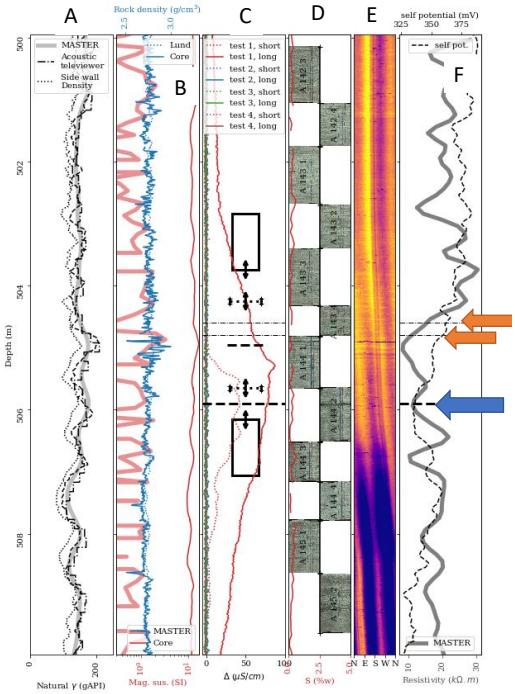

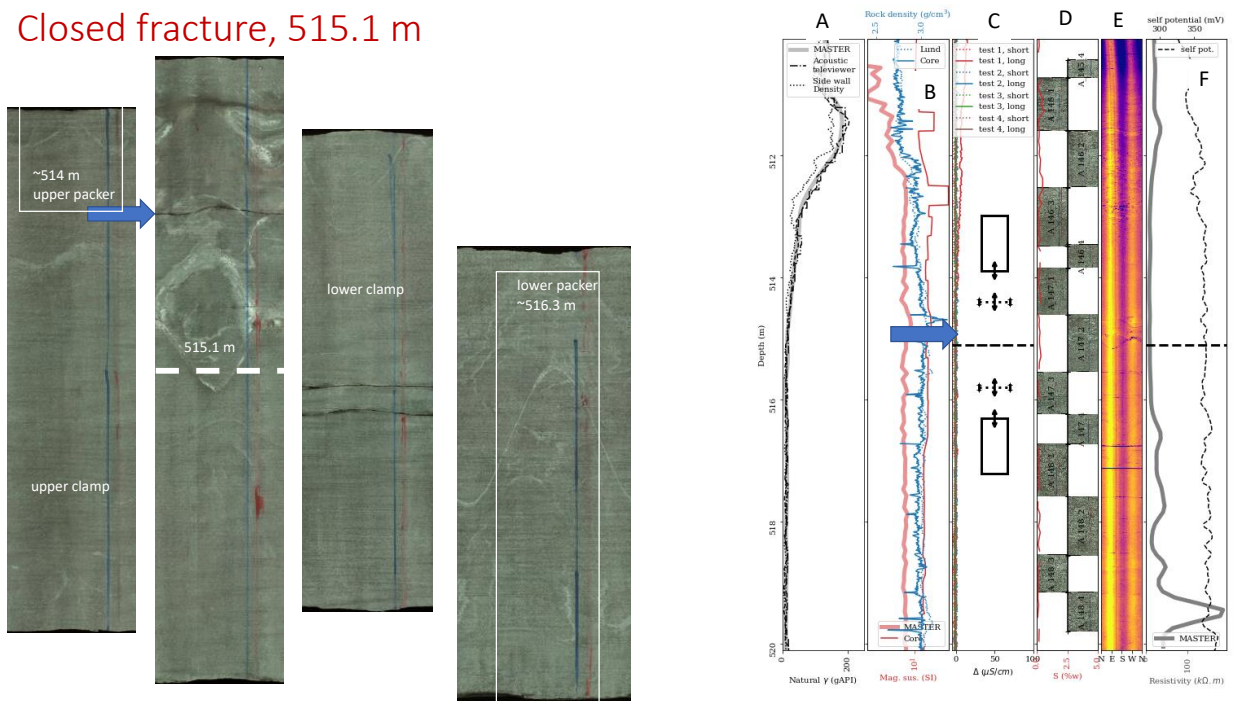

Figure 3-1. Composite logs of the three depths of 485.2, 505.9, and 515.1 m studied with the SIMFIP in the COSC-1 borehole during the 2019 field campaign. The left images represent core photos for each section, along with the locations of the packers and clamps from the SIMFIP tool. The geometry of the SIMFIP system (packers and clamps) is portrayed in Figure 3-2a. On the right, column A represents a suite of gamma log runs taken (these were used to help register the depth of the tool precisely), column B shows the magnetic susceptibility and rock density, column C shows the normalized conductivity values from FFEC logging (with positive changes indicating more saline and conductive fluids from formation waters being discharged into the dilute borehole), column D shows the unrolled core photographs along with plotted variations in S contents (wt. %) of the core samples, column E depicts the acoustic televiewer log image for the borehole interval (from Wenning et al., 2017), and column F depicts rock electrical resistivity and self-potential log measurements. Data from Dessirier et al. (submitted).

3.2 Detection of Flowing Fractures with a Distributed Water Resistivity Probe

3.2.1 Instrument setup and measurement protocol

The conductivity probe is attached to the upper part of the SIMFIP probe (Figure 3-2a). It consists of an array of 63 electrodes (originally 64) with 62 intervals of 10 cm each in between them, measuring electrical resistivity at regular time intervals by applying a voltage that is compared with a voltage across a resistor of known resistance (Figure 3-2b and c), hereby obtaining a continuous resistivity profile. An electrical conductivity sensor (EC) was integrated into the gamma logging tool that was lowered into the borehole together with the conductivity probe (Figure 3-2a). It provided actual conductivity measurements at a single point immediately above the conductivity probe, allowing for comparison of the conductivity data and transformation of the relative resistivity values of the probe into absolute conductivity values.

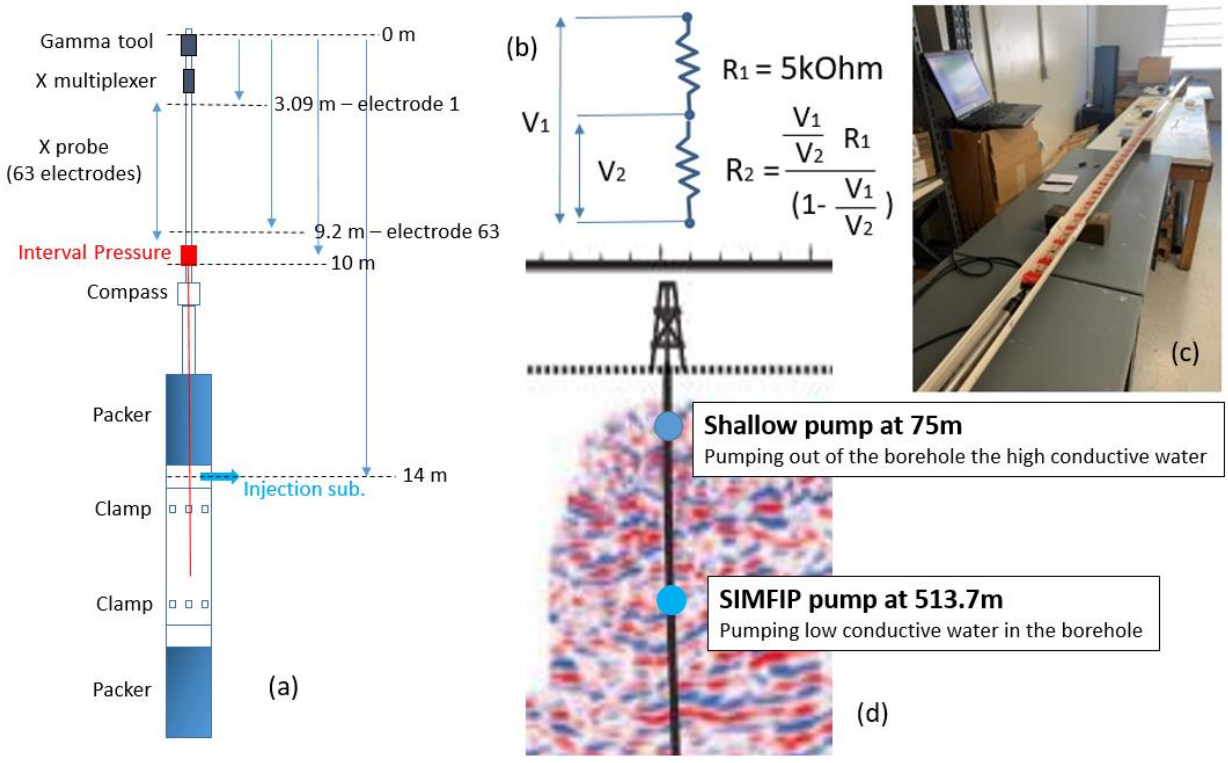

Figure 3-2. (a) – Schematic diagram of the SIMFIP probe including the resistivity probe and the gamma tool at the top (the gamma tool is used to localize the probe at depth). (b) - Concept of the resistivity measurement at each interval (R2) relative to a known resistance (R1) in the probe's control unit head. (c) - The 6.2 m long, 63 electrode probe laid out in a calibration trough. (d) – Deployment configuration of the resistivity measurement in the COSC-1 borehole (after Wenning et al., 2017).

The probe was deployed in the COSC borehole in order to profile the water resistivity between 502.87 and 509.07 m depth, a borehole interval where flowing fractures had previously been identified by FFEC measurements. After the probe was set at the interval and left to measure the conductivity of the present borehole fluid for a while in order to obtain a measurement baseline, freshwater from a nearby creek was pumped into the borehole 7.6 m below the probe (Figure 3-2d; also indicated by blue arrow in Figure 3-2a). In order to create a negative pressure gradient from the formation to the borehole, a shallow pump in the borehole at a 75 m depth was activated to draw down the hydraulic head in the borehole (Figure 3-2d). This was intended to stimulate flow of formation water out of flowing fractures into the borehole, where it could be detected by the conductivity probe.

Figure 3-3a shows the applied pumping rates at both depths and the borehole water pressure measured at the SIMFIP probe (Figure 3-2a for location of the pressure sensor in the probe). Freshwater injection below the conductivity probe started at 12:19 on June 16, 2019. At 13:20, the shallow pump at a 75 m depth was activated with a continuous pumping rate of 5 l/min. This operation introduced electric noise on the pressure sensor. At 13:48, the rate of the shallow pump was increased to 10 l/min, and the freshwater injection below the conductivity probe was ceased. At 15:01, the shallow pump achieved its maximum drawdown of 75 m and was turned off for ~25 min. At 15:25, the shallow pump was turned back on with a flow rate of ~6 l/min, which was lowered to 4.5 l/min at 16:13 to maintain a constant drawdown of 75 m. The conductivity

measurement was terminated at 16:08. Figure 3-3b is a schematic explanation of the water circulation induced in the borehole by the two pumps. Borehole initial water (dark blue color in Figure 3-3b) was replaced by fresh water (cyan blue color in Figure 3-3b) in a borehole interval much larger than the measuring zone. A part of the water was pumped out of the borehole by the shallow pump, but another significant part leaked in high permeability fractures intersecting the shallow borehole zone.

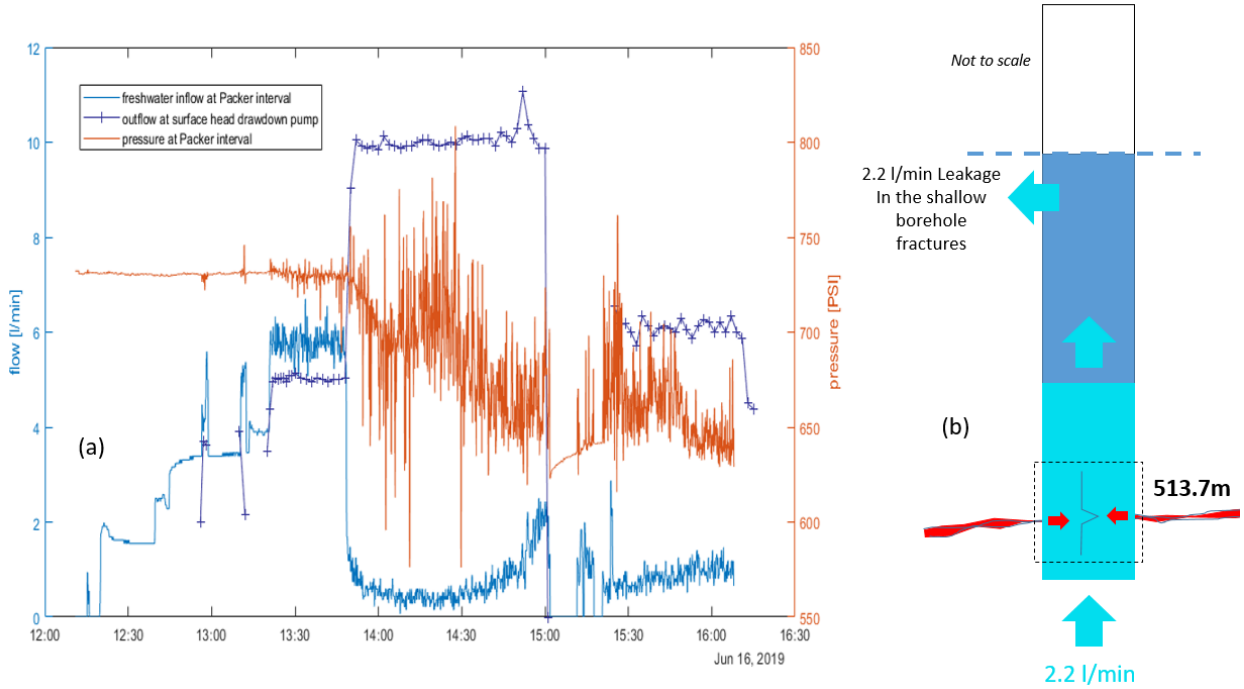

Figure 3-3. (a) – Injection freshwater flowrate, pumped borehole water flowrate and water pressure variations versus time; (b) – Water circulation in the borehole during the resistivity measurement.

3.2.2 Data processing

The raw data include a resistivity relative to a built-in resistor of 5kOhm, with 0 representing a perfectly conductive interval, and 1 representing a perfectly resistive interval between two contacts. Using the absolute conductivity measurement from the gamma tool, the relative resistivity measurements of the conductivity probe are transferred into absolute conductivity measurements in µS/cm. Variations of the measured conductivity along the probe due to the uneven placement in the borehole were corrected using baseline data collected prior to the test (when the probe was resting in an undisturbed column of water with an assumingly homogeneous conductivity).

After obtaining a baseline-corrected absolute conductivity value for each interval at every point in time, the data are analyzed along the time axis of the test (Figure 3-4). It can be seen that at the beginning at 12:53:29, roughly 30 minutes after the start of the freshwater injection, the higher conductive formation water was subsequently replaced by lower conductivity fresh water at each conductivity interval. However, at some intervals, a slightly higher conductive signal persists (Figure 3-4) for a time after freshwater was injected below, and before a large pressure gradient was caused by the shallow pump close to the surface. These "anomalies" for each interval were compared to similar water resistivity signals at a given time, and identified by previous FFEC tests and to borehole fracture locations observed on the acoustic logs (Figure 3-5).

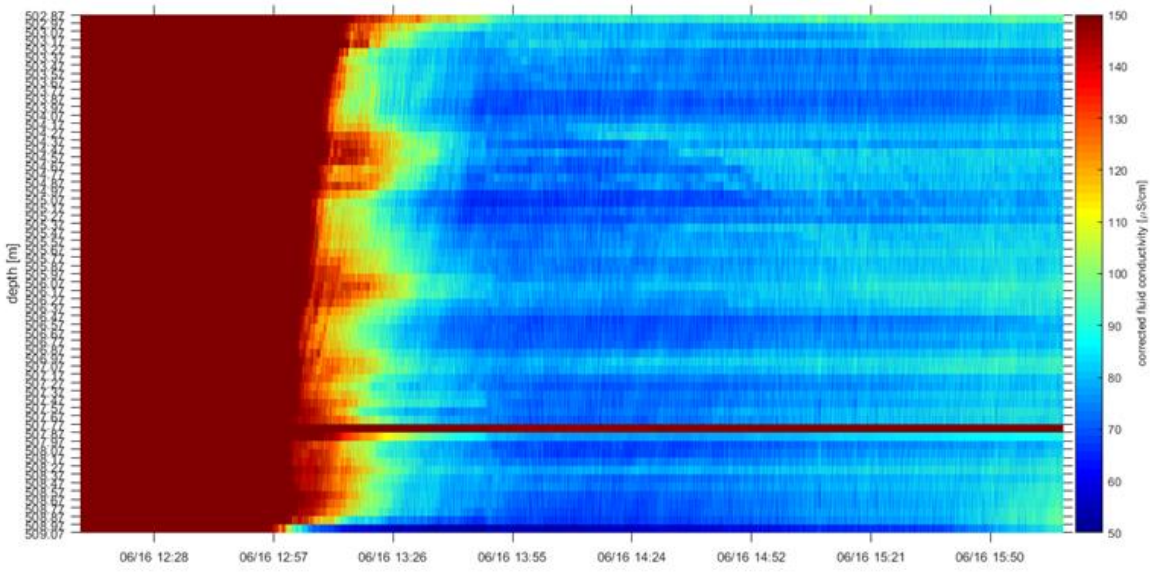

Figure 3-4. Borehole water absolute electrical conductivity variations with depth (vertical axis) and with time (horizontal axis)

3.2.3 Interpretation

After the borehole water was replaced with freshwater, but before the shallow pump was turned on to draw down the hydraulic head, a weak but consistent signal of persisting higher conductivities can be observed at two to three distinct interval regions (Figure 3-4). This is believed to be due to the presence of flowing fractures, allowing for a small inflow and diffusion of formation water into the borehole (Figure 3-3 and 3-5). Unfortunately, when the shallow pump was turned on in order to create a negative pressure gradient allowing for an increased inflow of formation water, it had the adverse effect of diminishing the signal. When the flowrate was turned up, the anomalies almost vanished. This is believed to be caused by the much stronger flow of freshwater past the probe, flushing the borehole completely with freshwater. However, the initial signal picked in the low-flow regime could be very well correlated with data from previous borehole logging, coring and FFEC measurements (Figure 3-5). Due to the high resolution of the distributed electrical resistivity measurements, 2 to 3 flowing fractures could be located within the broader resistivity anomaly.

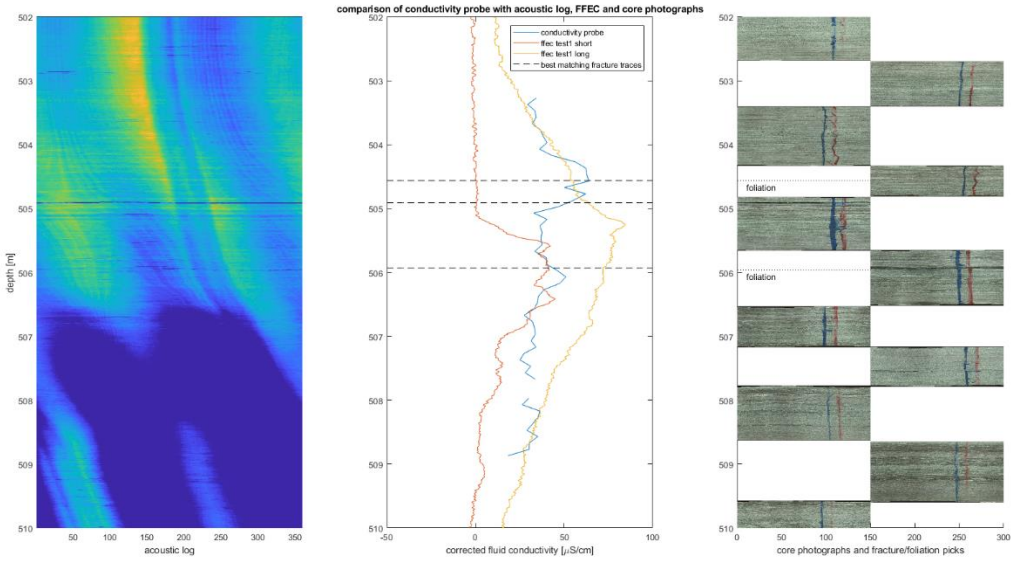

Figure 3-5. Left – Acoustic log showing traces of natural fractures; Middle – Borehole water conductivity variation with depth. The blue curve is the conductivity measured with the SIMFIP device. It is compared to conductivity signals captured by a moving FFEC probe in previous studies (Tsang et al., 2016; Doughty et al., 2017). There is a good correspondence of anomalies observed by the two methods. The SIMFIP conductivity may eventually show details, characterized by two to three conductivity peaks highlighting the possible existence of several flowing natural fractures. Right – Several fractures (denoted by dashed lines in center column) are observed on borehole cores at depths matching the observed conductivity anomalies.

3.3 In Situ Hydromechanical Testing of Fractures

3.3.1 Test setting and protocol

Three borehole intervals, each 2.41m long, have been tested:

- Test 1: An interval made of intact rock was selected between 484 and 486.4 m depth from the acoustic log observation in the field. Cross-checking with cores showed afterwards that this interval might be affected by two flat fractures at 484.9 and 486.2 m, with orientations roughly 247/13. These fractures appear sub-parallel to foliation. One is between the SIMFIP clamps, one is below the lower clamp.
- Test 2: Initially flowing fracture interval between 503.7 and 506.2 m depth. Flowing fractures were identified using a water resistivity measurement (Section 3.2) at 504.6, 504.8 and 505.9 m, respectively. This means that the two shallower fractures were between the SIMFIP clamps, while the deepest one is below the lower clamp. Fractures are relatively flat, more or less parallel to the foliation with dip direction and dip of 281/5 to 288/12, respectively.
- Test 3: Initially closed fracture between 513.9 and 516.3 m depth. No flow anomaly was observed in this interval in previous FFEC studies. This is why it is defined as affected by initially closed fractures, with one feature parallel to foliation (260-280/2-13) and the other representing a steeply dipping mineralized fracture (110/59). All fractures are located between the SIMFIP clamps.

The instrument used for the injection tests is a SIMFIP borehole probe, which allows for simultaneous measurements of fluid pressure and three-dimensional displacements at high frequency (Guglielmi et al.,

2013; 2015). The injection interval is isolated in the open hole using two inflatable rubber packers, with sliding sleeves straddled by a steel mandrel. A 0.49 m long and 0.1 m diameter pre-calibrated aluminum cage located between the two packers is clamped onto the borehole wall. When clamped, the cage is disconnected from the straddle packer system. As discontinuities intersected by the borehole interval are deforming as a result of the fluid injection into the interval, the cage allows obtaining angle-dependent strain measurements that are used to constrain the full three-dimensional displacement tensor and the three rotations of the upper anchor of the cage relative to the lower anchor. The maximum displacement range of the deformation cage is 0.7 and 3.5 mm in the axial and radial directions of the borehole, respectively, and the accuracy is $\pm 5 \times 10^{-6}$ m. A compass set on the probe provides the orientation of measurements with 0.1° accuracy. Thus, in further analyses, the displacements can be rotated into a geographic reference frame.

The displacement data are continuously logged together with pump parameters (pressure and flow rate). The pressure sensors allow for measurements over a pressure range from 0 to 20 MPa, with a 0.01 MPa accuracy. The relation between the compliance of the probe and the elastic response of the borehole wall was studied extensively through laboratory tests. It is shown that the device is ~10 times more compliant than the rock, and that the orientation and magnitude of displacements below the stimulation pressure strongly depends on the elastic anisotropy of the rock and on the coupling between the probe and the borehole wall. In theory, there should be no SIMFIP response for a uniform inflation of the pressurized interval in isotropic intact rock. In the field, the SIMFIP probe is capturing an elastic response, which depends on the SIMFIP's clamp compliance and clamping efficiency, orientation of the cage in the borehole and on the borehole wall geological heterogeneity. These different effects are removed from the signal during a pre-processing phase (see below). During each injection test, either the injection pressure or the injection flowrate is controlled by a pump set at the surface. The sampling frequency is 500 Hz. To facilitate analysis, the signal is down-sampled during pre-processing.

Packers were first inflated in order to seal the interval. Then, the displacement sensor was anchored to the borehole wall. Figure 3-6 shows the hydraulic cycles applied in the interval during each of the three performed tests. The protocol was practically the same for each interval:

- A pressure step-increase and step-decrease was first applied. Maximum pressure remained below the fracking or the stimulation pressure. This can be seen when the pressure at each step was constant. This cycle was used to (i) check the packers' sealing efficiency, and (ii) to test the SIMFIP clamping efficiency to the borehole wall. A linear relationship between the SIMFIP displacement and the pressure was used to apply the compensation related to the SIMFIP-borehole system mechanical response.
- The high-pressure stimulation cycles are then performed. The key idea is to produce a significant fracture displacement that will be later used to estimate the fracture mechanical properties and the state of stress. In the intact rock interval, this period corresponds to a succession of leak-off tests. In the two other intervals, pressure is initially increased step-by-step until fracture opening begins. Then, pressure is maintained for several minutes to grow the fracture away from the borehole influence. The interval is then shut-in for several minutes and finally bled off.
- The controlled pressure cycle is the last hydraulic cycle. Once the interval is fractured, or once a preexisting fracture is reactivated, this cycle's objective is to characterize the fracture's hydraulic properties. Pressure is maintained constant at different step values by varying the injection flowrate.

Pressures up to about 16 MPa and 2 to 4 l/min injection flowrates were applied during the tests performed in the COSC-1 borehole.

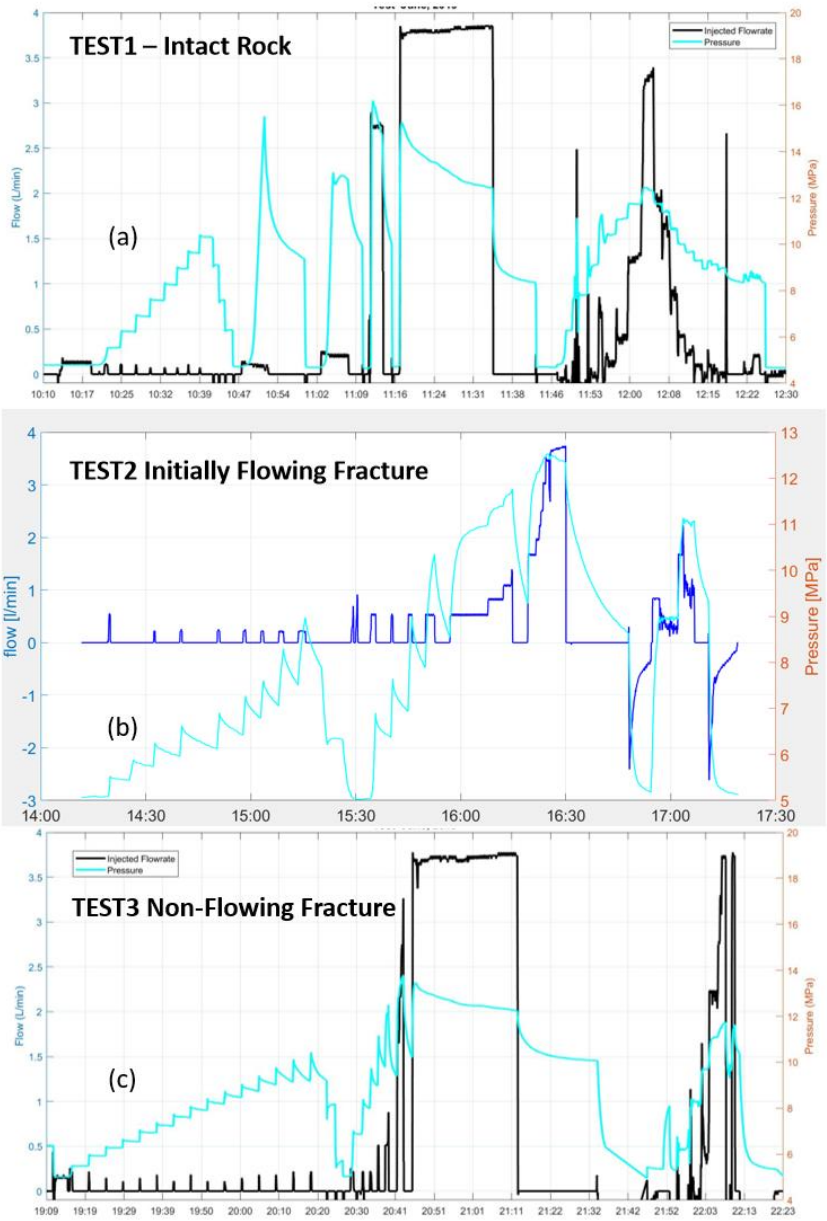

Figure 3-6. Hydraulic stimulation protocols applied in (a) – Intact rock interval (detailed analysis of the SRT test from 11:46 until 12:30 is shown in Figure 3-7), (b) – Initially flowing fractures interval (the higher pressure cycle conducted between 16:18 and 16:45 is detailed in Figure 3-8) and (c) – Non-flowing fractures interval (the fracture propagation period at 3.7 l/min injection flowrate from 20:42 to 21:11 is detailed in Figure 3-9).

3.3.2 Test Results

3.3.2.1 Synthesis of the activation pressures

Figure 3-6 and Table 3-1 summarize the key parameters deduced from the analysis of the SIMFIP tests. The breakdown pressures, which are the maximum pressures reached during the tests, vary from 12.5 to 16.15 MPa in the initially flowing fracture and intact rock interval, respectively. This pressure is considered

as a rough estimation of the fracture initiation, which is known to start at lower pressure (Detournay et al., 1997). The closed fracture interval displays an intermediate value of 13.79 MPa. The fracture propagation pressure, which is the pressure at which fluid-induced rupture propagates in the fracture, is consistent between all tests with values of 12.26 to 12.53 MPa. This pressure is picked at the end of the injection period, just before shut-in (Figure 3-6). The fracture opening pressure (FOP) and the fracture closing pressure (FCP) correspond to pressures when there is a sudden increase or decrease in the injection flowrate, caused by a hydraulic opening or closing of the activated fracture, respectively. The FOP/FCP increase with the depth of the tests with values of 9.25 MPa at Test 1 (485.2 m depth), about 11 MPa at Test 2 (506 m depth) and 11.7 MPa at Test 3 (515 m depth). This would correspond to a vertical stress gradient steeper than lithostatic, and this apparent depth-dependent variation may be locally perturbated around the activated fractures. Overall, these key pressures values do not differ much between tests although stronger contrast could have been expected due to the three contrasting interval geologies. Indeed, the fracture propagation pressures (FPP) are very close regardless of whether the interval contains initially flowing fractures, no flowing ones or intact rock. The FPP value is also close to what would be the expected vertical stress at the depth of the tests given a 2700 to 2800 kg/m^3 rock density (Hedin et al., 2016). Thus, the contribution of any rock or fracture strength to the FPP appears limited.

Table 3-1. Activated fractures, displacement modes and key activation pressures deduced from the three SIMFIP tests in COSC-1 borehole. See displacement vectors in Figures 3-7 to 3-9.

Test	Activated Fracture Depth/dd/d (m/degree/degree)	Mode	Displacement vector	Pressure Breakdown or max. (MPa)	Propagation Pressure (MPa)	FOP/FCP (MPa)
1 – Intact rock	484.9/246.6/12.9	Opening with shear increasing with fracture growth	AB	16.15	12.44	9.25 9.278
2 – Initial flowing fracture	505.9/288/12	Opening then shear at high Pressure	AB BC CD	12.53	12.53	10.98/11.55
3 – Closed Fracture	514.6/270/10 515.1/110/59	Mixed 2 fractures could be activated	AB CD DE EF	13.79	12.26	11.7/11.51

3.3.2.2 Test 1 – "Intact Rock"

Figure 3-6a shows that fracturing of the intact rock interval was conducted in 4 successive leak-off tests from 10:47 to 11:46 on June 18, 2019. It was followed by a pressure step-rate test from 11:46 until 12:30. All tests roughly show the same type of borehole displacement-vs-pressure responses. We focus on the final step rate test (SRT) test because, at this time, the rupture has propagated away from the borehole influence, and is more reflective of the *in-situ* fracture hydromechanical response. Figures 3-7a and b show a drastic change in the borehole displacements above 10MPa. It is the [AB] period from 12:03 to 12:10. It is about 1MPa above the FOP (Figure 3-7e), and it corresponds to a sharp non-linear increase in the injection flowrate. A large displacement offset remains when pressure is stepped down back to the initial borehole pressure, highlighting that some irreversible fracture displacement was triggered. Figures 3-7c and d show that this activation period is characterized by an upwards plunging $\underset{AB}{\rightarrow}$ vector oriented N0°. In detail, similar

displacement orientations of smaller magnitudes are detected immediately following FOP. If we consider the $\overrightarrow{AB}$ vector as representative of the opening of a mode 1 fracture, it should be parallel to the normal to the fracture plane. This gives a ~0/50° average orientation of the fracture. $\overrightarrow{AB}$ vector is also compatible with the opening with a reverse shear component of the 246/13 fracture observed on cores between the SIMFIP anchors.

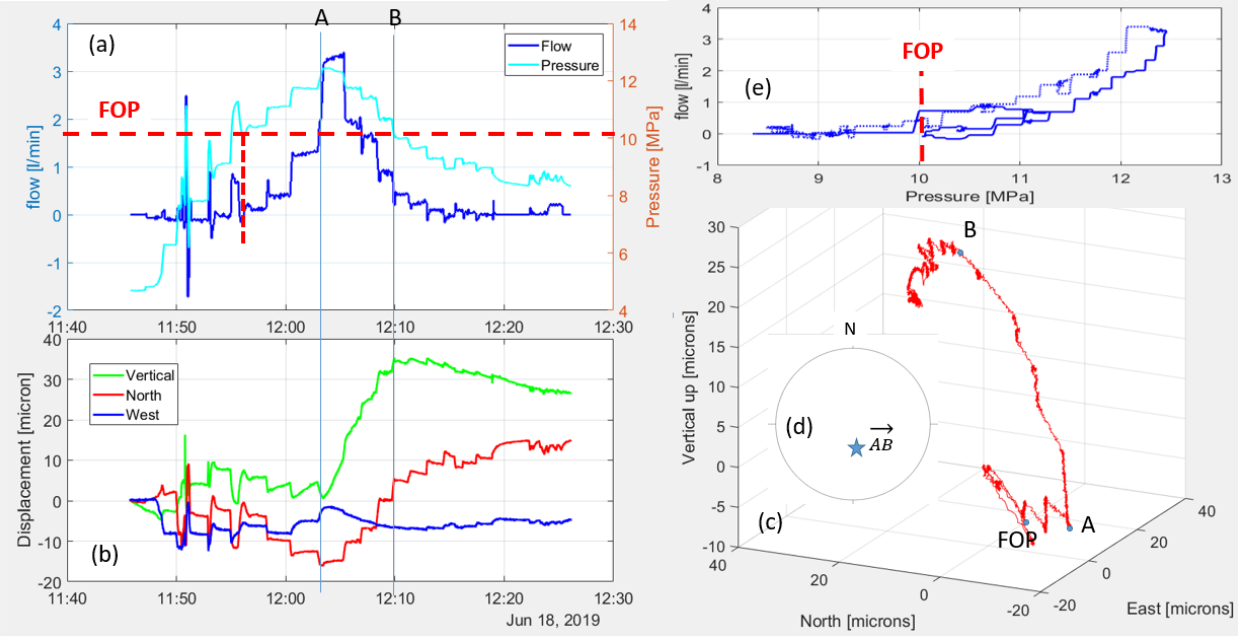

Figure 3-7. Test 1 pressure-displacement signals during the pressure-step-rate stimulation (see Figure 3-6a for location of this cycle in the entire test sequence). (a) – Pressure (light blue) and flowrate (dark blue). (b) – Displacements oriented in geographic coordinates. (c) – Three- dimensional displacement variation with time during the test. (d) – Stereographic lower hemisphere projection of $\overrightarrow{AB}$ displacement vector. (e) – Flowrate-vs-pressure curve (FOP is the Fracture Opening Pressure).

3.3.2.3 Test 2 – Initially Flowing Fracture

The initially flowing fractures were identified using a distributed water electrical conductivity probe test deployed at the interval depth before setting the SIMFIP test (see Section 3.2). As mentioned earlier, three flowing fractures were identified, two being between the SIMFIP anchors and one below. Displacements measured during activation of these fractures showed a contraction of the SIMFIP sensor, only compatible with the mechanical opening of the fracture located below the lower anchor. This test confirmed the initial hydraulic opening of the interval fractures since transient pressure steps were observed starting at the low pressures during the first pressure step rate cycle from 14:00 to 15:30 (Figure 3-6b). In Figure 3-8 we show details of the higher-pressure cycle conducted between 16:18 and 16:45 (Figure 3-6b), that produced the most significant borehole displacements. A large negative vertical displacement was observed while pressure was increased (Figure 3-8a and b). Compared to the horizontal northern and western displacements, which are relatively low, this shows that vertical movement is dominant and compatible with the opening of the gently dipping 288/12 fracture located below the SIMFIP anchors. The displacement

evolution is described by several vector directions rotating with time, and with the interval pressure (Figures 3-8c and d). During the fast pressure increase, vectors $\underset{OA}{\rightarrow}$ and $\underset{AB}{\rightarrow}$ show a sub-vertical displacement. The fracture is mainly opening. When injection pressure gets to 12.3 to 12.5 MPa, there is a drastic reorientation of the displacement vector characterized by a northern reverse movement on the fracture plane ($\underset{BC}{\rightarrow}$). After initial opening, the activated fracture is thus slipping at high pressure. When injection is shut-in, the fracture displays a mainly normal closing characterized by vector $\underset{CD}{\rightarrow}$, which is collinear to $\underset{OA}{\rightarrow}$ and $\underset{AB}{\rightarrow}$. Figure 3-8e shows no clear flowrate variation related to the fracture shearing period [BC], the sharp non-linear flowrate increase being associated to the [OB] normal opening period. Thus, Test 2 highlights two contrasting hydromechanical fracture responses: an initial normal opening at low to intermediate injection pressures followed by shear at high pressures.

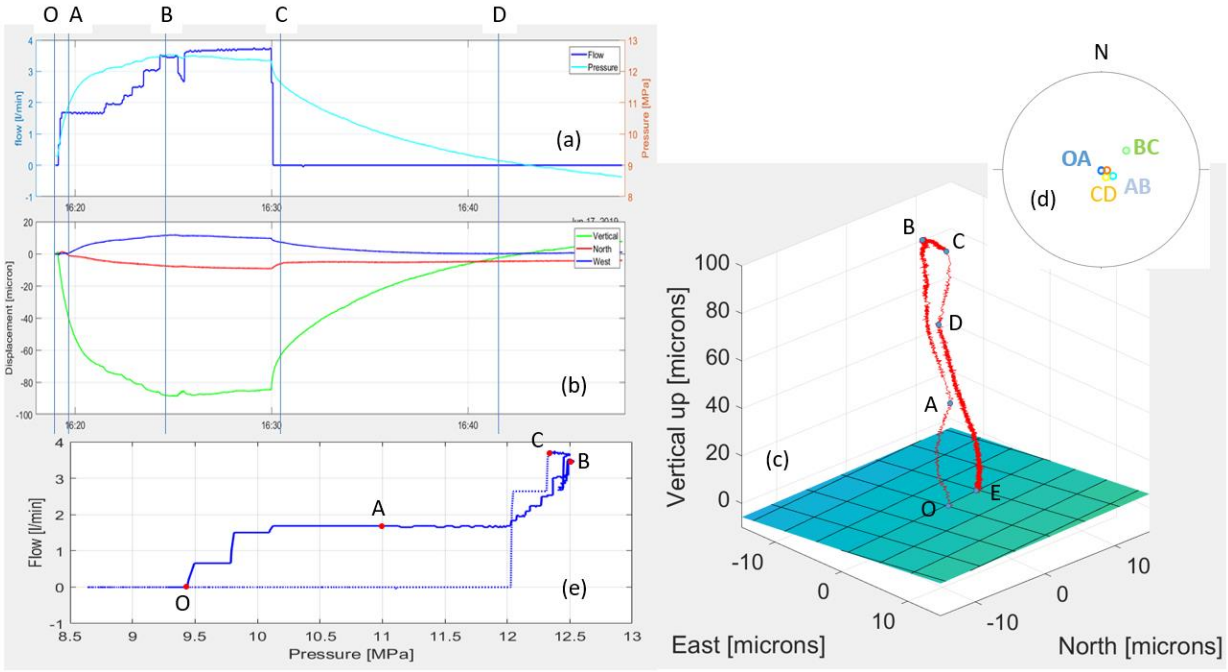

Figure 3-8. Test 2 pressure-displacement signals during the high-pressure stimulation cycle (see Figure 3-6b for location of this cycle in the entire test sequence): (a) Pressure (light blue) and flowrate (dark blue). (b) Displacements oriented in geographic coordinates. (c) Three-dimensional displacement variation with time during the test (the colored surface figures the initially flowing fracture plane). (d) Stereographic lower hemisphere projection of displacement vectors. (e) Flowrate-vs-pressure curve.

3.3.2.4 Test 3 – Initially Closed Fracture

The initially closed fractures were stimulated by applying increments of increasing pressure steps from 20:25 to 20:42 on June 17, 2019, until a clear hydraulic opening was observed, characterized by a pressure transient decay at the steps (Figure 3-6c). Then, a constant 3.7 l/min injection flowrate was applied from 20:42 to 21:11 to propagate the rupture in the fracture. At 21:11, the interval was shut-in until 21:32, and finally bled off. Figure 3-9 shows the hydromechanical response of the interval during the fracture propagation period at 3.7 l/min injection flowrate from 20:42 to 21:11. During this period, the fracture propagates away from the borehole's stress influence. It is considered as the most relevant period for the analysis of the *in situ* fracture's response. Compared to the two other test intervals, the displacements

display both a significant vertical and horizontal variation during the fracture propagation, highlighting shearing of the borehole (Figures 3-9a and b) although there is not much offset at the end of the test. Displacements evolve in a complex way, characterized by a general eastward and up-dip direction (Figures 3-9c and d), but with sharp reorientations in details. This highlights a much more complex interval stimulation than was observed in the two other tests. It could relate to the activation of the two families of fractures affecting the interval, respectively the 170/10 and 110/59 fractures both being between the SIMFIP anchors. $\underset{AB}{\rightarrow}$. and $\underset{EF}{\rightarrow}$. vectors match well with the opening of the flat-lying 170/10 fracture. Reorientation to $\underset{CD}{\rightarrow}$.and $\underset{DE}{\rightarrow}$. best match with dilatant shear along the 110/59 fracture. Figure 3-9e shows that flowrate increase is associated with the vertical displacement vectors, thus the normal opening of the flat-lying fracture. There is no flowrate variation during shearing of the 110/59 fracture.

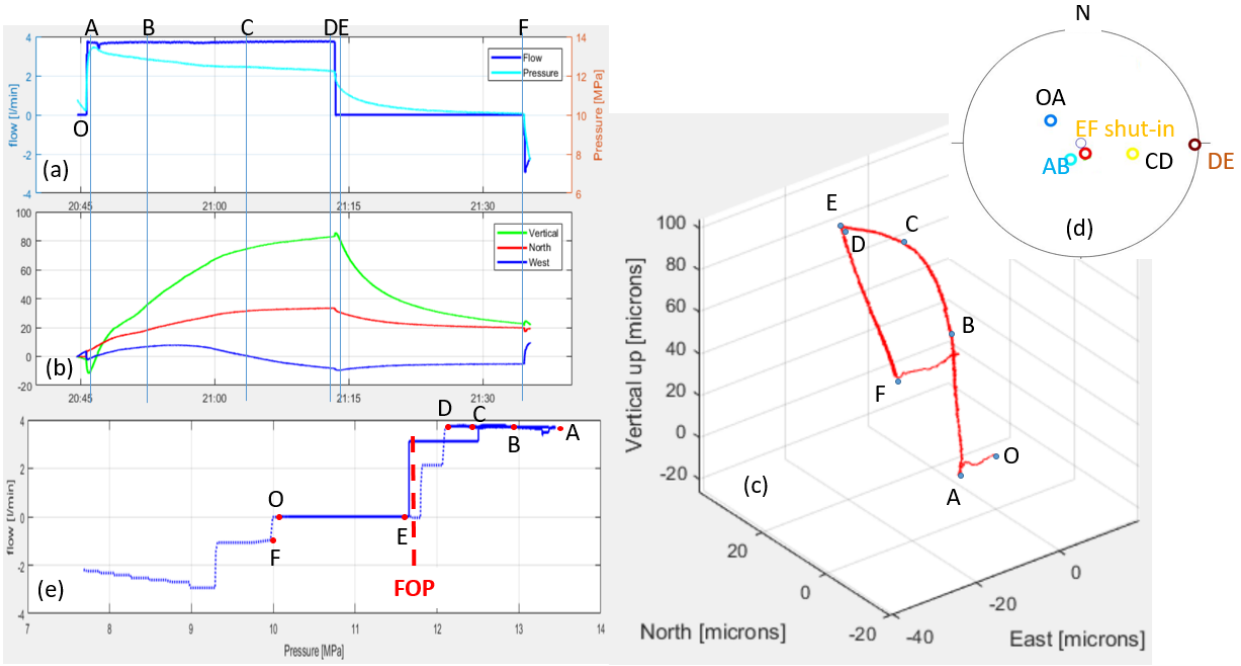

Figure 3-9. Test 3 pressure-displacement signals during the high-pressure fracture propagation cycle (see Figure 3-6c for location of this cycle in the entire test sequence). (a) Pressure (light blue) and flowrate (dark blue). (b) – Displacements oriented in geographic coordinates. (c) Three-dimensional displacement variation with time during the test. (d) Stereographic lower hemisphere projection of displacement vectors. (e) Flowrate-vs-pressure curve.

3.3.2.5 Synthesis of the activation displacements

In all tests, displacements are characterized by a dominant vertical orientation. Horizontal displacements are 1/4 to 1/10 the vertical ones in Test 3 and Tests 1&2, respectively. Displacement magnitudes are the same between tests, of about 10 to 100 micrometers. There is a very good correspondence between the main displacement variations and the hydraulic response to pressure stimulation. Figure 3-10 is a summary of the observed fracture activation modes. In Tests 1 and 2, it is mainly normal opening of the parallel-to-foliation fractures, with an irreversible slip component at the highest stimulation pressures. It is consistent with these intervals' geology consisting of foliation planes or flat-lying fractures. No clear new fracture may have been created by the stimulations (although this will require additional checking from post-testing image logging that should be conducted in June-July 2020 in the COSC-1 borehole). In Test 3, there is a more complex activation story possibly caused by the two fractures affecting the interval. The opening of

the flat-lying fracture competes with the reverse shearing of the steeply dipping 110/59 fracture. These two fractures, which were observed to be closed on the corresponding core samples, opened in the field within the same range of stimulation pressures as in the two other intervals. One possibility could be that in Test 3 and in Test 1, flat-lying fractures are closed but not sealed and can open under pressure. In Test 3, the in-filling material of the 110/59 fracture may not add much strength to the fracture that reactivated.

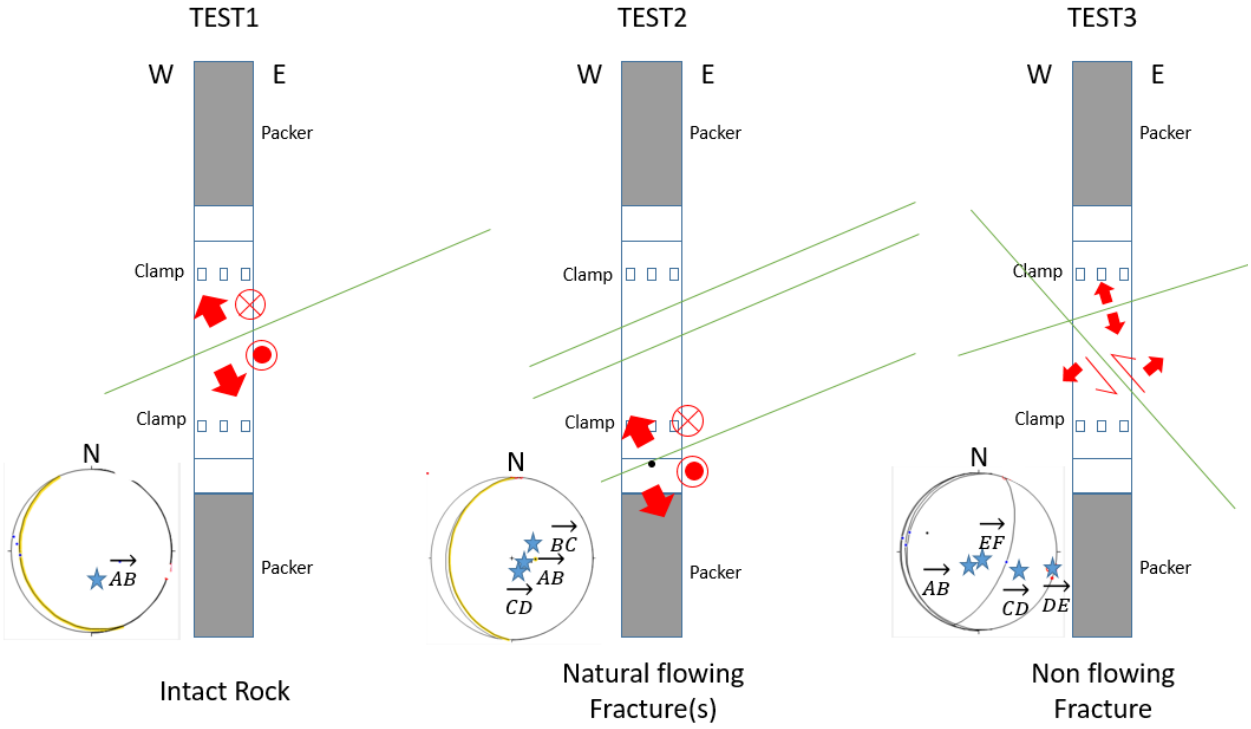

Figure 3-10. Fracture activation mechanisms deduced from in situ SIMFIP tests.

3.4 Stress Estimation from The Inversion of Displacement Data

The stress state is computed following the protocols on dislocation analysis during fluid injection and its application to stress inversion developed by Kakurina et al. (2019, and submitted). The protocol is based on inverting the SIMFIP borehole displacements vectors that have been identified in Section 3.3. We only consider the slip component of the displacement vector. The orientation of the vector together with the orientations of potentially reactivated fractures in the interval is the starting point for estimating the stress state from a single injection test. First, all possible reduced stress tensor solutions that fit the measured slip are searched. Second, the normal and vertical stress are matched on the reactivated fracture into the reduced stress ellipsoid. For the COSC-1 tests, the vertical stress was estimated by the weight of the overburden considering a 2700 kg/m^3 density (within the range of values reported by Hedin et al., 2016). The stress tensor is calculated using the orientation of the activated fractures in the intervals, their normal stress and the slip on these fractures, triggered during the fluid injection (Tables 3-1 and 3-2). We assume that the normal stress is equal to the fracture closing pressure (FCP) measured during the fluid injection (Section 3.3). We also assume that due to the vicinity of all the tests the slip may have triggered under the same stress state (or under a close variation of the stress). Nevertheless, we also conducted stress estimation by considering each test individually, in order to compare with the stress estimation from the three tests taken together. The input data for the stress inversion are given in Table 3-2.

Table 3-2. Input data used for the stress inversion from the COSC-1 SIMFIP tests

Test	Fault		Slip		Sense (1 - reverse)	FCP
	Dip dir.	Dip angle	Dip dir.	Dip angle		
1 (intact)	247	13	348	-3	1	9.28
2 (open)	288	12	53	-7	1	11.55
3 (closed)	110	59	282	-59	1	11.51

Firstly, we search for the reduced stress tensors, i.e., stress orientations (S1, S2 and S3) and stress ratio (R), for which the angular misfit between measured and calculated slip orientations is the smallest. When considering only one test at a time, there are several possible stress tensor solutions represented by the multiple colored dots in Figures 3-11a, c and e. The tensor's orientation is consistent between tests. It appears that all inversions display a sub-vertical σ_3 while σ_1 and σ_2 may shift to one another depending on the tests. When the three tests are considered all together, there is only one solution of the reduced stress tensor, which would have the angular misfit with all the measured slip of less than 10° (Figure 3-11g):

- σ_1=284.1/11.2 (red marker);
- σ_2=14.9/4.2 (blue marker);
- σ_3=125.0/78.0 (green marker),
- R=0.2.

The absolute principal stress magnitudes $\sigma_1, \sigma_2, \sigma_3$ are calculated by fitting the estimations of the fracture normal stresses σ_{n1} and σ_{n2} into the stress ellipsoid defined by the reduced stress state. We considered the normal stresses calculated on fractures 247/13 and 288/12, using equations below:

$$\begin{cases} R = (\sigma_2 - \sigma_3)/(\sigma_1 - \sigma_3), \\ \sigma_{n1} = l_1^2\sigma_1 + m_1^2\sigma_2 + n_1^2\sigma_3, \\ \sigma_{n2} = l_2^2\sigma_1 + m_2^2\sigma_2 + n_2^2\sigma_3, \end{cases}$$

where l_1, m_1, n_1 and l_2, m_2, n_2 are the direction cosines of the normal components of the fractures with respect to the principal stress axes.

When all tests are considered (Figure 3-11h), the magnitudes are $\sigma_1 = 11.82\ MPa$, $\sigma_2 = 9.77\ MPa$, $\sigma_3 = 9.26\ MPa$, respectively. Other combinations of the normal stresses of the fractures do not give a solution. When tests are taken separately, there is a strong variability of magnitudes between tests (Figures 3-11b, d and f), some values looking unrealistic given the COSC-1 borehole regional context.

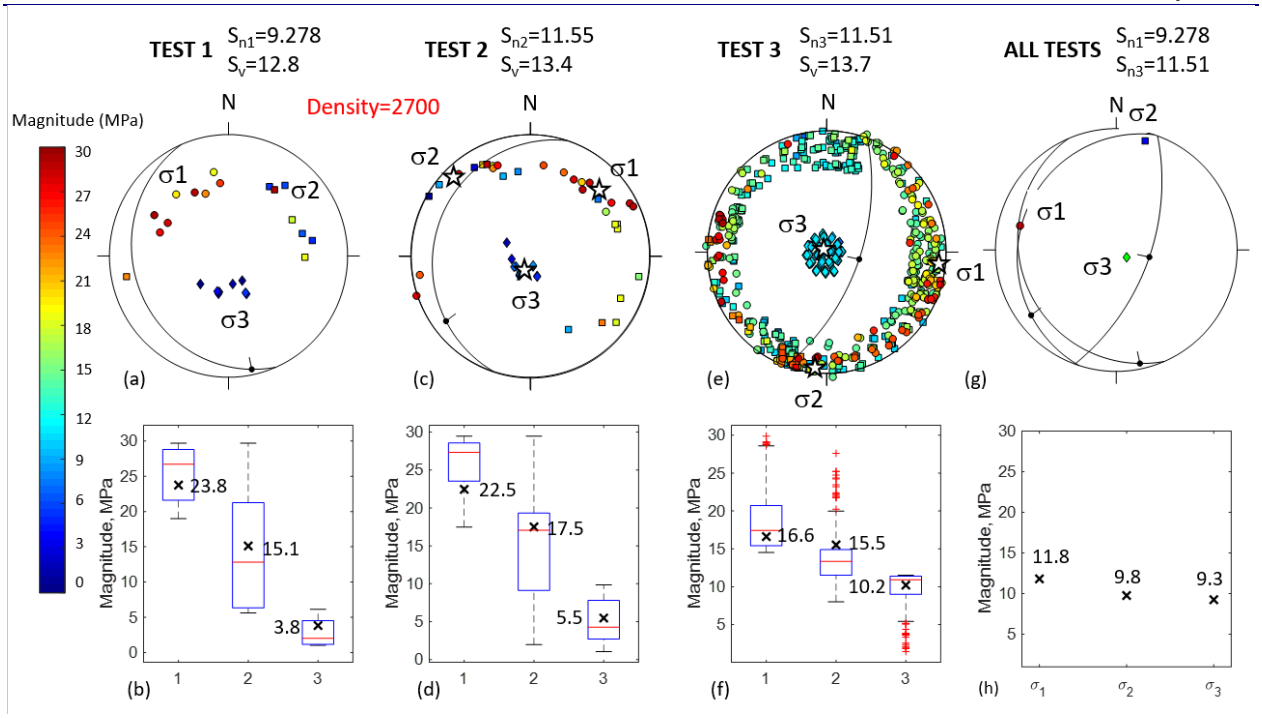

Figure 3-11. Stress inversion from SIMFIP displacement vectors and key interval pressures. Upper row shows the principal stresses orientation projected in a lower hemisphere stereogram (σ1 are circles, σ2 are squares, σ3 are diamonds, colors are stress magnitudes). Lower row shows the statistical variation of principal stress magnitude for each single inversion solution.

When the three tests are considered, we get a reverse stress regime in good accordance with the slightly reverse movements measured on all the activated fractures. Stress tensor horizontal stress orientation is in reasonable accordance with the one deduced from borehole breakout analyses (Wenning et al., 2017). The magnitude of the minimum principal stress appears lower than the weight of the overburden (which is about 13.8 MPa, considering a rock density of 2800 kg/m^3 at 500 m depth), which may look surprising. This approach assumes a homogeneous and constant pore pressure inside a non-deformable activated fracture, which results in an overestimation of the effective stress, and in an underestimation of the total normal stress applied on the fracture. Since here most of the fractures are sub-horizontal, it may explain the underestimated vertical stress.

Our approach gives an estimation of the potential full stress tensor (orientation and magnitude) taking advantage of the borehole displacements and pressures measured during the SIMFIP tests. The magnitudes of the principal stresses are close to each other, as it may be expected at the shallow depth of the tests. It is interesting to see that the estimated tensor is consistent with the one estimated from borehole breakouts (Wenning et al., 2017), observed at larger depths than the SIMFIP tests (below 600 m depth). It may show that although weaker, the stress regime is still reverse in the shallow crust. The tests showed a strong opening component of the stimulated fractures, which is not considered in our stress estimation, the slip component being a minor component of the observed fracture movements in comparison. In the next section, this stress tensor will be refined using a more exact numerical modeling of the tests.

3.5 Fully Coupled Numerical Analysis of the Simfip *In-Situ* Tests

3.5.1 Numerical model setting

We developed three-dimensional models of fractures in the three borehole intervals using the distinct element code 3DEC (Itasca Consulting Group, 2016). The code can be used to conduct fully coupled hydromechanical analysis of the fracture movement induced by the injections. Compared to the stress inversion approach (Section 3.4), the numerical modeling aims at studying the coupled hydromechanical processes of fluid diffusion in the activated fractures. We are interested in exploring how adding downhole displacement monitoring during a hydraulic stress test can help improve the fracture hydraulic conductivity dependency on its activation mode. We use a fully coupled hydromechanical approach to better assess the effects of the pore pressure profile evolution from the injection point into the stimulated fracture. The model domain has side-lengths of 20 m and contains the fractures activated in each interval (Figure 3-12).

We assume that the complex opening of the fractures observed in the field corresponds to a fault rupture is described by a generalized Coulomb failure criterion, including the possibility for failure in shear and in tension. The elastic hydromechanical response of the fracture is also included in the numerical model.

Injection of fluid leads to a change of pressure and fluid flow in the stimulated fracture, and consequently, to a change in stress over the fault surface and a change in aperture follow. It is assumed that the cubic law (Witherspoon et al., 1980) can be used to describe fluid flow in the fault:

$$Q = -\frac{b_h^3 \cdot w}{12\mu}\Delta P$$

where Q is the flow rate (m^3/s), ΔP is the increment in fluid pressure (Pa), μ_f is the viscosity of fluid (Pa.s), w is the fault width (m), and b_h is the hydraulic aperture (m), which is defined:

$$b_h = b_{ho} + \frac{\Delta\sigma_n'}{k_n} + \Delta u_s \cdot \tan\psi$$

where b_{ho} (m) is the initial aperture at zero normal stress, $\Delta\sigma_n'$ is the increment in effective normal stress, Δu_s (m) is the shear slip increment, and ψ is the dilation angle (°). Dilation occurs only as the fracture slips. The hydraulic aperture is linked to the permeability as follows:

$$k = \frac{b_h^2}{12}$$

Experimental and numerical analyses have showed that the cubic law is adequate to simulate fluid flow and hydromechanical effects along smooth surfaces (Brown, 1989; Zhang et al., 2019).

The numerical solution for fluid flow is based on the fluid domain network structure (Itasca Consulting Group, Inc., 2016). Each domain has a uniform fluid pressure and can communicate with the neighboring domains. Thus, the fluid flow is governed by the difference in pressure between adjacent domains. At each time step (Δt in s), the fluid pressure (P in Pa) is updated considering the net fluid flow and the domain volume change (ΔV):

$$P = P_0 + K_w Q\frac{\Delta t}{V} - K_w\frac{\Delta V}{V_m}$$

where P_0 is the initial fluid pressure, K_w (P_a) is the fluid bulk modulus, and $V_m = (V^t + V^{t-1})/2$ with V^{t-1} and V^t, the domain volumes (m^3) at previous (τ-1) and new (τ) times, respectively.

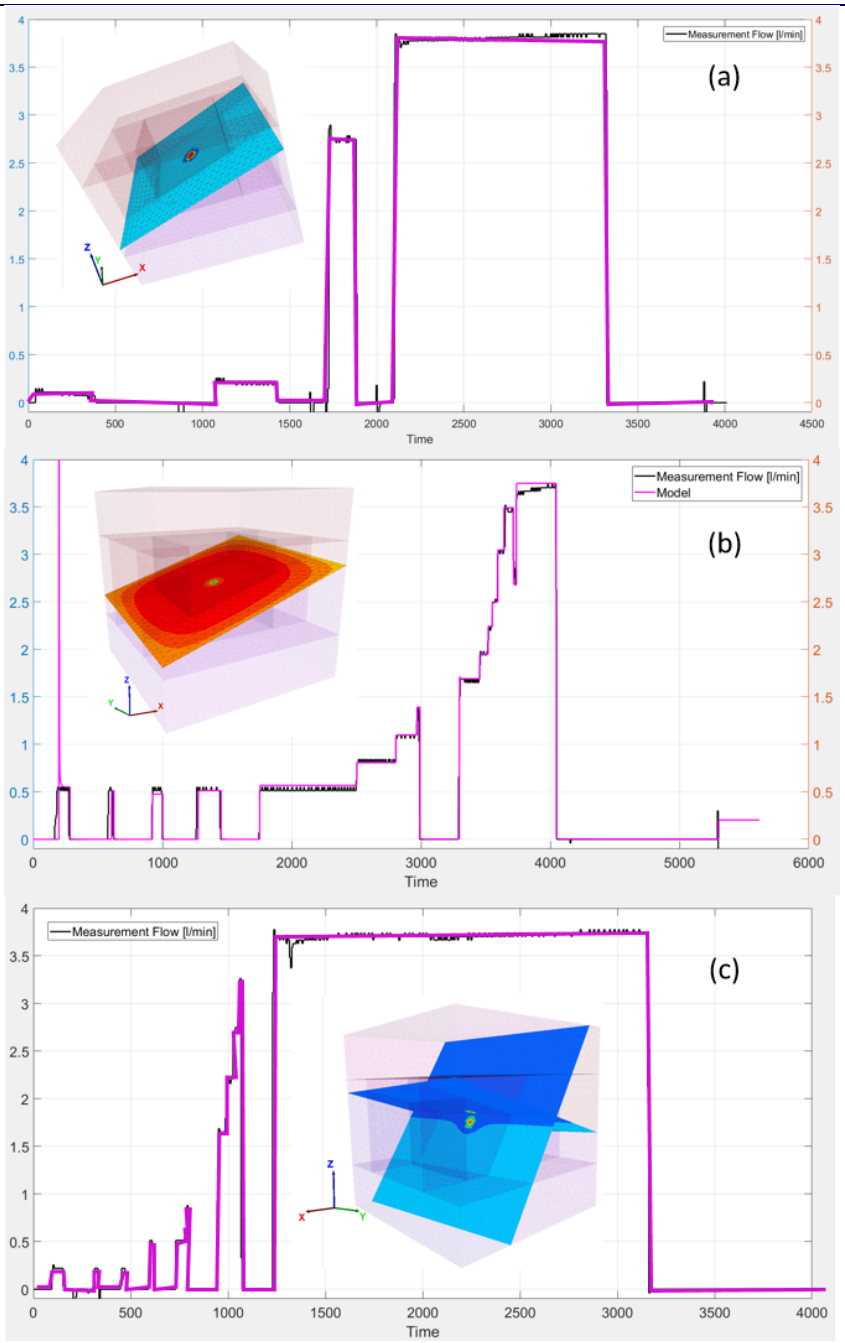

Figure 3-12. Numerical model geometry and injection flowrate history applied to the models of (a) Test 1, (b)– Test 2, and (c) Test 3. Blocks show the model with side lengths of 20 m. Colored planes are the geological fractures observed in each test interval. Injection point is the colored feature in the center of each model. Graphs show the flowrate injected in the field (black curve) and the flow rate history injected in the model (purple curve).

We used two different fluid flow modes to reproduce the observed fluid pressures:

(1) A variable permeability model (i.e. the cubic law and a value of hydraulic aperture that changes with the evolution of fault normal displacement). This flow mode was used to model the initially flowing fracture in Test 2;

(2) A variable permeability model activated at failure. We use the "crack flow model" implemented in 3DEC to simulate fluid flow in the activated parts in shear or tensile failure of the fracture plane, and prevent flow from occurring in the remaining elastic parts. This assumption is used to model the hydromechanical responses of the two initially closed intervals, during Tests 1 and 3 respectively.

The fault/fracture/rock properties used in the model are given in Table 3-3. The host rock is assumed to be linear elastic. The host rock matrix is considered impermeable. Fracture stiffness (K_n, K_s) are estimated from matching the initial reversible parts of the measured displacement-vs-pressure in situ curves. An initial hydraulic aperture is given to initiate the model. It is incrementally actuated during calculation iterations. Fracture friction, cohesion and tensile strength are given values found in the literature for this type of rock. These values are adjusted until a best match is observed between calculated and measured displacements. We start by applying the stress field estimated in Section 3.4 to all the models' boundaries. Stress magnitudes are then adjusted to match the magnitude and orientation of the measured displacements following the method developed in Guglielmi et al. (2020). A sensitivity study to the different model parameters is conducted but it is not described in this report. Here we focus on the comparison between the three tests. The field injection is simulated by applying the injection flowrate at the model's fault grid point coordinates (0, 0, 0) (purple curve in Figure 3-12) that theoretically represents the measured time-history of injection flowrate imposed in each interval during the in-situ tests. Normal and shear displacements of fractures and pore pressure are calculated at the injection point and compared to field measurements (Figures 3-13 to 15). First, the model is run to equilibrium to establish the initial static stress and pressure conditions. Then, the injection flowrate is applied (Figure 3-12).

Table 3-3. 3 DEC model parameters for Test 1–Intact rock, Test 2–Initially flowing fracture, and Test 3–initially closed fracture. Bulk and shear modulus were averaged from K3 perpendicular-to-foliation value in Wenning et al. (2017) and a Young's modulus used in Stephansson et al. (1991). Fracture properties were adjusted by trial and error in order to match calculated and measured SIMFIP displacements.

Parameters	**Units**	**Test 1**	**Test 2**	**Test 3**
Bulk modulus of rock *(K)*	GPa	33.3	33.3	33.3
Shear modulus of rock *(G)*	GPa	25	25	25
Rock density *(ρ_r)*	kg/m^3	2800	2800	2800
Fault elastic stiffness *(k_n, k_s)*	GPa/m	20, 1	3.3, 0.17	8.0, 0.3
Friction angle	(°)	25	25	25
Cohesion/Tensile strength	(MPa)	(0,0)	(0,0)	(0.2,0.2)
Initial hydraulic aperture *(a_{ho})*	μm	10	10	10
Dilation angle *(ψ)*	Degree	5	5	5
Initial fluid pressure *(P_o)*	MPa	6.2	6.2	6.2

Fluid Bulk modulus (K_w)	GPa	2	2	2
Fluid density (ρ_f)	kg/m^3	1000	1000	1000
Fluid viscosity (μ_f)	Pa.s	0.001	0.001	0.001
Stress (σ1,σ2,σ3)	(MPa)	(14.5,14.0,13.0)	(14.5,14.0,13.0)	(14.5,14.0,13.0)

3.5.2 Model results

Figure 3-13 shows the best fit of calculated pressure, fracture opening and shear to the experimental data measured during Test 1. To achieve a reasonable match, we considered a 246/13 fracture initially closed but with no cohesion and no tensile strength (Table 3-3). The initial pressure cycles 1 and 2 (until 1600 seconds) are underestimating the field breakdown pressures while a reasonable match is obtained during the two following cycles. This is explained by the adopted modeling protocol that assumes the presence of a preexisting fracture, thus neglecting any new fracture creation or propagation (this physics is not included in the current model). The two initial cycles might involve some fracturing of the interval to explain the much higher field breakdown pressures compared to the model. Cycles 3 and 4 are much better explained because the rupture has grown into a macroscopic fracture such as the one represented in our model. Nevertheless, shear displacements are poorly explained by the model. The model calculates an increasing slip with fracture growth. This is not clear in the field data where there is little slip in the field and dominant fracture opening. Indeed, the fracture's normal displacement is well reproduced by the model. The best fit is obtained at the last pressure cycle. We calculate a slightly reverse stress regime characterized by a stress tensor oriented as the one deduced from the inversion in Section 3.4. We get principal stress magnitudes (σ_1, σ_2, σ_3) = (14.5, 14.0, 13.0) MPa at the injection point, 2.7 to 4.2 MPa larger than the estimates of Section 3.4, and little difference between the values of the principal stresses. Such a difference can be related (i) to the inversion approach, which underestimates stresses (see Section 3.4) or (ii) to stress concentration effects that govern the fracture growth (and that are poorly captured by the numerical approach).

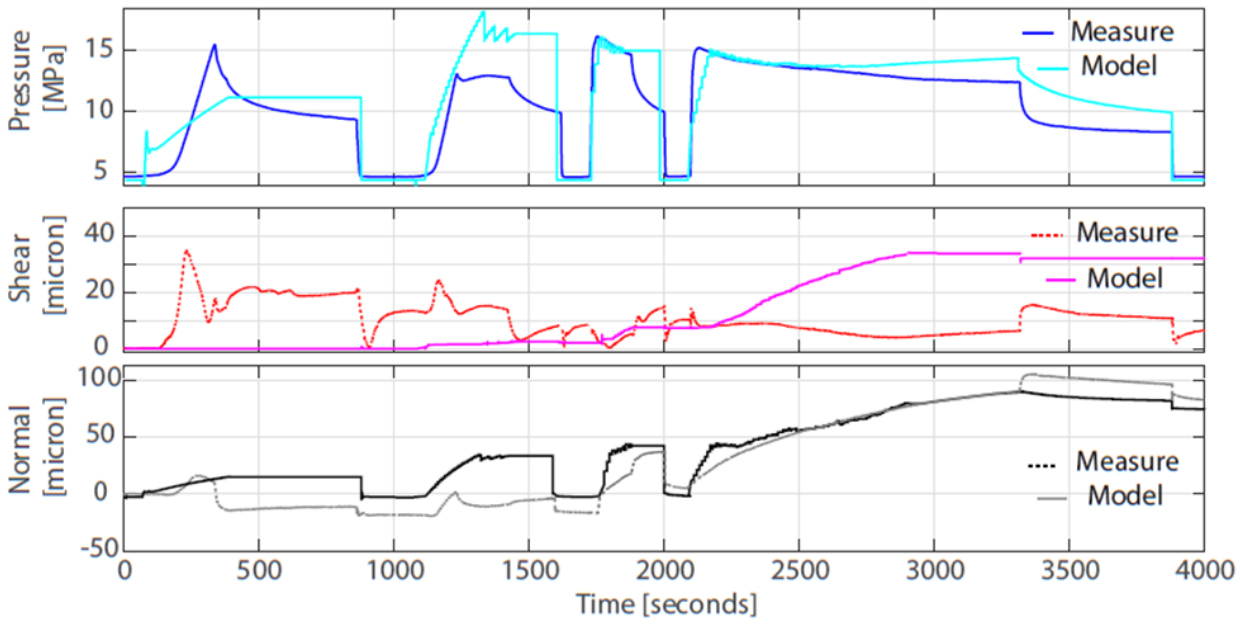

Figure 3-13. Comparison of pressure, normal opening and shear calculated with 3DEC (see model geometry in Figure 3.12a) with field measurements during Test 1 in intact rock.

Figure 3-14 shows the best fit of calculated pressure, fracture opening and shear to the experimental data measured during Test 2. There is a reasonable match of the model calculation to field data. The main difference lies in the model that does not accurately reproduce the transient pressure decays when injection is stopped (either during the initial cycles or during the shut-in at the end of the last cycle). Calculated pressure is always decaying much faster than the field pressure. This is explained by the relatively small size of the numerical model (20 m x 20 m x 20 m), and the very simple applied boundary conditions. The model better describes the injection source near-field hydromechanical response of the fracture than the far-field response, which is contained in the shut-in temporal evolution. The calculated shear displacements are small and in the range of the measured ones. Normal opening of the fracture is the dominant mechanism affecting fracture flow and the calculated pore pressure. We get the same state of stress as the one used in Test 1. The fracture shear and normal stiffness is estimated 6 times smaller in Test 2 than in Test 1. Thus, the flowing fracture appears much more deformable than the closed (or newly created) fracture in Test 1.

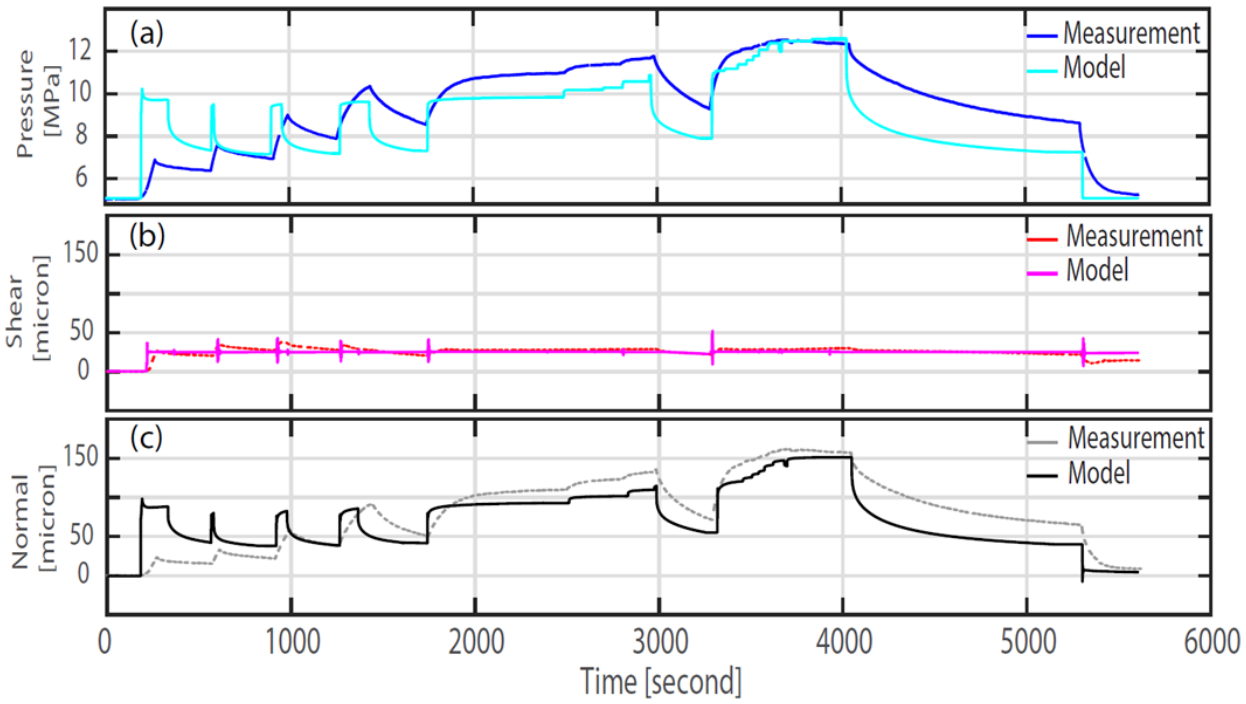

Figure 3-14. Comparison of pressure, normal opening and shear calculated with 3DEC (see model geometry in Figure 3.12b) with field measurements during Test 2 of the initially flowing fracture.

Figure 3-15 shows the best fit of calculated pressure, fracture opening and shear to the experimental data measured during Test 3. Here the model was stopped at about 1400 seconds because rupture reached the model's boundaries. This model is more complex than Tests 1 and 2 ones because it involves two cross-cutting fractures. We simultaneously inject half the measured flowrate in the center point of each fracture. Both fractures are affected by the same properties, and compared to Tests 1 and 2, we had to set a cohesion and a tensile strength equal to 0.2 MPa to match the displacement magnitudes. The same state of stress as in Tests 1 and 2 is calculated. The initial pressure and displacement steps are under-estimated until 500 seconds. After 500 seconds, the model reproduces reasonably well both pressure and displacement. We compare the calculated SIMFIP displacements (Figure 3-15c) to the field measurements (Figure 3-15b), because we do not a priori know which of the two fractures' movement explains the measured borehole displacements. A snapshot of the model's pore pressure shows that at 1000 seconds, most of the flow (red

patch) is going into the 110/59 fracture. We thus conclude that this fracture predominantly activated and explained the observed displacements.

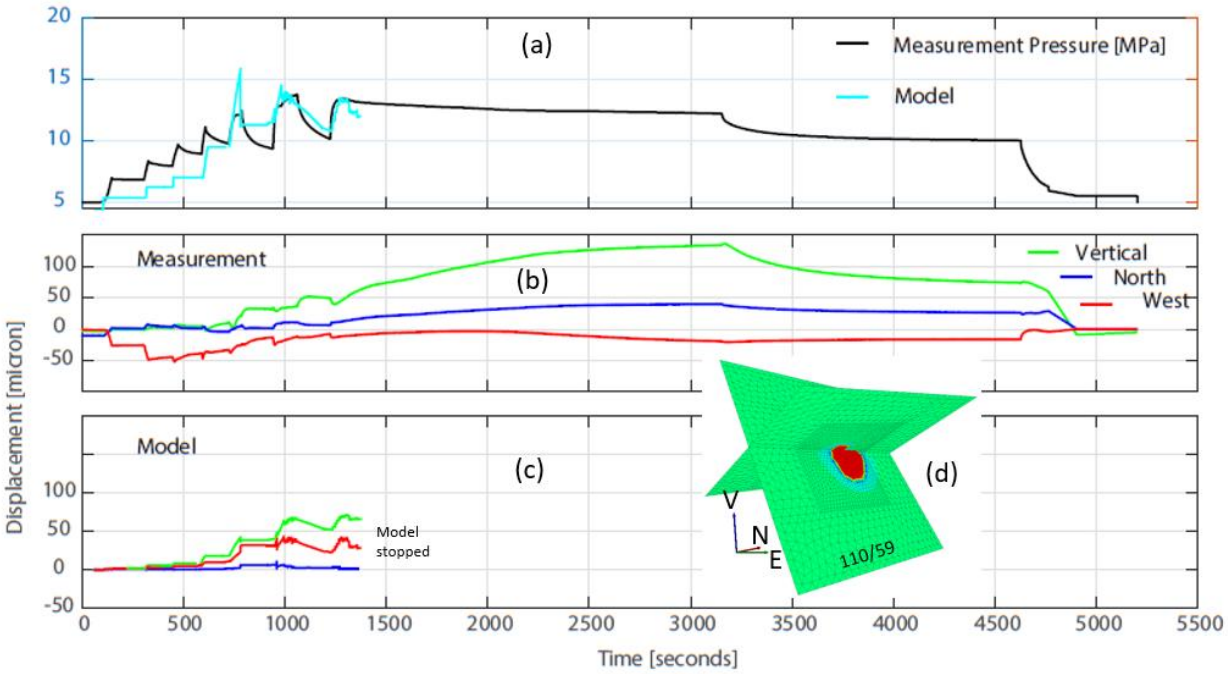

Figure 3-15. Test 3 closed fractures. (a) – Interval pressure. (b) – Measured SIMFIP displacements in geographic coordinates. (c) – Calculated SIMFIP displacements. (d) – Snapshot of fractures' pore pressure calculated at 1000 seconds (in this model flow is only allowed in the red patch which is growing with mechanical shear or tensile rupture of the predefined fracture surface).

3.5.3 Conclusions

The fully coupled numerical modeling of the three tested intervals allows for refining the estimate of the stress tensor, which is characterized by a slightly reverse stress regime, and an orientation consistent with the one deduced from the inversion of the SIMFIP displacement vectors. The same principal stress magnitudes (σ_1, σ_2, σ_3) = (14.5, 14.0, 13.0) MPa are used to reproduce all the tests.

The difference between the tests is explained by factor-of-6 difference in fracture stiffness and in strength and cohesion. The open-flowing fracture is also the less stiff fracture. The fracture activated in Test 1 has the highest stiffness. It can be an initially closed preexisting natural fracture sub-parallel to the foliation. Some observations on cores show that such a feature might exist, but the borehole logs do not show any preexisting fracture. It might also be a newly created fracture subparallel to the foliation, which could have provided weak planes for fracture nucleation. Test 3 shows that the 110/59 fracture with mineral infilling may reactivate under pressure even if affected with a moderate cohesion and tensile strength.

3.6 Conclusions of the Field Fracture SIMFIP Tests

Analyses of direct field pressure and displacements with an inversion method and with three-dimensional fully coupled forward numerical modeling allows for defining the activation sequence of fractures affecting the shallow crystalline crust at ~500m depth in the COSC-1 borehole. Flat-lying fractures subparallel to foliation open under variations of the normal effective stress in a slightly reversed stress regime. Planes reactivate at fracture opening pressures (FOP) as low as 9.3 MPa, about 3.7 MPa below the sub-vertical minimum principal stress. Our observations show that normal opening of fractures explains most of the flow leakage while shearing does not correlate with any change in the leakage flowrate. Borehole water electrical conductivity measurements highlight the natural leakage of some fractures before testing, while fracture displacements testing with a SIMFIP probe shows that fractures display 10-to-100 micrometer opening under a fluid pressure increase. The naturally flowing fractures appear more deformable than the closed ones for the same injection pressures. Sealed (mineralized) non-flowing fractures apparently do not display additional strength to behave differently from the closed fractures. They activate as easily as the other fractures given their orientation towards stress. The geology of the three different intervals give roughly the same leakage pressure and flow response under a comparable state of stress.

Next steps will be to analyze in detail the shut-in periods to get complementary information on the far-field connection of the fractures tested in intervals with other fractures existing in the surrounding host rock. In parallel, considering fracture mechanics in the numerical analyses will give an estimation of the stimulated fracture sizes. Numerical models tuned at the three intervals applied to other zones of the borehole will allow extending this approach to a statistical estimation of potential leakage of fractures under the state of stress defined in this study. All these steps combined should lead to a discrete fracture network including realistic individual fracture properties, and the variations of these properties with stress.

3.7 Laboratory Measurements of Transmissivity of Fractured Rock Cores

3.7.1 Introduction

This section summarizes laboratory work on anisotropic flow through fractures, which was conducted at LBNL in FY19-20. Previous work on anisotropic flow through natural fractures was completed for this project, but corresponding field transmissivity information was not available. Starting from FY18, measurements on artificial fractures were conducted to verify performance of the measurement system. During FY19-20, as a result of field work activities, three new core samples corresponding to the three zones examined by the SIMFIP were obtained and laboratory measurements were completed on one of these samples.

3.7.2 Experimental Design

Details of the experimental apparatus were described in previous reports (e.g., Dobson et al., 2017; Zheng et al., 2018). Transmissivity was measured over a range of effective stresses from 200 to 4000 psi in a custom constructed apparatus allowing water delivery to any of four inlets distributed at 45-degree increments around the circumference of the core, and to extract water from an outlet opposite to the inlet (Figure 3-16). The inlets and outlets are stainless steel half-tubes that run along the length of the core insuring contact with the fracture. A custom silicone rubber sleeve was manufactured to fit both around the core and inlet and outlet half-tubes to inhibit flow around the core. This sleeve was cast with silicone molding compound over a mockup of the setup to provide the proper fit. The pressure vessel was filled with water and confining pressure controlled by a high-pressure syringe pump. Flow through the fracture was driven using a second precision high-pressure syringe pump (Isco D-series). Confining pressure ranged from 200-4000 psi, depending on the core, and pressure in the sample was below 20 psi at all times.

Differential pressure measurements along the 60 mm flow path of the fracture was typically on the order of 0.1 – 1 psi, which necessitate adjustments of flow rate to maintain that range, depending on the transmissivity of the fracture.

To measure transmissivity, confining pressure is applied and a flow is applied to achieve a differential pressure across the fracture. Each channel was measured with a minimum of three flow rates, the resulting transmissivity was calculated, and the results from the three flow rates was averaged. In some cases, transmissivity was measured in both the forward and reverse direction.

Transmissivity was calculated using the following relationship:

$$Transmissivity\ (m^2/s) = \frac{Qg\rho l}{\Delta P w}$$

where Q is the volumetric flow rate (m^3/s), g is gravity, ρ is density, l is the fracture length, w is the fracture width, and P is pressure.

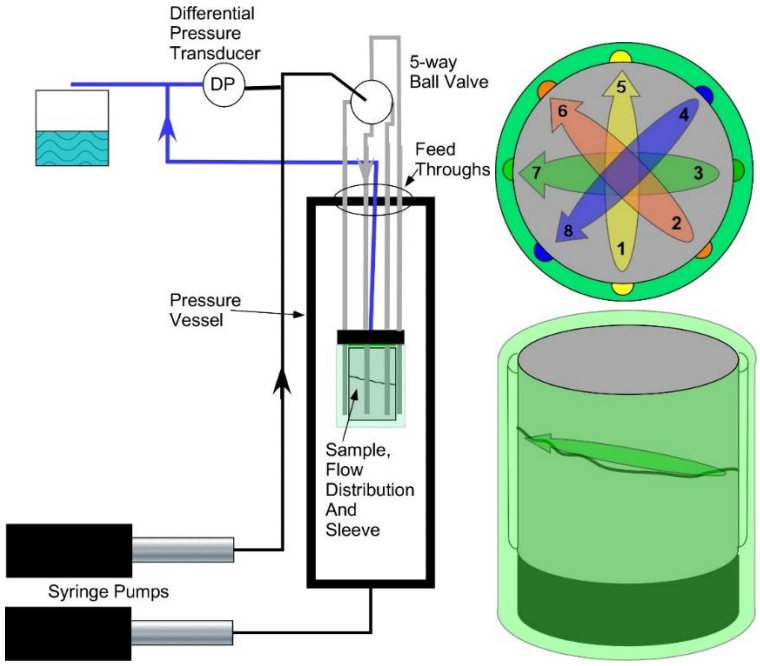

Figure 3-16. System schematic showing that the lower syringe pump controls confining pressure, and the upper syringe pump is used to inject water into the core. Two 5-way ball valves (one shown) control flow to the inlet tubes (1-4) and outlet tubes (5-8).

3.7.3 Core Descriptions

Three different artificial fracture (AF) Delrin cores were manufactured to be the same geometry as the rock cores (Figure 3-17). The AF1 core was solid except for one 1/16 in diameter horizontal hole through the center, and was designed to test whether circumferential flow could occur in the system. The second artificial fracture core (AF2) was the same size, but cut in half, with one side of the 'fracture' machined to have 4 rectangular channels, with cross sections of four channels of 0.26 mm^2, 0.50 mm^2, 1 mm^2, and 1.52 mm^2 to compare the results of measurements of transmissivity against predicted transmissivity based on this simple geometry. The third artificial fracture core (AF3) was also two-piece Delrin core with one side of the fracture etched with random paths placed in the system and tested with the same range of confining pressures used for the natural cores.

Natural fractures in core samples from the COSC-1 borehole were used in the apparatus to evaluate anisotropy with flow direction. Three cores were identified as usable in the apparatus due to geometry and condition of the fracture. Core 211-2 and 401-1 were measured previously, and Core 143-4 was received this FY (Figure 3-18). All cores were extracted from same borehole, but due to some alignment uncertainties the exact location of the extracted fracture in the borehole was uncertain. During field work in 2019 a new flowing fracture was studied, and core 143-4 was identified for comparison to field-measured transmissivity. Note that the X-ray CT scans shown in Figure 3-18 are taken without confining pressure, so apertures appear larger than they would during the measurement cycles.

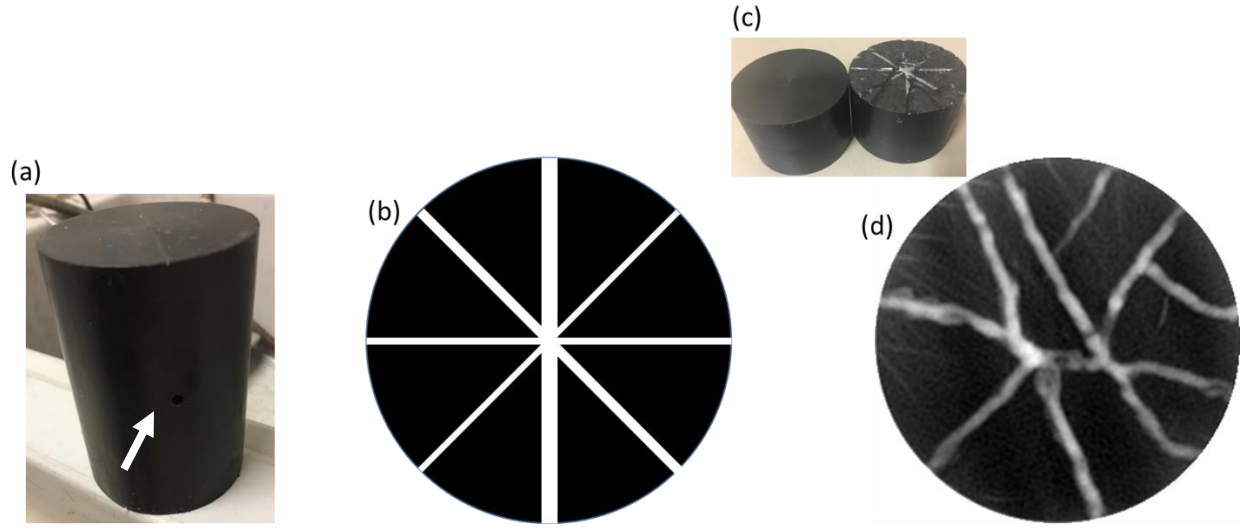

Figure 3-17. Artificial cores: (a) AF1, Delrin core with 1/16 in hole drilled through center. Hole is difficult to see but location indicated by arrow, (b) schematic of AF2 with lines representing rectangular channels, (c) image of AF3 Delrin core, and (d) AF3 cross section showing flow pathways.

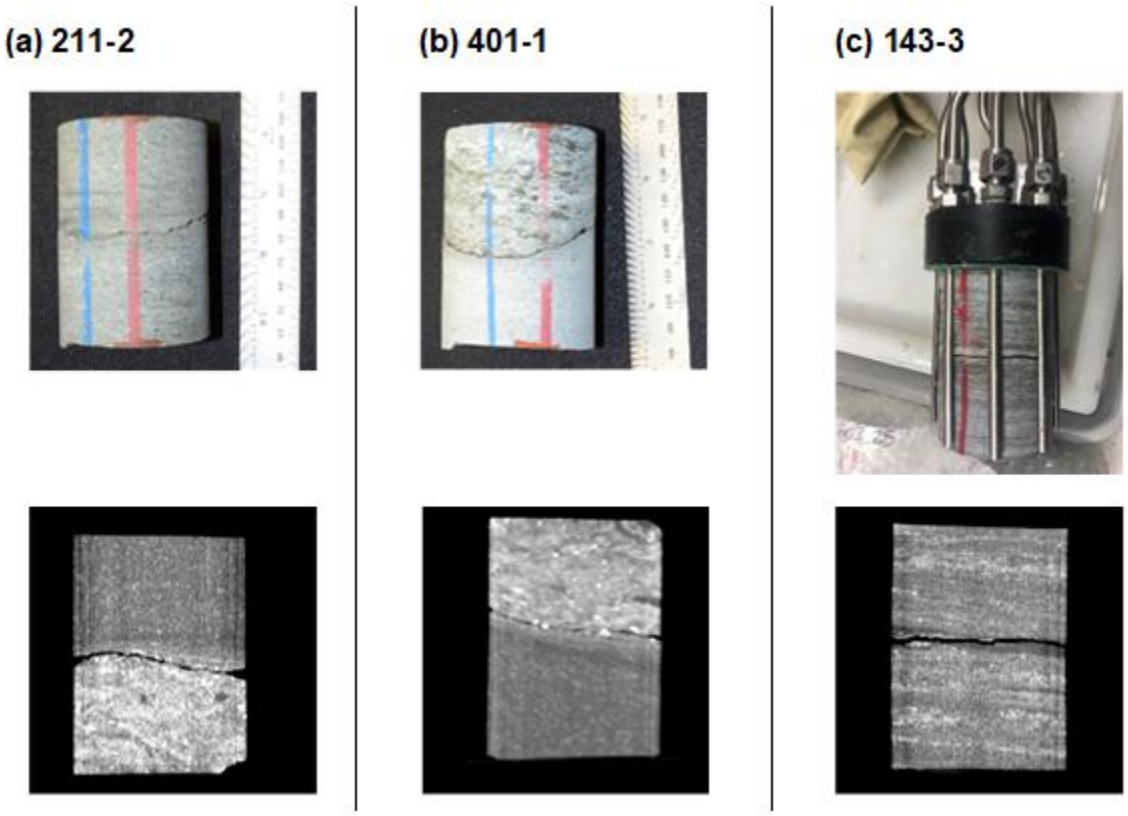

Figure 3-18. Natural Cores. Top row are images of fractures with 143-4 shown in core holder for experiment prior to the placement of the custom sleeve. Second row of images are x-ray CT scans of the fractures that were used for determination of average aperture.

3.7.4 Transmissivity Results

Transmissivity results for the artificial fractures are shown in Table 3-4. As reported previously, when AF1 was tested, the channel was aligned with the through-hole, and very low to no differential pressure was observed indicating that flow was not restricted. The T was recorded as infinite '∞', although if the flow rate was increased some flow restriction would have eventually been observed, but this was not attempted as it may have potentially damaged the apparatus. When the valves were adjusted to align away from the through-hole (solid Delrin), no flow was observed and the differential pressure steadily climbed until nearing the pressure limit of the flow system (20 psi), indicating that no flow occurred. Pressure was set on the no flow position (without the hole) for a period of 1 hour each, and no pressure drop was observed, further indicating that no circumferential flow occurred.

For AF2 and AF3, transmissivities were measured over a range of effective stresses (200 to 1100 psi) and flow rates. The flow rates were dependent on the core transmissivity and were adjusted to give a differential pressure within the range of the sensor. AF2, with the defined straight channels, as expected showed increasing T with channel size. However, for the smaller two channels not much difference was seen. This may be due to one of the fundamental difficulties of the apparatus, trapping of air bubbles in the flow path. With these small channels this could be a major problem, so plans are to repeat this measurement to confirm

results. For AF3, the results show minor differences in transmissivities for each channel. The differences in these channel geometries was due more to flow path length as opposed to flow cross section.

Transmissivity results for the natural fractures are shown in Table 3-5. These numbers represent an average number (n=10) differential pressure measurements at the confining pressure listed in the table and were measured for at least 3 flow rates. To measure each T value, there were first hundreds of measurements made for each of the flow paths to determine that the flow was stable and repeatable. The measurements started with low confining pressure and the confining pressure was gradually increased, raising the effective stress. In every case, settling of the fracture was observed, which was demonstrated by decreasing measured T with increasing confining pressure. After a few cycles the transmissivity decrease was no longer observed and a new set of measurements was taken with the 'settled' fracture. Results of the measurements as shown in Table 3-5 demonstrate that all three fractures have distinct permeability values, with the 211-2 fracture and the 143-4 fracture in the 10^{-5} m^2/s range, and the 401-1 showing lower permeability, in the 10^{-7} m^2/s range. Anisotropy differences are in the range of factors of 2 to 4, and some minor differences are seen in the measurements in the forward and reverse direction of 401-1.

Table 3-4. Results of measurements of transmissivity of the artificial fractures (AF).

	1 → 5 T (m^2/s)	**2 → 6** T (m^2/s)	**3 → 7** T (m^2/s)	**4→ 8** T (m^2/s)
AF-1	∞	0	0	0
AF-2	1.4×10^{-7}	2.2×10^{-7}	8.0×10^{-5}	1.3×10^{-4}
AF-3	4.0×10^{-5}	2.0×10^{-5}	5.7×10^{-5}	3.5×10^{-5}

Table 3-5. Results of measurements of transmissivity of the three fractures.

	Confining pressure (psi)	**1 → 5 (5→1)** T (m^2/s)	**2 → 6 (6→2)** T (m^2/s)	**3 → 7 (7→3)** T (m^2/s)	**4→ 8 (8→4)** T (m^2/s)
211-2	1000	4.0×10^{-5}	3.0×10^{-5}	1.0×10^{-4}	1.3×10^{-4}
401-1	1100	2.6×10^{-7} (2.1×10^{-7})	2.8×10^{-7} (2.3×10^{-7})	4.2×10^{-7} (3.3×10^{-7})	3.8×10^{-7} (2.3×10^{-7})
143-4	2000	3.0×10^{-5}	7.5×10^{-5}	7.4×10^{-5}	5.5×10^{-5}

3.7.5 Future Work

Future work will involve comparing current laboratory measurements with field measurements of transmissivity to help understand if this measurement technique is realistically representing transmissivities measured in the field. In addition, some additional work is in process measuring the aperture of the natural

fractures to aid in numerical modelling. Finally, the large number of measurements of transmissivity in the lab will undergo further statistical testing to verify differences observed with flow path are significant.

3.8 Numerical Modeling of Previous Core Experiments

3.8.1 Motivation

We want to gain insight into laboratory experiments on fluid flow through fractured cores. Experiments are run by imposing flow *Q* between pairs of ports surrounding the core and measuring the pressure difference (DP). This is done at a series of confining pressures between 200 and 4500 psi. Typical flow rates used are 5, 10, 15, and 20 cm^3/s. Then we use DP and Q with Darcy's law to determine the transmissivity T of the flow paths.

Figure 3-19a and Table 3-6 summarize results from previous years' work for Core 211-2. After a preliminary "settling period", T does not vary with confining pressure, and the T dependence on Q closely conforms to Darcy's law. There are consistent T differences between port pairs, with flow paths 4-8 and 3-7 showing higher T than flow paths 1-5 and 2-6, suggesting that the fracture may have anisotropic transmissivity, as illustrated schematically in Figure 3-18b. The goal of the modeling study is to investigate this hypothesis.

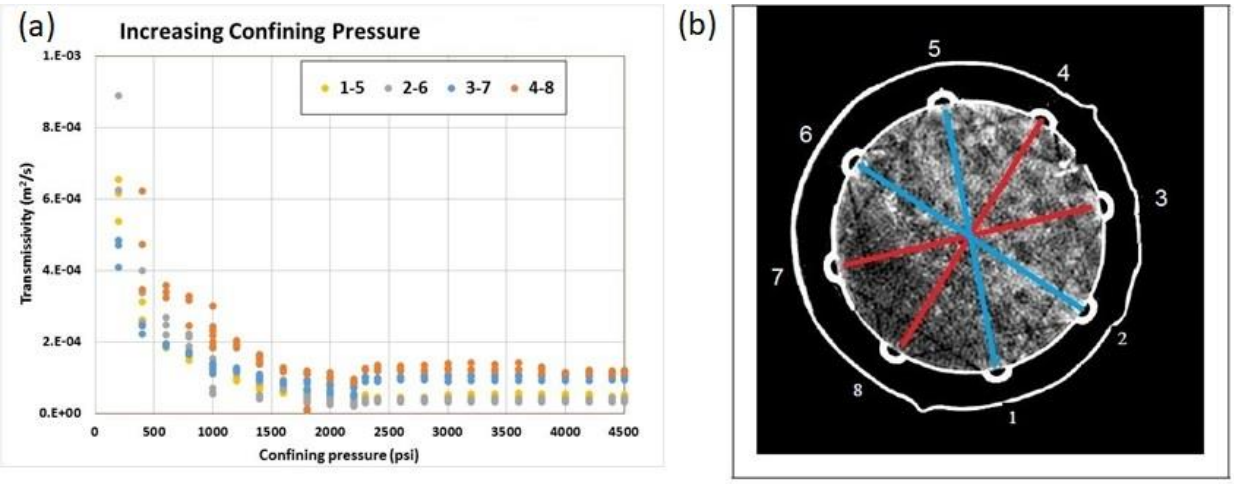

Figure 3-19. Results from previous year's lab experiments (Dobson et al., 2016, 2017; Zheng et al., 2018) on Core 211-2. (a) transmissivity T inferred from pressure difference DP between different port pairs. (b) schematic interpretation of T variations, with red indicating high-T flow paths and blue indicating low-T flow paths. Ports are labeled by number from 1 to 8. Note that in subsequent images the core is rotated so that Port 8 is on top.

Table 3-6. Summary of T values from previous years' studies on Core 211-2.

Port Pair	T (m^2/s)	Ratio T/T_{max}	Comment
4-8	1.3E-4	1.00	Maximum T
3-7	1.0E-4	0.77	High T
1-5	4E-5	0.31	Low T
2-6	3E-5	0.23	Minimum T

3.8.2 Data Used

The primary data used to develop the numerical model is the aperture distribution obtained by x-ray CT scanning the core, shown in Figure 3-20. The scan is composed of 512 x 512 measurements, at a spatial resolution 0.195 mm. The core itself, about 6 cm in diameter, is represented by a smaller number of measurements, 310 x 310. In the scan, measurements are ordered from left to right (I) and top to bottom (J). In order to plot the picture right-side up (by convention with Port 8 on top), a variable oppJ = -J is used. A threshold of 999 microns is applied, so any measurements greater than 999 are shown as 999. The port locations are visible in Figure 3-20. Ports are half-tubes with a diameter of 4.5 mm. The summary of T results from previous years are labeled on Figure 3-20, and detailed in Table 3-6.

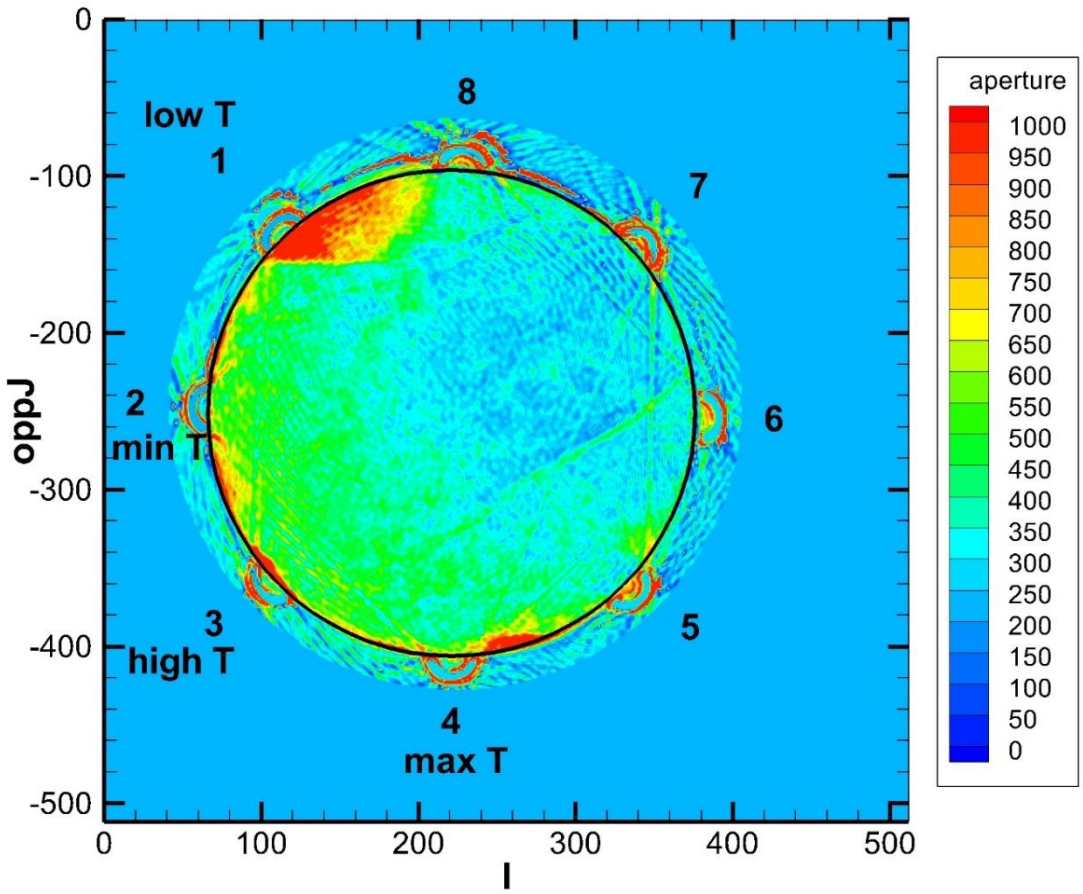

Figure 3-20. Core 211-2 scanned aperture distribution (microns) with a threshold of 999. The black circle is the interpreted edge of the core, which will be used for numerical model development, described below.

Figure 3-21 shows the distribution of apertures from the scan of Core 211-2. The arithmetic mean aperture is 292 microns. Note that values of 999 and 250 do not all represent actual measurements: 999 is the upper threshold and 250 is the background aperture outside the core. These values are omitted from averaging.

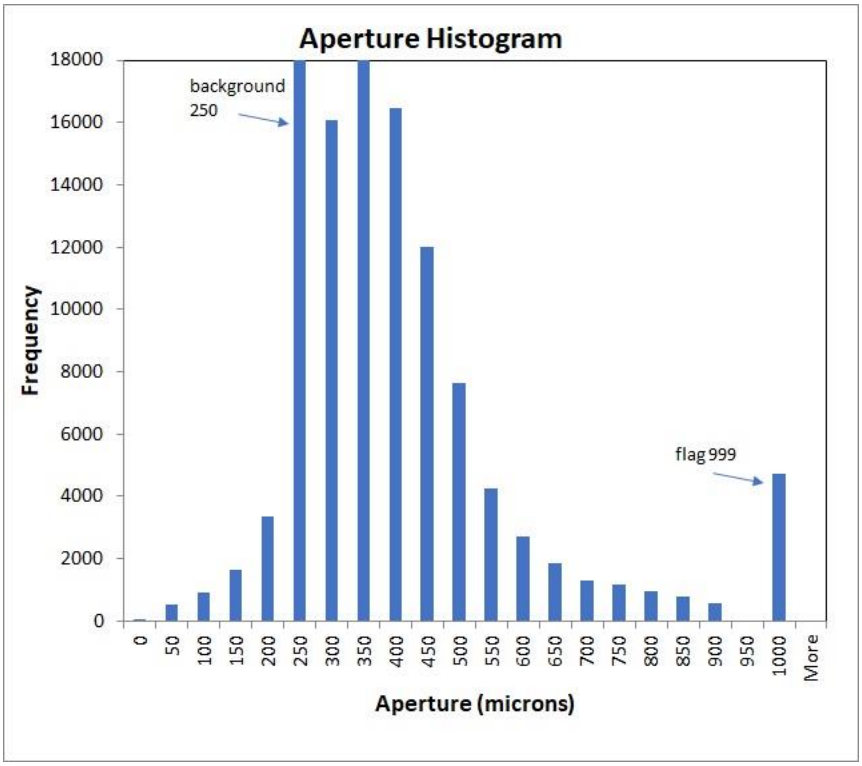

Figure 3-21. Aperture distribution for Core 211-2.

3.8.3 Model Development

3.8.3.1 General

The numerical simulator used is TOUGH3 with equation of state package EOS1, which considers a single-component (water). Here, we consider water as a single-phase liquid, flowing under isothermal conditions.Lab experiments were done at multiple confining pressures resulting in different effective stresses, with the presumption that the aperture distribution changes with confining pressure (effective stress). Here we just use one fixed aperture distribution, equivalent to one confining pressure. Furthermore, we just use one flow rate, Q = 10 cm^3/s (0.01 kg/s), since the lab experiments verified that DP was proportional to Q.

3.8.3.2 Create Grid

The scan represents the aperture distribution in the core with resolution of 0.195 mm, on a 310 x 310 grid. For computational efficiency, it was decided to use grid blocks 0.39 mm wide, on a 155 x 155 grid. The grid generator AMESH was used to create a two-dimensional regular rectangular grid with uniform thickness to represent the fracture. As described below, the variable aperture will be represented by a variable permeability field.

3.8.3.3 Assign aperture distribution as permeability field

Because the model grid resolution is half that of the scan, arithmetic averaging over 2 by 2 squares of scan measurements is done to create an aperture distribution for the model. Then the cubic law is used to convert aperture to a permeability modifier (PM) for each grid block. Specifically

$$PM = (b/b_{avg})^3$$

where b is the aperture for the model grid block, and b_{avg} = 292 microns is the average aperture.

After the permeability modifiers are applied, the model is trimmed to a circle shown in Figure 3-20. Ports are assigned as adjacent high-permeability grid blocks by visual inspection of Figure 3-20. The resulting model is shown in Figure 3-22.

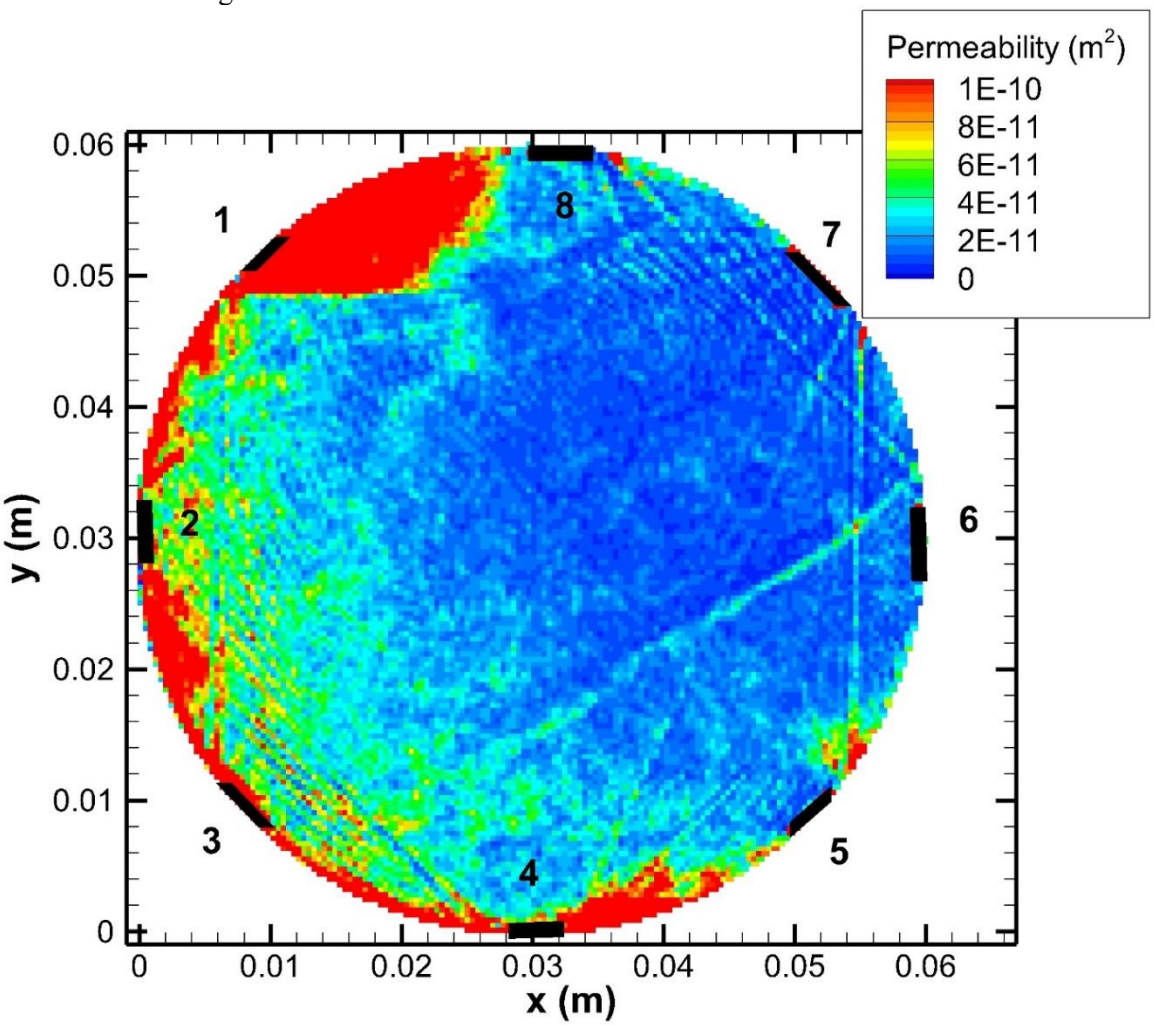

Figure 3-22. Permeability distribution for the numerical model of Core 211-2. Port locations are shown by black bars. Some of the high permeability pathways are X-ray CT artifacts.

Figure 3-23 shows the distribution of permeability modifiers, sorted from small to large over the 18,603 grid blocks of the model. Permeability modifiers range from approximately 0.01 to 30. A few grid blocks have the upper threshold permeability, which is shown by a permeability modifier of 40.

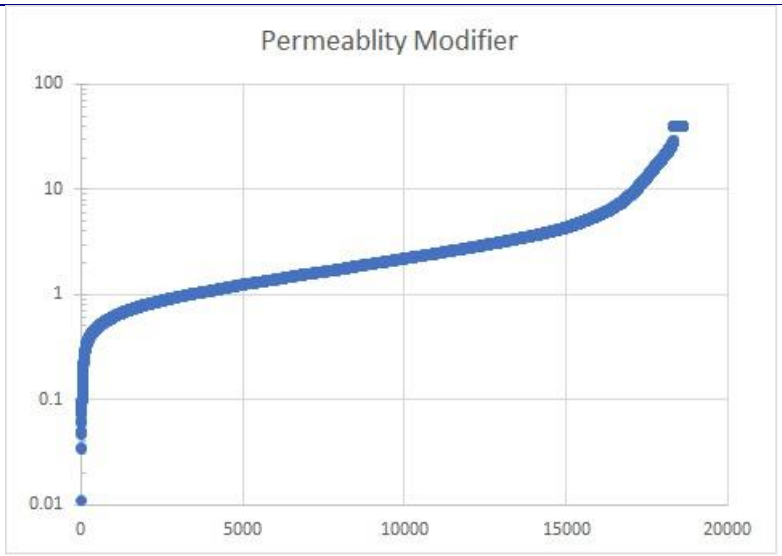

Figure 3-23. Distribution of permeability modifiers used to represent the variable aperture of Core 211-2.

3.8.3.4 Assign source and sinks to ports

Port locations are identified from Figure 3-20, and port grid blocks are given a separate material type in the TOUGH3 model. This material has a high porosity (0.99) and permeability (about 1000 times higher than the fracture permeability). Each port is about 10 grid blocks wide. The center grid block of each port is assigned as a source (ports 1, 2, 3, 4) or sink (ports 5, 6, 7, 8). The simulation period is divided into four time periods. During each period one pair of ports (1 and 5, 2 and 6, 3 and 7, 4 and 8) is assigned a positive flow rate of 0.01 kg/s at the source port and a negative flow rate of -0.01 kg/s at the sink port, with all other flow rates being zero for that time period.

3.8.3.5 Other properties

The porosity is set to 0.5 and rock compressibility is set to 1E-9 Pa^{-1}. The base permeability is calculated from the cubic law for the average aperture, and is 2E-12 m^2. For each grid block, base permeability is multiplied by the permeability modifier for that grid block.

3.8.4 Results

3.8.4.1 Pressure

In the laboratory experiments, typical pressure differences for a flow rate of 10 cm^3/s were less than 1000 Pa, whereas in the preliminary simulations with the numerical model they were about ten times greater. So, the first adjustment made to the model was to increase the base permeability and the port permeability each by a factor of ten. Unfortunately, the model would not run stably with such high port permeability. Therefore, the port permeability was returned to its original value (1E-9 m^2) and the base permeability was reduced to 1E-11 m^2. With these changes, the model runs stably and typical pressure changes are the same order of magnitude as obtained in the lab.

Plotting pressure as a function of time for the sources and sinks (not shown) indicates that steady state is achieved rapidly, within 0.01 s. Thus, each of the four time periods for the model, during which flow occurs for different port pairs, is set at 0.01 s. Figure 3-24 shows the pressure distributions at the end of each time period.

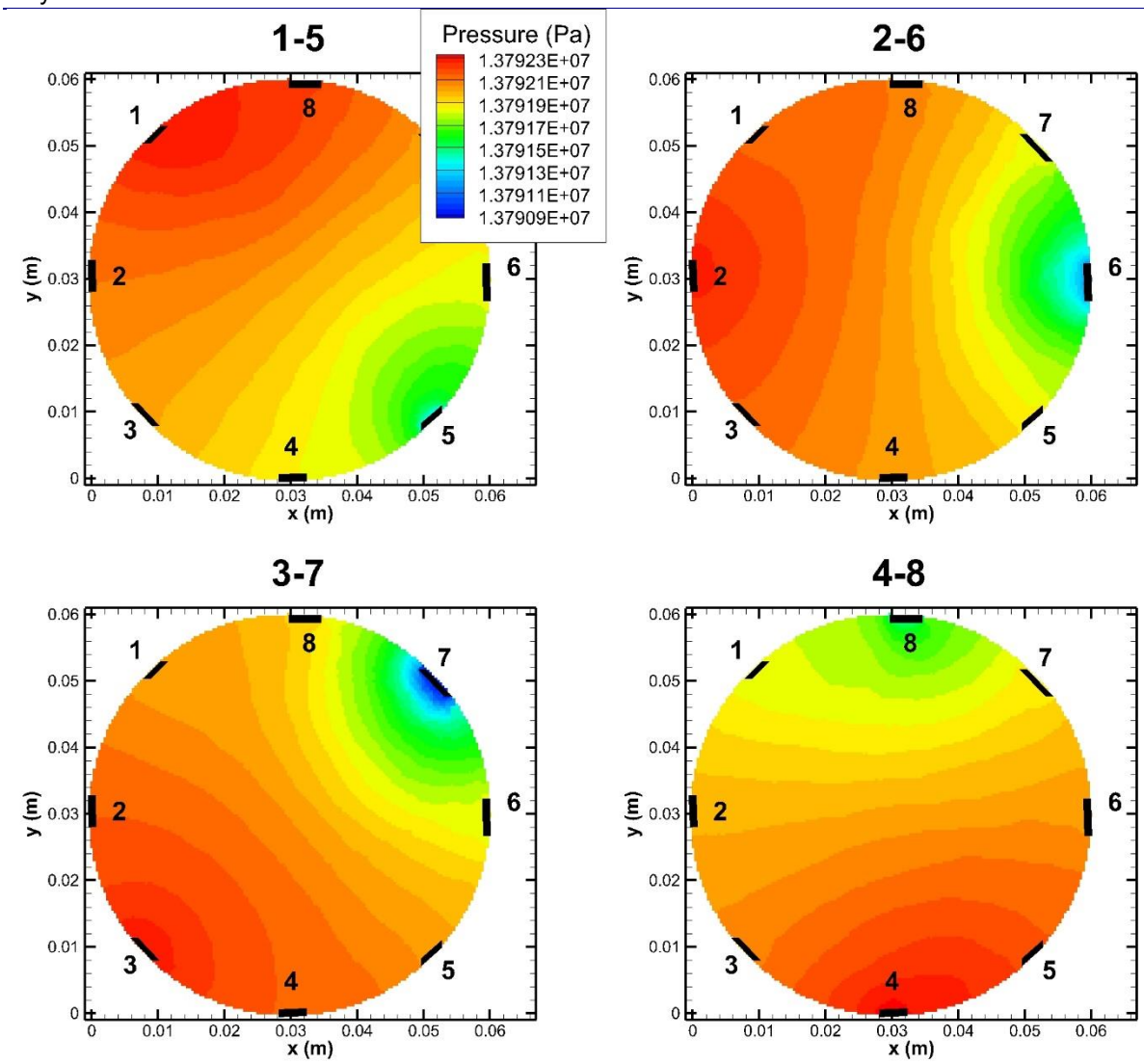

Figure 3-24. Modeled steady-state pressure distributions for the four different port pairs.

Table 3-7 summarizes the pressure differences (DP) for the four port pairs. Since DP is inversely proportional to transmissivity T, DP/DPmin = 1/(T/Tmax), which can be compared to lab values. There is reasonable agreement between model and lab for the high-permeability flow paths 4-8 and 3-7, but the model transmissivity for the low-permeability flow paths 1-5 and 2-6 is too high.

Table 3-7. Comparison of model and lab transmissivity results

Port Pair	Model DP (Pa)	Model DP/DPmin	Model T/Tmax	Lab T/Tmax
4-8	862	1.00	1.00	1.00
3-7	1385	1.61	0.62	0.77
1-5	927	1.07	0.93	0.31
2-6	1141	1.32	0.76	0.23

3.8.4.2 Flow field

It is valuable to examine the flow field across the fracture, to see what the T values inferred from the pressure difference represent. One way to plot the flow field is as a vector plot, but the great variation in flow magnitude near and far from ports makes it very difficult to interpret such plots. A better means of visualizing the flow field is by plotting streamtraces. Figure 3-25 shows the grid near Port 1. In this representation, grid block centers are at the intersections of the black lines. The blue circles identify grid blocks that represent the port, and the filled blue circle represents the source grid block. Streamtraces (red lines) are initiated along a line that spans the extent of the port. For each port pair, the same number of streamtraces are initiated.

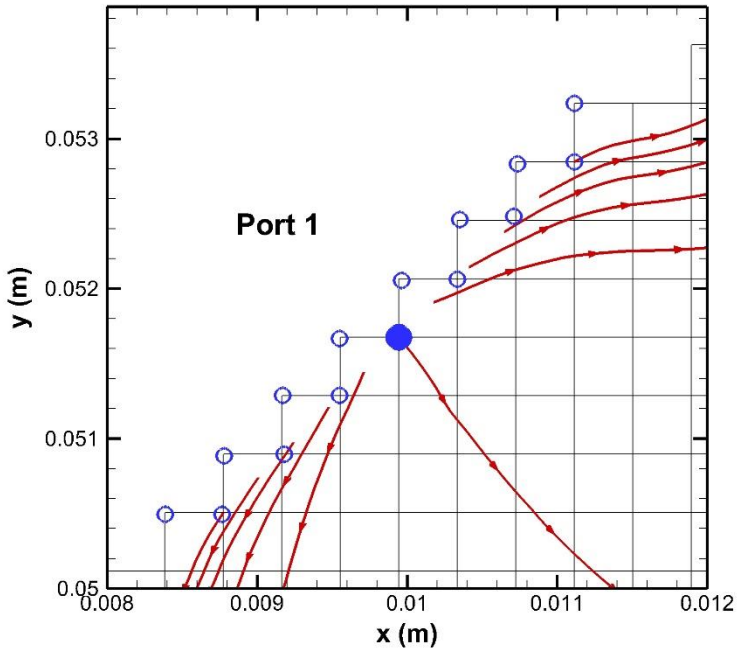

Figure 3-25. Detail of numerical grid around Port 1, illustrating how streamtraces are initiated.

Streamtrace plots are shown in Figure 3-26. The focusing of the streamtraces in the high-permeability portion of the core is apparent.

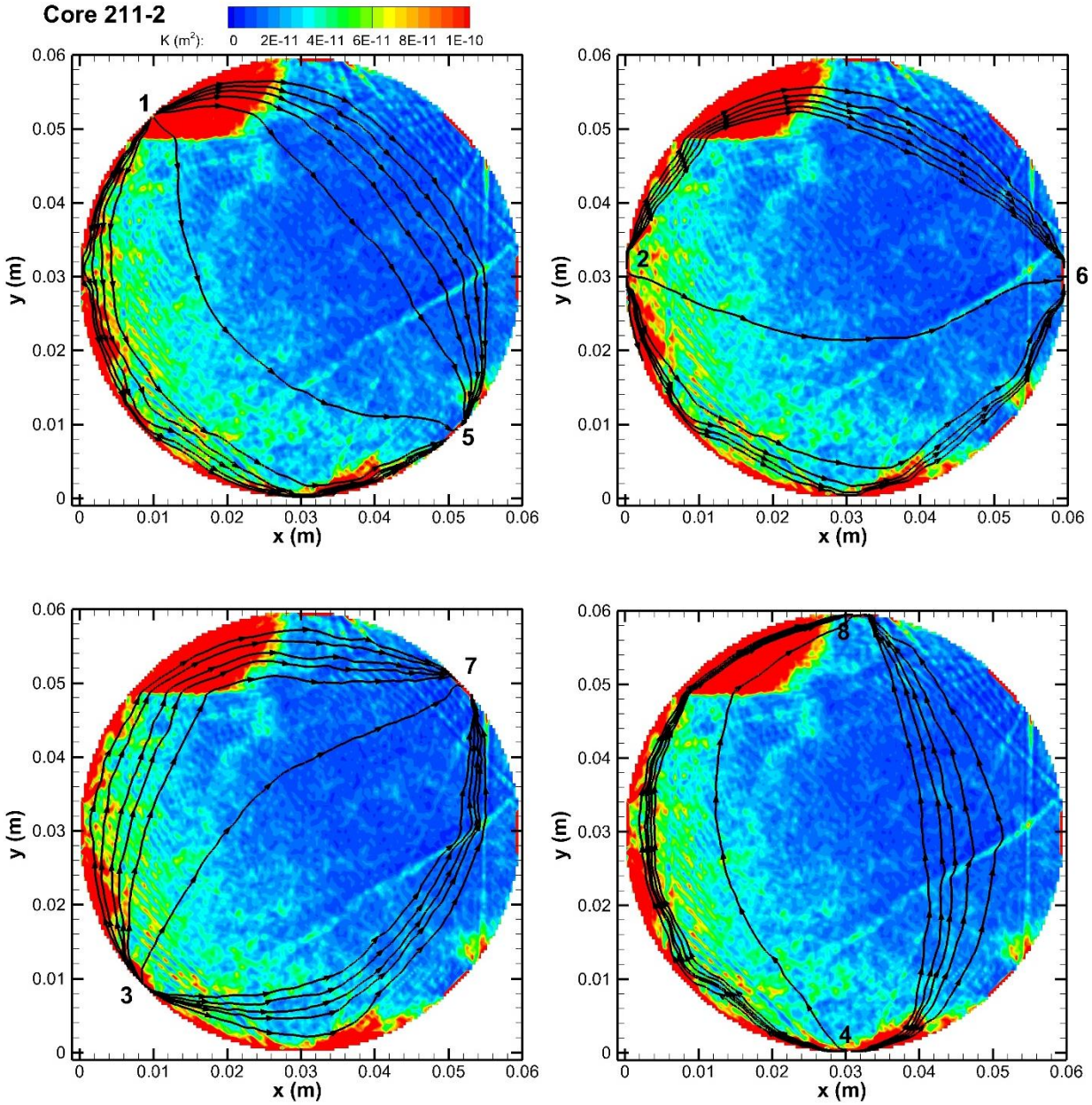

Figure 3-26. Streamtrace plots showing modeled flow field.

3.8.5 Discussion

The original premise to explain the variability in transmissivity T between different port pairs (Table 3-7) was that the fracture T field was anisotropic. Examination of the flow fields does not support the hypothesis that flow is controlled by an overall anisotropic transmissivity distribution, but rather by local heterogeneity. However, model results for T values for different port pairs are not completely consistent

with lab results (Table 3-7), so these conclusions must be seen as preliminary. An additional shortcoming of the model is that when a port is not being used for inflow or outflow during a given flow period, it still has a high permeability, and some of the flow paths near the outer edge of the core deviate from the path they should be taking and go through these high-permeability locations.

The model can be adjusted to try to better replicate lab results. Technical adjustments such as redrawing the black circle in Figure 3-20 that denotes the model outer boundary to include less of the very high permeability around the circumference of the core might be helpful, as will a more sophisticated representation of the ports. At a more conceptual level, the aperture distribution obtained by the scan might be decreased by a constant amount, to represent closing of the fracture due to increased confining pressure. Once the model better reproduces the lab results for transmissivity for various port pairs, its flow paths will be more reliable.

Because the model here is so much smaller than typical TOUGH3 models, which usually cover many meters or even many kilometers, care had to be taken to ensure that small spatial scales, short time scales, and small pressure differences were properly resolved. For example, in the main TOUGH3 output, not enough significant figures of pressure are shown to indicate that any change in pressure occurs when flow between ports is imposed. However, internally, TOUGH3 does use enough significant figures to properly calculate small pressure changes, and these are recorded in subsidiary output files.

3.8.6 Conclusion and Future Work

Numerical simulation of the laboratory experiments on flow through fractured cores demonstrated that the method works in principle, but model improvements are needed to make a compelling case that the model really captures the essence of lab behavior. Preliminary modeling results suggest that fracture anisotropy is not the dominant feature producing variable transmissivity values for flow between different port pairs, but rather local heterogeneity in the aperture distribution is responsible.

Technical and conceptual adjustments to the model, described in the previous section, will be carried out in an attempt to improve agreement between model and lab results.

Additionally, models will be developed of other cores whose aperture distribution has been scanned. Now that technical details involving creating models on these small spatial and time scales have been worked out, creating other models will be more efficient.

3.9 Overall Summary

In Section 3, we presented the results of investigations conducted by LBNL researchers in collaboration with the Collisional Orogeny in the Scandinavian Caledonides (COSC) scientific team. The research activities were conducted using the COSC-1 borehole as a testbed to evaluate the hydrology of a crystalline basement environment. This research is aimed at providing insights on the problem of nuclear waste disposal in crystalline formations. In June of 2019, the LBNL team deployed a unique borehole monitoring tool, called Step-rate Injection Method for Fracture In-situ Properties (SIMFIP), to measure real-time 3D mechanical deformation of rock within three intervals of the COSC-1 borehole. The following field tests were carried out: pressure buildup tests, pressure falloff tests, and constant flow rate tests for each of the three intervals. Two approaches were used to evaluate the stress conditions: an inversion of the displacement data, and a fully coupled numerical simulation of fracture stimulation and fluid flow using the distinct element code 3DEC. These analyses provided insights into the stress state for the borehole intervals, as well as how the fractures responded to hydraulic stimulation. Laboratory and modeling

investigations were conducted on COSC-1 core samples that correspond with the borehole intervals tested in the field. Future research activities include conducting modeling to assess far-field effects of the hydraulic stimulation of these intervals, additional rock property measurements on selected core samples, and obtaining new borehole televiewer images to better characterize the fractures that were opened at each of the three tested intervals with the application of the SIMFIP. Our collaborators at Uppsala University are conducting additional numerical simulations of the fracture flow tests. Preliminary results of these investigations were presented "virtually" at the 2020 EGU annual meeting (Basirit et al., 2020; Tatomir et al., 2020). The COSC team is currently drilling a new deep borehole (COSC-2), so there may be additional opportunities for conducting tests in this new well.

3.10 References

Basirat, F., Tsang, C.-F., Tatomir, A., Guglielmi, Y., Dobson, P., Cook, P., Juhlin, C., and Niemi, A. (2020) Analysis of flow and pressure data for the estimation of fracture generation and propagation – first model results from coupled hydromechanical experiments in COSC-1 borehole in deep crystalline rock, Åre, Sweden, EGU General Assembly 2020, Online, 4–8 May 2020, https://doi.org/10.5194/egusphere-egu2020-7914, 2020

Bieniawski, Z.T. (1989) Engineering rock mass classifications: a complete manual for engineers and geologists in mining, civil, and petroleum engineering.

Wiley-Interscience, 40–47. ISBN 0-471-60172-1.

Bossart, P., and Mazurek, M. (1991) Grimsel Test Site—structural geology and water flow-paths in the migration shear-zone. Nagra Tech Rep NTB 91–12, Nagra, Wettingten, Switzerland.

Bredehoeft, J.D., and Maini, T. (1981) Strategy for radioactive waste disposal in crystalline rocks. Science, 423 (4505), 293–296.

Brown, D. (1989) The flow of water and displacement of hydrocarbons in fractured chalk reservoirs. In: Fluid Flow in Sedimentary Basins and Aquifers. J. C. Goff and B. P. Williams, eds., Geological Society London, 201–218.

Chen, L., De'Haven Hyman, J., Lei, Z., Min, T., Kang, Q., Rougier, E., and Viswanathan, H. (2019) Effect of fracture density on effective permeability of matrix-fracture system in shale formations. In: Geological Carbon Storage: Subsurface Seals and Caprock Integrity, S. Vialle, J. Ajo-Franklin, and J.W. Carey, eds., AGU Geophysical Monograph 238, John Wiley & Sons, 137–146.

Cherry, J.A., Alley, W.M., and Parker, B.L. (2014) Geologic disposal of spent nuclear fuel – An earth science perspective. The Bridge, Spring 2014, 51–59.

David, C., Wassermann, J., Amann, F., Klaver, J., Davy, C., et al., (2018a) KG2B, a collaborative benchmarking exercise for estimating the permeability of the Grimsel granodiorite – Part 1: measurements, pressure dependence and pore-fluid effects, Geophysical Journal International, 215, 799–824.

David, C., Wassermann, J., Amann, F., Klaver, J., Davy, C., et al., (2018b) KG^2B, a collaborative benchmarking exercise for estimating the permeability of the Grimsel granodiorite-Part 2: modelling, microstructures and complementary data. Geophysical Journal International, 215 (2), 825-843.

Dessirier, B., Tsang, C.F., Hedayati, M., Lorenz, H., Juhlin, C., and Niemi, A. (submitted) A study of correlations of geophysical and geochemical logs with hydrogeologic features in a 2.5-km deep borehole in crystalline rock. Paper submitted for publication to Hydrogeology Journal.

Detournay, E., and Carbonell, E. (1997) Fracture mechanics analysis of the breakdown process in minifracture or leakoff test. SPE paper 28076, Soc. Pet. Eng. Prod. Facil., 12, 195–199.

Dobson, P., Tsang, C.F., Doughty, C., Ahonen, L., Kietäväinen, R., Juhlin, C., Rosberg, J.E., Borglin, S., Kneafsey, T., Rutqvist, J., Zheng, L., Xu, H., Nakagawa, S., and Nihei, K. (2017) Deep borehole field test activities at LBNL 2017. US DOE Spent Fuel and Waste Science and Technology, SFWD-SFWST-2017-000046, LBNL Report 2001043, 118 p.

Dobson, P., Tsang, C.-F., Kneafsey, T., Borglin, S., Piceno, Y., Andersen, G., Nakagawa, S., Nihei, K., Rutqvist, J., Doughty, C.,and Reagan, M. (2016) Deep borehole field test research activities at LBNL. US DOE Spent Fuel and Waste Science and Technology, FCRD-UFD-2016-000438, LBNL Report 1006044, 124 p.

Doughty, C., Tsang, C.F., Rosberg, J.E., Juhlin, C., Dobson, P.F., and Birkholzer, J.T. (2017) Flowing fluid electrical conductivity logging of a deep borehole during and following drilling: estimation of transmissivity, water salinity and hydraulic head of conductive zones. Hydrogeology Journal, 25, 501–517.

Follin, S., Hartley, L., Rhén, I., Jackson, P., Joyce, S., Roberts, D., and Swift, B. (2014) A methodology to constrain the parameters of a hydrogeological discrete fracture network model for sparsely fractured crystalline rock, exemplified by data from the proposed high-level nuclear waste repository site at Forsmark, Sweden. Hydrogeology Journal, 22, 313–331.

Guglielmi, Y., Cappa, F., Avouac, J.-P., Henry, P., and Elsworth, D. (2015) Seismicity triggered by fluid injection–induced aseismic slip. Science, 348(6240), 1224.

Guglielmi, Y., Cappa, F., Lançon, H., Janowczyk, J.B., Rutqvist, J., Tsang, C.F., and Wang, J.S.Y. (2013) ISRM Suggested Method for Step-Rate Injection Method for Fracture In-Situ Properties (SIMFIP): Using a 3-Components Borehole Deformation Sensor, in The ISRM Suggested Methods for Rock Characterization, Testing and Monitoring: 2007–2014, edited by R. Ulusay, Springer-Verlag, Wein, doi:DOI: 10.1007/978-3-319-07713-0.

Guglielmi, Y., Cook, P., Dobson, P., Nakagawa, S., Zheng, L., Niemi, A., Juhlin, C., Lorenz, H., Rosberg, J.-E., Dessirier, B., Tsang, C.-F., Tatomir, A., Basirat, F., Lundberg, E., Almqvist, B., Borglin, S., and Doughty, C. (2019) Crystalline Disposal R&D at LBNL: FY19 Progress Report. US DOE Spent Fuel and Waste Science and Technology, LBNL Report 2001221, 32 p.

Guglielmi, Y., Nussbaum, C., Rutqvist, J., Cappa, F., Jeanne, P. and Birkholzer, J. (2020) Estimating perturbed stress from 3-D borehole displacements induced by fluid injection in fractured or faulted shales. Geophys. J. Int., 221, 1684–1695.

Hadgu, T., Karra, S., Kalinina, E., Makedonska, N., Hyman, J.D., Klise, K., Viswanathan, H.S., and Wang, Y. (2017) A comparative study of discrete fracture network and equivalent continuum models for simulating flow and transport in the far field of a hypothetical nuclear waste repository in crystalline host rock. Journal of Hydrology, 553, 59–70.

Hedin, P., Almqvist, B., Berthet, T., Juhlin, C., Buske, S., Simon, H., Giese, R., Krauß, F., Roseberg, J.-E., and Alm, P.-G. (2016) 3D reflection seismic imaging at the 2.5 km deep COSC-1 scientific borehole, central Scandinavian Caledonides. Tectonophysics, 689, 40–55.

Itasca Consulting Group (2016) 3DEC, 3-Dimensional Distinct Element Code. Itasca Consulting Group, Minneapolis, MN.

Kakurina, M., Guglielmi, Y., Nussbaum, C., and Valley, B. (2019) Slip perturbation during fault reactivation by a fluid injection. Tectonophysics, 757, 140–152.

Kakurina, M., Guglielmi, Y., Nussbaum, C., and Valley, B. (submitted). Stress state estimation from fluid induced fault dislocation data. Paper submitted for publication to Tectonophysics.

Keusen, H.R., Ganguin, J., Schuler, P., and Buletti, M. (1989) Grimsel Test Site: Geology. NAGRA, Baden, Technical Report 87-14 (NTB 87-14E).

Lajtai, E.Z., Duncan, E.J.S., and Carter, B.J. (1991) The effect of strain rate on rock strength, Rock Mechanics and Rock Engineering, 24: 99. https://doi.org/10.1007/BF01032501

Lorenz, H., Rosberg, J.E., Juhlin, C., Bjelm, L., Almqvist, B.S.G., Berthet, T., Conze, R., Gee, D.G., Klonowska, I., Pascal, C., Pedersen, K., Roberts, N.M.W., and Tsang, C.F. (2015) COSC-1 –drilling of a subduction-related allochthon in the Palaeozoic Caledonide orogen of Scandinavia, Scientific Drilling, 19, 1–11.

Makedonska, N., Jafarov, E., Doe, T., Schwering, P., Neupane, G., and the EGS Collab team. (2020) Simulation of injected flow pathways in geothermal fractured reservoir using discrete fracture network model. Proceedings, 45th Workshop on Geothermal Reservoir Engineering, Stanford University, SGP-TR-216, 12 p.

Stephansson, O., Ljunggren, C. and Jing, L. (1991) Stress measurements and tectonic implications for Fennoscandia. Tectonophysics, 189, 317-322.

Tatomir, A., Basirat, F., Tsang, C.-F., Guglielmi, Y., Dobson, P., Cook, P., Juhlin, C., and Niemi, A. (2020) Coupled Hydro-Mechanical Modeling of Fracture Normal Displacement and Fluid Pressures during a SIMFIP (step-rate injection method for fracture in-situ properties) Test, EGU General Assembly 2020, Online, 4–8 May 2020, https://doi.org/10.5194/egusphere-egu2020-7387, 2020

Tsang, C.F., Rosberg, J.E., Sharma, P., Berthet, T., Juhlin, C., and Niemi, A. (2016) Hydrologic testing during drilling: application of the flowing fluid electrical conductivity (FFEC) logging method to drilling of a deep borehole. Hydrogeology Journal, 24, 1333–1341.

Wenning, Q.C., Berthet, T., Ask, M., Zappone, A., Rosberg, J.-E., and Almqvist, B.S.G. (2017) Image log analysis of in situ stress orientation, breakout growth, and natural geologic structures to 2.5 km depth in central Scandinavian Caledonides: Results from the COSC-1 borehole. Journal of Geophysical Research Solid Earth, 122, 3999–4019.

Witherspoon, P.A., Cook, N.G.W., and Gale, J.E. (1981) Geologic storage of radioactive waste: Field studies in Sweden. Science, 211 (4485), 894–500.

Witherspoon, P.A., Wang, J.S.Y., Iwai, K., and Gale, J.E. (1980) Validity of cubic law for fluid flow in a deformable rock fracture. Water Resour. Res., 16(6), 1016–1024.

Zhang, F., Damjanac, B., and Maxwell, S. (2019) Investigating Hydraulic Fracturing Complexity in Naturally Fractured Rock Masses Using Fully Coupled Multiscale Numerical Modeling. Rock Mech. Rock Eng. https://doi.org/10.1007/s00603-019-01851-3

Zheng, L., Deng, H., Nakagawa, S., Kim, K., Kneafsey, T., Dobson, P., Borglin, S., Doughty, C., Voltolini, M., Tsang, C.F., Dessirier, B., Wenning, Q., and Juhlin, C. (2018) Crystalline Disposal R&D at LBNL: FY18 Progress Report. US DOE Spent Fuel and Waste Science and Technology, LBNL Report 2001177, 71 p.

4. DISCRETE FRACTURE NETWORK MODELING

4.1 Introduction

In this section, we present two studies concerning the transport of solutes through crystalline rock. In the first study, we investigate the transport of waterborne substances in subsurface fractured bedrock. Many model-based studies assume fractures to be smooth planes, which is an acknowledged simplification. However, real-world fractures are known to have rough surface asperities. In our study, we account for fracture roughness by assuming textures with different connectivity structure and investigate how these impacts waterborne transport in bedrock. We demonstrate that this type of fracture roughness can control important features of flow and waterborne mass transport. Specifically, most of the mass will generally arrive later than expected when compared to a smooth fracture plane assumption. However, we also observe that a small percentage of mass can, under certain circumstances, arrive earlier than what would be expected if smooth fracture planes are assumed. This observation means that the assumption of smooth fracture planes should generally be considered a conservative simplifying assumption in the context of subsurface storage. Still, it is less likely to be accurate when considering early mass arrival. This study is in direct alignment with the current focus of the SKB task force Task 10 that is focusing on flow channelization in fracture media and supports crystalline international.

In the second study, we investigate the relative impact of advective transport compared to retention due to matrix diffusion. Flow and solute transport through low-permeability fractured media at short time scales is generally determined by fractures and the interconnected networks that they form. However, at longer time scales, matrix diffusion, where solutes are exchanged between flowing regions (fractures) and non-flowing regions (matrix) via molecular diffusion, also influences solute transport. A long-standing question in this area of research is the relative impact of matrix diffusion on power-law scaling in the tails of the solute transport breakthrough curve, which are observed in field and laboratory experiments. While classical theory requires that matrix diffusion produces a decay rate of time to the -3/2 power, deviations have also been observed. We address this question through the development of a new theory that elucidates how interactions between two critical physical processes (advection and matrix diffusion) can produce either the classical -3/2 decay rate or alternative decay rates based on two dimensionless parameters. Our theoretical predictions are validated against particle tracking simulations using a high-fidelity three-dimensional discrete fracture network simulator. Matrix diffusion is considered a front-line defense for the retardation of radionuclides. This work thus directly supports GDSA crystalline work, which is concerned with the effectiveness of matrix-diffusion for the retardation of radionuclides.

4.2 Advective Transport in Discrete Fracture Networks with Connected and Disconnected Textures Representing Internal Aperture Variability

4.2.1 Introduction

Analyses of flow and transport in sparsely fractured rock is important for several applications, including understanding how bedrock environments function as barriers to contaminant migration. This is especially relevant for applications such as long-term storage of spent nuclear fuel in subsurface repositories, where crystalline rocks are considered particularly favorable due to their geological stability, low fracture intensity, and low advective flow rates, combined with strong hydrogeochemical retention properties (Cvetkovic et al., 1999; Tsang et al., 2015; Tsang & Neretnieks, 1998). This is because the natural geological environment can delay transport of radionuclides by retention processes, allowing for more time for decay processes to occur, and thereby limiting release to the biosphere. However, due to the geological complexity of fractured bedrock, there are still significant challenges in understanding the effects of heterogeneity on fluid flow and solute transport (Neuman, 2005; Tsang et al., 2015).

Model-based investigations of flow and transport in sparsely fractured rock generally adopt a discrete fracture network (DFN) approach because it is well-adapted for numerical representation of the geometric complexity of fractures (Cacas et al., 1990; de Dreuzy et al., 2012; Frampton & Cvetkovic, 2010, 2011; Hyman et al., 2015, 2016; Lang et al., 2014; Long et al., 1982; Maillot et al., 2016). A key to modeling advective-dispersive transport in fractured rock is adopting a Lagrangian framework which involves quantifying pathway travel times and another quantity denoted as *the hydrodynamic control of retention* (Cvetkovic et al., 1999, 2004). Both of these quantities strongly depend on flow channeling, which in turn depends on the underlying heterogeneity in hydraulic and material properties of fractures and the rock matrix. The hydrodynamic control of retention is useful for applications because it quantifies the flow-dependence of solute retention properties (Cvetkovic & Frampton, 2010, 2012; Frampton & Cvetkovic, 2007a, 2007b; Painter et al., 2008).

Fractures have significant variability in their aperture structure because of surface roughness (Brown, 1987; Brown et al., 1995; Hakami & Larsson, 1996; Nicholl et al., 1999; Thompson & Brown, 1991) which is caused by different mechanical and geochemical generation processes (Aydin et al., 2006; Pollard & Aydin, 1988). Studies indicate internal fracture variability structure may follow power-law distributions (Brown & Scholz, 1985; Pyrak-Nolte et al., 1992) or lognormal distributions (Johns et al., 1993; Keller, 1998; Thörn & Fransson, 2015). However, most DFN models generally assume constant hydraulic properties (aperture, permeability or transmissivity) within the plane of individual fractures, typically not due to model limitations, but rather because of a lack of suitable field information. This reflects the challenges involved in measuring fracture aperture and its variability at multiple scales for in-situ field conditions.

Several studies have shown that textures with heterogeneous connectivity structures can strongly impact flow channeling both in porous media (Fiori et al., 2010; Gotovac et al., 2009; Vasco et al., 2016; Zinn & Harvey, 2003) and in single fractures (Brown, 1987; Detwiler & Rajaram, 2007; Nicholl et al., 1999; Zou et al., 2015, 2017b). Relatively few studies have investigated effects of internal fracture variability in networks of fractures, with a range of results indicating minor to notable effects on transport (Cvetkovic & Frampton, 2010; de Dreuzy et al., 2012; Frampton et al., 2018; Makedonska et al., 2016; Painter, 2006; Zou et al., 2017a). Thus, the effects of internal fracture variability on flow and transport in fracture networks is not fully understood, especially for cases where the internal fracture variability is represented by textures that have a strong connectivity structure.

The main aim of this work is to investigate how internal fracture variability with different connectivity structure impacts flow and transport in random discrete fracture networks. Two scales of heterogeneity are conceptualized, one at the scale of individual fractures and another at the scale of the network consisting of multiple fractures. At the single-fracture scale, different textures are used to describe permeability (or aperture) of the fracture, so that each fracture has an internal variability. This corresponds to heterogeneity at a local scale. At the scale of the DFN, the network geometric and topological structure also causes heterogeneity, which here is denoted as a network-scale heterogeneity. This generally originates from variability in fracture orientations, lengths, and densities. Thereby, the overall flow and transport behavior through the system will generally depend on combined effects of the small-scale and large-scale heterogeneities.

Then, the specific objectives are to investigate to what extent local-scale versus network-scale heterogeneity control flow and transport. We expect local-scale heterogeneity and connectivity structure within individual fractures to exert dominant control on flow and transport provided the fracture network is sufficiently simple, i.e. corresponding to a sufficiently small number of fractures with few intersections. On the other hand, we expect large-scale heterogeneity and topological structure of the network to exert dominant control on transport for sufficiently complex networks, i.e. for a sufficiently large number of fractures and fracture intersections.

This is investigated by performing Monte Carlo sampling of DFN realizations, where internal fracture variability is accounted for and several DFN domain sizes are considered (Table 4-1). Different textures

are used for representing internal variability and are considered with a range of correlation lengths relative to fracture length, which serves to control local-scale heterogeneity and connectivity structure of individual fractures. Specifically, we adopt the approach developed by Zinn & Harvey (2003) for creating a triad of textures with distinguished classes of connectivity structure, but which preserve critical common statistical properties, enabling fair comparisons. The texture structures are generated from a multi-variant Gaussian distribution (Section 4.2.2.1), where one texture case corresponds to a structure with medium values of permeability being well-connected (denoted as the Gaussian case), another with high values being well-connected (the Connected case), and a third with low values being well-connected (the Disconnected case). The different domain sizes correspond to an increasing number of fractures and fracture intersections, thereby representing an increasing complexity in network-scale heterogeneity and structure.

Table 4-1. Simulation cases

Domain size, label	**DS 1**	**DS 2**	**DS 3**	**DS 5**	**DS 7**
Domain size, LxLxL (m^3)	1x1x1	2x2x2	3x3x3	5x5x5	7x7x7
Fracture orientation (rad)	Uniform in range (0, 2π)				
Fracture size (m^2)	Constant LxL = 2x2				
Texture types for fracture variability	Constant, Gaussian, Connected, Disconnected				
Mean and st. dev. of aperture (m)	1e-4, 6.9e-5				
Mean and st. dev. of permeability (m^2)	8.3e-10, 2.5e-9				
Correlation lengths, λ (m)	0.05, 0.15, 0.25, 0.5				
Simulation cases per domain size	13 (=3 textures x 4 corr lengths + 1 const case)				
Realizations per sim case*	162	124	63	44	43
Average fractures per sim case	2.09	4.26	7.13	21.82	45.46
Average intersections per sim case	1.09	4.01	10.65	42.57	59.57
Average intersections per fracture	0.52	0.94	1.49	1.95	1.31

* After removal of non-connected (non-percolating) DFNs

4.2.2 Modeling Approach

Flow and transport are modelled through interconnected fracture networks using the discrete fracture network (DFN) approach where fractures are explicitly represented as *N-1* dimensional objects in *N* dimensional space; specifically, fractures are 2D planes in a 3D domain. Every stochastically generated fracture is assigned a location, shape, size, orientation, and permeability on the basis of user-assigned probability distributions. For the purpose of this study, uniformly distributed orientations are used, and fractures size is constant (Table 4-1). The fractures connect and form a network through which flow and transport is simulated. A mesh is generated on the DFN and a discretization of the governing equations for flow and transport are numerically integrated thereon.

The computational suite dfnWorks (Hyman et al., 2015) is used to generate the DFN, solve the steady-state flow equations, and determine transport properties through the system. dfnWorks uses a feature rejection algorithm for meshing (FRAM) (Hyman et al., 2014) to generate three-dimensional fracture networks and the LaGriT meshing toolbox to generate conforming Delaunay triangulation of the DFN. The parallelized subsurface flow and reactive transport code PFLOTRAN (Lichtner et al., 2015) is used to numerically integrate the governing flow equations for steady state flow. An extension of the Walkabout particle tracking method (Makedonska et al., 2015; Painter et al., 2012) is used to determine pathlines through the

DFN and simulate solute transport. Further details of the suite, its abilities, applications, and references for detailed implementation can be found in (Hyman et al., 2015).

4.2.2.1 Internal Fracture Aperture Variability

One of the key aspects of dfnWorks is the detailed control one has over the mesh resolution within a fracture. This feature is critical for the focus of this study, which is characterizing the effects of aperture variability on upscaled transport properties. To account of this variability in the simulations, the aperture of each fracture is represented as a stationary random field and variable aperture values are assigned to the nodes of the Delaunay triangulation of each fracture. In dfnWorks, FRAM (Hyman et al., 2014) is used to create a mesh that is composed of triangular elements that conform to the lines of intersection on each fracture. The dual mesh of the Delaunay triangulation is a Voronoi tessellation of the fracture, which is the mesh used by PFLOTRAN to obtain the steady-state distribution of pressures and volumetric flow rates in the DFN. The variable aperture values are assigned to the nodes of the Delaunay triangulation, which are the cells centers of the Voronoi tessellation. Geometrically, these Voronoi cells are two-dimensional, but computationally they are three-dimensional control volumes. The volume of each control cell is the surface area of the two-dimensional Voronoi cell multiplied by the aperture assigned to node at the cell center. We select a sufficiently small mesh resolution such that correlation lengths in random field are properly resolved. Moreover, we use a uniform sized mesh. We consider several correlation lengths, as described below, and for consistency we use the same mesh size for all simulations being the one that resolves the smallest correlation lengths, i.e., the finest resolution.

It is cumbersome to create a correlated multi-variant Gaussian field on an unstructured mesh. There are several methods to do so, such as sequential Gaussian sampling and Kriging, but these methods scale poorly with a large number of nodes in the mesh, which is the case here. To address this issue, we developed an efficient method to generate these fields using a modification of the methods of Hyman & Winter (2014), which was designed to stochastically generate three-dimensional pore spaces. Let f denote the triangulation of a fracture. First, a realization of a random field u is created on f. Independent identically distributed (i.i.d.) random variables sampled from a continuous uniform distribution on the closed interval [0, 1] are assigned to every node in f. Then u is convolved with a symmetric multi-variant Gaussian G with standard deviation σ^2 to create a correlated random topography T,

$$T = \int df\, G(\sigma^2) * u \tag{4-1}$$

where $*$ denotes convolution. The correlation length of the field T depends on σ^2 and the central limit theorem ensures that T is a multi-variant Gaussian field.

However, the numerical convolution of the field u with the Gaussian kernel is challenging on an unstructured mesh. We address this issue by generating a structured Cartesian grid with uniform cell size on a rectangular plane with dimensions slightly larger than the fracture under consideration, let us call this g. The grid resolution of g is the same as the mesh resolution on the f. Every node in g is assigned an i.i.d. random variable sampled from a continuous uniform distribution on the closed interval [0, 1], call this v. Let $\hat{v}$ and $\widehat{G(\sigma^2)}$ denote the Fourier transform of v and $G(\sigma^2)$, where the latter is defined on g. Recall that point wise multiplication in Fourier space corresponds to convolution in Fourier space. Therefore, the product of these transformed fields in Fourier space is equivalent to convolution in real space and we can obtain T_g on g by

$$T_g = F^{-1}[\widehat{G(\sigma^2)} \cdot \hat{v}] \tag{4-2}$$

where F^{-1} denotes the inverse Fourier transform. The resulting field T_g is projected π onto the f (the unstructured mesh), π: $T_g \rightarrow$ T to assign a value of the correlated multi-variant Gaussian field to every node in f.

In practice the projection is performed using barycentric interpolation and a fast Fourier transform is used to map the values into Fourier space, which is possible as g is a rectangle discretized by a structured Cartesian grid with uniform resolution. The method is efficient for both single fractures, because no conditionally sampled values need to be generated, as in sequential Gaussian sampling or Kriging, and each field can be created independently and in parallel. The latter is possible because we do not constrain the correlated multi-variant Gaussian fields to align at intersections.

Using the field T we then generate three different correlated structures by applying the methods of Zinn & Harvey (2003). These methods are agnostic to whether the fields are defined on a structured or unstructured mesh. First, T is transformed to a standard normal $Y_1 \sim N(0,1)$, i.e. with zero mean and unit variance. Note that this does not change the correlation length of the field. Then the absolute value of Y_1 is taken, $Y^* = |Y_1|$. This transformation shifts the extreme values (high and low) to be high values. Values close to the zero become low values.

Thereafter, the PDF of Y^* is converted to a univariate Gaussian distribution by mapping the CDF of Y^* to a standard normal pointwise using the transformation

$$Y_2 = \sqrt{2}\,\mathrm{erf}^{-1}\left(-1 + 2\,\mathrm{erf}\frac{Y^*}{\sqrt{2}}\right) \tag{4-3}$$

This transformation slightly changes the correlation length of the field. However, the change is consistent and equal to 1.68, and Y_2 is modified by this factor in order to preserve correlation length (Zinn & Harvey, 2003). The third field Y_3 is obtained by reflecting Y_2 across 0.

Aperture values are assigned as $b_i = Exp(Y_i)$ for the three fields *i*. The field b_1 is then referred to as the Gaussian texture, b_2 as the Connected texture, and b_3 as the Disconnected texture. In the Gaussian texture, medium values of aperture (or permeability) in the field are well-connected, in the Connected texture, high values are well-connected, and in the Disconnected texture, low values are well-connected.

4.2.2.2 Flow and Transport Simulation

We consider the steady-state flow of an isothermal single-phase fluid that fully saturates the DFN. Flow within each Voronoi control volume in the DFN is modelled using Darcy's law

$$q = -k(x) \cdot \nabla P \tag{4-4}$$

where, $q = Q/A$ (L/T) is specific discharge, Q (L^3/T) volumetric flow rate, A (L^2) cross-sectional area, P (Pa) pressure, and k (L^2) permeability at the cell center x, which we assume to be determined by the cubic law

$$k(x) = b(x)^2/12 \tag{4-5}$$

Note that this dependence of permeability on the aperture implies that variations in the aperture field are amplified in the permeability field. Darcy's Law (4) along with conservation of flow

$$\nabla \cdot Q = 0 \tag{4-6}$$

is used to derive an elliptic equation for pressure throughout the entire domain

$$\nabla \cdot (A(x)b(x) \cdot \nabla P) = 0 \tag{4-7}$$

A hydraulic gradient in the DFN along the x-axis is created by applying Dirchelet boundary conditions on the x boundaries of the domain (Figure 4-1). No flow boundary conditions are applied along y and z boundaries. Through the solution to the previous equation and prescribed boundary conditions one obtains the volumetric flow rates throughout the domain. The methods of Makedonska et al. (2015) and Painter et al. (2012) are used to obtain the Eulerian velocity field $u(x)$ throughout the network and conduct particle tracking.

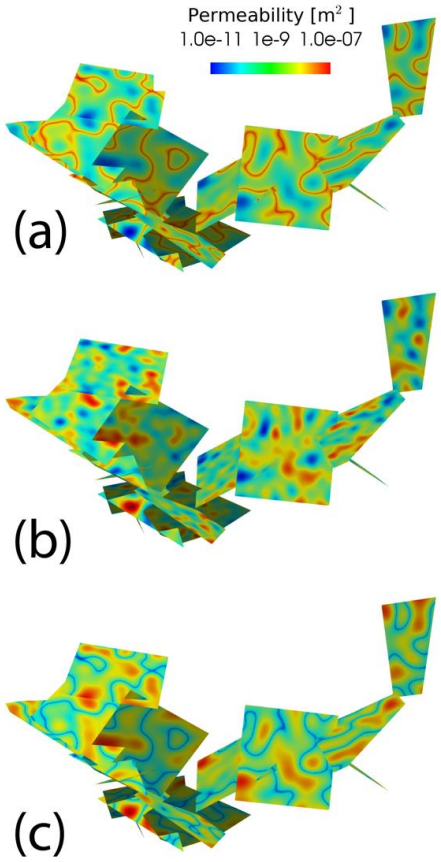

Figure 4-1. Example of a DFN realization for domain size DS7 (7x7x7 m^3). Showing the (a) Connected, (b) Gaussian, and (c) Disconnected texture cases, all cases with correlation length λ=0.25 m.

Transport through the network is conceptualized by a stochastic Lagrangian approach following Cvetkovic et al. (1999); Cvetkovic & Dagan (1994). A passive solute is represented by a plume of indivisible, inert particles that follow the advective flow field obtained by particle tracking through the DFN. We denote the ensemble of particles as Ω where each particle has a unique initial position along the inflow boundary $x_0 = (0, y, z)$. The pathline of a particle starting at x_0 is given by the trajectory equation

$$\frac{\mathrm{d}}{\mathrm{d}t}x(t,x_0) = v(x(t,x_0)) \tag{4-8}$$

where the Lagrangian velocity $v(x(t,x_0))$ is given in terms of the Eulerian velocity $u(x)$ as

$$v(x(t,x_0)) = u[x(t,x_0)]. \tag{4-9}$$

The transport time τ of a particle to exit the domain is given by the first passage time

$$\tau(x_0) = \min_t \text{ s.t. } [\, x(t,x_0) > L \,] \tag{4-10}$$

where L is the length of the domain. The cumulative distribution of travel times for all particles in a DFN is then given by

$$\Psi(t) = \int \mathrm{d}\Omega \, H[t - \tau(x_0)] \tag{4-11}$$

where $H[\cdot]$ is the Heaviside function. At fracture intersections a complete mixing rule is applied where the number of particles exiting in a given direction is proportional the outgoing flux (Berkowitz et al., 1994).

4.2.3 Simulation and Configurations

Multiple DFN realizations are generated in five domain sizes (DS), where each increase in domain size corresponds to an increasing number of stochastically generated fractures and fracture intersections (Table 4-1). For each domain size, the three texture cases describing internal variability of permeability within the fracture plane are considered. A fourth case where all fractures have a constant permeability is used as a reference case. The three textures have the same mean and variance and the permeability values adhere to the same log-normal distribution, but the textures differ in connectivity structure, as described in Subsection 2.2.2.1. An example realization of the DFN at domain size DS7 with the three texture cases is shown in Figure 4-1.

For each texture case, four correlation lengths are considered (Table 4-1). Fractures have a constant size, representing squares of 2x2 m2 (unless trimmed by the domain boundary), hence correlation lengths correspond to 1/40, 2/40, 5/40 and 10/40 of the fracture length scale. The small correlation length corresponds to a structure with very small-scale variability and the largest to a structure with large scale variability relative to the size of the fractures. This amounts to 13 simulation cases per domain size, or 65 in total. For each case, multiple DFN realizations are performed, typically ranging between 43 and 162 (Table 1-1), yielding a total of approximately 6000 DFN simulations.

For each realization, a constant generic hydraulic gradient along the *x*-axis is assumed and the steady-state flow solution is computed, and thereafter particle tracking is conducted on the resulting flow field. Particles are injected uniformly along each fracture intersecting the inflow boundary and tracked to the outflow boundary. Travel times are logged, yielding a set of arrival times for that realization. The travel times from multiple realizations computed in this way are then collected into a data set, which represents an aggregate of several samples out of the ensemble of possible realizations. The travel times of the aggregated data set

are then analyzed in terms of cumulative arrival time distributions and sample statistics (median and percentiles).

Travel time comparisons are made between the different textures for different correlation lengths and domain sizes (corresponding to different number of fractures and intersections in the network). Note the three textures and the constant permeability reference case are assigned to each realization of the DFN. Thus, for a given DFN realization, effects of the different textures can be compared since the underlying network is the same. The comparison is conducted by normalizing the travel times of the cases with variable texture by the corresponding case with constant permeability, thus enabling consistent comparisons between cases.

4.2.4 Results

Resulting empirical cumulative arrival time distributions (CDFs) and the complement of the cumulative distributions (CCDFs) are impacted by the textures representing internal fracture variability (Figure 4-2; only showing selected cases). The spread in arrival times for the case without texture (solid black) is due solely to the structure of the DFN because all fractures have the same constant permeability. Units are omitted because the DFN and boundary conditions are generic and the focus here is on relative differences between cases.

The increase in domain size delays travel times and increases the spread and variability in arrival times (Figure 4-2). Regardless of correlation length and domain size, the Connected case (dash-dotted red) has consistently earliest arrival times, the Disconnected case (dashed green) has latest arrivals, and the Gaussian case (dotted blue) resides in between. This behavior is in agreement with previous studies of 2D porous media, single fractures, and a synthetic four-fracture system (Frampton et al., 2018; Gotovac et al., 2009; Zinn & Harvey, 2003). Also, the texture cases have greater variability in arrival times compared to the Constant reference case, especially for larger correlation lengths (Figure 4-2b,d).

The CCDFs shown in Figure 4-2 highlight the behavior of late particle arrivals, which is more prominent for the large domain size DS7 (Figures 4-2c and 4-2d). As correlation length increases, the density of late arrivals increases slightly, especially for the Disconnected texture case. The Gaussian case yields slightly lower densities of late arrivals, followed by the Connected case and Constant case, which have even lower densities of late arrivals.

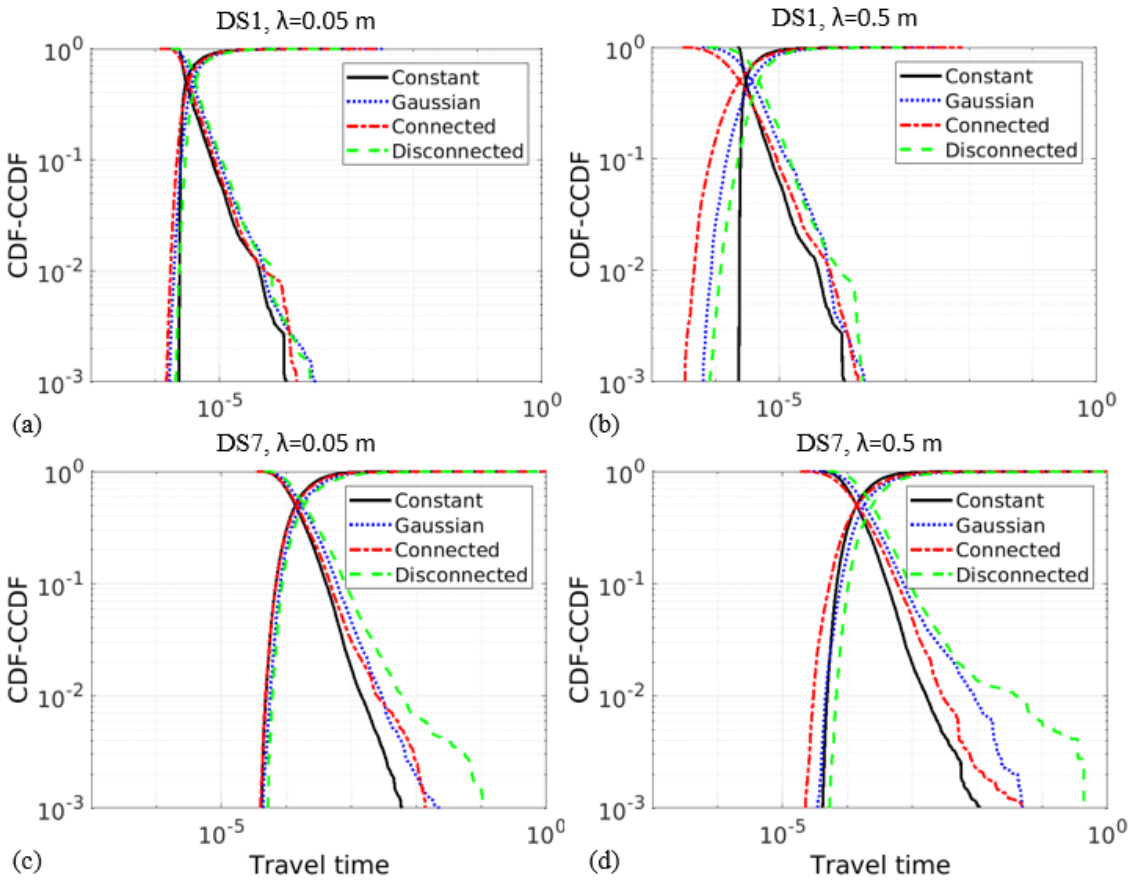

Figure 4-2. Cumulative and complement of the cumulative travel time distributions for the different texture cases from selected simulation cases. (a) Domain size DS1 with correlation length λ=0.05 m, (b) DS1 with λ=0.5 m, (c) DS7 with λ=0.05 m, and (d) DS7 λ=0.5 m. Units for travel times intentionally omitted, see main text.

Normalized median travel times versus domain size for all correlation lengths are shown in Figure 4-3 and Figure 4-4. The normalization is achieved by dividing the median travel time for each texture case with the median travel time of the corresponding constant reference case. Thereby, the resulting values indicate the relative deviation with respect to the reference case, where values less than unity indicate transport occurs faster than the corresponding case with constant permeability. This enables a clear comparison of the effects of texture and their different connectivity structure while accounting for the structure of the underlying DFN realization and focusing specifically on bulk (50%) mass arrival.

The normalized median travel times demonstrate the general consistency expected from previous studies, where the Connected case has shortest travel time, followed by the Gaussian case, and the Disconnected case has longest travel time (Figure 4-3). This is consistent for these network simulations regardless of domain size and correlation length. For all texture cases, the smallest correlation length λ=0.05 m is generally closest to unity (Figure 1-3a), and the largest correlation length λ=0.5 m is generally farthest from unity (Figure 4-3d), with correlation lengths λ=0.15 m and λ=0.25 m (Figure 1-3b and Figure 1-3c) generally residing in between.

The Connected texture case exhibits normalized median travel times which are below unity, i.e. indicating transport is faster than the Constant case (Figure 4-4a). This occurs for domain sizes DS1 to DS5 and correlation lengths λ=0.15 m to λ=0.5 m, where the travel times are typically about 80-95% of the

Connected texture. For the smallest correlation length λ=0.05 m, and, however, the median times are just above unity, typically about 1.05 to 1.1 times greater than the Constant case. Also, the Connected texture displays a convergence towards or just above unity for all correlation lengths as domain size increases to DS7.

The Gaussian texture cases have normalized median travel times between 1.1 to 1.3 times greater than the Constant case considering all correlation lengths (Figure 4-4b). For this texture, correlation length generally has little impact on median travel times for a given domain size, although the largest correlation length generally has largest median time.

The Disconnected texture cases have normalized median times from about 1.3 to over 1.7 times greater than the Constant case (Figure 4-4c). There is notable spread for different correlation lengths, where the small correlation lengths have shortest median travel times and the large correlation lengths have longest times. Also, there is a tendency for the times to increase with increasing domain size, and the largest deviation from the reference case is obtained for correlation lengths λ=0.25 m and λ=0.5 m at DS7.

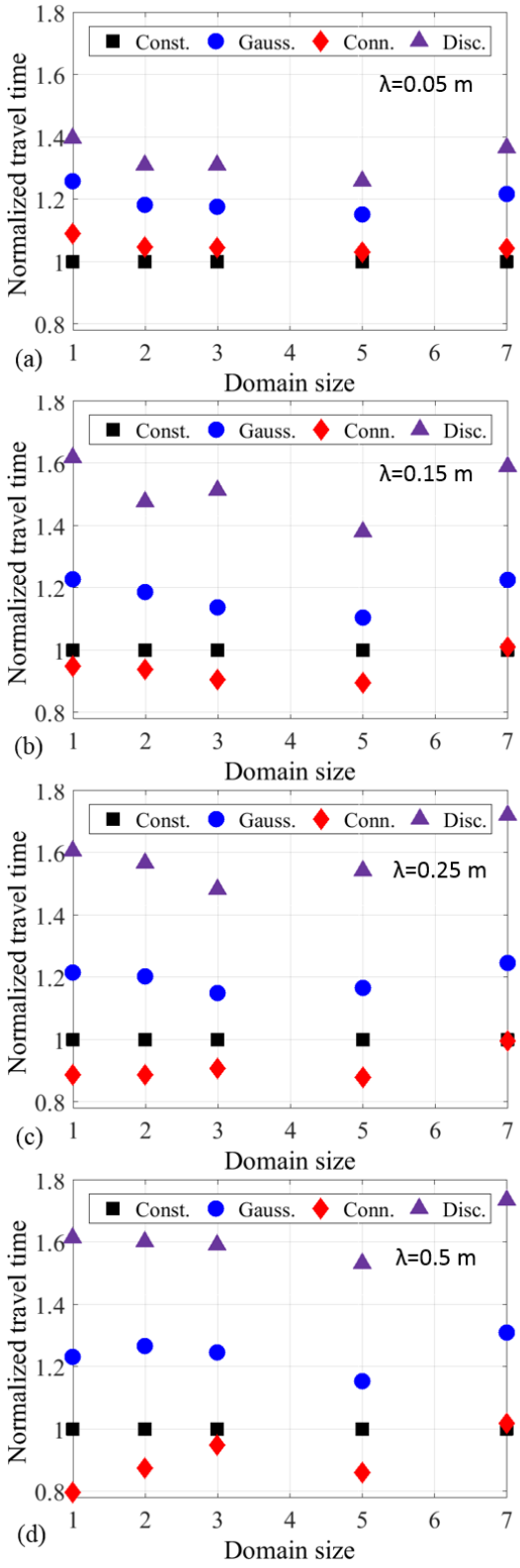

Figure 4-3. Normalized median arrival times against domain size DS grouped by texture with correlation length (a) λ=0.05 m, (b) λ=0.15 m, (c) λ=0.25 m, and (d) λ=0.5 m.

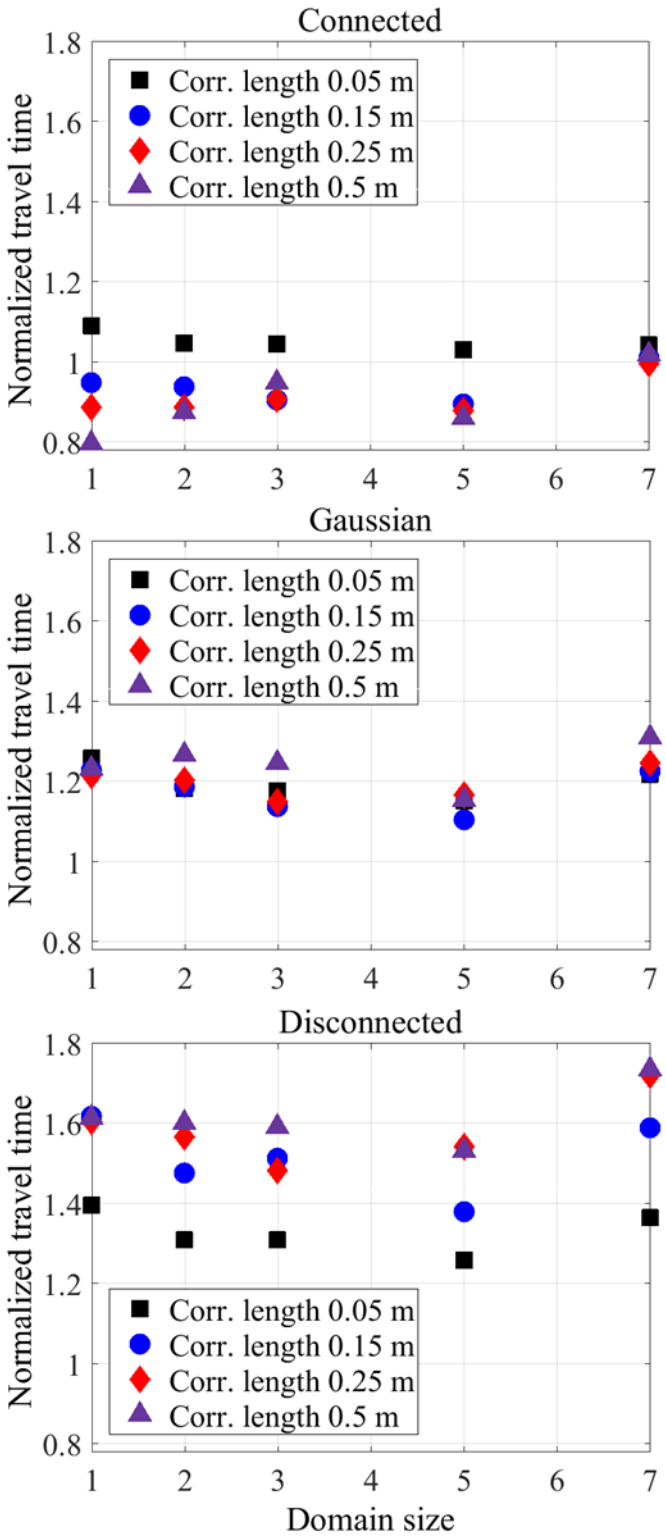

Figure 4-4. Normalized median arrival times against domain size DS grouped by correlation length for the (a) Connected texture case (b) Gaussian texture case, and (c) Disconnected texture case.

Normalized travel times for the first five percent of particle arrivals are shown in Figure 1-5. The normalization is achieved by dividing the 0.05 densities of the CDFs of a given texture case with the corresponding Constant reference case.

Early arrivals are notably influenced by texture, more so than corresponding median values presented above. The Connected texture case notably decreases travel times, where large correlation length further decreases early arrivals (Figure 4-5a). However, as domain size increases, the travel times increase. Interestingly, this appears to converge asymptotically towards unity, i.e. towards the Constant reference case. This is most apparent for the small correlation length λ=0.05 m (black squares), but with similar behavior also for the larger correlation lengths, although not reaching unity for the domain sizes considered. This indicates that the Connected texture can decrease travel times for early arrivals.

The Gaussian texture case also exhibits a similar change both with respect to changing correlation length as well as domain size (Figure 4-5b). Here, however, the increase in travel times for early arrivals with increasing domain size appears to converge to a value above unity, approximately 1.1. Again, this is most apparent for the smallest correlation length, but the behavior is consistent for all four correlation lengths considered.

The Disconnected texture case also exhibits travel time increase for early arrivals with increasing domain size, however it does not display a clear convergence (Figure 4-5c). Also, note all arrivals are greater than unity for all correlation lengths and domain sizes except for the smallest domain size DS1. Also, note there is not apparent convergence to an asymptote as domain size increases for the scales considered. This indicates that the Disconnected texture is causing an increase in travel time even for early arrivals and which seems to persist with increasing scale, which is a different behavior when compared to the Connected and Gaussian textures above.

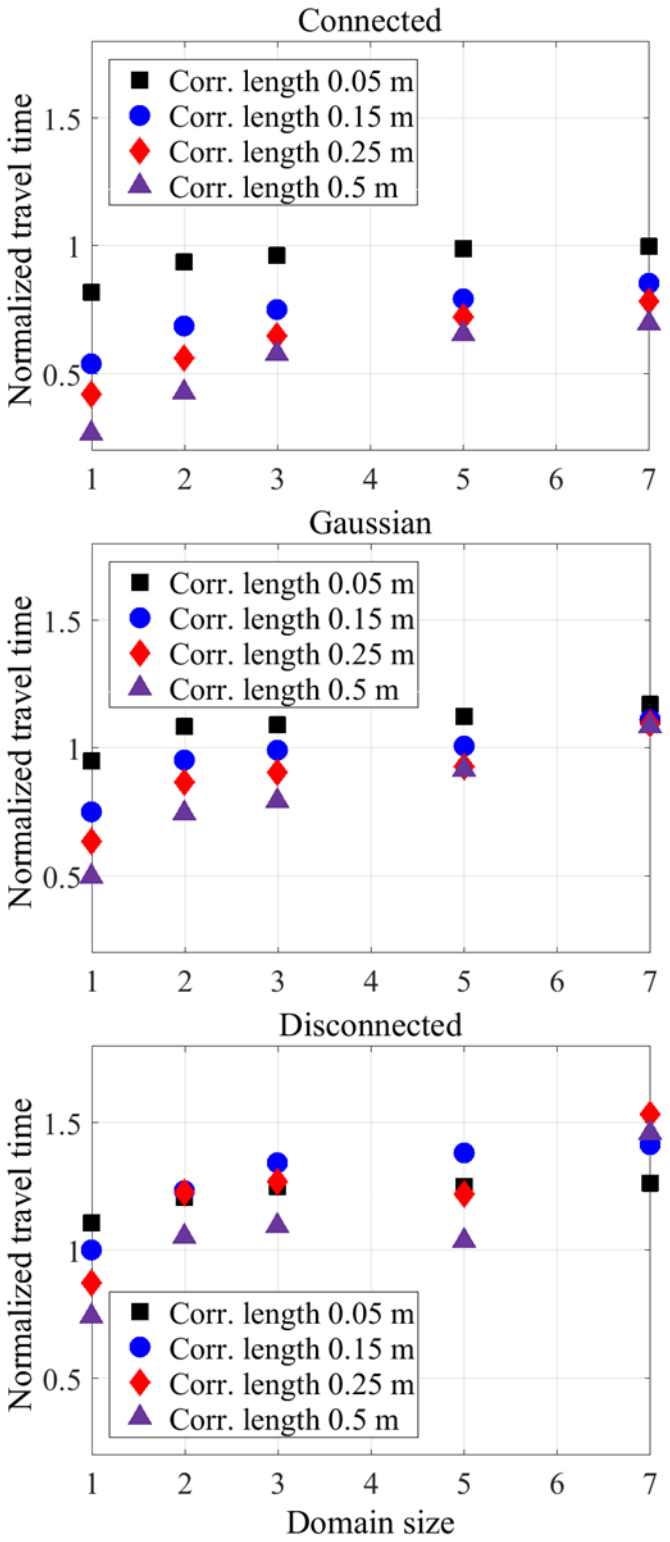

Figure 4-5. The 5-percentile arrival times against domain size DS grouped by correlation length for the (a) Connected texture case (b) Gaussian texture case, and (c) Disconnected texture case.

4.2.5 Discussion

The provided results demonstrate the effects of increasing correlation length and domain size on median particle travel times. Note that the small domain size DS1 typically consists of two fractures with one intersection only (Table 4-1). As domain size increases, the number of fractures and intersections increase; the large domain size DS7 typically consists of about 45 fractures with about 60 intersections. Also, the average number of intersections per fracture increases from about 0.5 to about 1.3 as domain size increases from DS1 to DS7. Then, for small correlation lengths and the smallest domain size, the CDFs of particle transport times for cases with texture are very similar to the case without texture (Figure 4-2a), indicating that at this correlation length (1/40 of fracture length scale) the textures do not significantly impact travel times, despite the network being insignificant (i.e. the DFN typically consisting of only two fractures). As correlation length increases, the CDFs exhibit greater spread in travel times (Figure 4-2b), yielding earlier first arrivals and later late arrivals. As the network size increases, the variability between texture cases increases notably (Figure 4-2c,d), especially for the case with larger correlation length (1/4 of fracture length scale; Figure 4-2d).

This is also apparent from the normalized median travel times, where the cases with small correlation length yield relatively similar median values (Figure 4-3a), and where the differences increase as correlation length increases (Figure 4-3b-d). The Connected case exhibits shorter median travel times than the reference case for intermediate correlation lengths, which converge towards unity as domain size increases to DS7 (Figure 4-4a). The Gaussian and Disconnected textures however exhibit longer median travel times than the reference case for all correlation lengths and domain sizes. The medians of the Gaussian case are approximately 1.1 to 1.3 times longer than the reference case, and a slight increase with domain size and correlation length is discernible (Figure 1-4b). The Disconnected case produces a tendency of increasing median travel times with increasing correlation length, e.g. from about 1.3 to over 1.7 depending on domain size (Figure 4-4c).

Thus, the general effect of the Connected texture is to decrease travel times, provided correlation length is sufficiently large compared to fracture size. Here, the smallest correlation length has only a minimal effect on travel time. However, as correlation length increases, to 3/40, 1/8 and 1/4 of fracture length scale (λ=0.15 m, λ=0.25 m and λ=0.5 m, respectively), the Connected texture decreases travel times, especially for bulk mass arrival (Figure 1-4a) and early arrivals (Figure 4-5a).

The differences in transport behavior can be understood by the connectivity structures of the textures, combined with the underlying structure of the discrete fracture network. The Connected texture consists of features with high permeabilities being well-connected within each fracture. As correlation length increases, the high-permeability structures increase and extend to larger contiguous portions within each fracture, thereby producing fractures with extensive, well-connected high permeability features throughout. This enhances flow channeling with increased particle speeds locally within individual fractures.

However, the attraction to high-permeability regions within fractures has to be restarted each time a particle enters an intersection to a new fracture because there is no continuity in permeability between two fractures at an intersection. This is because the random fields used for creating texture are independently generated for each fracture. Although there is correlation in permeability within the plane of a given fracture, there is no correlation between different fractures along common intersections in the network. That is, the correlation structure inherent in textures are obstructed by the geometry of the fracture network. Thus, flow channeling and associated increased particle speeds are restricted by the network-scale structure of the DFN.

Connected high-permeability structures are not present in the Gaussian or Disconnected cases. The Gaussian texture corresponds to features with medium permeabilities being well-connected, and the Disconnected texture to low-permeabilities being well-connected. As correlation length increases and such

features encompass larger contiguous portions of the fracture plane, travel times increase with respect to the constant permeability reference case. This is because the well-connected regions residing within each fracture plane pertain to medium or low permeability values, and serve to, on average, reduce particle speed.

For the Disconnected case, regions of high permeability are disconnected and intersected by contiguous regions of low permeability, causing an overall reduction in particle speed. Also, the discontinuity in permeability between fracture intersections serves to further delay transport, since particles still need to restart the process of attraction to high-permeability regions upon entering a new fracture. Thus, for the Disconnected case, there is a dual retardation effect of contiguous regions of low permeability within fractures combined with intersections between fractures causing speed reduction.

As the domain scale and hence number of fractures in the network increases, the number of intersections experienced by particles traveling with the flow field also increases (Table 4-1). This impacts travel times differently depending on texture. For the Connected case, as particles experience a greater number of intersections, their travel times are to a greater extent controlled by the network connectivity and discontinuities caused by intersections, rather than the local internal variability of fractures with well-connected continuous high permeability structures. Thus, a trade-off occurs between local-scale continuous connectivity which enhances transport, versus network-scale discontinuity (due to absence of correlation between fractures) retarding transport. This balance depends on the size of the network and, essentially, on the number of intersections. As domain size increases, median travel times approach the median time corresponding to the constant permeability reference (which embodies the network-scale structure); for the largest domain size the median travel times are on par with the reference case (Figure 4-4a).

For the Disconnected case, travel time is increased both by the local low-permeable contiguous regions within each fracture plane, as well as by the effect of discontinuity in permeability at fracture intersections. As particles experience a greater number of intersections with increasing domain size the combined effect is to retard transport and travel time is further increased (Figure 4-4c).

For the Gaussian case, it appears that the combined effect of local fracture medium permeabilities being well-connected causes a general, but only minor delay with respect to the constant permeability reference case. It is not sufficient to cause a significant scale-dependent accumulation of increased travel times as the domain scale increases (Figure 4-4b). This is consistent with previous studies of DFN transport based on lognormal internal variability fields (e.g. Makedonska et al., 2016; Painter, 2006).

4.2.6 Conclusions

This study investigates effects of assuming internal fracture variability in aperture and permeability on flow and transport in discrete fracture networks. The simulations are designed to address three main critical controls of local-scale and network-scale heterogeneity and structure.

First, three permeability textures are considered, corresponding to a connected-type structure (high permeabilities well-connected), a disconnected-type structure (low permeabilities well-connected), and an intermediate connectivity-type case (medium permeabilities well-connected). The approach used to generate the textures preserves the mean and variance, enabling fair comparisons. A fourth case with the mean permeability value as a constant, i.e. without internal variability, is used as a reference case.

Second, the correlation lengths of the texture cases are varied between 1/40 and 1/4 of the fracture length scale. This serves to control the effect of the connectivity structures within the plane of individual fractures, i.e. is a critical control of local-scale variability and hence small-scale transport behavior.

Third, the domain size used to generate the discrete fracture network is systematically increased, yielding a series of simulation cases with increasing complexity, i.e. increasing number of fractures and fracture intersections. This serves to control the network-scale geometrical and topological structure and hence large-scale transport behavior.

The main general conclusion of this study is that the local-scale fracture texture properties can impact transport at the scale of the network. A general effect regardless of texture type is an increase in the variability of arrival times when compared against the assumption of smooth fractures, i.e. when no texture is assumed (constant permeability). This corresponds to an increase in dispersion. Specific conclusions from this study are as follows.

Textures which correspond to connected-type structures (Connected cases) decrease travel times, but the decrease is limited by the scale and complexity of the network. The local high-permeable continuous structures within individual fractures serve to decrease travel times, however as particles enter new fractures the discontinuity in permeability at intersections impedes further travel time decrease. Thus the decrease in travel time is limited by the number of fractures and fracture intersections particles experience, i.e. is constrained by the network-scale structure. Hence, there is a trade-off between small-scale enhancement and large-scale impediment of transport. This means bulk mass arrival is accelerated with respect to a smooth fracture plane assumption only for strong connectivity structures and relatively simple networks.

Textures which correspond to disconnected-type structures (Disconnected case) increase travel times, an effect which is further amplified by discontinuity in permeability at intersections between fractures, i.e. by the network-scale DFN structure. Hence, transport is impeded both by small-scale and large-scale structures. This means that bulk mass arrival is notably delayed with respect to a smooth fracture plane assumption for weak connectivity structures and more complex networks.

Textures which correspond to intermediate-type structures (Gaussian case) do not significantly impact median travel times regardless of network-scale DFN structure. There is a general increase in median times regardless of domain size, and only a minor effect of an increased variability in arrival times with increasing correlation length. Hence, transport is mainly controlled by large-scale structures. This means that bulk mass arrival is slightly delayed with respect to a smooth fracture plane assumption for intermediate (classical) connectivity structures, regardless of network complexity.

The early mass arrival (here considered on a basis of the first 5 percent of the travel time distribution) is more notably influenced by texture. Both the connected-type and intermediate-type textures (Connected and Gaussian cases) decrease the 5-percentile arrival times compared to the reference case of assuming smooth fractures, indicating an accelerated early mass arrival. Nonetheless, this effect is also constrained by network complexity, such that the early arrival times indicate a convergence towards an asymptote as the number of fractures and intersections in the network increases.

4.2.7 References

Aydin, A., Borja, R. I., & Eichhubl, P. (2006). Geological and mathematical framework for failure modes in granular rock. *Journal of Structural Geology*, *28*(1), 83–98. https://doi.org/10.1016/j.jsg.2005.07.008

Berkowitz, B., Naumann, C., & Smith, L. (1994). Mass transfer at fracture intersections: An evaluation of mixing models. *Water Resources Research*, *30*(6), 1765–1773. https://doi.org/10.1029/94WR00432

Brown, S. R. (1987). Fluid flow through rock joints: The effect of surface roughness. *Journal of Geophysical Research: Solid Earth*, *92*(B2), 1337–1347. https://doi.org/10.1029/JB092iB02p01337

Brown, S. R., & Scholz, C. H. (1985). Broad bandwidth study of the topography of natural rock surfaces. *Journal of Geophysical Research: Solid Earth*, *90*(B14), 12575–12582. https://doi.org/10.1029/JB090iB14p12575

Brown, S. R., Stockman, H. W., & Reeves, S. J. (1995). Applicability of the Reynolds Equation for modeling fluid flow between rough surfaces. *Geophysical Research Letters*, *22*(18), 2537–2540. https://doi.org/10.1029/95GL02666

Cacas, M. C., Ledoux, E., Marsily, G. de, Tillie, B., Barbreau, A., Durand, E., et al. (1990). Modeling fracture flow with a stochastic discrete fracture network: calibration and validation: 1. The flow model. *Water Resources Research*, *26*(3), 479–489. https://doi.org/10.1029/WR026i003p00479

Cvetkovic, V., & Dagan, G. (1994). Transport of kinetically sorbing solute by steady random velocity in heterogeneous porous formations. *Journal of Fluid Mechanics*, *265*(1), 189. https://doi.org/10.1017/S0022112094000807

Cvetkovic, V., & Frampton, A. (2010). Transport and retention from single to multiple fractures in crystalline rock at Äspö (Sweden): 2. Fracture network simulations and generic retention model. *Water Resources Research*, *46*(5), W05506. https://doi.org/10.1029/2009WR008030

Cvetkovic, V., & Frampton, A. (2012). Solute transport and retention in three-dimensional fracture networks. *Water Resources Research*, *48*(2), W02509. https://doi.org/10.1029/2011WR011086

Cvetkovic, V., Selroos, J. O., & Cheng, H. (1999). Transport of reactive tracers in rock fractures. *Journal of Fluid Mechanics*, *378*, 335–356.

Cvetkovic, V., Painter, S., Outters, N., & Selroos, J. O. (2004). Stochastic simulation of radionuclide migration in discretely fractured rock near the Äspö Hard Rock Laboratory. *Water Resources Research*, *40*(2), W02404.

Detwiler, R. L., & Rajaram, H. (2007). Predicting dissolution patterns in variable aperture fractures: Evaluation of an enhanced depth-averaged computational model. *Water Resources Research*, *43*(4).

de Dreuzy, J.-R., Méheust, Y., & Pichot, G. (2012). Influence of fracture scale heterogeneity on the flow properties of three-dimensional discrete fracture networks (DFN). *Journal of Geophysical Research*, *117*(B11). https://doi.org/10.1029/2012JB009461

Fiori, A., Boso, F., de Barros, F. P. J., De Bartolo, S., Frampton, A., Severino, G., et al. (2010). An indirect assessment on the impact of connectivity of conductivity classes upon longitudinal asymptotic macrodispersivity. *Water Resources Research*, *46*(8), W08601. https://doi.org/10.1029/2009WR008590

Frampton, A., & Cvetkovic, V. (2007a). Upscaling particle transport in discrete fracture networks: 1. Nonreactive tracers. *Water Resources Research*, *43*(10), W10428. https://doi.org/10.1029/2006WR005334

Frampton, A., & Cvetkovic, V. (2007b). Upscaling particle transport in discrete fracture networks: 2. Reactive tracers. *Water Resources Research*, *43*(10), W10429. https://doi.org/10.1029/2006WR005336

Frampton, A., & Cvetkovic, V. (2010). Inference of field-scale fracture transmissivities in crystalline rock using flow log measurements. *Water Resources Research*, *46*(11), W11502. https://doi.org/10.1029/2009WR008367

Frampton, A., & Cvetkovic, V. (2011). Numerical and analytical modeling of advective travel times in realistic three-dimensional fracture networks. *Water Resources Research*, *47*(2), W02506. https://doi.org/10.1029/2010WR009290

Frampton, A., Hyman, J. D., & Zou, L. (2018). Advective transport in a synthetic discrete fracture system with internal variability in permeability. In *52nd US Rock Mechanics / Geomechanics Symposium* (Vol. 18–932). Seattle, Washington, USA.

Gotovac, H., Cvetkovic, V., & Andricevic, R. (2009). Flow and travel time statistics in highly heterogeneous porous media. *Water Resources Research*, *45*(7). https://doi.org/10.1029/2008WR007168

Hakami, E., & Larsson, E. (1996). Aperture measurements and flow experiments on a single natural fracture. *International Journal of Rock Mechanics and Mining Sciences & Geomechanics Abstracts*, *33*(4), 395–404. https://doi.org/10.1016/0148-9062(95)00070-4

Hyman, J. D., & Winter, C. L. (2014). Stochastic generation of explicit pore structures by thresholding Gaussian random fields. *Journal of Computational Physics*, *277*, 16–31. https://doi.org/10.1016/j.jcp.2014.07.046

Hyman, J. D., Gable, C. W., Painter, S. L., & Makedonska, N. (2014). Conforming Delaunay Triangulation of Stochastically Generated Three Dimensional Discrete Fracture Networks: A Feature Rejection Algorithm for Meshing Strategy. *SIAM Journal on Scientific Computing*, *36*(4), A1871–A1894. https://doi.org/10.1137/130942541

Hyman, J. D., Karra, S., Makedonska, N., Gable, C. W., Painter, S. L., & Viswanathan, H. S. (2015). dfnWorks: A discrete fracture network framework for modeling subsurface flow and transport. *Computers & Geosciences*, *84*, 10–19. https://doi.org/10.1016/j.cageo.2015.08.001

Hyman, J. D., Aldrich, G., Viswanathan, H., Makedonska, N., & Karra, S. (2016). Fracture size and transmissivity correlations: Implications for transport simulations in sparse three-dimensional discrete fracture networks following a truncated power law distribution of fracture size. *Water Resources Research*, *52*(8), 6472–6489. https://doi.org/10.1002/2016WR018806

Johns, R. A., Steude, J. S., Castanier, L. M., & Roberts, P. V. (1993). Nondestructive measurements of fracture aperture in crystalline rock cores using X ray computed tomography. *Journal of Geophysical Research: Solid Earth*, *98*(B2), 1889–1900. https://doi.org/10.1029/92JB02298

Keller, A. (1998). High resolution, non-destructive measurement and characterization of fracture apertures. *International Journal of Rock Mechanics and Mining Sciences*, *35*(8), 1037–1050. https://doi.org/10.1016/S0148-9062(98)00164-8

Lang, P. S., Paluszny, A., & Zimmerman, R. W. (2014). Permeability tensor of three-dimensional fractured porous rock and a comparison to trace map predictions. *Journal of Geophysical Research: Solid Earth*, *119*(8), 6288–6307. https://doi.org/10.1002/2014JB011027

Lichtner, P. C., Hammond, G. E., Lu, C., Karra, S., Bisht, G., Andre, B., et al. (2015). *PFLOTRAN User Manual: A Massively Parallel Reactive Flow and Transport Model for Describing Surface and Subsurface Processes* (No. LA-UR--15-20403, 1168703). https://doi.org/10.2172/1168703

Long, J. C. S., Remer, J. S., Wilson, C. R., & Witherspoon, P. A. (1982). Porous media equivalents for networks of discontinuous fractures. *Water Resour. Res.; (United States)*, *18:3*(3). https://doi.org/10.1029/WR018i003p00645

Maillot, J., Davy, P., Goc, R. L., Darcel, C., & Dreuzy, J. R. de. (2016). Connectivity, permeability, and channeling in randomly distributed and kinematically defined discrete fracture network models. *Water Resources Research*, *52*(11), 8526–8545. https://doi.org/10.1002/2016WR018973

Makedonska, N., Painter, S. L., Bui, Q. M., Gable, C. W., & Karra, S. (2015). Particle tracking approach for transport in three-dimensional discrete fracture networks: Particle tracking in 3-D DFNs. *Computational Geosciences*, *19*(5), 1123–1137. https://doi.org/10.1007/s10596-015-9525-4

Makedonska, N., Hyman, J. D., Karra, S., Painter, S. L., Gable, C. W., & Viswanathan, H. S. (2016). Evaluating the effect of internal aperture variability on transport in kilometer scale discrete fracture networks. *Advances in Water Resources*, *94*, 486–497. https://doi.org/10.1016/j.advwatres.2016.06.010

Neuman, S. P. (2005). Trends, prospects and challenges in quantifying flow and transport through fractured rocks. *Hydrogeology Journal*, *13*(1), 124–147.

Nicholl, M. J., Rajaram, H., Glass, R. J., & Detwiler, R. (1999). Saturated flow in a single fracture: evaluation of the Reynolds Equation in measured aperture fields. *Water Resources Research*, *35*(11), 3361–3373. https://doi.org/10.1029/1999WR900241

Painter, S., Cvetkovic, V., Mancillas, J., & Pensado, O. (2008). Time domain particle tracking methods for simulating transport with retention and first-order transformation. *Water Resources Research*, *44*(1). https://doi.org/10.1029/2007WR005944

Painter, S. L. (2006). *Effect of single-fracture aperture variability on field-scale transport*. Swedish Nuclear Fuel and Waste Management Co., Stockholm (Sweden). Retrieved from https://inis.iaea.org/collection/NCLCollectionStore/_Public/37/036/37036157.pdf

Painter, S. L., Gable, C. W., & Kelkar, S. (2012). Pathline tracing on fully unstructured control-volume grids. *Computational Geosciences*, *16*(4), 1125–1134. https://doi.org/10.1007/s10596-012-9307-1

Pollard, D. D., & Aydin, A. (1988). Progress in understanding jointing over the past century. *GSA Bulletin*, *100*(8), 1181–1204. https://doi.org/10.1130/0016-7606(1988)100<1181:PIUJOT>2.3.CO;2

Pyrak-Nolte, L. J., Myer, L. R., & Nolte, D. D. (1992). Fractures: Finite-size scaling and multifractals. *Pure and Applied Geophysics*, *138*(4), 679–706. https://doi.org/10.1007/BF00876344

Thompson, M. E., & Brown, S. R. (1991). The effect of anisotropic surface roughness on flow and transport in fractures. *Journal of Geophysical Research: Solid Earth*, *96*(B13), 21923–21932. https://doi.org/10.1029/91JB02252

Thörn, J., & Fransson, Å. (2015). A new apparatus and methodology for hydromechanical testing and geometry scanning of a rock fracture under low normal stress. *International Journal of Rock Mechanics and Mining Sciences*, *79*, 216–226. https://doi.org/10.1016/j.ijrmms.2015.08.015

Tsang, C.-F., & Neretnieks, I. (1998). Flow channeling in heterogeneous fractured rocks. *Reviews of Geophysics*, *36*(2), 275–298.

Tsang, C.-F., Neretnieks, I., & Tsang, Y. (2015). Hydrologic issues associated with nuclear waste repositories. *Water Resources Research*, *51*(9), 6923–6972. https://doi.org/10.1002/2015WR017641

Vasco, D. W., Pride, S. R., & Commer, M. (2016). Trajectory-based modeling of fluid transport in a medium with smoothly varying heterogeneity. *Water Resources Research*, *52*(4), 2618–2646. https://doi.org/10.1002/2015WR017646

Zinn, B., & Harvey, C. F. (2003). When good statistical models of aquifer heterogeneity go bad: A comparison of flow, dispersion, and mass transfer in connected and multivariate Gaussian hydraulic conductivity fields. *Water Resources Research*, *39*(3). https://doi.org/10.1029/2001WR001146

Zou, L., Jing, L., & Cvetkovic, V. (2015). Roughness decomposition and nonlinear fluid flow in a single rock fracture. *International Journal of Rock Mechanics and Mining Sciences*, *75*, 102–118. https://doi.org/10.1016/j.ijrmms.2015.01.016

Zou, L., Jing, L., & Cvetkovic, V. (2017a). Modeling of flow and mixing in 3D rough-walled rock fracture intersections. *Advances in Water Resources*, *107*, 1–9. https://doi.org/10.1016/j.advwatres.2017.06.003

Zou, L., Jing, L., & Cvetkovic, V. (2017b). Shear-enhanced nonlinear flow in rough-walled rock fractures. *International Journal of Rock Mechanics and Mining Sciences*, *97*, 33–45. https://doi.org/10.1016/j.ijrmms.2017.06.001

4.3 Matrix Diffusion in Fractured Media: New Insights into Power-Law Scaling of Breakthrough Curves

4.3.1 Introduction

Flow and solute transport through low-permeability/low-porosity fractured media at short time scales is generally determined by fractures and the structure of the interconnected networks that they form. However, at longer time scales, a variety of other processes become relevant and transport behavior is also influenced by interactions with the surrounding rock matrix. One of the most important processes is matrix diffusion where solutes are exchanged between flowing regions (fractures) and non-flowing regions (matrix) via molecular diffusion and has a profound influence on transport in fractured rock (Grisak & Pickens, 1980; Neretnieks, 1980; Tang, Frind, & Sudicky, 1981). The influence of matrix diffusion depends on a variety of physical properties including matrix porosity, matrix diffusivity, retardation factor, and the local advective gradient (Carrera et al., 1998; Zhou, Liu, Molz, Zhang, & Bodvarsson, 2007). The transport of solutes entering the matrix is retarded when compared to solutes that do not (Maloszewski & Zuber, 1985; Maloszewski & Zuber, 1993; Neretnieks, 1980), and slow back-diffusion from contaminated rock matrix blocks can drastically limit remediation efforts (Kueper, Stroo, Vogel, & Ward, 2014). Thus, the proper characterization of matrix diffusion's impact on transport through low-permeability fractured media is critical for a range of applications including predictive modeling of environmental restoration of contaminated sites (National Research Council, 1996; S. Neuman, 2005; VanderKwaak & Sudicky, 1996), aquifer storage and management (Kueper & McWhorter, 1991), hydrocarbon extraction (J. D. Hyman et al., 2016; Middleton et al., 2015), long-term storage of spent civilian nuclear fuel (Joyce, Hartley, Applegate, Hoek, & Jackson, 2014),and CO_2 sequestration (Jenkins, Chadwick, & Hovorka, 2015).

Breakthrough curves of solutes in fractured media commonly display anomalous transport behavior (Berkowitz & Scher, 1995; Cushman & O'Malley, 2015) with powerlaw tailing behavior $P(t) \sim t^{-\alpha+1}$. In the classical model of matrix diffusion for uniform flow in a single fracture adjacent to a semi-infinite matrix, the power-law tail decays with an exponent of -3/2 (Hadermann & Heer, 1996; Maloszewski & Zuber, 1985; Tsang, 1995). For a finite matrix block width, the late-time tail becomes steeper and decays exponentially (Maloszewski & Zuber, 1985). However, some tracer tests in fractured rock exhibit breakthrough curves with sustained power-law tails, but with exponents different from -3/2 (Becker & Shapiro, 2000; Haggerty, Fleming, Meigs, & McKenna, 2001; Meigs & Beauheim, 2001). Three classes of models have been invoked to explain this behavior: (i) multi-rate mass transfer models (Carrera et al., 1998; Haggerty, McKenna, & Meigs, 2000), which invoke diffusion in finite matrix blocks of various sizes, geometries and/or pore-scale heterogeneity of diffusivities, and appropriate parameterization for the distribution of exchange rates between fracture and matrix that captures these complexities. Haggerty et al. (2001, 2000) showed that breakthrough curves from the single well injection-withdrawal tests at the Waste Isolation Pilot Plant (WIPP) Dolomite site, which exhibit sustained power-law tails with decay exponents between -2.1 and -2.2, can be explained based on multi-rate models with log-normal, gamma or power-law distributed diffusion rate coefficients. They also suggested that at the relatively small scale of these tests, the behavior is controlled by multi-rate mass transfer, and that the influence of heterogeneous and/or transient advection may be neglected. (ii) multi-channel advection-dispersion models (Becker & Shapiro, 2003), which involve non-interacting channels with varying apertures and mean travel times, but no matrix diffusion. Becker and Shapiro (2003) showed that the non-diffusive (inferred from lack of differentiation between tracers with different diffusivity) tailing of breakthrough curves at the Mirror Lake Granite site (Becker & Shapiro, 2000), which exhibited sustained power-law tails with decay exponents around -2, can be explained based on a model of advection-dispersion in multiple channels with distinct apertures and mean advective travel times. (iii) generalized non-Fickian transport models such as the continuous-time

random walk (CTRW) and fractional-order transport models (Benson, Wheatcraft, & Meerschaert, 2000; Berkowitz, Cortis, Dentz, & Scher, 2006; Dentz, Gouze, Russian, Dweik, & Delay, 2012; S. Fomin, Hashida, Chugunov, & Kuznetsov, 2005; S. A. Fomin, Chugunov, & Hashida, 2011), whose mathematical properties inherently generate anomalous transport and power-law tails with decay exponents related to parameters in these models. For example, Geiger, Cortis, and Birkholzer (2010) interpreted simulations in fracture network-matrix models of flow and transport using a CTRW approach, and demonstrated how the CTRW memory/retention functions can be chosen to obtain the best fit to BTC, even those that do not exhibit a decay exponent of -3/2. However, establishing relationships between these model parameters and underlying physical parameters is an active area of research (De Anna et al., 2013; Hakoun, Comolli, & Dentz, 2019; S. P. Neuman & Tartakovsky, 2009)

The multi-scale structure of a fracture network results in heterogeneous advection and advective travel time distributions across multiple flowpaths, thus influencing large-scale long-term transport in fractured rock. One of the critical outstanding questions in this context is how the interaction between matrix diffusion and in-fracture transport processes in complex fracture networks impacts the late-time behavior of breakthrough curves. Recently developed high-resolution discrete fracture network (DFN) simulators offer an excellent opportunity to explore this question. Previous results suggest that breakthrough curves in fracture networks exhibit power-law tails, even in the absence of matrix diffusion (J. Hyman, Dentz, Hagberg, & Kang, 2019; Kang, Lei, Dentz, & Juanes, 2019; Painter, Cvetkovic, & Selroos, 2002). A specific question is the extent to which these power-law tails modify and/or are modified by the influence of matrix diffusion, and the conditions under which the influence of matrix diffusion dominates. To address this question, we incorporated matrix diffusion into the dfnWorks simulator (J. D. Hyman, Karra,et al., 2015), using the time-domain random walk approach presented by Delay and Bodin (2001). Even in relatively simple fracture networks with semi-infinite domain matrix diffusion, we observe an early-time regime where the tail of the travel time distribution follows the decay exponent of the advective travel time distribution and then transitions into a late-time regime where the decay exponent either approaches -3/2 or deviates systematically from -3/2. We propose a theoretical model to explain the simulation results, which clarifies that deviations from the -3/2 exponent occur if the advective travel time distribution decays relatively slowly (i.e. $t^{-(1+\alpha)}$, with $\alpha < 1$). Our results suggest a new mechanism for power-law breakthrough curve tails in fractured rock, involving the interaction/competition between complex heterogeneous advection and matrix diffusion. This mechanism is distinct from the multi-rate mass transfer and multi-channel advection-dispersion mechanisms noted above and provides justification and guidance for parameterizing generalized non-Fickian transport models.

4.3.2 Discrete Fracture Network Simulations: Particle travel time distributions

To investigate the influence of matrix diffusion on power-law scaling of particle travel time distributions in fractured media, we design three sets of semi-generic networks (they do not represent a specific field-site but have attributes that are based on field observations). Each set contains ten networks composed of uniformly sized square fractures with edge lengths of 1 meter within cuboid domain with dimensions of 20 m × 10 m ×10 m. Note that power-law tails in advective travel time distributions does *not* require a power-law distribution of fracture lengths (J. D. Hyman & Jiménez-Martínez, 2018; Painter et al., 2002). Fracture orientations are uniformly distributed over the unit sphere and fracture centroids are uniformly distributed within the domain, which mimics disordered fractures networks observed in the field (e.g., Klint et al., 2004). We prescribe the networks in terms of the fracture intensity, total fracture surface area per unit volume which is commonly referred to as P_{32} (Dershowitz & Herda, 1992) (set 1: 2.8, set 2: 3.2, set 3: 3.6). The mean and standard deviation of the final P_{32} values, once isolated fractures are removed (they

do not contribute to flow) is: set 1 - 1.27 (± 0.11); set 2 - 2.14 (± 0.25); set 3 - 2.91 (±0.09). The networks with larger fracture intensity require more fractures, because the fractures are monodisperse and exhibit higher network densities and better connectivity.

Fracture apertures are uniform within each fracture and equal to $b = 10^{-4}$m, which is a physically reasonable aperture value for a 1-meter fracture in crystalline rock under assumptions of a positively correlated power law relationship between fracture size and radius (Svensk Kärnbränslehantering AB, 2010). While it is well-documented that aperture variability leads to local dispersion within an individual fracture (Boutt, Grasselli, Fredrich, Cook, & Williams, 2006; Cardenas, Slottke, Ketcham, & Sharp, 2007; Detwiler, Rajaram, & Glass, 2000; Kang, Brown, & Juanes, 2016), recent high-fidelity DFN simulations in fracture networks have shown that aperture variability does not significantly influence behavior at the network scale, breakthrough curve (Frampton, Hyman, & Zou, 2019; Makedonska et al., 2016) or effective permeability (de Dreuzy, Méheust, & Pichot, 2012), except at high aperture variance or long correlation lengths relative to the domain size. Rather, it is the fracture network structure that controls flow and transport behavior.

Flow in the fracture network is modeled using the Reynolds equation (Zimmerman & Bodvarsson, 1996), which is limited to low Reynolds number flow regimes. Each fracture is meshed with a conforming Delaunay triangulation so the velocity field within each fracture is resolved (J. D. Hyman, Gable, Painter, & Makedonska, 2014). Solute transport through the flow field is simulated using a particle tracking approach (Makedonska, Painter, Bui, Gable, & Karra, 2015). One network from our set is shown in Fig. 4-6 where fractures are colored by pressure and particle pathlines are colored by velocity highlighting the spatially variable flow field within the network and individual fractures even though the fracture apertures are uniform. Even for purely advective transport, these velocity variations along particle pathlines lead to dispersion of the particle plume, which results in a wide distribution of advective particle travel times. Our approach thus implicitly represents the influence of dispersion by resolving velocity variations within fractures.

The travel time of a purely advective particle $t_f(\mathbf{a}, L)$ starting at an initial position $\mathbf{a}$ at time $t = 0$ is given by the integral

$$t_f(\mathrm{a};\, L) = \int_0^{\ell(L)} \frac{d\ell'}{||v(a,\ell'||} \,, \tag{4-12}$$

where ℓ is the particle pathline length, $\ell(L)$ is the minimum pathline length such that the particle exits the domain at a linear distance L and v(a; t) is the Lagrangian velocity sampled along the pathline x(a, ℓ), which is given in terms of the Eulerian velocity u(x); v(a; ℓ) = u[x(a; ℓ)]. We consider both resident (uniform) and flux-weighted injection modes into the networks (Kreft & Zuber, 1978) and particle behavior at intersections is determined using a complete mixing rule (Sherman, Hyman, Bolster, Makedonska, & Srinivasan, 2018). Denoting the plume of particles as

$$P(t_f) = \frac{1}{M} \int d\Omega\, \delta[t_f\,(a, L) - t_f] \,. \tag{4-13}$$

We refer to (4-13) as the breakthrough curve (BTC). For purely advective particles, powerlaw tails in (4-13) are caused by large values of t_f(a; L) due to particles entering low-velocity regions and/or recirculation regions within u(x) where they are retained for extended durations.

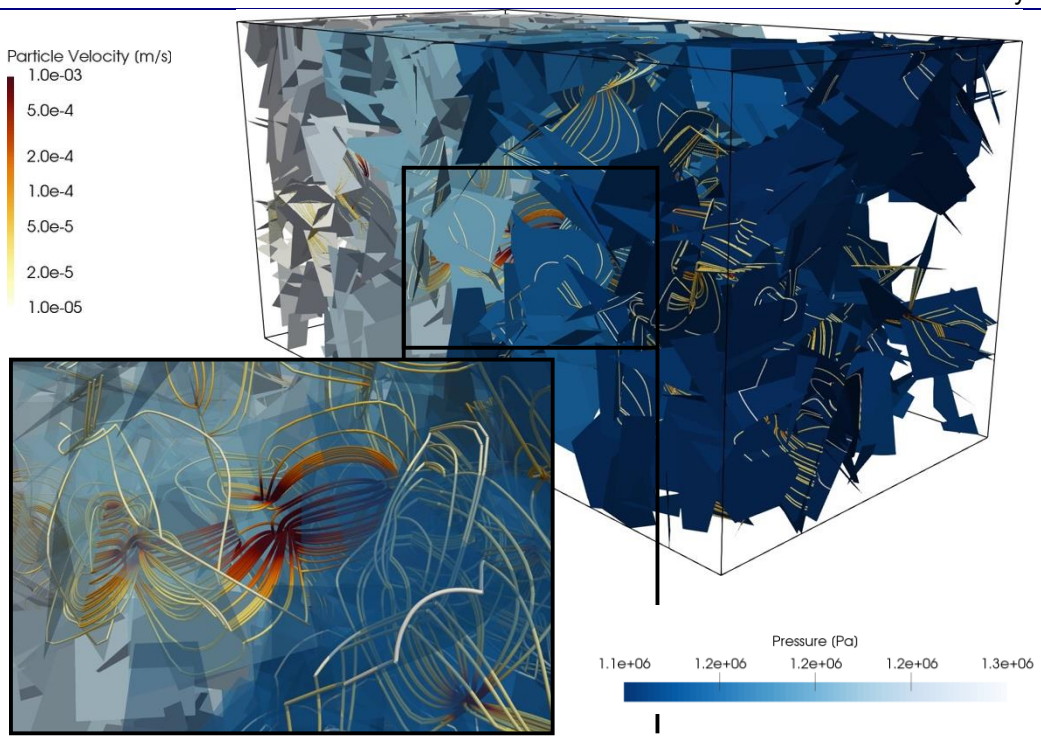

Figure 4-6. Particle pathlines (colored according to their velocities) within a fracture network (fractures are colored by pressure). The complex network structure along with individual fracture geometry results in a spatially variable velocity field within individual fractures that is sampled by the ensemble of particles.

Figure 4-7 shows multiple travel time distributions obtained from a set of particle tracking simulations in one of our networks to demonstrate how these low velocity regions are manifested in the tail of $P(t_f)$. The difference between the two simulations is the initial positions of particles; flux-weighted (left) and resident (right). The blue circles are the purely advective BTCs (4-13), the tails of which both exhibit the aforementioned power-law scaling ($Ct^{-\alpha+1}$) due to retention in low-velocity regions, but the decay rate, i.e., exponent of the power-laws, are different. The simplest probability distribution that can describe this power-law tail behavior is a Pareto distribution

$$P(t_f) \sim \frac{\alpha t_{f,min}^{\alpha}}{t_f^{\alpha+1}}, \; t_f > t_{f,min}. \tag{4-14}$$

where $t_{f,\min}$ denotes the minimum advective travel time across the population of streamlines. Note that (4-14) is a mathematical representation that provides excellent fits to the tail of the advective travel time distributions; it is not prescribed in the simulations and may not accurately represent the rising limb and behavior near the peak of the BTC. In this network realization, we observe a faster decay $\alpha = 1.85$ for flux-weighted injection than under resident injection $\alpha = 0.69$. More particles sample low-velocity regions under resident injection, which leads to a broader distribution of travel times and slower decay rate (Frampton & Cvetkovic, 2009; J. D. Hyman, Painter, Viswanathan, Makedonska, & Karra, 2015; Kang, Dentz, Le Borgne, Lee, & Juanes, 2017).

Particles can be retained for even longer durations due to matrix diffusion. We account for matrix diffusion using a time domain random walk (TDRW) where the total travel time of a particle is the linear superposition of the advective travel time within individual fractures and time spent in the matrix (Delay & Bodin, 2001). The adopted TDRW methodology implicitly includes variable advective travel times of particles along different streamlines within an individual fracture, i.e.,

local dispersion, which is in contrast to previous TDRW implementations in DFN models where longitudinal dispersion was either sampled from prescribed distributions or neglected entirely (Bodin, Porel, & Delay, 2003; Delay & Bodin, 2001; Painter, Cvetkovic, Mancillas, & Pensado, 2008). Moreover, the TDRW is applied for particle travel times in individual fractures rather than the total travel time through the network as in Karra, Makedonska, Viswanathan, Painter, and Hyman (2015) which used a different TDRW method coupled with dfnWorks to account for matrix diffusion (Painter & Mancillas, 2009). Thus, the adopted TDRW accounts for the possibility of particles entering and exiting the matrix multiple times as they pass through the network.

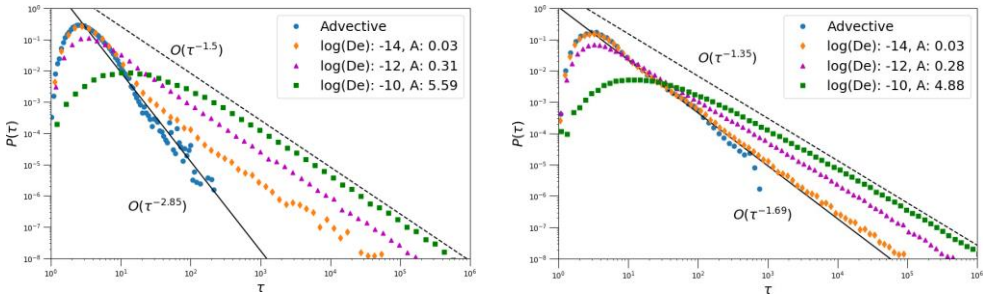

Figure 4-7. Particle travel time distribution for two networks. In the left subfigure the Pareto distribution has a exponent $\alpha = 1.85$ and in the right $\alpha = 0.69$. The purely advective PDF is plotted as as blue circles and empirical PDFs with matrix diffusion for different values of A: $O(10^{-2})$: orange diamonds, $O(10^{-1})$: magenta triangles, $O(10^{0})$: green squares. Solid black line is a Pareto with the decay rate estimated using the maximum likelihood estimator for the advective PDF. Dashed black lines are the theoretical predictions for asymptotic decay rates: $-3/2$ for $\alpha > 1$ (left) and $-(1 + \alpha/2)$ for $\alpha < 1$ (right).

The additional BTCs shown in Fig. 4-7 are particle tracking simulations from the same network and initial positions that also include matrix diffusion using the TDRW. For an illustrative exploration of the strength of matrix diffusion, we fix the matrix porosity at $\varphi = 0.1$ and consider three values of matrix diffusivity D_e [m^2/2]: $\log(D_e) = -10$ (green squares), -12 (purple triangles), -14 (orange diamonds). For the lowest values of D_e (orange), the BTC follows the purely advective BTC closely in the early part of the tail, before exhibiting a break in slope and approach to a different late-time power-law decay rate. For the intermediate value of D_e (purple), the peak is damped slightly in comparison to the purely advective BTC, and the late-time power law decay rate is approached more rapidly. For the highest value of D_e (green), the peak is damped significantly and the BTC directly approaches the late-time power law decay, without following the purely advective BTC during the early time portion of the tail. For $\alpha = 1.85$ (left), the BTCs for all cases exhibit a late-time power-law decay rate of -3/2, which corresponds to the classical signature of matrix diffusion. However, for $\alpha = 0.69$ (right), the BTCs for all cases converge to a power-law decay rate of -1.35, rather than -3/2. In the next section, we present a theoretical analysis of the combined influence of matrix diffusion and the advective travel time distribution to explain these features. Specifically, we derive a criterion for deviation from the -3/2 decay rate of the BTC considering matrix diffusion and relate it to the decay rate exponent of the purely advective BTC described by α and provide an explanation for the break in slope between the early and late time decay rates in the case of weak matrix diffusion.

4.3.3 Theoretical Insights: Matrix Diffusion and Advective Travel Time Distributions

Considering a population of streamlines within a fracture network, we combine the distribution of advective travel times of particles, $P(t_f)$, and the conditional distribution of travel times influenced by matrix diffusion along any individual streamline, $P(t|t_f)$, to obtain the distribution of total travel time of particles:

$$P(t) = \int_{t_{f,min}}^{t} P(t|t_f)\ P(t_f)\ dt_f\ , \tag{4-15}$$

where $t_{f,\min}$ denotes the minimum advective travel time. We have already shown that the tail of $P(t_f)$ can be well-modeled by a Pareto distribution (4-14), so we turn our attention to a suitable model to account for matrix diffusion.

For a pulse injection into a single uniform fracture surrounded by an infinite matrix, Maloszewski and Zuber (1985) derived an analytical solution considering only advection within the fracture. The probability density function of travel times exiting the fracture may be obtained from their solution as:

$$P(t|t_f) = \begin{cases} \frac{at_f}{\sqrt{\pi}(t-t_f)^{\frac{3}{2}}}\ exp\ \left(\frac{-a^2{t_f}^2}{(t-t_f)}\right) & if\quad t > t_f\ , \\ 0 & if\quad t \le t_f\ . \end{cases} \tag{4-16}$$

where t_f is the advective travel time through a fracture, and

$$a\ = \frac{\emptyset\sqrt{D_e}}{b}. \tag{4-17}$$

Here, ϕ is the matrix porosity, D_e is the matrix diffusivity, and b is the fracture aperture. Note that (4-16) exhibits a late-time decay rate of −3/2 associated with classical matrix diffusion. As long as a is constant along a streamline, (4-16) is valid even for streamlines along which the advection velocity varies (Cvetkovic, Selroos, & Cheng, 1999). To obtain first-order insights into the interaction between matrix diffusion and a power-law advective travel time distribution, we use (4-14) and (4-16) in (4-15), assuming a constant a. In future work, we will explore the influence of correlations between aperture and fracture length, which may imply correlations between the effective value of a and the travel time along a streamline. Our DFN simulations employed a constant value for a in each DFN realization.

It is convent to non-dimensionalize the variables involved in (4-14)-(4-16) as follows:

$$\tau\ = \frac{t}{t_{f,min}}\ ,\quad \tau_f\ = \frac{t_f}{t_{f,min}}\ ,\quad A = a\sqrt{t_{f,min}} = \frac{\emptyset\sqrt{D_e t_{f,min}}}{b}\ . \tag{4-18}$$

The corresponding dimensionless advective, conditional and total travel time probability density functions are

$$P(\tau_f)\ = \frac{\alpha}{{\tau_f}^{\alpha+1}}.\ \tau_f > 1\ , \tag{4-19}$$

$$P(\tau|\tau_f) = \begin{cases} \frac{A\tau_f}{\sqrt{\pi}(\tau-\tau_f)^{\frac{3}{2}}}\ exp\ \left(\frac{-A^2{\tau_f}^2}{(\tau-\tau_f)}\right) & \tau > \tau_f\ , \\ 0 & \tau \le \tau_f \end{cases} \tag{4-20}$$

and

$$P(\tau) = \int_1^{\tau} \frac{A\tau_f}{\sqrt{\pi}(\tau-\tau_f)^{\frac{3}{2}}}\ exp\ \left(\frac{-A^2{\tau_f}^2}{(\tau-\tau_f)}\right) \frac{\alpha}{{\tau_f}^{\alpha+1}}\ d\tau_f\ . \tag{4-21}$$

Three important limiting behaviors result from (4-21) and explain the decay rate of the breakthrough curves in different regimes. First, we note that (4-16) in non-dimensional form is essentially a Lévy distribution with parameters ($\tau_f, 2A^2\ \tau f^2$). Because the Lévy distribution belongs to the class of stable distributions, as the scale parameter $2A^2\ \tau f^2 \rightarrow 0$, its limiting behavior is well-approximated by the Dirac-delta measure $\delta(\tau-\tau_f)$. Thus, for values of A and τ such that $A\tau \ll 1$, $A\tau_f \ll 1$ over the entire range of the integral (4-16), $P(\tau|\tau_f)$ may be approximated by $\delta(\tau-\tau_f)$, and $P(\tau) \approx P(\tau_f)$. In other words, for weak matrix diffusion, or at small dimensionless times, the breakthrough curve follows the advective travel time PDF (the range of dimensionless times for which this behavior may be expected is $\tau \ll 1/A$). Considering the behavior for large dimensionless time τ, it can be shown that

$$P(\tau) \sim \frac{A^\alpha \alpha}{2\sqrt{\pi}}\, \tau^{-1-\alpha/2}\, \Gamma\left(\frac{1-\alpha}{2}, \frac{A^2}{\tau}\right), \quad \tau \gg 1, \quad A^2\tau \gg 1\ . \tag{1-22}$$

Where $\Gamma(\cdot,\cdot)$ denotes the upper incomplete Gamma function. Based on the Maclaurin series expansion of $\Gamma(\cdot,\cdot)$, we demonstrate two alternative decay rates for large τ depending on the value of α. For $\alpha > 1$ (advective travel time PDF decays sufficiently fast), the decay rate is -3/2. However, if $\alpha < 1$ (advective travel time PDF decays sufficiently slowly), the decay rate is $-(1 + \alpha/2)$.

Thus, the behavior of breakthrough curves impacted by matrix diffusion in fractured rock is controlled by two dimensionless parameters: A and α representing two physical features of the system. α describes the decay rate of the purely advective breakthrough curve, which is a manifestation of how particles sample the fluid velocity field, and A, which describes the potential for prolonged retention in the matrix. In general, if (4-14) holds for the advective travel time distribution, the breakthrough curve will exhibit two distinct decay rates in different dimensionless time ranges, with a break in-between:

$$\tau \ll \frac{1}{A}: \qquad P(\tau) \sim \tau^{-(1+\alpha)}\ , \tag{1-23a}$$

$$\tau \gg \frac{1}{A^2}, \tau \gg 1: \quad P(\tau) \sim \tau^{-\left(1+\frac{\alpha}{2}\right)},\ \alpha < 1; \quad P(\tau) \sim \tau^{-\frac{3}{2}}, \alpha > 1\ . \tag{1-23b}$$

Note that A depends on fracture and matrix properties and first advective breakthrough time ($t_{f,\min}$). Thus, even at the same field site, A is a scale-dependent quantity in so far as $t_{f,\min}$ increases with distance between the location of solute injection and breakthrough curve measurement. For $A > 1$, the first or early-time regime shown in (4-23a) will not be observed, because by definition $\tau > 1$, cf. equations (4-18) and (4-21). However, the late-time approximation(4-22) and regimes (1-23b) are expected to be observed regardless of A, clarifying that the -3/2 decay rate associated with the behavior in the single-fracture infinite-matrix diffusion model will be observed only if the advective travel time distribution decays sufficiently rapidly ($\alpha > 1$). As noted above, deviations from the -3/2 decay rate have been previously explained based on finite matrix block sizes and the multi-rate model (Haggerty et al., 2001), multi-channel advection-dispersion (Becker & Shapiro, 2003). The theoretical analysis presented in this section illustrates a new mechanism for deviation from the -3/2 decay rate, even in the case of a semi-infinite matrix width: one involving retention in low velocity regions of the advective flow field, manifested in power-law tail of the advective travel time distribution, and diffusion into the surrounding matrix.

4.3.4 Comparison between Numerical Simulations and Theoretical Results

We estimate the exponent of the Pareto distribution α that best fits the tail of the empirical purely advective travel time distributions obtained from our set of DFN simulations (described in Sec. 4.3.2) using a Maximum Likelihood Estimator. We define the tail of the distribution as the empirical

PDFs beyond the peak. Goodness-of-fit metrics confirm that the Pareto distributions provide reasonable fits to the data. The values of α range between 0.24 and 3.8 and we partition the simulations based on whether $\alpha < 1$ or $\alpha > 1$ and the value of A to facilitate the evaluation of theoretical results presented in Section 1.3.3. Out of the 60 purely advective simulations, there are 19 networks where $\alpha < 1$ and 41 where $\alpha > 1$.

We consider pairs of the matrix porosity φ [−] and matrix diffusion coefficient D_e [m^2 /s] of $\varphi = 0.01$, 0.02, 0.05, 0.10 and $\log(D_e) = -10, -11, -12, -13, -14$. These values encompass a wide range based on previously reported field studies, although lower D_e values are typically associated with lower φ values (Zhou et al., 2007). While we consider pairs of φ and D_e, the controlling dimensionless parameter is $A = \phi\sqrt{D_e t_{f,min}}/b$, which varies between networks due to differences in $t_{f,\min}$ for the same values of ϕ and D_e, as b is constant throughout the network. Values of A range from O(10^{-3}) to O(10), with larger values indicating stronger matrix diffusion. For each DFN and injection mode, 21 empirical probability distributions (BTCs) are generated using $\approx 10^5$ particles. Increasing the number of particles beyond this point did not significantly change results. In sum, 1260 particle tracking simulations were performed (60 purely advective and 1200 that include matrix diffusion via the TDRW algorithm). The mean pressure gradient was selected to observe travel times when $A\tau \ll 1$ and $A\tau \gg 1$ to explore our theoretical predictions.

Revisiting Fig. 4-7 which shows the travel time distributions of two network realizations with different values of the Pareto exponent; $\alpha = 1.85$ (left) and $\alpha = 0.69$ (right). For $\alpha = 1.85$ (> 1), the theory predicts a decay rate of $-3/2$ as $A\tau \rightarrow \infty$ which is also observed in the DFN simulations. For $\alpha = 0.69$ (< 1), the theory predicts a decay rate of $-(\alpha/2+1) = -1.35$ as $A\tau \rightarrow \infty$, which is also observed in the DFN simulations. Moreover, the predicted break in the slope between the early-time (1-23a) and late-time (1-23b) for lower values of A is observed. This feature is more pronounced in the network where $\alpha > 1$ (left). The peaks of the distributions for the purely advective case (blue) and $A = 0.03$ (orange) almost exactly overlay each other and at $\tau \approx 10$, the orange markers make an abrupt deviation from the advective BTC and subsequently exhibit a decay rate of $-3/2$. For the two higher values of A in this network, we do not observe the decay rate of underlying Pareto, we only observe the decay rate of $-3/2$, which is also in line with the theoretical analysis because the influence of matrix diffusion is already quite strong $A^2\tau$ 1 thereby masking the influence of the advective travel time distribution.

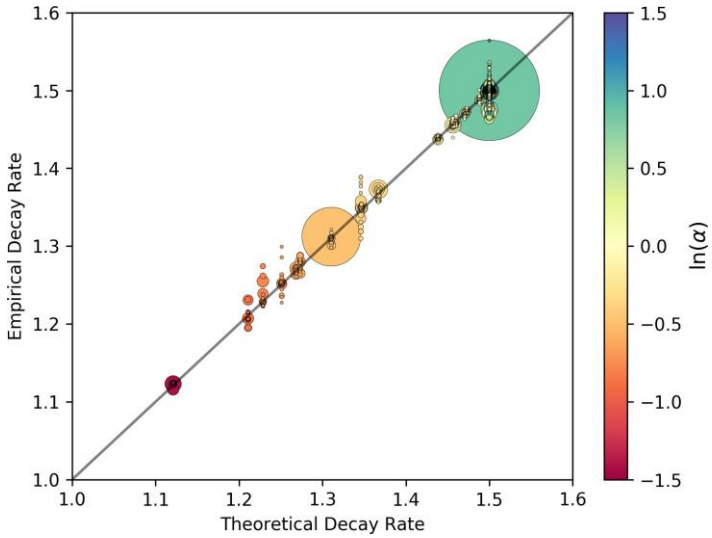

Figure 4-8. One-to-one plot of theoretical asymptotic breakthrough curve decay rate against DFN simulation data for 1198 simulations. Marker size is scaled by A (larger markers for higher values) and color denotes ln(α) value. α ranges between 0.24 and 3.8. For all values of both A and α, there is good agreement between our theoretical predictions and DFN simulations.

Figure 4-8 shows a one-to-one plot of the decay rate from numerical simulations (computed by fitting a power-law to the tail of the empirical PDF beyond the peak and break, i.e., late times) plotted against the theoretical values. 1198 out of the 1200 simulations that include matrix diffusion are plotted. The two networks omitted had too low particle densities at late times to provide adequate data for estimating power-law scaling. Marker size is scaled by A (larger markers for higher values), which fall into the range $O(10^{-3} - 10^{1})$ and color denotes the natural ln(α) value. Values of $\alpha < 1$ are colored between red and yellow and values of $\alpha > 1$ are colored green. For all values of α and A the agreement between the DFN simulations and theory is quite good, mean relative error of 0.004 (±0.009). Note that there is slightly better agreement for larger values of A, which indicates that even for stronger matrix diffusion where a decay rate of -3/2 would be expected, we observe systematic deviations from −3/2 when $\alpha < 1$.

4.3.5 Discussion and Conclusions

The presented theory, which is corroborated by high-fidelity three-dimensional discrete fracture network simulations, provides new insights into the scaling behavior of breakthrough curves in fractured media. In particular, we have identified a new mechanism for deviations from the classical −3/2 decay rate associated with matrix diffusion that involves interactions between matrix diffusion and complex heterogeneous advection at the fracture network scale (manifest as a slowly decaying power-law advective travel time distribution, $P(t_f) \sim t^{-(1+\alpha)}$, with $\alpha < 1$). For the case of uniform advection, as in the Maloszewski and Zuber (1985) model or for a single streamline, the advective travel time distribution is a delta function, and (4-21) reduces to (4-16), exhibiting the -3/2 decay rate characteristic of matrix diffusion. When the advective travel time distribution falls off relatively rapidly ($\alpha > 1$), the overall behavior is similar to the uniform advection case. The late-time tail is dominated by the influence of retention by matrix diffusion along all streamlines

(because the rising limb and peak along all streamlines pass by within a relatively short duration) and hence shows the -3/2 decay rate. However, when the advective travel time distribution decays relatively slowly ($\alpha < 1$), the late-time tail reflects the influence of both the rising limb/advective tail from transport along slow streamlines, and the matrix diffusion tail from fast streamlines, and thus deviates from -3/2. The manner in which these contributions are weighted is controlled by the dimensionless advective travel time distribution in the integral in (1-21), leading to a decay rate of $(1+\alpha/2)$ rather than -3/2. The threshold of $\alpha = 1$ (when $1+\alpha/2 = 3/2$) demarcates these two regimes. It is interesting to note that the $(1+\alpha/2)$ decay rate with $\alpha < 1$ is observed even when A is large (i.e. strong matrix diffusion), highlighting the influence of a slowly decaying advective travel time distribution. The mechanism for deviation from the -3/2 decay rate identified here (i.e. a slowly decaying advective travel time distribution combined with the influence of matrix diffusion) is distinct from the previously proposed finite matrix block width (Maloszewski & Zuber, 1985); multi-rate mass transfer (Haggerty et al., 2001), and multi-channel advection-dispersion (Becker & Shapiro, 2003) mechanisms. Our analysis involves strictly physical parameters and can thus provide a basis for relating parameters in generalized non-Fickian transport models to underlying physical mechanisms.

We also identified other scale-dependent aspects of when the influence of matrix diffusion is manifest in breakthrough curves. The theory identifies a dimensionless parameter that weighs the relative influences of variable advective travel time and matrix diffusion, $A\tau$, where $A = \frac{\phi\sqrt{D_e t_{f,min}}}{b}$ is a dimensionless measure of the strength of matrix diffusion at time scales on the order of the fastest advective travel times ($t_{f,\min}$) and $\tau = t/t_{f,\min}$ is a dimensionless total travel time. The regime $A\tau \ll 1$ is identified as a regime where the influence of matrix diffusion is weak, and the breakthrough curve tail is controlled by the decay rate of the advective travel time distribution. The late-time decay rates mentioned above will be observed in the regimes $\tau \gg 1$ and $A^2\tau \gg 1$. A novel feature of this non-dimensionalization is the inclusion of $t_{f,\min}$ in A. This clarifies that the expected behavior of breakthrough curves is scale (time) dependent; even at the same site, different behavior may be observed in tracer tests at different scales. For small-scale tracer tests (smaller $t_{f,\min}$), or if $A \ll 1$ (weak matrix diffusion), non-diffusive tailing reflecting the advective travel time distribution could be observed over relatively long-time scales (10^1-10^2 times the first breakthrough time). Such behavior has in fact been documented in previous work, e.g. Becker and Shapiro (2000). If the breakthrough curves are observed for sufficiently long duration and concentrations are above detection limit, a break in slope and transition may be observed in breakthrough curves. At larger scales (larger $t_{f,\min}$), matrix diffusion will influence the breakthrough curves. The DFN simulations considered here cover four orders of magnitude in A (10^{-3}–10^1). Across this range, we observed the early time advection-controlled regime and break in slope for smaller values of A. However, if the simulations were run with a smaller hydraulic gradient (slower velocities, larger $t_{f,\min}$), we may not have observed the early-time regime.

One important feature of our theoretical approach is that the overall breakthrough curve is expressed in relation to the advective travel time distribution, which already captures complexities associated with heterogeneous flow velocities, networks structure and advection loops. It could thus avoid the apparent scale-dependence of effective matrix diffusivities resulting from using a single fracture constant velocity model to estimate transport parameters by fitting breakthrough curves, e.g. (Liu, Zhang, Zhou, & Molz, 2007; Zhou et al., 2007). With regard to such applications of our theoretical approach for the interpretation of field tracer data, a key is the use of tracers with varying molecular diffusivities, especially high-molecular weight tracers or particulate tracers with very low diffusivities (Becker & Shapiro, 2000; Jardine et al., 1999; Maloszewski, Herrmann, & Zuber, 1999; Reimus et al., 2003), that can constrain the advective travel time distribution in the absence of matrix diffusion effects.

In general, solute dispersion arises from both velocity variations produced by the network structure and the smaller-scale velocity variations resulting from aperture variability within fractures. Although the assumption of a constant a in our analysis is a restriction, it is a first step towards understanding behavior in more complex fractured rock masses, where a varies spatially due to the dependence on the fracture aperture b. As a result, the advective travel time along a streamline may be correlated with an average value of a, requiring an alternative treatment of (1-15) and (1-16). Additional processes that should be considered in future work include exchange of solute between streamtubes, e.g. between preferential flow paths and stagnant zones within fractures (Becker & Shapiro, 2000; Neretnieks, 2006; Roubinet, De Dreuzy, & Tartakovsky, 2013; Zhou et al., 2007), adsorption, transformation between chemical species, and finally heterogeneity in fracture and finally heterogeneity in fracture aperture and matrix properties, i.e. spatially variable a, which requires additional theoretical investigation. In future extensions of our approach, we will focus on incorporating in-fracture mass transfer and dispersion into our analysis, adapting the concepts used by Delay and Bodin (2001) and also address the influence of finite matrix block size (Haggerty et al., 2001; Maloszewski & Zuber, 1985). Most discrete fracture network models are restricted to low Reynolds number flows, and the representation of fluid fluxes between the fractures and rock matrix is approximate, neglecting Brinkman effects for instance. Thus, their applicability to fractured karst or fracture networks in a relatively permeable rock matrix (e.g. sandstone) is limited.

4.3.6 References

Becker, M. W., & Shapiro, A. M. (2000). Tracer transport in fractured crystalline rock: Evidence of nondiffusive breakthrough tailing. *Water Resour. Res.*, *36* (7), 1677–1686.

Becker, M. W., & Shapiro, A. M. (2003). Interpreting tracer breakthrough tailing from different forced-gradient tracer experiment configurations in fractured bedrock. *Water Resour. Res.*, *39* (1).

Benson, D. A., Wheatcraft, S. W., & Meerschaert, M. M. (2000). Application of a fractional advection-dispersion equation. *Water Resour. Res.*, *36*(6), 1403–1412.

Berkowitz, B., Cortis, A., Dentz, M., & Scher, H. (2006). Modeling non-fickian transport in geological formations as a continuous time random walk. *Rev. Geophys.*, *44* (2).

Berkowitz, B., & Scher, H. (1995).On characterization of anomalous dispersion in porous and fractured media. *Water Resour. Res.*, *31* (6), 1461–1466.

Bodin, J., Porel, G., & Delay, F. (2003). Simulation of solute transport in discrete fracture networks using the time domain random walk method. *Earth Planet. Sc. Lett.*, *208* (3-4), 297–304.

Boutt, D. F., Grasselli, G., Fredrich, J. T., Cook, B. K., & Williams, J. R. (2006). Trapping zones: The effect of fracture roughness on the directional anisotropy of fluid flow and colloid transport in a single fracture. *Geophys. Res. Lett, 33(21).*

Cardenas, M. B., Slottke, D. T., Ketcham, R. A., & Sharp, J. M. (2007). Navier-Stokes flow and transport simulations using real fractures shows heavy tailing due to eddies. *Geophys. Res. Lett.*, *34* (14).

Carrera, J., Sánchez-Vila, X., Benet, I., Medina, A., Galarza, G., & Guimerà, J. (1998). On matrix diffusion: formulations, solution methods and qualitative effects. *Hydrogeol. J.*, *6* (1), 178–190.

Cushman, J. H., & O'Malley, D. (2015). Fickian dispersion is anomalous. *J. Hydrol.*, *531*, 161–167.

Cvetkovic, V., Selroos, J., & Cheng, H. (1999). Transport of reactive tracers in rock fractures. *J. Fluid Mech.*, 378, 335–356.

De Anna, P., Le Borgne, T., Dentz, M., Tartakovsky, A. M., Bolster, D., & Davy, P. (2013). Flow intermittency, dispersion, and correlated continuous time random walks in porous media. *Phys. Rev. Lett*., *110(18)*, 184502.

de Dreuzy, J.-R., Méheust, Y., & Pichot, G. (2012). Influence of fracture scale heterogeneity on the flow properties of three-dimensional discrete fracture networks (dfn). *J. Geophys. Res. Sol. Ea.*, *117* (B11).

Delay, F., & Bodin, J. (2001). Time domain random walk method to simulate transport by advection-dispersion and matrix diffusion in fracture networks. *Geophys. Res. Lett.*, *28* (21), 4051–4054.

Dentz, M., Gouze, P., Russian, A., Dweik, J., & Delay, F. (2012). Diffusion and trapping in heterogeneous media: An inhomogeneous continuous time random walk approach. *Adv. Water Resour.*, *49* , 13–22.

Dershowitz, W. S., & Herda, H. H. (1992). Interpretation of fracture spacing and intensity. In *The 33th us symposium on rock mechanics (USRMS)*.

Detwiler, R. L., Rajaram, H., & Glass, R. J. (2000). Solute transport in variable-aperture fractures: An investigation of the relative importance of taylor dispersion and macrodispersion. *Water Resour. Res.*, *36* (7), 1611–1625.

Fomin, S., Hashida, T., Chugunov, V., & Kuznetsov, A. (2005). A borehole temperature during drilling in a fractured rock formation. *International Journal of Heat and Mass Transfer* , *48* (2), 385–394.

Fomin, S. A., Chugunov, V. A., & Hashida, T. (2011). Non-fickian mass transport in fractured porous media. *Adv. Water Resour.*, *34* (2), 205–214.

Frampton, A., & Cvetkovic, V. (2009). Significance of injection modes and heterogeneity on spatial and temporal dispersion of advecting particles in two-dimensional discrete fracture networks. *Adv. Water Resour.*, *32* (5), 649–658.

Frampton, A., Hyman, J., & Zou, L. (2019). Advective transport in discrete fracture networks with connected and disconnected textures representing internal aperture variability. *Water Resour. Res.*, *55* (7), 5487–5501.

Geiger, S., Cortis, A., & Birkholzer, J. (2010). Upscaling solute transport in naturally fractured porous media with the continuous time random walk method. *Water Resour. Res.*, *46*(12).

Grisak, G., & Pickens, J.-F. (1980). Solute transport through fractured media: 1. the effect of matrix diffusion. *Water Resour. Res.*, *16* (4), 719–730.

Hadermann, J., & Heer, W. (1996). The grimsel (switzerland) migration experiment: integrating field experiments, laboratory investigations and modelling. *J. Contam. Hydrol.*, *21* (1-4), 87–100.

Haggerty, R., Fleming, S. W., Meigs, L. C., & McKenna, S. A. (2001). Tracer tests in a fractured dolomite: 2. analysis of mass transfer in single-well injection-withdrawal tests. *Water Resour. Res.*, *37* (5), 1129–1142.

Haggerty, R., McKenna, S. A., & Meigs, L. C. (2000). On the late-time behavior of tracer test breakthrough curves. *Water Resour. Res.*, *36* (12), 3467–3479.

Hakoun, V., Comolli, A., & Dentz, M. (2019). Upscaling and prediction of lagrangian velocity dynamics in heterogeneous porous media. *Water Resour. Res.*, *55* (5), 3976–3996.

Hyman, J., Dentz, M., Hagberg, A., & Kang, P. K. (2019). Linking structural and transport properties in three-dimensional fracture networks. *J. Geophys. Res. Sol. Ea.*, *124* (2), 1185–1204.

Hyman, J. D., Gable, C. W., Painter, S. L., & Makedonska, N. (2014). Conforming Delaunay triangulation of stochastically generated three dimensional discrete fracture networks: A feature rejection algorithm for meshing strategy. *SIAM J. Sci. Comput., 36*(4), A1871–A1894.

Hyman, J. D., & Jiménez-Martínez, J. (2018). Dispersion and mixing in three-dimensional discrete fracture networks: Nonlinear interplay between structural and hydraulic heterogeneity. *Water Resour. Res.*, *54* (5), 3243-3258.

Hyman, J. D., Jiménez-Martínez, J., Viswanathan, H., Carey, J., Porter, M., Rougier, E., . . . Makedonska, N. (2016). Understanding hydraulic fracturing: a multi-scale problem. *Phil. Trans. R. Soc. A*, *374* (2078), 20150426.

Hyman, J. D., Karra, S., Makedonska, N., Gable, C. W., Painter, S. L., & Viswanathan, H. S. (2015). dfnWorks: A discrete fracture network framework for modeling subsurface flow and transport. *Comput. Geosci.*, *84* , 10–19.

Hyman, J. D., Painter, S. L., Viswanathan, H., Makedonska, N., & Karra, S. (2015). Influence of injection mode on transport properties in kilometer-scale three-dimensional discrete fracture networks. *Water Resour. Res.*, *51* (9), 7289–7308.

Jardine, P., Sanford, W., Gwo, J., Reedy, O., Hicks, D., Riggs, J., & Bailey, W. (1999). Quantifying diffusive mass transfer in fractured shale bedrock. *Water Resour. Res*., *35*(7), 2015–2030.

Jenkins, C., Chadwick, A., & Hovorka, S. D. (2015). The state of the art in monitoring and verification—ten years on. Int. *J. Greenh. Gas. Con*., *40*, 312–349.

Joyce, S., Hartley, L., Applegate, D., Hoek, J., & Jackson, P. (2014). Multi-scale groundwater flow modeling during temperate climate conditions for the safety assessment of the proposed high-level nuclear waste repository site at forsmark, sweden. *Hydrogeol. J.*, *22* (6), 1233–1249.

Kang, P. K., Brown, S., & Juanes, R. (2016). Emergence of anomalous transport in stressed rough fractures. *Earth Planet. Sc. Lett.*, *454* , 46–54.

Kang, P. K., Dentz, M., Le Borgne, T., Lee, S., & Juanes, R. (2017). Anomalous transport in disordered fracture networks: spatial markov model for dispersion with variable injection modes. *Adv. Water Resour.*. doi: 10.1016/j.advwatres.2017.03.024

Kang, P. K., Lei, Q., Dentz, M., & Juanes, R. (2019). Stress-induced anomalous transport in natural fracture networks. *Water Resour. Res.,* 55 (5), 4163-4185.

Karra, S., Makedonska, N., Viswanathan, H. S., Painter, S. L., & Hyman, J. D. (2015). Effect of advective flow in fractures and matrix diffusion on natural gas production. *Water Resour. Res.*, *51* (10), 8646–8657.

Klint, K., Gravesen, P., Rosenbom, A., Laroche, C., Trenty, L., Lethiez, P., . . . Tsakiroglou, C. (2004). Multi-scale characterization of fractured rocks used as a means for the realistic simulation of pollutant migration pathways in contaminated sites: a case study. *Water Air Soil Poll.*, *4* (4-5), 201–214.

Kreft, A., & Zuber, A. (1978). On the physical meaning of the dispersion equation and its solutions for different initial and boundary conditions. *Chem. Eng. Sci.*, *33* (11), 1471–1480. doi: 10.1016/0009-2509(78)85196-3

Kueper, B. H., & McWhorter, D. B. (1991). The behavior of dense, nonaqueous phase liquids in fractured clay and rock. *Groundwater* , *29* (5), 716–728.

Kueper, B. H., Stroo, H. F., Vogel, C. M., & Ward, C. H. (Eds.). (2014). *Chlorinated solvent source zone remediation*. Springer.

Liu, H., Zhang, Y., Zhou, Q., & Molz, F. (2007). An interpretation of potential scale dependence of the effective matrix diffusion coefficient. *J. Contam. Hydrol.*, *90* (1-2), 41–57.

Makedonska, N., Hyman, J. D., Karra, S., Painter, S. L., Gable, C. W., & Viswanathan, H. S. (2016). Evaluating the effect of internal aperture variability on transport in kilometer scale discrete fracture networks.*Adv. Water Resour.*, *94* , 486–497.

Makedonska, N., Painter, S. L., Bui, Q. M., Gable, C. W., & Karra, S. (2015). Particle tracking approach for transport in three-dimensional discrete fracture networks. *Computat. Geosci.*, *19* (5), 1123–1137.

Maloszewski, P., Herrmann, A., & Zuber, A. (1999). Interpretation of tracer tests performed in fractured rock of the lange bramke basin, germany. *Hydrogeol. J.*, *7* (2), 209–218.

Maloszewski, P., & Zuber, A. (1985). On the theory of tracer experiments in fissured rocks with a porous matrix. *J. Hydrol.*, *79* (3-4), 333–358.

Maloszewski, P., & Zuber, A. (1993). Tracer experiments in fractured rocks: matrix diffusion and the validity of models. *Water Resour. Res.*, *29* (8), 2723–2735.

Meigs, L. C., & Beauheim, R. L. (2001). Tracer tests in a fractured dolomite: 1. experimental design and observed tracer recoveries. *Water Resour. Res.*, *37* (5), 1113–1128.

Middleton, R., Carey, J., Currier, R., Hyman, J., Kang, Q., Karra, S., . . . Viswanathan, H. (2015). Shale gas and non-aqueous fracturing fluids: Opportunities and challenges for supercritical CO_2. *Appl. Energ.*, *147* , 500–509.

National Research Council. (1996). *Rock fractures and fluid flow: contemporary understanding and applications*. National Academy Press.

Neretnieks, I. (1980). Diffusion in the rock matrix: An important factor in radionuclide retardation? *J. Geophys. Res. Sol. Ea.*, *85* (B8), 4379–4397.

Neretnieks, I. (2006). Channeling with diffusion into stagnant water and into a matrix in series. *Water Resour. Res.*, *42* (11).

Neuman, S. (2005). Trends, prospects and challenges in quantifying flow and transport through fractured rocks. *Hydrogeol. J.*, *13* (1), 124–147.

Neuman, S. P., & Tartakovsky, D. M. (2009). Perspective on theories of non-fickian transport in heterogeneous media. *Adv. Water Resour.*, *32* (5), 670–680.

Painter, S. L., Cvetkovic, V., Mancillas, J., & Pensado, O. (2008). Time domain particle tracking methods for simulating transport with retention and first-order transformation. *Water Resour. Res.*, *44* (1).

Painter, S. L., Cvetkovic, V., & Selroos, J.-O. (2002). Power-law velocity distributions in fracture networks: Numerical evidence and implications for tracer transport. *Geophys. Res. Lett.*, *29* (14), 20-1–20-4.

Painter, S. L., & Mancillas, J. (2009). *MARFA version 3.2. 2 user's manual: Migration analysis of radionuclides in the far field* (Tech. Rep.). Swedish Nuclear Fuel and Waste Management Co.

Reimus, P., Pohll, G., Mihevc, T., Chapman, J., Haga, M., Lyles, B., . . . Sanders, P. (2003). Testing and parameterizing a conceptual model for solute transport in a fractured granite using multiple tracers in a forced-gradient test. *Water Resour. Res.*, *39* (12).

Roubinet, D., De Dreuzy, J.-R., & Tartakovsky, D. M. (2013). Particle-tracking simulations of anomalous transport in hierarchically fractured rocks. *Comput. Geosci.*, *50* , 52–58.

Sherman, T., Hyman, J. D., Bolster, D., Makedonska, N., & Srinivasan, G. (2018). Characterizing the impact of particle behavior at fracture intersections in three-dimensional discrete fracture networks. *Phys. Rev. E*.

Svensk Kärnbränslehantering AB. (2010). *Data report for the safety assessment SR-site (TR-10-52)* (Tech. Rep.). Svensk Kärnbränslehantering AB.

Tang, D., Frind, E., & Sudicky, E. A. (1981). Contaminant transport in fractured porous media: Analytical solution for a single fracture. *Water Resour. Res.*, *17* (3), 555–564.

Tsang, Y. (1995). Study of alternative tracer tests in characterizing transport in fractured rocks. *Geophys. Res. Lett.*, *22* (11), 1421–1424.

VanderKwaak, J., & Sudicky, E. (1996). Dissolution of non-aqueous-phase liquids and aqueous-phase contaminant transport in discretely-fractured porous media. *J. Contam. Hydrol.*, *23* (1-2), 45–68.

Zhou, Q., Liu, H.-H., Molz, F. J., Zhang, Y., & Bodvarsson, G. S. (2007). Field-scale effective matrix diffusion coefficient for fractured rock: Results from literature survey. *J. Contam. Hydrol.*, *93* (1-4), 161–187.

Zimmerman, R. W., & Bodvarsson, G. S. (1996). Hydraulic conductivity of rock fractures. *Transport Porous Med.*, *23* (1), 1–30.

4.4 Conclusions

In this section, we presented two studies concerning the transport of solutes through crystalline rock. In the first, we examined the impact of different textures in fracture apertures. In the second, we studied the relative effect of matrix diffusion compared to advective transport. These studies lay the foundations for our work in the upcoming year. Concerning crystalline international, we will continue to study how various geophysical attributes of fractures and the networks they form leads to flow channelization, which is in-line with the directions of Task 10 in the SKB task force. We will examine both single fracture and network scale attributes. We will develop measurements to quantify the degree of flow channeling being observed, which are currently lacking in the literature. For GDSA, we will focus on the integration of alternative representations of matrix diffusion, be they computational or analytical. We will develop improved simulation tools to better account for the combined effects of fractures and the surrounding matrix. In addition to these new capabilities, we will also develop novel analysis tools to characterize simulation outputs better. We will also seek to upscaled analytical methods to account for retention due to matrix diffusion. The development of parsimonious upscaled transport models that can effectively incorporate the effects of fracture heterogeneity, initial condition, and matrix diffusion is critical for predictive purposes, and uncertainty quantification as many realizations of the model can be performed at low computational cost compared to 3D DFN simulations.

5. ALTERATION TO CLAY COLLOIDS IN ALKALINE, LOW-IONIC STRENGTH SOLUTIONS AT ELEVATED TEMPERATURE AND EXPERIMENTS TO QUANTIFY ANISOTROPY OF BENTONITE SWELLING

5.1 Introduction

Bentonite clays, part of the smectite group of clay minerals, find wide applications in various industries due to their high cation exchange capacities and swelling potential. Their proposed use as a barrier material in High Level Radioactive Waste (HLRW) repositories follows a precedent set in use as landfill liner materials and toxic waste repository liners (Kolstad et al., 2004). Bentonite clay features as an exterior barrier and back-fill material between the host rock and waste canister in several designs for deep geologic containment of HLRW. Bentonite has several properties that favor it for this application. Its low hydraulic conductivity when compressed and its high cation exchange capacity help protect the waste canister from outside water and contain any leakage of radionuclides. Its swelling properties offer the possibility that bentonite could swell into water conduits from the host rock and within the clay, sealing them and decreasing the chance of water intrusion into the waste canister (Villar and Lloret, 2008). In order to accurately predict the performance of bentonite clays in this environment it is necessary to understand the properties of bentonite clays by themselves. Two major thrusts in the study of bentonites for use in HLRW repositories are the behavior of bentonite colloids and their interactions with different radionuclides, and the swelling and erosional properties of bentonite barrier materials (Akinwunmi et al., 2019; Birgersson et al., 2011; Missana et al., 2003, 2014; Moreno et al., 2010; Norrfors et al., 2015, 2016; Reid et al., 2015). Previous work has addressed numerous scenarios affecting colloids ability to sorb and transport radionuclides, including radionuclide concentration, colloid mineralogy, groundwater pH, ionic strength, and potentially redox as reviewed in Kersting et al. (2003) and Reimus et al. (2017). This study addresses two additional potential alterations to bentonite that could occur in a HLRW setting: 1. high temperature alteration of bentonite colloids and 2. swelling and/or erosion of the bentonite upon hydration owing to intrusion of variable ionic strength groundwater. Both are important for the safety assessment of bentonite as a barrier material in HLRW repositories (Alonso et al., 2018).

In the previous report, we demonstrated that the colloids in the Chancellor groundwater from the Nevada Test Site sorb and transport radionuclides more effectively than a synthetic colloid solution of comparable chemistry (Viswanathan et al., 2019). Unlike freshly prepared colloid solutions typically used in lab experiments, groundwater at the test site experienced temperatures up to 75°C and was in place for several decades prior to collection. Therefore, experiments were designed to test whether these effects (i.e., aging and heating the colloids with sorbed radionuclides) might increase colloid-facilitated transport of radionuclides. Most recently, we showed that aging FEBEX colloids spiked with ^{137}Cs for 1200 hours increased the colloids' ability to transport ^{137}Cs through a series of columns by 10% (Telfeyan et al., 2020). We attributed the correlation between aging and sorption capacity to the increased time allowed for ^{137}Cs to migrate to the strong, less abundant sites (i.e., frayed edge sites) on the colloids.

The effect of heat on colloid stability and sorption capacity is less straightforward, however. Colloidal stability is governed by the balance of repulsion between the double layers of the particles and attractive (Van der Waals) forces, which varies as a function of ionic strength, temperature and pH. García-García et al. (2006) describe how both the DLVO and kinetic theories suggest that increasing temperature should result in less stable colloidal suspensions. Increasing temperature reduces the diffuse electrical double layer thickness which is responsible for stabilizing the electrostatic repulsion. Additionally, increasing temperature increases particle collision frequency and therefore aggregation rate (García-García et al., 2006, 2009). However, experiments by García-García et al. (2006) reveal the opposite behavior: colloidal stability slightly increases with increasing temperatures up to 80°C, which they attribute to the flat geometry

of bentonite and the different origin of the surface charge on bentonite particles. The negative charge at the face of a bentonite particle is constantly negative owing to isomorphic substitution, which is independent of temperature, and DLVO calculations suggest the repulsive component actually increases with increasing temperature (García-García et al., 2006). These and other studies (e.g., Tarì et al., 2000; Lu et al., 2003) on the effects of temperature on colloid stability assume peak repository temperatures of ~80˚C. However, temperatures ranging from 100-200˚C were chosen for the present experiments as current proposals for thermal management strategies of hard-rock backfilled disposal concepts suggest that backfill materials have a peak temperature tolerance of at least 200ºC (Liljenfeldt et al., 2017). At these even higher temperatures, there are additional considerations, such as the much lower dielectric constant of water and the potential for mineralogical and morphological alteration to the bentonite, which would affect its sorption capacity, both by potentially increasing its surface area and through transformation to a potentially more sorptive phase.

Another factor potentially affecting predictions of HLRW long-term stability is bentonite swelling and erosion. Many studies have investigated the swelling of bentonite clays in the micro-scale by observing them under Environmental Scanning Electron Microscopy (ESEM) and Transmission Electron Microscopy (TEM) or have investigated constrained swelling pressure measured via oedometer as a proxy for the unconstrained volumetric swelling of bentonite (Herbert et al., 2008; Komine, 2004; Komine and Ogata, 1994; Laird, 2006; Zhang et al., 2016). They have found among other things that the ionic strength and valence of electrolyte solutions strongly affects the swelling rate, swelling pressure, and final volume of bentonite (Komine and Ogata, 1994; Zhang et al., 2016). Recent efforts in computationally modeling bentonite swelling indicate that varying swelling rate may introduce anisotropy in the swelling of a bentonite pellet (Liu and Kang, personal communication). Anisotropy in swelling could have implications for modeling the erosion of a bentonite barrier, especially in the context of safety assessment.

Erosion of the bentonite barrier poses a risk for transport of radionuclides from the near-field repository to the far-field environment. The ability of bentonite to adsorb radionuclides onto its large surface area is part of what makes it attractive as a barrier material, preventing the release of dissolved radionuclides into the environment. However, that same property poses a risk of enhanced transport of those radionuclides should bentonite with sorbed radionuclides erode (Reimus and Boukhalfa, 2014). The behavior and interactions of various radionuclides when adsorbed onto bentonite colloids are the subject of numerous past and ongoing studies (Birgersson et al., 2009; Missana et al., 2003, 2008, 2018). Understanding the conditions under which bentonite erodes and the extent of that erosion are vital to predicting bentonite behavior in both the repository and surrounding environments.

The above mentioned methods for assessing bentonite swelling using swelling pressure, (e.g., Komine, 2004; Komine and Ogata, 1994; Zhang et al., 2016) are not well suited to assessing changes to the shape of a bentonite pellet as it swells due to their requiring a fully constrained swelling setup. A method that allows for visual evaluation of the swelling pellet is necessary for linking analyses of swelling and analyses of potential changing pellet geometry.

5.2 Methods and Materials

5.2.1 Column Studies at Elevated Temperature

All column experiments in this study employed a solution of synthetic Chancellor groundwater with FEBEX bentonite at a concentration of approximately 100 mg/L as described previously (Viswanathan et al., 2018, 2019). Two types of columns were conducted in this study. The first employs the repeat injection method discussed in previous milestone reports, and the set up was described in Viswanathan et al. (2019). Two minicolumns were constructed from Teflon tubing and packed with crushed analcime (75-200 nm) (Table 5-1). The elemental composition of the analcime and the mineralogy of the FEBEX are reported in Telfeyan et al. (2020). A concentrated solution of FEBEX colloids in synthetic Chancellor was spiked with

^{137}Cs ($7.3 \cdot 10^{-13}$ M) and subsequently heated in autoclaves for 2 weeks at 200ºC. The solution was then diluted and settled to remove large particles and diluted again to a colloid concentration of 100 mg L^{-1}. The solution was then spiked with a conservative tracer (^{3}HHO) and injected via a 60 mL Monoject™ syringe at a rate of 0.5 mL hr^{-1} into the first analcime column. Eluent was collected in glass test tubes arranged in a FOXY Jr. Fraction Collector programmed to collect sample every hour for the first 24 hours and then every 6 hours (3 mL collections) thereafter. Select samples from the first column were analyzed for ^{137}Cs, ^{3}HHO and colloid concentration. The remaining eluent was then collected and injected into the second analcime column. This eluent was collected in the same increments as described for the first column and was also analyzed for ^{137}Cs, ^{3}HHO and colloid concentration. These column experiments were interpreted using the colloid-facilitated transport models described in (Reimus, 2017; Reimus et al., 2017).

Table 5-1. Summary of parameters for columns and solutions used in the first set of column experiments. FEBEX was spiked with ^{137}Cs and heated for 2 weeks at 200˚C prior to preparation of the colloid solution for injection into an analcime column at room temperature. In the lower half of the table, the parameters for the granodiorite column heated in-situ are presented.

Column ID	Analcime Mass (g)	Pore volume (mL)	Column Length (cm)	Column Inner Diameter (cm)	Injection Volume (mL)	Injection Conc. Cs (M)	Injection Conc. ^{137} Cs (cpm/mL)
Heated FEBEX 1	10	3.31	11	0.8	120	$9.8 \cdot 10^{-13}$	25
Heated FEBEX 2	10	3.23	11	0.8	120	$2.7 \cdot 10^{-13}$	7
	Granodiorite Mass (g)						
200ºC Column	4.71	1.77	43		140	$2.6 \cdot 10^{-7}$ M	

A separate series of column studies was conducted to test the difference between pre-heating the colloids, as in the experiment above, and heating the colloid solution in-situ using a heated column apparatus. In order to understand the effect of elevated temperature on colloid properties in the absence of sediment, an experiment was conducted with a solution of FEBEX colloids (~100 mg L^{-1} colloid solution in synthetic Chancellor water) passed through an empty Teflon-lined stainless steel column encased in a ThermoScientific Linderg Blue Programmable Oven. The temperature was increased from 100˚C to 150˚C and 200˚C (pressure 1000 PSI), and eluent was collected from each interval. The eluent was analyzed for colloid concentration, colloid surface charge, and Scanning Electron Microscopy (SEM).

Following the characterization of colloids subjected to high temperatures, the column was packed with crushed granodiorite from the Grimsel Site (75-200 nm). A FEBEX solution similar to the above experiments was prepared. Non-radiological CsCl was added to 140 mL of FEBEX colloid solution (~100 mg L^{-1}) to a concentration of $2.6 \cdot 10^{-7}$ M Cs (Table 5-1). Although a lower concentration of Cs was desired in order to compare with previous experiments, non-radiological Cs was required for the laboratory with the high temperature furnace. The concentration was therefore prepared to be 100 times the detection limit of the mass spectrometer, which is $3.0 \cdot 10^{-9}$ M. The solution was then left for approximately 6 months, as it was previously shown that aging the colloids after spiking with Cs allows for Cs to diffuse to the strong sites on the colloids and sorb more strongly. The solution was then spiked with 10 ppm Br, as LiBr, to serve as a conservative tracer prior to injection through the granodiorite column. The flow rate was set to 3 mL

hr^{-1}, and samples were collected every 20 min for the first 2 hours and every hour thereafter. The column maintained a temperature of 200°C and a pressure of 1000 PSI for the duration of the experiment.

5.2.2 Analytical Methods for Column Evaluation

In order to determine changes in electrochemical properties of the FEBEX colloids due to temperature, the eluent colloids from the column experiments were analyzed for zeta potential, size and concetration. A Malvern Zetasizer Nano with a folded capillary cell was used to measure the eletrophoretic mobility of the colloids, from which the zeta potential was determined using the Henry equation with Smoluchowski approximation. The Zetasizer was also used to measure the distribution of colloid diameter, and the average value was reported. For both size and zeta potential, measurements were conducted at 22°C, and 3 independent runs were averaged to determine the measurment. An Agilent 8453 UV-vis Spectrophotometer equiped with a blue filter was employed to determine the colloid concentration as described in Telfeyan et al. (2020). Absorbance values at 700 nm were taken as background values subtrated from the absorbance at 400 nm, which showed the greatest sensitivity to colloids. The colloid concentration was determined by drying a known volume of the FEBEX suspension and weighing the difference, accounting for total dissolved solids. All UV-vis measurements were then determined as a fraction of the unaltered FEBEX suspension of known concentration.

^{137}Cs and ^{3}HHO concentrations were determined by liquid scintillation counting (LSC) on a PerkinElmer 1220 Quanitllus™ desinged for low level counting. Between 0.5 and 2 mL of sample was diluted with deionized water to a volume of 4 mL and combined with 16 mL of Optima Gold AB scintillantion cocktail in plastic liquid scintillation vials. Each sample was counted 3 times, and count times varied from 1 hour to 16 hours, depending on sample concentration. Non-radiological Cs was determined on an inductively coupled plasma mass spectrometer (ICP-MS), and Br concentrations were determined by ion chromatography (IC).

The colloidal suspensions that were injected into the empty column at elevated temperatures were collected for imaging analysis to determine if mineralogical changes had occurred. The eluent was collected after each temperature interval and poured through a ThermoScientific Nalgene vacuum filtration unit with a 0.02 μm size filter to collect the colloids. The dried colloidal material was then transferred to a carbon-taped mount for scanning electron microscopy (SEM). SEM analysis was conducted on an FEI™ Inspect F SEM equipped with Energy dispersive X-ray spectroscopy (EDS) for elemental analysis.

5.2.3 Bentonite Erosion Laboratory Experiments

Experiments were conducted to visually analyze the swelling of small pellets of MX80 bentonite in two and three dimensions under different ionic strength salt solutions. Pellets were created by compressing 0.015 g of powdered unprocessed commercial MX80 bentonite into an approximately 3.2 mm diameter by 1.25 mm height cylindrical pellet to give a dry density of 1.49 g/cm^3.

In order to test swelling in two dimensions, an apparatus was constructed using the top and bottom of a petri dish with a 3-D printed spacer separating them by the same height as the pellet. The top and bottom are sealed to the spacer with silicone rubber, and two small holes are drilled in the top as a water inlet and outlet. The spacer has a projection of known dimensions which provides a scale for the pellet swelling.

The whole apparatus is then placed on the stage of a Zeiss Stemi 2000-C inspection microscope with a canon Rebel 3t digital camera attached. The camera is set to take thirty images at an interval of five seconds followed by ten images at an interval of thirty seconds, and then the water-electrolyte solution is introduced. The camera records through the microscope the vertically constrained two-dimensional swelling of the bentonite pellet over the course of three minutes and twenty seconds. Solutions tested were deionized water, 0.2 mM NaCl, 2.0 mM NaCl, and 20 mM NaCl.

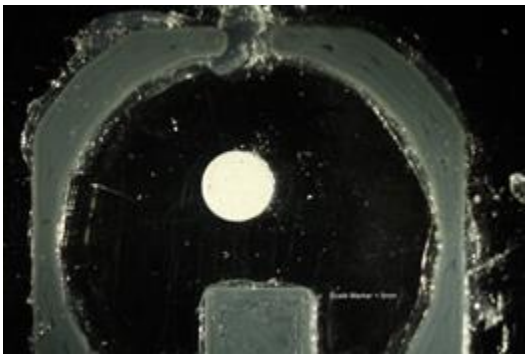

Figure 5-1. The constrained (2D) swelling setup in the microscope stage. The projection in the lower half of the image is a known dimension of 5-mm and serves as a scale marker for image analysis.

To test three-dimensional swelling, two cameras were used. One from the top, as described above, and one from the side. The side-view images were used to assess swelling vertically, and volume was estimated by assuming the pellets remain roughly cylindrical. For the unconstrained, three-dimensional tests, pellets were attached to frosted glass microscope slides in order to fix them in place. Tests were conducted in cube-shaped 50-mm optical glass cuvettes to ensure a clear undistorted view of the swelling pellet from the side. The Canon DSLR camera was mounted to a tripod and fitted with a macro lens in order to capture the side-on images. A Super Eyes B005 USB microscope was used to capture the top-down images. As in the vertically constrained two-dimensional swelling tests, the camera was set up to take 40 images at a 5-second interval after pre-swelling images were taken. The USB microscope was set up to take a video for the duration of the experiment and still images were extracted from the video at the same interval as the camera stills.

5.2.4 Image Analysis of Bentonite Erosion

Images were analyzed using the open source ImageJ software developed by the National Institute of Health. A color threshold analysis was performed to differentiate the pellet from its background. It was found that for the images in this study, the YUV color space (as opposed to RGB, HSV, or Lab) was most useful for differentiating the bentonite pellets from the background and from the gel dispersion that is thrown off as the pellet swells. Ideal threshold positions in that color space will vary with lighting conditions, but the threshold is held constant throughout the analysis of one test to provide a consistent benchmark for change in area. The threshold analysis produces a binary mask which is used as the input for the particle analysis function in ImageJ. This analysis measures and displays the number of pixels in an object that fits the criteria entered. It is also possible, and useful to set an equivalency between pixels and a distance measure such as millimeters. If that is done, the particle analysis function will also display the area of the particle in mm^2. The binary mask generated using the threshold analysis can also be used to investigate shape descriptors and how they change with swelling rate. In order to investigate shape descriptors however, the binary masks must be modified to remove the irregularity of the perimeter of the mask. If the masks are left unmodified, the shape descriptors will be very strongly influenced by the variations in the roughness of the edge of the particle. In order to smooth the edges of the pellet masks, a Gaussian blur with a radius of 2 mm was applied to the masks, and then a threshold was applied to produce another, smoothed binary from which the particle analysis was performed. The shape descriptors used in this method are the circularity and aspect

ratio measures which are inbuilt into the particle analyzer in ImageJ. Circularity compares the area of the particle to its perimeter and displays those as a ratio.

$$cicularity = 4 \cdot \pi \cdot \frac{area}{perimeter^2} \quad (5\text{-}1)$$

A perfect circle has a circularity of 1.0, and the least circular possible shape has a circularity approaching 0.0. As the bentonite pellets start near perfectly circular, circularity measurements below the starting measurement are interpreted to indicate anisotropy in swelling. Aspect ratio measures the difference in diameter between the largest circle that touches two points on the particle, and the smallest circle that fits entirely within the particle.

$$aspect\ ratio = \frac{major\ axis}{minor\ axis} \quad 52\text{-}2)$$

Aspect ratio increases as the pellet gets less circular, so higher aspect ratios are interpreted to represent higher swelling anisotropy. Change in area over five seconds is calculated as a proxy for the instantaneous swelling rate and is used to compare shape descriptors at a given swelling rate.

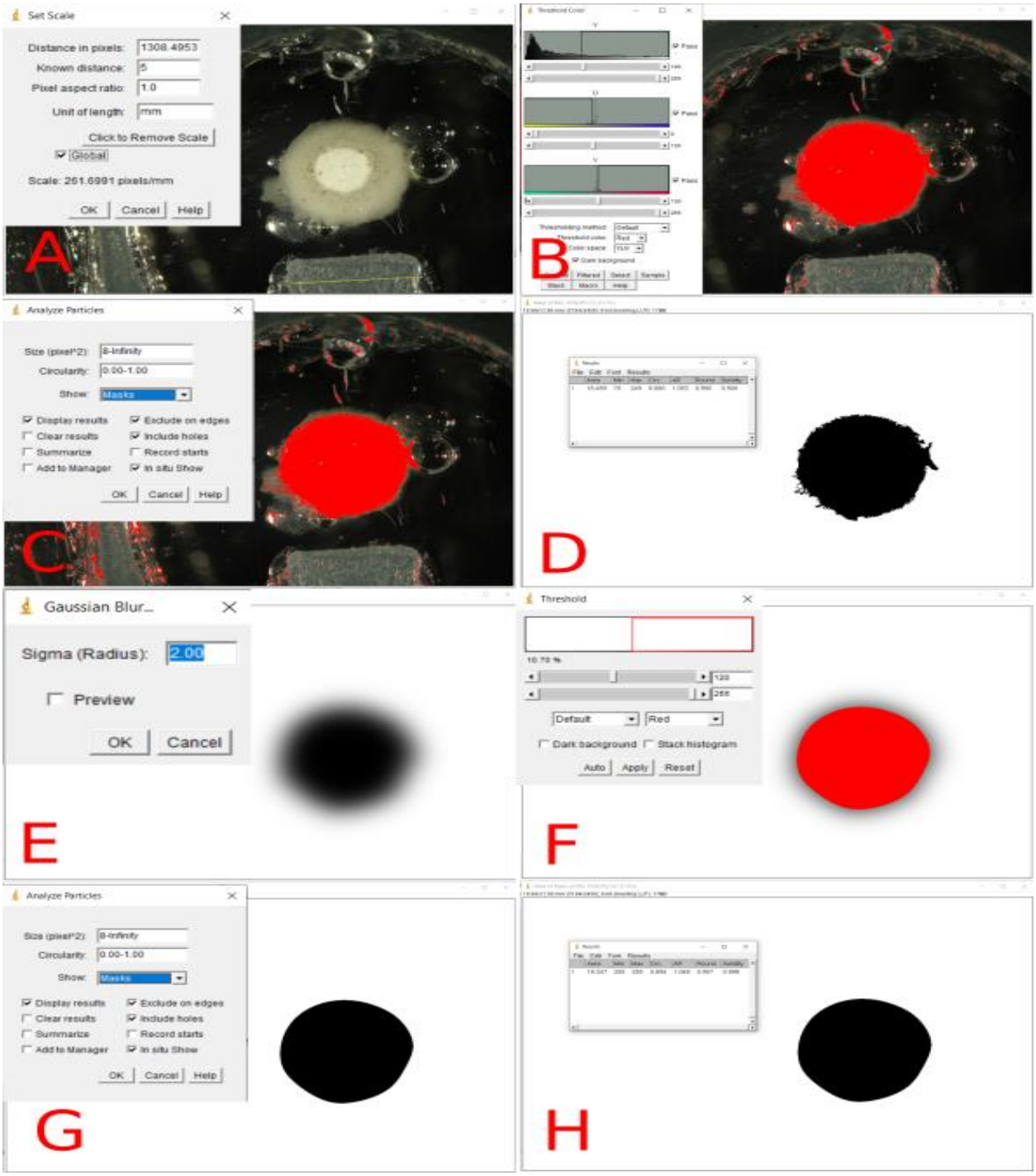

Figure 5-2. A visual representation of the image analysis process. A) Setting the scale. B) Using color thresholding to differentiate the pellet from its background and any gel suspensions it may create. C) Using the ImageJ particle analyzer to find the area of the pellet. D) Results of area analysis. E) Using the Gaussian blur function to blur the pellet mask. F) Using the threshold function to pull the general smoothed shape of the pellet out of the blurred image. G) Using the particle analyzer to access shape descriptors of the now smoothed pellet. H) The shape results.

5.3 Results

5.3.1 Column Studies at Elevated Temperature

Breakthrough of the colloids that were heated for 2 weeks at 200°C, conservative tracer (^{3}HHO), and ^{137}Cs eluting through a column packed with analcime at room temperature are shown in Figure 5-3. The conservative tracer indicates the breakthrough of the injectate and the beginning of column flushing. The breakthrough of about 60% of the colloid concentration relative to the starting pre-injection concentration occurs immediately, suggesting there is some filtration of the colloids by the analcime. The colloid concentration increases to 100% by the conclusion of the experiment. The breakthrough of ^{137}Cs follows a similar trend as that of the colloids, although at much lower concentrations. Only ~10% of the initial ^{137}Cs elutes initially, increasing to 40% by the conclusion of the experiment. Additionally, no detectable ^{137}Cs was measured in eluent fractions filtered through 0.02 μm filters, indicating that all ^{137}Cs occurred in the colloidal phase.

The model interpretations for column 1 are shown as dashed lines in Figure 5-3. A 2-site sorption model was used, and initial simulations used the same sorption and desorption rate constants as previous experiments with the FEBEX colloids spiked with ^{137}Cs eluting through an analcime column (Viswanathan 2018; Telfeyan et al., 2020). However, previous experiments did not show substantial initial filtration of the colloids by the analcime, so a reversible filtration and resuspension term for the colloids was necessary (Table 5-2). Additionally, the initial simulation failed to reproduce the increase in ^{137}Cs between 600 and 800 hours (gold dashed line in Figure 5-3). Increasing the sorption rate constants for the both the first and second site on the colloids was necessary to simulate this increase. Assuming all aspects of the colloid preparation are similar except for the heating to 200°C for 2 weeks, this column result suggests that pre-heating the colloids results in slightly greater sorption of ^{137}Cs to the analcime. However, the best fit for the model would benefit from an error-minimizing approach, although such an exercise would be difficult due to the inherent scatter from UV-vis and LSC measurements.

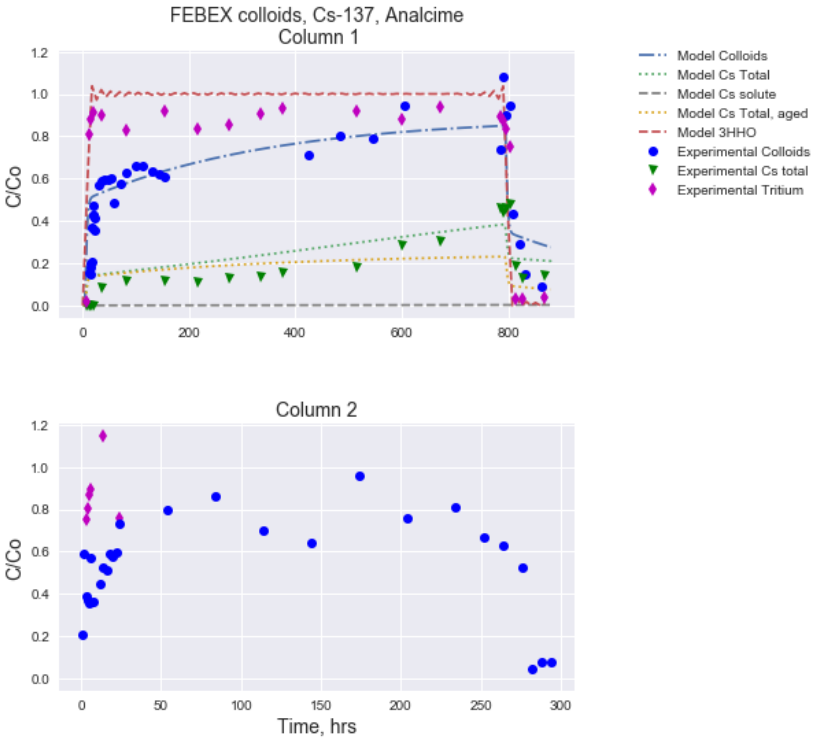

Figure 5-3. Results from the sequential injection column experiment consisting of FEBEX colloids spiked with ^{137}Cs and heated for 2 weeks at 200°C and a ^{3}HHO tracer. The top figure shows the results from the first column, including breakthrough of ^{3}HHO, colloids, and ^{137}Cs with corresponding model matches. The dashed line labeled "Model Cs Total, aged" shows the model results using the parameters from the aged FEBEX colloids used in the experiments described in Viswanathan et al. (2018) and Telfeyan et al., 2020. The bottom figure shows the breakthrough results of ^{3}HHO tracer and colloids through the second column.

The zetapotential and size of select eluent samples was also measured and compared to the injectate values. The FEBEX solution had a zetapotential of -46 mV and an average size ranging from 504 to 581 nm, which is slightly more negative compared to previous FEBEX colloid solutions (~-27 - -35 mV; Viswanathan et al., 2018). The three eluent samples measured for zetapotential ranged from -38 to -48 mV, and the seven samples measured for average size ranged from 355 to 545 nm, indicating that no to minimal changes to the bentonite colloid size or charge occurred.

Table 5-2. Model parameters used to match the column experiment data of Figure 5-3. The sorption site densities were kept the same as in Viswanathan et al. (2018). Different colloid reversible and irreversible filtration rates were necessary to simulate the filtration of colloids by the analcime

Parameter	Value
$k_{ac,1}$ (Site 1 sorption rate constant), ml/g-hr	30,000
$k_{ca,1}$ (Site 1 desorption rate constant), hr^{-1}	0.6
$C_{ac,max,1}$ (Site 1 sorption site density), mol/g	5×10^{-8}
$k_{ac,2}$ (Site 2 sorption rate constant), ml/g-hr	900
$k_{ca,2}$ (Site 2 desorption rate constant), hr^{-1}	0.0001
$C_{ac,max,2}$ (Site 2 sorption site density), mol/g	7×10^{-9}
k_{filt} (Irreversible filtration rate of colloids) hr^{-1}	0.015
Reversible filtration rate of colloids hr^{-1}	0.075
Resuspension rate of colloids hr^{-1}	0.004

The eluent from the first column was collected and injected into a fresh analcime column (column 2). The breakthrough curves of colloids and conservative tracer are shown in Figure 5-3. ^{3}HHO values in samples after the initial breakthrough were discarded owing to analytical issues with the ^{3}HHO measurements. Therefore, the full profile of the injection could not be characterized. The colloids, however, show near immediate breakthrough and decrease upon introduction of the flush solution with minimal tailing. In contrast to the first column, breakthrough of the colloids through the second column reaches 80% immediately and stays relatively constant during the full injection. The concentration of ^{137}Cs was not significantly larger than the blank concentration, suggesting any breakthrough of ^{137}Cs was too low to be detected. Therefore, no attempts were made to model the data. The lack of ^{137}Cs eluting through the second column suggests that ^{137}Cs was not as strongly sorbed to the colloids as previous experiments which showed 10% recovery of ^{137}Cs through a second analcime column. This result is in contrast to the above observation that the sorption rate constants needed to be increased to simulate the results from the first column. In this experiment and in the previous experiment (Viswanthan et al., 2018; Telfeyan et al., 2020), the ^{137}Cs eluting through the second column was near the detection limit of the LSC. Such low ^{137}Cs concentrations were selected to interrogate the sorption of ^{137}Cs to strong sites on the colloids, but the limitations of both the model and the LSC suggest that no firm conclusions regarding the relative sorption capacity of the hydrothermally altered bentonite can be made, except to say that it is very similar to the aged colloids used in the Viswanathan et al. (2018).

The SEM images taken of these colloids after heating and prior to spiking with ^{137}Cs and ^{3}HHO were discussed in a previous milestone (Viswanathan, 2019). SEM and EDS analysis indicated that some morphological and potentially mineralogical changes to the FEBEX occur at 200ºC. Specifically, the typical platy texture of the bentonite was partially replaced with small spheres. EDS capabilities were limited at time of the analysis, so questions remained regarding the composition of the newly formed spheres. EDS conducted during the studies discussed below attempted to address these questions.

In order to ascertain how temperature affects colloids' sorption capacity in the absence of sediment, column studies were conducted at elevated temperatures. A solution of 100 mg/L FEBEX colloids in synthetic Chancellor groundwater was injected into an empty Teflon-lined stainless steel column heated incrementally from 100˚C to 150˚C and 200˚C. Both the electrochemical and mineralogical changes to the FEBEX were determined. The change in colloid concentration, size, and charge as a function of temperature are shown in Figure 5-4. No change in colloid size or charge is apparent, but a decrease in colloid concentration is observed, especially at 200˚C. These measurements were taken at room temperature, and

it is not known how letting the solutions cool prior to measurement may affect the values. Future experiment should attempt to make the UV-vis measurements at elevated temperature if possible.

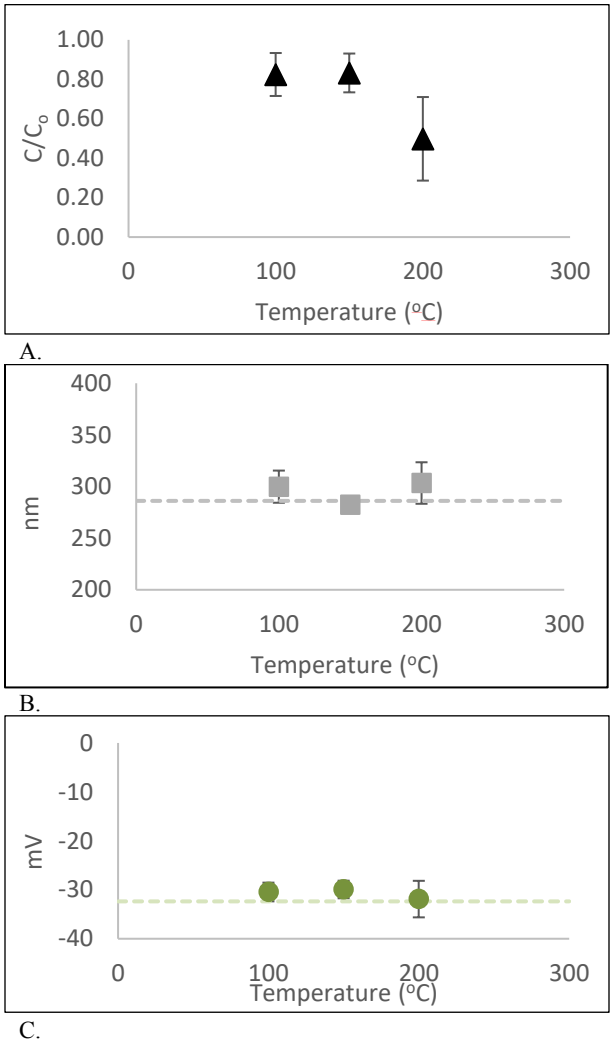

Figure 5-4. Colloid concentration (A), size (B), and charge (C) as a function of temperature measured from a solution of FEBEX colloids in synthetic Chancellor groundwater passed through a column heated to 100ºC, 150ºC, and 200ºC in the absence of sediment. The dashed lines in B. and C. indicate the size and charge of the room temperature FEBEX solution, respectively.

Eluent that was not used for UV-vis or zetasizer analysis was collected and vacuum filtered (0.02 µm) to isolate the colloids for SEM analysis. Colloids analyzed after passing through the column at 100˚C showed slight erosion at the edges of the bentonite but were still predominantly aluminosilicate minerals. At 200˚C, both morphological and mineralogical changes are apparent. Similar to SEM-EDS studies reported in last year's milestone, the SEM-EDS analysis in Figure 5-5 shows the presence of Ca-O phases formed from the FEBEX solution heated to 200˚C.

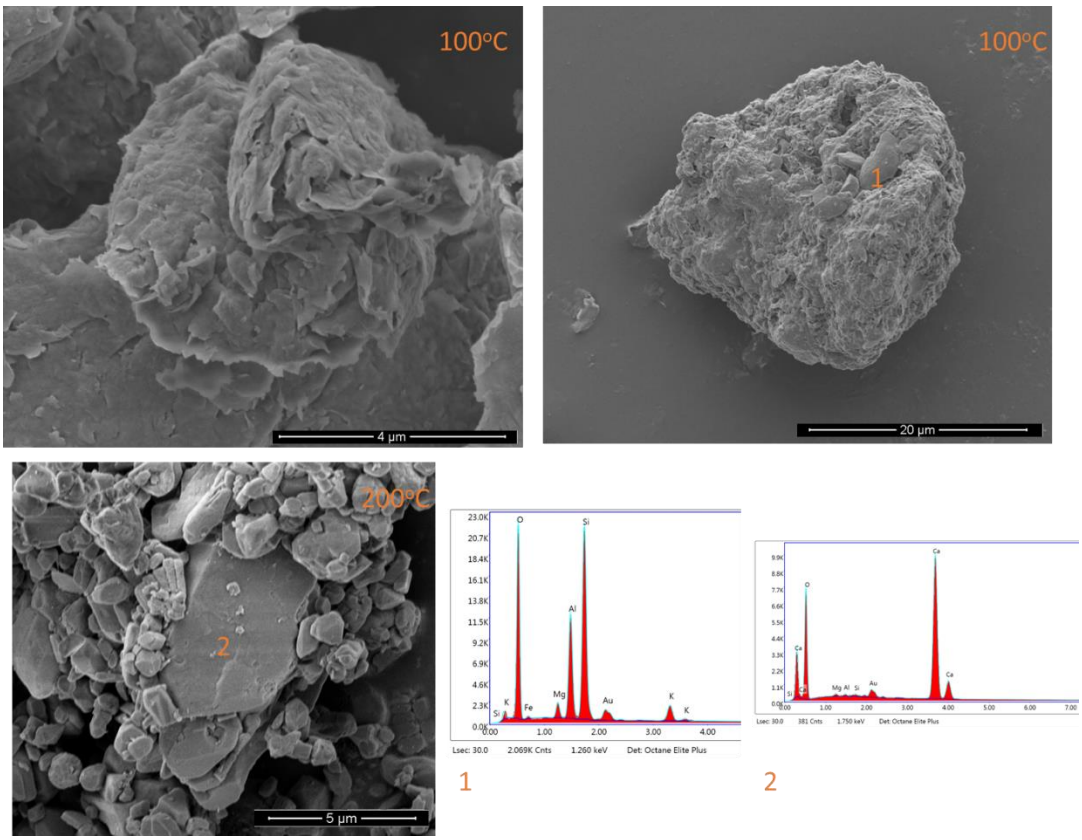

Figure 5-5. SEM image of FEBEX clay passed through an unpacked column at 100°C and 200°C.

The final column experiment involved injecting FEBEX colloids that were spiked with 35 ppb ($2.6 \cdot 10^{-7}$ M) non radiological Cs and aged for 6 months through a column of granodiorite heated in-situ to 200°C. The breakthrough of the conservative tracer (Br) and colloids relative to the starting concentrations, as well as the zetapotential and size of the colloids are shown in Figure 5-6. There is substantial scatter in the colloid concentration measurements initially, which may be due to the large amount of dead volume in the tubing of the heated column apparatus. The Br breakthrough supports this idea and indicates that nearly 12 mL of flushing solution elutes prior to breakthrough of the colloid solution. Colloid concentrations then drop to around 40% of starting concentration for approximately 25 hours before dropping to less than 10%. The zetapotential of 4 eluent samples is more negative than the injection value, whereas the average size of the colloid particles is greater than or the same as the injection value. Only four samples were measured owing to the small volume of sample available. Analysis of Cs is still undergoing, and remaining eluent will be filtered for SEM analysis as described above. Any remaining eluent will be used for additional zetasizer measurements.

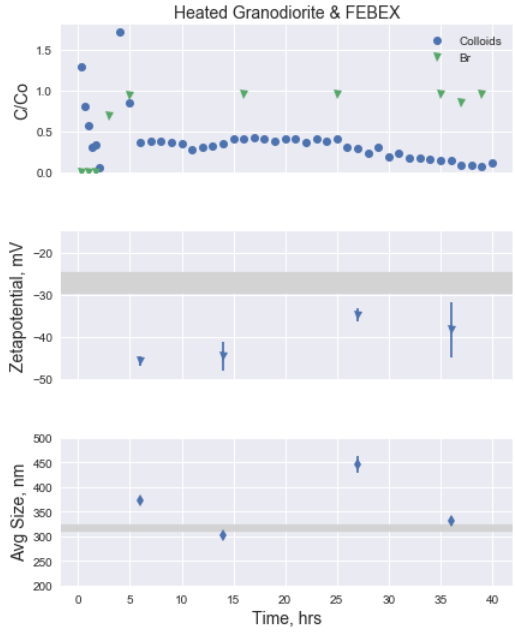

Figure 5-6. Breakthrough of FEBEX colloids and conservative tracer (Br) through a granodiorite column heated in-situ to 200°C, zetapotential, and size of eluent colloids relative to starting zetapotential and size. The grey line indicates injectate values, and the width of the line indicates the standard deviation.

5.3.2 Bentonite Erosion Experiments

For each swelling experiment, the two data sets generated in these tests were change in area over time, and change in shape descriptors (i.e., circularity and aspect ratio) over time. Because the bentonite pellets were constrained vertically, meaning they could only swell outwards and not upwards, the top-down change in area is considered an adequate descriptor of swelling. The change in pellet area over the five seconds between each analysis is used as a proxy for swelling rate. Swelling is also displayed as a percentage of total swelling as in Komine (2004). Circularity, a metric native to the analysis functionality of ImageJ which compares the perimeter of a shape to its area, is used as a proxy for the anisotropy of swelling—if the originally circular bentonite pellet is now less circular, it is assumed to have swelled anisotropically to a degree.

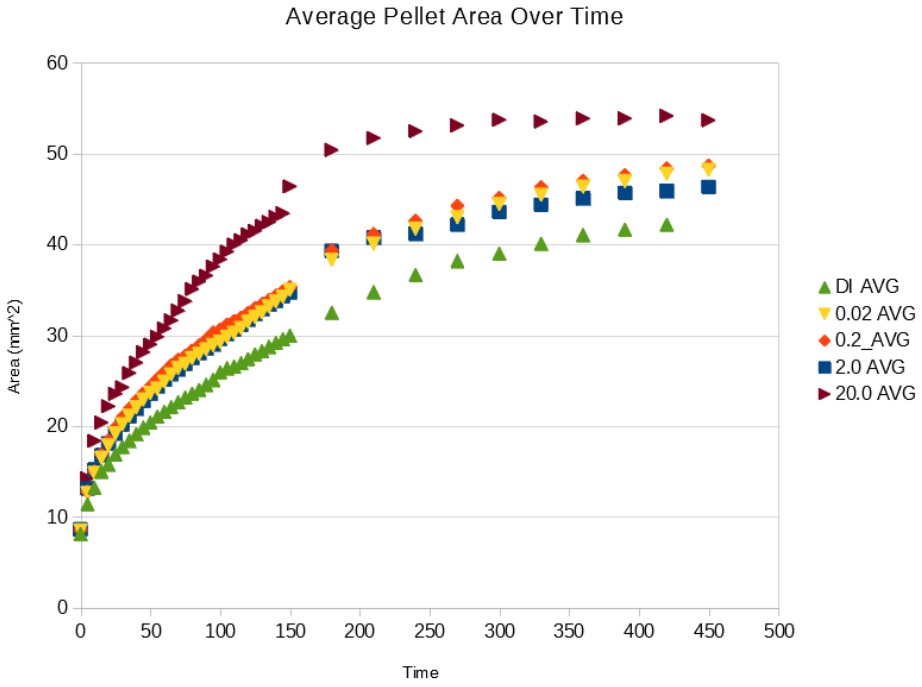

Figure 5-7. Average change in area over time for .015 g cylindrical bentonite pellets. Experiments were performed in triplicate.

Due to inconsistencies in constrained swelling apparatus and COVID-19 related inability to conduct lab work, the results of experiments to date do not show the expected relationships between salt solution concentration and swelling rate where swelling is expected to decrease with increasing solution strength. What the current data set may show, however, is that the effect of the available surface area for water to interact with the compressed bentonite compared to the volume of the pellet has a very large effect on how fast the bentonite is able to take on water and swell. Testing the swelling and wetting of pellets of different diameters could be used to elucidate this relationship. The large discrepancy between the swelling of weaker solutions and that of the 20 mM is due to the pellets losing cohesion and completely disintegrating in the 20 mM solutions and the inability of the image analysis method to discriminate between a pellet disintegrating and a pellet swelling. The tests run using DI water were conducted using constraining apparatuses which used a different petri dish in their construction and which seemingly held the pellet more firmly than the other apparatuses used, slowing wetting and thus swelling. The third iteration of the 0.02 mM and 0.2 mM solutions used similarly constructed constraining apparatuses to the DI water tests and correspondingly show lower swelling rates. When displaying only these runs, the areas show the expected relationship between swelling and solution concentration.

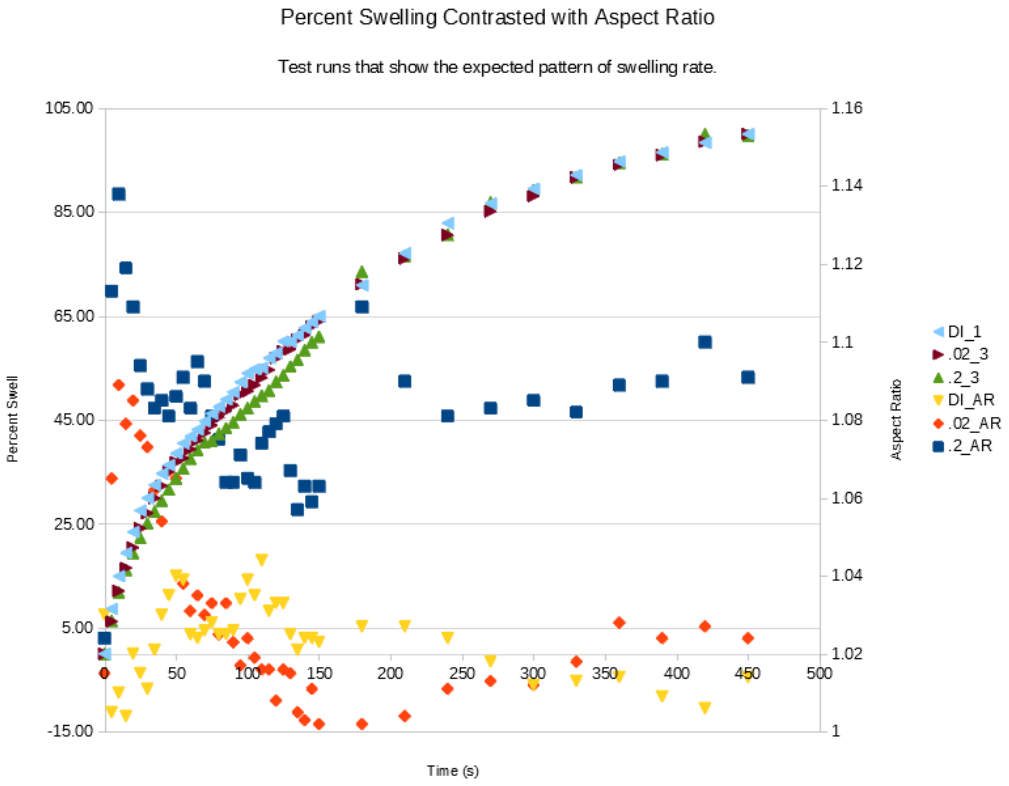

Figure 5-8. Graph showing the percent swelling of the three best constrained tests which show behavior similar to what is expected from bentonites swelling in different strength solutions. Also shown are the changes in aspect ratio of the pellets over swelling.

5.4 Discussion

The objective of the high-temperature colloid experiments was to interrogate the effects of temperature on both the electrochemical properties of colloids as well as mineralogical and morphological changes to the bentonite. The first set of experiments isolated the effects of mineralogical and morphological changes to the bentonite because the transport experiment was conducted at room temperature. The SEM images of the heated bentonite were presented in Viswanathan et al. (2019). Unfortunately, the EDS was not operational at the time of most of the analyses so the elemental composition of most of the grains could not be determined. However, morphological changes to the bentonite are apparent. Specifically, the edges of the bentonite show fraying and alteration to numerous small spheres on the order of 1 µm, indicating that the surface area of the bentonite increased. From the EDS data that was available, the presence of Ca-O spheres was apparent, and, combined with the visual observations of the clay, may suggest minor formation of calcium silicate hydrate (C-S-H) or calcium aluminate silicate hydrate (C-A-S-H). Such phases are the main cement hydration products formed at the interface between cement and bentonite in a repository setting (e.g., Fernández et al., 2016; Missana et al., 2018). However, it is unclear how such phases could form as the only addition of Ca to the system is the minor amount added from the Chancellor water. The SEM analysis performed on the colloids injected into a heated column show similar results to the colloids heated in an autoclave. At 100ºC, some fraying of the bentonite edges occurs, but the mineralogy largely indicates clay. At 200˚C, however, the morphology of the clay is largely different, and the EDS analysis

indicates some conversion to a Ca-O dominant mineral (Fig. 5-5). Additional SEM and potentially X-Ray Diffraction are planned to better identify these new phases.

The second column and third column experiments test the effects of heating the colloids during transport, which will incorporate both electrochemical changes to the colloids and mineralogical changes to the bentonite. Garcìa-Garcìa et al. (2006) show that temperature influences colloid stability mostly by affecting the repulsive force on colloids with minimal influence on the Van-der-Waals force. At temperatures up to 80°C, increasing the temperature was shown to increase the repulsion and therefore increase the colloid stability (Garcìa-Garcìa et al., 2006). However, at 200°C, temperature will also affect the dielectric constant of the medium (water) and potentially the bentonite, although the effects of temperature on bentonite's dielectric constant have not been determined. The column experiments presented here, both through sediment and in the absence of sediment, suggest that colloid concentration decreases to 40-50% relative to the starting concentration at high temperature. However, the zeta potential either stays the same, as in the experiment with no sediment, or decreases, as in the experiment with granodiorite. Furthermore, the average size of the colloids does not change significantly with temperature. Therefore, the zeta potential and size measurements cannot explain the decrease in colloid concentration at high temperature. Changes to the medium and the interaction of bentonite with the medium are likely responsible for the drop in concentration. To better envision the effects of temperature on the double layer electrostatic energy ($V_{repulsive}$) between the colloids, DLVO prediction were made according to the equations in Garcìa-Garcìa et al. (2006). This repulsion term was calculated both without decreasing the zeta potential as shown in Figure 5-4C (Figure 5-9A) and with decreasing the zeta potential to represent the experiment summarized in Figure 5-6 (Figure 5-9B). With and without changing the zeta potential results in decreased $V_{repulsive}$, which can be attributed to the lower dielectric constant of water at elevated temperature (Table 5-3). However, the decrease is much greater if the surface potentials are equal. Future experiments should attempt to address the discrepancy between the results of the heated column experiments with and without sediment. Additionally, large differences in zeta potential and surface potential can occur (Missana and Adell, 2000), and exploring different methods of calculating the surface potential would be worthwhile. Attempts to simulate the Van der Waals force were not made owing to the numerous potential values reported for the Hamaker constant of bentonite. This constant is difficult to determine experimentally (Missana and Adell, 2000) and any effects of temperature on this constant are not well understood but are assumed to be minimal (Garcìa-Garcìa et al., 2006).

It should also be noted that all experiments were conducted with synthetic Chancellor water which has optimum pH (8.5-9) and ionic strength (0.005 M) for colloid stability. Either increasing the ionic strength or decreasing the pH would lower the stability of colloids (Garcìa-Garcìa et al., 2009). In fact, Missana and Adell (2000) argue that the DLVO theory is inappropriate for montmorillonite, especially at pH below the point of zero charge where the clay's edge charges are positive, resulting in aggregation between colloid edge and faces that cannot be accounted for in the DLVO theory. Additionally, the DLVO theory cannot account for the effects of hydration energy or swelling energy, which may increase the attraction between colloids (Missana and Adell, 2000). With these constraints in mind, the exercise shown in Figure 5-9 simply demonstrates how changing the temperature term and dielectric constant of water lead to a reduced $V_{repulsive}$ term, which helps explain some of the reduction in colloid concentration observed in the above experiments. However, further theoretical and experimental simulations would be worthwhile to better explain the observed drop in colloid concentration by nearly 50%, especially considering that the morphological changes suggest that hydrothermally altered colloids will have a greater sorption capacity.

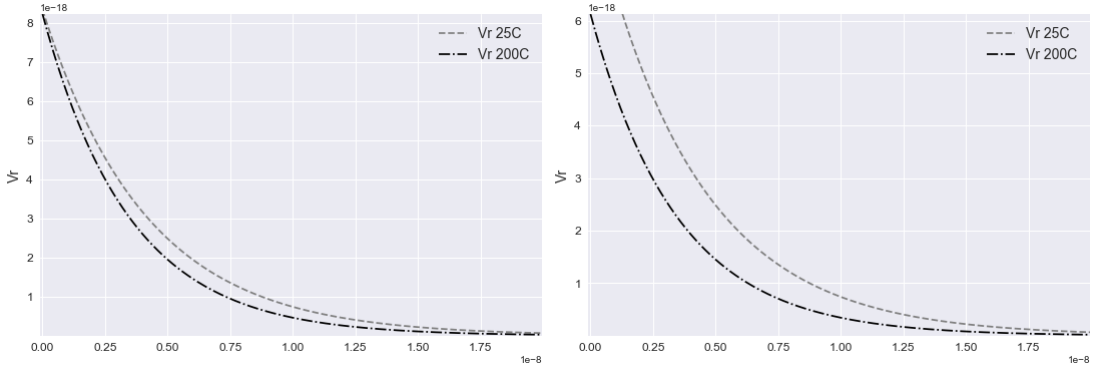

Figure 5-9. $V_{repulsive}$ calculations based on the DLVO theory using parameter estimates from measurements of FEBEX colloids. A. using the more negative surface potential at 200˚C, B. using the same surface potential for both temperatures.

Table 5-3. Parameters used to calculate $V_{repulsive}$

Parameter	Value	Units	Description
R	1.6e-7	m	Particle radius determined from zetasizer
n_0	4.6e24	l^{-1}	1000*N_a*Mi, number of ions per cubic meter
k_B	1.38e-23	$J{\cdot}K^{-1}$	Boltzmann constant
T	T_1: 298.15, T_2: 373.15	K	Absolute temperature
e	1.60217e-19	C	Charge of an electron
N_a	6.02213e23	mol^{-1}	Avogadro's number
ε_0	at T_1: 78.54, at T_2:35		Dielectric constant of water, Machmudah et al., 2017
ε_r	8.854e-12	F m^{-1}	Permittivity of a vacuum
$\Sigma(z_i^2*M_i)$	0.010889		Derived from ionic strength
ϕ_0	-0.2 - -0.15	V	Surface potential, derived from zeta potential according to Garcia-Garcia (2009)

The bentonite erosion experiments were largely focused on developing methods for quantifying important parameters for input into bentonite swelling models. Specifically, the above experiments demonstrate that anisotropy in bentonite swelling can be represented and quantified by simple microscopy and image analysis. Upcoming work will focus on refining the above outlined methods for 2-D and 3-D swelling tests to produce data. First the constrained (2-D) swelling experiments will be refined in order to eliminate inconsistencies in the pellet constraining apparatus that contributed to variance between tests in the data presented here. Then, tests using the refined 2-D swelling testing protocol will be performed in triplicate using the same NaCl solutions as in the above reported tests. 2-D swelling tests will also be performed with bentonite pellets of varying diameters in order to test the effect of wetting time on swelling. Following that, tests using the unconstrained, 3-D swelling method detailed above will be performed in triplicate using the same NaCl solutions as above. Farther in the future, experiments for measuring erosion of the bentonite pellet as it swells will be devised and performed.

5.5 References

Akinwunmi, B., Sun, L., Hirvi, J. T., Kasa, S., and Pakkanen, T. A. (2019). Influence of temperature on the swelling pressure of bentonite clay. *Chemical Physics*, *516*(June 2018), 177–181. https://doi.org/10.1016/j.chemphys.2018.09.009

Alonso, U., Missana, T., Fernández, A. M., and García-Gutiérrez, M. (2018). Erosion behaviour of raw bentonites under compacted and confined conditions: Relevance of smectite content and clay/water interactions. *Applied Geochemistry*, *94*(April), 11–20. https://doi.org/10.1016/j.apgeochem.2018.04.012

Birgersson, M., Börgesson, L., Hedström, M., Karnland, O., and Nilsson, U. (2009). *Bentonite erosion*. *TR-09-34*(December), 171.

Birgersson, M., Hedström, M., and Karnland, O. (2011). Sol formation ability of Ca/Na-montmorillonite at low ionic strength. *Physics and Chemistry of the Earth*, *36*(17–18), 1572–1579. https://doi.org/10.1016/j.pce.2011.07.017

Fernández, R., González, L., Ruiz, A. I., and Cuevas, J. (2016). Formation of C-A-S-H phases from the interaction between concrete or cement and bentonite. *Clay Minerals, 51*(2), 223-235. doi:10.1180/claymin.2016.051.2.09

Garcìa-Garcìa, S., Jonsson, M., Wold, S., (2006). Temperature effect on the stability of bentonite colloids in water. *Journal of Colloid and Interface Science*, *298*, 694-705. https://doi.org/10.1016/j.jcis.2006.01.018

Garcìa-Garcìa, M., Wold, S., S., Jonsson, (2009). Effects of temperature on the stability of colloidal montmorillonite particles at different pH and ionic strength. *Applied Clay Science*, *43*, 21-26. https:// doi: 10.1016/j.clay.2008.07.011

Herbert, H. J., Kasbohm, J., Sprenger, H., Fernández, A. M., and Reichelt, C. (2008). Swelling pressures of MX-80 bentonite in solutions of different ionic strength. *Physics and Chemistry of the Earth*, *33*(SUPPL. 1). https://doi.org/10.1016/j.pce.2008.10.005

Kersting, A. B., Reimus, P. W., Abdel-Fattah, A., Allen, P. G., Anghel, I., Benedict, F. C., ... & Neu, M. P. (2003). *Colloid-facilitated transport of low-solubility radionuclides: A field, experimental, and modeling investigation* (No. UCRL-ID-149688). Lawrence Livermore National Lab (LLNL), Livermore, CA (United States).

Kolstad, D. C., Benson, C. H., and Edil, T. B. (2004). Hydraulic Conductivity and Swell of Nonprehydrated Geosynthetic Clay Liners Permeated with Multispecies Inorganic Solutions. *Journal of Geotechnical and Geoenvironmental Engineering*, *130*(12), 1236–1249. https://doi.org/10.1061/(ASCE)1090-0241(2004)130:12(1236)

Komine, H. (2004). Simplified evaluation for swelling characteristics of bentonites. *Engineering Geology*, *71*(3–4), 265–279. https://doi.org/10.1016/S0013-7952(03)00140-6

Komine, H., and Ogata, N. (1994). Experimental study on swelling characteristics of compacted bentonite. *Canadian Geotechnical Journal*, *31*(4), 478–490. https://doi.org/10.1139/t94-057

Laird, D. A. (2006). Influence of layer charge on swelling of smectites. *Applied Clay Science*, *34*(1–4), 74–87. https://doi.org/10.1016/j.clay.2006.01.009

Liljenfeldt, H., Banerjee, K., Clarity, J. B., Scaglione, J., Jubin, R. T., Sobes, V., Howard, R. L., Hardin, E., Price, L., Kalinina, E., Hadgu, T., Ilgen, A., Cryan, Cl. L., Carter, J., Severynse, T. F., Perry, F. (2017). *Summary of Investigations on Technical Feasibility of Direct Disposal of Dual-Purpose Canisters* (No. ORNL/SPR-2017/443). Oak Ridge National Lab (ORNL), Oak Ridge, TN (United States).

Lu, N., Reimus, P. W., Parker, G. R., Conca, J. L., and Triay, I. R. (2003). Sorption kinetics and impact of temperature, ionic strength and colloid concentration on the adsorption of plutonium-239 by inorganic colloids. *Radiochimica Acta*, *91*(12), 713-720.

Machmudah, S., Kanda, H., & Goto, M. (2017). Hydrolysis of Biopolymers in Near-Critical and Subcritical Water. In *Water Extraction of Bioactive Compounds* (pp. 69-107). Elsevier.

Missana, T. and Adell, A., (2000). On the applicability of DLVO theory to the prediction of clay colloids stability. *Journal of Colloid and Interface Science, 230*, 150-156. https://doi:10.1006/jcis.2000.7003

Missana, T., Alonso, U., Fernández, A. M., and García-Gutiérrez, M. (2018). Colloidal properties of different smectite clays: Significance for the bentonite barrier erosion and radionuclide transport in radioactive waste repositories. *Applied Geochemistry*, *97*(December 2017), 157–166. https://doi.org/10.1016/j.apgeochem.2018.08.008

Missana, T., Alonso, Ú., García-Gutiérrez, M., and Mingarro, M. (2008). Role of bentonite colloids on europium and plutonium migration in a granite fracture. *Applied Geochemistry*, *23*(6), 1484–1497. https://doi.org/10.1016/j.apgeochem.2008.01.008

Missana, T., Alonso, Ú., and Turrero, M. J. (2003). Generation and stability of bentonite colloids at the bentonite/granite interface of a deep geological radioactive waste repository. *Journal of Contaminant Hydrology*, *61*(1–4), 17–31. https://doi.org/10.1016/S0169-7722(02)00110-9

Missana, T., Benedicto, A., García-Gutiérrez, M., and Alonso, U. (2014). Modeling cesium retention onto Na-, K- and Ca-smectite: Effects of ionic strength, exchange and competing cations on the determination of selectivity coefficients. *Geochimica et Cosmochimica Acta*, *128*, 266–277. https://doi.org/10.1016/j.gca.2013.10.007

Missana, T., García-Gutiérrez, M., Mingarro, M., Alonso, U., (2018). Comparison between cesium and sodium retention on calcium silicate hydrate (C-S-H) pahses. *Applied Geochemistry, 98*, 36-44. https://doi.org/10.1016/j.apgeochem.2018.09.007

Moreno, L., Neretnieks, I., and Liu, L. (2010). Modelling of erosion of bentonite gel by gel / sol flow. *Engineering and Technology*, *November*.

Norrfors, K. K., Bouby, M., Heck, S., Finck, N., Marsac, R., Schäfer, T., Geckeis, H., and Wold, S. (2015). Montmorillonite colloids: I. Characterization and stability of dispersions with different size fractions. *Applied Clay Science*, *114*, 179–189. https://doi.org/10.1016/j.clay.2015.05.028

Norrfors, K. K., Marsac, R., Bouby, M., Heck, S., Wold, S., Lützenkirchen, J., and Schäfer, T. (2016). Montmorillonite colloids: II. Colloidal size dependency on radionuclide adsorption. *Applied Clay Science*, *123*, 292–303. https://doi.org/10.1016/j.clay.2016.01.017

Reid, C., Lunn, R., El Mountassir, G., and Tarantino, A. (2015). A mechanism for bentonite buffer erosion in a fracture with a naturally varying aperture. *Mineralogical Magazine*, *79*(6), 1485–1494. https://doi.org/10.1180/minmag.2015.079.6.23

Reimus, P. W., 2017. *Mathematical Basis and Test Cases for Colloid-Facilitated Radionuclide Transport Modeling in GDSA-PFLOTRAN* (No. LA-UR-26560). Los Alamos National Laboratory (LANL), Los Alamos, NM (United States).

Reimus, P. W., and Boukhalfa, H. (2014). *Chancellor Water Colloids : Characterization and Radionuclide Associated Transpor*t (No. LA-UR-14-2). Los Alamos National Laboratory (LANL) Los Alamos, NM (United States).

Reimus, P. W., Zavarin, M., and Wang, Y., 2017. *Colloid-Facilitated Radionuclide Transport: Current State of Knowledge from a Nuclear Waste Repository Risk Assessment Perspective* (No. LA-UR-16-26638). Los Alamos National Laboratory (LANL), Los Alamos, NM (United States).

Tarì, G., Olhero, S. M., Ferreira, J. M. F., (2000). Influence of temperature of electrostatically stabilized alumina suspensions. *Journal of Colloid and Interface Science, 231*, 221-227. https://doi.10.1006/jcis.2000.7112.

Telfeyan, K., Reimus, P. W., Boukhalfa, H., and Ware, S. D. (2020). Aging effects on Cesium-137 (137Cs) sorption and transport in association with clay colloids. *Journal of Colloid and Interface Science*, *566*, 316-326. https://doi.org/10.1016/j.jcis.2020.01.033

Villar, M. V., and Lloret, A. (2008). Influence of dry density and water content on the swelling of a compacted bentonite. *Applied Clay Science*, *39*(1–2), 38–49. https://doi.org/10.1016/j.clay.2007.04.007

Viswanathan, H., Boukhalfa, H., Chu, S., Makendonska, N., Hyman, J., Karra, S., Reimus, P., Telfeyan, K., (2019). *Crystalline and Crystalline International Disposal Activities* (LA-UR-19-24954). Los Alamos National Laboratory (LANL), Los Alamos, NM (United States).

Viswanathan, H., Boukhalfa, H., Chu, S., Hyman, J., Karra, S., Makendonska, N., Reimus, P., Telfeyan, K., (2018). *Crystalline and Crystalline International Disposal Activities* (LA-UR-18-27885). Los Alamos National Laboratory (LANL), Los Alamos, NM (United States).

Zhang, F., Ye, W. M., Chen, Y. G., Chen, B., and Cui, Y. J. (2016). Influences of salt solution concentration and vertical stress during saturation on the volume change behavior of compacted GMZ01 bentonite. *Engineering Geology*, *207*, 48–55. https://doi.org/10.1016/j.enggeo.2016.04.010

6. DECOVALEX2019 Task C Updated Modeling of Inflow and Recovery Experiments

The DECOVALEX 2019 project that was active between 2016 and 2019 has been completed. A final report on Task C has been written to document the modeling work on GREET (Groundwater REcovery Experiment in Tunnel) which was conducted at the Mizunami Underground Research Laboratory (Iwatsuki, et al., 2020). The experimental and modeling work is a good addition to the study of hydrology, hydrochemistry and geomechanics for geological nuclear waste disposal in fractured crystalline rocks. The study also provides an analysis of the effect of excavations and tunnelling on the geological environment of the host rock.

The complete modeling work on Task C that was done at Sandia National Laboratories is included in the final report. In this chapter recent modeling updates only are reported. This work is a continuation of DECOVALEX 19, Task C analysis reported in the 2017-2019 Crystalline Work Package progress reports (Wang et al., 2017-2019). The work for inflow analysis during the excavation of the Inclined Drift and the Closure Test Drift (CTD) has been updated to incorporate new data and to conduct new simulations using a base case domain. The new simulations also include statistical analysis for different fracture realizations. A sensitivity analysis was also conducted to study of the effect of domain size. A much larger mesh was selected to minimize boundary effects. The DFN model was upscaled to equivalent continuum for the base case domain and the much larger domain to generate relevant permeability and porosity fields for each case. The updated calculations for the inflow analysis are described in Section 6.1. New calculations have also been conducted to model the flooding of the plugged CTD and the resulting pressure recovery. The modeling includes matching of pressure and Cl experimental data at observation locations in 12MI33. The modeling was done for the 10 fracture realizations. The recovery simulations are described in Section 6.2. An analysis of effect of grid block size in DFN upscaling using the Oda method is given in Section 6.3. A summary of the work reported in this chapter is given in Section 6.4.

6.1 Update of modeling of inflow during tunnel excavation

Fracture characterization for the base case domain (200 m x 300 m x 200 m) and mesh was conducted using the method detailed in Wang et al. (2017, 2018, 2019). For this study 10 DFN realizations were generated to provide a measure of uncertainty. The DFN permeability and porosity results for the 10 realizations were upscaled (converted) to a continuum mesh for use in flow and transport simulations (Wang et al., 2018, Kalinina et al., 2018).

PFLOTRAN (Hammond et al., 2014) simulations were conducted using the method described in Wang et al. (2017, 2018, 2019). An initial condition run was made with the base case mesh to set hydrostatic pressure and Cl concentration gradient. A linear concentration gradient was assumed per GREET project specifications. As was previously done specified pressure and Cl boundary conditions were applied to the top, bottom and side domain boundaries. Flow and transport simulations were then conducted as the excavation progressed, applying constant atmospheric pressure boundary conditions at the tunnel walls to the excavated portion of the tunnel. The simulations ran for the duration of the excavation. The output of the 10 realizations provided inflow rate and pressure and Cl predictions at observation points.

In this section the effect of the boundary conditions set for the site-scale domain is studied by changing the domain size of the base case. For this study a larger domain size was used. A 1386 m x 1486 m x 806 m (vertical) domain was selected to conduct inflow simulations. The new mesh contains 2,352,987 grid blocks. The mesh includes the base case mesh together with progressively increasing grid block sizes. Discretization of the base case mesh and the new enlarged mesh are shown in Figures 1 and 2, respectively. For the larger domain the same DFN realizations as for the base case domain were used to produce upscaled equivalent continuum fracture model.

The same procedure as previously described (Wang et al., 2017-2019) was followed to estimate the inflow for the larger domain. Figure 3 shows experimental excavation data in terms of distance as a function of excavation time. Figure 4 shows predictions of inflow for the specified 10 DFN realizations. The plot shows predictions for the base case domain (smaller domain) and the larger domain, together with experimental data. Significantly reduced inflow was predicted for the larger domain. It indicates that assigning boundary conditions close to the tunnel significantly influences inflow predictions. Better matching of the observed data (data points) was obtained for the larger domain.

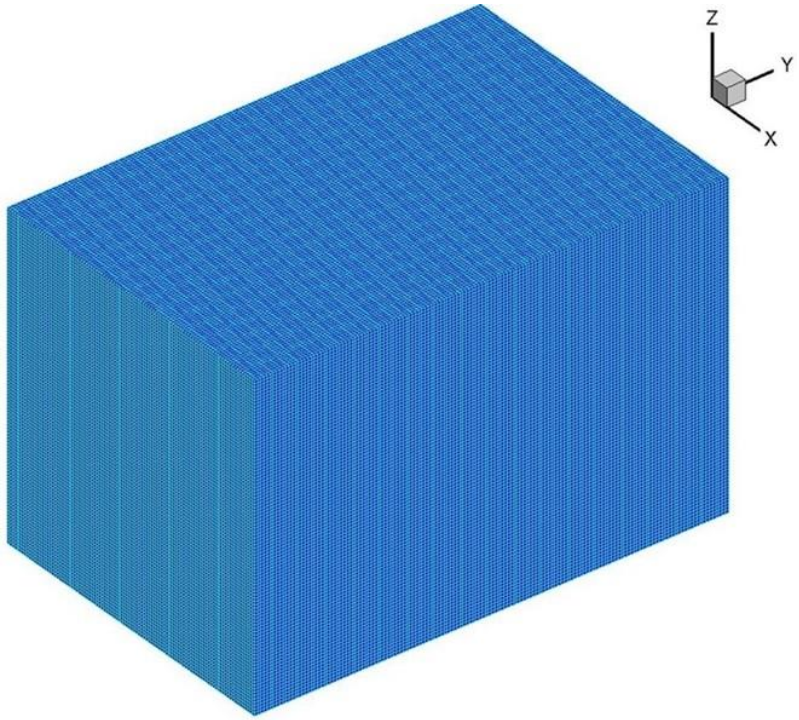

Figure 6-1. Base case site scale domain discretization

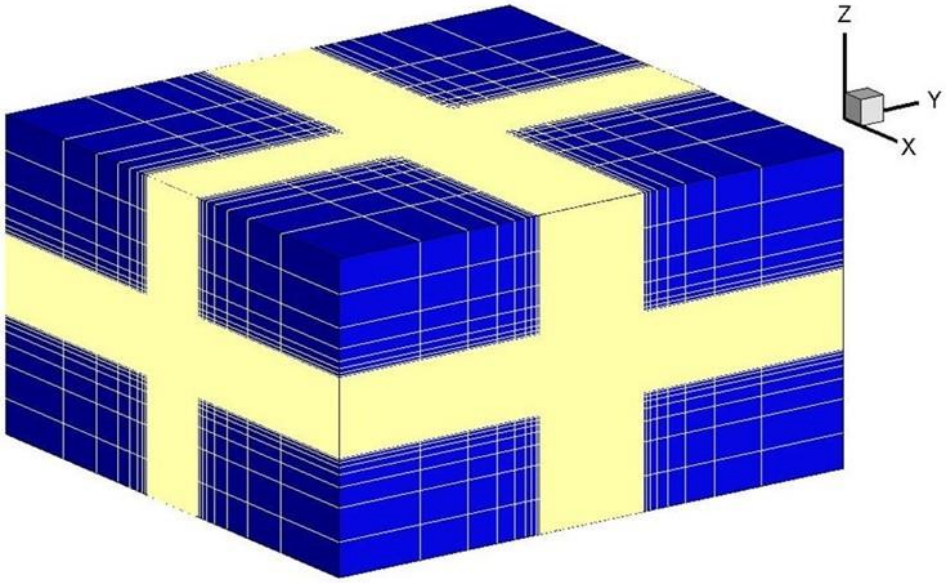

Figure 6-2. Discretization for the enlarged domain

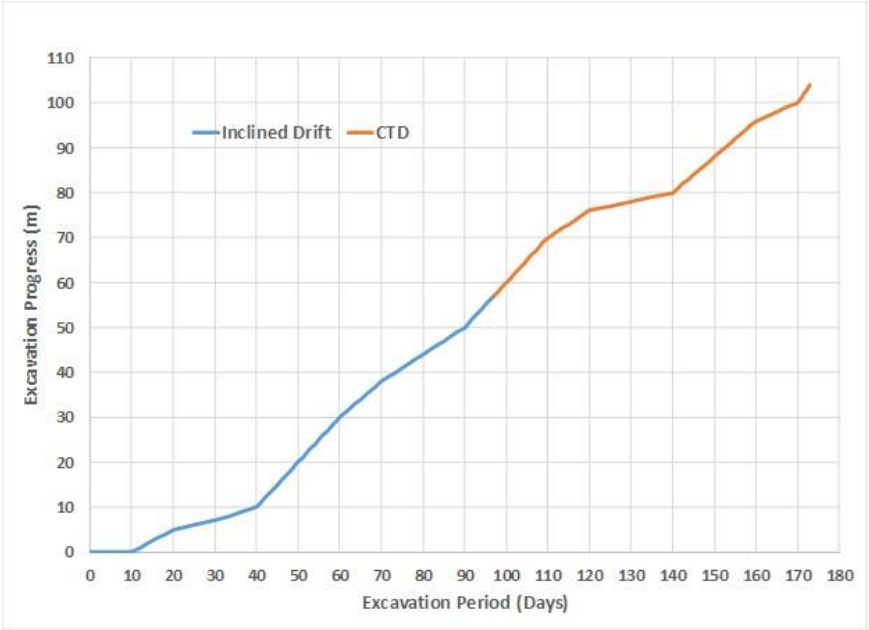

Figure 7-3. Data of excavation progress

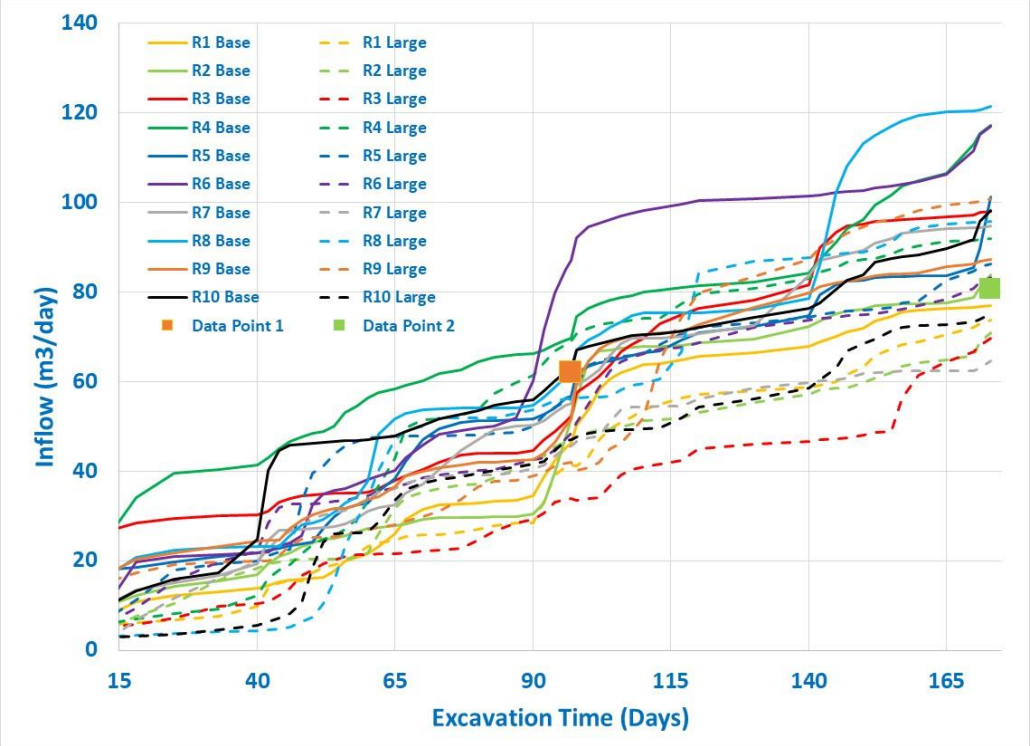

Figure 6-4. Inflow into Inclined Drift and CTD: Predictions for the base case and larger domains, together with experimental data. Data Point 1 is for inflow into Inclined Drift only and Data Point 2 is for combined inflow into the Inclined Drift and CTD.

6.2 Update of modelling of recovery during water filling experiment in CTD

The GREET project conducted further flow, transport and chemical tests after the excavation of the inclined drift and the CTD. The experiments include installing a concrete plug to isolate the CTD, filling the CTD with water and observing hydraulic and chemical recovery following the excavation of the tunnel. The timeline shown below indicates durations of major tests starting from the excavation of the tunnel.

- Incline drift and CTD excavation: 4/20/2013 to 10/14/2013
- Construction of impervious plug: 11/3/2014 to 6/2/2015
- First water-filling test (plug performance test): 8/24/2015 to 10/5/2015
- Injection of water to CTD at 500 m: 1/8/2016 to 1/25/2016
- CTD full of water: 1/25/2016 to 9/5/2017

In this section filling of the CTD with water and associated hydraulic and chemical recovery only are modelled. This covers the fourth and fifth bullets shown above. Results of flow and non-reactive transport simulations are presented.

For recovery simulations experimental data from the CTD and borehole 12MI33 were used. The initial conditions in the CTD and at the observation points is shown below.

- Initial pressure at CTD: 1 atm.
- Initial pressure data at observation points in Borehole 12MI33:
    - P1 = 3.822 MPa
    - P2 = 1.286 MPa
    - P3 = 1.76 MPa

- P4 = 3.48 MPa
- P5 = 3.79 MPa
- P6 = 3.357 MPa

Note that the experimental data also include data from borehole 13MI38. These data were not used in this study because the borehole has not been included in the fracture, flow and non-reactive transport models.

Figure 6-5 shows experimental pressure recovery data provided by the GREET project. The data includes pressure history at the CTD and the observation points in the monitoring borehole 12MI33. As would be expected the data show more visible pressure changes for observation points close to the CTD. JAEA project data shows that the concrete plug isolating the CTD did not function properly and that there was some leakage. The experimental leakage data are shown in Figure 6-6.

For flow simulations of the recovery phase the base case domain and mesh described in Section 6.1 were used. It was assumed that the shotcrete lined walls totally isolate the CTD from the inclined drift except at the floor of the CTD and the concrete plug (due to leakage). The inclined drift was also assumed to be isolated by the impermeable shotcrete except at the plug (also due to leakage). Permeability and porosity fields of the 10 fracture realizations were applied and the PFLOTRAN numerical code was used. Initial conditions were obtained by running the model using experimental initial condition data described above.The initial condition was obtained by setting the experimental initial pressure values (given above) for the observation points and running to steady state. The flow model was then run to one year (starting Jan. 7/2016) using the steady state as initial condition. Various approaches were utilized to match the measured data. Better results were obtained by applying the experimental CTD pressure history as a boundary condition at all CTD walls. Note that modeling flow and transport in the open CTD would require CFD simulations.

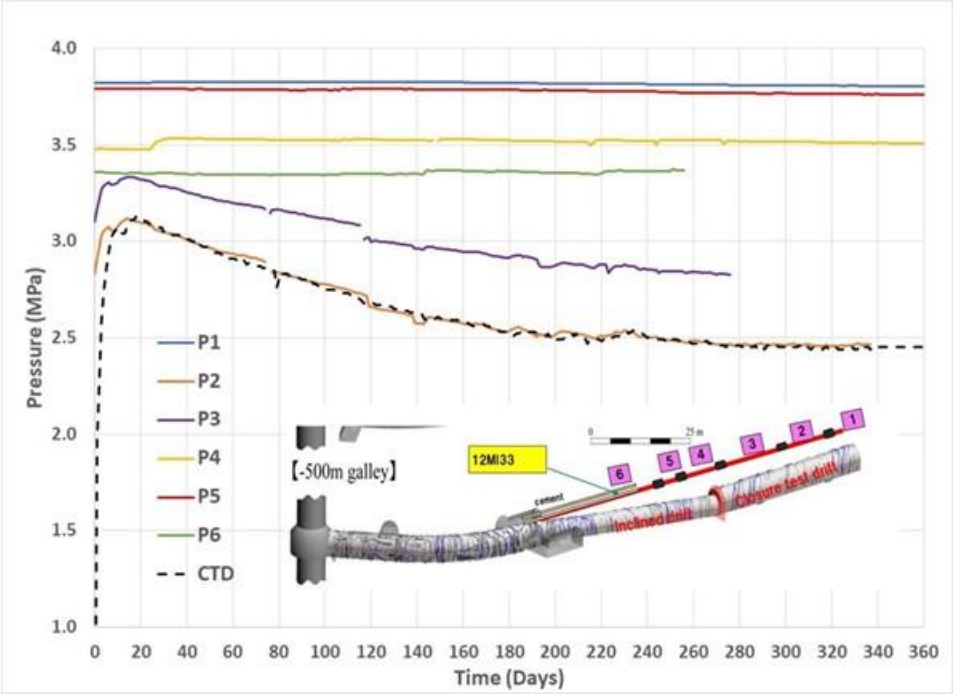

Figure 6-5. Experimental pressure recovery data in the CTD and at observation points in Well 12MI33

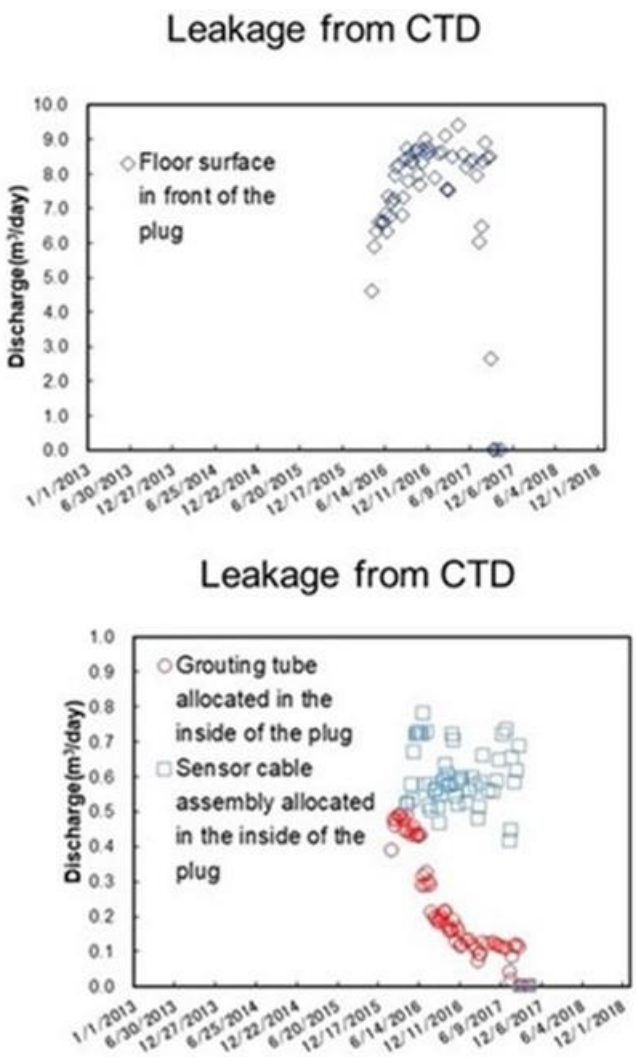

Figure 6-6. Experimental data of leakage from CTD during recovery experiment. Note that the upper figure includes leakage described in the lower figure

Figures 6-7 and 6-8 show predictions of pressure history at selected observation points in 12MI33 due to CTD water filling and post-filling pressure recovery. The figures show results for the fracture realizations together with the corresponding experimental data (dotted line). Figure 6-7 shows results for observation point P2. As shown in the figure, P2 is close to the CTD and is thus directly affected by the filling and recovery process. The experimental data shows pressure decreases over time. Predicted data for some of the simulations closely match the trend. Figure 8 shows pressure history results for observation point P6. The observation point is further to the left of the CTD and thus may not be as influenced by the CTD filling and recovery as the points to the right of it. The experimental data show almost constant pressure over time. The simulation results of some of the realizations match the experimental data.

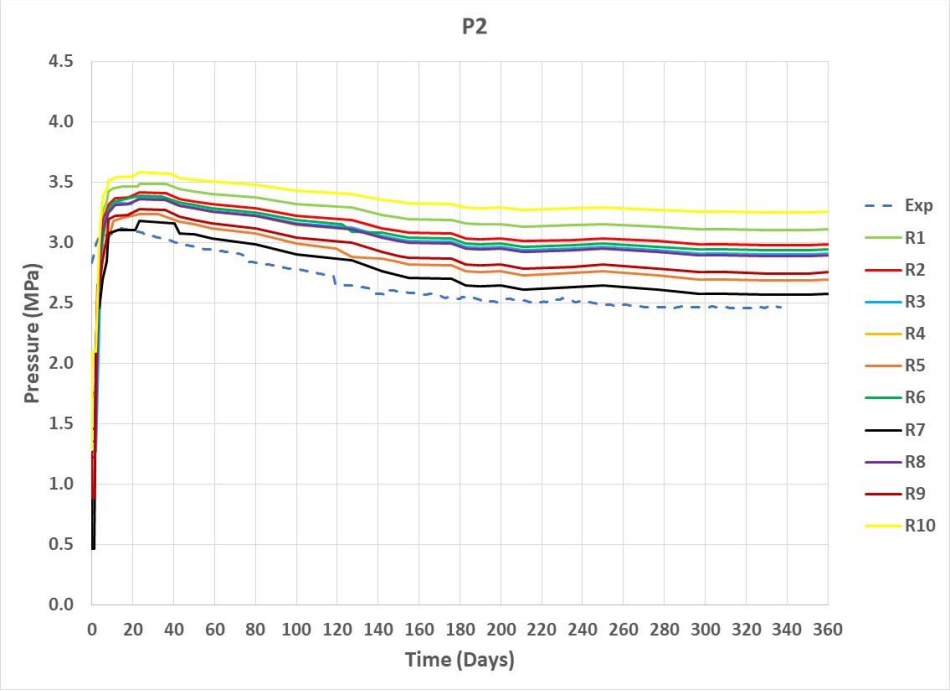

Figure 6-7. Predicted pressure recovery at Observation Point 2 (P2) in 12MI33 for 10 fracture realizations. The figure also includes experimental data for P2.

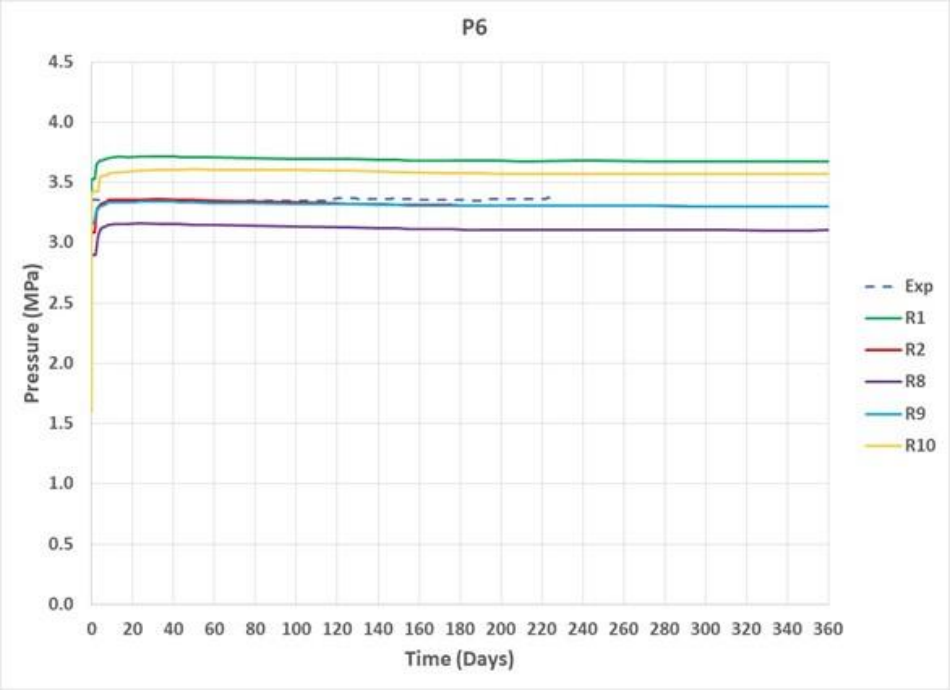

Figure 6-8. Predicted pressure recovery at Observation Point 6 (P6) in 12MI33 for 10 fracture realizations. The figure also includes experimental data for P6.

For the transport simulations the same procedure as that of the flow simulations was followed. Initial conditions were obtained by running the model using experimental initial condition data described below.

- Initial Cl concentration at CTD: 475 mg/L (0.013398 M)
- Initial Cl concentration data at observation points in Borehole 12MI33:
    - P1 = 438 mg/L (0.012354 M)
    - P2 = 377 mg/L (0.010634 M)
    - P3 = 274 mg/L (0.007729 M)
    - P4 = 215 mg/L (0.006064 M)
    - P5 = 594 mg/L (0.016755 M)
    - P6 = 333 mg/L (0.009393 M)

The above concentration data were converted to molarity for use in PFLOTRAN (given in parenthesis). The conversion equation used was:

$$Conc.in\ M = \frac{Conc.in\ mg/L}{1000\ x\ 35.453} \qquad (6\text{-}1)$$

with the molecular weight of Cl was 35.453 g/mol.

The initial concentrations at the CTD and the observation points in 12MI33 were used to generate the steady state conditions for the 10 fracture realizations. The non-reactive transport simulations then used the steady state conditions to model the recovery process. As with the flow simulations, the transport simulations used the experimental CTD Cl concentration gradient as boundary conditions on all the walls of the CTD. For all the transport simulations longitudinal dispersivity of 20.0 m and diffusion coefficient of 10^{-12} m^2/s were applied. The results were sensitive to longitudinal dispersivity but a selected value was not universally applicable to model concentrations at every observation point. Thus, a value of 20.0 m was selected for this study.

Simulation results are shown in Figures 6-9 to 6-12. Figures 6-9 and 6-10 show Cl concentration distributions at the beginning and end of the simulation times for Realization 2. Figures 6-11 and 6-12 show predictions of Cl concentration history at selected observation points in 12MI33 due to CTD water filling and post-filling pressure recovery. The figures show results for the fracture realizations together with the corresponding experimental data (dotted line). In general, matching Cl concentration data was not as smooth as that of pressure matching. Cl concentrations are highly sensitive to the hydrologic changes. However, prediction results are close to experimental data for some of the realizations.

Figure 6-11 shows results for observation point P2. The predicted concentrations for the 10 realizations span a wide range. However, some of the predicted data are close to the experimental data at later times. Figure 6-12 shows Cl concentration history results for P6. The observation point is further to the left side of the CTD. The results show that the predictions for all the realizations slightly overpredict the experimental data. However, some of the predicted data are close to the experimental data.

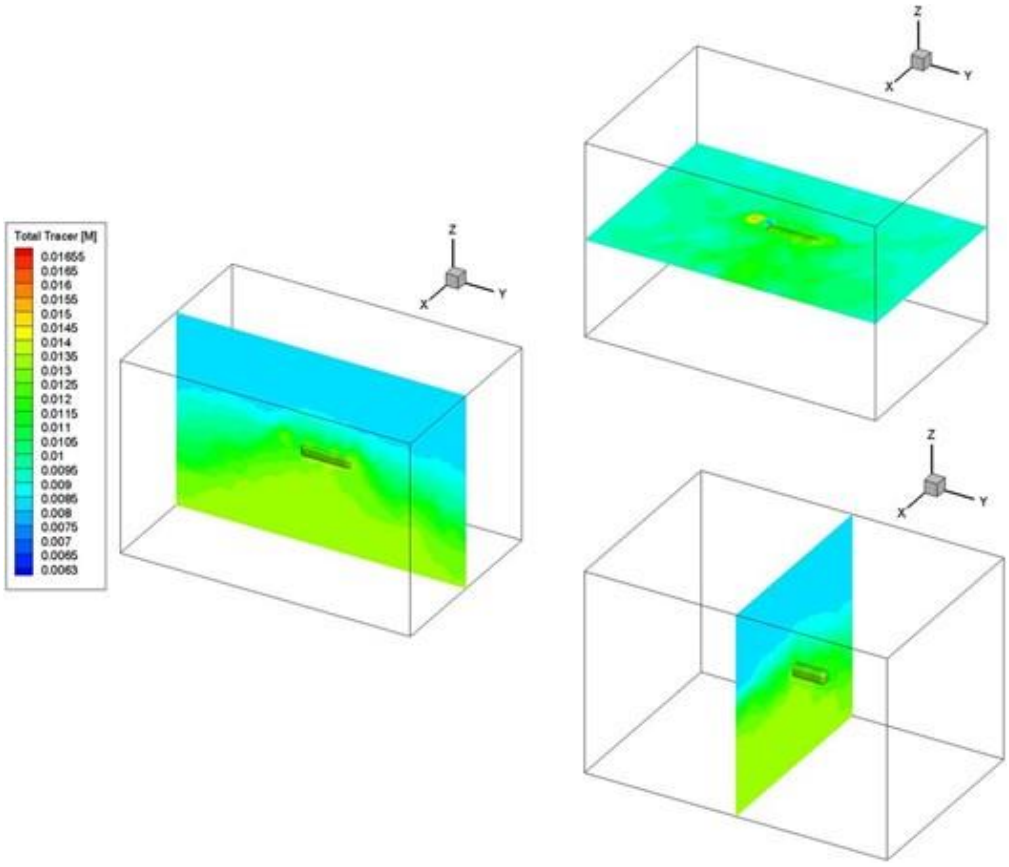

Figure 6-9. Predicted Cl distribution along tunnel axis at the beginning of the simulation for the base case domain. Results are for Realization 2.

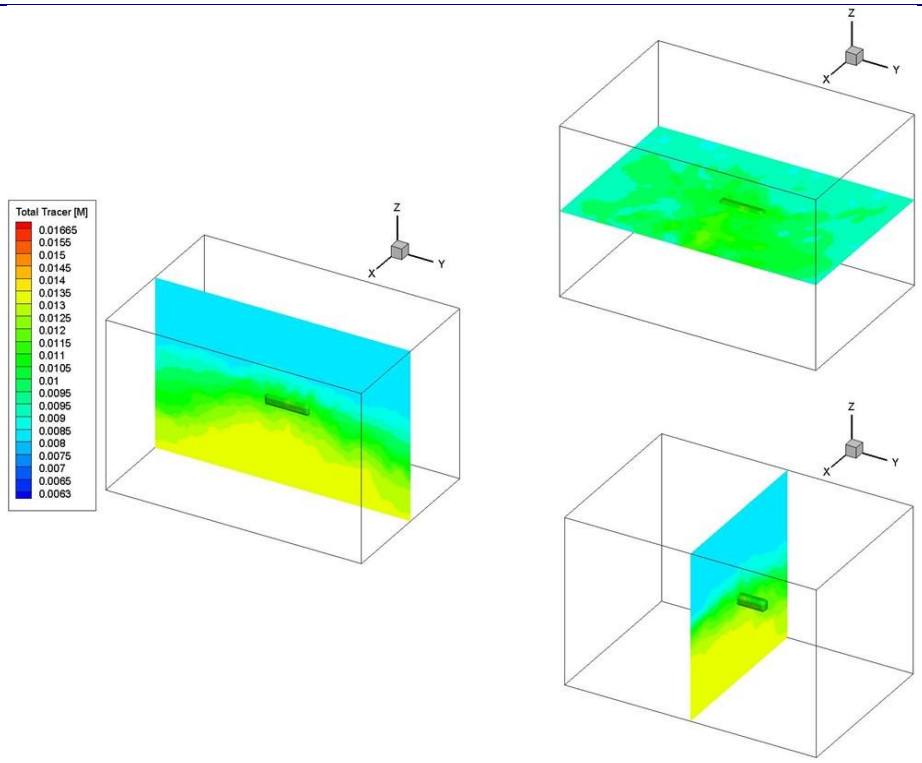

Figure 6-10. Predicted Cl distribution along tunnel axis after 360 days simulation time for the site-scale domain. Results are for Realization 2.

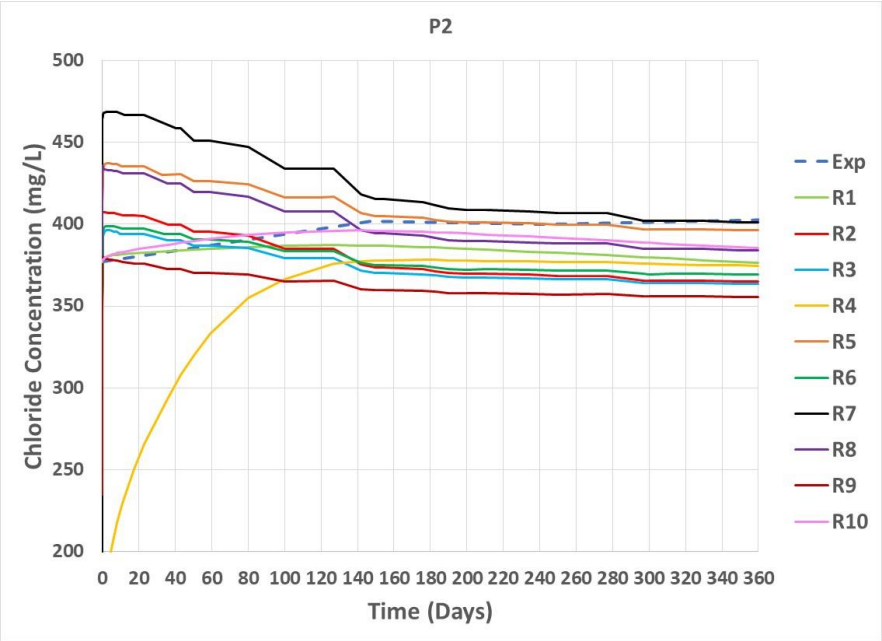

Figure 6-11. Predicted Cl concentration during recovery at Observation Point 2 (P2) in 12MI33 for 10 fracture realizations. The figure also includes experimental data for P2.

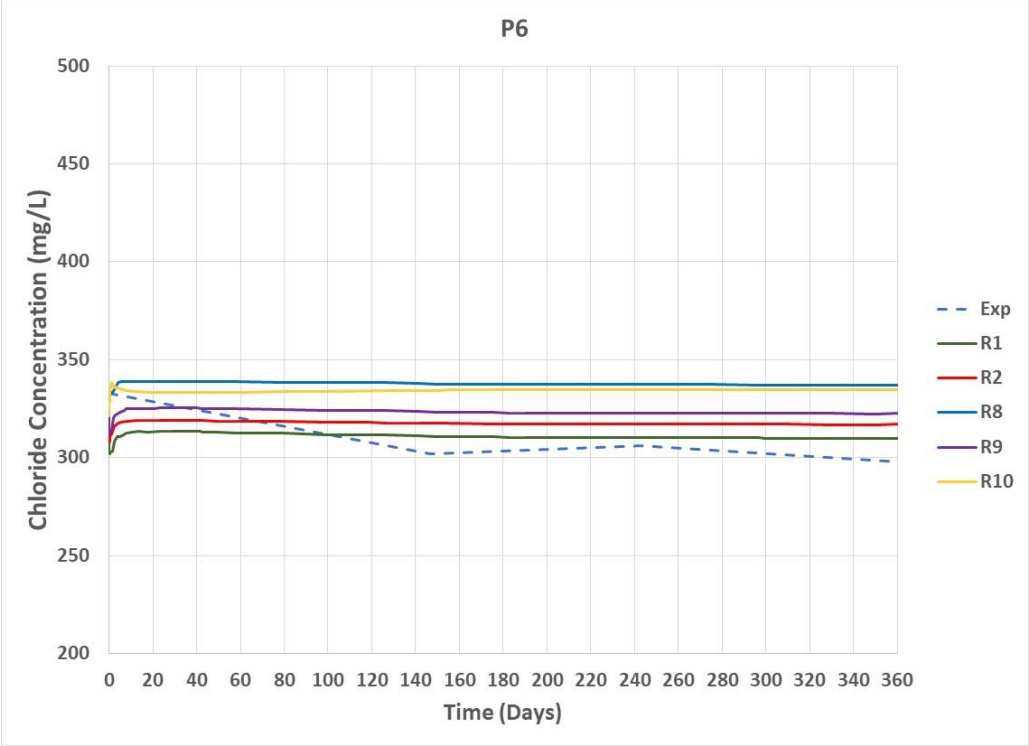

Figure 6-12. Predicted Cl concentration during recovery at Observation Point 6 (P6) in 12MI33 for 10 fracture realizations. The figure also includes experimental data for P6.

6.3 Effect of grid block size during DFN upscaling

In this section modeling analysis was conducted to study the effect of grid block size for upscaling of DFN to a continuum for the site-scale base case domain size of 200 m x 300 m x 200 m. For the simulations described in this chapter the DFN model was upscaled to continuum using the FracMan software (Golder, 2017). FracMan has various methods to upscale fracture network properties to grid blocks. The method used in this analysis to upscale permeability is the Oda method, a geometric based upscaling method. The Oda method (1985) calculates permeability (hydraulic conductivity) tensors in all directions for a grid block. The method scales the fracture isotropic permeability by the ratio of fracture volume and the volume of the grid block. For a given grid block with known fracture areas and transmissivities obtained from the DFN model, FracMan calculates a fracture tensor by adding the individual fractures weighted by their area and transmissivity:

$$F_{ij} = \frac{1}{V}\sum_{k=1}^{N} A_k T_k n_{ik} n_{jk} \qquad (6\text{-}2)$$

F_{ij} = fracture tensor
V = grid block volume
N = total number of fractures in grid block
A_k = area of fracture k
T_k = transmissivity of fracture k
n_{ik}, n_{jk}= components of a unit normal to the fracture k

Oda's permeability tensor assumes that the fracture tensor (F_{ij}) expresses fracture flow as a vector along the fracture's unit normal. Assuming the fractures are impermeable in a direction parallel to their unit normal, the fracture tensor must be rotated into the planes of permeability:

$$k_{ij} = \frac{1}{12}\left(F_{kk}\delta_{ij} - F_{ij}\right) \quad (6\text{-}3)$$

k_{ij} = permeability tensor
δ_{ij} = Kroenecker delta
Fracture porosity (ϕ) of the grid block is calculated as:

$$\phi = \frac{1}{V}\sum_{k=1}^{N} A_k b_k \quad (6\text{-}4)$$

where b_k is the aperture of fractur k. Grid block porosity (P33) was obtained from FracMan as fracture volume (area x aperture) divided by the grid block volume.

To study effect of grid block size results of flow and tracer transport were utilized. In the analysis different grid block sizes were considered for the same domain and DFN realization. The DFN was upscaled to the continuum grid for each grid block size. Figures 6-13 and 6-14 show permeability and porosity fields for selected grid block sizes. The figures show that spatial permeability and porosity distributions are affected by the grid block size selected. Effective permeability and tracer breakthrough were estimated using flow and transport simulations. The PFLOTRAN numerical code was used for the flow and transport simulations.

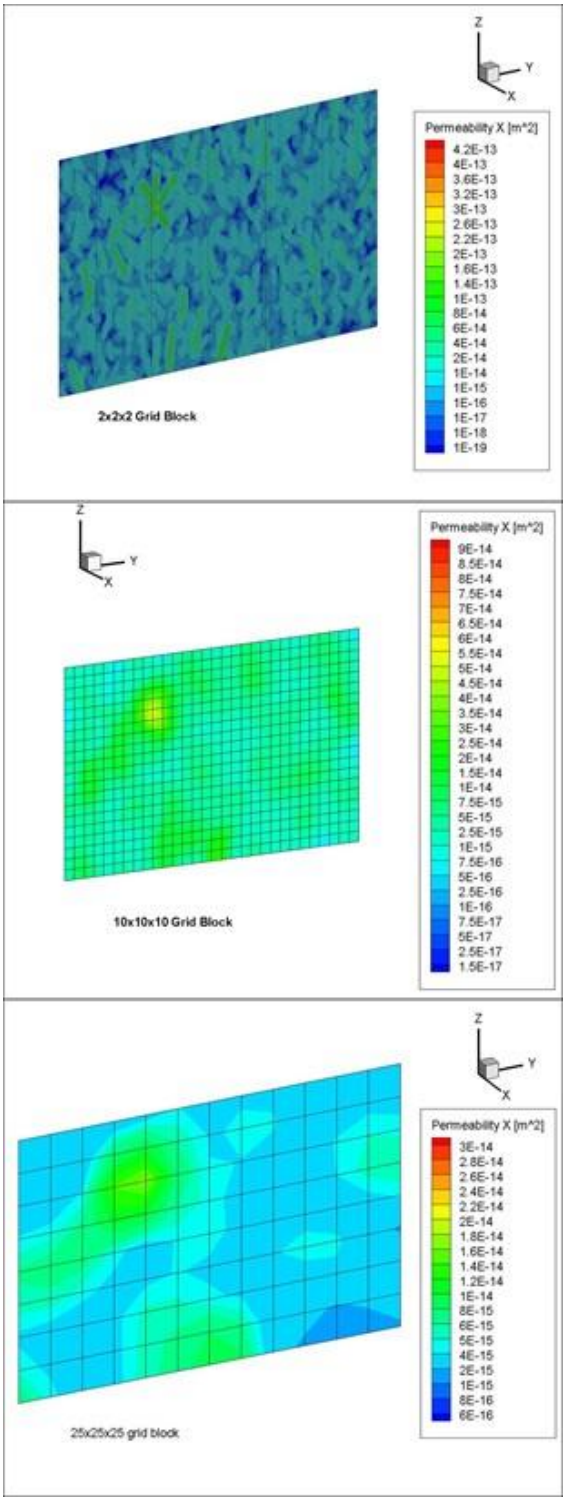

Figure 6-13. Slices of permeability distributions for grid block sizes of 2m x 2m x 2m, 10 m x 10 m x 10m and 25 m x 25 m x 25 m for the base case domain (200 m x 300 m x 200 m) and DFN Realization 2.

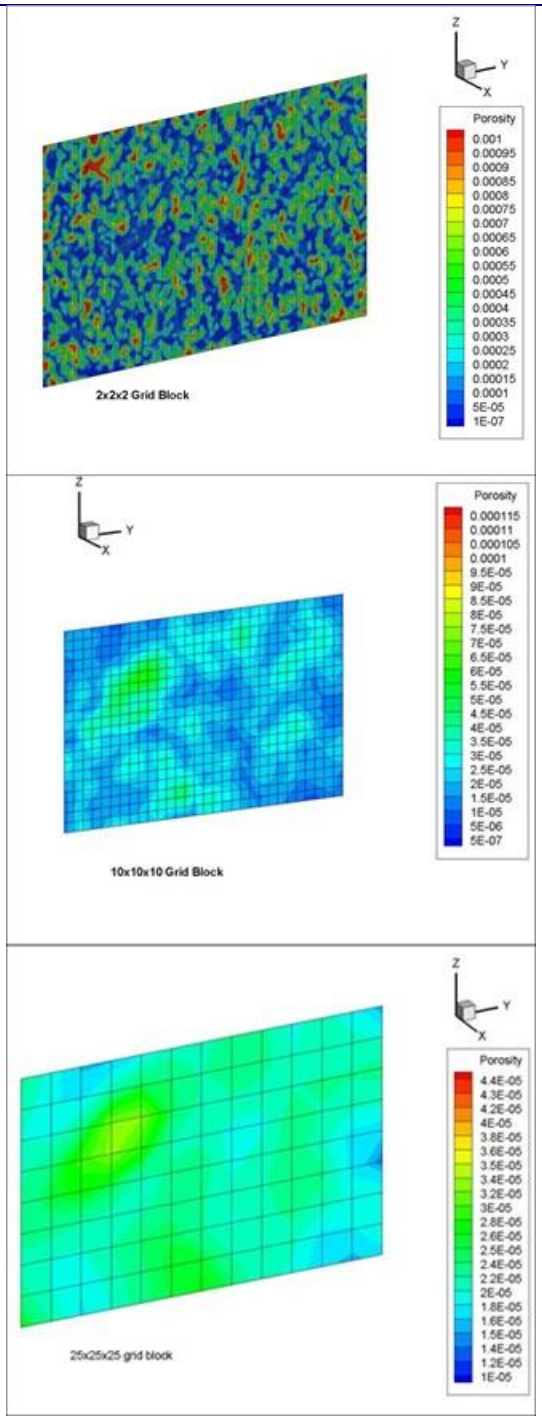

Figure 6-14. Slices of porosity distributions for grid block sizes of 2m x 2m x 2m, 10 m x 10 m x 10m and 25 m x 25 m x 25 m for the base case domain (200 m x 300 m x 200 m) and DFN Realization 2.

Flow-based effective permeability representing the entire fractured rock domain was calculated using Darcy's law and liquid flux at steady state. Flow simulations were carried out using the upscaled permeability and porosity fields for one of the realizations (Realization 2) to estimate the flow-based effective permeability representing the entire domain. A pressure gradient of 1000 Pa was imposed between the south and north faces of the simulation domain (Length = 300 m and cross-sectional area = 40000 m^2). The resulting calculated effective permeability for various grid block sizes is shown in Figure 15. The curve represents a power law relationship between grid block size and effective permeability.

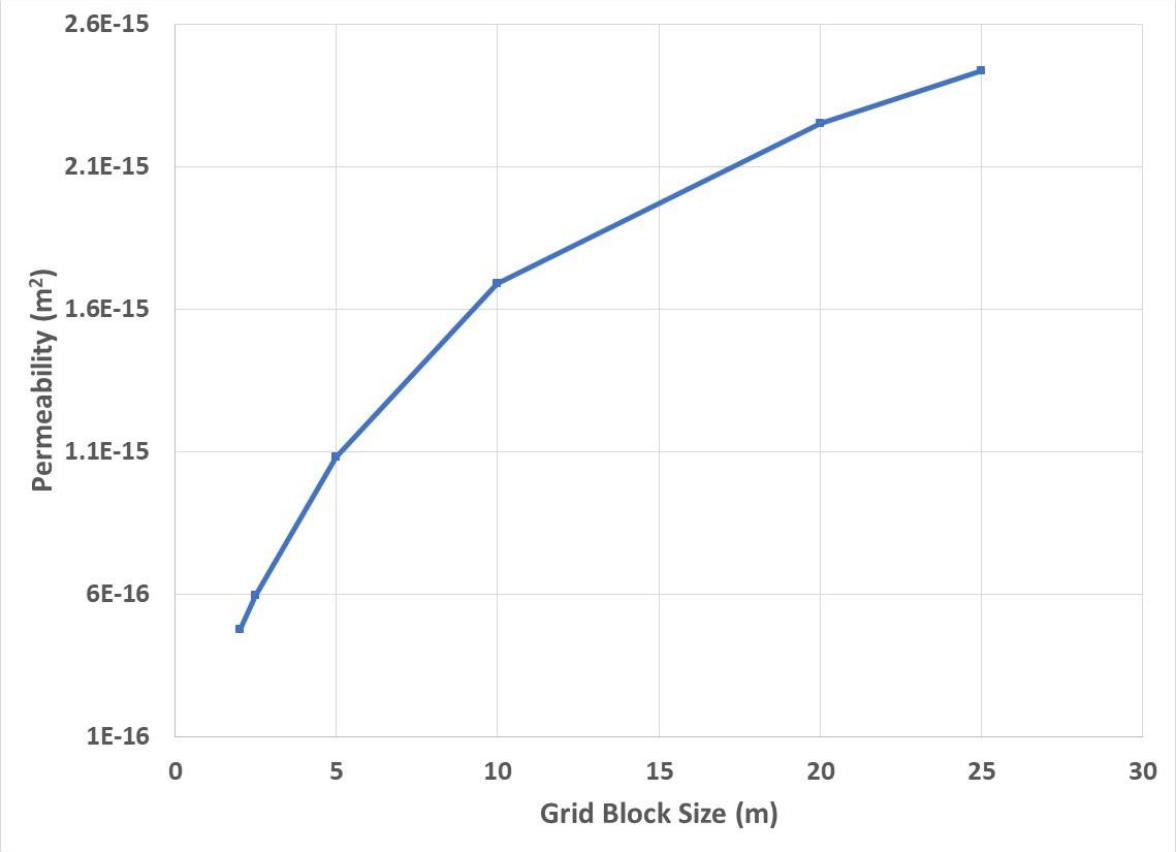

Figure 6-15. Predicted effective permeability vs. grid block size

Transport calculations were also conducted using the steady-state flow field. A tracer concentration gradient was imposed between the south and north faces of the simulation domain. The resulting calculated breakthrough curves for different grid block sizes are shown in Figure 6-16. Figure 6-17 shows distributions of tracer at 10 years simulation time for selected grid block sizes.

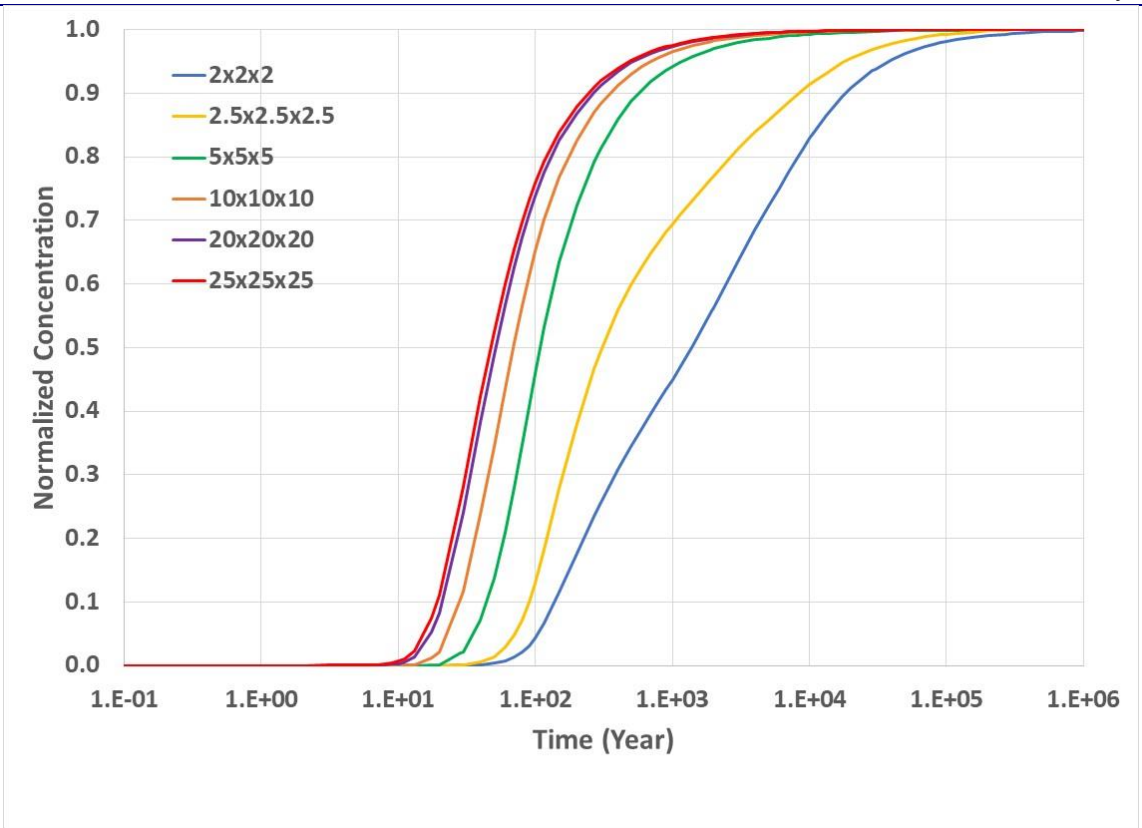

Figure 6- 6. Breakthrough curves of tracer transport for different grid block sizes

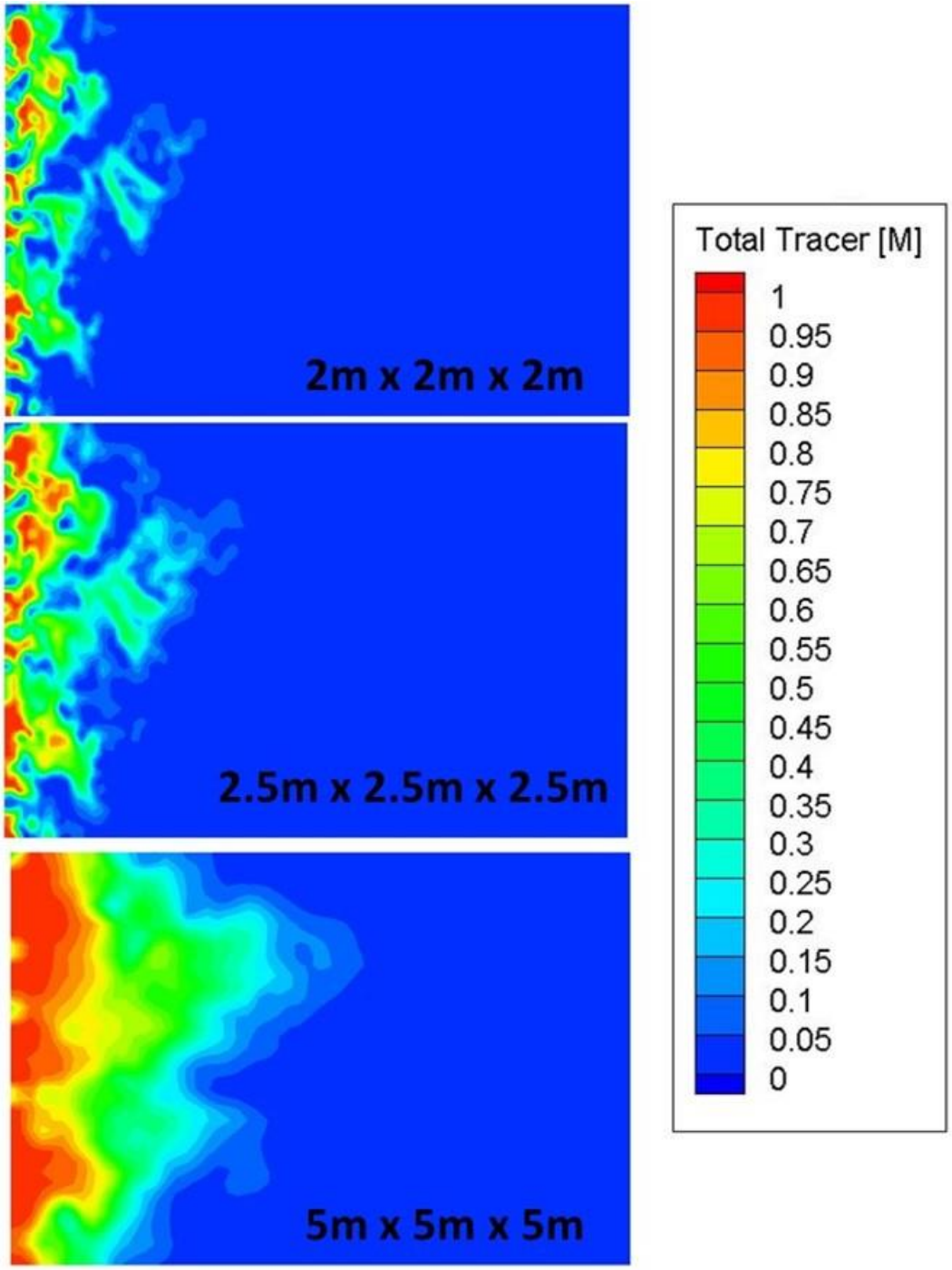

Figure 6-17. Distribution of tracer at 10 years simulation time for selected grid block sizes

Both the effective permeability and breakthrough curves show that upscaling using the Oda method is affected by grid block size. Figure 18 illustrates that depending on the grid block size selected, upscaling would result in different grid block permeability values. There is a need to compare different upscaling methods to optimize grid block size for a specified problem. The upscaled results maybe compared to results from direct DFN simulations and simulations using particle tracking.

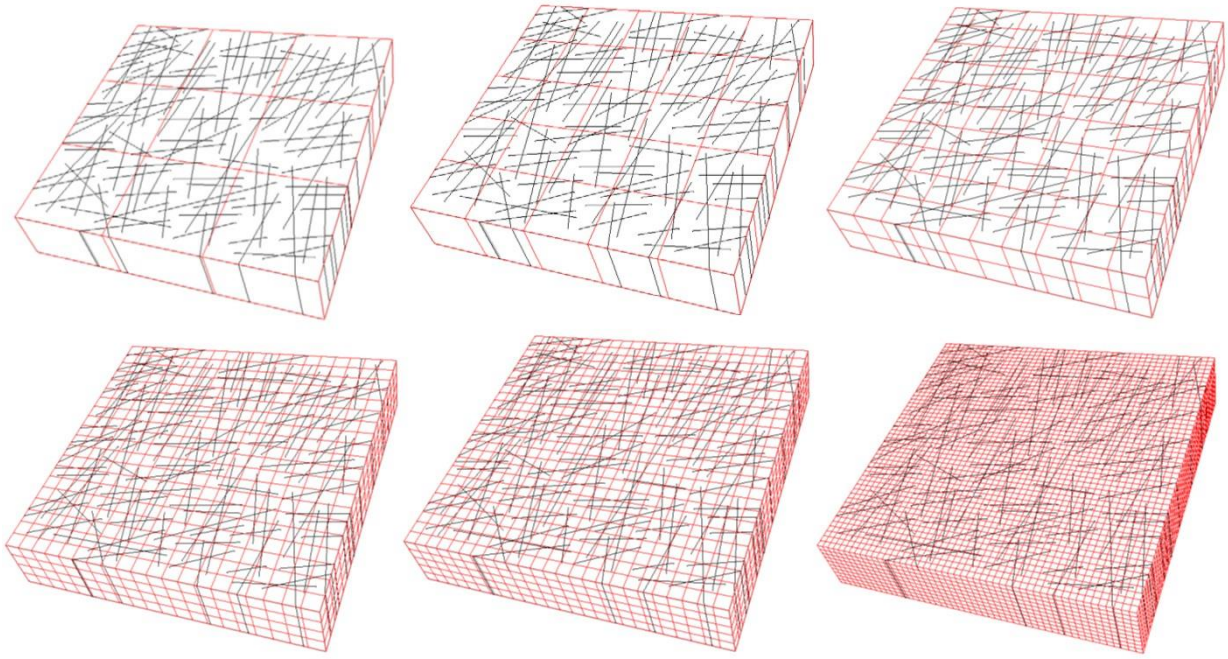

Figure 6-18. Fractures and grid block size (Wang et al., 2008)

6.4 Summary of DECOVALEX19 Task C modeling

Updated modeling analyses were conducted on DECOVALEX Task C inflow and recovery simulations. The inflow simulations included a study of boundary conditions related to domain size by comparing inflow results for the base case domain (200 m x 300 m x 200 m) with that of a much larger domain (1386 m x 1486 m x 806 m). The comparisons were done for all ten fracture realizations. Pressure distribution simulation results for one of the realizations show that the site-scale domain exhibited boundary effects while the larger domain had no such effects (Wang et al., 2019). As a result, the inflow results for the 10 realizations using the larger domain show significantly reduced values compared to the base case domain. Thus, the inflow is better predicted with the larger domain.

Updated simulations were also conducted to model water-filling of the plugged CTD and resulting pressure recovery. For the analysis the base case domain with domain size of 200 m x 300 m x 200 m was used. The 10 upscaled fracture realizations were also used to provide permeability and porosity distributions. Simulation results were compared with project experimental data. The results show that pressure predictions of many of the 10 realizations closely match the experimental data at the observation points in 12MI33. Reasonable results were also obtained for predictions of chloride concentrations at most of the observation points. Additional analysis will be conducted to study high chloride concentrations at Observation Point P5. Further sensitivity study would also be needed with a larger number of DFN realizations to better match the experimental inflow and recovery data.

For this study upscaling of DFN to a continuum grid was conducted using the Oda method. The Oda method is an efficient geometric method to calculate grid block permeability without the use of flow simulations. However, it relies on well-connected fracture networks and thus tends to over-predict grid block

permeability (Golder, 2017). In this work the Oda method was used to study the effect of grid block size on flow and transport. Simulations have shown that results are highly dependent on grid lock size. Further study is needed to optimize grid block size for flow and transport simulations in fractured rock using upscaled permeability and porosity. Comparison of different upscaling methods would need to be studied to obtain better upscaling.

6.5 References

Golder Associates, Inc., 2017: Interactive Discrete Feature Data Analysis, *Geometric Modeling and Exploration Simulation, FracMan Manual.* Golder.

Hammond, G. E., Lichtner, P. C., and Mills, R. T., 2014: *Evaluating the Performance of Parallel Subsurface Simulators: An Illustrative Example with PFLOTRAN*, Water Resources Research, 50, doi:10.1002/2012WR013483 (2014).

Iwatsuki, T., Ishibashi, M., Onoe, H., Ozaki, Y., Hadgu, T., Jove-Colon, C.F., Kalinina, E., Wang, Y., Balvin, A., Hokr, M., Landa, J., Šembera, J., Zeman, J., 2020: DECOVALEX-2019 Task C final report, LBNL-2001264.

Kalinina, E., Hadgu, T., Wang, Y., Ozaki, Y., and Iwatsuki, T. 2018: Development and Validation of a Fracture Model for the Granite Rocks at Mizunami Underground Research Laboratory, Japan", *Pro. 2nd Int. Discrete Fracture Network Conference,* Seattle, Washington, June 20-22, 2018.

Oda, M., 1985: Permeability tensor for discontinuous rock masses, *Geo technique*. ICE Publishing, **35** (4), pp. 483–495.doi: 10.1680/geot.1985.35.4.483.

Wang, Y., T. Hadgu, E. A. Kalinina, J. Jerden, V. K. Gattu, W. Ebert, H. Viswanathan, J. Hyman, S. Karra, N., Knapp, N. Makedonska, P. Reimus, K. Telfeyan, P. M. Fox, P. S. Nico, M. Zavarin, E. Balboni, and C. Atkins-Duffin. 2017: Evaluation of Spent Fuel Disposition in Crystalline Rocks: FY17 Progress Report, Spent Fuel and waste Disposition, SFWD-SFWST-2017-000007, September, 2017.

Wang, Y., T. Hadgu, E. A. Kalinina, J. Jerden, V. K. Gattu, W. Ebert, H. Viswanathan, H. Boukhalfa, S. Chu, J. Hyman, S. Karra, N., Knapp, N. Makedonska, P. Reimus, K. Telfeyan, L. Zheng, H. deng, S. Nakagawa, K. Kim, T. Kneafsey, P. Dobson, S. Borglin, C. Doughty, M. Voltolini, M. Zavarin, E. Balboni, and C. Atkins-Duffin, 2018: Evaluation of Spent Fuel Disposition in Crystalline Rocks: FY18 Progress Report, Spent Fuel and waste Disposition, M2SF-18SN010302051, September, 2018.

Wang et al., 2019: Evaluation of Spent Fuel Disposition in Crystalline Rocks: FY19 Progress Report, Spent Fuel and waste Disposition.

Wang, H., Forster, C., Deo, M., 2008: Simulating naturally fractured reservoirs: comparing discrete fracture network models to the upscaled equivalents, Annual Convention, San Antonio, Texas.

7. FUEL MATRIX DEGRADATION MODEL PARAMETERIZATION EXPERIMENTS AND MODEL DEVELOPMENT

7.1 Introduction

The purpose of this project is to develop, test and implement a process model that provides the degradation rate of spent nuclear fuel under a wide range of conditions that can be readily incorporated into the geologic disposal safety assessment (GDSA) performance assessment (PA) code to provide reliable radionuclide source terms over the service life of a deep geologic repository. The fuel matrix degradation (FMD) model described herein was developed for this purpose and is currently being updated, optimized and tested. The FMD model is an electrochemical reactive-transport model built using fundamental redox kinetics and thermodynamics. It is based on the Canadian Mixed Potential Model (CMPM) of Shoesmith and King, 1998, Shoesmith et al., 2003 and King and Kolar 2003 but quantifies the attenuating effect of H_2 on the spent fuel degradation rate and has been customized for application in the ongoing spent fuel and waste science and technology (SFWS) campaign.

The continuing development and implementation of the FMD model addresses two high level Features, Events, and Processes (FEPs) that are recognized as high R&D priorities for the SFWS campaign (Wang et al., 2014). The addressed FEPs include 2.1.02 (waste form) and 2.1.03 (waste container), which correspond to the high priority research topics P19 (Development of waste form degradation model) and P20 (Development of new waste package concepts and models for evaluation of waste package performance for long-term disposal) identified by Wang et al., 2014.

Specifically, the FMD model employs mixed potential theory to calculate the degradation rate of UO_2 by accounting for all major interfacial anodic and cathodic reactions. The major phenomena included in the FMD model are:

- Hydrogen (H_2) production from steel corrosion within a breached waste package,
- Alpha radiolysis and radiolytic oxidant (e.g., H_2O_2) generation as a function of fuel burn-up,
- Growth of a porous layer of uranyl oxyhydroxide and/or uranyl peroxide corrosion phases,
- Complexation of dissolved uranium by carbonate,
- Temperature variations of reaction rates,
- One-dimensional diffusion of all chemical species to and from the fuel and steel surfaces,
- Bulk solution reactions such as the oxidation of ferrous iron by O_2 and radiolytic H_2O_2.

The most important process included in the FMD model that was not addressed in the original CMPM is the oxidation of dissolved H_2 at the spent fuel surface (Jerden et al., 2015). The H_2 generated by steel corrosion in leaching experiments with spent fuel and simulated spent fuel has been seen to decrease the fuel degradation rate by as much as three orders of magnitude compared to the same tests performed in the absence of steel (e.g., Röllin et al., 2001, Ollila, 2008). How this H_2 effect is represented in the FMD model is discussed in Section 2 below.

Jerden et al., 2017 discussed including a corroding steel surface as a source of H_2 in the FMD model (FMDM version 3). One notable finding from that work is the extensive coupling between the corrosion of waste package components and the corrosion of spent fuel, which must be taken into account to accurately predict radionuclide source terms. As discussed in Jerden et al., 2017, the Eh and pH conditions within a breached waste package will evolve with time due to the coupled reactions of alloy corrosion, radiolysis, and spent fuel dissolution.

Depending on the waste package design, various waste package components will be in electrical contact when contacted by seepage water. Galvanic coupling and galvanically-induced corrosion will affect the dissolution rates of the individual waste components: the corrosion rate of the most susceptible component (which serves as the anode) will be accelerated and corrosion of the more noble component(s) (serving as the cathode) will decrease. In this study, initial tests were conducted to measure the behaviors of the individual materials as they equilibrated under various test conditions. Future tests will be performed to measure corrosion rates of various coupled systems using a recently developed method. This will permit modeling of various waste package designs. Implementation of the metal corrosion model with the FMD model is demonstrated here by using rates measured for individual metals. More extensive experimental and modeling work is needed to accurately represent the dynamics of in-package chemistry, galvanically-induced alloy corrosion, and fuel degradation.

In Jerden et al., 2019, we discussed ongoing experimental work to measure the corrosion rates of waste package alloys and the parameterization of this information for use in the latest version of the FMD model (FMDM version 4). Here, we discuss electrochemical experiments that are being performed to parameterize the FMD model (V.4).

As summarized in Jerden et al., 2019, the FMD model has been successfully integrated with the GDSA-PA code PFLOTRAN. The flow of information within the integrated FMDM – GDSA-PA model is summarized in Figure 7-1. The prototype in-package chemistry (IPC) model identified in Figure 1 has been implemented in the reactive transport code X1t, which is a module within the Geochemist's Workbench software package. This IPC model is referred to as a "prototype" because it is anticipated that a different version of the in-package chemistry model will be required to facilitate integration with other GDSA process models (including the FMD model).

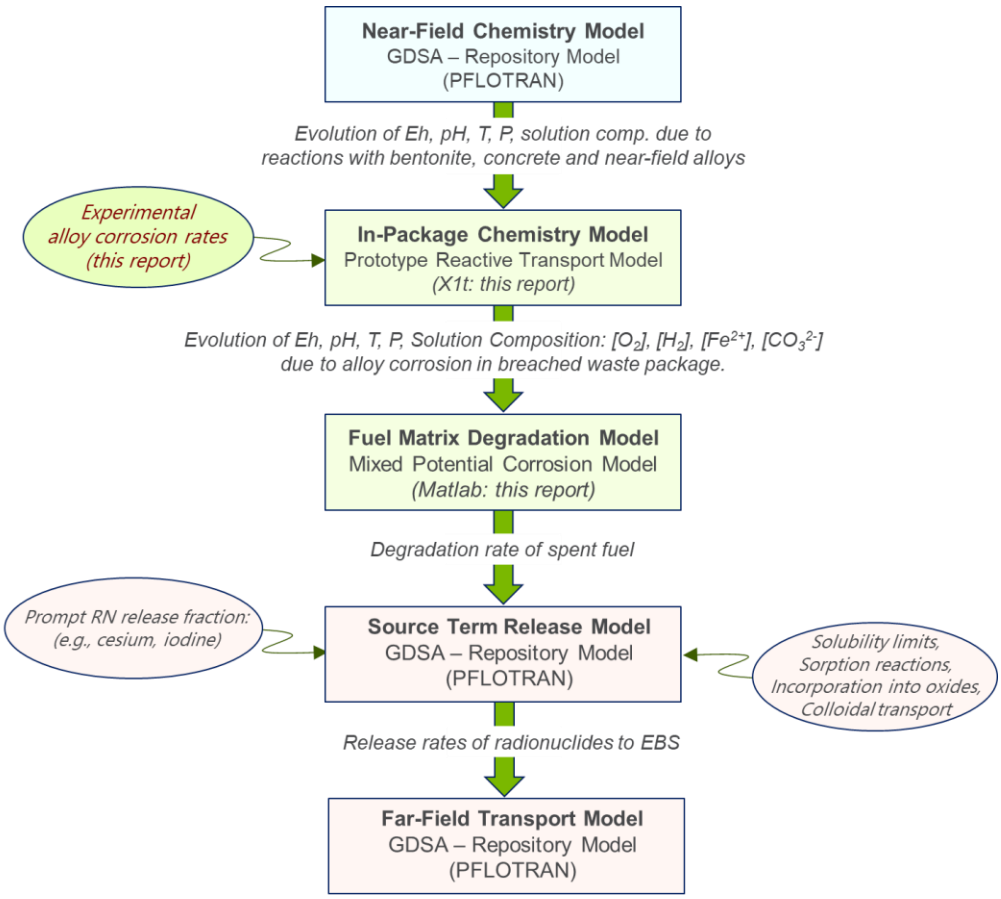

Figure 7-1. Flow chart summarizing how the X1t in-package chemistry model and FMD model from this report combine with GDSA-PA models to calculate source term.

7.2 The Fuel Matrix Degradation Model

The FMD model is based on fundamental electrochemical principals, mixed potential theory, and traditional mass balance and reactive transport relationships (King and Kolar, 1999) to determine the degradation rate of the fuel. Specifically, the FMD model calculates the dissolution rate of spent fuel as a function of the interfacial corrosion potential (E_{corr}), at which all of the anodic and cathodic half reactions occurring at the fuel/solution boundary are kinetically balanced with no net electron transfer. The dissolution rate (which corresponds to an anodic current due to the oxidation of U^{4+} to U^{6+}) is relatively high under oxidizing conditions above the U(IV)/U(VI) threshold potential, but significantly lower at potentials where only solubility-limited chemical dissolution of U^{4+} occurs.

The threshold potential for U(IV)/U(VI) oxidative dissolution depends on pH, as shown in Figure 2, and on the water chemistry. Under the reducing conditions envisioned in argillite and crystalline rock repositories, the Eh of the solution is expected to be below -0.1 V_{SHE} between pH 7 – 9 (Laaksoharju et al., 2008), which is well below the U(IV)/U(VI) threshold. However, the radiolysis of water by spent fuel to form H_2O_2 and other radiolytic oxidants can cause localized oxidizing conditions that drive the Eh far above the threshold for oxidative dissolution of the fuel, i.e., into the U(VI) stability field. The shaded area in Figure 2 shows the possible range of in-package conditions due to radiolysis. Thus, the FMD model must have the capability to address a pH range from about 4 to 11 and Eh values spanning the range of water stability.

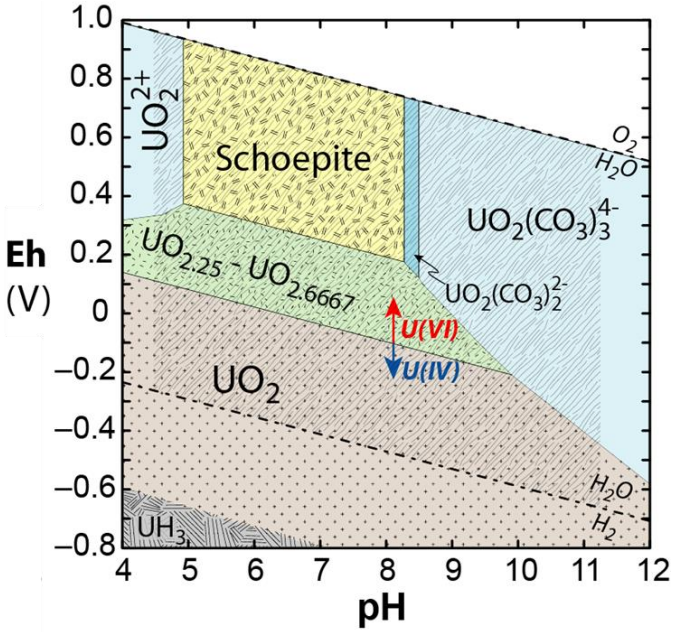

Figure 7-2. Pourbaix diagrams for uranium speciation showing possible range of conditions within a breached waste package due to radiolysis (shaded gray region). This diagram was drawn for a solution with $1x10^{-6}$ molal uranium and $1x10^{-4}$ molal carbonate. Eh is relative to standard hydrogen electrode (SHE).

A number of experimental and modeling studies have shown that the oxidative dissolution of spent fuel in anoxic environments is counteracted by the catalyzed oxidation of H_2 on fission product alloy phases referred to as the Ru ε-phase or noble metal particles (NMP) (e.g., Broczkowski et al., 2005, Shoesmith, 2008, Grambow, et al., 2010). This phenomenon, which we refer to as the H_2 effect, has been reported to decrease spent fuel dissolution rates by up to 3 orders of magnitude in comparison to the maximum dissolution rates attained in the absence of H_2 (e.g., Röllin et al., 2001, Ollila, 2008). The major goal of the

ongoing FMD model development work is to implement an accurate model that quantifies the generation and accumulation of H_2 and its influence on spent fuel degradation rates.

Two main sources of H_2 in the repository will be: (1) the radiolysis of in-package solutions, and (2) the anoxic corrosion of steels and other alloys present within the breached waste package and in the surrounding EBS and nearfield. Of these H_2 sources, alloy corrosion has been shown to be, by far, the most important (e.g., Johnson and King, 2003, Turnbull, 2009). Therefore, we must account for alloy corrosion within a breached waste package to accurately represent the effect of H_2 on spent fuel degradation rates. To this end, the FMD modeling work has expanded to include the quantification of alloy corrosion as a source of H_2 (e.g., Jerden et al., 2017, Jerden et al., 2018, Jerden et al., 2019).

Our on-going work addresses the coupling between the corrosion of waste package components and the spent UO_2 fuel. As shown in Jerden et al., 2017 and Jerden et al., 2019, the Eh and pH conditions within a breached waste package will evolve with time due to coupled reactions of alloy corrosion, radiolysis, and spent fuel dissolution. The latest FMD model accounts for radiolysis and takes a step towards accounting for coupled processes by linking alloy corrosion kinetics and fuel degradation rates. However, more experimental and modeling work is needed to more accurately model the dynamic relationship between spent fuel degradation and in-package alloy corrosion.

7.2.1 Fuel Matrix Degradation Model Functionality

The key processes represented in the latest version of the FMD model include:

- The generation of radiolytic oxidants as a function of fuel burn-up,
- The NMP □□-phase)-catalyzed oxidation of H_2, which protects the fuel from oxidative dissolution,
- The precipitation and growth of a uranyl oxyhydroxide (schoepite) corrosion layer that blocks radiolysis at the fuel/solution interface and slows the diffusion of reactants to and from the fuel surface,
- The complexation of uranyl by carbonate,
- The destruction of O_2 and radiolytic H_2O_2 by ferrous iron within the bulk solution,
- Temperature variations of reaction rates (by Arrhenius equations),
- The one-dimensional diffusion of all chemical species to and from the fuel and steel surfaces,
- The anoxic corrosion of alloy components to generate dissolved H_2 and oxidized metals (e.g., ferrous iron from steel).

As discussed above, the effect of H_2 oxidation is the most important of the above processes for determining the fuel dissolution rate and the radionuclide source terms (Jerden et al. 2015). The second most important effect is the oxidative dissolution of the fuel by the radiolytic oxidant H_2O_2 and its decomposition product O_2. In the FMD model, the H_2O_2 concentration is calculated using an analytical form of the radiolysis model developed at PNNL (Buck et al., 2014) and a burn-up/dose rate function derived from Radulescu, 2011.

The layout and reaction scheme of the FMD model is shown in Figure 7-3.

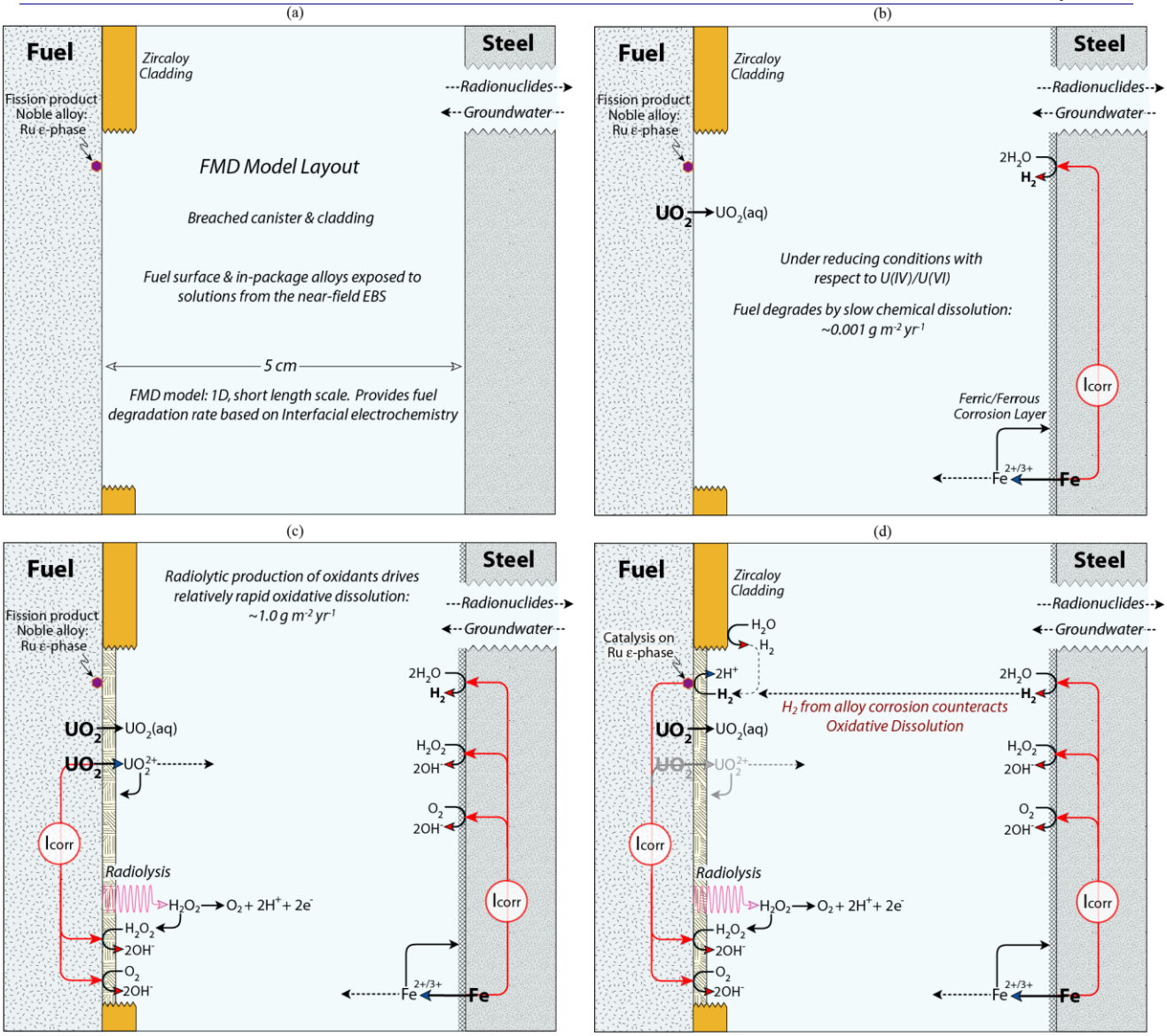

Figure 7-3. Schematic diagram showing the conceptual layout and reaction scheme for the fuel matrix degradation model and identifying other key processes that influence in-package chemistry and radionuclide mobilization (I_{corr} indicates corrosion current).

The steps involved in radionuclide release from spent fuel that are or will be represented in the FMD model are as follows:

- In a breached waste package, groundwater will infiltrate open spaces within the canister and begin to corrode in-package alloys.
- Alloy corrosion will produce H_2 even when the infiltrating groundwaters are electrochemically reducing with respect to the fuel. This is because the stability fields of carbon steels and stainless steels lie below the stability field of water, as shown in Figure 7-4.
- Assuming that the Zircaloy cladding has also been breached, the fuel will begin degrading when contacted by seepage water by either relatively rapid oxidative dissolution (~1 - 10 g/m^2 yr) or by

relatively slow chemical dissolution ($\leq 10^{-3}$ g/m^2 yr). The degradation pathway depends on the Eh and pH of the seepage water and the dissolved concentration of H_2.

- The prototype X1t in-package chemistry model calculates H_2 generation rates in this report, but these values will be computed within the FMD model in future iterations of the model.

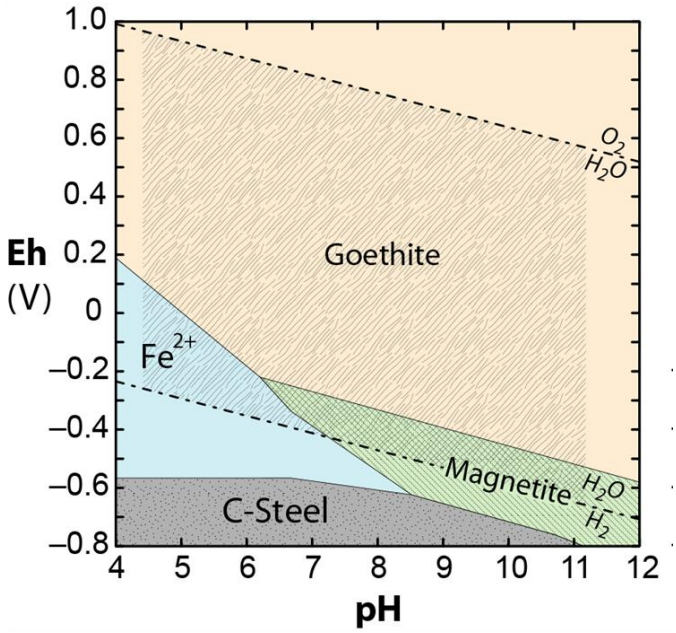

Figure 7-4. Pourbaix diagram showing the range of possible conditions within a breached waste package due to radiolysis (shaded gray region).

7.2.2 Breached Waste Package Environment

Simplified conceptual diagrams of a typical spent fuel waste package in a generic crystalline or argillite repository setting are shown in Figures 7-5 and 7-6 (adapted from Energy Solutions, 2015). These figures highlight the spatial arrangement of waste package components and key processes that the FMD model represents. As shown in Figures 7-5 and 7-6, the spent fuel assemblies will be surrounded by (and in close contact with) a number of alloy components within the waste package. These materials include carbon steel (C-steel), 316 stainless steel (316SS) and either borated aluminum or borated steel alloys. Another important material from the prospective of H_2 production in the repository is the Zircaloy cladding retaining the fuel pellets (gold or yellow in Figures 7-5 to 7-6). Although Zircaloy is not considered as a barrier to radionuclide release in the current FMD or GDSA PA models, Zircaloy corrosion could be an important source of H_2 and should be included in the FMD model. Quantifying the effect of Zircaloy corrosion in the FMD model is a subject of ongoing model development work.

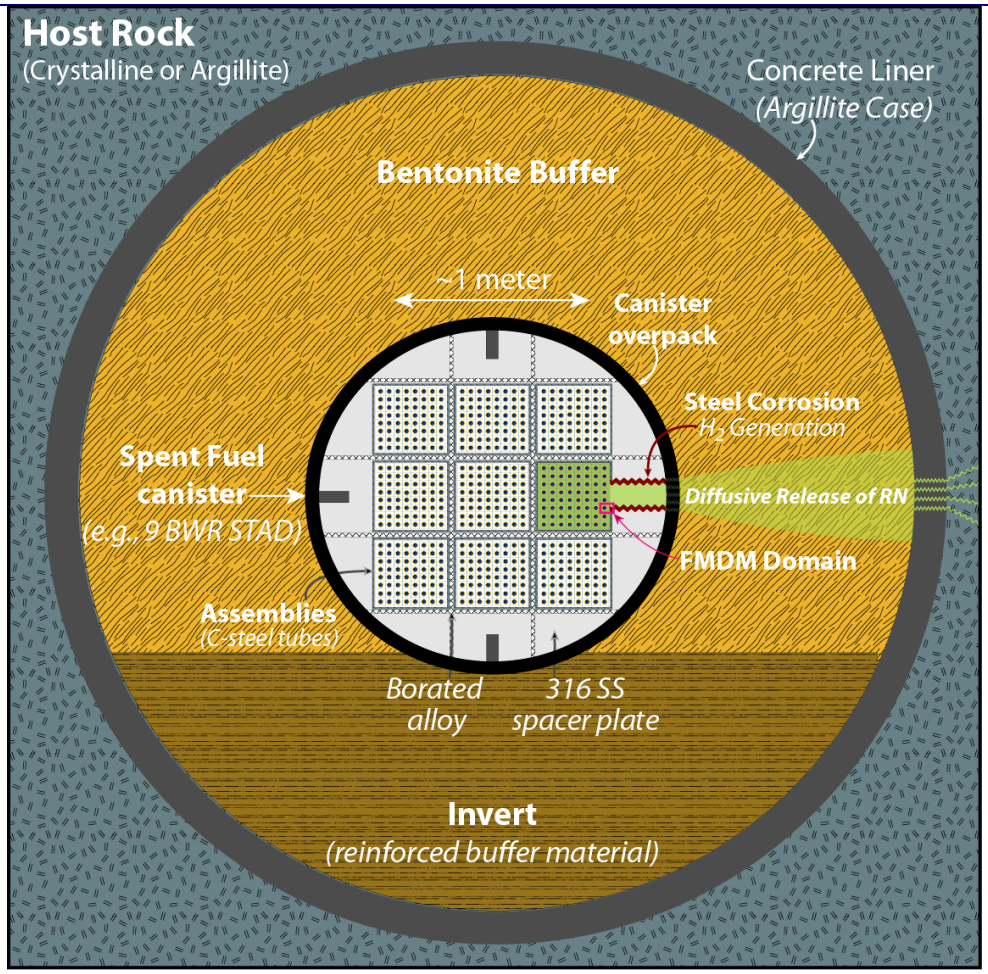

Figure 7-5. Conceptual diagram of a generic waste package showing a conceptual canister-breaching scenario. BWR STAD denotes a boiling water reactor standard transport, aging and disposal canister and RN denotes radionuclides (adapted from Energy Solutions, 2015).

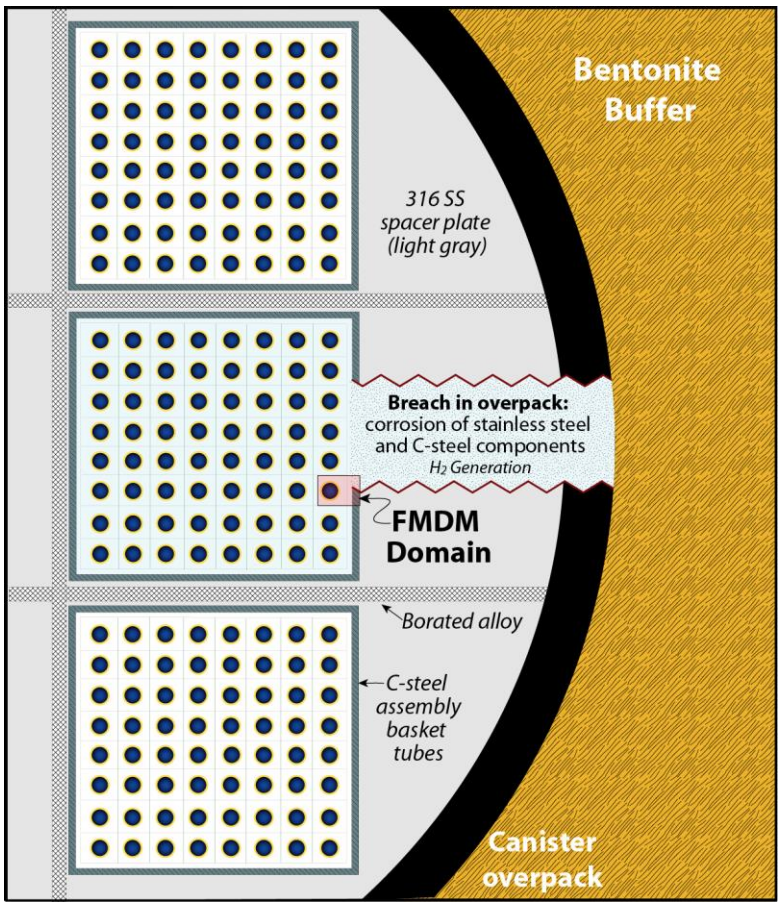

Figure 7-6. Conceptual diagram of a generic waste package showing a conceptual canister-breaching scenario (adapted from Energy Solutions, 2015).

7.3 Electrochemical Corrosion Experiments on In-Package Alloys: Kinetics of H_2 Generation

7.3.1 Hydrogen Producing Reactions

Accurate alloy corrosion rates that are measured under relevant disposal conditions are essential to model source term due to the dominant effect that H_2 produced from alloy corrosion has on the spent fuel dissolution rate (as discussed in Section 2). The half-cell reactions of particular interest for H_2 generation during the oxidation of relevant alloys are as follows:

$Fe \rightarrow Fe^{2+} + 2e^-$ (Reaction 1)

$2H_2O + 2e^- \rightarrow H_2 + 2OH^-$ (Reaction 2)
$2H^+ + 2e^- \rightarrow H_2$ (Reaction 3)

with the overall steel corrosion reactions

$Fe + 2H_2O \rightarrow H_2 + Fe^{2+} + 2OH^-$ (Reaction 4)
$Fe + 2H^+ \rightarrow H_2 + Fe^{2+}$ (Reaction 5)

Analogous reactions can be written for zirconium and aluminum alloys:

$Zr + 2H_2O \rightarrow 2H_2 + ZrO_2$ *(Baddeleyite)* (Reaction 6)
$Al + 3H_2O \rightarrow 1.5H_2 + Al(OH)_3$ *(Gibbsite)* (Reaction 7)

Reactions 4 - 7 provide the fundamental coupling between alloy corrosion and H_2 generation. The oxidation of minor alloy constituents (Cr, Mo, Ni, and Mn in steel and Sn in Zircaloy) will also contribute to the anodic current, but the oxidation of Fe (in steel), Al (in Boral), and Zr (in Zircaloy) will be dominant.

As discussed in Jerden et al., 2017, there is a wealth of literature on steel corrosion, but much of the previous work was not done under repository-relevant conditions. Studies that did use relevant solutions, such as bentonite pore waters (see reviews by Johnson and King, 2003 and King, 2007), involved batch style immersion tests that provided average cumulative rates rather than the instantaneous corrosion rates needed to parameterize and validate the in-package chemistry model.

Steel coupon immersion tests provide valuable information on the corrosion product mineralogy and the evolution of the chemical system. However, corrosion rates derived from immersion tests are based on cumulative mass loss measurements or corrosion layer thicknesses that do not indicate how the corrosion rate (and thus H_2 generation rate) varies with time or conditions (most importantly, with the solution Eh). Knowing these dependencies of the H_2 generation rate is essential for modeling spent fuel dissolution under evolving in-package chemical conditions.

During an immersion test with a passivating steel, most of the mass loss occurs before the steel surface is passivated. This may skew the average rate to high values. We need to know how the instantaneous corrosion rate controlling the H_2 generation changes as the conditions evolve to accurately represent the flux of H_2 in the FMD model. Electrochemical techniques allow us to measure instantaneous rates under carefully controlled chemical and redox conditions.

Electrochemical tests also quantify the effects of surface stabilization due to passivation and localized corrosion (such a pitting) that can only be qualitatively observed in coupon immersion tests. Furthermore, electrochemical methods can measure rates on the order of 10^{-3} g m^{-2} yr^{-1} (10^{-4} μm yr^{-1}). Therefore, electrochemical methods yield reliable corrosion rates for durable EBS materials (including 316 stainless steel and Zircaloy cladding) and provide dependencies on environmental conditions needed to predict the long-term generation of H_2 and attenuation of fuel degradation rates as the seepage water composition evolves.

7.3.2 Electrochemical Corrosion Test Method

The electrochemical corrosion experiments employ the standard three electrode method as described by Bard and Faulkner, 2001. The three-electrode cell used for the tests at Argonne consists of a 20 mL jacketed, borosilicate glass vessel with a mercury/mercurous sulfate reference electrode, a graphite counter electrode and a working electrode consisting of the alloy to be tested. A typical electrochemical cell and working electrode is shown in Figure 7-7. The voltages reported herein have been adjusted to the standard hydrogen electrode (SHE), which is the reference used in the FMD model.

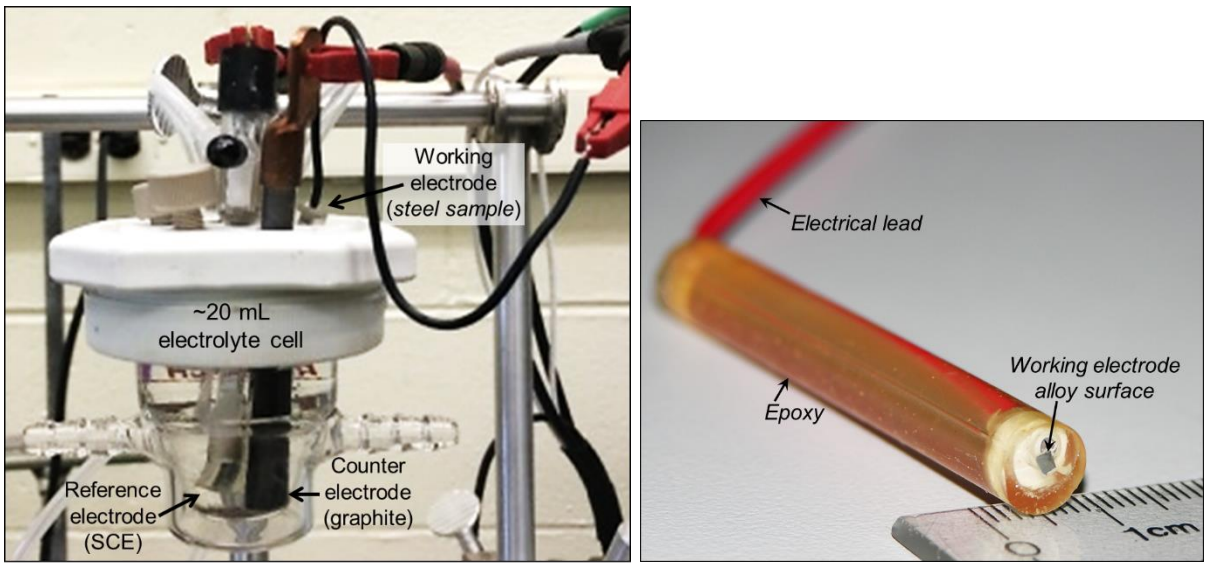

Figure 7-7. Three-electrode electrochemical cell used in Argonne electrochemical experiments (left) and an alloy working electrode (right).

In the electrochemical tests, the composition of the electrolyte is used to impose chemical effects, including pH, Cl^- concentration, and other solutes of interest, and a potentiostat is used to impose several surface potentials of interest, which can be significantly different than the Eh of the solution used in the test. The potentiostat allows a wide range of potentials to be applied to efficiently determine the effect of the solution redox (Eh) on the alloy corrosion and H_2 generation rates under controlled chemical conditions. In practice, a potentiodynamic scan is performed to measure the corrosion potential (E_{corr}) for the polished surface in the test solution and identify regions of active and passive behavior to be studied in subsequent potentiostatic tests. Several potentiostatic tests are conducted at voltages selected to measure the corrosion currents after stable passive layers have formed on passivating metals or after stable currents have been achieved by actively corroding metals. A stable current indicates that the surface has equilibrated under the

test conditions (pH, chloride concentration, temperature, applied potential) and is interpreted to represent the long-term corrosion rate under those conditions.

7.3.2.1 Comparison of Results from Electrochemical Tests and Coupon Immersion Tests

As discussed in Jerden et al., 2017, there are many studies in the literature addressing steel corrosion, but much of the previous work was not done under repository-relevant conditions. The studies that were done using relevant solutions, such as bentonite pore waters (see reviews by Johnson and King, 2003 and King, 2007), involved batch style immersion tests that provided average cumulative rates rather than the instantaneous corrosion rates needed to parameterize and validate the FMD model. The instantaneous corrosion rate refers to the oxidation reactions that result in the generation of H_2. The FMD model tracks the kinetics for diffusion of the generated H_2 to the fuel surface and its subsequent oxidation on noble metal particles.

The immersion tests quantify the cumulative extent of corrosion (based on the specimen mass loss or thickness of the corrosion layer) that occurs over a given test duration; they do not provide the instantaneous corrosion rates needed to determine H_2 generation rates (see Jerden et al., 2017). The difference between the cumulative rates from immersion tests and the instantaneous rates measured electrochemically is illustrated in Figure 7-8 (adapted from Jerden et al., 2017), where the blue curve represents the actual mass of a passivating metal such as 316 stainless steel that is oxidized during a coupon corrosion test. The blue curve shows that the majority of corrosion occurs prior to passive stabilization and little further corrosion occurs after that. At the end of the immersion test duration, the oxide layer is carefully removed, and the corroded coupon is weighed to determine the mass lost due to corrosion; two blue circles are included in Figure 8 to represent the extents of corrosion measured after two durations. The two tests only provide the average corrosion rates indicated by the dashed green lines in Figure 7-9 after those test durations. The corrosion behavior is not well-represented by the cumulative rates, which give an "artificial" dependence on the test duration. That is, the average rate will decrease with longer test durations even though most of the mass loss occurred early in the test.

The instantaneous rate of corrosion (which determines the H_2 generation rate at each point in time) is given by the slope of the blue curve. That rate decreases significantly after the surface passivates and becomes much lower than the average cumulative rate. In principle, an extensive series of immersion tests could be conducted for different durations to derive the mass loss curve, but the mass loss of a passivated surface will be too small to measure. Regardless, immersion test results do not indicate the dependence of the corrosion rate on the solution Eh that is needed for the FMD model. Immersion tests can only provide corrosion rates under the test conditions, which will drift as the solutions and specimen surfaces evolve. The electrochemical method employed for this study directly measures the metal oxidation rates needed to calculate H_2 generation rates in the FMD model under wide ranges of controlled redox and test conditions (Eh, pH, chloride concentrations).

The electrochemical tests can measure oxidation rates on the order of 10^{-3} g m^{-2} yr^{-1} (10^{-4} μm yr^{-1}) and quantify the effects of localized corrosion processes, such as pitting, and surface passivation on the corrosion rate. The electrochemical method provides reliable corrosion rates for durable EBS materials (including Zircaloy cladding) over the wide range of environmental conditions that could occur in a breached waste package that are needed to predict the generation of H_2.

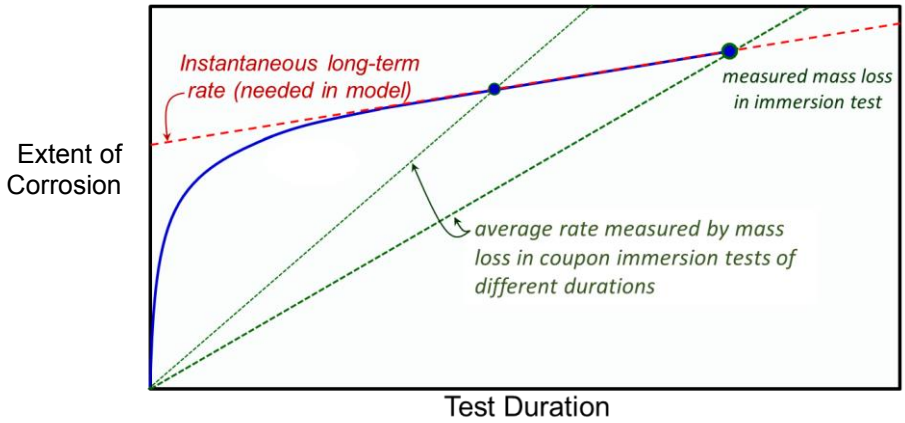

Figure 7-8. Conceptual diagram showing how mass loss measurements of steel corrosion rates in immersion tests yield rates that do not represent the corrosion kinetics (adapted from Jerden et al., 2017).

7.3.2.2 Data Analysis Method

Potentiostatic tests are conducted to monitor the current as the material surface interacts with the solution, which may result in passivation or active corrosion. In most cases, a steady current is achieved within a few days and indicates a constant corrosion rate. The steady current densities measured in the potentiostatic test are converted directly into alloy corrosion rates by using Faraday's Law which relates the cumulative charge transferred through the working electrode to the mass of metal oxidized during an experiment (Equation 7-1). Since the cumulative charge transferred is a function of the reaction current over time (Equation 7-2) we can use current densities measured during potentiostatic tests to calculate corrosion rates (Equations 7-3 and 4)

$$m = \frac{QM}{nF} \qquad \text{Equation 7-1}$$

where m is the mass of substance oxidized, Q is the total electric charge passed through the electrode substance, M is the molecular weight of the electrode substance, F is the Faraday constant, and n is the number of electrons transferred.

The cumulative electric charge Q is the integrated reaction current measured at the electrode:

$$Q = \int_0^t I(t)\, dt \qquad \text{Equation 7-2}$$

Where $I(t)$ is the reaction current measured at the electrode at time t. Therefore, the mass of material oxidized at the electrode surface can also be calculated from the measured reaction current at the electrode. If the corrosion current is constant, the mass corroded over an interval Δt can be calculated as:

$$m = \frac{I \cdot \Delta t\, M}{nF} \qquad \text{Equation 7-3}$$

and the rate can be calculated as

$$rate = \frac{m}{\Delta t} = \frac{IM}{nF}$$ Equation 7-4

The current and mass released can be normalized to the surface area of the electrode to give corrosion rates in units of g m^{-2} yr^{-1}, which can be converted to penetration rates in mm yr^{-1} using the density of the steel. It also gives the H_2 generation rate using the stoichiometry of Reactions 4 – 7 shown above.

Each electrochemical experiment involves the following sequence of steps:

- Electrochemical cleaning at a potential far below the corrosion potential of the material to remove any native oxide from the sample electrode,
- Potentiodynamic scans to determine E_{corr} of alloy under chemical conditions of interest,
- Potentiostatic holds (up to 8 days) at several relevant redox conditions to quantify effects of passivation,
- Periodic electrical impedance spectroscopy analyses to characterize the evolving properties of corroded surface,
- Detailed microscopy (reflected light, SEM/EDS) to characterize changes in alloy microstructures during test.

The results from these tests provide the following information:

- Corrosion rates for surfaces equilibrated under controlled environmental conditions,
- Electrical properties of the passivated surfaces to provide confidence in their long-term stability,
- Data to derive analytical expressions for key corrosion rate dependencies (Eh, pH, chloride concentration) to calculate evolution of H_2 concentrations in breached waste package,
- Corrosion products for further analyses.

The Butler-Volmer equation (as defined by Bard and Faulkner, 2001) relates the anodic current density to the applied over-potential as:

$$j_a = j_0 \cdot \exp\left(\frac{(1-\alpha)\cdot z\cdot F}{(R\cdot T)}(E - E_{eq})\right)$$ Equation 7-5

where j_a is the anodic current density (A m^{-2}), j_0 is the exchange current density (A m^{-2}), α is the charge transfer coefficient, z is the number of electrons involved in the corrosion reaction, F is the Faraday constant, R is the universal gas constant, T is absolute temperature, E_{eq} is the equilibrium electrode potential (E_{corr}) and E is the instantaneous electrode potential applied during the test. The Butler-Volmer equation is typically restricted to deviations from less than 0.2 V and the high applied potentials used to represent the range of conditions that could occur in a disposal system will likely result in deviations from Butler – Volmer behavior. The added effects of high pH and chloride concentrations may also lead to deviations. The dependencies can be represented using empirical relationships determined by plotting corrosion rate as a function of applied potential, pH, and chloride concentration. This approach allows us to define the analytical functions needed in the X1t in-package chemistry model to predict the H_2 generation rates (from alloy corrosion) over the wide range of relevant Eh and pH conditions to be input into the FMD model. The empirical dependencies of the alloy corrosion rates on pH and chloride are quantified in Section 7.3.3.

7.3.3 Results from Electrochemical Corrosion Tests

The test conditions and results from the electrochemical corrosion tests are shown in Tables 7-1 through 7-3 and the data trends are shown in Figures 7-9 through 7-30.

The effects of Eh, as represented by the applied potentials in the potentiostatic tests, are quantified in the IPC – FMD model using an exponential dependence consistent with the form of the Butler-Volmer equation (Equation 7-5). Preliminary empirical relationships for the effects of pH and chloride concentration on the alloy corrosion rates are being derived for data sets showing regular trends (Equations 6 – 21). Exponential functions provide reasonable quantitative descriptions of the data under most experimental conditions (Figures 11, 14, 16, 17, 18, and 26), though many deviations are not yet understood. Future experimental work will aim to better quantify the combined effects to provide more accurate analytical functions that quantify the alloy corrosion rate dependence on Eh, pH, chloride and temperature.

7.3.3.1 AISI 4320 Carbon Steel and Boral

The results for AISI 4320 carbon steel and Boral corrosion under different test conditions are provided in Table 7-1. Both the experimentally measured current densities (CD) and calculated corrosion rates (CR) are provided. A few corrosion tests that were run at potentials of -0.06 V_{SHE} and lower had net cathodic currents (i.e., negative values), indicating that the test potentials were lower than E_{corr} under those conditions. (Note that the value of E_{corr} increases as the surface passivates.) The cathodic currents indicate the rate of cathodic reactions catalyzed by the metal surface, including H_2 formation (Reaction 3 above).

Table 7-1. Current densities and corrosion rates from electrochemical corrosion tests on AISI 4320 (carbon steel) and Boral

Alloy	pH	NaCl (molal)	Quantity*	Volts vs. SHE					
				0.49	0.24	-0.06	-0.26	-0.44	-0.66
4320 (C-steel)	4	4.3E-03	CD	1.2E-02	----	----	----	----	----
			CR	1.1E+06	----	----	----	----	----
	7	4.3E-03	CD	1.4E-03	----	----	----	----	----
			CR	1.2E+05	----	----	----	----	----
	10	1.7E-09	CD	3.8E-07	1.9E-07	-6.6E-06	----	----	----
			CR	3.5E+01	1.7E+01	Cathodic	----	----	----
		4.3E-03	CD	1.5E-03	----	-1.7E-06	----	7.7E-05	-2.5E-05
			CR	1.4E+05	----	Cathodic	----	7.0E+03	Cathodic

		1.0E-01	CD	1.1E+00	1.5E-02	9.3E-04	----	----	----
			CR	9.7E+07	1.4E+06	8.5E+04	----	----	----
Boral	10	4.3E-03	CD	1.5E-03	5.8E-04	----	1.4E-04	----	----
			CR	4.4E+04	1.7E+04	----	4.2E+03	----	----

**CD = current density (A cm^{-2}), CR = Corrosion Rate (g m^{-2}yr^{-1}), ---- = not measured.*

The lowest carbon steel corrosion rate measured was 1.7 g m^{-2}·yr^{-1} for the test with 17 nanomolal NaCl, 0.24 V_{SHE}, and pH 10, while the highest carbon steel corrosion rate measured was 9.7×10^7 g m^{-2}·yr^{-1} at 100 millimolal NaCl, 0.49 V_{SHE}, and pH 10. The measured corrosion rates of carbon steel strongly depend on the concentration of NaCl. The effect of pH on the corrosion rate of carbon steel is not as significant as NaCl concentration. When NaCl is 4.3 millimolal and the potential is held at 0.49 V_{SHE}, the corrosion rate is highest at pH 4 (1.1×10^6 g m^{-2}·yr^{-1}) and approximately an order of magnitude lower at both pH 7 and pH 10.

Figure 7-9 presents selected potentiostatic scans from carbon steel experiments at pH 10, 0.1 molal NaCl, and potentials ranging from 0.49 V_{SHE} to -0.26 V_{SHE}. The current densities in these scans remain high and do not reach clearly stable values at the positive hold potentials in Figure 7-9. The high current densities are attributed to the lack of passivation for this alloy (the magnetite corrosion product layers are porous and do not electrochemically protect the alloy surface from future corrosion).

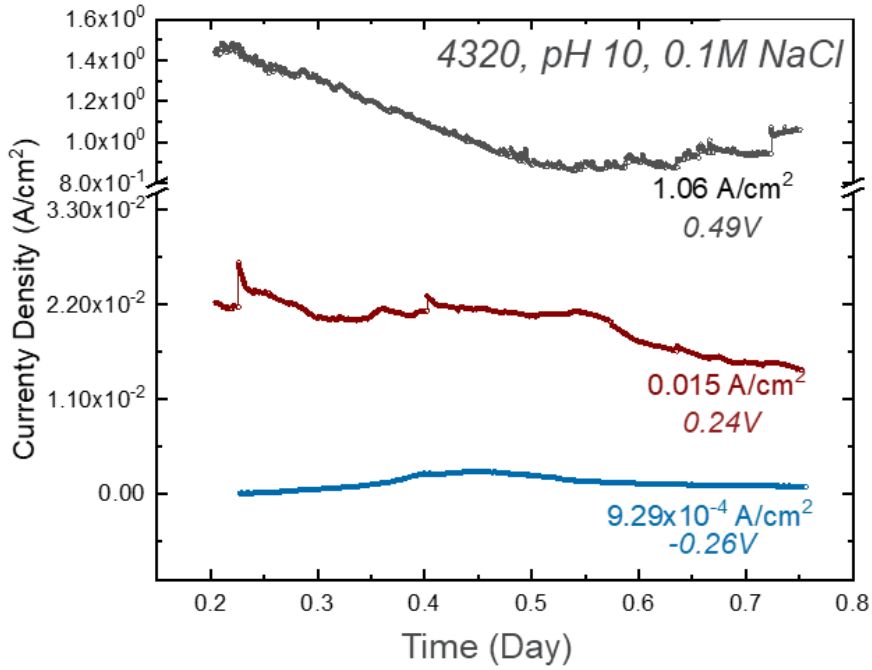

Figure 7-9. Potentiostatic tests on AISI 4320 (carbon steel) at pH 10, 0.1 molal NaCl, and 3 fixed potentials (V_{SHE}).

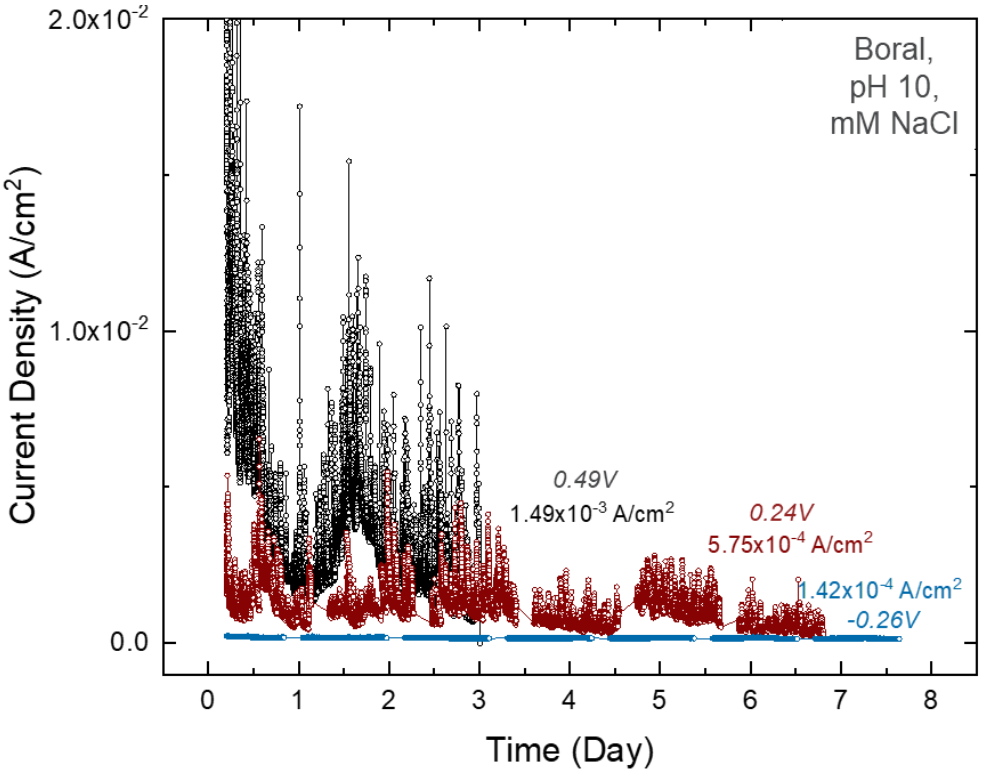

Figure 7-10. Potentiostatic test results on Boral at pH 10, 4.3 millimolal NaCl, and various fixed potentials (V_{SHE}).

The Boral corrosion rates, which were only measured at pH 10 and in 4.3 millimolal NaCl solution, are nearly the same order of magnitude as those measured for carbon steel under the same conditions (Table 7-1). Corrosion of the Al cladding of the Boral material forms porous aluminum oxide/hydroxide corrosion products that do not effectively passivate the surface and high corrosion rates persist. The currents measured in the potentiostatic tests with the Boral at pH 10, 4.3 millimolal NaCl, and positive hold potentials (i.e., 0.49 V_{SHE} and 0.24 V_{SHE}) are erratic during the measurement (Figure 7-10), probably due to pitting. The average of the current density values beyond Day 1 was used to calculate the corrosion rate.

Figure 7-11 shows the corrosion rate data trends for tests with carbon steel as a function of applied potential in different electrolyte compositions. The best-fit lines in the plot depict the relationship between corrosion rate and applied potential. The increase in the carbon steel corrosion rate with increasing NaCl concentration is clear in Figure 7-11.

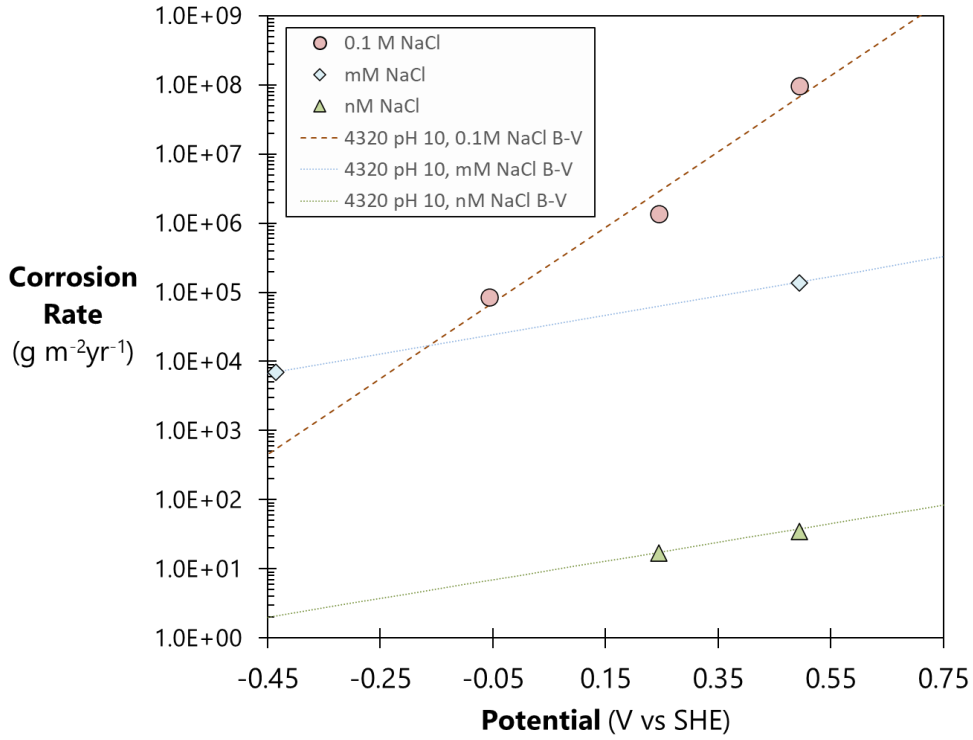

Figure 7-11. Corrosion rates plotted against potentiostatic fixed potentials (V_{SHE}) for AISI 4320 (carbon steel) at pH 10 and various NaCl concentrations overlaid with exponential best-fit lines (Equations 7-6 through 7-8).

The best trendline fits to the data shown in Figure 11 are exponential relationships:

For the 0.1 molal data the fit is:

$CR = 1.253x10^{5} \cdot \exp(12.683 \cdot E)$, R^2: 0.97 (Equation 7-6)

For the millimolal data the trend is:

$CR = 2.81x10^{4} \cdot \exp(3.193 \cdot E)$ (Equation 7-7)

And for the nanomolal data the trend is:

$CR = 8.413 \cdot \exp(2.879 \cdot E)$ (Equation 7-8)

The corrosion rates for AISI 4320 plotted as functions of pH and chloride concentrations are shown in Figures 7-12 and 7-13.

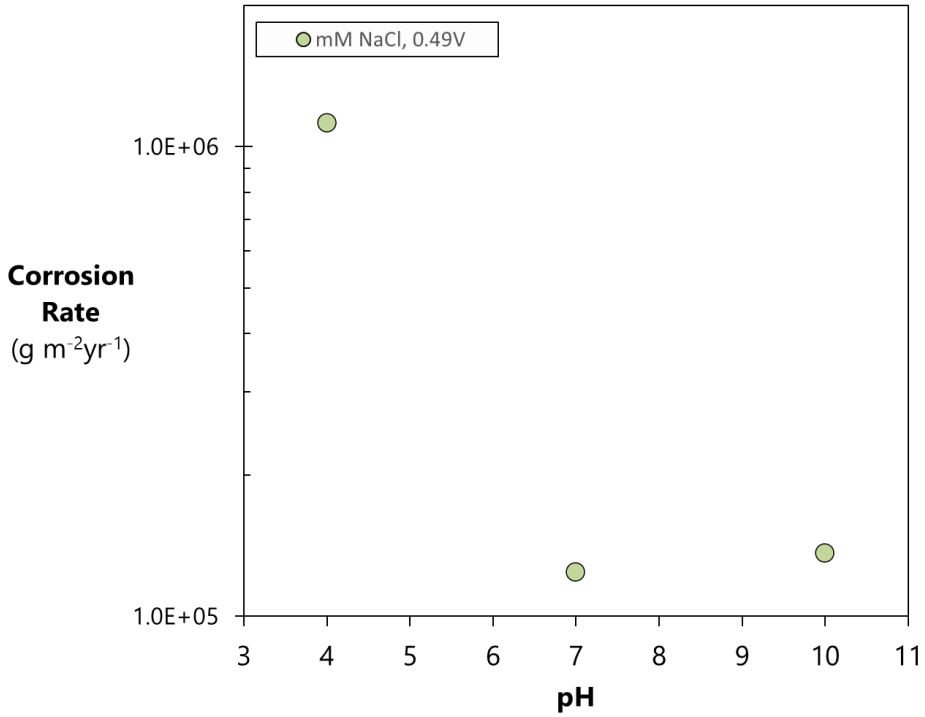

Figure 7-12. Corrosion rates plotted against pH for AISI 4320 (carbon steel) at 4.3 millimolal NaCl concentration and 0.49 V_{SHE}.

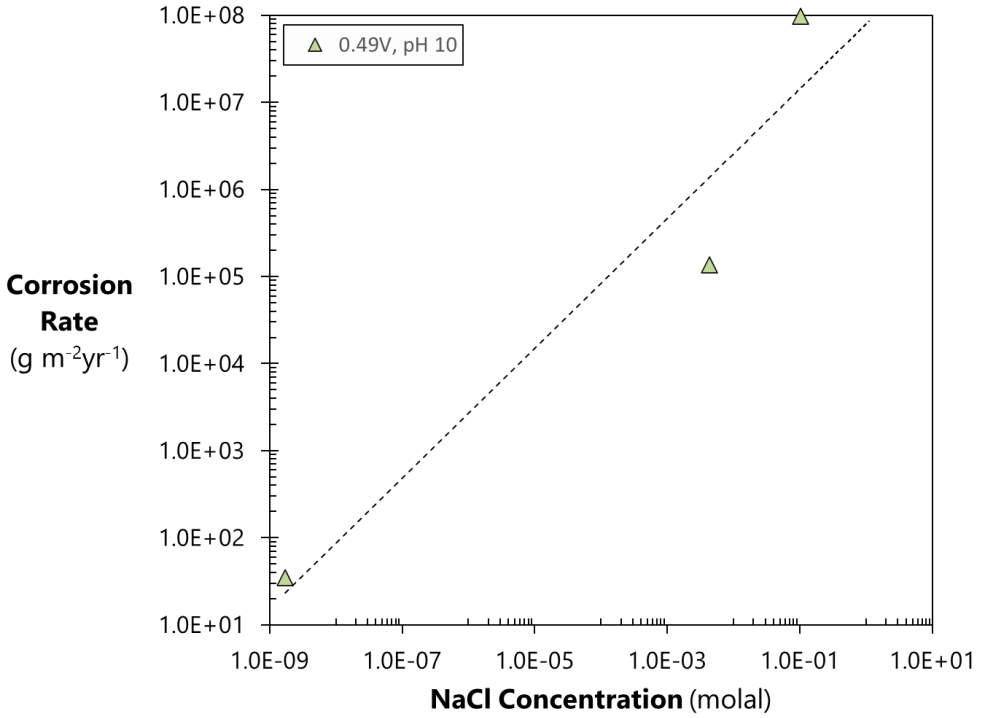

Figure 7-13. Corrosion rates plotted against pH for AISI 4320 (carbon steel) at pH 10 and 0.49 V_{SHE} (regression line is given in Equation 9).

The NaCl concentration dependence of the carbon steel corrosion rate is fit best by a power law:

$CR = 8.0x10^{7} \cdot [NaCl]^{0.7454}$, $R^2 = 0.918$ (Equation7- 9)

Figures 14 shows the corrosion rate data trends as a function of applied potential in different electrolyte compositions for the borated aluminum composite material Boral. The best-fit line in the plot depicts the relationship between the corrosion rate and redox potential.

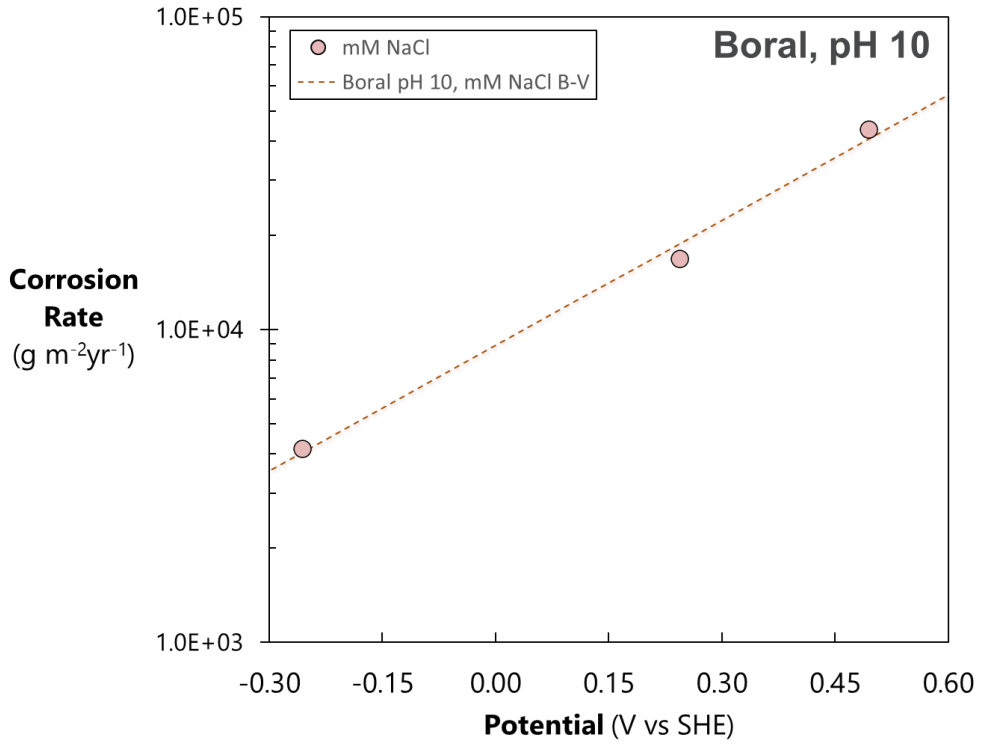

Figure 7-14. Corrosion rates plotted against potentiostatic fixed potentials (V_{SHE}) for Boral at pH 10 and 4.3 millimolal NaCl overlaid with an exponential best-fit line (Equation 10).

The best trendline fit to the corrosion rate data for Boral shown in Figure 14 is an exponential relationship:

$CR = 8.88x10^{3} \cdot \exp(3.086 \cdot E)$, R^2: 0.994 (Equation 7-10)

7.3.3.2 316 Stainless Steel

Table 7-2 reports the current densities and corrosion rates of 316 stainless steel measured at various pH, NaCl concentration, and hold potential. The highest corrosion rate (1.2×10^{3} g m^{-2} yr^{-1}) was measured in the solution containing 630 millimolal NaCl at pH 4 and held at 0.49 V_{SHE} and the lowest corrosion rate (1.2×10^{-2} g m^{-2} yr^{-1}) was measured in the solution containing 4.3 millimolal NaCl at pH 10 and held at 0.14 V_{SHE}. Many corrosion tests that were run below 0.14 V_{SHE}, and a few that were run above, showed net

cathodic currents (i.e., negative values for current density), signifying that measurement potentials were lower than E_{corr}.

Table 7-2. Current densities and corrosion rates from electrochemical corrosion tests on 316 stainless steel

Alloy	pH	NaCl (molal)	Quantity*	Volts SHE					
				0.49	0.34	0.24	0.14	-0.01	-0.26
316SS	4	1.7E-09	CD	7.1E-09	-1.8E-09	-1.3E-09	----	----	----
			CR	2.5E-02	*Cathodic*	*Cathodic*	----	----	----
		4.3E-03	CD	8.6E-09	2.7E-09	1.2E-09	-1.1E-09	----	----
			CR	7.2E-01	2.3E-01	1.0E-01	*Cathodic*	----	----
		1.0E-01	CD	7.1E-09	2.7E-09	1.5E-09	----	----	----
			CR	5.9E-01	2.3E-01	1.2E-01	----	----	----
		6.3E-01	CD	1.4E-05	3.3E-09	----	----	----	----
			CR	1.2E+03	2.8E-01	----	----	----	----
	7	1.7E-09	CD	3.2E-09	2.5E-09	7.0E-10	----	-3.2E-06	-2.5E-09
			CR	2.7E-01	2.1E-01	5.9E-02	----	*Cathodic*	*Cathodic*
		4.3E-03	CD	4.1E-08	3.4E-09	2.6E-09	4.3E-09	-1.7E-07	-8.2E-06
			CR	3.4E+00	2.9E-01	2.1E-01	3.6E-01	*Cathodic*	*Cathodic*
		1.0E-01	CD	1.2E-08	1.6E-09	3.9E-09	----	-6.4E-08	-4.5E-06
			CR	9.6E-01	1.3E-01	3.2E-01	----	*Cathodic*	*Cathodic*
		6.3E-01	CD	1.1E-08	1.3E-08	----	----	----	----
			CR	8.8E-01	1.0E+00	----	----	----	----
	10	1.7E-09	CD	5.1E-09	2.0E-10	1.9E-09	----	4.0E-10	-7.9E-06
			CR	4.3E-01	1.6E-02	1.6E-01	----	3.4E-02	*Cathodic*
		4.3E-03	CD	3.2E-09	1.0E-09	4.9E-10	1.4E-10	-1.5E-09	-3.8E-06
			CR	2.7E-01	8.5E-02	4.1E-02	1.2E-02	*Cathodic*	*Cathodic*
		1.0E-01	CD	2.0E-09	5.1E-09	-6.7E-10	----	-8.1E-08	-8.7E-06
			CR	1.7E-01	4.2E-01	*Cathodic*	----	*Cathodic*	*Cathodic*
		6.3E-01	CD	8.2E-10	2.9E-09	----	----	----	----
			CR	6.8E-02	2.4E-01	----	----	----	----

**CD = current density (A cm^{-2}), CR = Corrosion Rate (g $m^{-2}yr^{-1}$), ---- = not measured.*

Figure 7-15 presents representative data from potentiostatic tests on 316 stainless steel measured in solutions containing 17 nanomolal NaCl at pH 10 and at 3 designated hold potentials. The gaps in the current profiles are due to the performance of electrochemical impedance spectroscopy (EIS), the results of which will be discussed in a future report. The thickness of the curves are a result of the dynamic balance between anodic and cathodic reactions occurring of the electrode surface, and the higher values after about seven days were used to calculate corrosion rate. The corrosion currents stabilized relatively rapidly (after day 2) in tests at the higher potentials, coinciding with the passivation of the material by a thin chromium oxide layer. The surface did not passivate in the test at -0.26 V and a cathodic current occurred.

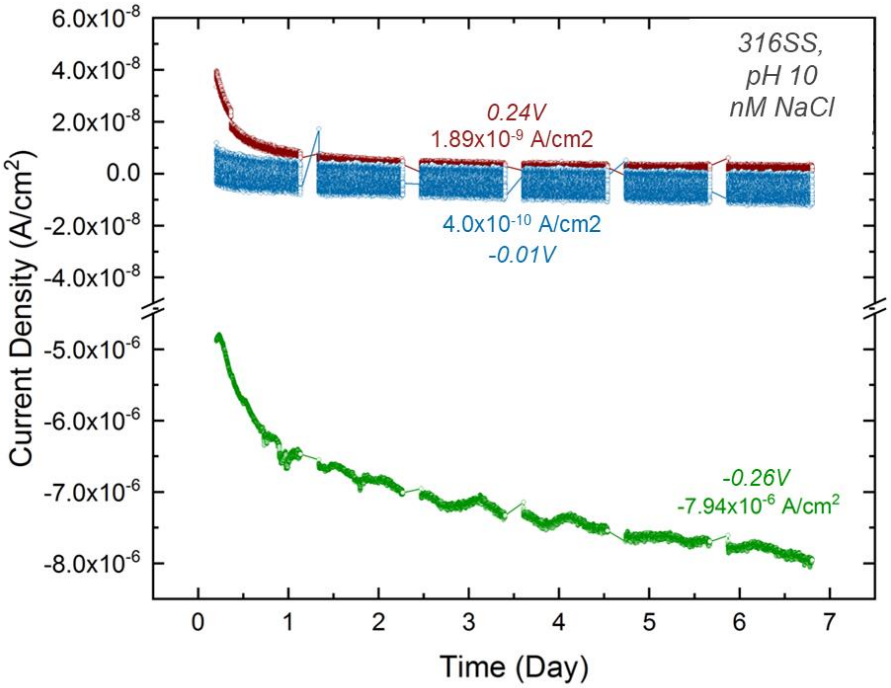

Figure 7-15. Potentiostatic test results on 316 stainless steel at pH 10, 17 nanomolal NaCl, and various fixed potentials (V_{SHE}).

In general, the corrosion rates of 316 stainless steel do not vary significantly with NaCl concentration at pH 4 and 7, which is apparent from the overlaid datasets in Figures 16 and 17, respectively. Representative best-fit lines are shown for the data collected in solutions of 4.3 millimolal NaCl for both plots (Figures 7-16 and 7-17). At pH 10, the corrosion rate of 316 stainless steel is dependent on NaCl concentration (Figure 7-18). For the hold potentials measured in this study, the corrosion rates in solutions of 1.7 nanomolal NaCl are approximately an order of magnitude greater than in solutions of 4.3 millimolal NaCl. However, in solutions of 0.1 molal NaCl and 1 molal NaCl, the corrosion rate unexpectedly decreases with increasing hold potential (Figure 7-18).

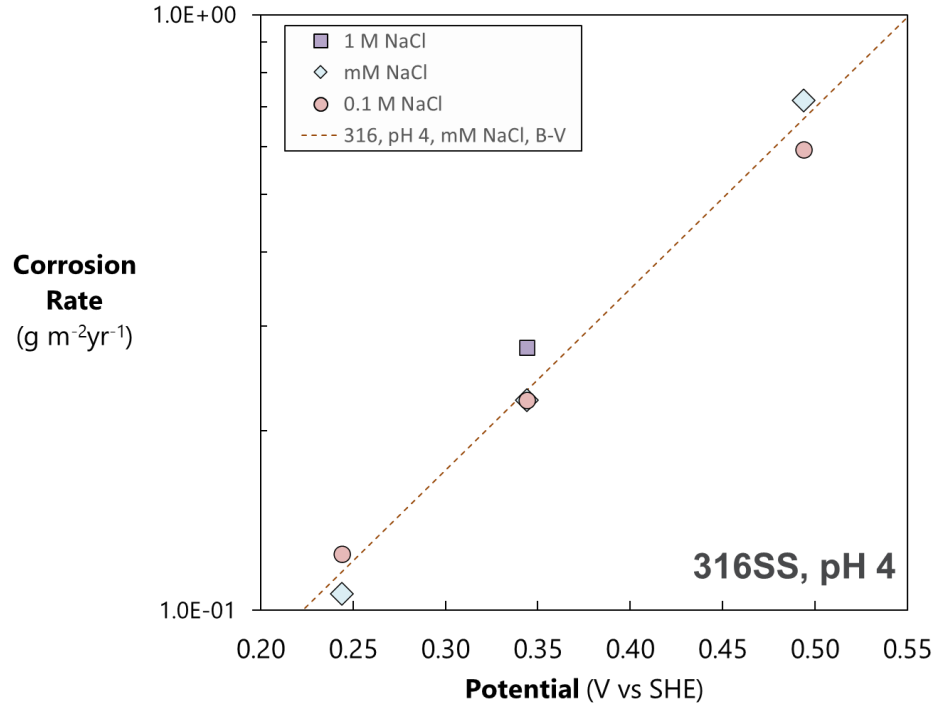

Figure 7-16. Corrosion rates plotted against potentiostatic fixed potentials (V_{SHE}) for 316 stainless steel at pH 4 and various NaCl concentrations overlaid with an exponential best-fit line (Equation 11).

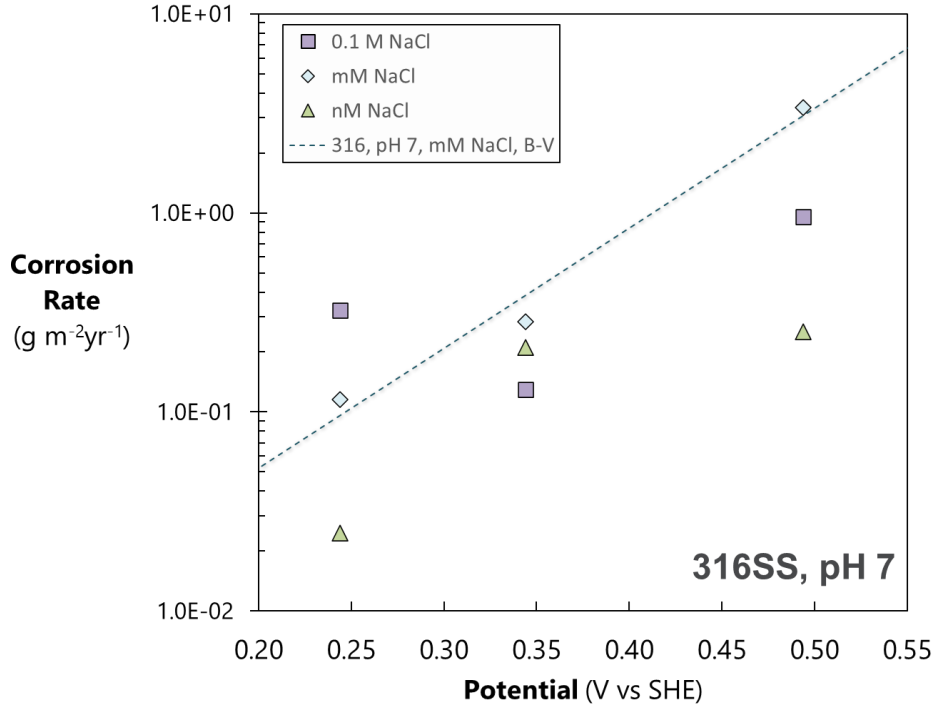

Figure 7-17. Corrosion rates plotted against potentiostatic fixed potentials (V_{SHE}) for 316 stainless steel at pH 7 and various NaCl concentrations overlaid with an exponential best-fit line.

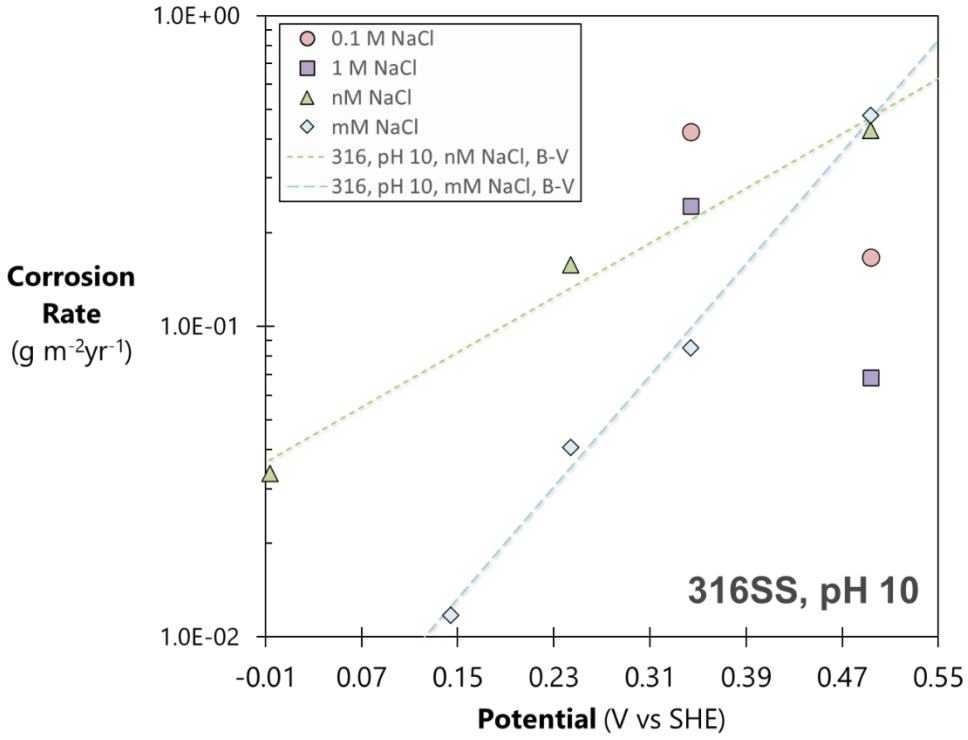

Figure 7-18. Corrosion rates plotted against potentiostatic fixed potentials (V_{SHE}) for 316 stainless steel at pH 10 and various NaCl concentrations overlaid with exponential best-fit lines (Equations 7-13 and 7-14).

The best fit trendlines for the corrosion rate data shown in Figures 7-16, 7-17 and 7-18 are exponential relationships:

for the stainless steel corrosion at pH 4 (Figure 7-16) the relationship for the 4.3 millimolal data is:

$CR = 1.64x10^{-2} \cdot \exp(7.638 \cdot E)$, R^2: 0.999 (Equation 7-11)

the relationship at pH 7 (Figure 17) for the 4.3 millimolal data is:

$CR = 3.4x10^{-3} \cdot \exp(13.734 \cdot E)$, R^2: 0.978 (Equation 7-12)

the relationship at pH 10 (Figure 18) for the 4.3 millimolal data is:

$CR = 2.8x10^{-3} \cdot \exp(10.33 \cdot E)$, R^2: 0.993 (Equation 7-13)

and the best fit trend for the nanomolal data shown in Figure 18 is:

$CR = 3.8x10^{-2} \cdot \exp(5.079 \cdot E)$, R^2: 0.985 (Equation 7-14)

The pH dependence of the 316 stainless steel corrosion rates are shown in Figures 7-19, 7-20 and 7-21.

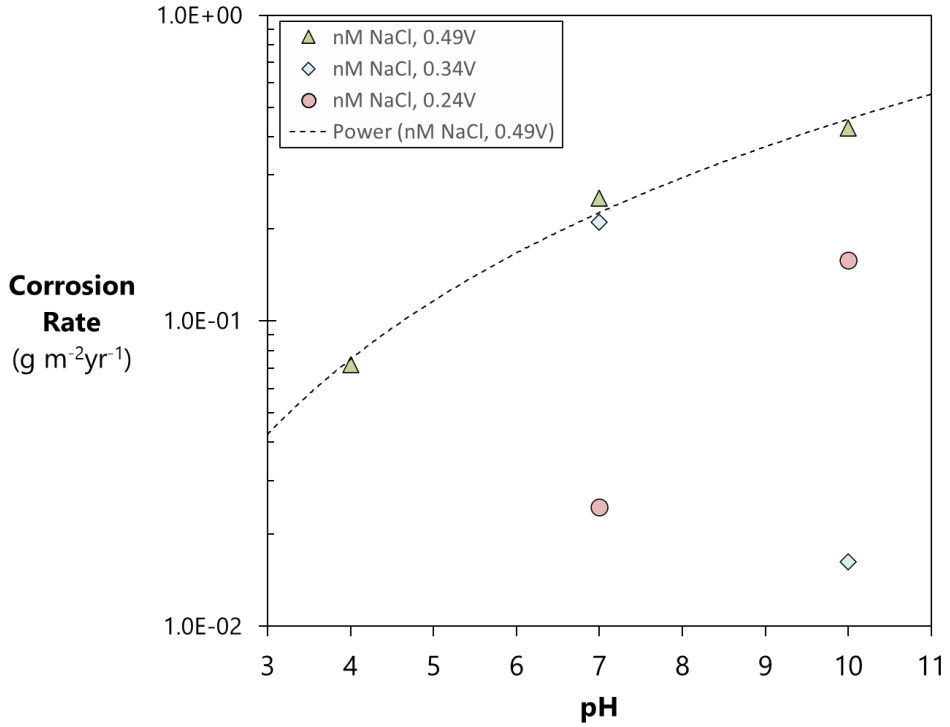

Figure 7-19. Corrosion rates plotted against pH for 316 stainless steel at 1.7 nanomolal NaCl concentration.

The best fit trend line for the pH dependence of the stainless steel corrosion rate at 0.49 V shown in Figure 19 is a power law function:

$CR = 0.0049 \cdot [pH]^{1.974}$, $R^2 = 0.989$ (Equation 7-15)

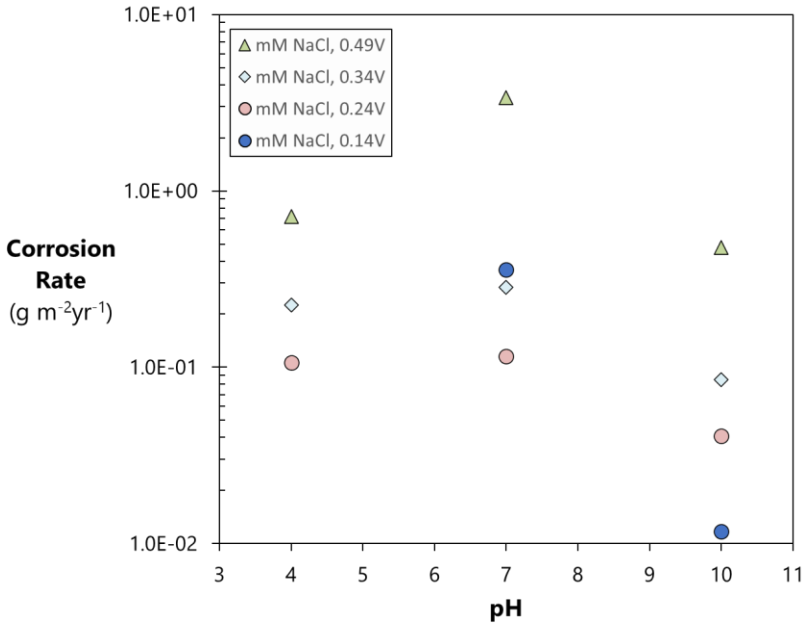

Figure 7-20. Corrosion rates plotted against pH for 316 stainless steel at 4.3 nanomolal NaCl concentration.

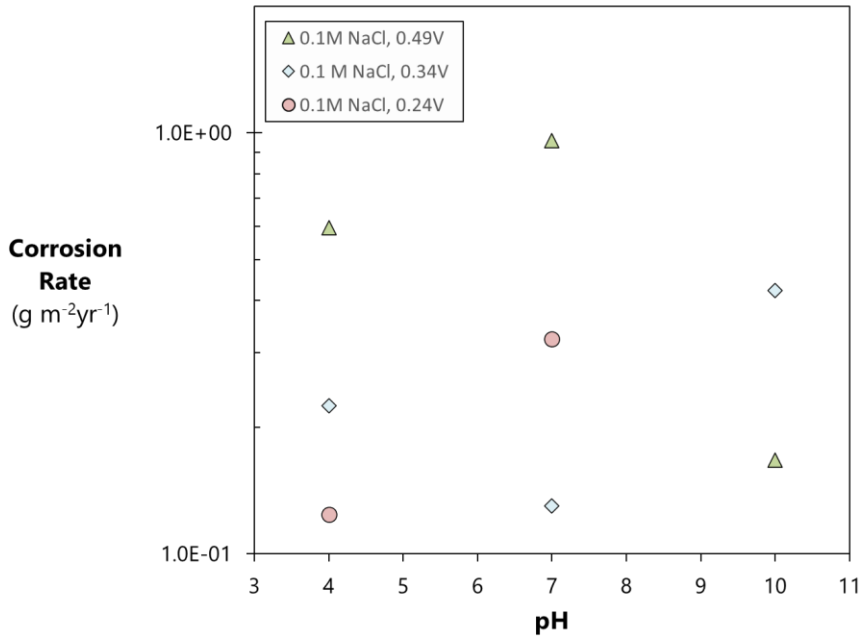

Figure 7-21. Corrosion rates plotted against pH for 316 stainless steel at 0.1 molal NaCl concentration.

The data shown in Figures 20 and 21 do not show regular trends for the stainless steel corrosion rate dependence on pH. The dependence of the stainless steel corrosion rate on salt concentration are shown in Figures 7-22, 7-23 and 7-24. These data generally do not show regular tends.

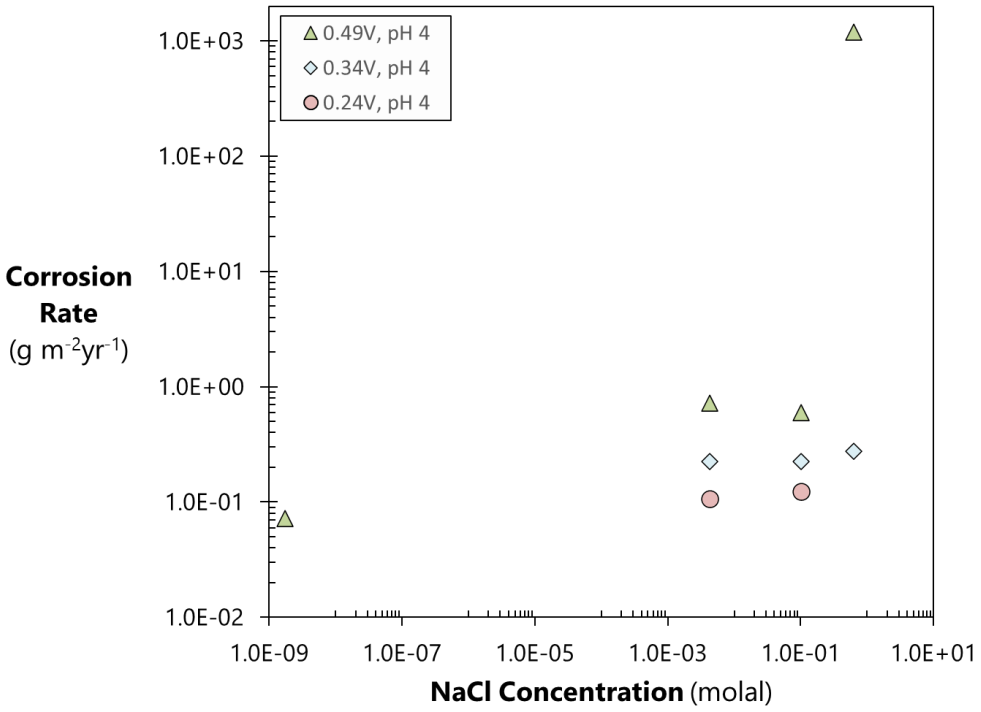

Figure 7-22. Corrosion rates plotted as a function of NaCl concentration 316 stainless steel at pH 4.

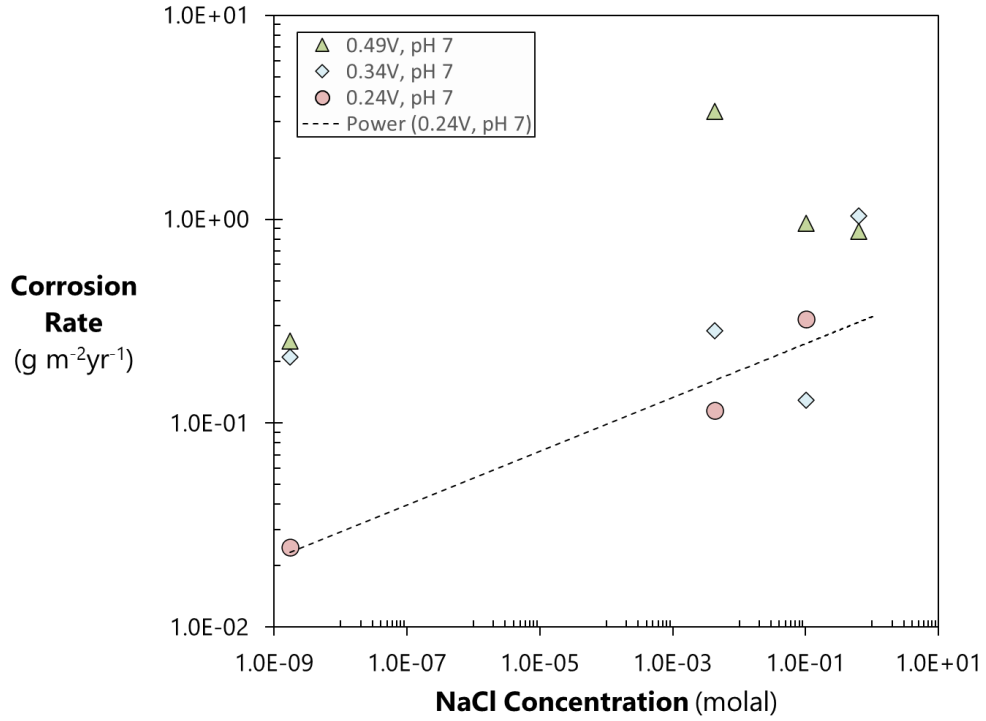

Figure 7-23. Corrosion rates plotted as a function of NaCl concentration 316 stainless steel at pH 7.

The stainless steel corrosion rate dependence on the NaCl concentrations for the 0.24 V data shown in Figure 7-23 is best fit by a power law:

$CR = 0.3326 \cdot [\mathrm{NaCl}]^{0.132}$, R^2: 0.943 (Equation 7-16)

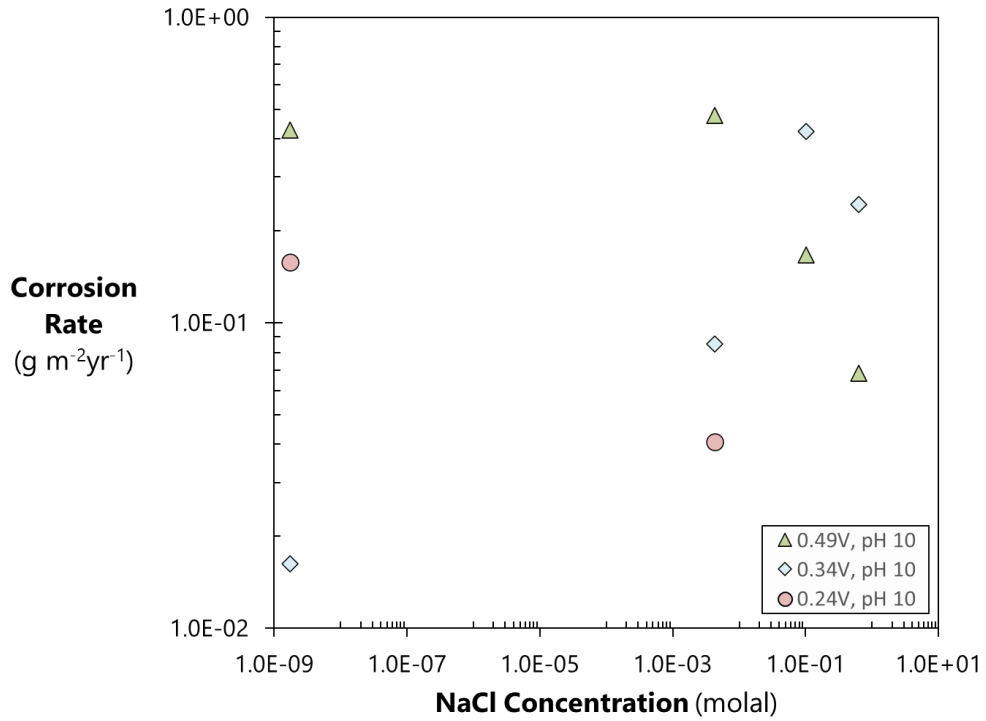

Figure 7- 24. Corrosion rates plotted as a function of NaCl concentration 316 stainless steel at pH 10.

7.3.3.3 Zircaloy-4

The corrosion test results for Zircaloy-4 are provided in Table 7-3. The highest measured corrosion rate (6.1×10^{-1} g m^{-2} yr^{-1}) is reported at pH 10, 100 millimolal NaCl, and 0.49 V_{SHE}, and the lowest measured corrosion rate, which is just an order of magnitude lower (5.4×10^{-2} g m^{-2} yr^{-1}), is reported at pH 10, 4.3 millimolal NaCl, and -0.01 V_{SHE}.

Table 7-3. Current densities and corrosion rates from electrochemical corrosion tests on Zircaloy-4

Alloy	pH	NaCl (molal)	Quantity*	Volts SHE				
				0.49	*0.34*	*0.24*	*-0.01*	*-0.46*
Zircaloy-4	4	1.7E-09	CD	1.1E-09	----	----	----	----
			CR	8.0E-02	----	----	----	----
		4.3E-03	CD	3.7E-09	2.7E-09	----	----	----
			CR	2.7E-01	2.0E-01	----	----	----
		1.0E-01	CD	4.6E-09	----	----	----	----
			CR	3.4E-01	----	----	----	----
	7	1.7E-09	CD	2.9E-09	----	----	----	----
			CR	2.2E-01	----	----	----	----
		4.3E-03	CD	2.5E-09	----	----	----	----
			CR	1.9E-01	----	----	----	----
		1.0E-01	CD	4.8E-09	----	----	----	----
			CR	3.6E-01	----	----	----	----
	10	1.7E-09	CD	2.6E-09	----	1.7E-09	----	----
			CR	1.9E-01	----	1.3E-01	----	----
		4.3E-03	CD	5.6E-09	----	2.5E-09	7.3E-10	-2.6E-07
			CR	4.2E-01	----	1.8E-01	5.4E-02	*Cathodic*
		1.0E-01	CD	8.2E-09	----	1.7E-09	1.4E-09	-4.0E-06
			CR	6.1E-01	----	1.3E-01	1.1E-01	*Cathodic*

CD = current density (A cm^{-2}), CR = Corrosion Rate (g $m^{-2}yr^{-1}$), **---- = not measured.*

Figure 7-25 depicts typical results from potentiostatic tests on Zircaloy-4. Steady state is reached relatively rapidly (by day 3) with very low current densities, which is due to the formation of a zirconium oxide layer that protects the surface from corrosion by limiting the diffusion of reactive chemical species. The corrosion rates of Zircaloy-4 are minimally affected by the NaCl concentration in solution, which is shown for tests at pH 10 in Figure 7-26. The dotted line in Figure 7-26 is the best-fit line for the data collected in solutions of 4.3 mM NaCl.

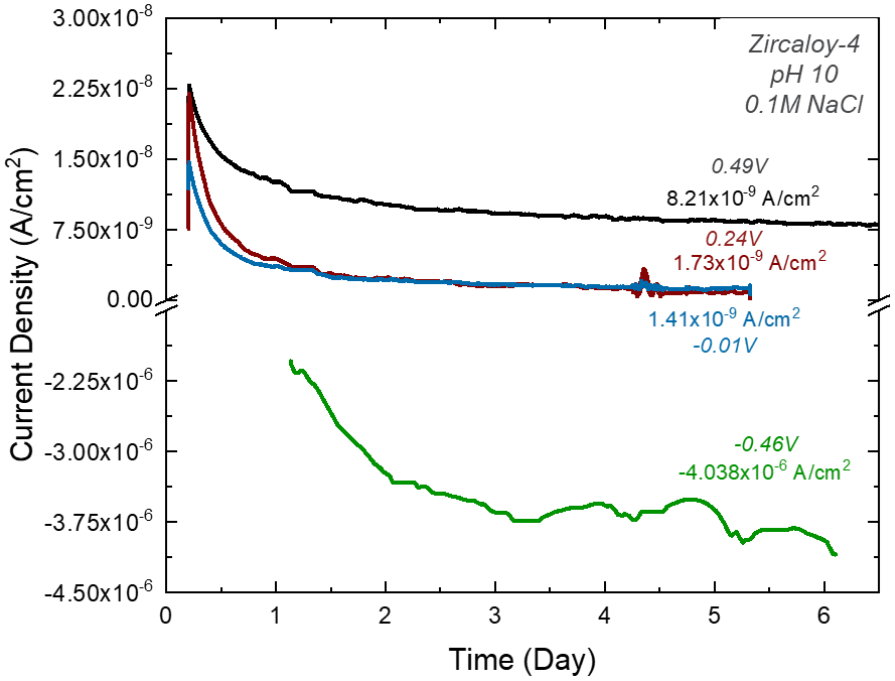

Figure 7-25. Potentiostatic test results on Zircaloy-4 at pH 10, 0.1 molal NaCl, and various fixed potentials (V_{SHE}).

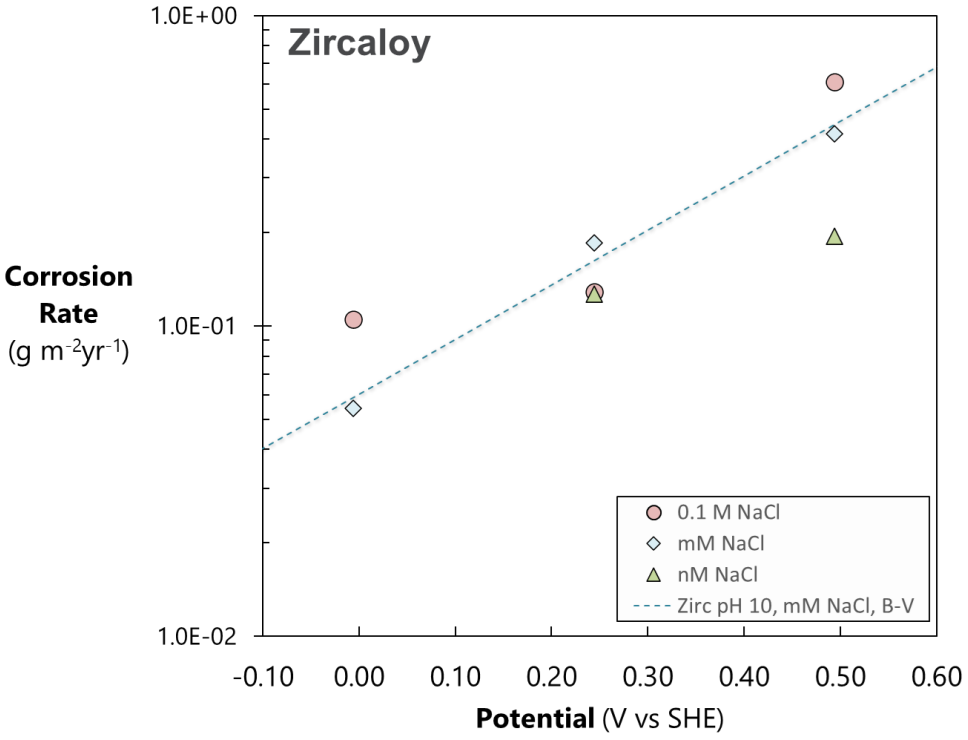

Figure 7-26. Corrosion rates plotted against potentiostatic fixed potentials (V_{SHE}) for Zircaloy-4 at pH 10 and various NaCl concentrations overlaid with an exponential best-fit line (Equation 7-17).

The dependence of the Zircaloy corrosion rate on potential is best fit by an exponential relationship. The best fit trend line for the 4.3 millimolal data in Figure 7-26 is:

$CR = 5.97x10^{-2} \cdot \exp(4.074 \cdot E)$, R^2: 0.987 (Equation 7-17)

The dependence of the Zircaloy corrosion rate on pH is shown in Figure 27. The trend lines shown in the plot are, for the 0.1 molal data:

$CR = 0.138 \cdot [\mathrm{pH}]^{0.5939}$, R^2: 0.72 (Equation 7-18)

And for the nanomolal data:

$CR = 0.021 \cdot [\mathrm{pH}]^{1.045}$, R^2: 0.78 (Equation 7-19)

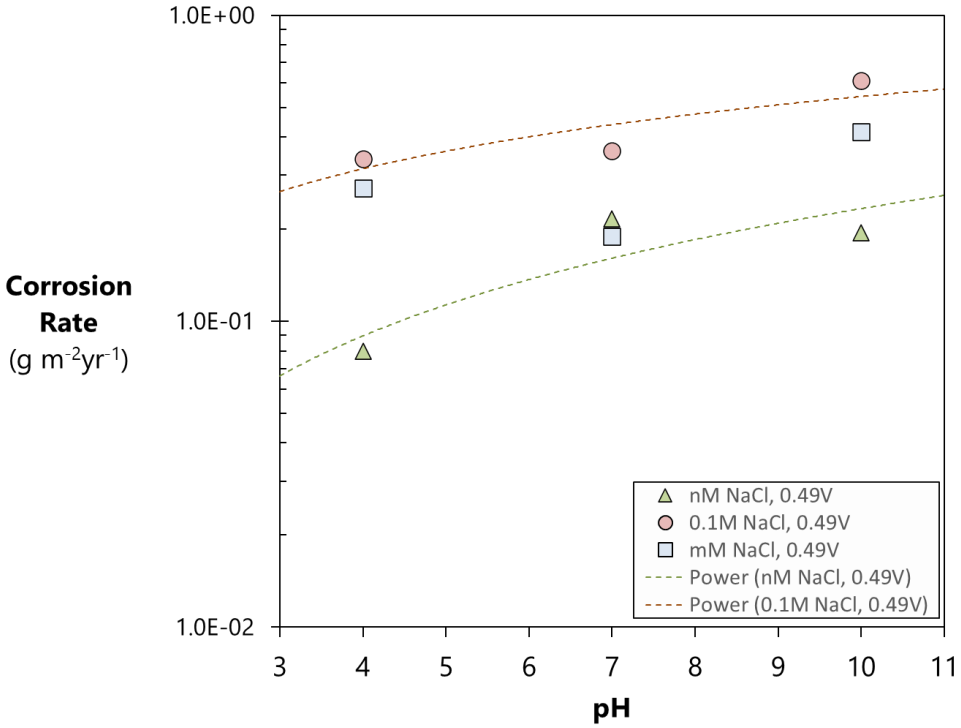

Figure 7-27. Corrosion rates plotted against pH for Zircaloy at 0.49 V_{SHE}. The trendlines shown are defined in Equations 7-18 and 7-19.

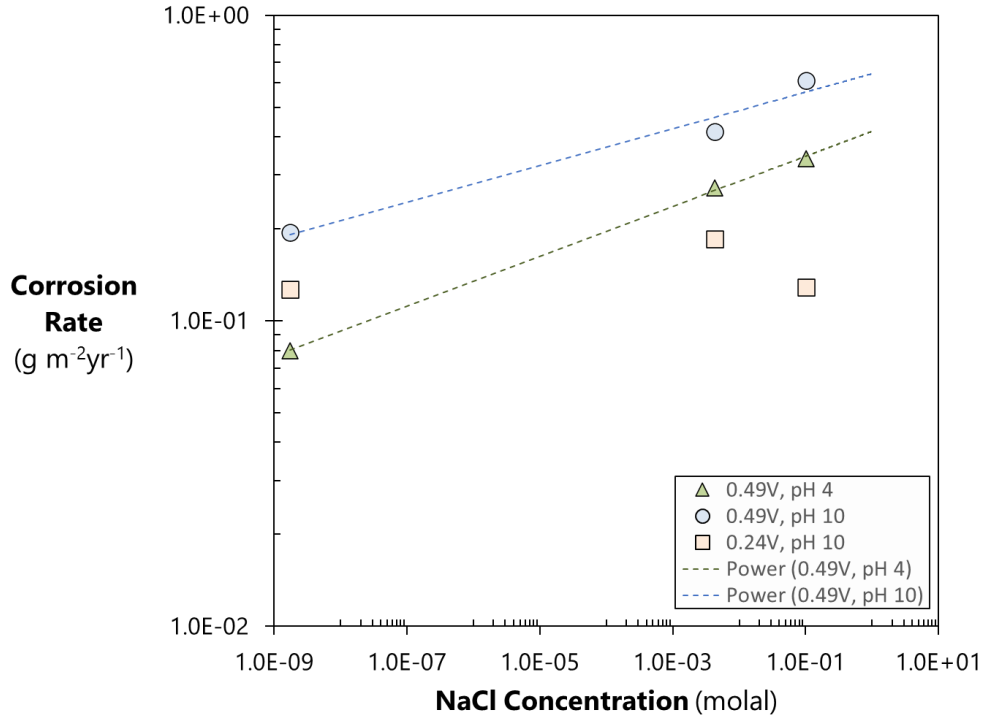

Figure 7-28. Zircaloy corrosion rates plotted as a function of NaCl concentration. The trendlines are defined in Equations 7-20 and 7-21.

The dependence of the Zircaloy corrosion rates on the chloride concentration (Figure 7-28) are best fit by the following power laws for the 0.49 V, pH 10 and 0.49 V, pH 10 data respectively:

$CR = 0.644 \cdot [\mathrm{NaCl}]^{0.0602}$, R^2: 0.972 (Equation7- 20)

$CR = 0.417 \cdot [\mathrm{NaCl}]^{0.0817}$, R^2: 0.999 (Equation 7-21)

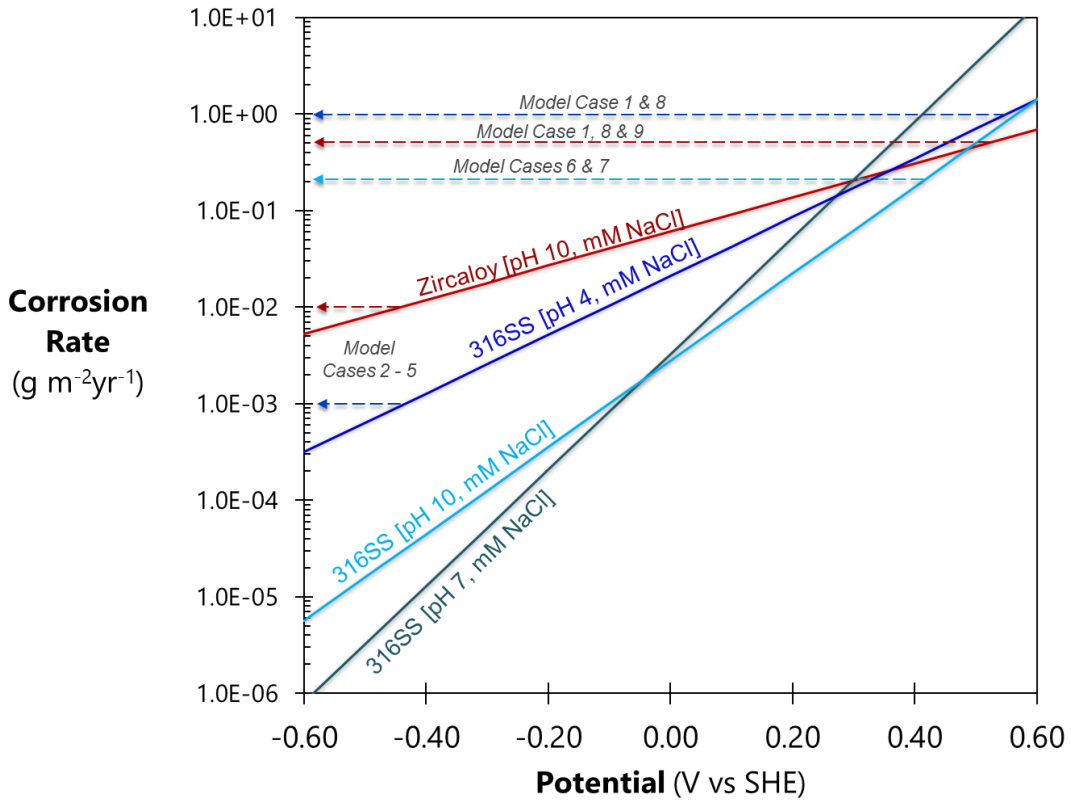

Figure 7-29. Comparisons of corrosion rate vs. potential (V_{SHE}) for 316 stainless steel and Zircaloy-4 at mM NaCl and a range of fixed pH values. The dotted lines indicate the corrosion rates used in the IPC – FMD model sensitivity runs discussed in Section 7.4 below.

7.3.4 Summary of Electrochemical Corrosion Tests

Figures 7-29 and 7-30 show the best fit trends for all of the electrochemical experiments described above. The dotted lines indicate the corrosion rates used for the IPC – FMD model sensitivity model runs discussed in Section 7.4 below. By comparing Figures 7-29 and 7-30, it is clear that, on average, carbon steel and Boral exhibit corrosion rates that are orders of magnitude higher than 316 stainless steel and Zircaloy-4. In addition, the corrosion rate of carbon steel at millimolal concentrations of NaCl is much greater than at nanomolal concentrations of NaCl. During electrochemical corrosion tests, a passivating layer that is effective at protecting the surface from corrosion does not build up on the carbon steel and Boral surface, which explains the high corrosion rates measured in this study. In contrast, effective metal oxide/hydroxide passivating layers do build up relatively quickly on 316 stainless steel and Zircaloy-4 surfaces, accounting for the low corrosion rates measured for these materials.

It should be noted that the relationships represented in Figures 7-29 and 7-30 were extrapolated based on the data sets shown in Figures 7-9 to 7-28 above. Future measurements will further quantify the alloy corrosion rate dependence on pH, chloride concentrations and temperature to produce more accurate and applicable analytical functions. The empirical relationships that describe the datasets shown in Figures7- 9 through 7-28 are shown in Table 7-4.

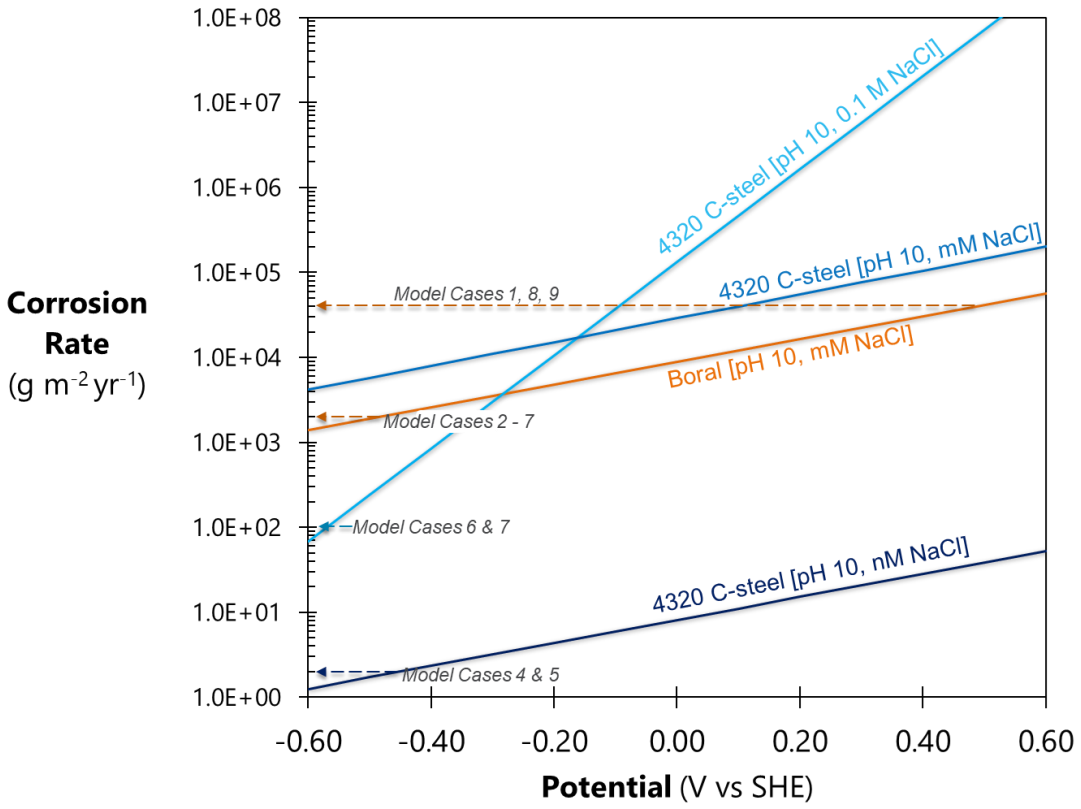

Figure 7-30. Comparisons of corrosion rate vs. potential (V_{SHE}) for AISI 4320 (carbon steel) and Boral at pH 10 and a range of NaCl concentrations. The dotted lines indicate the corrosion rates used in the IPC – FMD model sensitivity runs discussed in Section 7.4 below.

Table 7-4. Empirical functions (Equations 7-6 through 7-21) derived from the potentiostatic test results discussed in Section 7.3.3.

Alloy	Test Conditions	Empirical Function*	R^2
AISI 4320 (C-steel)	0.1 M NaCl, pH 10	$CR = 1.253x10^{5} \cdot \exp(12.683 \cdot E)$	0.97
AISI 4320 (C-steel)	4.3 mM NaCl, pH 10	$CR = 2.81x10^{4} \cdot \exp(3.193 \cdot E)$	*2 points*
AISI 4320 (C-steel)	1.7 nM NaCl, pH 10	$CR = 8.413 \cdot \exp(2.879 \cdot E)$	*2 points*
Boral	4.3 mM NaCl, pH 10	$CR = 8.88x10^{3} \cdot \exp(3.086 \cdot E)$	0.994
316SS	4.3 mM NaCl, pH 4	$CR = 1.64x10^{-2} \cdot \exp(7.638 \cdot E)$	0.999
316SS	4.3 mM NaCl, pH 7	$CR = 3.4x10^{-3} \cdot \exp(13.734 \cdot E)$	0.978
316SS	4.3 mM NaCl, pH 10	$CR = 2.8x10^{-3} \cdot \exp(10.33 \cdot E)$	0.993
316SS	1.7nM NaCl, pH 10	$CR = 3.8x10^{-2} \cdot \exp(5.079 \cdot E)$	0.985
Zircaloy-4	4.3 mM NaCl, pH 10	$CR = 5.97x10^{-2} \cdot \exp(4.074 \cdot E)$	0.987
316SS	0.49 V_{SHE}, 1.7 nM NaCl	$CR = 0.0049 \cdot [pH]^{1.974}$	0.989
Zircaloy-4	0.49 V_{SHE}, 0.1 M NaCl	$CR = 0.138 \cdot [pH]^{0.5939}$	0.72
Zircaloy-4	0.49 V_{SHE}, 1.7 nM NaCl	$CR = 0.021 \cdot [pH]^{1.045}$	0.78
AISI 4320 (C-steel)	0.49 V_{SHE}, pH 10	$CR = 8.0x10^{7} \cdot [NaCl]^{0.7454}$	0.918
316SS	0.24V_{SHE}, pH 7	$CR = 0.3326 \cdot [NaCl]^{0.132}$	0.943
Zircaloy-4	0.49 V_{SHE}, pH 10	$CR = 0.644 \cdot [NaCl]^{0.0602}$	0.972
Zircaloy-4	0.24V_{SHE}, pH 4	$CR = 0.417 \cdot [NaCl]^{0.0817}$	0.999

**CR: corrosion rate, E: the applied potential for the potentiostatic tests (represents Eh).*

7.4 In-Package Chemistry Simulation and the Fuel Matrix Degradation Model: Role of Alloy Corrosion

Building on the modeling approach described in Jerden et al., 2019, the 1-D reactive transport code X1t (a module within the Geochemist's Workbench (GWB) software package) was used to implement a prototype in-package chemistry (IPC) model that was coupled to the FMD model. The IPC model was used to track how the corrosion rates of in-package alloy components and the resulting H_2 concentrations evolve over a range of repository relevant time scales and conditions. The coupled FMD model determines how the spent fuel degradation rate changes based on H_2 concentration history calculated by the X1t IPC model. The models were parameterized using the experimental data discussed in Section 7.3 above.

The thermodynamic database used for this model was thermo.com.V8.R6 (Johnson et al, 2000) to which the steel reactants were added. The masses of the different steel components, their surface areas, and total solution volume were those given in the in-package chemistry model used for the YM TSPA (CRWMS, 2003). The alloy masses used for this model are shown in Table 7-5, and the initial groundwater composition, which is typical of an argillite rock repository environment, is shown in Table 7-6. The volume of solution used in the model was 4.1 m^3, which is based on the void volume within the spent fuel canister assumed in CRWMS, 2003.

Table 7-5. Alloy masses and specific surface areas used in the X1t in-package chemistry model (values are from CRWMS, 2003)

Materials	**Total Mass** (kg)	**Specific Surface Area** (m^2 g^{-1})
316 SS	$5.9x10^3$	$4.1x10^{-6}$
C-steel	$1.2x10^3$	$8.7x10^{-5}$
Aluminum alloy*	$1.9x10^2$	$2.8x10^{-4}$
Zircaloy cladding	$3.6x10^2$	$1.3x10^{-3}$
Spent Fuel	$2.9x10^4$	$1.6x10^{-5}$

**Indicated as "Boral" in discussion and figures below.*

Table 7-6. Initial solution composition used in X1t in-package chemistry model (from Fernandez et al., 2007). This composition is typical pore-water from the Opalinus clay.

Component	**Concentration** (molar)
pH	7.4
Na	$2.8x10^{-1}$
Ca	$2.3x10^{-2}$
K	$2.2x10^{-3}$
Mg	$2.1x10^{-2}$
Fe	$3.5x10^{-6}$
Cl^-	$3.3x10^{-1}$
SO_4^{2-}	$1.9x10^{-2}$
CO_3^{3-}	$5.2x10^{-3}$

SiO_2	$1.1x10^{-4}$

Figure 7-31 shows the flow of information for the coupled X1t – FMD model as well as the schematic layout and discretization of X1t IPC model. The alloy corrosion rates discussed in Section 7.3 above are used to parameterize the IPC model, which tracks in package the H_2 concentration based on its generation by alloy corrosion and its loss by diffusion/advection into the surroundings over the 100,000-year model time frame. The H_2 concentration evolution determines the spent fuel degradation rate as calculated by the FMD model.

The X1t model includes 21 reaction/diffusion cells (not shown in Figure 7-31) with the central cell including the materials shown in Table 7-2. The diffusion coefficient used for H_2 in all model cases was $6.0x10^{-5}$ cm^2/s (Turnbull, 2008). The porosity of the waste package cell was set to 80%, while the porosity in the bentonite and host rock cells were set to 30%.

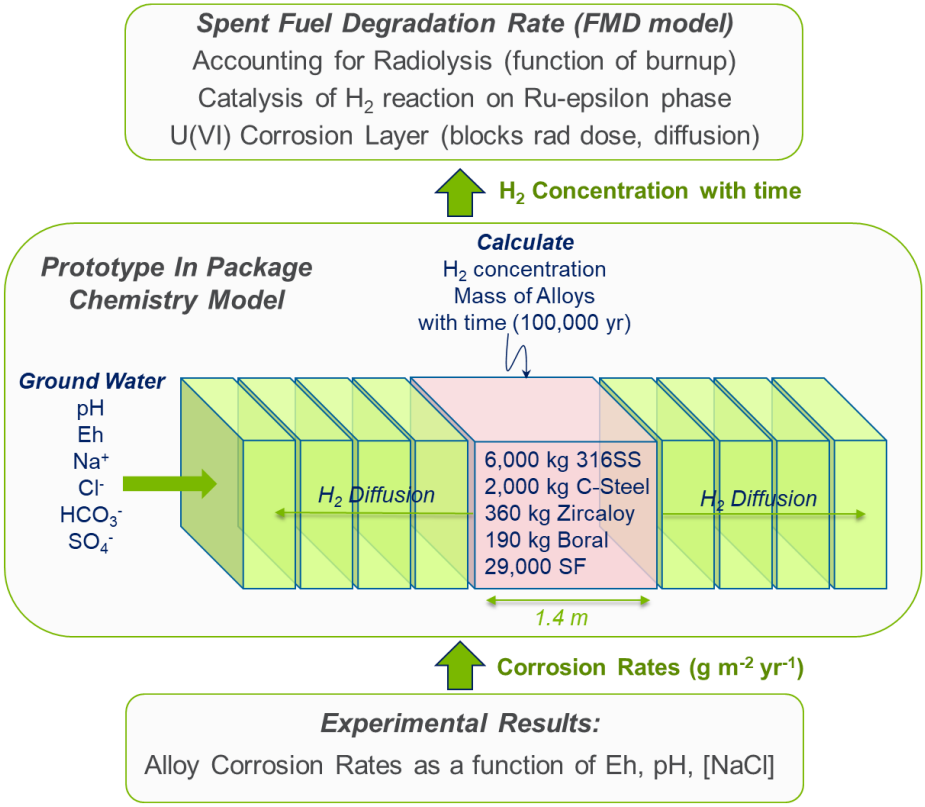

Figure 7-31. Flow of information for the coupled X1t prototype in-package chemistry and the FMD model.

Thus, the four main functions of the X1t IPC mode are to:

- Determine the amount of H_2 produced and accumulated over a range of relevant alloy corrosion rates.
- Quantify the kinetics of H_2 removal (by diffusion or advection) from the waste package cell containing the spent fuel.
- Track the dissolved H_2 concentration within the in-package solution based on the first two bullets.
- Provide the H_2 concentration as a function of time to the FMD model so that the spent fuel degradation rate can be calculated as the in-package environment evolves.

As discussed in Sections 7.1 and 7.2 above, the most significant processes accounted for in the FMD model include burnup dependent radiolysis, U(VI) corrosion layer formation and the catalytic oxidation of H_2 on the noble metal alloy. The H_2 oxidation process proves to be dominant, inhibiting oxidative dissolution of the fuel, when the H_2 concentration is greater than a certain threshold value as discussed in Jerden et al., 2019 and shown schematically in Figure 7-3 above. Results from FMD modeling (discussed below) show that the H_2 concentration threshold needed to shut down oxidative dissolution of the fuel depend on the burnup of the fuel. Higher burnup fuels produced more radiolytic oxidants per time and thus the amount of H_2 needed to overcome the radiolytic oxidative effect is higher. Therefore, sensitivity model runs were conducted using a higher fuel burn up value of 80 GWd/MTU and a relatively low burn up value of 30 GWd/MTU. Other variables investigated in the model sensitivity runs for this study include: steel corrosion rates for different conditions (Eh, pH, NaCl concentration) and the advective rate of solution within the waste package (Table 7-7).

It should be noted that the X1t IPC model represents a prototype or scoping model intended to inform future development of a more versatile in-package model that will be integrated within the GDSA framework and implemented in PFLOTRAN. There are several simplifying assumptions that the model currently uses that need to be replaced by more rigorous formulations in the future. The major simplifying assumptions are for the X1t IPC model are:

- The use of first order alloy corrosion rate expressions (parameterized using data described in Section 3) that do not account for the evolving surface area of the corroding alloy.
- The neglection of galvanic effects caused by alloys being in contact within the waste package.

The results of the X1t IPC model are thus preliminary and not meant to accurately represent actual repository scenarios. Rather, the results are meant to yield insights as to how changes in in-package alloy corrosion rates influence the spent fuel degradation rate over repository relevant conditions and time scales. To this end a set of sensitivity studies were run using the range of measured alloy corrosion rates presented in Section 7.3 above. Table 7-7 shows the conditions used for the sensitivity runs and Figures 7-32 to 7-37 show the modeling results. The solution Eh, pH and [NaCl] referred to in Table 7-7 are the conditions for the solution flowing into the waste package during corrosion. These variables can evolve with time depending on the balance between the rate of advection/diffusion of solute into the waste package and the rates of alloy corrosion. The specific surface areas used for the alloys for each model run are shown in Table 7-5 above. The corrosion rates chosen for each set of Eh, pH and NaCl concentration conditions are based on the empirical relationships shown in Figures 7-29 and 7-30 above.

Table 7-7. Conditions for sensitivity runs performed using the linked X1t IPC and FMD models. The corrosion rates chosen for these model runs span the range of rates measured in the electrochemical tests discussed in Section 3 above.

Model Case	Solution Eh[1]	pH[2]	[NaCl][3]	C-Steel ($g\ m^{-2}\ yr^{-1}$)	316 SS ($g\ m^{-2}\ yr^{-1}$)	Boral[4] ($g\ m^{-2}\ yr^{-1}$)	Zircaloy ($g\ m^{-2}\ yr^{-1}$)	Advection[5] (m/yr)
1	High	Low	High	$1.0x10^{6}$	$1.0x10^{0}$	$4.0x10^{4}$	$5.0x10^{-1}$	0 *(diffusion only)*
2	Low	Low	Low	$1.0x10^{6}$	$1.0x10^{-3}$	$4.0x10^{3}$	$1.0x10^{-2}$	0 *(diffusion only)*
3	Low	Low	Low	$1.0x10^{6}$	$1.0x10^{-3}$	$4.0x10^{3}$	$1.0x10^{-2}$	0.1
4	Low	High	Low	$2.0x10^{1}$	$1.0x10^{-3}$	$4.0x10^{3}$	$1.0x10^{-2}$	0 *(diffusion only)*
5	Low	High	Low	$2.0x10^{1}$	$1.0x10^{-3}$	$4.0x10^{3}$	$1.0x10^{-2}$	0.1
6	Low	High	High	$1.0x10^{2}$	$2.0x10^{-1}$	$4.0x10^{3}$	$1.0x10^{-2}$	0 *(diffusion only)*
7	Low	High	High	$1.0x10^{2}$	$2.0x10^{-1}$	$4.0x10^{3}$	$1.0x10^{-2}$	0.1
8	High	Low	Low	$1.0x10^{6}$	$1.0x10^{0}$	$4.0x10^{4}$	$5.0x10^{-1}$	0 *(diffusion only)*
9	High	Low	High	$1.0x10^{6}$	$1.0x10^{3}$	$4.0x10^{4}$	$5.0x10^{-1}$	0 *(diffusion only)*

[1] Low Eh denotes -0.6 V to -0.2 V (vs SHE) and high Eh denotes 0.2 V to 0.6 V (vs SHE).
[2] Low pH denotes a value of 4 and high pH refers value of 10 (as used in the experiments described above).
[3] Low [NaCl] denotes concentrations ranging from nanomolal to micromolal and high [NaCl] denotes concentrations ranging from 0.1 to 1 molal NaCl.
[4] Boral is a borated aluminum alloy commonly used as a neutron absorber in spent fuel storage canisters.
[5] Advection refers to the rate of groundwater discharge through the breached waste package.

Most of the corrosion rates used for the model runs are indicated on Figures 7-29 and 7-30 above. The corrosion rate for C-steel (AISI 4320) for the low pH model runs (Cases 1, 2, 3, 8 and 9) was $1.0x10^{6}$ g m^{-2} yr^{-1} (row 2, Table 7-1) and the high corrosion rate for 316SS used in model Case 9 is from high salt concentration, low pH data shown in row 8 of Table 7-2.

Each model run involved the following steps:

- The initial condition of the reactive transport domain (Figure 7-31):
    - All cells fully saturated with a solution of the composition shown in Table 7-6.
    - The model starts with the condition of a breached and fully saturated waste package.
    - The spent fuel is assumed to be contacted by the in-package solution.
- The age of the fuel is assumed to be 1100 years out of reactor. Therefore, the model assumes that the waste package failed and was filled with solution 1000 years after emplacement and that the fuel was 100 years out of reactor when it was emplaced.
- The four alloys (Table 7-5) are congruently reacted with the solution composition given in Table 7-6 at the rates specified in Table 7-7.
- Geochemist's Workbench (as implemented in X1t) was used to determine the evolution of the pH, Eh and speciation (solution and solids) of the simulated in-package solution corresponding to a given set of steel dissolution rates.
- The amount of H_2 produced and its distribution with time over the reactive transport domain (through diffusion and advection) are determined and quantified as fugacity and molal concentrations.
- Results from the in-package solution simulations (i.e. H_2 concentrations) are used as input to the FMD model, which is then used to calculate the spent fuel degradation rate.
    - Parameter values for the fuel environment are from Jerden et al., 2015.

  - Temperature was held constant at 25 °C for all runs.
  - Each model case included two fuel burnup values (30 GWd/MTU and 80 GWd/MTU) as indicated in the results shown below.
- The H_2 threshold concentrations for inhibiting oxidative fuel degradation is $1.0x10^{-3}$ molal for 80 GWd/MTU and $1.0x10^{-4}$ molal for 30 GWd/MTU.

Figure 7-32a shows the masses of the in-package alloys (blue) and the most abundant corrosion products (gray) over the simulation duration for Case 1 (Table 7-7). For these conditions (low Eh, High pH and relatively high NaCl concentrations) the model predicts that C-steel will be nearly completely corroded to magnetite around 20 years after the waste package has been breached and the aluminum alloy Boral will be nearly consumed approximately 400 years after the waste package breach. The production of around 10 kg of zirconium oxide indicates that a moderate amount of Zircaloy has corroded; however, most of the original alloy remains at the end of the simulation. Only minimal amounts (~100 grams) of 316 SS are predicted to corrode for the Case 1 model conditions.

The predicted in-package H_2 concentration for Case 1 is shown in Figure 7-32b. The initially high concentrations of over 1 molal are due to the sudden rise in H_2 fugacity caused by the relatively rapid corrosion of C-steel. Following the corrosion of C-steel and Boral the concentration reaches a long-term steady state concentration of $1.3x10^{-3}$ molal. This steady state concentration is due to the continued production of H_2 by Zircaloy that persists throughout the 100,000-year time frame of the model. This concentration is higher than the threshold concentrations for inhibiting oxidative fuel degradation for both fuel burnup values (Figure 7-32c).

Modeling Cases 2 and 3 have the same alloy corrosion rates (Table 7-7) and thus show the same alloy mass loss and corrosion products production with time, as shown in Figure 7-33(a). The difference between Cases 2 and 3 and Case 1 is that the Zircaoly, 316SS and Boral corrosion rates are all lower due to the low chloride concentration condition for these runs (see Figures 7-29 and 7-30 above). As with Case 1 the rapid corrosion of C-Steel leads to its consumption 20 years after the waste package breach. Boral persists for around 4,000 years, a factor of 10 longer than for the Case 1 conditions (Figure 7-33a). The slower corrosion of Zircaloy is indicated by the lack of significant zirconium oxide production (Figure 7-33a).

The H_2 concentrations for Cases 2 and 3 show similar trends but are off-set due to the presence of advective solution transport in Case 3 (light blue line in Figure 7-33b). Advection causes lower H_2 concentrations as it transports H_2 produced by corrosion out of the waste package cell at a rate faster than diffusion. The points on the curves shown in Figure 7-33b are the thresholds for inhibiting oxidative dissolution for the two different fuel burnups. The higher burnup fuel produces more radiolytic oxidants and thus requires a higher H_2 concentration to counteract oxidation. The threshold concentrations are 1.0 millimolal H_2 for the 80GWd/MTU case and 0.1 millimolal for the 30GWd/MTU fuel. The H_2 concentrations drop below these thresholds around the time when nearly all of the Boral is consumed. The spent fuel degradation rate for Case 2 increases to the oxidative dissolution rate at around 3,000 years, while the degradation rate for Case 3 (light red line, Figure 7-33c) increases to the oxidative dissolution rate around 2,200 years after waste package breach. This difference is due to the lower H_2 concentrations caused by advection.

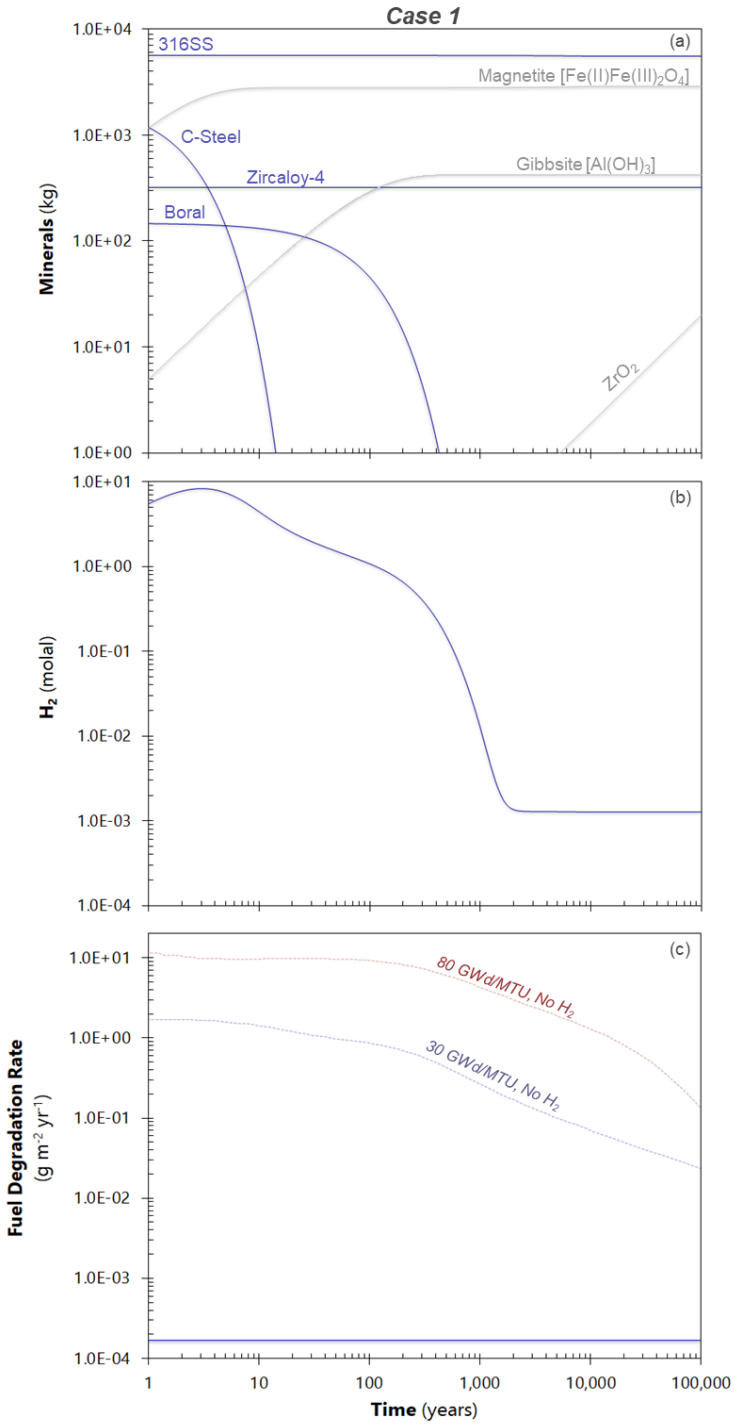

Figure 7-32. Results from the Case 1 model scenario (Table 7-7). The time axis refers to the time elapsed from the start of in-package corrosion (assumed to be 1000 years after emplacement). The fuel is assumed to be 1100 years old at time zero in these model runs. In the bottom plot (c), the solid line just below $2x10^{-4}$ g m^{-2} yr^{-1} is the calculated degradation rate for the Case 1 scenario representing the chemical dissolution rate of the fuel. The dotted lines show the degradation rates calculated for cases with no H_2 for a high burnup fuel (80 GWd/MTU) and a low burnup fuel (30 GWd/MTU).

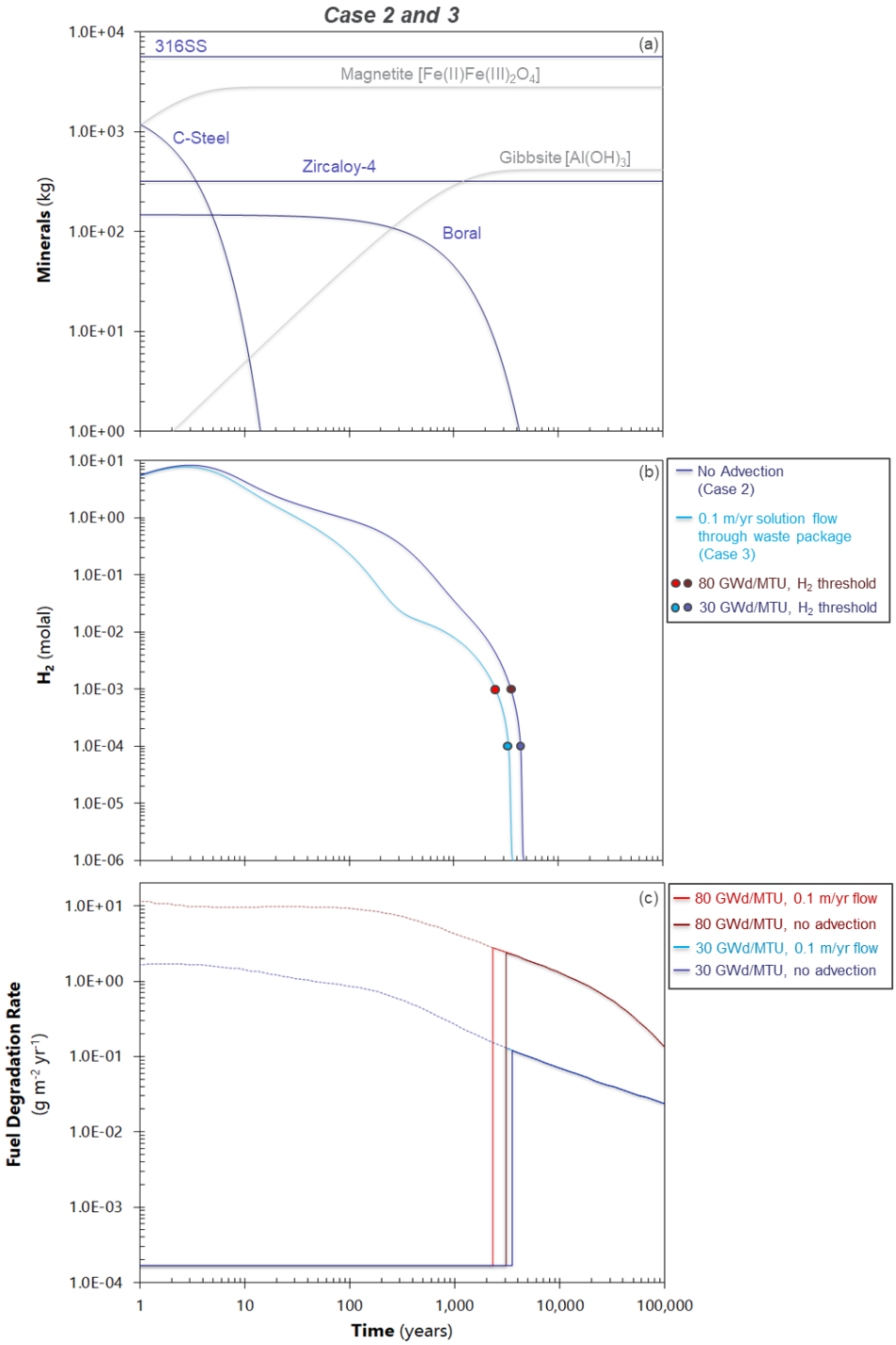

Figure 7-33. Results from the Case 2 and 3 model scenarios (Table 7-7). The time axis refers to the time elapsed from the start of in-package corrosion (assumed to be 1000 years after emplacement). The points in the middle plot (b) indicate the H_2 concentration thresholds for inhibiting oxidative fuel dissolution for the two different fuel burnups. In the bottom plot (c), the solid line just below $2x10^{-4}$ g m^{-2} yr^{-1} is the calculated chemical dissolution rate of the fuel. The dotted lines show the degradation rates calculated for cases with no H_2 for a high burnup fuel (80 GWd/MTU) and a low burnup fuel (30 GWd/MTU).

The results for modeling Cases 4 and 5 are shown in Figure 7-34. These Cases are for low Eh, high pH and low NaCl concentrations without and with advection respectively. The only difference between these Cases and Cases 3 and 4 are that the corrosion rate used for C-steel is considerably lower (see high pH, low NaCl empirical curve in Figure 7-29). For these runs the Boral is the first alloy to be consumed at around 4,000 years after the waste package breach, while the C-steel persists for the full 100,000-year model duration (Figure 7-34a). There is no significant corrosion of either 316SS or Zircaloy in these model cases.

Approximately 1,000 kg of C-steel is corroded to magnetite during the Cases 4 and 5 runs, which leads to relatively high H_2 concentrations throughout the model time frame (Figure 7-34b). The Case 4 H_2 concentration remains above the threshold concentration for inhibiting oxidative fuel dissolution for 100,000 year; however, when advection is accounted for (Case 5) the H_2 concentrations drop below the threshold values at 4,200 years for the 80 GWd/MTU fuel and at 90,000 year for the 30 GWd/MTU fuel (Figures 7-34b and 7-34c).

Modeling Cases 6 and 7 are for low Eh, high pH and high NaCl conditions (Table 7-7) and are differentiated from Cases 4 and 5 by a somewhat higher corrosion rates for C-steel, 316SS and Zircaloy. As shown in Figure 7-35a, Boral is predicted to be the first alloy consumed at around 4,000 years and C-Steel is predicted to persist until around 70,000 years. The H_2 concentration for Case 6 (no advection) remains above the threshold for inhibiting oxidative fuel dissolution until around 30,000 years for the 80 GWd/MTU fuel and around 40,000 years for the 30 GWd/MTU fuel. For Case 7 (with advection) the H_2 concentration remains above the H_2 threshold until around 20,000 years for the 80 GWd/MTU fuel and around 30,000 years for the 30 GWd/MTU fuel (Figures 7-35b and 7-35c).

Case 8 is for high Eh, low pH and low NaCl concentration conditions and thus involves relatively high alloy corrosion rates (Table 7-7). For this Case, C-steel is predicted to be nearly completely consumed within 20 years after waste package breach while Boral is consumed by year 400 (Figure 7-36a). Both 316SS and Zircaloy show minor amounts of corrosion as evidenced by the production of magnetite, goethite and zirconium oxide relatively late in the simulation time (>10,000 years) (Figure 7-36a). The H_2 concentration for Case 8 decreases to below the H_2 thresholds for inhibiting oxidative fuel dissolution at around 1,500 years (Figure 7-36b and 7-36c). Including advection for this model run did not produce significantly different results as those shown in Figure 7-36.

Figure 7-37 shows the results for Case 9, which is for high Eh, low pH and high NaCl concentration conditions. This case differs from Case 8 by the higher 316SS corrosion rate used. For this run, in addition to the C-steel and Boral being consumed by 20 years and 400 years respectively, the 316SS is also consumed by around the 5,500-year mark of the simulation (Figure 7-37a). Minor Zircaloy corrosion is indicated by the production of approximately 10 kg of zirconium oxide. Following the consumption of most the 316SS the ferric oxyhydroxide Goethite begins to replace the primary iron corrosion phase magnetite. This is due to the relatively oxidizing conditions assumed for the seepage water (Table 7-7).

The resulting H_2 concentration for Case 9 falls below the thresholds for inhibiting oxidative fuel dissolution around the time that most of the 316SS is consumed (~5,000 years). Due to the steep decrease in the H_2 concentration, the time at which the two different burnup fuels commence oxidative dissolution are the same (Figures 7-37a and 7-37b). Advective transport through the waste package did not significantly change the results for Case 9.

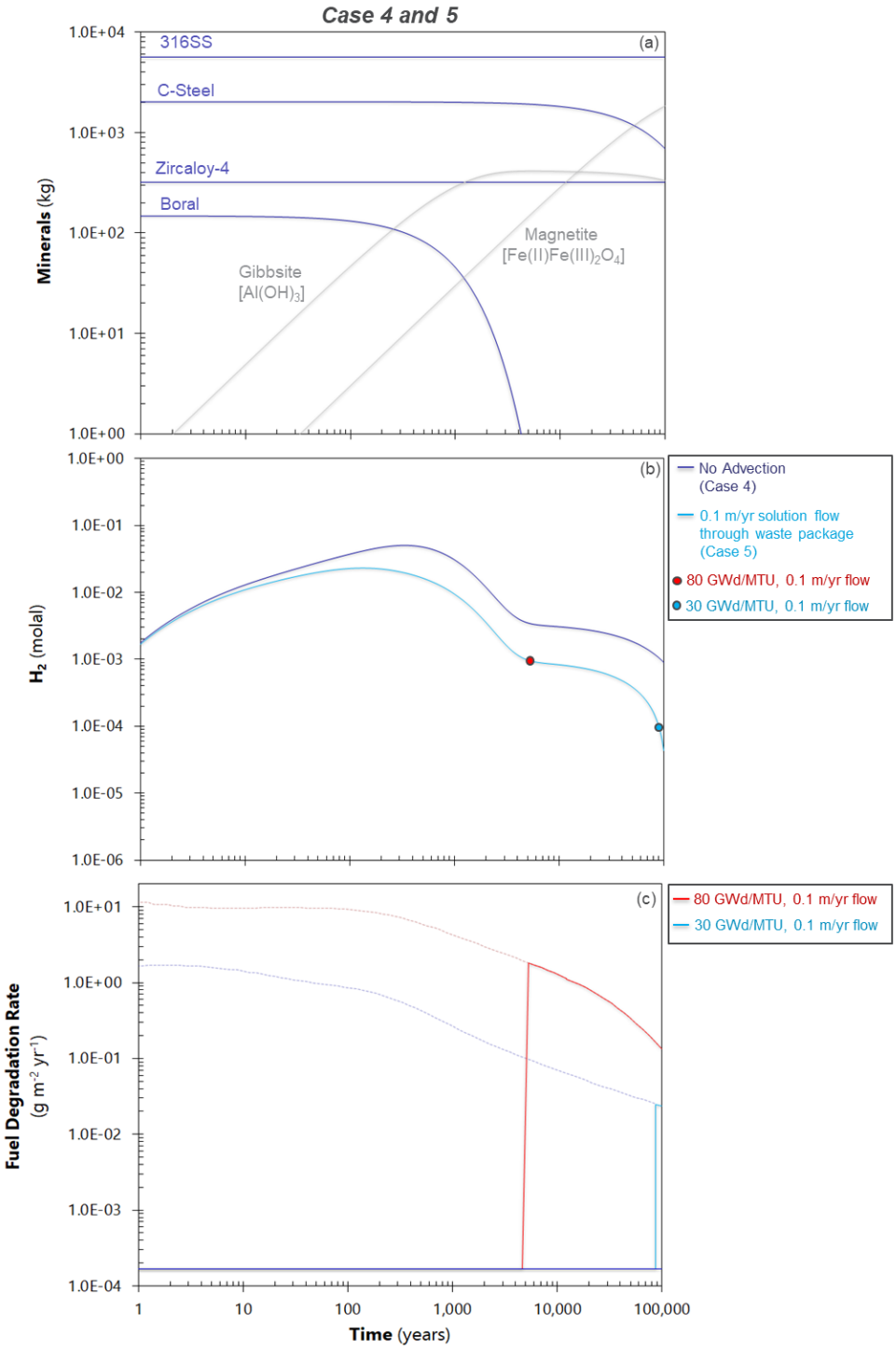

Figure 7-34. Results from the Case 4 and 5 model scenarios (Table 7-7). The time axis refers to the time elapsed from the start of in-package corrosion (assumed to be 1000 years after emplacement). The points in the middle plot (b) indicate the H_2 concentration thresholds for inhibiting oxidative fuel dissolution for the two different fuel burnups. In the bottom plot (c), the solid line just below $2x10^{-4}$ g m^{-2} yr^{-1} is the calculated chemical dissolution rate of the fuel. The dotted lines show the degradation rates calculated for cases with no H_2 for a high burnup fuel (80 GWd/MTU) and a low burnup fuel (30 GWd/MTU).

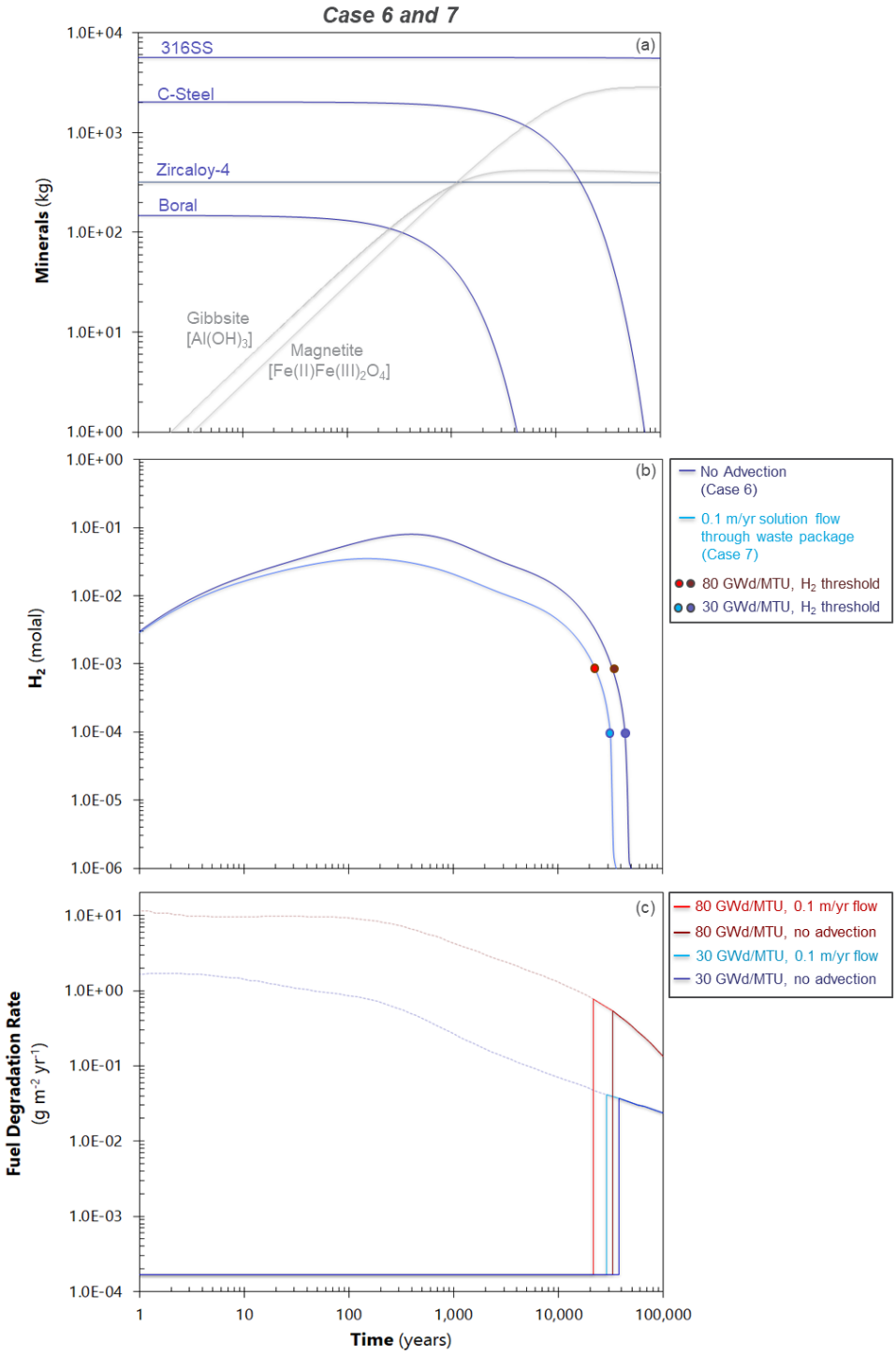

Figure 7-35. Results from the Case 6 and 7 model scenarios (Table 7-7). The time axis refers to the time elapsed from the start of in-package corrosion (assumed to be 1000 years after emplacement). The points in the middle plot (b) indicate the H_2 concentration thresholds for inhibiting oxidative fuel dissolution for the two different fuel burnups. In the bottom plot (c), the solid line just below $2x10^{-4}$ g m^{-2} yr^{-1} is the calculated chemical dissolution rate of the fuel. The dotted lines show the degradation rates calculated for cases with no H_2 for a high burnup fuel (80 GWd/MTU) and a low burnup fuel (30 GWd/MTU).

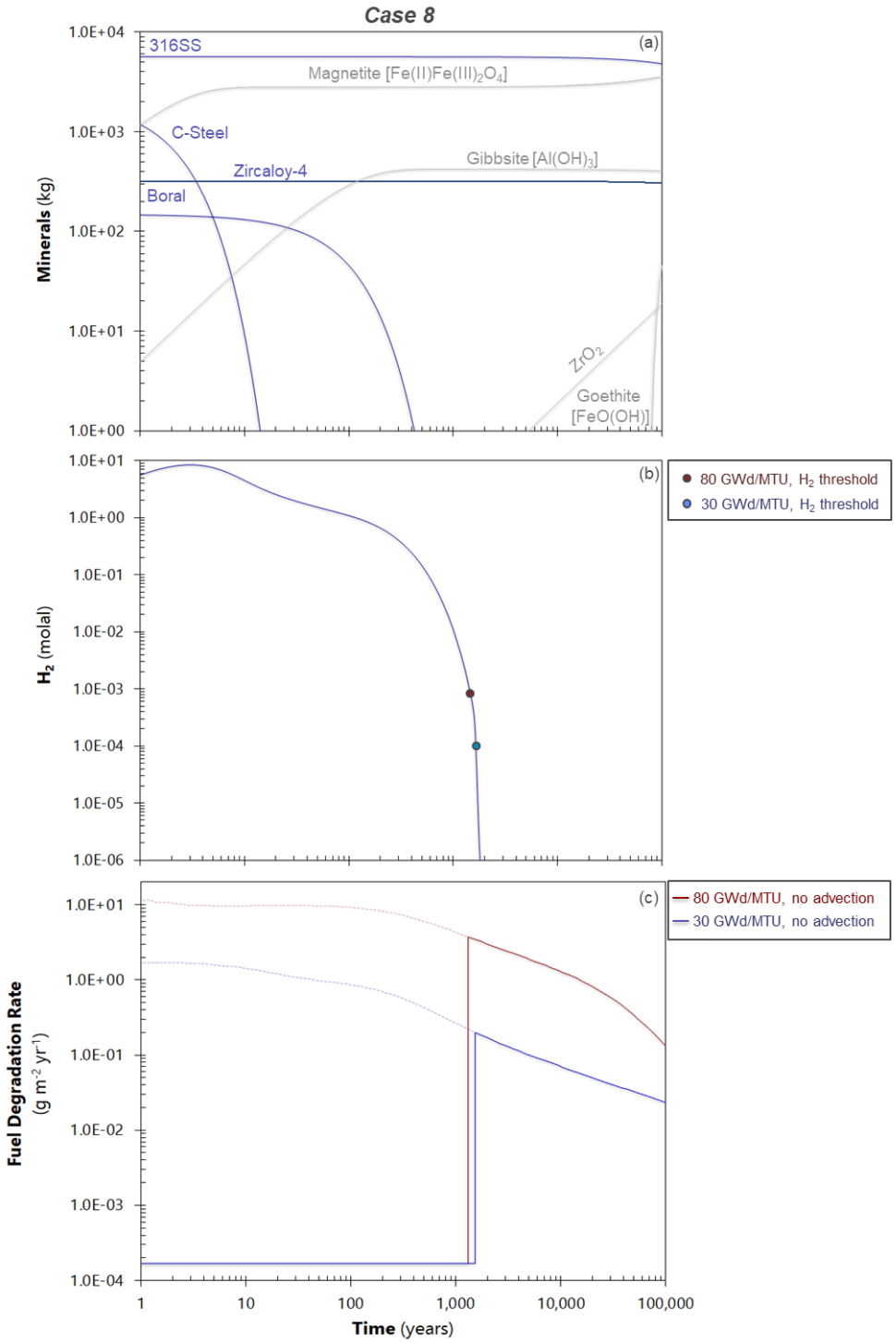

Figure 7-36. Results from the Case 8 model scenario (Table 7-7). The time axis refers to the time elapsed from the start of in-package corrosion (assumed to be 1000 years after emplacement). The points in the middle plot (b) indicate the H_2 concentration thresholds for inhibiting oxidative fuel dissolution for the two different fuel burnups. In the bottom plot (c), the solid line just below $2x10^{-4}$ g m^{-2} yr^{-1} is the calculated chemical dissolution rate of the fuel. The dotted lines show the degradation rates calculated for cases with no H_2 for a high burnup fuel (80 GWd/MTU) and a low burnup fuel (30 GWd/MTU).

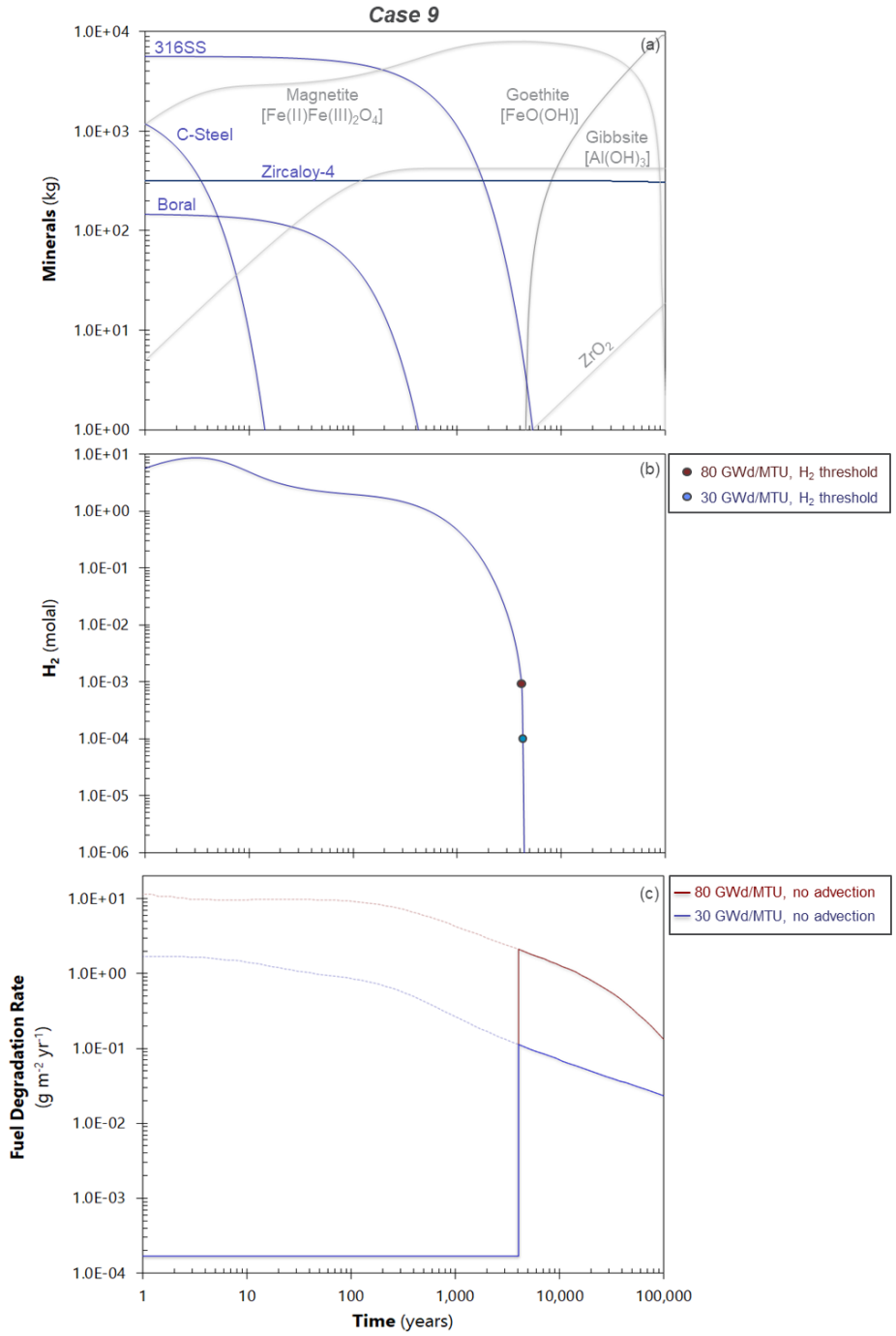

Figure 7-37. Results from the Case 9 model scenario (Table 7-7). The time axis refers to the time elapsed from the start of in-package corrosion (assumed to be 1000 years after emplacement). The points in the middle plot (b) indicate the H_2 concentration thresholds for inhibiting oxidative fuel dissolution for the two different fuel burnups. In the bottom plot (c), the solid line just below $2x10^{-4}$ g m^{-2} yr^{-1} is the calculated chemical dissolution rate of the fuel. The dotted lines show the degradation rates calculated for cases with no H_2 for a high burnup fuel (80 GWd/MTU) and a low burnup fuel (30 GWd/MTU).

7.5 Conclusions and Future Work

This report presents new results from a series of electrochemical corrosion tests that provide information needed to parameterize the fuel matrix degradation (FMD) model and an associated prototype in-package chemistry (IPC) model. The data provide corrosion rates for the major in-package alloys over a range of relevant pH and redox conditions. The alloys tested are: 316L stainless steel (316SS), AISI 4320 carbon steel (C-steel), Zircaloy-4 and the borated aluminum composite material Boral. The range of conditions were: pH 4, 7 and 10, salt concentrations ranging from nanomolal to around one molal and several relevant potentials (see Tables 1 – 3). All tests were performed at laboratory ambient temperatures (~22°C). These electrochemical tests provide new insights into the corrosion behavior of these in-package alloys that traditional mass loss tests (coupon immersion) do not provide. The primary findings are as follows:

- Based on the trend lines shown in Figure 29, the corrosion rates for the carbon steel and Boral samples in millimolal salt solutions increase by a factor of approximately 10 over the relevant potential range of -0.6 V to 0.6 V (vs SHE). At higher salt concentrations (0.1 molal) carbon steel shows a dramatic increase in its corrosion rate (~ 6 orders of magnitude) over this potential range.
- The corrosion rate of carbon steel decreases from values greater than $1x10^5$ g m^{-2} yr^{-1} for all tests performed in millimolal (or greater) salt concentrations down to around 30 g m^{-2} yr^{-1} in tests run at the lowest salt concentration (around 1 nanomolal).
- Boral showed evidence of non-uniform corrosion at potentials greater than 0.24 V (vs SHE) (Figures 14).
- Based on the trend lines shown in Figure 30, the corrosion rate of 316 stainless steel tested in pH 7 and 10, millimolal salt solutions increases dramatically (by 7 orders of magnitude) over the relevant potential range of -0.6 V to 0.6 V (vs SHE). The increase in 316 stainless steel corrosion rates in tests performed in pH 4, millimolal salt solutions is less steep over this potential range (increasing by around 3 orders of magnitude) but yields higher corrosion rates at lower potentials (Figure 30).
- The trend line for Zircaloy in Figure 30 indicate that its corrosion rate increases by approximately 2 orders of magnitude over the relevant potential range of -0.6 V to 0.6 V (vs SHE).

The corrosion rates measured in electrochemical tests with individual alloys were used as direct input to demonstrate the coupled in-package chemistry (IPC) – fuel matrix degradation (FMD) model that is being developed to provide long-term spent fuel degradation rates as chemical conditions (Eh, pH, speciation) evolve within a breached waste package. The combined prototype IPC and FMD model discussed in Jerden et al., 2019 and this report has been updated in the current study to account for the new alloy corrosion rate data. The coupled fuel degradation/IPC model links the FMD mixed potential code with the reactive transport code X1t, which is a module within the Geochemist's Workbench (GWB) software package. The reactive transport model consists of a 1D domain discretized with 21 reaction diffusion cells and includes a single waste package cell, two cells within the bentonite backfill and then 19 other cells within the near-field host rock.

The concentration of dissolved H_2 is the key variable in the FMD model, therefore, being able to accurately model the evolution of H_2 within the waste package is essential for accurately predicting long-term spent fuel degradation rates. The prototype X1t, IPC model has been used successfully to calculate the amount of H_2 produced and accumulated within a breached waste package due to the corrosion of stainless steel, carbon steel, Boral and Zircaloy and the results are discussed above. The experimental results for individual alloys were used to exercise the model for a set of 9 new model cases (Table 7). This model uses the masses, surface areas and corrosion rates of each alloy to calculate the H_2 generation rate and tracks all relevant

chemical speciation reactions to provide information on in-package pH, Eh and chemistry for a 10^5-year generic repository simulation. The model includes both the diffusive and advective transport of dissolved H_2 away from the waste package to track the concentration over time.

The sensitivity runs performed with this combined prototype IPC - FMD model using the new in-package alloy corrosion data presented above resulted in the following observations:

- For model runs using the corrosion results from tests performed in pH 4 solutions, the in-package carbon steel is predicted to be consumed by corrosion within 20 years of the waste package being breached. This rapid corrosion causes a sharp maximum in H_2 fugacity and concentration. The concentration of H_2 does not decrease rapidly following the consumption of carbon steel due to H_2 production by the relatively rapidly corroding Boral materials.
- Boral is predicted to persist for around 400 years under high Eh conditions and for around 4,000 years under low Eh conditions. Boral is the major source of H_2 in model cases with rapid carbon steel consumption and slow stainless steel and Zircaloy corrosion (Cases 2 and 3, Figure 33).
- In most cases stainless steel and Zircaloy are predicted to persist for over 100,000 years after the waste package has been breached. This is due to their low corrosion rates as measured in the electrochemical experiments (below 0.01 g m^{-2} yr^{-1}). These alloys do produce H_2 as they slowly corrode, but the rate is too low to maintain the H_2 concentration above the threshold for inhibiting oxidative dissolution of the fuel for most cases. The exception being Case 1 where a stainless steel corrosion rate of 1 g m^{-2} yr^{-1} leads to a H_2 production rate that maintains the concentration below the oxidative dissolution threshold for the duration of the model time frame (Figure 33).
- The relatively low corrosion rates for stainless steel and Zircaloy (below 1 g m^{-2} yr^{-1} for all cases except one) lead to their persistence through the 100,000-year time frame for the simulations. These alloys produced H_2 throughout the model runs; however, the amount produced is small.
- Including a pore water advection rate of 0.1 m/yr through the waste package cell decreases the H_2 concentration by a factor of approximately 4. This leads to H_2 concentrations dropping below the threshold needed to inhibit oxidative dissolution of the fuel under some conditions (e.g., see Case 5, Figure 34).
- Under high Eh conditions, the model predicts that the in-package H_2 concentration will have a steep increase corresponding to the rapid corrosion of carbon steel and Boral during the first 400 years following the waste package breach, but will fall below the threshold for inhibiting oxidative fuel dissolution by approximately 1,500 years due to H_2 diffusion out of the waste package cell.

The results of this study confirm the conclusions and recommendations that were identified and discussed in Jerden et al., 2017, Jerden et al., 2018 and Jerden et al., 2019. Several of the information gaps identified in those studies remain, but the present study has demonstrated how electrochemical testing methods can be used to address the key information gaps. Clearly, the environmental dependencies of in-package alloy corrosion rates must be taken into account in the FMD model to represent the evolving conditions in a breached waste package. Electrochemical measurements of alloy corrosion rates provide values and dependencies on T, Eh, pH, and Cl^- conditions for active corrosion and after passivation and thus are essential for source term model parameterization and validation. However, the effects of Galvanic coupling on the long-term corrosion rates and analytical functions for the pH and chloride ion concentration effects remain to be determined. Also, galvanic coupling of fuel and alloys (particularly Zircaloy) must be assessed.

The primary information gaps that still need to be filled to reduce uncertainties in long-term spent fuel degradation and associated radionuclide source term modeling include the following:

- Corrosion rates for galvanically coupled alloys and fuel remain to be measured.
- A robust waste package breaching model based on reliable electrochemical measurements such as those described in this report, is needed to determine the time at which spent fuel degradation initiates. This is particularly important for high burnup fuels that will produce high concentrations of radiolytic oxidants if contacted by water at times less than 1000 years out of the reactor. The threshold concentration of H_2 needed to inhibit oxidative dissolution will be higher for "young" fuels relative to older fuels.
- The mechanism by which H_2 inhibits the oxidative dissolution of spent fuel remains uncertain. The mechanism is currently modeled in the FMD model as a catalytic process by which H_2 oxidation is energetically promoted on the surface of the Ru-epsilon phase particles (see Figure 3 above and Broczkowski et. al., 2005). However, other processes may also influence the H_2 effect on fuel dissolution such as the destruction of radiolytic oxidants (e.g., H_2O_2) by H_2 within the solution near the degrading fuel surface. Electrochemical tests performed on simulated spent fuel (e.g., lanthanide and noble metal doped UO_2) could be used to address this issue.
- Relatedly, any processes that counteract the mechanism by which H_2 suppresses oxidative fuel degradation need to be accounted for. There is some evidence that halides (particularly Br) may be capable of poisoning the catalytic properties of the Ru-epsilon phase particles (Metz et. al., 2008), although the process is not fully understood or quantified. Electrochemical tests on simulated noble metal particle bearing fuel could be used to address this issue.
- It is also important that any processes that consume H_2 within the breached waste package be quantified and taken into account in the IPC – FMD model. Two key processes known to consume H_2 that have not yet been fully quantified experimentally or included in the IPC model are microbial oxidation of H_2 (e.g., Bagnoud et al., 2016) and the chemical conversion of H_2 to sulfur species such as H_2S, HS^-, S^{2-}. These processes could lead to higher fuel degradation rates by decreasing H_2 concentrations within the breached waste package and need to be understood and quantified.

The use of tailored electrochemical methods such as those discussed in this report offer the most accurate and versatile means for quantifying the long-term degradation behavior of spent fuel because its primary degradation mechanism is electrochemical in nature. Future studies should build on the existing alloy corrosion database and electrochemical modeling techniques to fill the data gaps identified above.

7.6 References

Bard, A., Faulkner, L., "Electrochemical methods: Fundamentals and Applications", John Wiley and Sons, Inc., 2001

Bagnoud, A., Leupin, O., Schwyn B., Bernier-Latmani R., Rates of microbial hydrogen oxidation and sulfate reduction in Opalinus Clay rock, Applied Geochemistry 72 (2016) 42-50

Broczkowski, M. E.; Noël, J. J.; Shoesmith, D. W., "The inhibiting effects of hydrogen on the corrosion of uranium dioxide under nuclear waste disposal conditions" *Journal of Nuclear Materials*, vol. 346, pp. 16-23, 2005.

Buck E., Jerden, J., Ebert, W., Wittman, R., "Coupling the Mixed Potential and Radiolysis Models for Used Fuel Degradation," FCRD-UFD-2013-000290, 2013.

Buck, E., Mausolf, E., McNamara, B., Soderquist, C., Schwantes, J., "Nanostructure of Metallic Particles in Light Water Reactor Used Nuclear," *Journal of Nuclear Materials*, vol. 61, pp. 236–243, 2015.

Bethke, C.M., Yeakel, S. "The Geochemist's Workbench User's Guides, Version 10.0," Aqueous Solutions LLC, Champaign, Illinois, 2014.

CRWMS M&O 2003, "In-Package Chemistry Abstraction," ANL-EBS-MD-000037 REV 02., Las Vegas, Nevada: CRWMS M&O. ACC: MOL.20000418.0818, 2003.

Energy Solutions, "Generic Design for Small Standardized Transportation, Aging and Disposal Canister Systems," DOE Advisory and Assistance Services Contract Task Order 18, UPDATED FINAL REPORT, May 14, 2015, 317 p.

Fillmore, D.L., "Parameter Selection for Department of Energy Spent Nuclear Fuel to be Used in the Yucca Mountain License Application, Idaho National Engineering and Environmental Laboratory Report," INEEL/EXT-03-01032 Revision 1, October 2003

Gattu, V. K., Ebert, William L., Tehrani, N., Indacochea, J. E. "Electrochemical Measurements of Steel Corrosion for Modeling H_2 Generation." CORROSION 2018. NACE International, 2018.

Grambow, B., Bruno, J., Duro, L., Merino, J., Tamayo, A., Martin, C., Pepin, G., Schumacher, S., Smidt, O., Ferry, C., Jegou, C., Quiñones, J., Iglesias, E., Rodriguez Villagra, N., Nieto, J., Martínez-Esparza, A., Loida, A., Metz, V., Kienzler, B., Bracke, G., Pellegrini, D., Mathieu, Wasselin-Trupin, G., Serres, C., Wegen, D., Jonsson, M., Johnson, L., Lemmens, K., Liu, J., Spahiu, K., Ekeroth, E., Casas, I., de Pablo, J., Watson, C., Robinson, P., Hodgkinson, D., "Model Uncertainty for the Mechanism of Dissolution of Spent Fuel in Nuclear Waste Repository," European Commission, Final Report for MICADO Project, EUR 24597, 2010.

Jerden, J., Lee, E., Gattu, V, Ebert, W., "Fuel Matrix Degradation Model Development Update: Alloy Corrosion Rates and Hydrogen Generation", Report for Spent Fuel and Waste Science and Technology Project, Milestone #: M4SF-19AN010301013, ANL/CFCT-19/12, September 30, 2019

Jerden, J., Lee, E., Gattu, V, Ebert, W., "Results from In-Package Alloy Electrochemical Corrosion Experiments: Implications for Long-Term Spent Fuel Degradation", Report for Spent Fuel and

Waste Science and Technology Project, Milestone #: M3SF-19AN010301012, ANL/CFCT-19/2, March 19, 2018

Jerden, J., Gattu, V, Ebert, W., "Update on Validation and Incorporation of a New Steel Corrosion Module into Fuel Matrix Degradation Model", Report for Spent Fuel and Waste Science and Technology Project, Milestone #: M4SF-18AN010301017, August 6, 2018

Jerden, J., Frey, K., Ebert, W., "Spent Fuel Matrix Degradation and Canister Corrosion: Quantifying the Effect of Hydrogen", Report for Spent Fuel and Waste Science and Technology Project, Report #: SFWD-SFWST-2017-000039, February 28, 2017

Jerden J., Hammond, G., Copple J., Cruse, T., Ebert W., "Fuel Matrix Degradation Model: Integration with Performance Assessment and Canister Corrosion Model Development," FCRD-UFD-2015-000550, July 21, 2015

Jerden J. Frey K. Ebert W., "A Multiphase Interfacial Model for the Dissolution of Spent Nuclear Fuel, *Journal of Nuclear Materials*, vol. 462, pp. 135–146, 2015.

Johnson J, Anderson F, Parkhurst DL. Database thermo.com.V8.R6.230, Rev 1.11. Lawrence Livermore National Laboratory, Livermore, California; 2000

Johnson, L.H. and F. King, "Canister options for the disposal of spent fuel," Nagra Technical Report 02-11, 2003.

Kaesche, H., "Metallic Corrosion," National Association of Corrosion Engineers International, Houston, TX, 1985.

King F. and Kolar M., "Mathematical Implementation of the Mixed-Potential Model of Fuel Dissolution: Model Version MPM-V1.0," Ontario Hydro, Nuclear Waste Management Division Report No: 06819-REP-01200-10005 R00, 1999.

King F. and Kolar M., "The Mixed-Potential Model for UO_2 Dissolution MPM Versions V1.3 and V1.4," Ontario Hydro, Nuclear Waste Management Division Report No. 06819-REP-01200-10104 R00, 2003.

King, F., "Overview of a Carbon Steel Container Corrosion Model for a Deep Geological Repository in Sedimentary Rock," Nuclear Waste Management Organization Report TR-2007-01, March 2007, 71 p.

Laaksoharju M., Smellie, J., Tullborg, E-L., Gimeno, M., Hallbek, L., Molinero, J., Waber, N., "Bedrock hydrogeochemistry Forsmark site descriptive modeling SDM-Site Forsmark," SKB R-Report (R-08-47), SKB, Stockholm, Sweden, 2008.

Metz V., Loida A., Bohnert E., Schild D., Dardenne K., "Effects of Hydrogen and Bromide on the Corrosion of Spent Nuclear Fuel and γ-irradiated UO_2(s) in NaCl Brine," *Radiochim. Acta* 96, 637–648, 2008.

Miller, W.M., W.R. Alexander, N.A. Chapman, I.G. McKinley, and J.A.T. Smellie, "Natural analogue studies in the geological disposal of radioactive wastes," Studies in Environmental Sciences 57, Elsevier, Amsterdam (also Nagra Technical Report NTB 93-03), 1994.

Ollila, K., "Dissolution of Unirradiated UO_2 and UO_2 Doped with ^{233}U in Low- and High-Ionic-Strength NaCl Under Anoxic and Reducing Conditions," Posiva Working Report 2008-50, 2008.

Pastina B., and LaVerne, J. A. "Effect of Molecular Hydrogen on Hydrogen Peroxide in Water Radiolysis", Journal of Physical Chemistry A 105, 9316-9322, 2001.

Posiva, "Safety case for the disposal of spent nuclear fuel at Olkiluoto – Design Basis 2012," Eurajoki, Finland: Posiva Oy. POSIVA 2012-03. ISBN 978-951-652-184-1, 2012.

Radulescu, G., "Repository Science/Criticality Analysis," Oak Ridge National Laboratory, Reactor and Nuclear Systems Division, FTOR11UF0334, ORNL/LTR-2011, Oak Ridge National Laboratory, Oak Ridge, TN., 2011.

Röllin S., Spahiu K., Eklunda U., "Determination of Dissolution Rates of Spent Fuel in Carbonate Solutions Under Different Redox Conditions with a Flow-through Experiment," *Journal of Nuclear Materials*, vol. 297, pp. 231–243, 2001.

Shoesmith, D., Kolar, M., King, F., "A Mixed-Potential Model to Predict Fuel (Uranium Dioxide) Corrosion within a Failed Nuclear Waste Container" Corrosion, vol. 59, pp. 802-816, 2003.

Shoesmith, D., "The Role of Dissolved Hydrogen on the Corrosion/Dissolution of Spent Nuclear Fuel," Nuclear Waste Management Organization, Toronto, Ontario, Canada, TR-2008-19, November 2008.

Simpson, J.P. 1989, "Experiments on canister materials for Swiss high- level waste disposal projects, Part IV. National Cooperative for the Storage of Radioactive Waste Technical Report," NAGRA-NTB-89-19, 1989.

Turnbull, A. 2009, "A Review of the Possible Effects of Hydrogen on Lifetime of Carbon Steel Nuclear Waste Canisters NAGRA," Technical Report 09-04, July 2009.

Wang Y. et al., "Used Fuel Disposal in Crystalline Rocks: Status and FY14 Progress," FCRD-UFD-2014-000060, SAND2014, Sandia National Laboratories, Albuquerque, NM., 2014.

8. LEAD/LEAD-ALLOY AS A CORROSION-RESISTANT OUTER LAYER PACKAGING MATERIAL FOR HIGH LEVEL NUCLEAR WASTE DISPOSAL

8.1 Introduction

Owing to its carbon-neutral nature and high energy density, nuclear energy is an indispensable part of the total energy portfolio to address the climate change problem caused by anthropogenic carbon dioxide emission. Safe disposal of nuclear waste is critical for the development and sustainability of nuclear energy industries. In a deep geologic disposal system, HLW is placed in a canister/overpack, which constitutes one of the key components of a so-called multiple barrier system. The materials for a canister/overpack must satisfy several requirements, including the assurance of at least 1,000 years of containment capability (Asano and Aritomi, 2005); the avoidance of detrimental impacts on other barriers (Landolt et al., 2009); retrievability during the operational phase; the good radiation shielding ability; availability of raw material; reasonable structural strength/robustness; reasonable economics associated with raw material, fabrication, and handling; and ease of sealing and inspection (Landolt et al., 2009).

Various packaging materials have been proposed. Copper has been a candidate material for canisters/overpacks in the nuclear waste disposal programs in Finland (Raiko, 2005) and Sweden (Wersin, 1994; King et al., 2010). Similarly, carbon steel has been proposed in the nuclear waste disposal programs in Belgium, France, Japan, and Switzerland (King, 2013). In the Canadian nuclear disposal programs, a hybrid approach for the canister/overpack material has been considered, in which carbon steel is used as the material for the main body, with the outlayer being coated with copper as a corrosion resistance layer (Shoesmith, 2006). In the nuclear waste disposal programs in Argentina (Cassibba and Fernandez, 1989; Semino et al., 1993, 1996; Guasp et al., 2000), Brazil (Vicente, 2007), and Russia (Arustamov et al., 1999; Ojovan et al., 1999; 2003), lead/lead-based alloy has suggested as a candidate material for canisters/overpacks.; however, the technical feasibility of this concept yet needs to be demonstrated.

The materials mentioned above have their respective advantages and disadvantages. Copper has good corrosion resistance under sulfide-free reducing conditions, but it suffers from serious questions over the economics of its use, especially in view of the limited availability of copper resources, and its propensity to corrosion in a sulfide-bearing environment. The current price of copper ($3.29/lb) is about seven and four times of those for carbon steel ($0.50/lb) and lead ($0.87/lb), respectively (Infomine, 2018). In addition, copper is not suitable for a repository design concepts in an unsaturated zone where an oxidizing condition prevails. Under an oxic condition, the corrosion rate of copper is high, as the solubility of the corrosion product, malachite, $Cu_2CO_3(OH)_2$(cr), is rather high (Wersin et al., 1994). Carbon steel is rather economical in comparison with copper and has good mechanical strength. A major concern for its use is that hydrogen gas generated by the high corrosion rate may damage barrier properties of an engineered barrier system (EBS) and rock formations (Landolt et al., 2009). In addition, iron may promote microbial activity that could degrade the bentonite buffer (Liu et al., 2012; Stone et al., 2016a, 2016b; Haynes et al., 2018), as iron is a nutrient for microbes. Furthermore, carbon steel is not suitable for repository design concepts in unsaturated zones because the corrosion rate of iron is too high under an oxidizing condition. Regarding lead/lead-based alloy materials, the previous investigations have indicated that lead/lead-based alloy materials have excellent radiation shielding ability and very good resistance to corrosion, although the underlying mechanism is unclear.

The mechanical strength required for packing materials in a repository design is site-specific. For instance, the minimum mechanical strength required for a canister in the Finnish design concept is to withstand the total compressive stress of 14 MPa (the sum of 7 MPa pressure of 700 m groundwater and 7 MPa of bentonite swelling) (Raiko, 2005). The compressive strength of lead is usually not measured owing to its

creep behavior. Pure lead has a tensile strength of 12-13 MPa (ASM International, 2008). Lead alloys usually have much higher tensile strength. For example, Pb-Ca alloy has a tensile strength of 70 MPa (ASM International, 2008). Given the fact that the compressive strength of a material is generally higher (many times) than the tensile strength, lead or lead alloys should be able to withstand the total compressive stress that a waste canister will be subjected to in a hard rock repository. In an actual waste canister, the mechanical strength of the canister can also be enhanced by the inner layer(s) of package materials. In addition, the creep behavior of lead materials can provide another benefit for waste canister corrosion resistance. That is, creeping will relax the stress concentration induced during waste canister manufacture and emplacement, thus reducing the possibility for stress crack corrosion of the outer layer of the canister. In an actual waste canister, the mechanical strength of the canister is generally provided by the inner layer(s) of package materials.

In this study, we elucidate the underlying mechanism for corrosion resistance of lead/lead-based alloy materials and demonstrate the feasibility of the use of these materials in the outer layer of a waste container or package for HLW disposal. Our work is based on a previously unreported long-term corrosion test, a microstructural analysis of corrosion coupons, and a thermodynamic evaluation of corrosion product stabilities in relevant disposal environments.

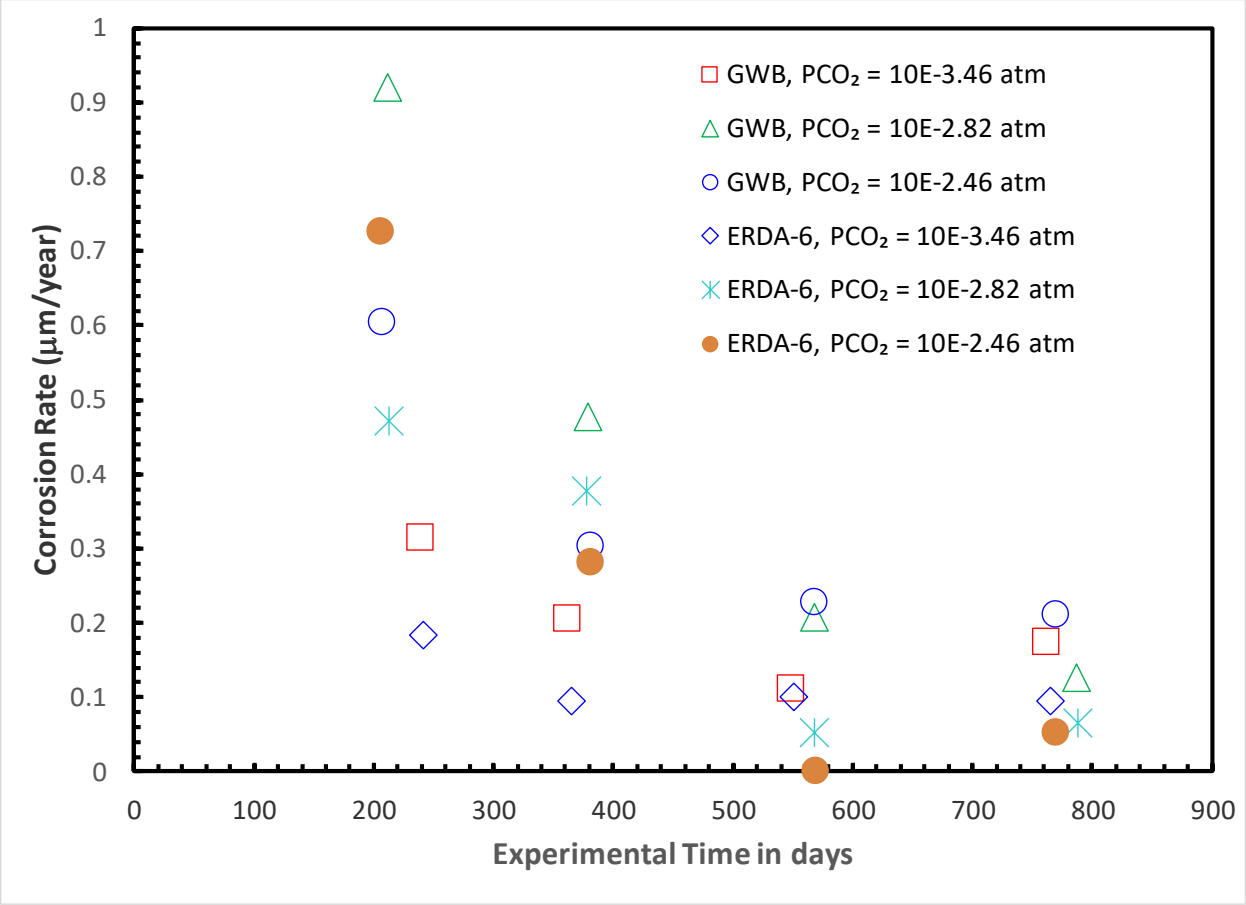

Figure 8-1. Corrosion rates of metallic lead determined at various experimental durations in the synthetic WIPP brines [i.e., GWB and ERDA-6 without organic ligands, see detailed descriptions in the text at P_{CO_2} = $10^{-3.46}$, $10^{-2.82}$, and $10^{-2.46}$ atm at 26°C (from Roselle, 2013)]

8.2 Methods

In corrosion experiments (Roselle, 2013), lead coupons with the specifications of QQ-L-171e Grade C Chemical lead, which contained 99.9 wt % of lead with trace amounts of other metals such as bismuth and copper, were used. The brines used followed the synthetic recipes for ERDA-6 and GWB from Xiong (2008). In some experiments, organic ligands, i.e., acetate, citrate, EDTA, and oxalate, which were present in the waste stream for the WIPP, were also added into the synthetic ERDA-6 and GWB. Corrosion experiments were conducted at 26ºC under the atmospheres of nitrogen and various desired partial pressures of CO_2 ($10^{-3.46}$, $10^{-2.82}$, and $10^{-2.46}$ atm.). Corrosion experiments were performed in a flow-through system. Corrosion products were characterized using XRD and SEM with Energy Dispersive Spectroscopy (EDS). Corrosion rates were determined based on weight loss data. Weight loss data were obtained according to the ASTM G1-03 procedure from ASTM International (2003).

In our thermodynamic calculations, the standard state for a solid phase is defined as its pure end-member with unit activity at temperatures and pressures of interest. The standard state of the solvent in aqueous solutions is pure solvent at temperatures and pressures of interest. The standard state for an aqueous solute is a hypothetical 1 molal ($mol \bullet kg^{-1}$) solution of infinite dilution at temperatures and pressures of interest. The computer code EQ3/6 Version 8.0a (Wolery et al., 2010; Xiong, 2011a) with the thermodynamic database DATA0.FM2 (Domski, 2015; Xiong and Domski, 2016) was employed for our thermodynamic calculations.

8.3 Results

Our long-term corrosion experiments on lead were conducted for ~800 days at 26ºC and P_{CO_2} ranging from 0 to $10^{-2.46}$ atm in high ionic strength solutions from the salt formations at the Waste Isolation Pilot Plant (WIPP) near Carlsbad, NM. Two brine were used for corrosion experiments: ERDA-6 (Energy Research Development Administration Well 6) representing a NaCl-rich brine from the Castile Formation (Popielak *et al*., 1983) and GWB (Generic Weep Brine) representing a Mg-Na-Cl-rich brine the Salado Formation at or near the stratigraphic horizon of the repository. The experiments were terminated at various experimental durations to constrain the time-dependent corrosion rate. Experimental results show a rapid decrease in corrosion rate with time for all P_{CO_2} conditions tested (Figure 8-1), clearly indicating passivation of Pb corrosion surfaces. The corrosion products in the experiments imposed with external P_{CO_2} were cerussite ($PbCO_3$) and tarnowitzite [$(Ca, Pb)CO_3$] (Figures 8-2A and 8-2B).

The rate measurements are corroborated well with a microstructural structural analysis of corrosion products. The corrosion products typically exhibit micro-pyramid forms (Figures 8-2A and 8-2B). These micro-pyramids form a dense layer of products that covers the whole corrosion surface (see Figure 8-2B for a close-up view). The similar micro-pyramids for cerussite have also been observed in other studies (e.g., Yuan et al., 2018). We attribute the formation of micro-pyramids for cerussite to its crystal habit of orthorhombic prisms commonly with twinning (Bowles et al., 2004).

We postulate that the low solubility of cerussite (see a detailed thermodynamic calculation below) and the morphology of cerussite are the key factors leading to lead passivation. That is, the low solubility of cerussite promotes a fast formation of a stable corrosion product layer, and the dense morphology of the corrosion product prevents a lead surface from further corrosion. Our experimental results and hypothesis are consistent with archaeological studies on lead artifacts. For instance, Reich et al. (2003) observed that the corrosion of the lead artifacts of ~2500 years was passivated, and the lead artifacts were protected by

the lead corrosion products (80 vol% of cerussite and 20 vol% of litharge, PbO). Additionally, the low catalytic nature of lead may also play a part role in its corrosion resistance.

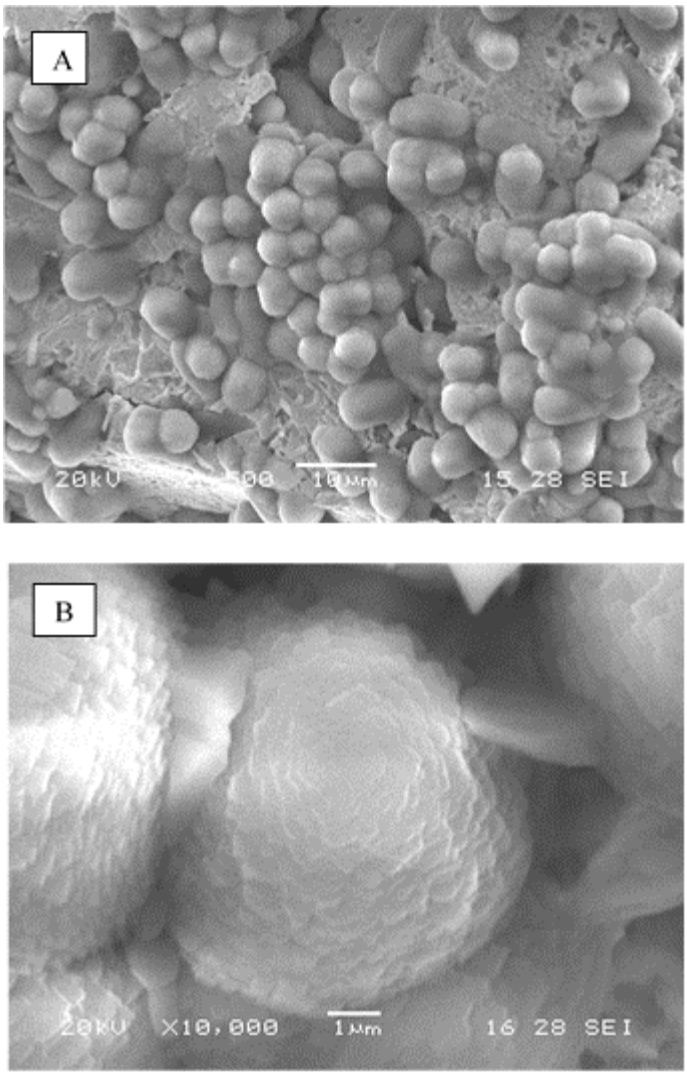

Figure 8-2. The images of lead corrosion experiments in ERDA-6 with an experimental duration of 6 months (Roselle, 2013). A - A SEM image for the experiment at $P_{CO_2} = 10^{-2.46}$ atm in ERDA-6 with organic ligands; B - A SEM image for the experiment at $P_{CO_2} = 10^{-2.82}$ atm in ERDA-6 without organic ligands.

In most waste disposal concepts, a canister or an overpack will be surrounded with a thick layer of buffer material such as bentonite. In such a configuration, the stability of the passivating layer will depend on the diffusion of Pb^{2+} in equilibrium with cerussite into bentonite buffer to cause cerussite dissolution (see Figure 8-3). The diffusion flux is solubility-dependent. If the solubility of cerussite is high, the diffusion will be

fast because of a steep concentration gradient. Conversely, if the solubility is low, the diffusion will be slow because of a low concentration gradient.

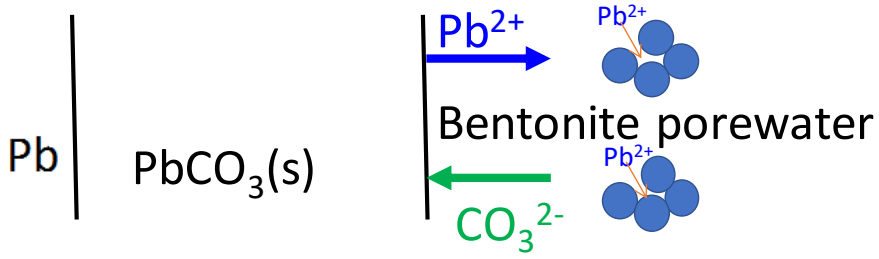

Figure 8-3. A conceptual envision of the further corrosion of a canister/overpack constructed with lead/lead-based alloy materials, limited by diffusion, in a geological repository. As the morphology of cerussite is dense micro-pyramid aggregates illustrated in Figure 2B, the above conceptual model represents only the top layer of micro-pyramids in contact with bentonite buffer. Bentonite particles are represented by dark-blue spheres with lead ions being adsorbed onto them.

We calculated the solubilities of cerussite in various disposal environments, based on a solubility model we recently developed (Xiong, 2015). Figure 8-4 shows solubilities of cerussite in three representative disposal environments: granitic rocks, high grade metamorphic rocks, and clay formations. In these environments, the pH ranges from ~7 to ~10, and carbonate concentrations range from ~3×10^{-4} mol•kg^{-1} to ~2×10^{-2} mol•kg^{-1}. Solubilities of cerussite in terms of total dissolved lead ($m_{\sum Pb}$) in equilibrium with the representative groundwaters and various bentonite porewaters are generally below 10^{-6} mol•kg^{-1} (Figure 7-3B). At such low concentrations, the dissolution of the passivating layer would be very slow, if there is any, and the passivating layer will persist for the whole repository time period. In addition, considering that the crystallinity and overgrowth of corrosion products continue to increase with time, it is reasonable to expect that the passivating mechanism elucidated above for lead corrosion would remain effective or even be reinforced as the time goes. In other words, the trend observed in our experiment - a decrease in corrosion rate with time - can be extrapolated beyond the experiment duration.

As mentioned earlier, the corrosion of copper by sulfide is a serious concern for canisters/overpacks constructed with copper outer layers, as Cu_2S instead of metallic copper is a thermodynamically stable phase in sulfide environments (King et al., 2010). In the presence of sulfide, lead could also be corroded as PbS (mineral name, galena). The relative stability of cerussite vs. galena can be evaluated according to the following reaction,

$$PbS(cr) + CO_2(g) + H_2O(l) = PbCO_3(cr) + H_2S(g) \qquad (8\text{-}1)$$

Based on the thermodynamic properties for the substances in Reaction (8-1), the stability fields of cerussite and galena were constructed (Figure 8-4). In this calculation, the thermodynamic properties for all substances except cerussite were from the CRC Handbook (Lide, 2004). The Gibbs free energy of formation for cerussite was calculated from the equilibrium constant for cerussite from Xiong (2015) in consistency with the CRC Handbook. The $\log(\frac{f_{H_2S}}{f_{CO_2}})$ was estimated from groundwater chemistry. It is clear from Figure 8-4 that cerussite has a large stability field that encompasses most of the disposal

environments considered. Figure 8-4 suggests that cerussite is the predominantly stable phase under various disposal conditions, implying the unlikelihood of sulfide corrosion for lead.

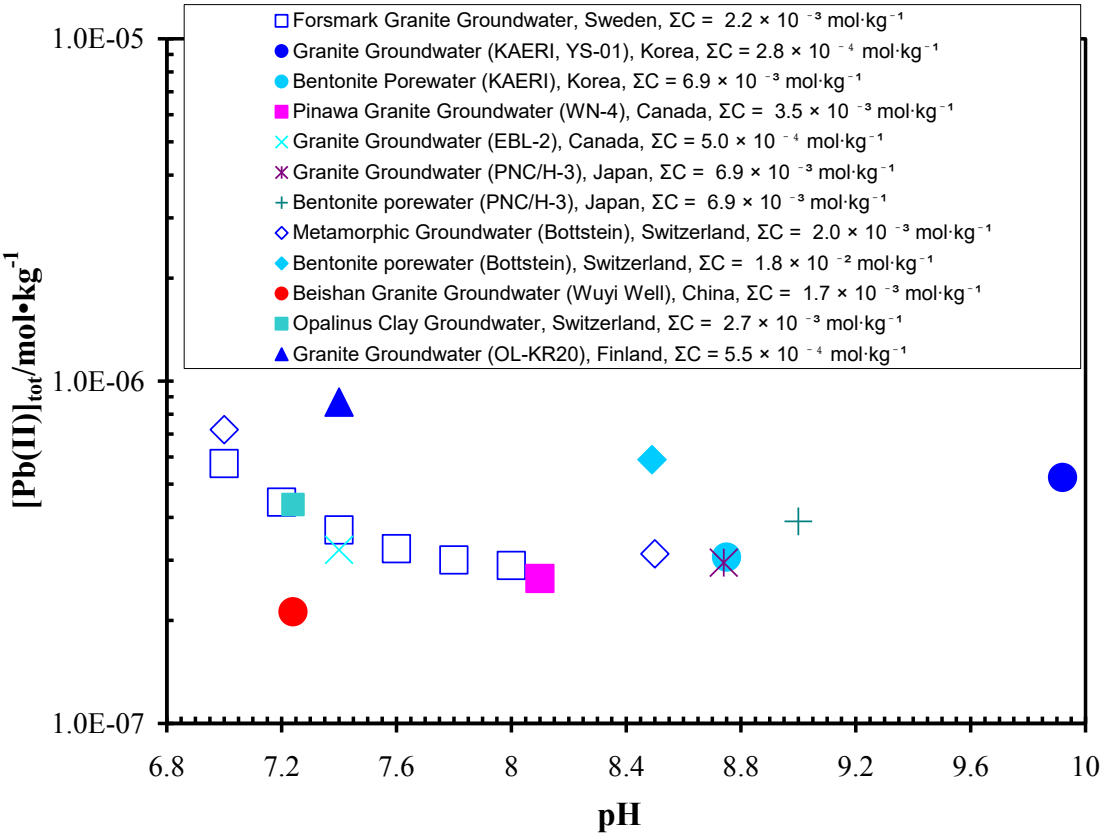

Figure 8-4. Solubilities of cerussite in terms of total molality of lead ($m_{\Sigma Pb}$) in equilibrium with various groundwaters as a function of pH. The geochemical compositions for these groundwaters represent those in the disposal concepts in crystalline rock formations (including high grade metamorphic rocks and granite) and clay formations. The chemical compositions for the reference granite groundwater from the borehole YS-01 and associated bentonite pore water, Korea, are from Baik et al. (2008). The chemical compositions for the Pinawa granite groundwater from the borehole WN-4 and for the East Bull Lake granite groundwater from the borehole EBL-2, Canada, are from Gascoyne et al. (1987). The chemical compositions for the granite groundwater from the borehole PNC/H-3 and for the bentonite porewater equilibrated with PNC/H-3, Japana, are from PNC (1992). The chemical compositions for the crystalline metamorphic rock groundwater from the Böttstein, Switzerland, are from NAGRA (1985), and for the bentonite porewater equilibrated with the Böttstein groundwater are from Curti (1993). The chemical compositions for the Beishan granite groundwater (Wuyi Well), China, are from Zhou et al. (2000). The chemical compositions for the Forsmark granite groundwater, Sweden, are from SKB (2006). The chemical compositions for the Olkiluoto granite groundwater, Finland, are from POSIVA (2010).

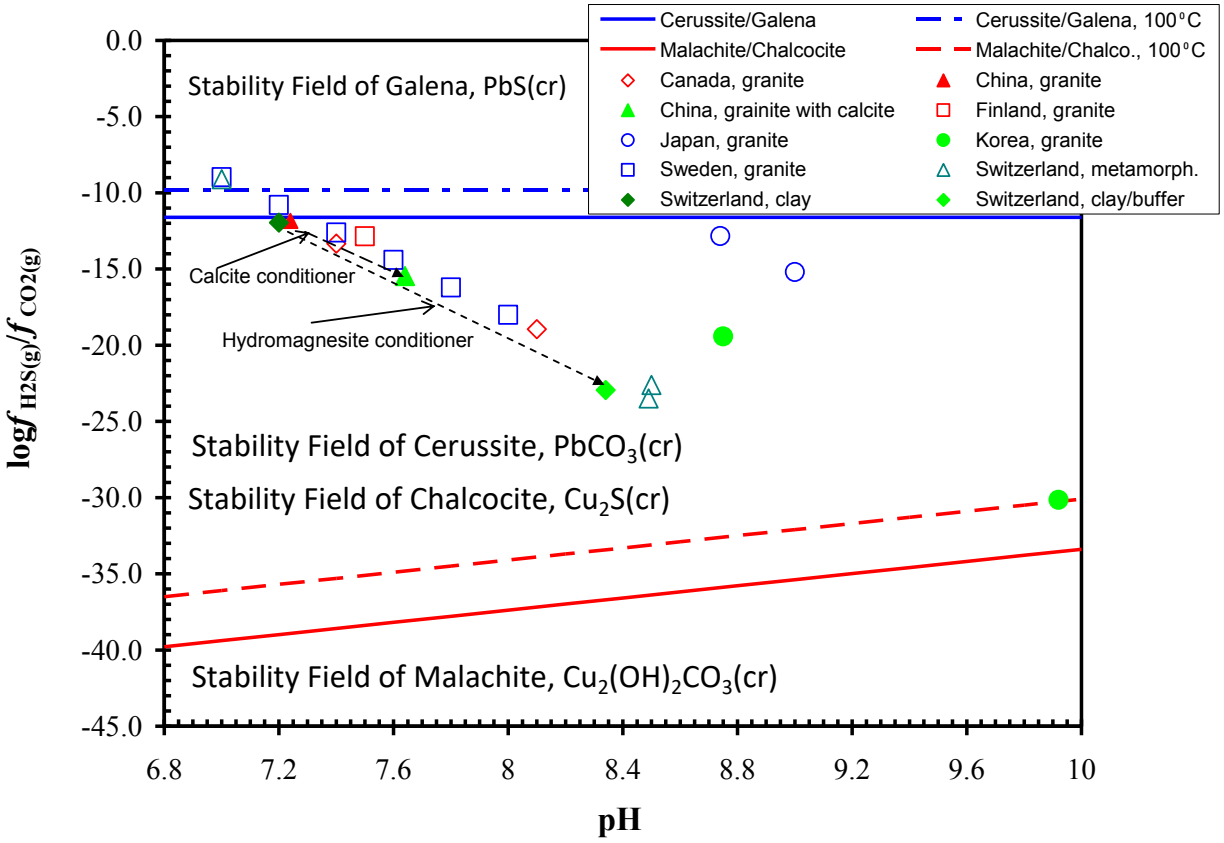

Figure 8-5. Stability fields of galena (PbS), cerussite ($PbCO_3$), chalcocite (Cu_2S), and malachite [$Cu_2(OH)_2CO_3$], with regard to lead and copper corrosion in the presence of carbon dioxide and sulfide, in the disposal concepts in crystalline rocks and clay formations. The sources for the geochemical compositions of the groundwaters in those disposal concepts are the same as those presented in Figure 3b. The solubility constant for hydromagnesite from Xiong (2011b) is used for calculations using hydromagnesite as a conditioner.

For comparison, in Figure 8-5, the stability fields of chalcocite (Cu_2S) and malachite [$Cu_2(OH)_2CO_3$] are also constructed according to the following reaction,

$$Cu_2S(cr) + CO_2(g) + 3H_2O(l) = Cu_2(OH)_2CO_3(cr) + H_2S(g) + H_2(g) \qquad (8\text{-}2)$$

Assuming unity for activity of water, $\log(\frac{f_{H_2S}}{f_{CO_2}})$ can be calculated by using the following equation,

$$\log(\frac{f_{H_2S}}{f_{CO_2}}) = \log K_2 - \log f_{H_2} \qquad (8\text{-}3)$$

The equilibrium constant for Reaction (2) (log K_2) were calculated using the Gibbs free energies of formation from the CRC Handbook for all substances except malachite. The Gibbs free energy of formation

for malachite was from Kiseleva et al. (1992). Fugacities of hydrogen at each pH were calculated using EQ3/6 Version 8.0a based on the chemical compositions of the groundwaters in various disposal concepts at an average Eh value of -150 mV. Figure 8-5 shows that $\log(\frac{f_{H_2S}}{f_{CO_2}})$ for the groundwaters in various disposal concepts are in the stability field of chalcocite under all pH conditions ranging from 6.8 to 10 and dictate that copper would be corroded by sulfide.

8.4 Discussion

Our investigation demonstrates that lead/lead-based alloy materials can be a good material for a waste package outer layer for HLW disposal given their excellent ability for radiation shielding and corrosion resistance, and favorable economics. In carbonate-bearing groundwaters characterized with a wide range of disposal concepts, the surface of lead will be passivated shortly after initial corrosion. The passivating layer subsequently will protect lead from further corrosion. The low solubility of cerussite would render the passivating layer stable and persistent over a whole repository time scale.

Copper is also excellent in corrosion resistance in reducing environments without sulfide. However, copper will suffer from severe corrosion if sulfide is present. In contrast, given its large stability field for cerussite in the space of f_{CO_2} vs. f_{H_2S}, lead is unlikely to suffer from such corrosion even if sulfide is present. Also, importantly, carbonate materials such as calcite and hydromagnesite can be used as a geochemical conditioner in a repository design to completely eliminate the sulfide corrosion issue for lead. As an illustration, we use calcite as a geochemical conditioner for the groundwater at the Beishan granite site, China, and hydromagnesite as a geochemical conditioner for the groundwater in the Opalinus clay formations, Switzerland. As shown in Figure 8-4, the geochemical conditions of the original Beishan groundwater are close to the boundary between cerussite and galena, although it is still on the side of cerussite (see the red triangle in Figure 8-4). However, if calcite is added, the water chemistry would shift towards the center of the cerussite stability field (the green triangle in Figure 8-4), thus further preventing the corrosion by sulfide. The same would happen to Opalinus groundwater, if hydromagnesite is added.

Although our corrosion experiments were conducted at 26°C and calculations were performed at 25°C, the results presented above are likely to provide a bounding case for elevated temperature situations because carbonates generally exhibit retrograde solubilities (i.e., their solubilities decrease with temperature). For instance, the solubility constant ($\log_{10} K$) for calcite has been shown to decrease about one order of magnitude and about two and half orders of magnitude at 100°C and 200°C (Barin and Platzki, 1995), respectively, in comparison with that at 25°C.

It is anticipated that cerussite would be a stable phase in a carbonate-bearing solution at an elevated temperature. Cerussite has been observed in hydrothermal ore deposits, active hydrothermal systems, and geothermal scales (e.g., Nakashima et al., 1995; Yakovenchuk et al., 2010; Wasch, 2014). In Figure 8-4, the dashed blue and red lines represent the boundaries of cerussite/galena and malachite/chalcocite at 100°C, respectively. In our calculations, we use the Gibbs-Helmholtz equation by assuming the change in enthalpy for Reaction (1) ($\Delta_r H$) is constant over the temperature range from 25°C to 100°C. Figure 8-4 illustrates that the stability field of cerussite does expand at 100°C in comparison with that at 25°C. We expect that our corrosion rates may be applicable to elevated temperatures, because of retrograde solubility of cerussite, considering the fact that the corrosion rate of a material is roughly correlated with the solubility of the passivating corrosion product, as exemplified by titanium and its corrosion product of TiO_2. Nevertheless, the extrapolation of the measured rates to an elevated temperature condition needs to be further evaluated.

One concern could arise that the usage of lead-based materials as packaging material for high level nuclear waste disposal could lead to a potential groundwater contamination. However, regardless of whether lead is used in waste packages, a large quantity of lead is already present in nuclear waste as waste streams and a fission product. For instance, the inventory of lead for the WIPP is predicted to be on the order of ~1.3×10^6 kg (Xiong et al., 2015), and it is regulated as a RCRA (Resource Recovery and Conservation Act) metal. Therefore, lead is already included in an existing regulatory framework for a repository. In addition, owing to the low solubility of cerussite and the surrounding bentonite layer (a standard design for many disposal concepts), the use of lead or lead alloy as the outer layer material should not create an additional burden for demonstrating regulatory compliance, as elaborated in the following. The US EPA guideline with regard to lead in drinking water is 0.015 mg/L (ATSDR, 2019), which is 7.2×10^{-8} mol•dm^{-3} ≈ 7.2×10^{-8} mol•kg^{-1}. The solubility of cerussite is < 10^{-6} mol•kg^{-1} at 25°C. As bentonite has strong absorption capacities for lead (Xu et al., 2008; Yang et al., 2010), with K_d of ~1250 mL/g (Xu et al., 2008) and sorption capacities of ~2.5 × 10^{-4} mol/g (Yang et al., 2010), lead aqueous species are strongly absorbed onto bentonite. Notice that the K_d and sorption capacities cited above are determined in acidic pH range (pH 3.5-4.0). As sorption capacities and K_d are optimal and much higher in the pH range from ~6 to ~10 (Yang et al., 2010), which is similar to the expected pH range in geological repositories, it is expected that much higher values for sorption capacities and K_d would be present in geological repositories. Combined with the extremely low hydraulic conductivity offered by bentonite, the lead concentrations released from the bentonite buffer material are expected below 7.2×10^{-8} mol•kg^{-1}.

8.5 Conclusions

Safe disposal of high-level nuclear waste (HLW) is a challenging problem world-wide. Corrosion-resistant waste packages constitute a key component of a multiple barrier system for waste isolation. Metallic copper has been proposed as an outer layer material for a waste package. However, a concern has been raised regarding potential copper corrosion induced by hydrogen sulfides in a reducing disposal environment. We here demonstrate that lead/lead-alloy materials could be an excellent alternative material for waste package outer layers, owing to their corrosion resistance (especially to hydrogen sulfide attack) and radiation-shielding capability. Our long-term corrosion experiments show that lead is passivated by its corrosion products, cerussite ($PbCO_3$) and tarnowitzite $(Ca,Pb)CO_3$, in carbonate-bearing groundwaters, because of the formation of a dense surface layer of corrosion products and the low solubility of the corrosion products. With its low solubility (<10^{-6} mol kg^{-1}), cerussite is more favored to form over galena (PbS) in a typical disposal environment; thus the issue of sulfide-induced metal corrosion as related to copper can be completely eliminated. If needed, the carbonate concentration in a repository can be conditioned with carbonate materials such as calcite or hydromagnesite to ensure cerussite precipitation. Furthermore, using lead/lead alloy will provide excellent radiation shielding for waste package transportation and repository operation.

8.6 References

Arustamov, A.E., Ojovan, M.I., Kachalov, M.B. Lead and lead-based alloys as waste matrix materials. *MRS Proceedings* **556**, 961–966 (1999).

Asano, H. and Aritomi, M., 2005. Long-term integrity of waste package final closure for HLW geological disposal, (I) Points at issue concerning 1,000 years containment capability of overpack. *Journal of nuclear science and technology* **42**, 470–479 (2005).

ASM International, 2008, Properties of Lead, Tech Note, Advanced Materials & Processes/September 2008, page 6;

https://www.asminternational.org/documents/10192/1885446/amp16609p61.pdf/18bfec41-661e-4ea1-b65c-8e9e9c6c6c73/AMP16609P61

ASTM International, 2003. ASTM G1-03, Standard Practice for Preparing, Cleaning, and Evaluating Corrosion Test Specimens, American Society for Testing and Materials (ASTM) International, West Conshohocken, PA, USA.

ATSDR (Agency for Toxic Substances & Disease Registry), 2019, Lead Toxicity: What Are U.S. Standards for Lead Levels? https://www.atsdr.cdc.gov/csem/csem.asp?csem=34&po=8

Baik, M.-H., Lee, S.-Y., Lee, J.-W., Kim, S.-S., Park, C.-K., Choi, J.-W. Review and compilation of data on radionuclide migration and retardation for the performance assessment of a HLW repository in Korea. *Nuclear Engineering and Technology* **40**, 593–606 (2008).

Barin, I., and Platzki, G., 1995, Thermochemical Data of Pure Substances (3rd Edition). New York, VCH.

Bowles, J.F.W., Anthony, JW, Bideaux, RA, Bladh, KW and Nichols, MC, 2004. Handbook of Mineralogy. Volume V. Borates, Carbonates, Sulfates. Tucson, Arizona (Mineral Data Publishing), 2003, ix+ 813 pp. ISBN0-9622097-0-8.

Cassibba, R.O., Fernandez, S. Lead corrosion behaviour in simulated media of an underground repository. *Journal of Nuclear Materials* **161**, 93–101 (1989).

Curti, E. Modeling bentonite porewaters for the Swiss high-level radioactive waste repository. NAGRA Tech. Rep., NTB 93-94, Wettingen, 85 pp (1993).

Domski, P.S. "Memo AP-173, EQ3/6 Database Update: DATA0.FM2" Memorandum to WIPP Records, October 27, 2015. Carlsbad, NM: Sandia National Laboratories. ERMS 564914 (2015).

Gascoyne, M., C. C. Davison, J. D. Ross, and R. Pearson. Saline groundwaters and brines in plutons in the Canadian Shield. *Saline Water and Gases in Crystalline Rocks*. P. Fritz and S. K. Frape (eds.). Geological Association of Canada, Waterloo, Ontario. Special Paper 33, 53–68 (1987).

Guasp, R., Lanzani, L, Bruzzoni, P., Cufre, W., Semino, C.J. Lead corrosion evaluation in high activity nuclear waste container (Argentina). *Extrapolation of short term observations to time periods relevant to the isolation of long lived radioactive waste*, p.27, IAEA-TECDOC-1177 (2000).

Haynes, H.M., Pearce, C.I., Boothman, C. and Lloyd, J.R. Response of bentonite microbial communities to stresses relevant to geodisposal of radioactive waste. *Chemical Geology* **501**, 58–67 (2018).

Infomine, http://www.infomine.com/investment/metal-prices, accessed in November 6, 2018.

King, F., Lilja, C., Pedersen, K., Pikanen, P., Vahanen, M. An update of the state-of-the-art report on the corrosion of copper under expected conditions in a deep geologic repository. Technical Report TR-10-67. Svensk Kärnbränslehantering AB, Swedish Nuclear Fuel and Waste Management Co, SE-101 24 Stockholm, Sweden (2010).

King, F. Container materials for the storage and disposal of nuclear waste. *Corrosion* **69**, 986–1011 (2013).

Landolt, D., Davenport, A., Payer, J., Shoesmith, D. A Review of Materials and Corrosion Issues Regarding Canisters for Disposal of Spent Fuel and High-level Waste in Opalinus Clay. Technical Report 09-02. NAGRA, Hardstrasse 73, CH-5430 Wettingen, Switzerland (2009).

Lide, D.R., CRC Handbook of Chemistry and Physics, 84th edition (2003-2004), CRC Press (2004).

Liu, D., Dong, H., Bishop, M.E., Zhang, J., Wang, H., Xie, S., Wang, S., Huang, L. and Eberl, D.D., 2012. Microbial reduction of structural iron in interstratified illite-smectite minerals by a sulfate-reducing bacterium. *Geobiology* **10**, 150–162 (2012).

NAGRA. Projekt Gewähr 1985. NAGRA Proj. Rep. NGB 85-09, Baden, 400 pp (1985).

Nakashima, K., Sakai, H., Yoshida, H., Chiba, H., Tanaka, Y., Gamo, T., Ishibashi, J.I. and Tsunogai, U., 1995. Hydrothermal mineralization in the Mid-Okinawa Trough. *Biogeochemical processes and ocean flux in the Western Pacific*, pp.487-508.

Ojovan, M.I., Guskov, A.V., Prozorov, L.B., Arustamov, A.E., Poluektov, P.P., Serebryakov, B.B.: Safety assessment of bore-hole repositories for sealed radiation sources disposal. *MRS Proceedings* **608**, 141–146 (1999).

Ojovan, M.I., Dmitriev, S.A., Sobolev, I.A.: Long-term safe storage and disposal of spent sealed radioactive sources in borehole type repositories. *Waste Management Conference Proceedings* **3**, 23–27 (2003).

PNC. Research and development on geological disposal of high-level radioactive waste: First progress report. PNC Tech. Rep. TN1410 93-018, Tokyo, 430 pp (1992).

Popielak, R.S., Beauheim, R.L., Black, S.R., Coons, W.E., Ellingson, C.T., and Olsen, R.. Brine Reservoirs in the Castile Formation, Waste Isolation Pilot Plant Project, Southeastern New Mexico. TME 3153. Carlsbad, NM: U.S. Department of Energy WIPP Project Office (1983).

POSIVA. *Models and Data Report 2010*. POSIVA 2010-01. Posiva Oy, Olkiluoto, Finland (2010).

Raiko, H. Disposal canister for spent nuclear fuel-Design report. *Posiva report*, *2*, p.61 (2005).

Reich S, Leitus G, Shalev S. Measurement of corrosion content of archaeological lead artifacts by their Meissner response in the superconducting state; a new dating method. *New Journal of Physics* **5**, 99.1-99.9 (2003).

Roselle, G.T. Anoxic Corrosion of Steel and Lead in Na-Cl +/- Mg Dominated Brines. Sandia National Laboratories, Albuquerque, New Mexico, SAND2013-3509C (2013).

Semino, C.J., Burkart, A., Garcia, M., Cassibba, R. Galvanic corrosion evaluation of high activity nuclear waste container metals components. Improvements in materials reliability in the back end of the nuclear fuel cycle, 1, p.132, IAEA-TECDOC-686 (1993).

Semino, C.J., Burkart, A.L., Garcia, M.E., Cassibba, R. Lead/carbon steel galvanic corrosion evaluation. *Journal of Nuclear Materials* **238**,198–204 (1996).

Shoesmith, D.W. Assessing the corrosion performance of high-level nuclear waste containers. *Corrosion* **62**, 703–722 (2006).

SKB. *Long-term safety for KBS-3 repositories at Forsmark and Laxemar – a first evaluation*. SKB TR-06-09. Svensk Kärnbränslehantering AB, Stockholm, Sweden (2006).

Stone, W., Kroukamp, O., Moes, A., McKelvie, J., Korber, D.R. and Wolfaardt, G.M. Measuring microbial metabolism in atypical environments: Bentonite in used nuclear fuel storage. *Journal of microbiological methods* **120**, 79–90 (2016a).

Stone, W., Kroukamp, O., McKelvie, J., Korber, D.R. and Wolfaardt, G.M. Microbial metabolism in bentonite clay: saturation, desiccation and relative humidity. *Applied Clay Science* **129**, 54–64 (2016b).

Vicente, R.: Disposal of disused sealed radiation sources in boreholes. WM'07 Conference, February 25 - March 1, 2007, Tucson, AZ (2007).

Wasch, L.J., 2014, Geothermal energy – Scaling potential with cooling and CO_2 degassing. TNO report, TNO 2013R1166, Netherland.

Wersin, P., Spahiu, K. and Bruno, J. *Kinetic modelling of bentonite-canister interaction. Long-term predictions of copper canister corrosion under oxic and anoxic conditions* (No. SKB-TR--94-25). Swedish Nuclear Fuel and Waste Management Co (1994).

Wolery, T.J., Xiong, Y.-L., and Long, J., Verification and Validation Plan/Validation Document for EQ3/6 Version 8.0a for Actinide Chemistry, Document Version 8.10. Carlsbad, NM: Sandia National laboratories. ERMS 550239 (2010).

Xiong, Y.-L., WIPP Verification and Validation Plan/Validation Document for EQ3/6 Version 8.0a for Actinide Chemistry, Revision 1, Document Version 8.20. Supersedes ERMS 550239. Carlsbad, NM. Sandia National Laboratories. ERMS 555358 (2011a).

Xiong, Y., Experimental determination of solubility constant of hydromagnesite (5424) in NaCl solutions up to 4.4 m at room temperature. *Chemical Geology*, *284*(3-4), pp.262-269 (2011b).

Xiong Y. Experimental determination of lead carbonate solubility at high ionic strengths: a Pitzer model description. *Monatshefte für Chemie-Chemical Monthly* **146**, 1433–43 (2015).

Xiong, Y.-L., Domski, P.S. Updating the WIPP Thermodynamic Database, Revision 1, Supersedes ERMS 565730. Carlsbad, NM: Sandia National Laboratories. ERMS 566047 (2016).

Xiong, Y.-L., McInroy, B., Zeitler, T., Clayton, D. DOE Response to EPA Comment 3-C-7 Lead Inventory, Gas Generation and Water Balance. Carlsbad, NM: Sandia National Laboratories. ERMS 564378 (2015).

Xu, D., Tan, X.L., Chen, C.L. and Wang, X.K., 2008. Adsorption of Pb (II) from aqueous solution to MX-80 bentonite: effect of pH, ionic strength, foreign ions and temperature. *Applied Clay Science*, *41*(1-2), pp.37-46.

Yakovenchuk, V.N., Ivanyuk, G.Y., Pakhomovsky, Y.A., Selivanova, E.A., Men'Shikov, Y.P., Korchak, J.A., Krivovichev, S.V., Dar'ya, V.S. and Zalkind, O.A., 2010. Punkaruaivite, $LiTi_2[Si_4O_{11}(OH)](OH)_2{\bullet}H_2O$, a new mineral species from hydrothermal assemblages, Khibiny and Lovozero alkaline massifs, Kola peninsula, Russia. *The Canadian Mineralogist*, *48*(1), pp.41-50.

Yang, S., Zhao, D., Zhang, H., Lu, S., Chen, L. and Yu, X., 2010. Impact of environmental conditions on the sorption behavior of Pb (II) in Na-bentonite suspensions. *Journal of hazardous materials*, *183*(1-3), pp.632-640.

Yuan, K., De Andrade, V., Feng, Z., Sturchio, N.C., Lee, S.S. and Fenter, P., 2018. Pb^{2+}–Calcite Interactions under Far-from-Equilibrium Conditions: Formation of Micropyramids and Pseudomorphic Growth of Cerussite. *The Journal of Physical Chemistry C*, *122*(4), pp.2238-2247.

Zhou, W.-B., Zhang, Z.-S., Li, M.-G. Modeling of water-glass and water-granite interaction in Beishan Area, Northwestern China. *Nuclear Backend Research* **7**, 85–90 (2001).

9. ENHANCEMENT OF THERMAL CONDUCTIVITY OF A BENTONITE BUFFER MATERIAL WITH COPPER MESHES FOR HIGH-LEVEL RADIOACTIVE WASTE DISPOSAL

9.1 Introduction

For the perceivable future, nuclear energy will continue to be an indispensable part of low-carbon energy for human society (Horvath and Rachlew, 2016). Safe disposal of high-level radioactive waste generated from nuclear power plants is critical to the sustainability of nuclear energy industry. In many disposal concepts, nuclear waste is first placed into a metal canister, which is then encased with a layer of bentonite buffer material acting as an engineered barrier to limit water and radionuclide release (Sellin and Leupin, 2013). Given its low thermal conductivity (~0.5 W/mK) (Hardin et al., 2012), this layer of buffer material together with a high heat generation waste package [such as a high burnup dual purpose canister (DPC)] may result in a high temperature on the package surface during the early stage of geologic disposal. A high surface temperature may directly impact the performance of the waste package as well as the surrounding buffer material as engineered barriers for waste isolation (IAEA, 1984). The potential impacts may include an enhanced waste package corrosion and a thermally induced mineral phase transformation of bentonite. Effective heat dissipation from waste packages thus becomes an important consideration for an engineered barrier system design.

Several options have been proposed to mitigate the potential thermal effects. For example, increasing the spacing between waste packages can reduce the surface temperature of a waste package by minimizing the thermal interference from neighboring packages. Thermal management tools have been developed for optimizing the waste loading of disposal footprint and the spacing between waste packages and drifts for a pre-specified thermal limit (Myers et al., 2015). The surface temperature of a waste package can also be reduced by placing the waste package in an interim storage facility for additional cooling before permanent disposal (Hardin et al., 2012). The problem with this approach is that, for a large package (such as a dual-purpose canister, as discussed below), a prohibitively long cooling time may be required. Heat dissipation from a waste package can also be improved by enhancing the thermal conductivity of the surrounding buffer material, for example, by adding a high-conductivity filler material such as quartz, graphite or even graphene to the original bentonite material (Jobmann and Buntebarth, 2009; Chen et al., 2018). However, one caveat with this option is that, to achieve a high thermal conductivity needed for effective heat dissipation, a large volume fraction of filler material is required (Chen et al., 2018). This requirement is dictated by the underlying mechanism for thermal conduction in a granular composite, in which a high thermal conductivity can be achieved only when the volume fraction of the filler material reaches a percolation threshold where the particles of the material become fully connected across the whole physical domain (Pietrak and Wiśniewski, 2015). Based on the percolation theory, the geometrical percolation threshold of overlapping ellipsoids is found to range from 0.2 to 0.6, depending on the aspect ratio of the ellipsoids (Garboczi wt al., 1995; Xie, 2003). Such a high-volume fraction of filler material introduced would inevitably alter the mechanical and hydrological properties of the original buffer material and therefore can potentially compromise the performance of buffer material as an engineered barrier for waste isolation.

9.2 Methods

A semi-analytical method was used in the thermal conduction calculation for an array of 81 DPCs in a crystalline disposal environment (Hardin et al., 2012). The repository is assumed to be at 500 m depth. An average ambient ground surface temperature of 15°C and a natural geothermal gradient of 25°C/km were

used. The disposal concept is based on DPCs placed in overpacks emplaced individually horizontally. The selected geometry for the analysis includes a drift diameter of 5.5 m and a waste package diameter of 2.0 m with 5.6 m length. Thermal conductivity of the crystalline host rock is assumed to be 2.5 W/m-K. Thermal loading of each DPC used in the thermal conduction calculation is given in Figure 9-1. Other parameters used in the calculation include:

- Each DPC contains 37-PWR assemblies with 60 GW-d/MT burnup.
- Drift spacing of 60 m
- Waste package spacing of 20 m (center-to-center)

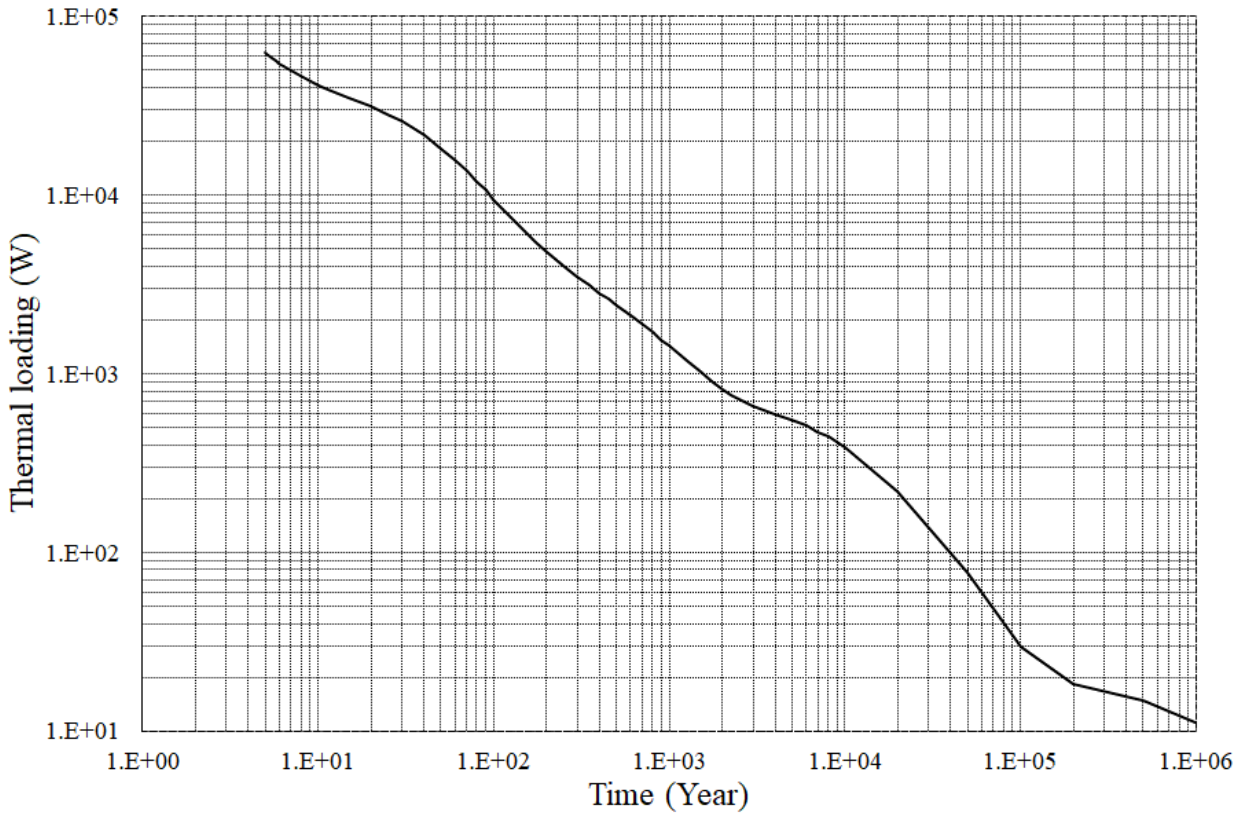

Figure 9-1. Thermal loading of a DPC containing 37 PWR assemblies (Hardin et al., 2012)

9.3 Results

In this communication, we focus on the enhancement of thermal conductivity of a buffer material. Different from any existing approach, in which a high-conductivity filler material is added to a buffer material as embedded particles (Chen et al., 2018), we here propose to use highly conductive copper wires or meshes to ensure the full percolation of the filler material across the whole physical domain of the buffer layer around a waste package to achieve a high heat dissipation rate for the package (Figure 9-2). For illustration, we apply this concept to a DPC.

A DPC is a large welded metal canister of about 2 meters in diameter, 5 meters long and 80 metric tons in weight (Hardin et al., 2015). Each DPC may contain up to 37 PWR assembles. Due to its high waste loading, a DPC is generally required to be cooled on the surface for an extended period, up to hundreds of years, before actual disposal. To evaluate the potential effect of the thermal conductivity of the buffer layer on thermal evolution of a DPC, we have performed heat conduction calculations for an array of DPCs, each containing 37 PWR assemblies, emplaced in a crystalline rock disposal environment (see Methods for details). The result for the central package of the array is presented in Figure 9-3.

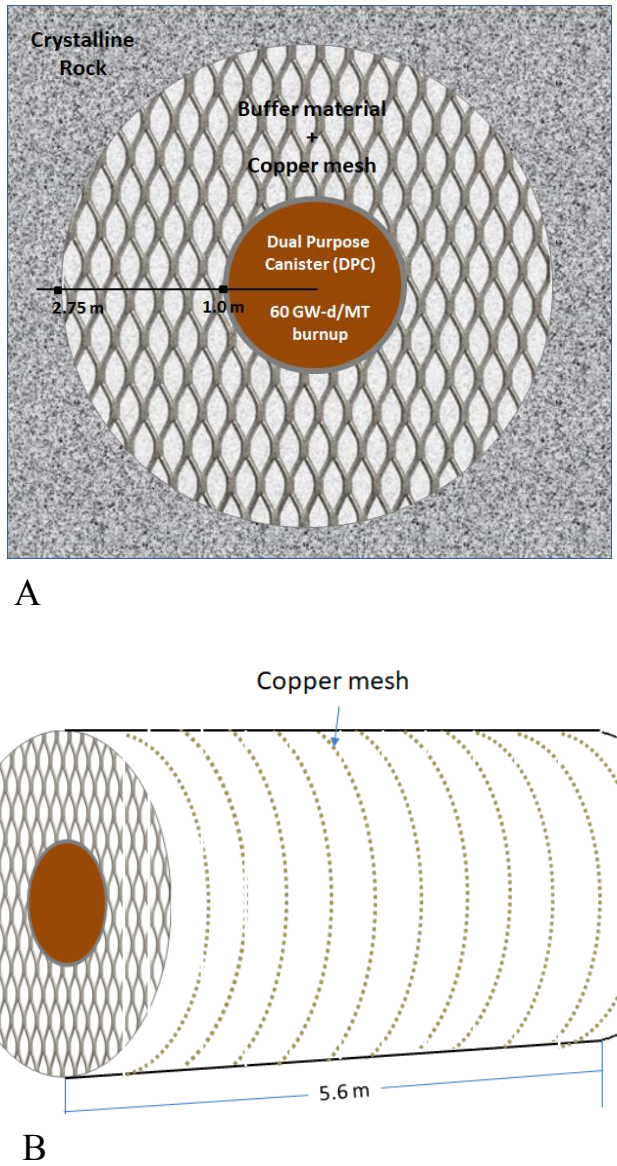

Figure 9-2. Emplacement of a dual purpose canister (DPC) surrounded by a bentonite buffer material with embedded copper meshes in a crystalline disposal environment.

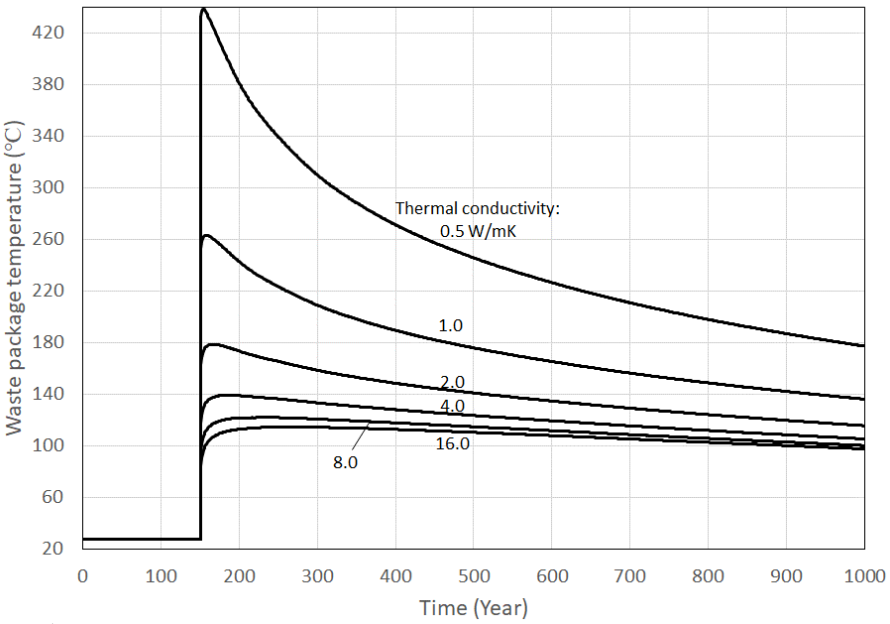

A

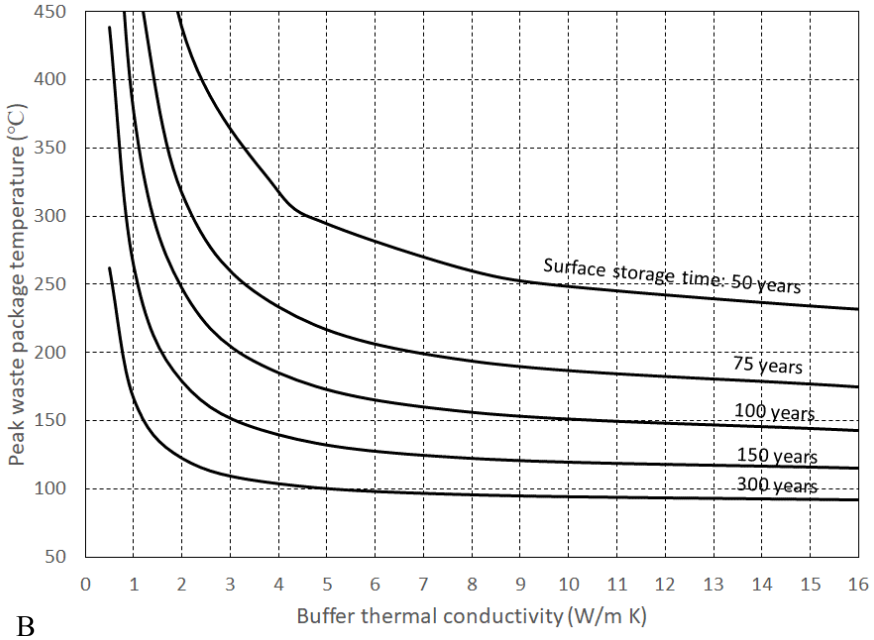

B

Figure 9-3. Surface temperature (A) and peak surface temperature (B) of a central dual purpose canister (DPC) predicted as a function of time or buffer material thermal conductivity. In A, the surface storage time of the DPC is assumed to be 150 years.

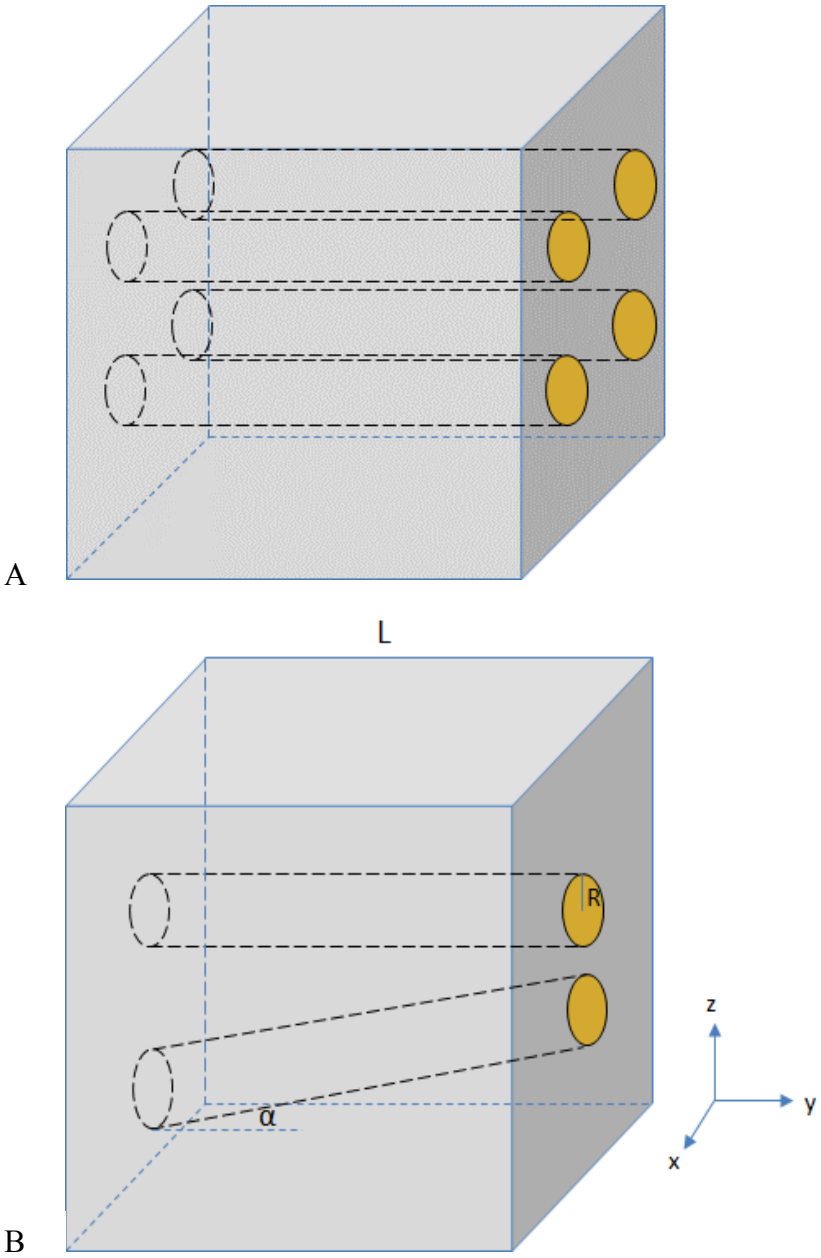

Figure 9-4. Geometric consideration for calculating effective thermal conductivity of bentonite with embedded copper wires.

The result shows that the peak surface temperature attains immediately after DPC emplacement (Figure 9-3A). This temperature highly depends on both surface storage time and the thermal conductivity of the buffer material (Figure 9-3B). Given a typical thermal conductivity of compacted bentonite (~0.5 W/mK) (Hardin et al., 2012), the peak surface temperature is predicted to reach up to 440 °C even if the canister has been cooled for 150 years prior to disposal (Figure 9-3A). Experimental observations indicate that at such a high temperature the swelling property of bentonite could significantly be altered (Yilmaz, 2011). Figure 9-3 shows that the enhancement of thermal conductivity of buffer material can reduce the peak

surface temperature by up to 300 °C. It is interesting to notice that this effect seems to level off beyond a thermal conductivity ranging from 5 to 10 W/mK, indicating that beyond this value the heat dissipation of a waste package becomes more limited by the ambient rock. This value is thus an optimal value we need to achieve for buffer material improvement.

Now we want to show that this value of thermal conductivity can be easily achieved by embedding a small volume fraction of copper wires or meshes into the buffer material layer. Let's examine a simple case where a parallel set of copper wires are embedded into a bentonite block as shown in Figure 9-4A. The effective thermal conductivity of the block can be calculated using Rayleigh's model (Pietrak and Wiśniewski, 2015):

$$k_e^{\parallel} = k_b + (k_c - k_b)\phi \quad (9\text{-}1)$$

$$k_e^{\perp} = k_b + \frac{2\phi}{C_1 - \phi + C_2(0.30584\phi^4 + 0.0013363\phi^8 + \cdots)} \quad (9\text{-}2)$$

with

$$C_1 = \frac{k_c + k_b}{k_c - k_b} \text{ and } C_1 = \frac{k_c - k_b}{k_c + k_b}$$

where $k_e^{\parallel}$ and $k_e^{\perp}$ are the effective thermal conductivities of bentonite with embedded copper wires in the directions parallel and perpendicular to the wires, respectively; k_b and k_c are the thermal conductivities of bentonite and metallic copper, respectively; and ϕ is the volume fraction of copper wires. For a wire oblique to the surface of the bentonite block, as shown in Figure 3B, the cross-section area of the wire on the surface of the bentonite block becomes $\pi R^2/\cos(\alpha)$. On the other hand, the wire length is increased to $L/\cos(\alpha)$. (See Figure 9-4B for the definition of parameters R, L, and α). As a result, the heat flux of an oblique wire is equivalent to that of a perpendicular wire. Thus, the thermal conductivity of the bentonite block is determined only by the number of copper wires that intercept both sides of the block, implying that equations (9-1) and (9-2) can apply to copper meshes. For a buffer layer surrounding a cylindric waste canister as shown in Figure 1, $k_e^{\parallel}$ and $k_e^{\perp}$ are the radial and axial thermal conductivities of the buffer material, respectively.

Using Equations (9-1) and (9-2), we have calculated the effective thermal conductivities of a bentonite layer with copper meshes embedded as a function of the volume fraction of copper, as compared to that experimentally determined value for a bentonite-graphene composite (Chen et al., 2018) (Figure 9-5A). It is clearly shown that, for a given volume fraction of an introduced material, copper meshes in the direction parallel to the meshes greatly outperform graphene. This is because, unlike graphene powder, which relies exclusively on the volumetric percolation, copper meshes ensure the full percolation from one side of the buffer material layer to another side. Remarkably, to achieve a needed thermal conductivity of ~5 W/mK, we only need to add 1 v% of copper meshes, much less than 20 v% needed for graphene. It is reasonable to expect that with such a small fraction of copper added the alteration to the mechanical and hydrological properties of the original bentonite material is expected to be minimal. In addition, the material cost for copper (~ $6/kg) is much less than that for graphene (> $100/kg).

Then the next question would be how many copper wires are needed for a unit cross-section area of a bentonite layer. For illustration, let's choose the wire diameter to be 2 mm. To attain 1% of copper volume, 1 m^2 cross-section area of bentonite layer needs to contain ~3185 copper wires. Thus, the spacing of the wires is about 1.8 cm, which can be viewed as either of the mesh size (the hole size) or the spacing between the neighboring meshes (Figure 1). Increasing the wire diameter would increase both the mesh size and the mesh spacing. Of course, the mesh size and the spacing between meshes don't have to be the same. By

reducing the mesh size, one can increase the spacing between the meshes, while maintaining a constant volume fraction of copper.

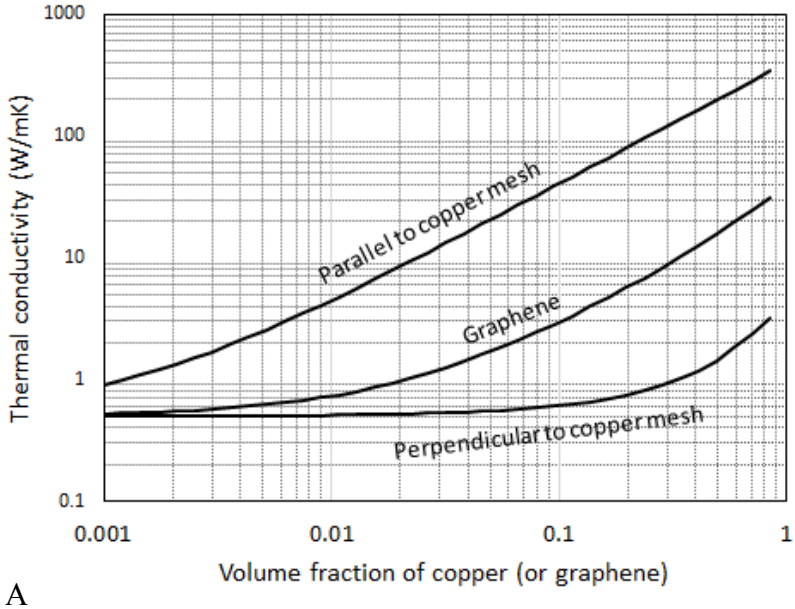

A

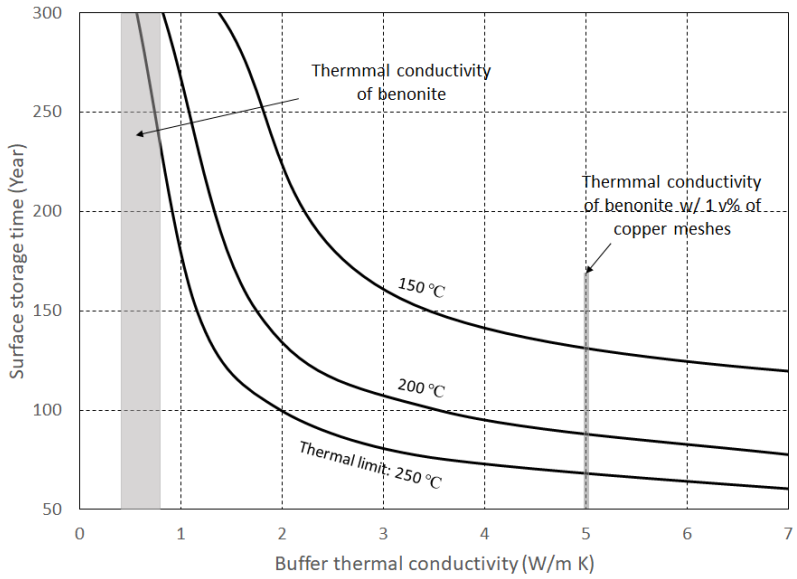

B

Figure 9-5. Effective thermal conductivity of bentonite calculated as a function of volume fraction of copper meshes embedded (A) and its effect on surface storage time of a waste package (B). Experimentally determined thermal conductivity for bentonite-graphene composite are from Chen et al., (2018). Thermal conductivities for copper and bentonite are chosen to be ~ 400 W/mK (Engineering ToolBox, 2005) and 0.5 W/mK (Hardin et al., 2012), respectively.

Figure 9-5B shows the effect of the thermal conductivity of buffer material on the surface storage time required for a DPC containing 37 PWR assemblies prior to permanent disposal in a crystalline disposal environment for various thermal limits. Let's choose a thermal limit of 200 ℃. This is a reasonable choice, since existing experimental observations indicate that the swelling index of bentonite would not significantly change until the temperature goes beyond 200 ℃ (Yilmaz, 2011). It can be seen in Figure 4B that adding 1 v% copper meshes is sufficient to reduce the required surface storage time from more than 300 years to ~ 75 years, thus significantly accelerating the process for direct disposal of DPCs and reducing the overall cost for disposal. Our calculation shows that this storage time can further be reduced to ~50 years by increasing the thermal conductivity to 10 W/mK, if we can expand the thermal limit for bentonite to 250 ℃.

9.4 Discussions

Two additional advantages can be incurred for using copper meshes. There is a concern with bentonite erosion that could potentially be caused by a dilute water intrusion into a repository system during a glaciation-deglaciation period (Neretnieks et al., 2009). In this case, the introduced copper meshes will reinforce the mechanical strength of bentonite strength and therefore minimize a potential bentonite erosion if it happens. In addition, in some design concepts, a waste canister will be fabricated with an inner layer of cast iron and an outer shell of metallic copper (30−50 mm in thickness) (Hedman et al., 2002). Despite its thermodynamic resistance to corrosion in anoxic environments, copper is known for being liable to sulfide-induced corrosion (Kong et al., 2017). The introduced copper meshes may help mitigate this potential problem. For a heat-generating waste, the evolution of a disposal system can be divided into an early thermal pulse period and a post-thermal pulse period (Zheng et al., 2015). The thermal pulse will generally lead to a drying out period for the buffer material. In this period, the introduced copper meshes will serve as an excellent heat conductor for heat dissipation of a waste canister. After the thermal pulse, if the groundwater contains dissolved sulfide, the introduced copper meshes can also serve as a sacrificial material for sulfide-induced corrosion, therefore protecting the outer copper layer of a waste canister from sulfide attack.

9.5 Conclusions

In high-level radioactive waste disposal, a heat-generating waste canister is generally encased with a layer of bentonite-based buffer material acting as an engineered barrier to limit water percolation and radionuclide release. The low thermal conductivity of bentonite (~ 0.5 W/mK) combined with a high thermal loading waste package may result in a high surface temperature on the package that can potentially impact the structural integrity of the package itself as well as the surrounding buffer material. We here show that the thermal conductivity of bentonite can be effectively enhanced by embedding copper meshes across the buffer layer to form fully connected high heat conduction pathways. A simple calculation based on Rayleigh's model indicates that a thermal conductivity value of 5 W/mK required for effective heat dissipation can be achieved simply by adding ~ 1 v % of copper meshes into bentonite. As a result, the peak surface temperature on a large waste package such as a dual-purpose canister can be reduced by up to 300 ℃, thus significantly reducing the surface storage time for waste cooling and therefore the overall cost for direct disposal of such waste packages. Because of the ensured full thermal percolation across the buffer layer, copper meshes turn out to be much more effective than any other materials currently suggested (such as graphene or graphite) in enhancing thermal conductivity of buffer material. Furthermore, the embedded copper meshes will help reinforce the mechanical strength of the buffer material, thus preventing the material from a potential erosion by an intrusion of dilute groundwater.

9.6 References

Chen, Y.-G., Liu, X.-M., Mu, X., Ye, W.-M., Cui, Y.-J., Chen, B., and Wu, D.-B. (2018) Thermal conductivity of compacted GO-GMZ bentonite used as buffer material for a high-level radioactive waste repository. Advances in Civil Engineering, 9530813.

Engineering ToolBox (2005) Thermal Conductivity of Metals, Metallic Elements and Alloys. Available at: https://www.engineeringtoolbox.com/thermal-conductivity-metals-d_858.html.

Garboczi, E. J., Snyder, K. A., Douglas, J. F. and Thorpe, M. F. (1995) Geometrical percolation threshold of overlapping ellipsoids. Physical Review E, 52(1), 819-828.

Hardin, E., Hadgu, T., Clayton, D., Howard, R., Greenberg, H., Blink, J., Sharma, M., Sutton, M., Carter, J., Dupont, M. and Rodwell, P. (2012) Repository Reference Disposal Concepts and Thermal Load Management Analysis. Sandia National Laboratories, Albuquerque, New Mexico, USA, FCRD-UFD-2012-000219 Rev. 2.

Hardin E., Banerjee, Carter, J., Clark, R., Clarity, J., Howard, R., Kalinina, E, and Scaglione, J. (2015) Investigations of dual-purpose canister direct disposal feasibility. WM2015 Conference, March 15-19, 2015, Phoenix, Arizona, USA.

Hedman, T., Nyström, A., and Thegerström (2002) Swedish containers for disposal of spent nuclear fuel and radioactive waste. C. R. Physique, 3, 903-913.

Horvath, A. and Rachlew, E. (2016) Nuclear power in the 21st century: Challenges and possibilities. Ambio, 45(S1), S38–S49; DOI 10.1007/s13280-015-0732-y.

IAEA (1984) Effects of Heat from High-Level Waste on Performance of Deep Geological Repository Components. International Atomic Energy Agency, Vienna, IAEA-TECDOC-319.

Jobmann, M. and Buntebarth, G. (2009) Influence of graphite and quartz addition on the thermo-physical properties of bentonite for sealing heating-generating radioactive waste. Applied Clay Science, 44, 206-210.

Kong, D.-C., Dong, C.-F., Xiao, K., and Li, X.-G. (2017) Effect of temperature on copper corrosion in high-level nuclear waste environment. Trans. Nonferrous Met. Soc. China, 27, 1431-1438.

Myers, S., Holton, D. and Hoch, A. (2015) Thermal dimensioning to determine acceptable waste package loading and spatial configurations of heat-generating waste packages. Mineralogical Magazine, 79(6), 1625-1632.

Neretnieks, I., Liu, L., Moreno, L. (2009) Mechanisms and models for bentonite erosion. Swedish Nuclear Fuel and Waste Management Co., TR-09-35.

Pietrak, K. and Wiśniewski, T. S. (2015) A review of models for effective thermal conductivity of composite materials. J. Power Technologies, 95(1), 14-24.

Sellin, P. and Leupin, X. L. (2013) The use of clay as engineered barrier in radioactive-waste management – A review. Clays and Clay Minerals, 61(6), 477-498.

Xie, Q. (2003) A percolation model of metal-insulator composites. Physica B, 325, 195-198.

Yilmaz, G. (2011) The effects of temperature on the characteristics of kaolinite and bentonite. Scientific Research and Essays, 6(9), 1928-1939.

Zheng, L., Rutqvist, Birkholzer, J. T., and Liu, H.-H. (2015) On the impact of temperatures up to 200 °C in clay repositories with bentonite engineer barrier systems: A study with coupled thermal, hydrological, chemical, and mechanical modeling. Engineering Geology, 197, 278-295.

10. PROCESS MODEL FOR RADIONUCLIDE INCORPORATION INTO CORROSION PRODUCTS

10.1 Introduction

This progress report (Level 4 Milestone Number M4SF-20LL010302042) summarizes research conducted at Lawrence Livermore National Laboratory (LLNL) within the Crystalline Activity Number SF-20LL010302041. The research is focused on actinide and radionuclide sequestration in steel corrosion products.

Fuel matrix degradation models suggest that the near field is likely to be reducing at the time of canister breaching, steel corrosion, and radionuclide release, but more oxidizing conditions may prevail in the far field. The incorporation of radionuclides into corrosion phases may limit the rate of radionuclide release by sequestering a portion of the radionuclide source term. For these reasons there is a need to evaluate the incorporation of Pu and other radionuclides into various Fe-oxide phases, and to understand the behavior of coprecipitated phases during mineral recrystallization processes and during re-oxidation events. Radionuclide coprecipitation with Fe minerals may impact long-term repository performance and is an ongoing research focus at Lawrence Livermore National Laboratory.

The effort described in this document is focused on identifying:

- The fate of plutonium during ferrihydrite to goethite recrystallization reported as a summary of a paper that will be submitted for publication at the end of June 2020
- Preliminary results on the coprecipitation of plutonium with magnetite and its behavior during exposure to oxidative solutions

Additionally, part of our effort for FY20 is focused on performing an assessment to identify the most critical radionuclides and data gaps associated with radionuclide interaction with corrosion products. Our goal is to summarize how radionuclides are expected to interact with Fe minerals relevant for the safety assessment of a geological repository. Upon completion of this assessment, we plan to perform supplementary experiments with radionuclides identified as playing a central role in repository performance assessment and to fill the knowledge gap. The radionuclides of interest include Tc, Se, Cl, I, and Np. Synthesis methods developed for Pu incorporation into oxidized and reduced iron oxide phases can be directly applied to radionuclides of specific interest to GDSA efforts. Here we report our literature review on Se and Tc interactions with various Fe minerals.

In addition to the corrosion effort, we planned to complete our analysis and modeling of Np(IV) diffusion through bentonite buffer material and provide diffusivity and retardation parameters for use in GDSA. These data are the first attempt to quantify the diffusion of the dominant Np oxidation state likely to be present under reducing repository conditions (i.e. Np(IV)). However, due to limited access to LLNL laboratories during the COVID-19 pandemic, completion of this task has been delayed and results will only become available in FY21.

10.2 Plutonium fate during ferrihydrite to goethite recrystallization

The fate of radionuclides, including Pu, during mineral formation and recrystallization processes is still not fully understood. Gaining a detailed, mechanistic, understanding of the interactions between iron (oxy)hydroxides and Pu is key to predicting the long-term stability and mobility of Pu in the natural and engineered environment.

The goal of this work is to assess the fate of Pu during the ubiquitous process of ferrihydrite to goethite recrystallization. We synthesized ferrihydrite with various amounts of Pu(IV) (3000, 1000 and 400 ppm) following either a coprecipitation (FH_C-3000, FH_C-1000, FH_C-400) or sorption process (FH_S-3000, FH_S-1000, FH_S-400), and then subsequently used this material to crystallize goethite (goethite samples recrystallized from Pu coprecipitated ferrihydrite: G-FH_C-3000, G-FH_C-1000, G-FH_C-400; goethite samples recrystallized from Pu sorbed ferrihydrite: G-FH_S-3000, G-FH_S-1000, G-FH_C-3000). We provide detailed extended x-ray absorption fine structure (EXAFS) spectroscopy, transmission electron microscopy (TEM) and acid leaching analysis to elucidate the nature of plutonium association with ferrihydrite and goethite.

Our results show that variations in synthetic routes have impacts on the nature of Pu associated with both the ferrihydrite precursor and the ferrihydrite recrystallization product (goethite). When a Pu containing solution is added to a ferrihydrite mineral (sorption route), a fraction of the Pu precipitates as PuO_2 nanoparticles and the remaining Pu fraction forms a complex on the mineral surface. After hydrothermal alteration to goethite, the PuO_2-like nanoparticles are preserved while a fraction of Pu is still present as a surface adsorbed species on the goethite mineral surface (Table 10-1, Figure 10-1). There is evidence that this adsorbed species is more weakly bound to goethite than to ferrihydrite, as evidenced by a decrease in the number of Pu-Fe scatterers identified in the respective sample (the LIII-edge EXAFS data and fit results for selected samples are reported in Figures 10-2 and 10-3). This observation suggests that Pu adsorbed to ferrihydrite may be mobilized during the recrystallization processes. The analysis of the supernatant after hydrothermal alteration of ferrihydrite to goethite showed a small increase in Pu concentration confirming that some Pu re-mobilization occurs during the mineral recrystallization process.

When ferrihydrite is precipitated directly from a solution containing Fe and Pu (coprecipitation route), no PuO_2-like nanoparticles are observed (Table 10-1). Although it is difficult to identify the exact nature of Pu in the sample due to a high degree of disorder, there is evidence that Pu is strongly bound to the ferrihydrite solids through a combination of adsorption and/or coprecipitation as evidenced by the high number of Pu-Fe scatters. In this sample, a fraction of Pu could coprecipitate with ferrihydrite and/or form a polynuclear inner sphere complex. The EXAFS data show that the Pu binding site changes significantly during ferrihydrite recrystallization to goethite, indicating that Pu is mobilized during hydrothermal alteration. However, only a small fraction of Pu in the highest Pu concentration sample (G-FH_C-3000) is remobilized to form PuO_2. In the lower concentration goethite samples (G-FH_C-1000, G-FH_C-400) Pu is strongly sorbed (either coprecipitated and/or adsorbed as inner sphere complex) to the goethite as evidenced by the high number of Pu-Fe scatterers, and PuO_2 is not observed. The acid leaching results support this conclusion by showing that less Pu is accessible to leaching in goethite formed via coprecipitation process, compared to the goethite formed via the sorption process. These observations confirm that that the nature of Pu associated with the mineral will affects the leachability of Pu from the solids (Figure 10-4).

Overall the results presented in this study provide valuable new insights into Pu(IV)- iron (oxy)hydroxide interactions in the natural and engineered environment and highlight the importance of understanding the fate of radionuclides during mineral recrystallization processes.

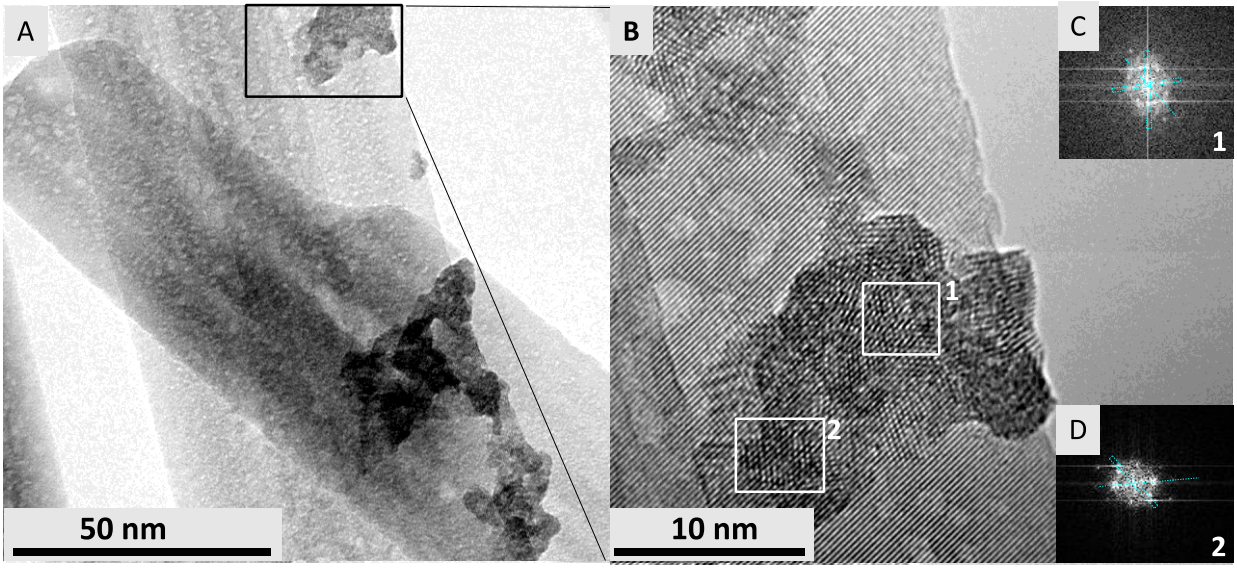

Figure 10-19. Pu nanoparticles on goethite G-FH$_S$-3000. (A) Low-magnification TEM image of large tabular goethite and intrinsic Pu nanoparticles (black inlet). (B) HRTEM image of Pu nanoparticles on goethite surface from inlet in (A); (C) and (D) FFT of HRTEM area 1 and 2 shown in panel (B), is consistent with the *fcc*, PuO_2 structure.

Table 10-8. Summary of EXAFS fits

Sample	Shell	N	R (Å)	σ^2 (Å^2)	E0 (eV)	*R* (%)
FH_S-3000	Pu-O	9(1)	2.31(1)	0.014(1)	-10.8(8)	8.0
	Pu-Fe	6(2)	3.39(1)	0.021(4)		
	Pu-Pu	3(1)	3.79(1)	0.008(1)		
FH_C-3000	Pu-O1	4.0(2)	2.41(1)	0.0053(7)*	-11.0(4)	3.5
	Pu-O2	3.0(1)	2.24(1)			
	Pu-Fe	8(1)	3.39(1)	0.023(2)		
G-FH_S-3000	Pu-O	8(1)	2.32(1)	0.010(1)	-11.4(8)	10.2
	Pu-Pu	4(1)	3.80(1)	0.003(1)		
G-FH_S-1000	Pu-O	8(1)	2.32(1)	0.008(1)	-11.7(7)	9.9
	Pu-Pu	4(1)	3.81(1)	0.001(1)		
G-FH_C-3000	Pu-O	6(1)	2.28(1)	0.013(2)	-12.6(12)	8.7
	Pu-Fe	1(1)	3.56(1)	0.003(4)		
	Pu-Pu	2(1)	3.80(1)	0.001(1)		
G-FH_C-1000	Pu-O	5(1)	2.21(1)	0.013(2)	-10.0(16)	13.3
	Pu-Fe	6(1)	3.17(4)	0.01(1)*		
	Pu-Fe	10(8)	3.49(2)			
G-FH_C-400	Pu-O	6(1)	2.20(2)	0.016(2)	-7.6(21)	12.2
	Pu-Fe	5(3)	3.19(2)	0.015(6)*		
	Pu-Fe	8(4)	3.47(2)			

* Indicates a tied σ^2 parameter (i.e. shared in two shells). N represents the coordination number assuming an amplitude reduction factor of 1; R denotes the interatomic distance; σ^2 represents the Debye Waller factor; ΔE0 represents the energy shift from the calculated energy fermi level.

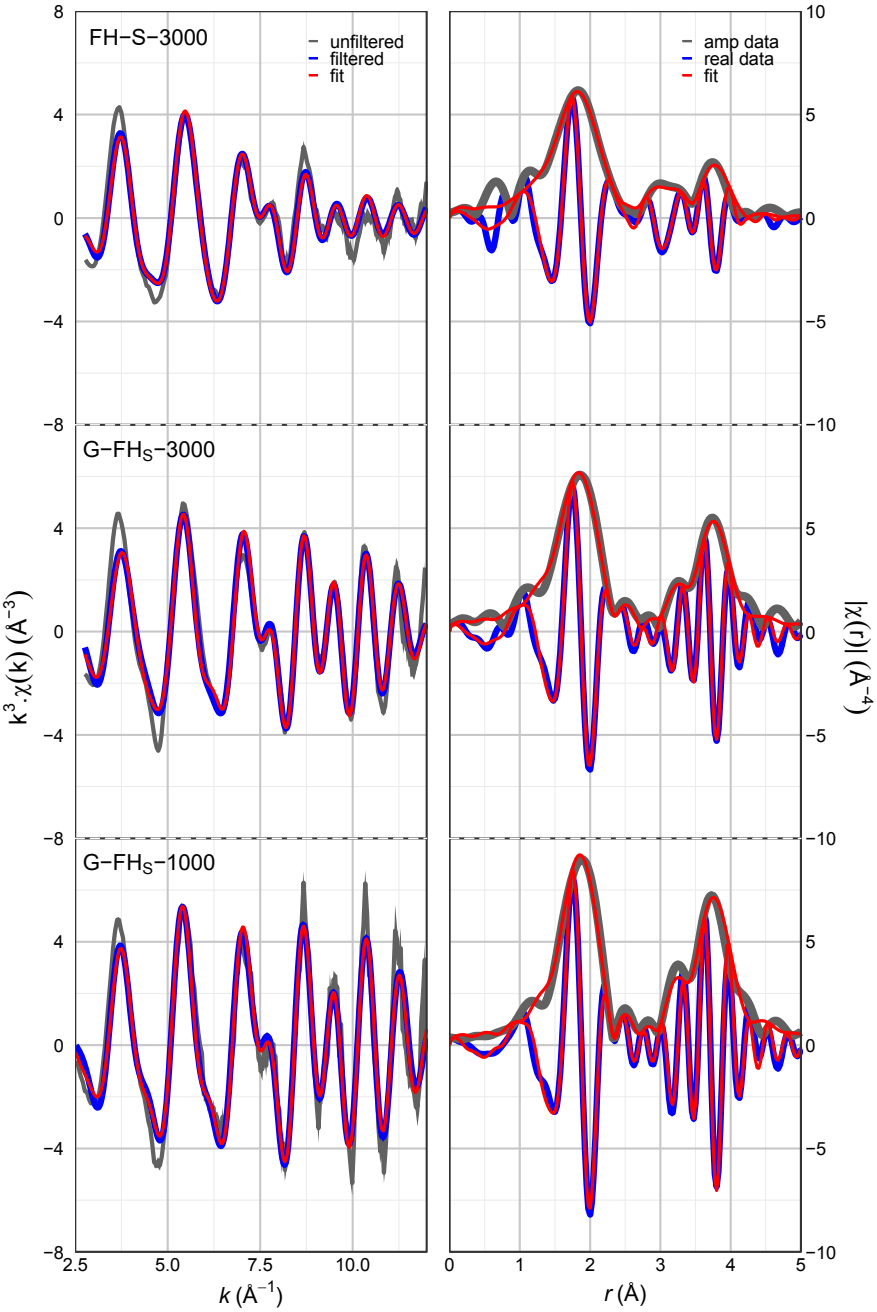

Figure 10-2. Pu L_{III}-edge EXAFS data and fit results for samples synthesized following the sorption method measured at 30 K. Left: Fourier transforms (FT) of the k-space data and fit. Vertical dashed lines indicate the fit range. Data were transformed between 2.5 and 12.5 $Å^{-1}$ by using a Gaussian window with a width of 0.3 $Å^{-1}$. The raw unfiltered data error bars (encompassed by the solid gray shaded area around the data set) were estimated by the standard deviation of the mean between traces. Right: EXAFS results in k-space. The filtered data and fit were back-transformed over the fit range.

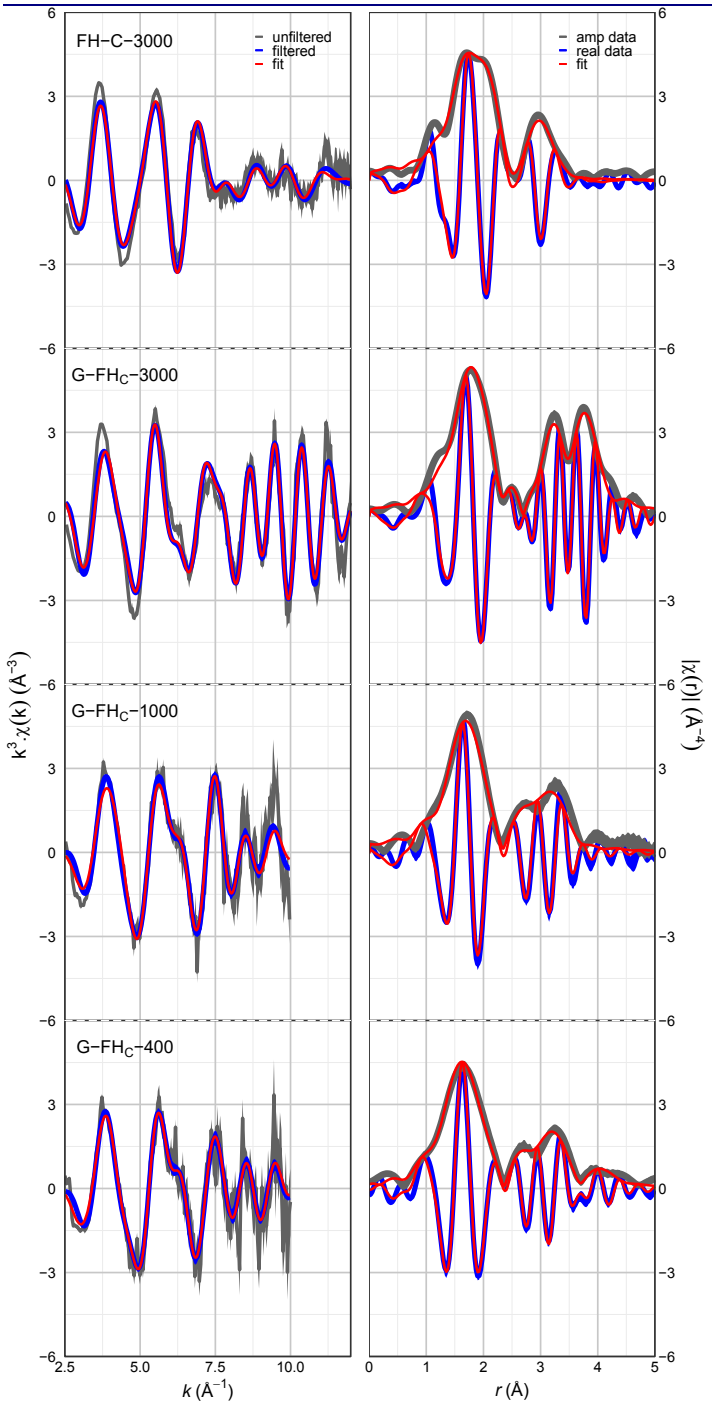

Figure 10-3. Pu L_{III}-edge EXAFS data and fit results for samples synthesized following the coprecipitation method measured at 30 K. Left: Fourier transforms (FT) of the k-space data and fit. Vertical dashed lines indicate the fit range. Data were transformed between 2.5 and a maximum of 12.5 $Å^{-1}$ by using a Gaussian window with a width of 0.3 $Å^{-1}$. The raw unfiltered data error bars (encompassed by the solid gray shaded area around the data set) were estimated by the standard deviation of the mean between traces. Right: EXAFS results in k-space. The filtered data and fit were back-transformed over the fit range.

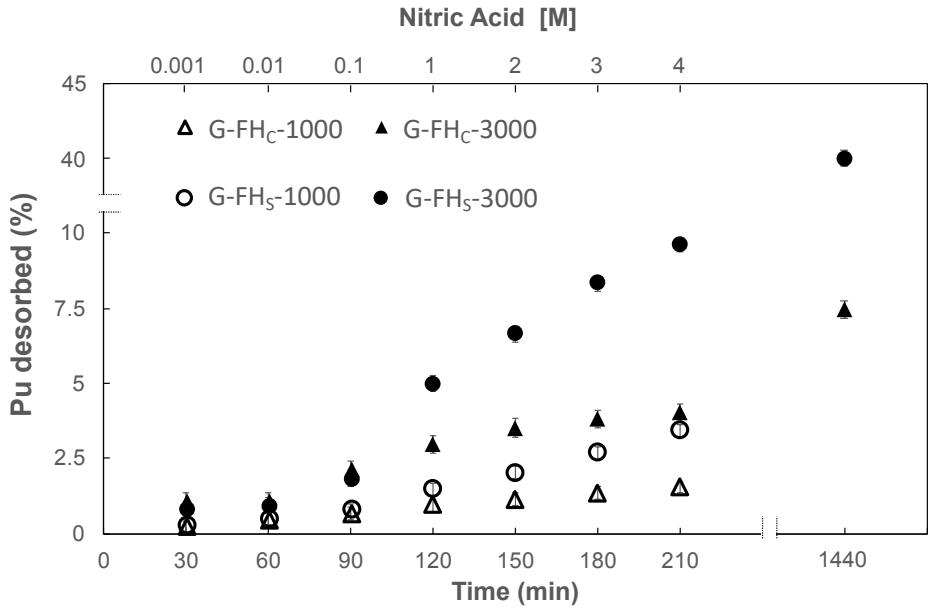

Figure 10-4. Leaching behavior of Pu in acidic solutions (0.001-4M) for goethite synthesized following the sorption (G-FH_S-3000, G-FH_S-1000) and coprecipitation (G-FH_C-3000, G-FH_C-1000) method. The acid leaching results show that overall more Pu is leached from goethite hydrothermally aged from ferrihydrite synthesized following the sorption than the coprecipitation method. A total of 9.6 ± 0.2% and 3.42 ± 0.3% are leached from G-FH_S-3000 and G-FH_S-1000, respectively, whereas in comparison 4.03(12)% and 1.54(8)% of Pu are leached in solution from G-FH_C-3000 and G-FH_C-1000, respectively. After 24 hours of leaching in 4 mol/L HNO_3, a total of 40(1)% of Pu is leached from G-FH_S-3000; whereas only 7.5(5)% of total Pu is leached from G-FH_C-3000.

10.3 Magnetite coprecipitation with plutonium: preliminary results

Pu-doped magnetite was synthesized in an anaerobic glovebox using a 0.1 M Fe(II)Cl_2 and 0.2 M Fe(III)Cl_3 prepared by dissolving the Fe salts in a degasses 0.3 M HCl solutions. An aliquot of ^{242}Pu(IV) 1.3×10^{-3} M solution was added to the Fe(III)Cl_3 solution prior to formation of any visible precipitate to achieve a Pu concentration of ~500 ppm in the solid.

The Fe(II) and Fe(III)/Pu solutions were slowly mixed on a stir plate to achieve a Fe(II)/Fe(III) molar ratio of 0.6. The pH of the mixed Fe(II)/Fe(III) solution was adjusted to ~9 using a degassed NH_4OH solution (28%v). The final product consisted of a black suspension that was left stirring for two hours in the glovebox (Mg-500). After two hours 1mL aliquot was centrifuged at 6000 rpm for 10 minutes, and results show that >99.9% Pu is associated with the solid (pH of mother liquor between 8-9). Pu aqueous concentration was measured for up to 60 days, but no significant changes were observed from the initial measurements suggesting that Pu is strongly associated to magnetite.

Aliquots of Pu-doped mineral suspensions of magnetite were rinsed from the synthetic mother liquors with degassed DI water and equilibrated with low ionic strength solution (10^{-3} mol/L $NaHCO_3$ and 5 Å~10^{-3} mol/L NaCl and pH 8) in a 0.1 g/10 mL suspension. The low ionic strength solution was degassed and

stored in anaerobic conditions. Replicate samples were exposed to oxygenated atmosphere conditions and were placed on rotators. The samples were oxygenated every two days by opening the sample vials and letting the solution equilibrate with the atmosphere. After 24 hours, 7 days, 14 days and 30 days, aliquots of the mineral suspension were centrifuged (6000 rpm, 10 minutes) and the aqueous Pu in suspension was measured. After 30 days 99% of Pu remains associated with the solid.

Aliquots of as synthesized magnetite (Mg-500) and of magnetite oxidized for 30 days (Mg-500-ox) were prepared for analyses at the Stanford Synchrotron Radiation Lightsource, Stanford (CA) and preliminary results are reported below. Figure 10-5 shows the background subtracted EXAFS data collected on Mg-500, as well as the corresponding Fourier transform. The data were modeled (Table 2) using two shells: 10(3) O scatterers at 2.53 Å; and 6(4) Fe scatterers at 3.57 Å. Due to time constraints during data collection, the data are of low quality so results are to be interpreted carefully. However, some information can be drawn from this dataset. The Pu-O distance of 2.52(3) Å is slightly larger that Pu(III)-O as expected in Pu(III) aqueous complexes (PuIII-O aq= 2.49 Å)[1] but could be indicative of a Pu(III) complex associated with the magnetite solid. The presence of Pu-Fe scatterers suggests that this complex may be strongly bound to the magnetite surface.

Figure 10-6 shows the background subtracted Pu LIII-edge EXAFS and corresponding Fourier transform (FT) for Pu coprecipitated with magnetite that was subsequently oxidized for 30 days. An unconstrained fit to the data is shown in Table 2. The data could be described with a 3 shell fit. These shells consisted of 2(2) Pu-O scatterers at 1.73(3) with a σ^2 of 0.01(3) Å.[2] The second shell was with 4(1) Pu-O scatters at 2.49 Å and the final shell was fit with 6(2) Pu-Fe scatterers at 3.54 Å. There is an indication in the sample of Pu-O_{ax} scatterers strongly implying that some plutonyl species are present in this sample however due to the large error bar associated with this value we are unable to accurately quantify the extent of oxidation. Furthermore, the Pu-O and Pu-Fe interatomic distances and the number of Pu-Fe scatterers correspond to the work presented in Kirsch et al. 2011[1] who interpreted their data as Pu(III) binding to the magnetite surface in a tridentate, trinuclear complex.

Analysis of the supernatant after 30 days of oxidation experiments showed that less than 1% Pu is released to solution during 30 days oxidation, suggesting that Pu associates strongly to magnetite and is retained upon exposure to oxidative conditions. Further efforts will need to be done to obtain higher quality x-ray absorption spectroscopy data. Increasing Pu concentration in the samples should improve data quality and reduce acquisition time.

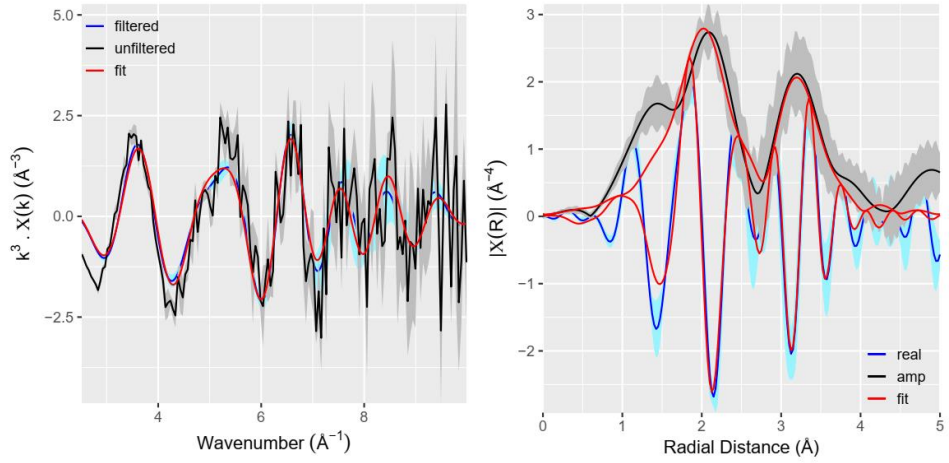

Figure 10-5. Left: background subtracted EXAFS collected on Mg-500. Right: corresponding Fourier transform. Fit was unconstrained.

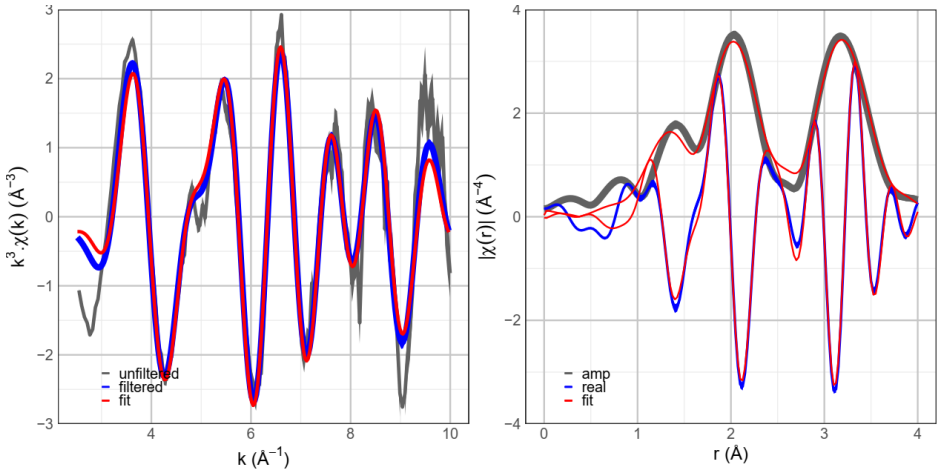

Figure 10-6. Pu coprecipitated with magnetite and subsequently oxidized. Left: Background subtracted Pu L_{III}-edge EXAFS. Right: Corresponding Fourier transform.

Table 10-9. Fitting statistics associated with Mag-500 and Mag-500-ox

Sample	Shell	N	R(Å)	σ^2 (Å^2)	E0 (eV)	*R* (%)
Mg-500	Pu-O	10(3)	2.52(3)	0.025(6)	-8.0	16.55
	Pu-Fe	6(4)	3.57(5)	0.01(1)		
Mg-500-ox	Pu-O	2(2)	1.73(3)	0.01(3)	-3.4(17)	9.97%
	Pu-O	4(1)	2.49(2)	0.011(4)		
	Pu-Fe	6(2)	3.54(1)	0.011(3)		

10.4 Technetium interactions with iron oxide minerals

10.4.1. Technetium inventory

Technetium (^{99}Tc) is a long lived (2.1×10^5 years), high yield (6%) fission product.[2-4] Atmospheric nuclear testing resulted in ~100 to 140 TBq of ^{99}Tc released to the atmosphere, much of which has been deposited and incorporated into sediments, and ~ 1000 TBq of ^{99}Tc (1 PBq) has been released through reprocessing of spent fuel.[5] At the Hanford Site, Washington State, nearly 1990 kg of ^{99}Tc (or 1.25 PBq) was produced between 1943 and 1987 and are waiting for final disposition.[6] Tc also continues to accumulate in large amounts due to active nuclear power generation with 21 kg of ^{99}Tc (13.2 TBq) produced annually in a large 1 GWe reactor.[2]

10.4.2. Oxidation state

Tc is a redox-sensitive element and its solubility and mobility in subsurface waters depend strongly on its oxidation state. The fundamental measurement that describes the stability of reduced and oxidized Tc is the TcO_4^-/TcO_2 couple expressed as[7]:

$$TcO_4^- + 4H^+ + 3e^- = TcO_2\,(s) + 2H_2O \qquad E_0 = 0.747\pm0.004V$$

The pertechnetate anion ($^{99}TcO_4^-$) is highly soluble in aqueous solution (~11 mol/L) and occurs in oxidizing environment (>200 mV) or when exposed to the atmosphere[8]. Even in its reduced oxidation state, Tc(IV) solubility (Tc =3.08×10^{-9} M or ~5200 pCi/L; ~190 Bq/L;[7]) does not restrict Tc concentrations to below the drinking water standard of 900 pCi/L (or 5.3X10-^{10}mol/L; ~33 Bq/L [9]).

While the predominance of reducing conditions is necessary for Tc reduction, the availability of electron donors is far more critical. For example, Cui and Eriksen, 1996 [10] showed that even under conditions in which ferrous iron (Fe(II)) activity in solution was relatively high, reduction kinetics of Tc(VII) were sluggish. In contrast, when Fe(II) is sorbed onto other mineral phases, surface-mediated heterogeneous catalysis becomes important and reduction of Tc(VII) to Tc(IV) takes place rapidly above pH 6.[11-13] The rapid disproportionation of Tc in valence states between (VII) and (IV) also inhibits the reduction of Tc(VII) and hinders complete transformation to Tc(IV) unless other factors come into play, such as surface-mediated catalysis:

3Tc(V) = 2Tc(IV) + Tc(VII)
3Tc(VI) =Tc(IV) +2Tc(VII)

Overall technetium (^{99}Tc) presents unique challenges to nuclear waste disposal due to the environmental mobility of pertechnetate (TcO_4^-) under aerobic conditions.[2-4]

10.4.3. Precipitation of Tc compounds and their solubility

The crystalline dioxide TcO_2 and its hydrated forms ($TcO_2\cdot nH_2O$), crystallize as the distorted rutile structure[14] with metal-oxygen bond lengths of 1.98 Å. The initial precipitation of Tc-O compounds occurs by the formation of short (monomeric to trimeric) chains that attach to mineral surfaces under most environmentally relevant conditions (Tc <10^{-5}M).[15] In hydrous Tc(IV) oxide monomers and polymers, the atomic arrangement of Tc and O are different from the $TcO_2\cdot nH_2O$ crystals precipitated biotically or abiotically from strongly supersaturated solutions. These monomers and polymers have octahedra in an edge-sharing arrangement and a Tc-Tc distance of 2.59 Å in the chains indicating that the formation of hydrated TcO_2-type compounds with the distorted rutile configuration may occur through a complex

rearrangement of these incipient molecular structures. The characterization of Tc(VII) crystalline structure is limited, however various reports show that bond lengths for the Tc(VII)-O are overall shorter (1.711 Å) than Tc(IV) compounds.[16, 17]

A number of investigators have undertaken measurements to determine the solubility of Tc(IV) in aqueous solution. Solubility determinations were made in a variety of different solutions, including natural and synthetic groundwater. Concentrations of Tc in equilibrium with hydrated TcO_2 solid compounds vary from 1×10^{-8} to 2.4×10^{-10}.[4, 7, 18-21] At pH interval between 4 and 10, the solubility depends on the nature of the substrate onto which the TcO_2 material precipitates.[7, 19-21]

The solubility of $TcO_2{\cdot}nH_2O$ was determined at high pH values (11.8 to 14.4) by Warwick et al., 2007.[22] They reported that above pH 13.5, the solubility of $TcO_2{\cdot}nH_2O$ increases linearly due likely to the formation of the $TcO(OH)_3^-$ species. The formation constant for the reaction is as follows:

$$TcO_2 \cdot nH_2O \rightarrow TcO(OH)_3^- + H^- + (n\text{-}2)H_2O \qquad \log K_2 = -21.6$$

The presence of carbonate species in the alkaline pH range can also increase the solubility of $TcO_2{\cdot}nH_2O$ with formation of $Tc(OH)_2CO_3^0$, $Tc(OH)_3CO_3^-$, $Tc(OH)(CO_3)_2^-$, and $Tc(OH)_2(CO_3)_2^{2-}$ complexes which may increase the solubility by a factor of ~2.5-10 times.[23, 24] Increase in Tc solubility was observed in chloride solutions (1×10^{-3} to 5 M NaCl) with formation of $TcCl_6^{2-}$ and $TcCl_4^0$ complexes[25] at relatively low pH[26], and in the presence of ubiquitous natural ligands such as humic substances.[27, 28]

In experiments with relatively high concentrations of Tc ($>10^{-5}$ M Tc), investigators have reported formation of colloids of Tc at moderately acidic (pH 4) conditions[29] and in alkaline media containing high concentrations of Cl^- and SO_4^{2-}.[30] The structure of the colloid particles was revealed by EXAFS to be one-dimensional chains of Tc(IV) in octahedral coordination that connect through edge-sharing of the polyhedral.[30] The Tc-Tc distance is 2.53 Å (253 pm), and the Tc-O bond lengths alternate between short (1.80 Å) and long (1.98 Å). Tc colloids will condense from pertechnetate solutions exposed to radiolysis at acid to near-neutral pH values.[31, 32] Radiolysis caused reduction of Tc(VII) and formation of Tc(IV) polymers and colloids, first as Tc(IV), then as $TcO_2{\cdot}nH_2O$ nanoparticles as the solution pH increased.[31, 32] The solubility of Tc(IV) is also complicated by the tendency of amorphous Tc dioxide [TcO_2(am)] to form more readily than its crystalline analog under most pH conditions. Like $TcO_2{\cdot}nH_2O$ the solubility of TcO_2(am) is pH-independent from acidic to alkaline conditions, but is a factor of 10 times more soluble.[18] Further, TcO_2 solubility is strongly influenced by heterogeneous precipitation kinetics on the surfaces or within Fe(II)-bearing phases. For Tc, precipitation is usually preceded by reduction of Tc(VII) to Tc(IV) and the rate of reduction is strongly controlled not only by the form of Fe(II) (aqueous, structural, or sorbed), but also by the identity of the phase associated with reduced iron (phyllosilicates v. iron oxides and hydroxides). The ability of Fe(II) to reduce Tc(VII) therefore depends on whether Fe(II) is a dissolved species, sorbed onto mineral surfaces, or is manifested in a structural role in the mineral. Principally, Fe(II) oxide, hydroxide and sulfide phases have been reported to facilitate the precipitation of Tc(IV) compounds. Investigations have shown that TcO_2 compounds will precipitate on the surfaces of magnetite ($[Fe^{2+}Fe^{3+}]O_4$)[10, 19], goethite [α-FeO(OH)][12], ferrihydrite [$Fe(OH)_3$][11], and "green rust".[33] The relative power of Fe(II) in its various forms to reduce Tc(VII) was given by [12] in this order: Fe(II) aqueous ~ Fe(II) sorbed onto phyllosilicates << structural Fe(II) in phyllosilicates << Fe(II) sorbed onto hematite and goethite. The association of Tc(IV) with structural Fe(II) has a profound influence on the rate of re-oxidation of Tc and it is discussed in detail below. Kobayashi et al., 2013[34] investigated the reduction/sorption of Tc(VII) in the presence of Fe(II) (magnetite, mackinawite and siderite) and Fe(III) (goethite and hematite) minerals. Their results showed that Tc reduction was only observed in the presence of the Fe(II) minerals demonstrating that Tc redox behavior strongly depends on the Eh values in solution

and independent of the chemicals used to fix redox conditions. A diagram illustrating the stability fields of the Tc species as a function of pH and E_h is displayed in Figure 10-7.

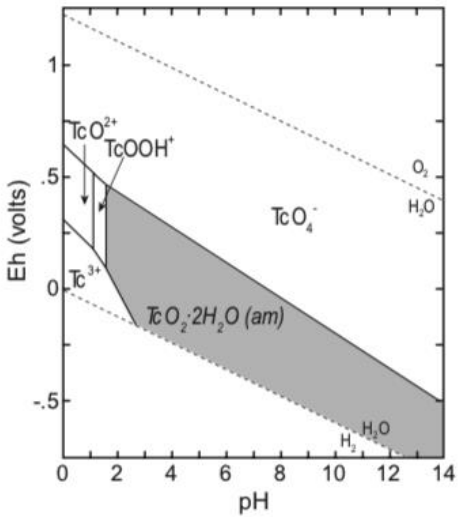

Figure 10-7. EH-pH diagram for Tc.[2] The shaded area represents the regions in which the amorphous solid $TcO_2 \cdot 2H_2O$ (am) is stable. Note that nearly the entire field for the species $TcO(OH)_2°$ is congruent with the stability field of $TcO_2 \cdot 2H_2O$(am).

10.4.4. Strategies for Tc disposal

Since the stable form of Tc under anaerobic conditions, Tc(IV), is not highly mobile the most effective method for preventing Tc migration is disposal in an anaerobic repository.[4] Another potential method for preventing Tc migration from a waste repository is stabilizing it within a durable waste form that can sequester ^{99}Tc until it has decayed. A general rule of thumb is that ten half-lives are sufficient to allow a radionuclide to decay; however, this period can be shorter or longer depending on the risks posed by the radionuclide.[35] In the U.S., all of the operational and proposed repositories for spent nuclear fuel (Yucca Mountain) and for fission products generated during plutonium production (Savannah River Site and Hanford Reservation) are aerobic and/or near-surface sites.[36-38] The disposal of ^{99}Tc in these aerobic repositories drives the interest in waste forms for ^{99}Tc that are stable in aerobic environments. Understanding sorption behavior of Tc is fundamental to determining repository performances over long period of time.

10.4.5. Technetium sorption processes: adsorption and coprecipitation

10.4.5.1. Technetium adsorption studies

Compared to the other radionuclides, much fewer sorption studies have been conducted to determine the sorption processes of Tc on mineral substrates. [39] Baston et al., 2002[18] measured Kd values for Tc(IV) sorption to Boom Clay at low Eh values (-230 mV) in conditions below the threshold of Tc(IV) reduction, and reported Kd values between 0.8 to 1.8 mL/g. In oxidizing systems, where pertechnetate is the dominant species, there is virtually no sorption of dissolved TcO_4^-. Autoradiographic analyses of rock and mineral thin sections contacted with $^{95m}TcO_4^-$ containing solutions, under oxic and anoxic conditions, have confirmed that virtually no sorption takes place in the presence of oxygen[40]. Overall the measured Kd for

typical geologic materials tends to be very low (Table 10-10). The Kd values of $Tc(VII)O_4^-$ species onto hematit [41], magnetite and goethite, as well as goethite-coated sands [42] are < 5.4 mL/g (Table 10-10). Sheppard and Sheppard (1986)[43] reported low values of Kd (<0.005 mL/g) measured on soils in lysimeter tests. Elwear et al., 1992[44] measured Kd values of pertechnetate on a variety of geologic materials and reported values of ≤2 mL/g. Kaplan and Serne, 1998[45] reported small positive to negative Kd values (<0.11 mL/g) for soils sampled from the Hanford Site, Washington State, and < 0.29 mL/g for Savannah Rivers site sediments.[42] These results reflect the electrostatic repulsion between the negatively-charged pertechnetate anion (TcO_4^-) and the negative surface charge carried by sedimentary materials in temperate climates at near-neutral pH values.

Table 10-10. Sorption Kd of Tc onto geologic materials

Study	Solution	Geologic material	K_d (mL/g)
Kaplan, 2002; Li and Kaplan, 2012[39, 42]	Tc(VII)	Sands coated with Fe_2O_3 (pH 3.2-6.8)	0-0.3
Sheppard and Sheppard, 1986[43]	Tc VII	lysimeter	
Palmer and Meyer, 1981[41]	Tc(VII)	magnetite	5.4
Palmer and Meyer, 1981[41]	Tc(VII)	hematite	0.8
Elwear et al., 1992[44]	Tc(VII)	geologic media	<2
Kaplan and Serne, 1998[45]	Tc(VII)	Hanford sediments	<0.11
Baston et al., 2002 [18]	Tc(IV)	Boom Clay	0.8-1.8

10.4.5.2. Technetium coprecipitation studies

Surface sorbed Fe(II) on Fe-bearing minerals under reducing conditions can promote surface mediated reduction of Tc(VII) to Tc(IV).[12] When Tc(VII) is reduced to Tc(IV), the concentration of Tc is well above that of saturation, and surface precipitates and colloids, rather than an aqueous complex, may form. Studies have shown that during this surface mediated Tc(VII) reduction process, reduced products consists of sorbed octahedral TcO_2 monomers and dimers. In some instances x-ray absorption spectroscopy studies have shown Fe(III) in the second coordination shell of Tc, indicating that Tc may become incorporated into the structure of various Fe-bearing minerals (discussed in detail below). The similarity of the ionic radius of six-coordinate Tc(IV), 0.645 Å, to that of Fe(III), 0.645 Å, suggests that Tc(IV) can replace Fe(III) in an iron oxide provided that the difference in charge is balanced.[46] There are a few reports in the literature that address the coprecipitation behavior of Tc in Fe bearing minerals including oxides, hydroxides, sulfides and clays and results are summarized below. Tc is mostly immobile under reducing conditions[4], so the coprecipitation of Tc with minerals such as magnetite, green rust or white rust may be favored. However these Fe(II) minerals are usually not stable under aerobic conditions, and the fate of coprecipitated Tc upon exposure could be an issue of concern. Fe(III) iron oxides like α-Fe_2O_3 are unstable towards reduction; however both hematite (α-Fe_2O_3) and goethite (α-FeOOH) are well known to be stable under aerobic conditions.[47-50] Results of coprecipitation studies are summarized in Table 4 and discussed in detail in the following paragraphs.

Table 10-11. Summary of Tc coprecipitation studies with Fe minerals (n.d= not determined in study; b.d.l.= below detection limit as reported by cited study)

Study	Mineral	Tc uptake (%)	Tc environment upon coprecipitation	Remobilized Tc (%) upon oxidation	Tc environment after oxidation
Zachara et al., 2007[11]	Ferrihydrite/ magnetite pH 7-8	100	Tc(IV) dimer bound in bidentate edge-sharing mode to octahedral Fe(III)	7% Tc(VII) pH 8 over 5 days oxygenation	n.d
	Ferrihydrite/ magnetite pH 6	0	n.d	n.d	n.d
Lukens and Saslow, 2018[51]	Hematite	82	Tc(IV) replaces Fe(III) octahedral site	5% 200 days in DI water (pH ~7)	Tc(IV) replacing Fe(III) in the hematite lattice
	Magnetite	97	Tc(IV) occupies octahedral site	12% 200 days in DI water (pH ~7)	n.d
Saslow et al., 2017[52]	$Fe(OH)_2$ to magnetite (Cr co-contaminant)	99.5	$TcO_2.H_2O$; TcO_4^-, < 17(5)% Tc incorporated into magnetite	n.d	nd
Pepper et al., 2003[33]	Green rust (sulfate and carbonate) High $NaNO_3$	99.8	Tc(IV) as surface complex (monomer, dimer) in a TcO_2-like environment	n.d.	On contact with air, the green rusts oxidize to poorly crystalline goethite, but the Tc environment is unchanged
Um et al., 2011[53]	Fe(II)-goethite (some magnetite)	>93	Tc(IV) replaces Fe(III) octahedral site	<5% over 180 days	Tc(IV) incorporated within the goethite mineral lattice is resistant to re-oxidation.
Um et al., 2012[54]	Fe(II)-goethite pellets	>100	Tc(IV) replaces Fe(III) octahedral site	<1% 120 days	XANES only the Tc(IV) oxidation state
McBeth et al., 2011[55]	Bio-magnetite	100	Short range Tc(IV)O_2 like environment , possible incorporation Tc(IV) replacement in Fe(III) octahedral site	<4%	Octahedrally coordinated Tc(IV) may be incorporated into the re-oxidized mineral product;
	Bio-siderite $FeCO_3$	84	Short range Tc(IV)O_2-like environment	<6.2%	Hydrous TcO_2-like coordination environments
	Bio-vivianite $Fe_3(PO_4)_2.8\ H_2O$	68	Short range Tc(IV)O_2 like environment	18.7% over 45 days oxidation	Octahedrally coordinated Tc(IV) may be incorporated into the re-oxidized mineral product;
	Fe(II) gel	100	Short range Tc(IV)O_2 like environment	<4% nitrate mediated oxidation	Hydrous TcO_2-like coordination environments
Yalçıntaş et al., 2016[56]	Magnetite	b.d.l.	Tc incorporation in Fe sites + Tc-Tc dimers sorbed	n.d.	n.d
	Mackinawite	b.d.l.	Tc-S like phase + TcO_2+H_2O (possible surface precipitates)	n.d.	n.d.

Study	Mineral	Tc uptake (%)	Tc environment upon coprecipitation	Remobilized Tc (%) upon oxidation	Tc environment after oxidation
Livens et al., 2004; Wharton et al., 2000[57, 58]	Mackinawite	98	Tc(IV)S_2-like species	n.d	Tc(IV) in an oxide, rather than a sulfide environment.
Marshall et al., 2014[59]	Ferrihydrite to magnetite (pH 10.3-13)	100	Tc(IV) was predominantly incorporated into the magnetite octahedral site in all systems studied	40 over 152 days (maghemite/goethite) in CO2 free air	Tc(IV) replacing Fe(III) in the magnetite/maghemite lattice

10.4.5.3. Tc coprecipitation process with Fe(II) and Fe(II)/Fe(III) oxy-hydroxides

Pepper et al.[33] reported that treatment of green rust (layered hydrous oxides containing both Fe(II) and Fe(III) and with interlayer sulfate or carbonate anions) with pertechnetate results in Tc(IV) incorporation into an iron oxide phase. Green rusts concentrates >99.8% of ^{99}Tc, present as $[TcO_4]^-$, from aqueous solution, even in the presence of high concentrations of $NaNO_3$, a common constituent of radioactive waste streams.[33] The mechanism of removal from solution appears to occur through a reduction process and formation of strong Tc(IV) surface complexes.[33] X-ray absorption spectroscopy shows that $[TcO_4]^-$ is reduced by reaction with both sulfate and carbonate forms of green rusts and is found in a TcO_2-like environment. On contact with air, the green rusts oxidize to poorly crystalline goethite, but the Tc environment is unchanged. There is no increase in Tc solubility associated with oxidation of the host green rust. This behavior suggests that green rusts may be useful in restricting Tc migration from repositories.[33] Treatment of alkaline solutions (pH=13.5) containing TcO_4^- and CrO_4^{2-} with white rust, $Fe(II)(OH)_2$, results in incorporation of both transition metals into the magnetite structure.[52]

Long term exposure of magnetite ($Fe^{(II/III)}{}_3O_4$) to pertechnetate solutions results in reduction of TcO_4^- to Tc(IV), and incorporation of Tc(IV) into the crystal lattice of Fe_3O_4.[34, 56] McBeth et al., 2011[55] added pertechnetate ($Tc(VII)O_4^-$) to samples of biogenic and abiotically synthesized magnetite at low concentration and higher concentration XAS experiments. Complete removal of Tc(VII) from solution was achieved in magnetite systems. In select, higher concentration Tc XAS experiments, XANES spectra showed reductive precipitation to Tc(IV). Low concentration re-oxidation experiments with air resulted in only partial remobilization of Tc. Upon exposure to air, the Tc bound to the Fe-minerals was resistant to oxidative remobilization. The resultant XANES spectra of the re-oxidized minerals showed Tc(IV)-like spectra in the re-oxidized Fe-phases. In this system Tc is largely recalcitrant to re-oxidation over medium-term timescales and there is spectroscopic evidence that Tc(IV) replaces Fe(III) in an octahedral site in the magnetite structure.[55] Biogenically derived vivianite ($Fe^{2+}Fe^{2+}{}_2(PO_4)_2 \cdot 8H_2O$) and siderite ($FeCO_3$) take up less Tc compared to biogenically derived magnetite, and overall higher Tc was released in solution upon oxidation.[55, 60]

Zachara et al., 2007[11] investigated the abiotic reduction of Tc(VII) by dissolved Fe(II) in pH 6–8 solutions under strictly anoxic conditions using an oxygen trap ($<7.5\times10^{-9}$ bar O_2). Tc(VII) was reduced rapidly and completely to a precipitated Fe–Tc(IV) form when 11 μM Tc(VII) was reacted with 0.4 mM Fe(II) at pH 7.0 and 8.0, while no significant reduction was observed over 1 month at pH 6.0, demonstrating that the reduction kinetics are strongly pH dependent. The Fe–Tc(IV) solid phase so formed is poorly ordered and dominated by Fe(II)-containing ferrihydrite with minor magnetite. Tc(IV) exhibited homogeneous spatial distribution within the precipitates with estimated composition of the solids is $Fe_T/Tc(IV) \approx 6$. Spectra

of the precipitate from X-ray Absorption Near-Edge Spectroscopy (XANES) analyses show that Tc is in the reduced form [Tc(IV)]. The molecular environment of Tc(IV) is consistent with an octahedral Tc(IV) dimer bound in bidentate edge-sharing mode to octahedral Fe(III) associated with surface or vacancy sites in ferrihydrite. The oxidation rate of sorbed Tc(IV) in the Fe–Tc precipitate is considerably slower than $Tc(IV)O_2{\cdot}nH_2O(s)$.

Initial adsorption of Tc(IV) onto ferrihydrite also resulted in incorporation of Tc(IV) in the resulting magnetite phase at high pH (10.5-13.1).[59] Subsequent air oxidation of the magnetite particles for up to 152 days resulted in only limited remobilization of the incorporated Tc(IV). X-ray absorption spectroscopy data indicated that the Tc(IV) was predominantly incorporated into the magnetite octahedral site in all systems studied. On re-oxidation in air, the incorporated Tc(IV) was recalcitrant to oxidative dissolution with less than 40% remobilization to solution despite significant oxidation of the magnetite to maghemite/goethite and all solid associated Tc remained as Tc(IV).

Computational studies found that Tc(IV) doping into the octahedral Fe sites in magnetite is possible, but other Tc oxidation states, especially Tc(V), may be present and several mechanisms can balance the charge mismatch created when Tc(IV) replaces Fe(III) on the octahedral site.[61] To achieve Tc doping into Fe_3O_4, charge may be balanced by either replacement of Fe(III) by Fe(II) or by creating octahedral vacancies, however overall Tc(IV) incorporation into magnetite is energetically favorable.[61]

Overall mixed Fe(II)/Fe(III) precipitates of this nature may form in anoxic sediments or groundwater. The overall results of studies summarized in this section suggest that once Tc is immobilized as sorbed/precipitated Tc(IV) in Fe(II)/Fe(III) minerals, its remobilization upon the return of oxidizing conditions may be limited.

10.4.5.4. Tc coprecipitation process with Fe(II) containing sulfides and silicates

Livens et al.[57] showed that reduced Tc is harbored by mackinawite (tetragonal FeS) and EXAFS data indicates the presence of Tc-S bonds. During re-oxidation mackinawite forms goethite [α-FeO(OH)], yet Tc remains in the reduced state. The EXAFS evidence indicates that Tc(IV) bonds switch from S to O suggesting that Tc(IV) may be incorporated into the goethite structure. Because of the identical size of the Tc(IV) and Fe(III) cations, this is a plausible substitution, provided that a charge-compensating ion is present or the solid forms a defect structure. These results were similar to those reported by Wharton et al.[58] in that FeS solids oxidized, but Tc remained reduced as was associated with O, rather than S, after re-oxidation. Tc incorporated into Fe(II)-bearing phyllosilicates along cracks or defect trails could also be reduced to Tc(IV), albeit more slowly than the mineral-surface mediated reduction mechanism.[12, 15, 62] Fe-bearing di- and trioctahedral phyllosilicates in various states of weathering are common in most sedimentary deposits and may be an important sink for reduced Tc. As reported by Fredrickson et al.[62] reduced Tc incorporated into diffusion- limited spaces, such as in phyllosilicates, is resistant to oxidation, whereas Tc(IV) on unprotected mineral surfaces rapidly re-oxidizes when contacted by air or oxidizing solutions.

10.4.5.5. Tc coprecipitation process with Fe(III) minerals

Lukens and Saslow[51] showed that coprecipitation of hematite (alpha-Fe_2O_3) with TcO_4^- in acidic conditions results in >80% Tc incorporation in the mineral structure, corresponding to a 2.2%wt uptake of Tc by the hematite structure. Leeching studies showed that that less <5% Tc are remobilized in 200 days of exposure to oxidative conditions. Incorporation of Tc into hematite has also been studied computationally, and up to 2.6 wt.% of isolated Tc(IV) can be accommodated by hematite when the charge is balanced by reduction of a neighboring Fe(III) site to Fe(II).[50] Although pertechnetate incorporation is found to be unfavorable, incorporation of small amounts of Tc(IV) (at least 2.6 wt. %) is energetically feasible.

Tc-doped goethite has been investigated both experimentally and computationally. [53, 54, 61] Um et al. 2011[53] demonstrated that Fe(II) sorbed to goethite efficiently catalyzes the reduction of Tc in deionized water and complex solutions that mimic the chemical composition of caustic waste scrubber media. Analyses of the Tc-bearing solid products by XAFS indicate that all of the Tc(VII) was reduced to Tc(IV) and that the latter is incorporated into goethite or magnetite as octahedral Tc(IV). Batch dissolution experiments, conducted under ambient oxidizing conditions for more than 180 days, demonstrated a very limited release of Tc to solution (27μg Tc/g solid). When crystals of goethite are furthered "armored" by an additional layer of precipitated goethite the armoring isolates the reduced ^{99}Tc(IV) from oxidizing agents. [54] Monolithic pellets formed from "armored" maintained Tc as a reduced species even after 120 days of oxidative leaching (pH = 7.2 and I = 0.05 M). The results of this study indicate that Tc can be immobilized in a stable, low-cost Fe oxide matrix that is easy to fabricate and these findings can be useful in designing long-term solutions for nuclear waste disposal.[54]

Collectively, these studies indicate that co-precipitation of Tc with an iron (oxy)hydroxide, sulfide, "green rust" or siderite provide a good medium of immobilization for Tc and remobilization upon oxidation is limited. Further, these studies indicate that Tc incorporated into phyllosilicates is resistant to re-oxidation. The Tc(IV) in this case is associated with structural Fe and the resistance to re-oxidation appears to be subject to the limitation of oxygen diffusion into the phyllosilicates. These observations have implications for the designing a durable medium to immobilize Tc from liquid waste and additionally they provide insights into environmental and geological conditions that limit Tc mobility in the subsurface, which provide insight into canister corrosion impacts on Tc release and long-term contaminant mitigation.

10.5. Selenium interactions with Fe oxide minerals

10.5.1. Selenium

The trace element selenium (Se) is of special concern because of the extremely fine line between its opposing properties: at low concentrations, it is an essential nutrient for many organisms, at slightly higher quantities, however, it becomes a toxic contaminant.[63] Of concern are therefore not only Se-deficient agricultural soils in certain regions of the world, but also Se contaminations of soils or wastewaters caused by natural and/or anthropogenic factors. [63, 64]

In addition, selenium occurs in high-level nuclear waste (HLW) in the form of radionuclide ^{79}Se, which plays an important role in long-term safety assessments of deep geological repositories.[65] ^{79}Se is produced by nuclear fission and it is produced with a yield of about 0.04% [7] and is a component of spent nuclear fuel, high-level radioactive wastes resulting from processing spent fuel, and radioactive wastes associated with the operation of nuclear reactors and fuel reprocessing plants. The assumed concentration ^{79}Se in high-level radioactive waste is 10^{-7} mol/L and could amount to 10^{-10} mol/L in the biosphere.[66, 67]

^{79}Se is a pure beta-emitting nuclide, which poses a challenging task for reliable, quantitative determination of its half-life due to vulnerable radiometric and mass spectrometric methodologies, both requiring chemical purification in advance for the removal of interfering activity and isobars. The most recent measurements of ^{79}Se half-life report a value of $3.27(8)\times10^{5}$.[65] Due to its long half-life, it is one of only a few nuclides that determine the long-term radiological impact and of a repository on the environment.[68, 69]

10.5.2. Oxidation state

In nature selenium can occur in five different oxidation states (-II, -I, 0, IV, VI) and standard potential for redox reaction are reported in Table 10-12. Selenium species of the oxidation states Se(-II), Se(-I) and Se(0)

are characterized by forming sparingly soluble compounds, including metal selenides or elemental Se.[66] By contrast in the two higher oxidations states, selenium forms the soluble oxyanions selenite [$Se^{IV}O_3^{2-}$] and selenate [$Se^{VI}O_4^{2-}$], which are generally highly mobile due to their limited interaction with geological materials.[66, 70, 71] In soils in contact with the atmosphere for example, the thermodynamically favored Se species are the oxyanions selenate [Se(VI)] and selenite [Se(IV)]. The oxidation state is therefore the key factor determining the biogeochemical behavior of selenium, since parameters such as solubility, mobility, bioavailability and toxicity mainly depend on the occurrence of dissolved selenium species.[72, 73]

The selenium oxidation state in high level waste and the accompanying dominant selenium species depends on the waste type. Recent research has demonstrated that ^{79}Se occurs as Se(−II) in spent nuclear fuel.[74, 75] Due to the reducing conditions predicted in deep repositories, formation of mobile selenium species is unlikely, however, it cannot be fully excluded that oxidation processes induced by long-term irradiation could lead to a oxidation to Se(VI).[76] The fate of selenium in the near-field of high-level radioactive waste also depends on the Se valence state in vitrified glasses which are part of the technical barrier in the multibarrier concept for HLW disposal.[70] The expected predominant selenium oxidation state in vitrified HLW arising from nuclear fuel reprocessing plants is Se(IV) in the form of selenite.[76]

For these reasons it is imperative to understand the mobility of oxidized and reduced forms of Se in oxidizing and reducing conditions, to better determine long-term safety and performance of nuclear repository.

Table 10-12. Standard potential of Se redox reactions from Seby et al.[67]

Redox reactions	*Standard potential (V)*
Se(0)/Se(–II)	
$Se(s) + 2H^+ + 2e^- \Leftrightarrow H_2Se(aq)$	– 0.115
$Se(s) + H^+ + 2e^- \Leftrightarrow HSe^-$	– 0.227
$Se(s) + 2e^- \Leftrightarrow Se^{2-}$	– 0.641
Se(IV)/Se(0)	
$H_2SeO_3(aq) + 4H^+ + 4e^- \Leftrightarrow Se(s) + 3H_2O$	0.740
$HSeO_3^- + 5H^+ + 4e^- \Leftrightarrow Se(s) + 3H_2O$	0.780
$SeO_3^{2-} + 6H^+ + 4e^- \Leftrightarrow Se(s) + 3H_2O$	0.903
Se(VI)/Se(IV)	
$HSeO_4^- + 3H^+ + 2e^- \Leftrightarrow H_2SeO_3(aq) + H_2O$	1.090
$HSeO_4^- + 2H^+ + 2e^- \Leftrightarrow HSeO_3^- + H_2O$	1.008
$HSeO_4^- + H^+ + 2e^- \Leftrightarrow SeO_3^{2-} + H_2O$	0.760
$SeO_4^{2-} + 4H^+ + 2e^- \Leftrightarrow H_2SeO_3(aq) + H_2O$	1.139
$SeO_4^{2-} + 3H^+ + 2e^- \Leftrightarrow HSeO_3^- + H_2O$	1.060
$SeO_4^{2-} + 2H^+ + 2e^- \Leftrightarrow SeO_3^{2-} + H_2O$	0.811

10.5.3. Precipitation of Se compounds and their solubility

Selenium can react with inorganic cations to give solid phases that can be responsible for its immobilization. Precipitation/ dissolution reactions govern selenium solubility only in reduced conditions with formation of solid elemental selenium and metal-selenide((Se(-2)).[77-80] Under reduced conditions, metal-selenide minerals are found to limit the Se solubility.[80] The most stable minerals are Cu_2Se(s) in acid soils and PbSe(s) and SnSe(s) under neutral to alkaline conditions.[80] In groundwater with a potential value lower than 0 mV, FeSe(s), ZnSe(s) and MnSe(s) can exist.[67] Equilibrium thermodynamic calculation have shown that elemental Se,FeSe(s) (achavalite) or $FeSe_2$(s) (ferroselite) can control Se solubility.[78, 81] Elemental Se has a wide stability field under acid conditions and formation of achavalite is favored for neutral to alkaline conditions. A mixed solid solution phase can also be formed with selenide substituting for sulfide and precipitated FeS will contain FeSe.[67] These observation of Se compounds solubility suggests that the chemistry of selenium is closely related to those of iron sulfides.[67]

Metal-selenate minerals are too soluble to persist in aerated soils and among different metal-selenite precipitates, only $MnSeO_3$(s) can be formed in strongly acid soils.[80]

10.5.4. Sorption processes: adsorption, surface mediated reduction and coprecipitation

10.5.4.1. Adsorption studies

The fate of dissolved Se(IV) and Se(VI) species in subsurface systems is primarily determined by interaction with mineral phases, including processes such as adsorption, incorporation, and reductive precipitation, which are the key immobilization mechanisms.[70, 82] However, most natural materials like clays or silicate minerals show only a restricted retention capacity for Se oxyanions.[83] In this context, crystalline iron (oxyhydr)oxide minerals (e.g. hematite and goethite) and their metastable precursors (e.g. ferrihydrite) are of great importance as they are widespread in nature and capable of anion sorption.[84, 85] This is the reason why, in particular, the mechanisms of Se oxyanion adsorption to iron oxide surfaces have been investigated in detail by a large number of previous studies.

Adsorption of Se(IV) and Se(VI) onto iron oxides can be very efficient at lower pH but is limited under near-neutral and alkaline pH conditions.[86-90] This tendency is independent of the type of iron oxide, since alkaline conditions generally lead to the formation of a negative charge at the iron oxide surface and therefore to a poor adsorption of anionic species.[71] Moreover, all iron oxides show a relatively high adsorption capacity for Se(IV) and there is only little release of Se(IV) with increasing ionic strength.

Unlike Se(IV), adsorption of Se(VI) is much lower and is strongly influenced by the presence of competing anions.[91-95] Most authors suggest the difference between Se(IV) and Se(VI) adsorption is due to the nature of the chemical attachment and the formation of different types of adsorption complexes.

Spectroscopic investigations as well as surface complexation modeling reveal that the adsorption of Se(IV) onto iron oxides is usually the result of inner-sphere complexation[71] with a mostly bidentate character, e.g. for hematite.[88, 96] By contrast, the poor adsorption of Se(VI) and the strong impact of competing anions has been attributed to the formation of outer-sphere complexes.[91] However, more recent studies suggest that adsorption of Se(VI) can occur via both inner-sphere and outer-sphere complexation.[94, 97] The type of surface complexation depends on pH, ionic strength, the nature of the iron oxide mineral and its surface loading.[71, 98]

Several anions can be in competition with selenium ion sorption. Kim et al.[99] analyzed the influence of carbonate and silicate on the sorption of selenium ions onto magnetite. Se(IV) was sorbed onto magnetite very well below pH 10, but silicate and carbonate hindered its sorption onto magnetite. On the other hand, little Se(VI) was sorbed onto magnetite in neutral and weak alkaline solutions even though silicate or carbonate was not contained in the solutions. Seby et al.[67] report the following sequences for selenium sorption anion competitions on goethite: phosphate > silicate ~ citrate > molybdate > bicarbonate/carbonate > oxalate > fluoride > sulphate.[67]

Although a considerable amount of Se sorption data has been obtained under aerobic conditions, where selenite and selenate species are dominant, the data obtained under reducing conditions are limited and the sorption data for Se(-II) species are scarce. Iida et al.[100] performed batch sorption experiments of Se(-II) under reducing conditions to investigate the sorption behavior of selenium onto granodiorite, sandy mudstone, tuffaceous sandstone, and their major constituent minerals and accessory minerals (Table 10-13). The author conclude that minor phases present in granodiorite and sandstone, mainly biotite and pyrite, are important minerals with respect to the sorption behavior of Se onto rocks. Selected published K_d values for Se(-II), Se(V) and Se(VI) are reported in Table 10-13.

Table 10-13. Selected sorption K_d of Se onto geologic materials

Study	Se	Geologic material	Kd (as reported)
Borsig (2018)[101]	Se(VI)	magnetite (pH=9-9.3)	2.14-4.72 Log K_d (L/kg)
	Se(IV)	magnetite (pH=9-9.3)	4.7-5.16 Log K_d (L/kg)
Missana (2009)[83]	Se(IV)	smectite (pH 3-8)	500 mL/g (pH 3); 100 mL/g (pH 8)
		illite (pH 3-8)	150 mL/g (pH 3); 75 mL/g (pH8)1
Loyo(2008) [102]	Se(IV)	magnetite (pH 5)	3500-3600 mL/g
		magnetite (pH 10)	170 mL/g
		Fe/Fe_3C (pH 5)	3640-3800 mL/g
		Fe/Fe_3C (pH 10)	388-410 mL/g
Kim (2012) [99]	Se(IV)	magnetite (pH 7)	2000 mL/g
		magnetite pH 7 (10mmol/L carbonate-)	1300 mL/g
		magnetite (pH 9)	1200 mL/g
		magnetite (pH 9)	300 mL/g
	Se(VI)	magnetite a(6-8) (10mmol/L carbonate-)	no sorption
Fevrier (2007)[103]	Se(IV)	soil (sterile)	16 L/kg
		soil (non-sterile)	130 L/kg
Iida (2011) [100]	Se(-II)	granodiorite (pH 8.5-11.5)	$2.2x10^{-4}$ to $4 x10^{-3}$ m^3/kg
	Se(-II)	sandy mudstone (pH 8.5-11.5)	$3.3x10^{-2}$ to $5.6x10^{-2}$ m^3/kg
	Se(-II)	tuffaceous sandstone (pH 8.5-11.5)	$2.9x10^{-2}$ to $8.2x10^{-2}$ m^3/kg

10.5.4.2. Surface mediated reduction of selenium

The oxidation state of dissolved selenium oxyanions can be reduced by Fe(II). Although the presence of dissolved Fe(II) generally favors the selenium reduction process,[104] a reduction only by dissolved Fe(II) is not possible due to the difference in reduction potentials of the redox couples.[105] It is known however that for the reduction by Fe(II) to occur, Se needs to interact with the surface of Fe(II) mineral[106] and various mineral phases that contain Fe(II) are able to reduce selenium oxyanions under anoxic conditions. This reduction process has been observed for magnetite[107] , iron(II) hydroxide[108, 109], green rust[110-112] as well as elemental iron,[113-116], iron(II) sulfides[107, 117] or Fe^{2+} adsorbed on clay minerals[118].

Since reduction of selenium oxyanions causes the formation of sparely soluble compounds, this interaction generally results in the immobilization of selenium. These selenium compounds are either elemental Se or iron selenides like FeSe and Fe_7Se_8, and the nature of the products varies depending on the iron-bearing phases, the hydrogeochemical conditions, and the reduction kinetics. Kinetic rather than thermo-dynamic control of reduction products may explain why the majority of the above-mentioned studies showed the formation of elemental Se(0)[106, 108-110, 112, 118, 119] and only a few studies identified iron selenides.[107, 113, 120] This can be attributed to the fact that reduction to Se(-II) and formation of iron selenides is limited to a rapid reduction of selenium oxyanions.[107]

10.5.4.3. Coprecipitation studies

The coprecipitation and structural incorporation of a metal species in a mineral host can be relevant in cases where mineral phases interact with dissolved species during their formation or transformation, including recrystallization or sorption induced crystal growth. Since the formation pathway of crystalline iron oxides commonly includes amorphous metastable intermediates [121], such processes are very common in natural systems like soils. Oxyanion incorporation or occlusion by Fe(II) and Fe(II/III) minerals has been shown for Se(IV) [122], P(V)[123], As(V)[124, 125], and Tc(VII)[50]. For this reason, it is conceivable that a retention mechanism on the basis of incorporation also exists for the both Se oxyanions, Se(IV) and Se(VI), and that such mechanisms could affect the migration of dissolved Se species.

In reducing conditions, where reduced Se species are more stable, pyrite (FeS_2) and mackinawite (FeS) are expected to be the most dominant Fe(II) minerals. Pyrite is the most common near-surface iron sulfide, well-known for its capacity to incorporate elements up to several mol%.[126-129] Pyrite is also part of host rocks and bentonite backfills considered for use in HLW repositories[130-133] and could form from the corrosion of steel containers containing vitrified nuclear waste. Due to the similarities in geochemical behavior and ionic radii of Se(-II) and S(-II), iron sulfide minerals are likely host for selenide incorporation.

In the following sections we will discuss studies that have addressed the coprecipitation and structural incorporation of selenium in various Fe minerals, and a summary of the results is reported in Table 10.14.

Table 10.14. Summary of Se coprecipitation studies with Fe minerals (n.d.= not determined in study)

Study	Mineral	Se form	Se uptake (%)	Se behavior upon coprecipitation
Borsig et al 2018[101]	Magnetite (pH 9.2)	Se(IV) Se(VI)	100% 100% (10^{-4}-10^{-3} mol/L); 30% 10^{-2} mol/L	Reduction of Se(IV) or Se(VI) to Se(-II) causes the formation of nanoparticulate iron selenide [FeSe] phase. Progressive oxidation of Fe(II) hydroxide and green rust into magnetite leads to oxidation of Se(-II) to Se(0) (gray elemental selenium)
Missana et al. (2009) [134]	Magnetite (pH <5): adsorption studies at pH<5 showed magnetite dissolution and coprecipitation of Se species	Se(IV)	n.d.	Ferric selenite formation is the predominant retention process at higher selenite concentrations (>1 x10^{-4} M) and pH < 5
Diener 2011[135]	Pyrite, mackinawite (pH 4.5-5)	Se(-II)	98.9% (pyrite); 95.4% (mackinawite); 99.2% (amorphous FeS); 98.1% (mixed iron sulfide phases)	Focused ion beam analysis shows an inhomogeneous Se distribution with a higher accumulation in the center of the pyrite grains, probably due to the progressive depletion of Se from solution with regard to S.
Diener 2012[136]	Pyrite, mackinawite (pH 3.7-5)	Se(-II) Se(IV)	98.6 - 99.98 % 99.5%	In supersaturated solutions: substitution of S(-I) by Se(-I) in Se-doped pyrite and of S(-II) by Se(-II) in Se-doted mackinawite. At lower concentrations and in case of a slower precipitation : Se(-II) and Se(IV) retention by incorporation is coupled with a change in the oxidation state and selenium is incorporated as Se(0) into pyrite without structural bonding.
Francisco (2018)[137]	Ferrihydrite (pH 5-10)	Se(IV)	94-99% During aging, the behavior of Se(IV) varied with pH. At pH 5, Se was retained in the solid. At pH 10, a fraction of Se(IV) was released in solution.	Se(IV) was retained within the crystalline post-aging products and possibly occluded in nanopore and defect structures.
Borsig 2017 [138]	Ferrihydrite to hematite (pH 7.5)	Se(IV) Se(VI)	100% 15%	Se oxidation state is not changed during adsorption or coprecipitation. Se coprecipitation leads to the occurrence of a resistant, non-desorbable Se fraction. Se initially adsorbs to the ferrihydrite surface, but after the transformation of ferrihydrite into hematite, it is mostly incorporated by hematite.

10.5.4.4.Se coprecipitation process with Fe(II) and Fe(II)/Fe(III) oxy-hydroxides

Borsig et al.[101] investigated the immobilization of dissolved Se(IV) and Se(VI) during the formation of magnetite in coprecipitation experiments based on the progressive oxidation of an alkaline, anoxic Fe(II) system at pH 9.2. Results showed a high retention of selenium oxyanions during the mineral formation process. The authors show that this immobilization is due to the reduction of Se(IV) or Se(VI), resulting in the precipitation of sparingly soluble trigonal elemental selenium compounds. These selenium compounds formed in all coprecipitation products following magnetite formation. Time-resolved analysis of selenium speciation during magnetite formation and detailed spectroscopic analyses of the solid phases showed that selenium reduction occurred under anoxic conditions during the early phase of the coprecipitation process via interaction with Fe(II) hydroxide and green rust. This early selenium interaction leads to the formation of a nanoparticulate iron selenide phase [FeSe], which is oxidized and transformed into gray trigonal elemental selenium during the progressive oxidation of the aquatic system. Selenium is retained regardless of whether the oxidation of the unstable iron oxides leads to the formation of pure magnetite or other iron oxide phases, e.g. goethite.

Missana et al.[134] studied Se(IV) retention by magnetite using both surface complexation modeling and x-ray absorption spectroscopy (XAS) to characterize the processes of adsorption, reduction, and dissolution/co-precipitation. Results showed that at higher selenite concentrations ($>1\times10^{-4}$M) and pH<5 the precipitation of ferric selenite (SeIV-Fe) is the predominant retention process of Se onto magnetite.

10.5.4.5. Se coprecipitation process with sulfides

Selenium is often associated with sulfides such as pyrite, a frequent minor constituent of host rocks and bentonite backfills considered for radioactive waste disposal. Diener and Neumann[135] investigated the uptake of Se by pyrite (FeS_2) and mackinawite (FeS). More than 98% of the Se added to solutions was taken up by the Fe sulfide minerals. Focused ion beam analysis shows an inhomogeneous Se distribution with a higher accumulation in the center of the pyrite grains, probably due to the progressive depletion of Se from solution with regard to S. The results imply that pyrite and its precursor phase, mackinawite, are efficient in removing selenium from solution, and this may contribute in reducing the mobility of ^{79}Se released from radioactive waste.

Diener et al.[136] investigated the incorporation mechanisms of Se(-II) and Se(IV) into pyrite and mackinawite by x-ray absorption spectroscopy to determine the relevance of iron sulfides to Se retention and the type of structural bonding. The syntheses of pyrite and mackinawite occurred via direct precipitation in batches and also produced coatings on natural pyrite in mixed-flow reactor experiments under anoxic conditions at Se concentrations in the solutions of up to 10^{-3} mol/L. The Se uptake >98.6% suggesting a high potential for retention. XAFS results indicate a substitution of sulfur by selenide during instantaneous precipitation in highly supersaturated solutions only. In selenide doped mackinawite, S(-II) was substituted by Se(-II), resulting in a mackinawite-type compound. S(-I) is substituted by Se(-I) in selenide-doped pyrite, yielding a FeSSe compound as a slightly distorted pyrite structure. Under slighter supersaturated conditions, XAFS results indicate an incorporation of S(-II) and Se(IV) predominantly as Se(0). This study shows that a substitution of S by Se in iron sulfides is probable only for highly supersaturated solutions under acidic and anoxic conditions, however under closer equilibrium conditions, Se(0) is expected to be the most stable species.

10.5.4.6. Se coprecipitation process with Fe(III) minerals

Francisco et al.[137] studied the coprecipitation behavior of Se(IV) with ferrihydrite at different pH values to determine how Se(IV) associates with ferrihydrite and how Se(IV) coordination changes with ferrihydrite aging and recrystallization. Results show that despite efficient removal, the mode and stability of Se(IV) retention in the coprecipitates varied with pH. At pH 5, Se(IV) is removed dominantly as a ferric selenite-like phase intimately associated with ferrihydrite, while at pH 10, it is mostly present as a surface species on ferrihydrite. Similarly, the behavior of Se(IV) and the extent of its retention during phase transformation varied with pH. At pH 5, Se(IV) remained completely associated with the solid phase despite recrystallization to hematite, whereas it was partially released back into solution at pH 10. Regardless of this difference in behavior, TEM and XAS results show that Se(IV) is retained within the crystalline products and possibly occluded in nanopore and defect structures. These results demonstrate a potential long-term immobilization pathway for Se(IV) even after phase transformation.

Borsig et al.[138] also studied the immobilization of Se oxyanions during the crystallization of hematite from ferrihydrite. In coprecipitation studies, hematite was synthesized by the precipitation and aging of ferrihydrite in an oxidized Se(IV) or Se(VI) containing system (pH 7.5). Aqueous chemistry data of these batch experiments revealed the complete uptake of all available Se(IV), while the retention of Se(VI) was low (max. 15% of Se). The study shows that during the crystallization of hematite from ferrihydrite, interacting Se oxyanions are not adsorbed but mainly incorporated into hematite. This incorporation process follows the previous adsorption of Se oxyanions onto ferrihydrite and takes place during the subsequent transformation of amorphous ferrihydrite into crystalline hematite. The incorporation mechanism itself results from a direct linkage between the Se oxyanions and the hematite phase but is not attributed to substitution or occupation of crystallographic sites within the hematite crystal lattice. The incorporated Se oxyanion species are bound to the hematite phase in a way that is similar to surface adsorption complexes – outer-sphere complexes for Se(VI) and innersphere complexes for Se(IV). Compared to simply adsorbed Se oxyanions, the retention of the incorporated Se fraction is very resistant even at alkaline pH conditions at least as long as the hematite mineral remains stable.

Collectively, these studies indicate that sorption processes of Se with Fe(III)(oxy)hydroxide, Fe(II) sulfide, and Fe(II/III) minerals provide a good medium of immobilization for Se. Key factors that affect removal of Se from solution include mineral formation pathways, presence of Fe(II), pH and redox potential, and presence of competing anions.

Regarding the behavior of selenium in the geosphere, reductive selenium precipitation represents an efficient mechanism to immobilize dissolved selenium oxyanions. Processes like these should be considered in safety assessments of HLW disposal sites, as they may affect the migration of the radionuclide ^{79}Se as it interacts with secondary iron oxides in the near-field.

Although there is a significant body of literature discussing sorption processes of Se species with various reduced Fe minerals (Fe(II) and mixed Fe(II/FeIII)), there is a lack of information regarding the fate of Se species during re-oxidation and recrystallization reaction. Future studies should focus on determining the retention mechanisms of Se species after extended disposure to oxidative conditions, as has been done for Tc.

10.6. Future FY21 work

To mimic our ferrihydrite to goethite mineralization experiments, we are planning on performing magnetite experiments where Pu will be sorbed to a mineral precipitate precursor first, then aged to the desired mineral phase (green rust or magnetite). Our goal is to understand if differences in association of Pu to the precursor material will affect bonding of Pu to the final crystalline solid. In the magnetite synthesis a Fe-precipitate forms starting at pH>3. Our plan is to add Pu to the $Fe(III)Cl_3$ once the pH> 3 precipitate has formed. Then we will proceed with the synthesis as described above.

We also plan on expanding our literature review of radionuclides relevant to nuclear waste repository (i.e. Np, I and Cl) performance assessment, perform additional corrosion experiments for radionuclides with limited information in the literature (e.g. iodine), and evaluate the overall impact that nuclear waste repository corrosion processes on radionuclide release and long-term performance of nuclear waste repositories.

10.7. References

1. Kirsch, R.; Fellhauer, D.; Altmaier, M.; Neck, V.; Rossberg, A.; Fanghanel, T.; Charlet, L.; Scheinost, A. C., Oxidation state and local structure of plutonium reacted with magnetite, mackinawite, and chukanovite. *Environmental Science & Technology* **2011,** *45*, (17), 7267-7274.
2. Icenhower, J. P.; Qafoku, N. P.; Zachara, J. M.; Martin, W. J., THE BIOGEOCHEMISTRY OF TECHNETIUM: A REVIEW OF THE BEHAVIOR OF AN ARTIFICIAL ELEMENT IN THE NATURAL ENVIRONMENT. *American Journal of Science* **2010,** *310*, (8), 721-752.
3. Pilkington, N. J., The solubility of technetium in the near-field environment of a radioactive waste repository. *Journal of the Less Common Metals* **1990,** *161*, (2), 203-212.
4. Kunze, S.; Neck, V.; Gompper, K.; Fanghänel, T., Studies on the Immobilization of Technetium under Near Field Geochemical Conditions. *Radiochimica Acta* **1996,** *74*, (Supplement), 159-164.
5. Schulte, E. H.; Scoppa, P., SOURCES AND BEHAVIOR OF TECHNETIUM IN THE ENVIRONMENT. *Science of the Total Environment* **1987,** *64*, (1-2), 163-179.
6. Darab, J. G.; Smith, P. A., Chemistry of technetium and rhenium species during low-level radioactive waste vitrification. *Chemistry of Materials* **1996,** *8*, (5), 1004-1021.
7. Meyer, R. E.; Arnold, W. D.; Case, F. I.; Okelley, G. D., Solubilities of Tc(Iv) Oxides. *Radiochimica Acta* **1991,** *55*, (1), 11-18.
8. Boyd, G. E., Osmotic and Activity-Coefficients of Aqueous Natco4 and Nareo4 Solutions at 25-Degrees-C. *Journal of Solution Chemistry* **1978,** *7*, (4), 229-238.
9. EPA EPA facts about Technetium-99. https://semspub.epa.gov/work/HQ/175252.pdf
10. Cui, D. Q.; Eriksen, T. E., Reduction of pertechnetate by ferrous iron in solution: Influence of sorbed and precipitated Fe(II). *Environmental Science & Technology* **1996,** *30*, (7), 2259-2262.
11. Zachara, J. M.; Heald, S. M.; Jeon, B. H.; Kukkadapu, R. K.; Liu, C. X.; McKinley, J. P.; Dohnalkova, A. C.; Moore, D. A., Reduction of pertechnetate Tc(VII) by aqueous Fe(II) and the nature of solid phase redox products. *Geochimica Et Cosmochimica Acta* **2007,** *71*, (9), 2137-2157.
12. Peretyazhko, T.; Zachara, J. M.; Heald, S. M.; Jeon, B. H.; Kukkadapu, R. K.; Liu, C.; Moore, D.; Resch, C. T., Heterogeneous reduction of Tc(VII) by Fe(II) at the solid-water interface. *Geochimica Et Cosmochimica Acta* **2008,** *72*, (6), 1521-1539.
13. Peretyazhko, T.; Zachara, J. M.; Heald, S. M.; Kukkadapu, R. K.; Liu, C.; Plymale, A. E.; Resch, C. T., Reduction of Tc(VII) by Fe(II) sorbed on Al (hydr)oxides. *Environmental Science & Technology* **2008,** *42*, (15), 5499-5506.
14. Colton, R., Chemistry of Rhenium and Technetium. *Journal of the Less-Common Metals* **1966,** *11*, (2), 147-&.

15. Fredrickson, J. K.; Zachara, J. M.; Balkwill, D. L.; Kennedy, D.; Li, S. M. W.; Kostandarithes, H. M.; Daly, M. J.; Romine, M. F.; Brockman, F. J., Geomicrobiology of high-level nuclear waste-contaminated vadose sediments at the Hanford Site, Washington State. *Applied and Environmental Microbiology* **2004,** *70*, (7), 4230-4241.
16. Krebs, B.; Hasse, K.-D., Refinements of the crystal structures of KTcO4, KReO4 and OsO4. The bond lengths in tetrahedral oxoanions and oxides of d0 transition metals. *Acta Crystallographica Section B* **1976,** *32*, (5), 1334-1337.
17. Bandoli, G.; Mazzi, U.; Roncari, E.; Deutsch, E., Crystal structures of technetium compounds. *Coordination Chemistry Reviews* **1982,** *44*, (2), 191-227.
18. Baston, G. M. N.; De Canniere, P. R.; Ilett, D. J.; Cowper, M. M.; Pilkington, N. J.; Tweed, C. J.; Wang, L.; Williams, S. J., Technetium behaviour in Boom Clay - a laboratory and field study. *Radiochimica Acta* **2002,** *90*, (9-11), 735-740.
19. Farrell, J.; Bostick, W. D.; Jarabek, R. J.; Fiedor, J. N., Electrosorption and reduction of pertechnetate by anodically polarized magnetite. *Environmental Science & Technology* **1999,** *33*, (8), 1244-1249.
20. Eriksen, T. E.; Ndalamba, P.; Bruno, J.; Caceci, M., The Solubility of TcO2 · nH2O in Neutral to Alkaline Solutions under Constant pco2. **1992,** *58-59*, (1), 67.
21. Meyer, R. E.; Arnold, W. D.; Case, F. I. *The solubility of electrodeposited Tc(IV) oxides*; NUREG/CR-4865; ORNL-6374; Other: ON: DE87013034 United States Other: ON: DE87013034 NTIS, PC A02/MF A01 - GPO. HEDB English; ; Oak Ridge National Lab., TN (USA); Nuclear Regulatory Commission, Washington, DC (USA). Office of Nuclear Regulatory Research: 1987; p Medium: X; Size: Pages: 20.
22. Warwick, P.; Aldridge, S.; Evans, N.; Vines, S., The solubility of technetium(IV) at high pH. *Radiochimica Acta* **2007,** *95*, (12), 709-716.
23. Liu, D. J.; Yao, J.; Wang, B.; Bruggeman, C.; Maes, N., Solubility study of Tc(IV) in a granitic water. *Radiochimica Acta* **2007,** *95*, (9), 523-528.
24. Langmuir, D., *Aqueous Environemntal Geochemistry*. Upper Saddle River, New Jersey, Prentice Hall: 1997.
25. Hess, N. J.; Xia, Y.; Rai, D.; Conradson, S. D., Thermodynamic Model for the Solubility of TcO2· xH2O(am) in the Aqueous Tc(IV) – Na+ – Cl− – H+ – OH− – H2O System. *Journal of Solution Chemistry* **2004,** *33*, (2), 199-226.
26. Lieser, K. H.; Bauscher, C., Technetium in the Hydrosphere and in the Geosphere .1. Chemistry of Technetium and Iron in Natural-Waters and Influence of the Redox Potential on the Sorption of Technetium. *Radiochimica Acta* **1987,** *42*, (4), 205-213.
27. Boggs, M. A.; Minton, T.; Dong, W. M.; Lomasney, S.; Islam, M. R.; Gu, B. H.; Wall, N. A., Interactions of Tc(IV) with Humic Substances. *Environmental Science & Technology* **2011,** *45*, (7), 2718-2724.
28. Gu, B. H.; Dong, W. M.; Liang, L. Y.; Wall, N. A., Dissolution of Technetium(IV) Oxide by Natural and Synthetic Organic Ligands under both Reducing and Oxidizing Conditions. *Environmental Science & Technology* **2011,** *45*, (11), 4771-4777.
29. Maes, A.; Geraedts, K.; Bruggeman, C.; Vancluysen, J.; Rossberg, A.; Hennig, C., Evidence for the interaction of technetium colloids with humic substances by X-ray absorption spectroscopy. *Environmental Science & Technology* **2004,** *38*, (7), 2044-2051.
30. Vichot, L.; Ouvrard, G.; Montavon, G.; Fattahi, M.; Musikas, C.; Grambow, B., XAS study of technetium(IV) polymer formation in mixed sulphate/chloride media. *Radiochimica Acta* **2002,** *90*, (9-11), 575-579.
31. Sekine, T.; Narushima, H.; Suzuki, T.; Takayama, T.; Kudo, H.; Lin, A.; Katsumura, Y., Technetium(IV) oxide colloids produced by radiolytic reactions in aqueous pertechnetate solution. *Colloids and Surfaces a-Physicochemical and Engineering Aspects* **2004,** *249*, (1-3), 105-109.

32. Sekine, T.; Narushima, H.; Kino, Y.; Kudo, H.; Lin, M. Z.; Katsumura, Y., Radiolytic formation of Tc(IV) oxide colloids. *Radiochimica Acta* **2002,** *90*, (9-11), 611-616.
33. Pepper, S. E.; Bunker, D. J.; Bryan, N. D.; Livens, F. R.; Charnock, J. M.; Pattrick, R. A. D.; Collison, D., Treatment of radioactive wastes: An X-ray absorption spectroscopy study of the reaction of technetium with green rust. *Journal of Colloid and Interface Science* **2003,** *268*, (2), 408-412.
34. Kobayashi, T.; Scheinost, A. C.; Fellhauer, D.; Gaona, X.; Altmaier, M., Redox behavior of Tc(VII)/Tc(IV) under various reducing conditions in 0.1 M NaCl solutions. **2013,** *101*, (5), 323.
35. Hebel, L. C.; Christensen, E. L.; Donath, F. A.; Falconer, W. E.; Lidofsky, L. J.; Moniz, E. J.; Moss, T. H.; Pigford, R. L.; Pigford, T. H.; Rochlin, G. I.; Silsbee, R. H.; Wrenn, M. E.; Committee, A. P. S. C. R.; Frauenfelder, H.; Cairns, T. L.; Panofsky, W. K. H.; Simmons, M. G., Report to the American Physical Society by the study group on nuclear fuel cycles and waste management. *Reviews of Modern Physics* **1978,** *50*, (1), S1-S176.
36. DOE DOE's License Application for a High-Level Waste Geologic Repository at Yucca Mountain. https://www.nrc.gov/waste/hlw-disposal/yucca-lic-app.html
37. Mann, F. M. *Integrated Disposal Facility Risk Assessment*; United States, 2003; p 162.
38. SRR Closure & Waste Disposal Authority Aiken, S. *PERFORMANCE ASSESSMENT for the SALTSTONE DISPOSAL FACILITY at the SAVANNAH RIVER SITE*; SRR Closure & Waste Disposal Authority Aiken, SC 29808: Aiken, SC 29808, 2009.
39. Li, D.; Kaplan, D. I., Sorption coefficients and molecular mechanisms of Pu, U, Np, Am and Tc to Fe (hydr)oxides: A review. *Journal of Hazardous Materials* **2012,** *243*, 1-18.
40. Vandergraaf, T. T.; Ticknor, K. V.; George, I. M., Reactions Between Technetium in Solution and Iron-Containing Minerals Under Oxic and Anoxic Conditions. In *Geochemical Behavior of Disposed Radioactive Waste*, American Chemical Society: 1984; Vol. 246, pp 25-43.
41. Palmer, D. A.; Meyer, R. E., Adsorption of technetium on selected inorganic ion-exchange materials and on a range of naturally occurring minerals under oxic conditions. *Journal of Inorganic and Nuclear Chemistry* **1981,** *43*, (11), 2979-2984.
42. Kaplan, D., Influence of surface charge of an Fe-oxide and an organic matter dominated soil on iodide and pertechnetate sorption. *Radiochim Acta* **2002,** *91*, 173-178.
43. Sheppard, M. I.; Sheppard, S. C., Technetium Behaviour in Soils of the Canadian Precambrian Shield. In *Technetium in the Environment*, Desmet, G.; Myttenaere, C., Eds. Springer Netherlands: Dordrecht, 1986; pp 131-141.
44. Elwear, S.; German, K. E.; Peretrukhin, V. F., Sorption of Technetium on Inorganic Sorbents and Natural Minerals. *Journal of Radioanalytical and Nuclear Chemistry-Articles* **1992,** *157*, (1), 3-14.
45. Kaplan, D. I.; Serne, R. J., Pertechnetate Exclusion from Sediments. **1998,** *81*, (2), 117.
46. Muller, O.; White, W. B.; Roy, R., Crystal chemistry of some technetium-containing oxides. *Journal of Inorganic and Nuclear Chemistry* **1964,** *26*, (12), 2075-2086.
47. Ramanaidou, E.; Nahon, D.; Decarreau, A.; Melfi, A. J., Hematite and goethite from duricrusts developed by lateritic chemical weathering of Precambrian banded iron formations, Minas Gerais, Brazil. *Clays and Clay Minerals* **1996,** *44*, (1), 22-31.
48. Shuster, D. L.; Vasconcelos, P. M.; Heim, J. A.; Farley, K. A., Weathering geochronology by (U-Th)/He dating of goethite. *Geochimica et Cosmochimica Acta* **2005,** *69*, (3), 659-673.
49. Yapp, C. J., Climatic implications of surface domains in arrays of δD and δ18O from hydroxyl minerals: goethite as an example. *Geochimica et Cosmochimica Acta* **2000,** *64*, (12), 2009-2025.
50. Skomurski, F. N.; Rosso, K. M.; Krupka, K. M.; McGrail, B. P., Technetium Incorporation into Hematite (alpha-Fe2O3). *Environmental Science & Technology* **2010,** *44*, (15), 5855-5861.
51. Lukens, W. W.; Saslow, S. A., Facile incorporation of technetium into magnetite, magnesioferrite, and hematite by formation of ferrous nitrate in situ: precursors to iron oxide nuclear waste forms. *Dalton Transactions* **2018,** *47*, (30), 10229-10239.
52. Saslow, S. A.; Um, W.; Pearce, C. I.; Engelhard, M. H.; Bowden, M. E.; Lukens, W.; Leavy, I. I.; Riley, B. J.; Kim, D.-S.; Schweiger, M. J.; Kruger, A. A., Reduction and Simultaneous Removal

of 99Tc and Cr by Fe(OH)2(s) Mineral Transformation. *Environmental Science & Technology* **2017,** *51*, (15), 8635-8642.

53. Um, W.; Chang, H. S.; Icenhower, J. P.; Lukens, W. W.; Serne, R. J.; Qafoku, N. P.; Westsik, J. H.; Buck, E. C.; Smith, S. C., Immobilization of 99-Technetium (VII) by Fe(II)-Goethite and Limited Reoxidation. *Environmental Science & Technology* **2011,** *45*, (11), 4904-4913.
54. Um, W.; Chang, H.; Icenhower, J. P.; Lukens, W. W.; Serne, R. J.; Qafoku, N.; Kukkadapu, R. K.; Westsik, J. H., Iron oxide waste form for stabilizing (TC)-T-99. *Journal of Nuclear Materials* **2012,** *429*, (1-3), 201-209.
55. McBeth, J.; Lloyd, J.; Law, G.; R. Livens, F.; T. Burke, I.; Morris, K., *Redox interactions of technetium with iron-bearing minerals*. 2011; Vol. 75, p 2419-2430.
56. Yalçıntaş, E.; Scheinost, A. C.; Gaona, X.; Altmaier, M., Systematic XAS study on the reduction and uptake of Tc by magnetite and mackinawite. *Dalton Transactions* **2016,** *45*, (44), 17874-17885.
57. Livens, F. R.; Jones, M. J.; Hynes, A. J.; Charnock, J. M.; Mosselmans, J. F. W.; Hennig, C.; Steele, H.; Collison, D.; Vaughan, D. J.; Pattrick, R. A. D.; Reed, W. A.; Moyes, L. N., X-ray absorption spectroscopy studies of reactions of technetium, uranium and neptunium with mackinawite. *Journal of Environmental Radioactivity* **2004,** *74*, (1-3), 211-219.
58. Wharton, M. J.; Atkins, B.; Charnock, J. M.; Livens, F. R.; Pattrick, R. A. D.; Collison, D., An X-ray absorption spectroscopy study of the coprecipitation of Tc and Re with mackinawite (FeS). *Applied Geochemistry* **2000,** *15*, (3), 347-354.
59. Marshall, T. A.; Morris, K.; Law, G. T. W.; Mosselmans, J. F. W.; Bots, P.; Parry, S. A.; Shaw, S., Incorporation and Retention of 99-Tc(IV) in Magnetite under High pH Conditions. *Environmental Science & Technology* **2014,** *48*, (20), 11853-11862.
60. Thorpe, C. L.; Boothman, C.; Lloyd, J. R.; Law, G. T. W.; Bryan, N. D.; Atherton, N.; Livens, F. R.; Morris, K., The interactions of strontium and technetium with Fe(II) bearing biominerals: Implications for bioremediation of radioactively contaminated land. *Applied Geochemistry* **2014,** *40*, 135-143.
61. Smith, F. N.; Um, W.; Taylor, C. D.; Kim, D.-S.; Schweiger, M. J.; Kruger, A. A., Computational Investigation of Technetium(IV) Incorporation into Inverse Spinels: Magnetite (Fe3O4) and Trevorite (NiFe2O4). *Environmental Science & Technology* **2016,** *50*, (10), 5216-5224.
62. Fredrickson, J. K.; Zachara, J. M.; Plymale, A. E.; Heald, S. M.; McKinley, J. P.; Kennedy, D. W.; Liu, C. X.; Nachimuthu, P., Oxidative dissolution potential of biogenic and abiogenic TcO2 in subsurface sediments. *Geochimica Et Cosmochimica Acta* **2009,** *73*, (8), 2299-2313.
63. Lenz, M.; Lens, P. N. L., The essential toxin: The changing perception of selenium in environmental sciences. *Science of The Total Environment* **2009,** *407*, (12), 3620-3633.
64. Winkel, L. H. E.; Johnson, C. A.; Lenz, M.; Grundl, T.; Leupin, O. X.; Amini, M.; Charlet, L., Environmental Selenium Research: From Microscopic Processes to Global Understanding. *Environmental Science & Technology* **2012,** *46*, (2), 571-579.
65. Jörg, G.; Bühnemann, R.; Hollas, S.; Kivel, N.; Kossert, K.; Van Winckel, S.; Gostomski, C. L. v., Preparation of radiochemically pure 79Se and highly precise determination of its half-life. *Applied Radiation and Isotopes* **2010,** *68*, (12), 2339-2351.
66. Séby, F.; Potin-Gautier, M.; Giffaut, E.; Borge, G.; Donard, O. F. X., A critical review of thermodynamic data for selenium species at 25°C. *Chemical Geology* **2001,** *171*, (3), 173-194.
67. Seby, F.; Potin-Gautier, M.; Giffaut, E.; Donard, O. F. X., Assessing the speciation and the biogeochemical processes affecting the mobility of selenium from a geological repository of radioactive wastes to the biosphere. *Analusis* **1998,** *26*, (5), 193-198.
68. Olyslaegers, G.; Zeevaert, T.; Pinedo, P.; Simon, I.; Prohl, G.; Kowe, R.; Chen, Q.; Mobbs, S.; Bergstrom, U.; Hallberg, B.; Katona, T.; Eged, K.; Kanyar, B., A comparative radiological assessment of five European biosphere systems in the context of potential contamination of well water from the hypothetical disposal of radioactive waste. *Journal of Radiological Protection* **2005,** *25*, (4), 375-391.

69. Barescut, J. C.; Gariel, J. C.; Péres, J. M.; Février, L.; Martin-Garin, A., Biogeochemical behaviour of anionic radionuclides in soil: Evidence for biotic interactions. *Radioprotection* **2005,** *40*, (S1), S79-S86.
70. Grambow, B., Mobile fission and activation products in nuclear waste disposal. *Journal of Contaminant Hydrology* **2008,** *102*, (3), 180-186.
71. Fernández-Martínez, A.; Charlet, L., Selenium environmental cycling and bioavailability: a structural chemist point of view. *Reviews in Environmental Science and Bio/Technology* **2009,** *8*, (1), 81-110.
72. Winkel, L. H. E.; Vriens, B.; Jones, G. D.; Schneider, L. S.; Pilon-Smits, E.; Banuelos, G. S., Selenium Cycling Across Soil-Plant-Atmosphere Interfaces: A Critical Review. *Nutrients* **2015,** *7*, (6), 4199-4239.
73. Nothstein, A. K.; Eiche, E.; Riemann, M.; Nick, P.; Winkel, L. H. E.; Gottlicher, J.; Steininger, R.; Brendel, R.; von Brasch, M.; Konrad, G.; Neumann, T., Tracking Se Assimilation and Speciation through the Rice Plant - Nutrient Competition, Toxicity and Distribution. *Plos One* **2016,** *11*, (4).
74. Curti, E.; Puranen, A.; Grolimund, D.; Jädernas, D.; Sheptyakov, D.; Mesbah, A., Characterization of selenium in UO2 spent nuclear fuel by micro X-ray absorption spectroscopy and its thermodynamic stability. *Environmental Science: Processes & Impacts* **2015,** *17*, (10), 1760-1768.
75. Curti, E.; Froideval-Zumbiehl, A.; Günther-Leopold, I.; Martin, M.; Bullemer, A.; Linder, H.; Borca, C. N.; Grolimund, D., Selenium redox speciation and coordination in high-burnup UO2 fuel: Consequences for the release of 79Se in a deep underground repository. *Journal of Nuclear Materials* **2014,** *453*, (1), 98-106.
76. Bingham, P. A.; Connelly, A. J.; Cassingham, N. J.; Hyatt, N. C., Oxidation state and local environment of selenium in alkali borosilicate glasses for radioactive waste immobilisation. *Journal of Non-Crystalline Solids* **2011,** *357*, (14), 2726-2734.
77. Masscheleyn, P. H.; Patrick, W. H., Biogeochemical Processes Affecting Selenium Cycling in Wetlands. *Environmental Toxicology and Chemistry* **1993,** *12*, (12), 2235-2243.
78. Masscheleyn, P. H.; Delaune, R. D.; Patrick, W. H., Biogeochemical Behavior of Selenium in Anoxic Soils and Sediments - an Equilibrium Thermodynamics Approach. *Journal of Environmental Science and Health Part a-Environmental Science and Engineering & Toxic and Hazardous Substance Control* **1991,** *26*, (4), 555-573.
79. Masscheleyn, P. H.; Delaune, R. D.; Patrick, W. H., Transformations of Selenium as Affected by Sediment Oxidation Reduction Potential and Ph. *Environmental Science & Technology* **1990,** *24*, (1), 91-96.
80. Elrashidi, M. A.; Adriano, D. C.; Workman, S. M.; Lindsay, W. L., Chemical-Equilibria of Selenium in Soils - a Theoretical Development. *Soil Science* **1987,** *144*, (2), 141-152.
81. Hatten Howard, J., Geochemistry of selenium: formation of ferroselite and selenium behavior in the vicinity of oxidizing sulfide and uranium deposits. *Geochimica et Cosmochimica Acta* **1977,** *41*, (11), 1665-1678.
82. Chen, F. R.; Burns, P. C.; Ewing, R. C., Se-79: geochemical and crystallo-chemical retardation mechanisms. *Journal of Nuclear Materials* **1999,** *275*, (1), 81-94.
83. Missana, T.; Alonso, U.; Garcia-Gutierrez, M., Experimental study and modelling of selenite sorption onto illite and smectite clays. *Journal of Colloid and Interface Science* **2009,** *334*, (2), 132-138.
84. Roh, Y.; Lee, S. Y.; Elless, M. P., Characterization of corrosion products in the permeable reactive barriers. *Environmental Geology* **2000,** *40*, (1-2), 184-194.
85. Adegoke, H. I.; Adekola, F. A.; Fatoki, O. S.; Ximba, B. J., Sorptive Interaction of Oxyanions with Iron Oxides: A Review. *Polish Journal of Environmental Studies* **2013,** *22*, (1), 7-24.
86. Balistrieri, L. S.; Chao, T. T., Adsorption of Selenium by Amorphous Iron Oxyhydroxide and Manganese-Dioxide. *Geochimica Et Cosmochimica Acta* **1990,** *54*, (3), 739-751.
87. Zhang, P. C.; Sparks, D. L., Kinetics of Selenate and Selenite Adsorption Desorption at the Goethite Water Interface. *Environmental Science & Technology* **1990,** *24*, (12), 1848-1856.

88. Duc, M.; Lefevre, G.; Fedoroff, M.; Jeanjean, J.; Rouchaud, J. C.; Monteil-Rivera, F.; Dumonceau, J.; Milonjic, S., Sorption of selenium anionic species on apatites and iron oxides from aqueous solutions. *Journal of Environmental Radioactivity* **2003,** *70*, (1-2), 61-72.
89. Martínez, M.; Giménez, J.; de Pablo, J.; Rovira, M.; Duro, L., Sorption of selenium(IV) and selenium(VI) onto magnetite. *Applied Surface Science* **2006,** *252*, (10), 3767-3773.
90. Rovira, M.; Giménez, J.; Martínez, M.; Martínez-Lladó, X.; de Pablo, J.; Martí, V.; Duro, L., Sorption of selenium(IV) and selenium(VI) onto natural iron oxides: Goethite and hematite. *Journal of Hazardous Materials* **2008,** *150*, (2), 279-284.
91. Hayes, K. F.; Roe, A. L.; Brown Jr, G. E.; Hodgson, K. O.; Leckie, J. O.; Parks, G. A., In situ x-ray absorption study of surface complexes: Selenium oxyanions on α-FeOOH. *Science* **1987,** *238*, (4828), 783-786.
92. Su, C. M.; Suarez, D. L., Selenate and selenite sorption on iron oxides: An infrared and electrophoretic study. *Soil Science Society of America Journal* **2000,** *64*, (1), 101-111.
93. Rietra, R. P. J. J.; Hiemstra, T.; van Riemsdijk, W. H., Comparison of selenate and sulfate adsorption on goethite. *Journal of Colloid and Interface Science* **2001,** *240*, (2), 384-390.
94. Jordan, N.; Ritter, A.; Foerstendorf, H.; Scheinost, A. C.; Weiss, S.; Heim, K.; Grenzer, J.; Mucklich, A.; Reuther, H., Adsorption mechanism of selenium(VI) onto maghemite. *Geochimica Et Cosmochimica Acta* **2013,** *103*, 63-75.
95. Jordan, N.; Ritter, A.; Scheinost, A. C.; Weiss, S.; Schild, D.; Hubner, R., Selenium(IV) Uptake by Maghemite (gamma-Fe2O3). *Environmental Science & Technology* **2014,** *48*, (3), 1665-1674.
96. Catalano, J. G.; Zhang, Z.; Fenter, P.; Bedzyk, M. J., Inner-sphere adsorption geometry of Se(IV) at the hematite (100)-water interface. *Journal of Colloid and Interface Science* **2006,** *297*, (2), 665-671.
97. Wijnja, H.; Schulthess, C. P., Vibrational spectroscopy study of selenate and sulfate adsorption mechanisms on Fe and Al (hydr)oxide surfaces. *Journal of Colloid and Interface Science* **2000,** *229*, (1), 286-297.
98. Fukushi, K.; Sverjensky, D. A., A surface complexation model for sulfate and selenate on iron oxides consistent with spectroscopic and theoretical molecular evidence. *Geochimica Et Cosmochimica Acta* **2007,** *71*, (1), 1-24.
99. Kim, S. S.; Min, J. H.; Lee, J. K.; Baik, M. H.; Choi, J. W.; Shin, H. S., Effects of pH and anions on the sorption of selenium ions onto magnetite. *Journal of Environmental Radioactivity* **2012,** *104*, 1-6.
100. Iida, Y.; Tanaka, T.; Yamaguchi, T.; Nakayama, S., Sorption Behavior of Selenium(-II) on Rocks under Reducing Conditions. *Journal of Nuclear Science and Technology* **2011,** *48*, (2), 279-291.
101. Borsig, N.; Scheinost, A. C.; Shaw, S.; Schild, D.; Neumann, T., Retention and multiphase transformation of selenium oxyanions during the formation of magnetite via iron(II) hydroxide and green rust. *Dalton Transactions* **2018,** *47*, (32), 11002-11015.
102. López de Arroyabe Loyo, R.; Nikitenko, S. I.; Scheinost, A. C.; Simonoff, M., Immobilization of Selenite on Fe3O4 and Fe/Fe3C Ultrasmall Particles. *Environmental Science & Technology* **2008,** *42*, (7), 2451-2456.
103. Fevrier, L.; Martin-Garin, A.; Leclerc, E., Variation of the distribution coefficient (K-d) of selenium in soils under various microbial states. *Journal of Environmental Radioactivity* **2007,** *97*, (2-3), 189-205.
104. Tang, C.; Huang, Y. H.; Zeng, H.; Zhang, Z., Reductive removal of selenate by zero-valent iron: The roles of aqueous Fe2+ and corrosion products, and selenate removal mechanisms. *Water Research* **2014,** *67*, 166-174.
105. Chakraborty, S.; Bardelli, F.; Charlet, L., Reactivities of Fe(II) on Calcite: Selenium Reduction. *Environmental Science & Technology* **2010,** *44*, (4), 1288-1294.
106. Chen, Y.-W.; Truong, H.-Y. T.; Belzile, N., Abiotic formation of elemental selenium and role of iron oxide surfaces. *Chemosphere* **2009,** *74*, (8), 1079-1084.

107. Scheinost, A. C.; Kirsch, R.; Banerjee, D.; Fernandez-Martinez, A.; Zaenker, H.; Funke, H.; Charlet, L., X-ray absorption and photoelectron spectroscopy investigation of selenite reduction by FeII-bearing minerals. *Journal of Contaminant Hydrology* **2008,** *102*, (3), 228-245.
108. Murphy, A. P., Removal of selenate from water by chemical reduction. *Industrial & Engineering Chemistry Research* **1988,** *27*, (1), 187-191.
109. Zingaro, R. A.; Carl Dufner, D.; Murphy, A. P.; Moody, C. D., Reduction of oxoselenium anions by iron(II) hydroxide. *Environment International* **1997,** *23*, (3), 299-304.
110. Myneni, S. C. B.; Tokunaga, T. K.; Brown, G. E., Abiotic Selenium Redox Transformations in the Presence of Fe(II,III) Oxides. *Science* **1997,** *278*, (5340), 1106-1109.
111. Johnson, T. M.; Bullen, T. D., Selenium isotope fractionation during reduction by Fe(II)-Fe(III) hydroxide-sulfate (green rust). *Geochimica et Cosmochimica Acta* **2003,** *67*, (3), 413-419.
112. Scheidegger, A. M.; Grolimund, D.; Cui, D.; Devoy, J.; Spahiu, K.; Wersin, P.; Bonhoure, I.; Janousch, M., Reduction of selenite on iron surfaces: A micro-spectroscopic study. *Journal De Physique Iv* **2003,** *104*, 417-420.
113. Olegario, J. T.; Yee, N.; Miller, M.; Sczepaniak, J.; Manning, B., Reduction of Se(VI) to Se(-II) by zerovalent iron nanoparticle suspensions. *Journal of Nanoparticle Research* **2010,** *12*, (6), 2057-2068.
114. Yoon, I.-H.; Kim, K.-W.; Bang, S.; Kim, M. G., Reduction and adsorption mechanisms of selenate by zero-valent iron and related iron corrosion. *Applied Catalysis B: Environmental* **2011,** *104*, (1), 185-192.
115. Liang, L.; Yang, W.; Guan, X.; Li, J.; Xu, Z.; Wu, J.; Huang, Y.; Zhang, X., Kinetics and mechanisms of pH-dependent selenite removal by zero valent iron. *Water Research* **2013,** *47*, (15), 5846-5855.
116. Ling, L.; Pan, B. C.; Zhang, W. X., Removal of selenium from water with nanoscale zero-valent iron: Mechanisms of intraparticle reduction of Se(IV). *Water Research* **2015,** *71*, 274-281.
117. Bruggeman, C.; Maes, A.; Vancluysen, J.; Vandenmussele, P., Selenite reduction in Boom clay: Effect of FeS2, clay minerals and dissolved organic matter. *Environmental Pollution* **2005,** *137*, (2), 209-221.
118. Charlet, L.; Scheinost, A. C.; Tournassat, C.; Greneche, J. M.; Géhin, A.; Fernández-Martı´nez, A.; Coudert, S.; Tisserand, D.; Brendle, J., Electron transfer at the mineral/water interface: Selenium reduction by ferrous iron sorbed on clay. *Geochimica et Cosmochimica Acta* **2007,** *71*, (23), 5731-5749.
119. Cannière, P.; Maes, A.; Williams, S.; Bruggeman, C.; Beauwens, T.; Maes, N.; Cowper, M., Behaviour of Selenium in Boom Clay. State-of-the-art report. **2010**.
120. Scheinost, A. C.; Charlet, L., Selenite Reduction by Mackinawite, Magnetite and Siderite: XAS Characterization of Nanosized Redox Products. *Environmental Science & Technology* **2008,** *42*, (6), 1984-1989.
121. Schwertmann, U.; Cornell, R. M., Iron oxides in the laboratory. In *Iron Oxides in the Laboratory*, Wiley-VCH Verlag GmbH: 2000; pp i-xviii.
122. Liu, J.; Liang, C.; Zhang, H.; Tian, Z.; Zhang, S., General Strategy for Doping Impurities (Ge, Si, Mn, Sn, Ti) in Hematite Nanocrystals. *Journal of Physical Chemistry C* **2012,** *116*, (8), 4986-4992.
123. Galvez, N.; Barron, V.; Torrent, J., Effect of phosphate on the crystallization of hematite, goethite, and lepidocrocite from ferrihydrite. *Clays and Clay Minerals* **1999,** *47*, (3), 304-311.
124. Bolanz, R. M.; Wierzbicka-Wieczorek, M.; Caplovicova, M.; Uhlik, P.; Gottlicher, J.; Steininger, R.; Majzlan, J., Structural Incorporation of As5+ into Hematite. *Environmental Science & Technology* **2013,** *47*, (16), 9140-9147.
125. Das, S.; Essilfie-Dughan, J.; Hendry, M. J., Fate of adsorbed arsenate during phase transformation of ferrihydrite in the presence of gypsum and alkaline conditions. *Chemical Geology* **2015,** *411*, 69-80.

126. Abraitis, P. K.; Pattrick, R. A. D.; Vaughan, D. J., Variations in the compositional, textural and electrical properties of natural pyrite: a review. *International Journal of Mineral Processing* **2004,** *74*, (1-4), 41-59.
127. Morse, J. W., Interactions of Trace-Metals with Authigenic Sulfide Minerals - Implications for Their Bioavailability. *Marine Chemistry* **1994,** *46*, (1-2), 1-6.
128. Morse, J. W.; Luther, G. W., Chemical influences on trace metal-sulfide interactions in anoxic sediments. *Geochimica Et Cosmochimica Acta* **1999,** *63*, (19-20), 3373-3378.
129. Rickard, D.; Luther, G. W., Chemistry of iron sulfides. *Chemical Reviews* **2007,** *107*, (2), 514-562.
130. Bildstein, O.; Trotignon, L.; Perronnet, M.; Jullien, M., Modelling iron-clay interactions in deep geological disposal conditions. *Physics and Chemistry of the Earth* **2006,** *31*, (10-14), 618-625.
131. De Craen, M.; Van Geet, M.; Wang, L.; Put, M., High sulphate concentrations in squeezed Boom Clay pore water: evidence of oxidation of clay cores. *Physics and Chemistry of the Earth* **2004,** *29*, (1), 91-103.
132. Gaucher, E.; Robelin, C.; Matray, J. M.; Negral, G.; Gros, Y.; Heitz, J. F.; Vinsot, A.; Rebours, H.; Cassagnabere, A.; Bouchet, A., ANDRA underground research laboratory: interpretation of the mineralogical and geochemical data acquired in the Callovian-Oxfordian formation by investigative drilling. *Physics and Chemistry of the Earth* **2004,** *29*, (1), 55-77.
133. Joseph, C.; Schmeide, K.; Sachs, S.; Brendler, V.; Geipel, G.; Bernhard, G., Sorption of uranium(VI) onto Opalinus Clay in the absence and presence of humic acid in Opalinus Clay pore water. *Chemical Geology* **2011,** *284*, (3-4), 240-250.
134. Missana, T.; Alonso, U.; Scheinost, A. C.; Granizo, N.; García-Gutiérrez, M., Selenite retention by nanocrystalline magnetite: Role of adsorption, reduction and dissolution/co-precipitation processes. *Geochimica et Cosmochimica Acta* **2009,** *73*, (20), 6205-6217.
135. Diener, A.; Neumann, T., Synthesis and incorporation of selenide in pyrite and mackinawite. *Radiochimica Acta* **2011,** *99*, (12), 791-798.
136. Diener, A.; Neumann, T.; Kramar, U.; Schild, D., Structure of selenium incorporated in pyrite and mackinawite as determined by XAFS analyses. *Journal of Contaminant Hydrology* **2012,** *133*, 30-39.
137. Francisco, P. C. M.; Sato, T.; Otake, T.; Kasama, T.; Suzuki, S.; Shiwaku, H.; Yaita, T., Mechanisms of Se(IV) Co-precipitation with Ferrihydrite at Acidic and Alkaline Conditions and Its Behavior during Aging. *Environmental Science & Technology* **2018,** *52*, (8), 4817-4826.
138. Börsig, N.; Scheinost, A. C.; Shaw, S.; Schild, D.; Neumann, T., Uptake mechanisms of selenium oxyanions during the ferrihydrite-hematite recrystallization. *Geochimica et Cosmochimica Acta* **2017,** *206*, 236-253.

11. THERMODYNAMIC DATABASE FOR GENERIC DISPOSAL SYSTEM ASSESSMENT

11.1. Introduction

This progress report (Level 4 Milestone Number M4SF-20LL010302082) summarizes research conducted at Lawrence Livermore National Laboratory (LLNL) within the Crystalline International Collaborations Activity Number SF-20LL010302081. The activity is focused on our long-term commitment of engaging our partners in international nuclear waste repository research. This includes participation in the Nuclear Energy Agency Thermochemical Database (NEA TDB) Project (Cindy Atkins-Duffin) and development of methodologies for integrating US and international thermodynamic databases for use in SFWST Generic Disposal System Assessment (GDSA) efforts.

LLNL is supporting the overall objectives of the Disposal Research (DR) Crystalline International Collaborations Research and Development (R&D) control account. The objective of this control account is to advance our understanding of long-term disposal of spent fuel in crystalline rocks (including both granitic and metamorphic rocks) and to develop necessary experimental and computational capabilities to evaluate various disposal concepts in such media. LLNL efforts in the Crystalline International Collaborations work package are focused on the following:

Continued engagement with the NEA TDB project through the support of Dr. Atkins-Duffin as the SFWST representative for international thermodynamic database development effort. This effort ensures that US GDSA model efforts are aligned with internationally accepted practices for repository performance assessment calculations.

- Dr. Cindy Atkins-Duffin is the Executive Group (EG) liaison to the TDB Cements team and will help coordinate the completion of the Cements report.
- Coordinating and integrating LLNL thermodynamic database efforts (Argillite DR workscope) with international efforts to ensure that GDSA model efforts are performed using internationally accepted thermochemical data.

In FY20, we focused on our longterm commitment to engaging our partners in international nuclear waste repository research. This includes participation in the Nuclear Energy Agency Thermochemical Database Project (Cindy Atkins-Duffin), thermodynamic database collaborations (Tom Wolery), and surface complexation model international collaborations (Mavrik Zavarin).

In FY19 we developed mechanisms for integration of NEA-TDB thermochemical data (new electronic database made available in 2018) with LLNL's thermodynamic databases. A short code was written to import new data and export formatted databases for use in Geochemists Workbench and other reactive transport codes. This effort was coordinated with the Argillite work package database development efforts. The goal for FY20 was to test this code for providing a new downloadable database that will be hosted on LLNL's thermodynamics website which incorporates NEA-TDB data into the LLNL database where appropriate.

As part of our international engagement with surface complexation model development, FY20 efforts included the assimilation of sorption data collected by our international RES3T team partners at the Helmholtz Zentrum Dresden Rossendorf. These data are in the process of being incorporated into LLNL's sorption database and will increase our database to approximately 20,000 individual measurements. A summary of that data will be provided in the Argillite International Collaborations FY20 M4 milestone report.

11.2. Nuclear Energy Agency Thermochemical Database Program

11.2.1 History of Project

The Nuclear Energy Agency (NEA) Thermochemical Database Program was conceived of and initiated with the goal to: 1) make available a comprehensive, internally consistent, internationally recognized database of selected chemical elements; 2) meet the specialized modeling requirements for safety assessments of radioactive waste and; 3) prioritize the critical review of relevant data for inorganic compounds and complexes containing actinides. Data from other elements present in radioactive waste are also critically reviewed as well as compounds and complexes of the previously considered elements with selected organic ligands.

The objective of the Program is to produce a database that contains data for all the elements of interest in radioactive waste disposal systems; document why and how the data are selected; give recommendations based on original experimental data, rather than compilation and estimates; document the sources of experimental data; provide an internally consistent thermodynamic parameters, and treat solids and aqueous species of the elements of interest for nuclear storage performance assessment calculations.

The qualification of existing data is conducted using documented Guidelines which include several components. A Technical Review is conducted by subject matter experts who critically review experimentally-determined literature data; reanalyze the data as necessary; and select data for inclusion in the database. Upon completion of the Technical Review, a Peer Review is undertaken. A second, independent panel of reviewers ensure that the technical reviewers followed the review Guidelines. A Comment Resolution component ensures that the Technical Reviewers address the comments made by the Peer Reviewers. At this time the volume is readied for final publication.

11.2.2 History of Phases and New Phase 6 Efforts

Phase I of the NEA-TDB program was conducted between 1984 and 1998. Initial review volumes included Uranium, Americium, Technetium, Neptunium/Plutonium.

Phase II of the NEA-TDB program updated all the actinide volumes. The update is contained in a single volume. Added in this phase were Nickel, Selenium, Zirconium, and the compounds and complexes of the reviewed elements with selected organic ligands - EDTA, ISA, oxalate, and citrate. The Program also conducted a workshop, “The Use of Thermodynamics Databases in Performance Assessment.” The phase ran from 1998-2003.

Phase III of the NEA-TDB program saw the introduction of a second product, State-of-the-Art reports. The first such report covered solid solutions of interest to nuclear waste management. Thorium, Iron (part I), and Tin volumes were added to the published collection.

Phase IV of the NEA-TDB program, conducted from 2008-2014, started the second portion of the Iron review; review of Molybdenum, and; review of Auxiliary Data which includes species and compounds necessary to describe aqueous chemistry of Aluminum and Silicon, data on inorganic species and compounds of elements such as Iodine, Boron, Magnesium, Calcium, Strontium, and Barium.

Phase 5 of the NEA-TDB program, conducted from 2014-2019 took on a second update to actinide and fission product volumes, and two State-of-the-Art reviews - Cement Minerals and High Ionic Strength

Aqueous Systems. The design and development of a new TDB electronic database that is compatible with PHREEQC was undertaken.

Phases 6 of the NEA-TDB program was officially started in February 2019 with all participating member parties having signed the Framework Agreement. The First Meeting of the Management Board (MB) and the Executive Group (EG) were held at the NEA in Paris February 19-20, 2019. Lena Evins (Sweden-SKB) was elected Chair of the MB and Stephane Brassinnes (ONDRAF/NIRAS- Belgium) Vice Chair. Canada and the Netherlands joined the Programme for this Phase. Elected to the Executive Group were Chair Marcus Altmaier (INE-Germany), Cindy Atkins-Duffin (DOE/LLNL-USA), Benoit Made (ANDRA-France), Pascal Reiller (CEA Saclay – France), and Kastriot Spahiu (SKB (retired)-Sweden. In process projects from Phase 5 were brought forward to Phase 6.

The current status of the Phase 6 program and the associated reviews are:

- **Iron (Part II) Volume** – Published online (NEA TDB website) in January, 2020.
- **2nd Update of the Actinides Volume** – Issues with the Uranium chapter were identified and then resolved by members of the review team. The final draft is now in preparation by the TDB staff before transmittal to the NEA publishing group. Publication of this volume is anticipated in the summer of 2020.
    - This volume will contain a dedication to the late Ingmar Grenthe, renown chemist and one of the founders of the TDB project
- **Ancillary Data Volume** – The full draft volume is now in the peer review process. Carlos Jove-Colon (USA) is one of the peer reviewers.
- **Molybdenum Data Volume** – This review continues to struggle with delivery of information from the team to the NEA and to other teammates. Several rescoping and personnel assignments have been put into place. The EG will take a more visible management role in this project.
- **Cements State of the Art Report** – The team provided a new schedule to the EG. They had not delivered the individual drafts and internal reviews in December as described in their previous schedule of work. The new schedule indicates the individual draft will now be completed by September 2020. Internal reviews would commence in the following summer. There will be a scheduled videoconference at the end of June to status their progress.
- **High Ionic Strength Solutions State of the Art Report** – The deadline for the completion of the first drafts and of all internal reviews was February 2020. A progress report received in April indicated a three month delay in the delivery of the first drafts. The latest information received by the EG is that "there is progress, but it is slow."
- **Organics Update** – The initiation report work is underway. The literature search is projected to be complete by the end of July and the final initiation report submitted by the end of October for review by the MB for their November meeting.
- **Lanthanides Volume** – The initiation team has indicated they intend to submit their final report by the end of June.
- **High Temperature State of the Art Report** – The initiators have submitted a document containing a synopsis of the topics that will be covered and the organization of their initiation report.
- **TDB course** – planned to be held in Paris, November 2020 – The webpage and final outline are available online, including the registration page. Possible impact to this activity from COVID 19 will be evaluated at some later time.

The NEA has announced there will be no "in person" meetings convened for NEA projects through this calendar year. Plans are in progress to convene the annual meeting in November of the Management Board and the Executive Group by virtual means.

11.3. An Interactive SUPCRT Data Tool for Adding New Species and Outputting New Data Files for Reactive Transport Codes

11.3.1 Introduction

The goal of this task is to create software to help manage thermodynamic database files as new and improved data become available. The software will ensure that users adding data to databases do so in way that is correct, convenient, consistent with existing data, and in a form immediately useful for reactive transport modeling.

The task consists of two main efforts:

1. Method to add thermodynamic data for new species, or replace thermodynamic data for existing species to the existing database
2. Produce a new data file for the user-specified reaction path code (e.g. PHREEQC, EQ3/6, GWB etc.) that contains the new or modified data formatted for the code of choice.

We choose for this version of the software to work from the SUPCRT data base developed by Helgeson and others at UC Berkeley (Helgeson et al., 1974a,b, 1976, 1981). Our starting file is the SUPCRT version that has been augmented with additional data by Chen Zhu and co-workers at Indiana University and referred to as SUPCRTBL (Zimmer et al., 2016).

We have chosen to use the scripting language Tcl/Tk to create the software. Tcl can be used with all major platforms and Tk provides easy creation of a graphical interface for convenient and fool-proof user input.

11.3.2 Progress to date

The first task we identified was to code a method to read in the SUPCRT data file and write reactions between all the species (or user-selected subset of species). This would be done using the user-selected set of "basis species" that are specific to the reactive transport code the user is targeting. This code reads in and stores all the data in SUPCRT and allows later manipulation needed to add new species or modify existing ones as desired.

The first version of code to carry out this task was completed in the Fall of 2019. However, in carrying out this work, we identified two additional needs to complete this task. The first involves correcting numerous formatting inconsistencies in the SUPCRT data file that cause our script to fail. Error checking to alert the user was one option, but would necessitate the user having to edit the data file to correct the problem. Because our high-level goal is to make robust software that would not involve user editing (which might not even be an option for some users), we decided to use the script itself to check for and correct these errors. This task was time-consuming and in some ways more difficult than the main task. This task continued on through the end of the year.

The second need is to include phase change data in the algorithm. Although these data are probably not necessary for most applications that we envision (low temperature aqueous systems), the data may be needed for some modeling at elevated temperatures (corrosion near reactors or heated HLW etc.) and

providing for this capability now will be much easier than inserting it later. Work on this task is not expected to be difficult, but has not yet started. The SUPCRT data file contains phase change data for many solids. These data will be carried forward along with an input option to add additional phase change data.

11.3.3 Next steps

The next step is a front end (including GUI) to allow a user to input new or revised data into the SUPCRT database. The code will make sure the data is entered correctly and in a way that is internally consistent with the existing data.

The final step is to provide coding to format the SUPCRT output for the reactive transport code of choice. Both of these steps will take advantage of the code already written to read in the data file and write reactions. We anticipate that these last two steps will take the same amount or less effort than effort to date.

The final task is to take the list of balanced chemical reactions and log K data and re-write it in the format of the desired reactive transport code. This work has not yet been started, but is not expected to involve anything other than providing the correct output format for each code. No additional data manipulation should be needed.

11.3.4 Summary

Work is in progress to produce a software tool to add new species and to produce enhanced data files for reactive transport codes relevant to the SFWST Generic Disposal System Assessment (GDSA) efforts. The tool is built around the SUPCRT data base as amended by Chen Zhu and co-workers (SUPCRTBL). The code is meant to be used by someone wanting to add new data to SUPCRT and ensure that it is internally consistent with the existing data. The code will produce a new version of the data file needed to run any of several reactive transport codes. Currently we plan to produce files for PHREEQC, EQ3/6, and GWB. Additional file configurations can be readily added to support the GDSA efforts. Furthermore, our code can readily be modified to use data files other than SUCPRT as the starting database. In particular, this code will be applicable to the modified SUPCRT code under development in the Argillite work package and led by T. Wolery for use in the US SFWST Generic Disposal System Assessment (GDSA) efforts. A key goal is to facilitate the integration of US SFWST thermodynamic database development with international thermodynamic database compilations (e.g. the NEA-TDB radiochemical thermodynamic data).

A continuing focus for FY21 efforts will be to support the US participation in the NEA-TDB effort and developing mechanisms for integration of NEA-TDB thermochemical data (new electronic database made available in 2018) with LLNL's thermodynamic databases that support the SFWST GDSA activities. This effort is coordinated with the Argillite work package database development efforts. The goal is to provide a downloadable database that will be hosted on LLNL's thermodynamics website which incorporates NEA-TDB data into the LLNL database where appropriate. Updating thermodynamic databases and enhancement of our database integration code to ensure that SFWST GDSA efforts are based on current and internationally accepted thermodynamic data will be a key focus in the next fiscal year.

11.4. References

Helgeson H. C. and Kirkham, D. H. (1974a) Theoretical prediction of the thermodynamic behavior of aqueous electrolytes at high pressures and temperatures: I. Summary of the thermodynamic/electrostatic properties of the solvent. *Am. J. Sci.* 274, 1089-1198.

Helgeson H. C. and Kirkham, D. H. (1974b) Theoretical prediction of the thermodynamic behavior of aqueous electrolytes at high pressures and temperatures: II. Debye-Hiickel parameters for activity coefficients and relative partial molal properties. *Am. Jour. Sci.* 274, 1199-1261.

Helgeson H. C. and Kirkham, D. H. (1976) Theoretical prediction of the thermodynamic behavior of aqueous electrolytes at high pressures and temperatures: III. Equation of state for aqueous species at infinite dilution. *Am. Jour. Sci.* 276, 97-240.

Helgeson H. C., Kirkham D. H., and Flowers G. C. (1981) Theoretical prediction of the thermodynamic behavior of aqueous electrolytes at high pressures and temperatures: IV. Calculation of activity coefficients, osmotic coefficients, and apparent molal and standard and relative partial molal properties to 600°C and 5 kb. *Am. Jour. Sci.* 281, 1249-1546.

Zimmer K., Zhang Y., Lu P., Chen Y., Zhang G., Dalkilic M., and Zhu (2016) SUPCRTBL: A revised and extended thermodynamic dataset and software package of SUPCRT92. *Computers & Geosciences* 90 (Part A), 97-111.

12. ILLITIZATION OF SODIUM AND POTASSIUM SMECTITE

12.1 Introduction

The Spent Fuel & Waste Science & Technology (SFWST) program under the U.S. Department of Energy Office of Spent Fuel Waste Disposition (SFWD), is focused on research and development activities related to storage, transportation, and disposal of used nuclear fuel and high-level nuclear waste. Within the disposal campaign, various host rock media, which include salt, crystalline, and argillite, are being investigated to advance the understanding and performance of long-term isolation. With respect to crystalline and argillite repositories, characterization of buffer materials proposed for geotechnical barrier media (i.e., bentonite) concerning heat-generating nuclear waste is critical for performance assessment and evaluation of the safety case. The final design of the repository (i.e. waste package spacing, heat output, water and heat properties of the rock, etc.) and barrier systems will determine the maximum temperatures experienced, where predictions vary among international programs (100ºC to >200ºC). Elevated temperatures can result in chemical alterations of the buffer material, such as illitization, reducing plasticity and swelling behavior. The process of illitization, in particular, is derived from both natural and synthesized experimental samples, where environmental conditions for natural systems are not well established. Therefore, it is imperative for laboratory experiments to aid in evaluation of certain conditions that control illitization, such as the work presented here.

Illitization is the formation of illite from smectite clay occurring by diagenetic processes in nature. The rate and extent of illitization is known to be affected by the concentration of silica and potassium, as well as time, temperature, initial chemical composition of material, solution chemistry, and pressure. The transformation from smectite to illite has been most commonly observed in natural samples taken from various aged formations and at multiple depths of lithologies. This type of process, also known as burial diagenesis, occurs under fairly long geologic timescales and is temperature controlled solely by geothermal gradients. Alternatively, hydrothermal systems can reproduce these earth processes on much shorter timescales to help better understand the effect of the various conditions mentioned above, particularly solution/clay ratio and fluid composition. Many experimental studies with various conditions have been carried out to investigate the conversion of smectite to illite within hydrothermal settings (Inoue, 1983; Velde and Vasseur, 1992; Huang et al., 1993; Roaldset et al., 1998; Mosser-Ruck et al., 2001; Ferrage et al. 2011; among others). For instance, Huang et al. (1993) estimated the stoichiometric relationship of the reaction (Equation 12-1) based on their empirical kinetic model and assuming aluminum conservation and substitution. Nevertheless, the rate associated with conversion, along with the path of particular reaction mechanisms, remain unresolved.

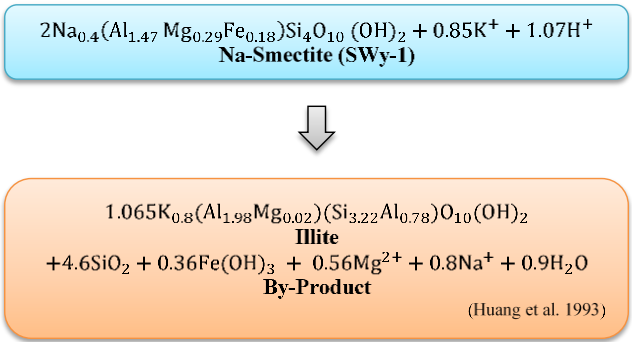

Equation 12-1

Two main process mechanisms, with several others hypothesized over the decades, are thought to occur during transformation from smectite to illite: 1) dissolution/recrystallization and 2) solid-state transformation. The first is a continuous transformation of smectite layers to illite where complete dissolution of the parent mineral is followed by the nucleation and growth of the new mineral. During conversion under certain conditions, the smectite crystallites become unstable, subsequently dissolving into more stable silicate phases (illite/smectite, vermiculite, illite, chlorite, micas, and zeolite (Inoue, 1995)). The solid-state transformation typically involves a fluid that acts as a catalyst to drive the gradual alteration, layer-by-layer, of the parent mineral (Cuadros and Linares, 1996). Either transformation process can occur during illitization.

Temperature continues to be an important factor for conversion and is a main concern for a repository with heat-generating waste. The activation energy of illitization, dependent on temperature, can vary greatly (ranging from 4 to 30 kcal; Meunier and Velde, 2004) with other parameters as well, leading to uncertainty within kinetic models (Huang et al., 1993; Ferrage et al., 2011). Roaldset et al. (1998) assessed the effect of temperature by performing hydrothermal experiments ranging from 180°C to 350°C, with two concentrations of KCl (1.0 N and 0.01 N) for a duration of 24 hours and a solution/clay ratio slightly over 300. Through XRD analysis, Roaldset et al. observed in the 1.0 N KCl case, the percentage of structural smectite decreased for temperatures above 200°C with optimal temperatures for nearly complete conversion of smectite to illite, taking place at 240°C. In the lower concentration case, 0.01 N, illitization began at 50°C higher than the 1.0 N KCl case (250°C), and completed at 300°C. This also indicated when a higher concentration of potassium is in the system, the temperature needed is lower for the illitization process to begin.

Many other studies have found the dependence not only on temperature, but on potassium, either in the clay interlayer or reactor solution, to convert as well (Eberl, 1977; Inoue, 1983; Huang et al, 1993; Cuadros and Linares, 1996; Whitney, 1990; Mosser-Ruck et al., 2001). For instance, Huang et al. (1993) varied the concentration of KCl solution from 0.1 M to 6 M in their conversion reactions of Na-smectite along with temperature (250°C to 325°C) and liquid/solid loading from 5 to 10. Similar to Roaldset et al. (1998), Huang et al. (1993) found through XRD patterns the amount of illitic layers increase in shorter time periods with higher concentrations of KCl in the system at each temperature.

Cuadros and Linares (1996) XRD analyses confirmed that, for the most extreme conditions of time, K^+ concentration, and temperature, the extent of transformation of smectite to illite was 15%. XRD was able to show complete transformation of smectite to illite starting from a pure smectite mineral. The amount of dissolved silica was shown to be influenced by increasing K^+ concentrations, temperature and reaction time. It was observed that there was a rapid rate of dissolution between 0 and 30 days and after this, a much slower steady rate of silica dissolved from 30 to 180 days. Cuadros and Linares stated that this phenomenon could be attributed to two stages of dissolution. Firstly, that non crystalline siliceous phases, cristobalite, plagioclase, quartz and smectite are rapidly dissolved within the first 30 days. The second stage is attributed to silica dissolved as a result of smectite to illite transformation. However, the amount of clay used in their studies (5 grams to 25 mL solution) is much higher compared to conditions in this study.

The amount of silica in the system is directly correlated with the water to rock ratio in the reaction and has been shown to alter the reactivity of the system (Howard and Roy, 1985; Whitney, 1990; Cuadros and Linares, 1996). However, only a select number of experimental endeavors vary this ratio or analyzed solution concentrations to fully examine the effect. Also, most studies, previously mentioned, use a small liquid to solid ratio, meaning there is a large amount of silica in the system, which could be inhibiting certain processes from occurring for full transformation.

This study focuses primarily on expanding the current knowledge about the following variables influencing the rate and extent of illitization: initial clay composition of starting smectite materials, variation of the interlayer cation within the smectite structure, and variation of silica content (liquid to clay ratio) and solution chemistry of reactor fluid. Length of reaction time was varied and two types of reactor fluid were used, thereby aiding in the determination of the driving factors that illicit the physicochemical changes needed for illitization and certain conditions to achieve complete illitization.

12.2 Experimental Approach

Sample Preparation: To relate to bentonite material, the sodium form smectite (SWy-2) from the Clay Minerals Society Source Clays was chosen as a starting material to conduct illitization studies. The clay was first crushed by mortar and pestle, and sieved to obtain less than 75μm particle size fractions (#200 sieve). To further remove impurities, less than 2 μm clay particles were obtained from suspension after settling of the 75 μm size for 23.3 hours in a 1000 mL graduated cylinder with deionized water (100 solid to liquid loading up to 30 cm) . After carefully pouring off the supernatant, the less than 2 μm settled portion is collected, dried at 60°C, and crushed again via mortar and pestle. A potassium rich environment was desired to facilitate ideal conditions for conversion. Therefore, the 2 μm SWy-2 Na-form was also cation exchanged with 1M KCl to produce the K-form smectite. The cation exchange involved subsequent saturation with 1M KCl solution, followed by removal of any excess chloride (i.e. no precipitant in $AgNO_3$ solution).

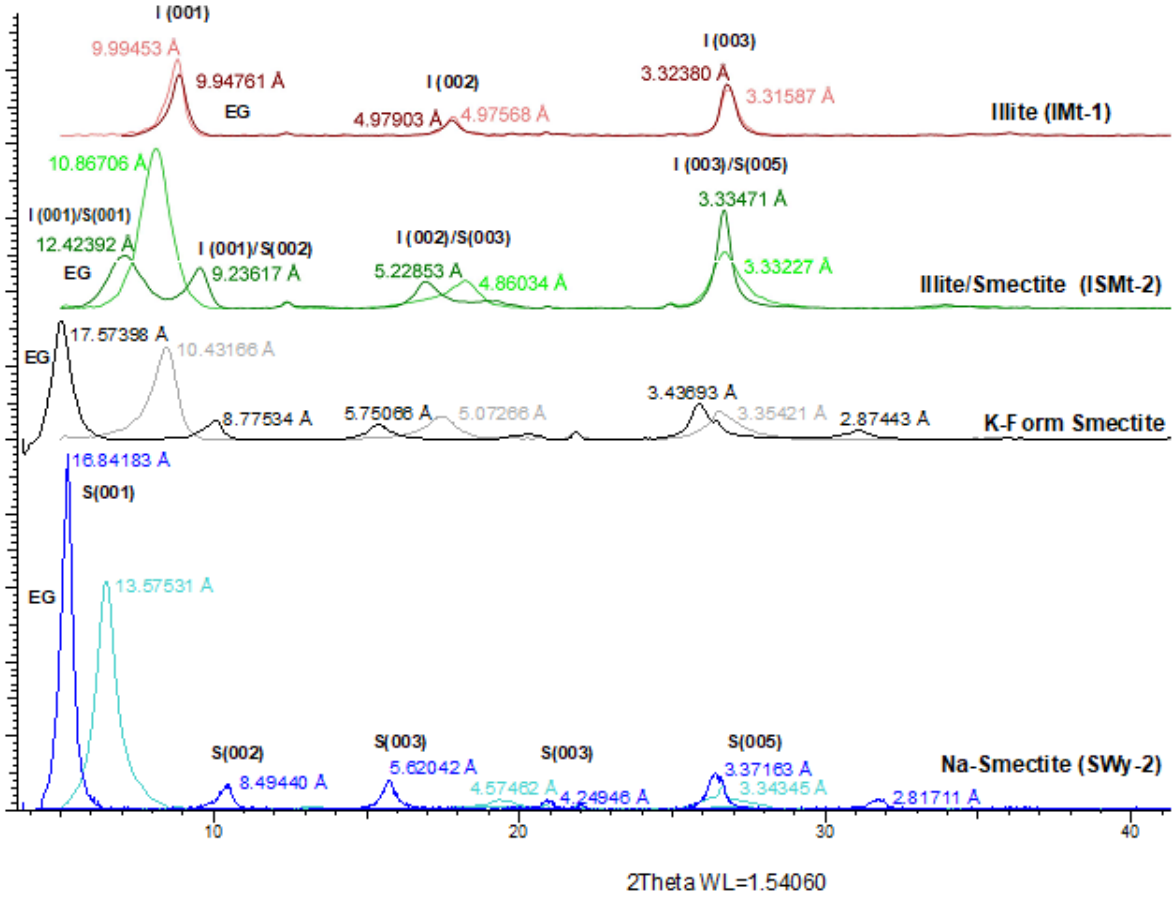

Figure 12-1: XRD spectra of source clays from the Clay Mineral's Society, along with potassium exchanged smectite. Air-dried oriented mounts were made for each and subsequently glycolated (EG).

A compilation of XRD scans, shown in Figure 12-1, from raw source clays such as Wyoming Na-smectite (SWy-2), discrete illite (IMt-1), illite/smectite 60:40 (ISMt-2) and also SWy-2 clay exchanged with 1M KCl to replace interlayer Na-cations with K-cations, resulting in K-form smectite. The curves are arranged in a manner to distinguish the differences in d-spacings and peak responses of each untreated clay type, going from smectite to illite. The responses of each clay type are comparable to those in other literature (Moore and Reynolds, 1997; Cuadros and Linares, 1996; Roaldset et. al, 1998; Ferrage et. al, 2011), where illite experiences little to no swelling upon glycolation, and smectite samples swell, shifting the 001 peak to a lower º2-θ or higher d-spacing. The identification of smectite can also be accomplished via saturation of the clay with K and subsequent heating to 300C; it will produce an XRD spectra akin to illite. Although, the clay wasn't heated to 300C after saturation with KCl in these studies, it is observable that the air-dried "K-Form Smectite" produces an XRD spectra that is similar to that of illite, with a 001 reflection at ~10.4 Å (Moore and Reynolds, 1997). This shift is a distinguishable feature between K-smectite and Na-smectite. Also typical to other data, the illite/smectite (ISMt-2) response shows the characteristic double reflection after glycolation between 5-10º 2-θ, which is important for identification of mixed layer clays going forward.

Thermal Alteration Experiments: The reactor liquid to solid clay ratio is known to affect illitization rates, and yet has only marginally been focused on in previous studies. Therefore, the approach in this study was to alter liquid to solid ratios reacted within 200 mL acid digestion Parr Vessels, thereby examining if there is a critical point for conversion. Due to maximum temperatures that can be seen in repository settings (Zheng et al., 2017), 200ºC was chosen for our reactions. In order to mitigate potential hazards by using the Parr Vessel reactors, liquid volumes were limited to 150 mL. To determine the most ideal mass of clay for conversion, the amount of smectite needed to convert to 1 mole of illite was calculated based on their respective stoichiometric equations and the solubility of SiO_2 at 200ºC. The optimal amount of smectite calculated in volumes of 150 mL was 0.169g, yielding a liquid to solid ratio of approximately 1000. Subsequent loadings of 500 and 100 were used to compare conversion rates. Additionally, time scales of 7 days were used for all loadings, where longer periods of 14, 56, and 112 days were used for the ideal 1000 loading case. Reactor fluid consisted of 1M KCl and water to determine the result of a potassium rich environment.

Table 12-15: List of reacted samples and corresponding conditions.

Clay Type	Solution	Loading	Time (days)	Naming Convention
Na-Form Smectite	1M KCl	100	7	Na-100-KCl-7
		500	7	Na-500-KCl-7
		1000	7	Na-1000-KCl-7
			56	Na-1000-KCl-56
			112	Na-1000-KCl-112
	DI water	100	7	Na-100-DI-7
		500	7	Na-500-DI-7
		1000	7	Na-1000-DI-7
			14	Na-1000-DI-14
K-Form Smectite	1M KCl	100	7	K-100-KCl-7
		500	7	K-500-KCl-7
		1000	7	K-1000-KCl-7
			56	K-1000-KCl-56
			112	K-1000-KCl-112
	DI water	100	7	K-100-DI-7
		500	7	K-500-DI-7
		1000	7	K-1000-DI-7
			14	K-1000-DI-14

Analysis Techniques: After being heated for the allotted time of study, the Parr Vessel reactors were removed and allowed to cool to room temperature. Once opened, the reactor solution and solid clay particles were separated. Readings of the solution pH were taken, and the clay particles were rinsed for excess chloride removal followed by drying in the oven at 60ºC. Once dried, the solid portions were weighed and recorded to calculate the amount of dissolved solids in solution given the starting mass for each reaction.

A Bruker D2 Phaser Desktop X-ray diffraction (XRD) instrument with CuK α radiation was used for the identification and peak position changes of the crystalline structure to determine extent of conversion after

reaction. Oriented mounts were made from the reacted clay by adding 0.1 g to 1 mL of a 70:30 water: ethanol mixture and sonicating for approximately one minute. The solution was transferred, via carefully pipetting in a circular motion, to a zero-background silicon wafer mount. The wafer was delicately transferred to a 60ºC oven to dry before analyzing on the XRD (2-θ domain from 3-70º at 0.2 second step-size). Solvation of the dried oriented mounts with ethylene glycol was also performed to determine any swelling characteristics. The sample was placed on an elevated platform in a chamber saturated with ethylene glycol vapor, which was then transferred to an oven for 24 hours at 60°C. The sample is immediately taken to be analyzed on the XRD with identical settings as above.

For elemental analysis of the collected liquid samples, a Perkin Elmer inductively coupled plasma – optimal emission spectrometer (ICP-OES) Optima8000, equipped with a constant internal standard of 1ppm Sc was used. Samples reacted in 1M KCl were diluted with 2% nitric acid to factors of 10 for analysis of Fe, Mg, Na, Ca, Si and Al and 1000 for analysis of K. Samples reacted in deionized water only required a dilution factor of 10 for all elements.

12.3 Results & Discussion

Figures 12-2 and 12-3 display the reaction products for Na-form and K-form smectite reacted in deionized (DI) water. These findings are considered a baseline for illitization studies because it gives insight into how various smectites behave under hydrothermal conditions and specifically how the interlayer cation plays a role in driving illitization. Apart from a slight variation in degrees-2θ, the glycolated reaction products are similar to the starting untreated Na and K-form smectites. There is an observed disparity in air-dried samples; the 001 reflections appear at higher degrees 2-θ and lower d-spacings as the loading is decreased. This could possibly be due to the collapse of the interlayers as the smectite is dehydrated. Many illitization studies have been carried out in the past on the effects of K concentration in solution ([K]) and even focus on similar starting materials, bentonite, K and Na-smectites, to carry out the reaction (Mosser-Ruck, 2011; Roaldset et. al, 1998, Ferrage et, al, 2011; Huang et al, 1993; Cuadros and Linares, 1996; Inoue, 1983). None have emphasized the impact of Na-form and K-form smectite on illitization under hydrothermal conditions without an added K-source. Whitney and Northop (1988) experimented with Wyoming bentonites reacted in distilled water and found that temperatures 250°C and above result in a decrease in expandability. The experiments unique to this paper were run at 200°C. The interlayer, as indicated by the (001) peak, shows a greater collapse for smaller loadings (100) over larger loadings (1000) for the air-dried conditions. However, it is apparent that the reaction products still have the ability to swell and expand through ethylene glycolation (EG). The EG reaction products show a (001) peak shift between 16.7 Å to 17.4 Å; Na-form reaction products have slightly higher (001) reflections for glycolated samples than K-form smectite. The (001) reflection measured for the untreated Na-form and K-form EG smectite was approximately 16.8 and 17.5 Å, respectively. The (001) reflections for the reaction products show that there is slightly less expansivity of K-smectite layers than for untreated K-smectite. The Na-form smectite reaction products, however, show more expansivity than untreated Na-form smectite due to higher d-spacing values. There are no findings on the XRD curve that indicate mixed-layer illite/smectite, nor discrete illite within the reaction products. Therefore, solution chemistry is an important factor in illitization. Even with an ideal interlayer cation for the starting material (K-form smectite), illitization requires a higher amount of K^+ ions present, even in the presence of high temperatures and pressures. Presented below are the findings for smectite minerals reacted in 1M KCl.

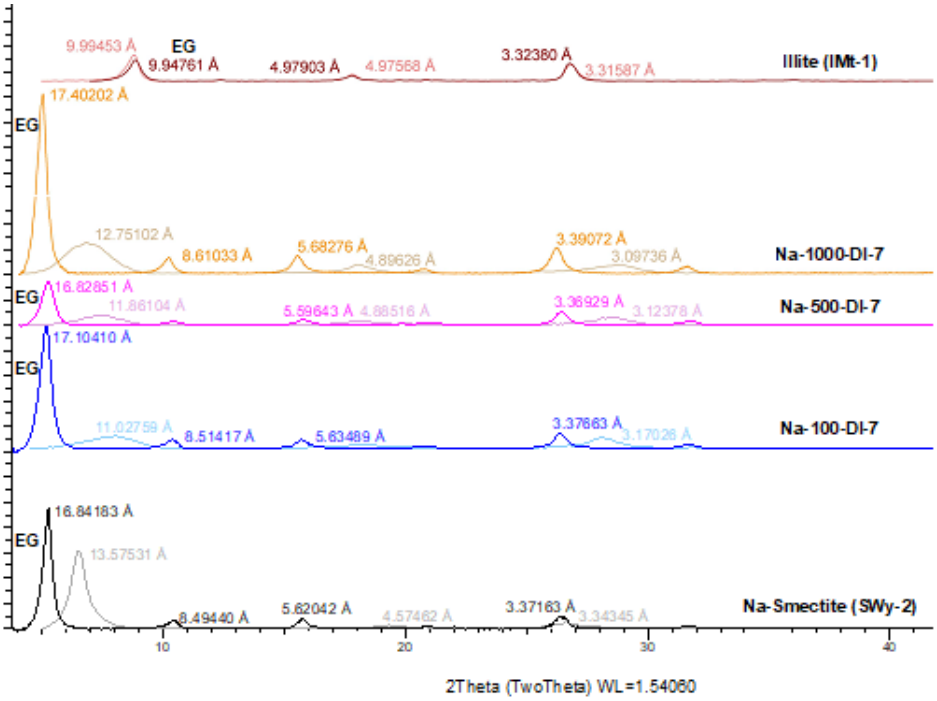

Figure 12-2: XRD spectra for Na-smectite (SWy-2) reacted in water for 100, 500 and 1000 solution/clay ratios. Air-dried oriented mounts were made for each and subsequently glycolated (EG).

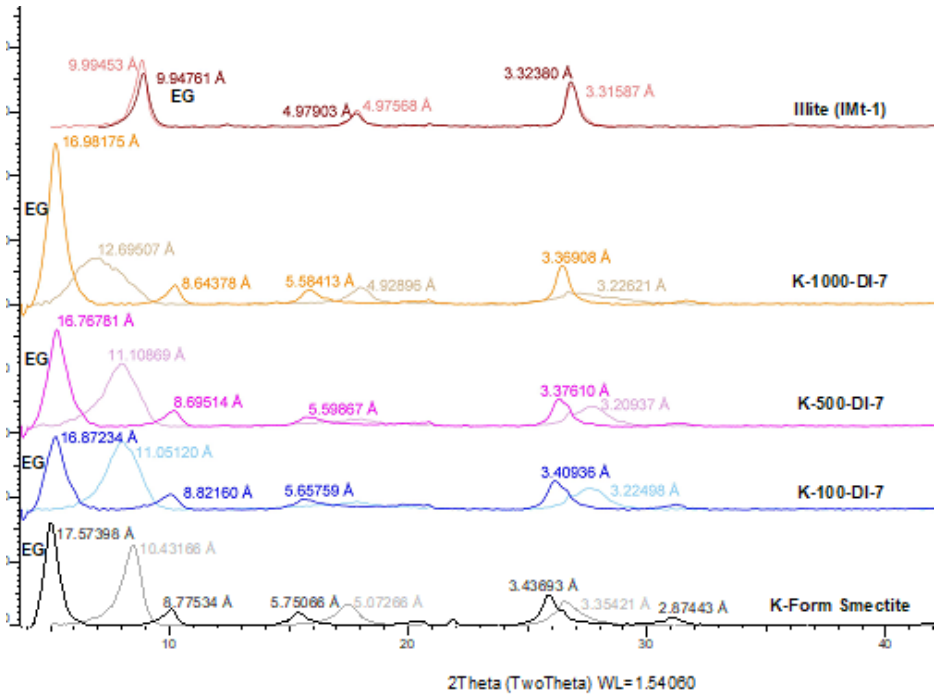

Figure 12-3: XRD spectra for K-Form Smectite reacted in water for 100, 500 and 1000 solution/clay ratios.

Figures 12-4 and 12-5 are a compilation of XRD scans for Na-Form smectite reacted in 1M KCl. Figure 12-4 shows the influence of solution/clay ratio on illitization. The solution/clay ratios used here are among the largest of illitization studies found in literature (Mosser-Ruck, 2001; Ferrage et. al, 2011; Huang et al, 1993; Cuadros and Linares, 1996; Kaufhold and Dorhman, 2010; Whitney and Norhthrop, 1988, Howard and Roy 1985). Inoue et. al 1983 and Roaldset et. al, 1998 both report loadings of ~105 and ~300 respectively. However, no other studies were found to have loadings as high as 1000, which could very well be the ideal loading for formation of discrete illite under the accompanying conditions. First, it should be noted that the peak intensities for the untreated Na-Form smectite are much higher than those of the reaction products. Perhaps this is suggestive of higher water content within the interlayer of the smectite clay as described in Ho et. al. (2020). There is a dramatic decrease in d-spacing for both the air-dried and the glycolated samples from 100 to 1000 loadings. The reaction time was initially kept constant across all loadings, at 7 days' time. There is a visible shift of the glycolated (001) reflection from 16.8 Å (a characteristic peak for glycolated smectite) for untreated starting material, to 14.5Å, 12.6 Å and 11.5 Å as solution/clay ratio is increased (100, 500, 1000, respectively). This indicates a decrease in swelling capacity of the material, more typical characteristic of an illitic clay. The air-dried samples of the reaction products do in fact show a shift towards 10 Å; the reflections are 10.2 Å, 10.2 Å and 10.4 Å respectively from 100 to 1000 loadings. This is reasonable due to 1M KCl being the solution in which the clay was reacted and, as reported above, K saturation of smectite can lead to a shift in d-spacing to 10 Å, akin to illite (Moore and Reynolds, 1997).

The parameters in these studies for solution/clay ratio allowed for the identification of the most ideal ratio for illitization; the 1000 loading case. The factor of reaction time was then varied to determine whether increasing reaction times would further drive the process of smectite to illite transformation. This study is consistent with authors mentioned above in regard to reaction time parameters. Figure 12-5 shows the collection of data for the 1000 loading cases arranged in increasing extent of time. A reaction time of 112 days is attributed with the most minimal shift in the (001) peak; observed to be ~0.21 Å post-glycolation. The XRD responses of reacted clays do not display similar characteristics to the spectra for illite/smectite (Figure 12-1), suggesting that the mineralogical transformation post-reaction is representative of a material largely analogous to discrete illite. The XRD results show that there are certain layers within the reaction product that can expand, like smectite, as seen in EG samples. The air-dried XRD spectra of Na-1000 at 56 days produces a (001) reflection at 10.31 Å which is the most similar to that of illite. The (003) peak for illite can be seen near 4.98 Å (Moore and Reynolds, 1997). For all reaction times, the (003) peak position is shifted, except for the 112-day sample, which is another indication of reduced swelling capabilities and illitic characteristics. This data suggests that for natural bentonite systems, where Na^+ ions occupy the interlayer space of smectite minerals, the reaction smectite undergoes to produce illite is attainable with high temperatures (200 °C), a solution/clay loading of 1000, the presence of potassium ions (K^+) and reaction times as low as 7 days. It is even more apparent that 112 days of reaction time produces reaction products that are closest in crystalline spectra to that of pure illite.

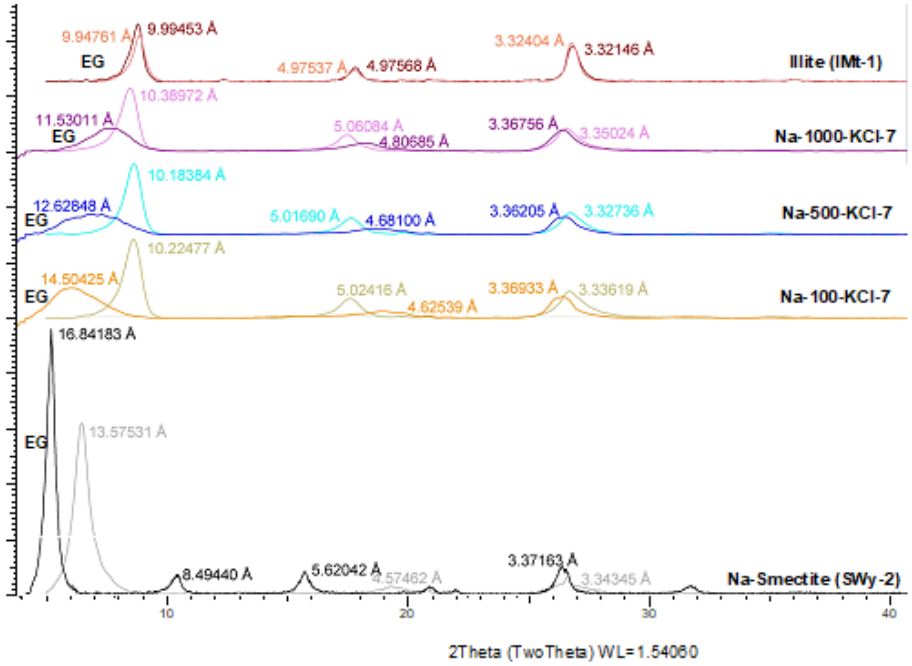

Figure 12-4: XRD spectra for Na-Form Smectite reacted in 1M KCl for 100, 500 and 1000 solution/clay ratios for duration of 7 days.

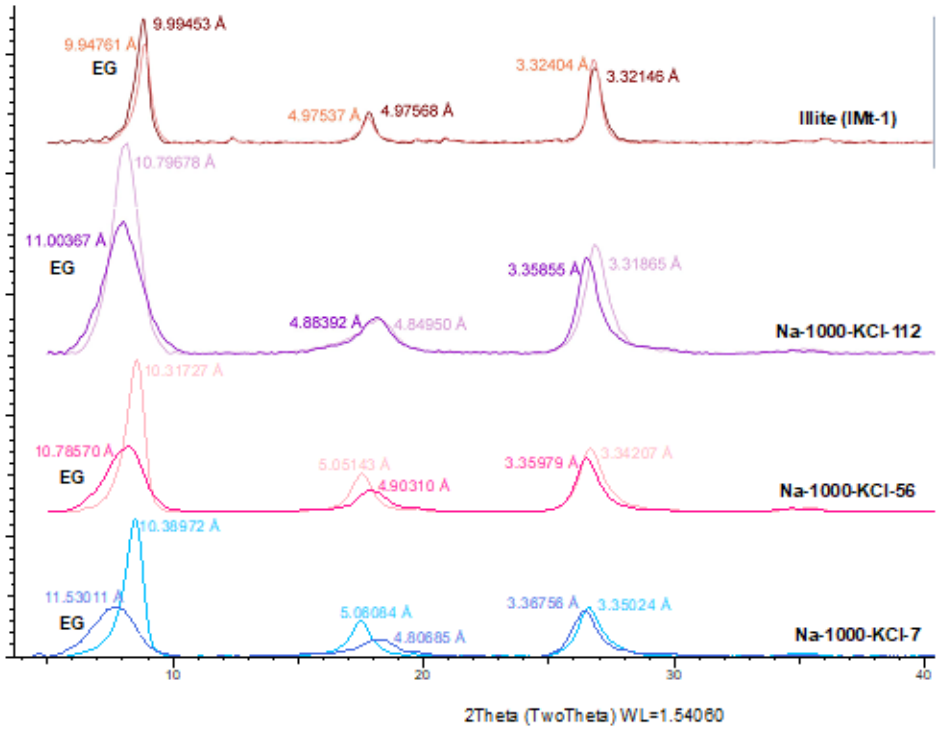

Figure 12-5: XRD spectra for Na-Form Smectite reacted in 1M KCl for 1000 solution/clay loading for varying reaction times.

Figures 12-6 and 12-7 show the XRD results for K-exchanged smectite that was reacted in 1M KCl. Figure 12-6 shows the influence of the solution/clay ratio for a reaction time of 7 days. Once again, similar to the Na-form smectite, the reaction products show a trend of less expandability as the loading is increased. The (003) peak of the glycolated samples can also be seen to shift less and tend to get closer to the air-dried (003) peak as loading is increased. Note that there is a (001) reflection at lower degrees-2θ for "K-smectite (SWy-2)" as opposed to SWy-2 in its natural, Na-Form. This peak is closer to that of illite: 10 Å. Once again, ethylene glycolation exposes the interlayer swelling capabilities of reacted samples, as indicated by the left peak shift that takes place for the (001) peaks for EG samples. The (001) EG peak, however, repeats the same trend as shown for the Na-smectite reaction products, the reflection begins to adjust itself closer to 10.7 Å, as the loading and reaction time increase (Figure 12-7); 112 and 56 day samples have a (001) relection at 10.7 Å under EG conditions. The reaction products produced after 112 days also shows an air-dried (001) reflection at ~10.19 Å, which is very close to the raw illite (IMt-1) samples. These studies have shown that complete illitization is achievable at short reaction times and lower temperatures than have been studied prior (Ferrage et. al, 2011; Huang et. al, 1993; Mosser-Ruck et. al, 2001; Whitney and Northrop 1988). That K-Form smectite clays shows favorability to produce illite over natural Na-smectite is not proven by XRD analysis. There seems to be a hairline shift towards illitic XRD spectra for K-smectite EG conditions compared to Na-smectite, but no dramatic shifts can be concluded. The elements that are commonly found in nature, such as Na and K in this report, if present as the interlayer cation of bentonite do not show major difference in the process of illitization.

These results from XRD analysis suggest that the external presence of K^+ is needed in order to drive illitization, for a time range spanning 7 to 112 days. K-exchanged smectite does not have enough K^+ to fully convert smectite to illite at 200°C. Introducing 1M KCl to the system, does in fact drive illitization for the loadings identified in this study. It is uncertain, however, as to how much K^+ or what concentration of K with be sufficient for complete conversion to take place under the same conditions of solution/clay loading, temperature and pressure. Solely changing the exchanged interlayer cation to K^+ does not have a large effect on illitization when reacted in DI water. However, when reacted in 1M KCl, the interlayer cation is insignificant on extent of illitization since both types of smectites produce discrete illite, discernible after as little as 7 days. The reaction products are more similar to illite and do not display characteristics similar to that of mixed layer illite smectite. However, some of the layers within the clay reaction products still have the ability to expand and, therefore, may contain some smectite layers intermixed in the clay.

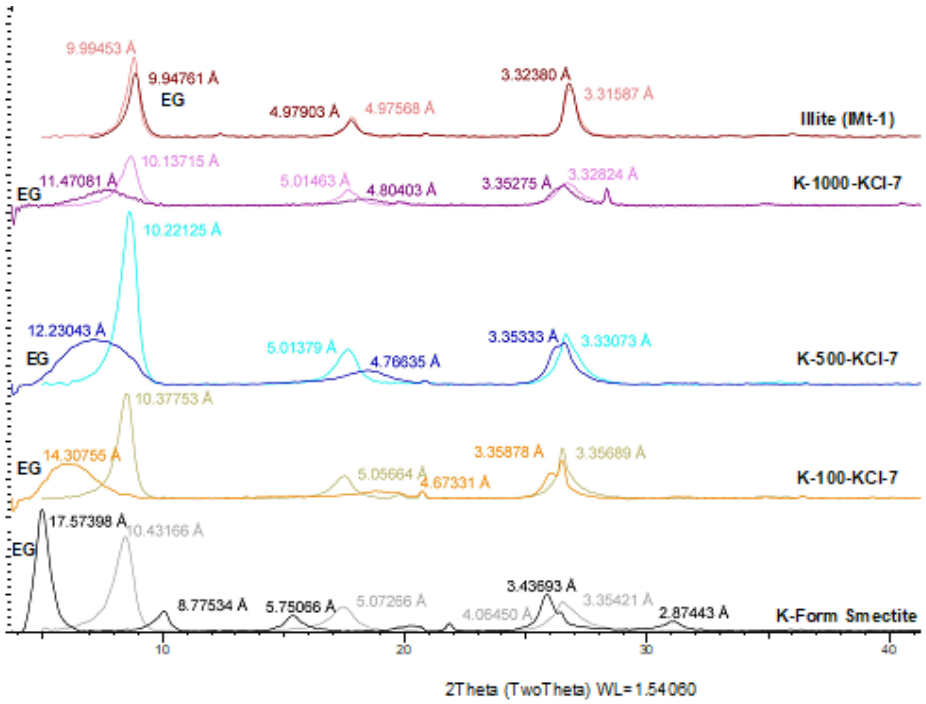

Figure 12-6: XRD spectra for K-Form Smectite reacted in 1M KCl for 100, 500 and 1000 solution/clay ratios for a duration of 7 days.

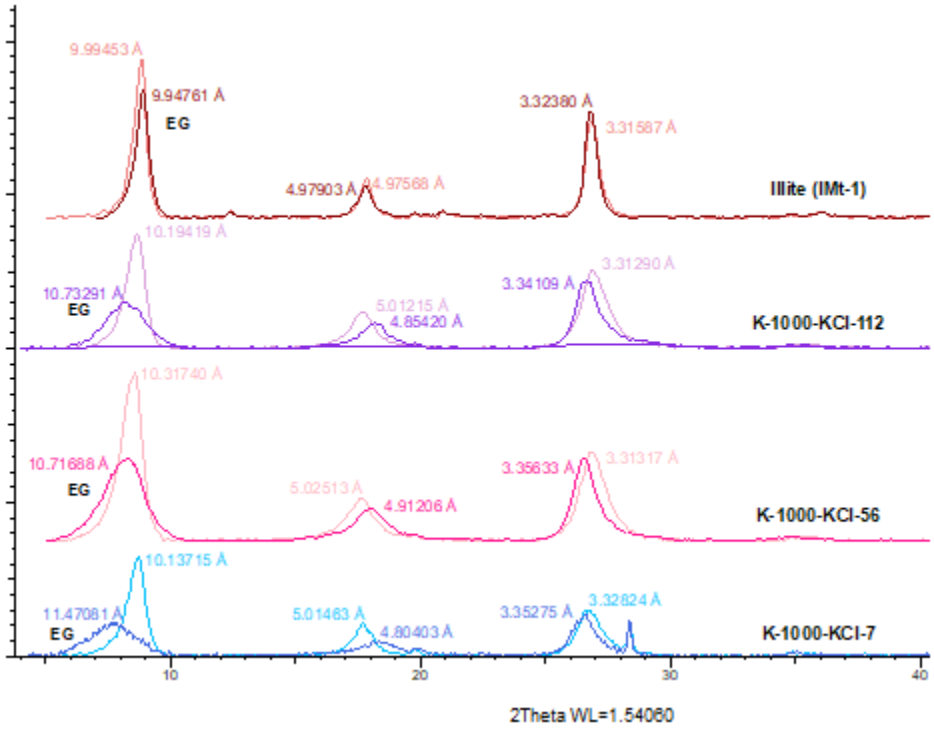

Figure 12-7: XRD spectra for K-Form Smectite reacted in 1M KCl for 1000 solution/clay ratios for varying reaction times.

A major factor influencing illitization is the concentration of silica in the system. With the induction of high temperatures and pressures to the environment during reaction, the amount of silica dissolved can be captured in the fluid products. The amount of dissolved silica (Si), measured by ICP, of the reactor fluid after hydrothermal alterations is shown in Figure 12-8 for cases reacted in 1M KCl.

The results for clay reacted in KCl solution show that the concentration of Si dissolved increases for smaller loadings. The 1000 case, for the 7-day reaction time, shows the least amount of dissolved silica, while the 100 loading showed the highest concentration of silica dissolved. Furthermore, there is a greater concentration of silica that is dissolved upon extending reaction time; 56 days of reaction time provides more time for silica to be released from the smectite as opposed to only 7 days for the 1000 loading. However, as the reaction time is extended to 112 days for the 1000 loading case there is little disparity of dissolved silica between 56 and 112 days. Therefore, the length of reaction time reaches a threshold after which the amount of silica released remains nearly constant. Upon comparison of Na-Form and K-Form smectite, the amount of dissolved silica for K-Form smectite is shown to surpass that of its counterpart for 100, 500 and 1000 loading cases reacted for 7 days. The amount of dissolved silica is equalized between the two clay types as the reaction time is extended. The results at 56 days shows that the amount of dissolved silica is comparable for both forms of smectite; the interlayer cation has does not affect the amount of dissolved silica between the two clay types after 56 day reaction times. It is important to note that for Illite (IMt-1/IMt-2), as reported in Martin (1980), "Data Handbook for Clay Minerals and Other Non-metallic Minerals", the chemical composition of SiO_2 within illite is 49.3% and will have less SiO_2 than smectite clays (62.9%).

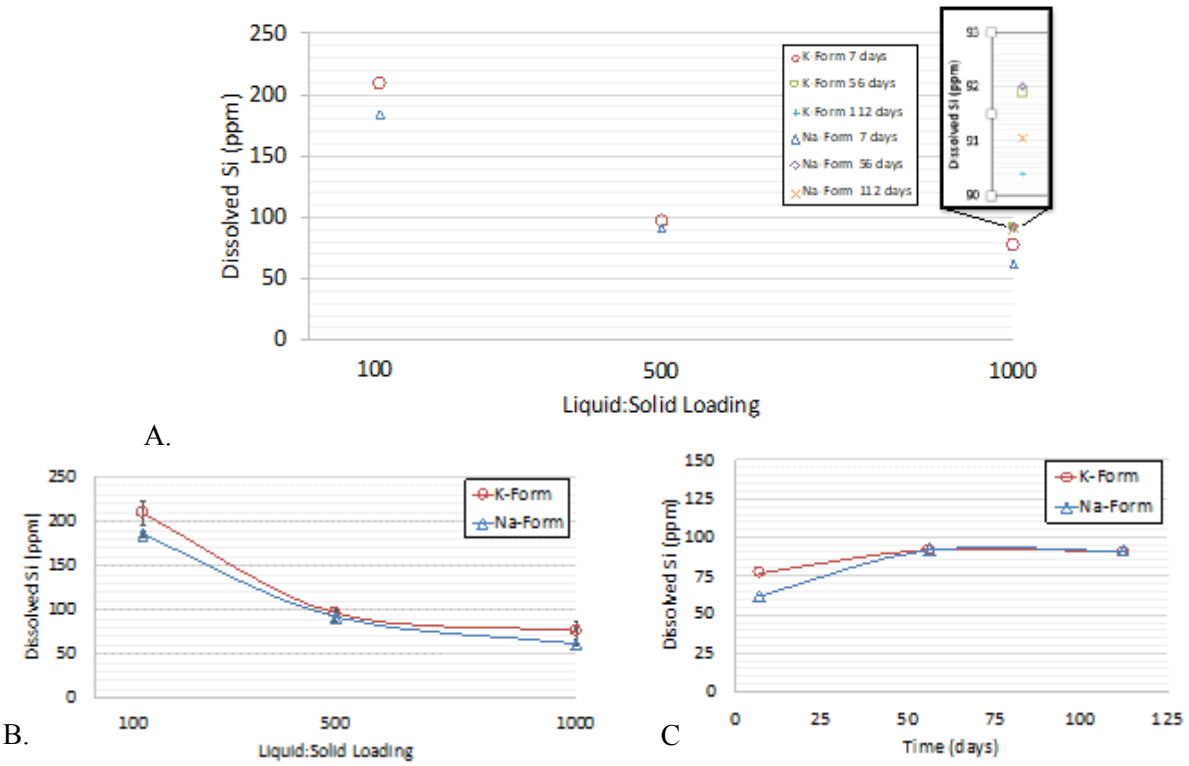

Figure 12-8: Dissolved silica concentration (ppm) obtained from solution after reaction. A. Loading vs. dissolved silica concentration for all samples reacted in 1M KCl over various durations. B. Samples reacted in 1M KCl for a duration of 7 days with various loadings. C. Dissolved silica concentration over time for samples of 1000 loading case with 1M KCl.

12.4 Conclusion

In order to accurately predict engineered barrier functions for heat generating nuclear waste, illitization experiments were conducted to explore the effects of clay loading in the system, the role of potassium, either as an interlayer cation or within the surrounding solution, and extended durations on transformation. The results indicate transformation can happen rather fast, within 7 days, under the appropriate conditions (1M KCl and 1000 loading) regardless of the stable interlayer cation typically found in nature (i.e., Na or K). Contrary to other studies, there does not appear to be an intermediate mixed-layer clay step of illite/smectite, as shown by XRD spectra. The results also do not precisely follow any previously proposed mechanisms found in literature, which may indicate a new mechanism and/or additional experimental work needed. Further studies will incorporate various temperature conditions and altering the concentration of the KCl solution. Additionally, the integration of elements not found in natural soil systems, but introduced through human processes, such as Cs^+ and $NH4^+$ ions, will be investigated.

12.5 References

Clay Minerals Society, 2020. http://www.clays.org/sourceclays_data.html

Cuadros, J., Linares, J., 1996. Experimental kinetic study of the smectite-to-illite transformation. Geochimica et Cosmochimica Acta. 60, No. 3, 439-453.

Eberl, D., Hower, J., 1977. The hydrothermal transformation of sodium and potassium smectite into mixed-layer clay. Clays Clay Miner. 25, 215–227.

Ferrage, E., Vidal, O., Mosser-Ruck, R., Cathelineau, M., Cuadros, J., 2011. A reinvestigation of smectite illitization in experimental hydrothermal conditions: Results from X-ray diffraction and transmission electron microscopy. Amer. Miner. 96, 207-223.

Ho, T.A, Wang, Y., Jove-colon C.M. Virtue X-Ray Diffraction Study of Homogenous Smectite Hydration (to be submitted).

Howard, J.J., Roy, D.M., 1985. Development of layer charge and kinetics of experimental smectite alteration. Clays and Clay Minerals 33, No. 2, 81-88.

Huang, W.L., Longo, J.M., Pevear, D.R., 1993. An experimentally derived kinetic model for smectite-to-illite conversion and its use as a geothermometer. Clay and Clay Minerals 41, No. 2, 162-177.

Inoue, A., 1983. Potassium fixation by clay minerals during hydrothermal treatment. Clays and Clay Minerals 31, No. 2, 81-91.

Inoue, A., 1995. Formation of clay minerals in hydrothermal environments, in: Origin and Mineralogy of Clays: Clays and the Environment. 268-329.

Kaufhold, S. Dorhman, R., 2010. Stability of bentonites in salt solutions II. Potassium chloride solution-Initial step of illitization?. Applied Clay Science, 49, 98-107.

Martin, R.T., 1980. Data Handbook for Clay Materials and Other Non-Metallic Minerals. Clays Clay Miner. 28, 160.

Moore and Reynolds, 1997. X-Ray Diffraction and the Identification and Analysis of Clay Minerals. Second Edition, 226-298.

Mosser-Ruck, R., Pironon, J., Cathelineau, M., Trouiller, A., 2001. Experimental illitization of smectite in a K-rich solution. Eur. J. Mineral. 13, 829-840.

Roaldset, E., Wei, H., Grimstad, S., 1998. Smectite to illite conversion by hydrous pyrolysis. Clay Minerals 33, 147-158.

Velde, B., Vasseur, G., 1992. Estimation of the diagenetic smectite to illite transformation in time-temperature space. Amer. Miner. 77, 967-976.

Whitney, G., 1990. Role of water in the smectite-to-illite reaction. Clays and Clay Minerals 38-4, 343-350.

Whitney, G., Northop, H.R., 1988. Experimental investigation of the smectite to illite reaction: Dual reaction mechanisms and oxygen-isotope systematics. Amer. Miner. 73, 77-90.

Zheng, L., Rutqvist, J., Xu, H., Birkholzer, J.T., 2017. Couple THMC models for bentonite in an argillite repository for nuclear waste: Illitization and its effect on swelling stress under high temperature. Eng. Geo., 230, 118-129.

13. SUMMARY AND PERSPECTIES

Significant progress has been made in FY20 in both experimental and modeling arenas in evaluation of used fuel disposal in crystalline rocks, especially in model demonstration using field data obtained from international collaborations. The work covers a wide range of research topics identified in the R&D plan. The major accomplishments are summarized below:

- *Discrete Fracture Network Development:* Many model-based studies assume fractures to be smooth planes. However, real-world fractures are known to have rough surface asperities. We accounted for fracture roughness by assuming textures with different connectivity structure and investigate how this impacts transport behavior. We demonstrated that this type of fracture roughness could control important features of flow and waterborne mass transport. We also investigated the relative impact of advective transport compared to retention due to matrix diffusion. Flow and solute transport through low-permeability fractured media at short time scales is generally determined by fractures and the interconnected networks that they form. However, at longer time scales, matrix diffusion, where solutes are exchanged between flowing regions (fractures) and non-flowing regions (matrix) via molecular diffusion, also influences solute transport. A long-standing question in this area of research is the relative impact of matrix diffusion on power-law scaling in the tails of the solute transport breakthrough curve, which are observed in field and laboratory experiments. While classical theory requires that matrix diffusion produces a decay rate of time $t^{-3/2}$, deviations have also been observed. We address this question through the development of a new theory that elucidates how interactions between two critical physical processes (advection and matrix diffusion) can produce either the classical -3/2 decay rate or alternative decay rates based on two dimensionless parameters. Our theoretical predictions were validated against particle tracking simulations using a high-fidelity three-dimensional discrete fracture network simulator.
- *Understanding bentonite swelling behaviors and colloid stability:* We addressed uncertainties related to bentonite behavior under disturbances, such as high temperature or swelling induced by changes in groundwater ionic strength and to understand the implications for colloid-facilitated transport of radionuclides. Column experiments were designed to test the effects of temperature on bentonite mineralogy and electrochemical properties. In the first experiment, bentonite spiked with ^{137}Cs was heated for 2 weeks at 200°C prior to making a dilute colloid solution to inject through a series of analcime columns. Another experiment involved injecting a similar colloid solution through a granodiorite column heated in-situ to 200°C. The results suggest that morphological and mineralogical changes to the bentonite occur, potentially increasing its sorption capacity. By contrast, elevated temperatures also reduce the repulsive force between colloids, lowering their stability. The colloid concentration of the solution eluting through the columns heated to 200°C dropped by roughly half, indicating that colloids are less stable at high temperature. The zeta potential and average diameter of the colloids, however, showed minimal changes from the increased temperature. A new method was also developed to quantify the anisotropy of bentonite swelling in order to inform bentonite swelling and erosion models. Solutions of variable ionic strength were introduced to pressed bentonite pellets, and images were taken over time through a microscope. The swelling rate and circularity were quantified at set time steps to relate anisotropy to swelling rate as predicted by simulations.

- *Rock testing capability development:* We have developed a high pressure (up to 10,000 psi), high temperature (up to 200˚C) triaxial loading system to enable long-term (days to months) laboratory experiments of flow simultaneously on multiple core samples under temperature, mechanical, and chemically controlled conditions. We also used the system for permeability measurements of granite samples obtained from the Grimsel Underground Research Laboratory.
- *In-situ evaluation of transmissive fractures:* Lawrence Berkeley National Laboratory (LBNL) conducted in-situ transmissive fracture testing in collaboration with the Collisional Orogeny in the Scandinavian Caledonides (COSC) scientific team. The research activities were conducted using the COSC-1 borehole as a testbed to evaluate the hydrology of a crystalline basement environment. This research is aimed at providing insights on the problem of nuclear waste disposal in crystalline formations. In June of 2019, the LBNL team deployed a unique borehole monitoring tool, called Step-rate Injection Method for Fracture In-situ Properties (SIMFIP), to measure real-time 3D mechanical deformation of rock within three intervals of the COSC-1 borehole. The following field tests were carried out: pressure buildup tests, pressure falloff tests, and constant flow rate tests for each of the three intervals. Two approaches were used to evaluate the stress conditions: an inversion of the displacement data, and a fully coupled numerical simulation of fracture stimulation and fluid flow using the distinct element code 3DEC. These analyses provided insights into the stress state for the borehole intervals, as well as how the fractures responded to hydraulic stimulation. Laboratory and modeling investigations were conducted on COSC-1 core samples that correspond with the borehole intervals tested in the field.
- *Model validation for fluid flow and transport in fractured rocks:* Updated modeling analyses were conducted on DECOVALEX Task C inflow and recovery simulations. The inflow simulations included a study of boundary conditions related to domain size by comparing inflow results for the base case domain (200 m x 300 m x 200 m) with that of a much larger domain (1386 m x 1486 m x 806 m). The comparisons were done for all ten fracture realizations. Pressure distribution simulation results for one of the realizations show that the site-scale domain exhibited boundary effects while the larger domain had no such effects. As a result, the inflow results for the 10 realizations using the larger domain show significantly reduced values compared to the base case domain. Thus, the inflow is better predicted with the larger domain. Updated simulations were also conducted to model water-filling of the plugged CTD and resulting pressure recovery. For the analysis the base case domain with domain size of 200 m x 300 m x 200 m was used. The 10 upscaled fracture realizations were used to provide permeability and porosity distributions. Simulation results were compared with project experimental data. The results show that pressure predictions of many of the 10 realizations closely match the experimental data at the observation points in 12MI33. Reasonable results were also obtained for predictions of chloride concentrations at most of the observation points. For this study upscaling of DFN to a continuum grid was conducted using the Oda method. The Oda method is an efficient geometric method to calculate grid block permeability without the use of flow simulations. However, it relies on well-connected fracture networks and thus tends to over-predict grid block permeability. In this work the Oda method was used to study the effect of grid block size on flow and transport. Simulations have shown that results are highly dependent on grid lock size.
- *Fuel Matrix Degradation Model Parameterization:* Electrochemical experiments were conducted to quantify the corrosion rates of the four most abundant alloys that make up the internal components of a typical spent fuel waste package (316 stainless steel, carbon steel, and aluminum alloy and Zircaloy-4) at several pH values and chloride concentrations. These rates were used to determine the amount of

hydrogen gas generated during anoxic corrosion and to parameterize a prototype in-package chemistry (IPC) model that has been integrated with the fuel matrix degradation (FMD) model. The combined model provides spent fuel degradation rates over a range of Eh, pH and chemical conditions relevant for argillite and crystalline rock repository environments. This combined model was developed by coupling the FMD model with the reactive transport code X1t, which is a module within the Geochemist's Workbench (GWB) software package. The reactive transport model was used to calculate the amount of H_2 produced and accumulated within a breached waste package due to the corrosion of stainless steel, carbon steel, aluminum alloys and Zircaloy based on the corrosion rates measured in the experiments. The environmental dependencies of in-package alloy corrosion rates must be taken into account in the FMD model to represent the range of conditions that can occur in a breached waste package. Instantaneous alloy corrosion rates and environmental dependencies (Eh, pH, Cl, T) are needed to calculate the spent fuel degradation rates used to define the radionuclide source term in a repository system performance assessment. The electrochemical measurements of alloy corrosion rates provide values and dependencies on T, Eh, pH, and Cl^- conditions that are needed for source term model parameterization and validation for carbon steel and aluminum alloy, which corrode actively, and for 316 stainless steel and Zircaly-4, which passivate.

- *Waste package material development:* Corrosion-resistant waste packages constitute a key component of a multiple barrier system for waste isolation. Metallic copper has been proposed as an outer layer material for a waste package. However, a concern has been raised regarding potential copper corrosion induced by hydrogen sulfides in a reducing disposal environment. We here demonstrate that lead/lead-alloy materials could be an excellent alternative material for waste package outer layers, owing to their corrosion resistance (especially to hydrogen sulfide attack) and radiation-shielding capability. Our long-term corrosion experiments show that lead is passivated by its corrosion products, cerussite ($PbCO_3$) and tarnowitzite $(Ca,Pb)CO_3$, in carbonate-bearing groundwaters, because of the formation of a dense surface layer of corrosion products and the low solubility of the corrosion products. With its low solubility ($<10^{-6}$ mol kg^{-1}), cerussite is more favored to form over galena (PbS) in a typical disposal environment; thus, the issue of sulfide-induced metal corrosion as related to copper can be completely eliminated. If needed, the carbonate concentration in a repository can be conditioned with carbonate materials such as calcite or hydromagnesite to ensure cerussite precipitation. Furthermore, using lead/lead alloy will provide excellent radiation shielding for waste package transportation and repository operation.
- *Enhancement of bentonite thermal conductivity:* In high-level radioactive waste disposal, a heat-generating waste canister is generally encased with a layer of bentonite-based buffer material acting as an engineered barrier to limit water percolation and radionuclide release. The low thermal conductivity of bentonite (~ 0.5 W/mK) combined with a high thermal loading waste package may result in a high surface temperature on the package that can potentially impact the structural integrity of the package itself as well as the surrounding buffer material. We showed that the thermal conductivity of bentonite could be effectively enhanced by embedding copper meshes across the buffer layer to form fully connected high heat conduction pathways. A simple calculation based on Rayleigh's model indicates that a thermal conductivity value of 5 W/mK required for effective heat dissipation can be achieved simply by adding ~ 1 v % of copper meshes into bentonite. As a result, the peak surface temperature on a large waste package such as a dual-purpose canister can be reduced by up to 300 °C, thus significantly reducing the surface storage time for waste cooling and therefore the overall cost for direct disposal of such waste packages. Because of the ensured full thermal percolation across the buffer layer, copper meshes turn out to be much more effective than any other materials currently suggested (such as graphene or graphite) in enhancing thermal conductivity of buffer material. Furthermore, the embedded copper meshes will help reinforce the mechanical strength of the buffer material, thus preventing the material from a potential erosion by an intrusion of dilute groundwater.

- *Understanding radionuclide incorporation into corrosion products:* The incorporation of radionuclides into corrosion phases may limit the rate of radionuclide release by sequestering a portion of the radionuclide source term. We performed a literature review on Se and Tc interactions with various Fe minerals to identify the most critical radionuclides and data gaps associated with radionuclide interaction with corrosion products. We synthesized ferrihydrite with various amounts of Pu(IV) (3000, 1000 and 400 ppm) following either a coprecipitation or sorption process and then subsequently used this material to crystallize goethite. We performed extended x-ray absorption fine structure (EXAFS) spectroscopy, transmission electron microscopy (TEM) and acid leaching analysis to elucidate the nature of plutonium association with ferrihydrite and goethite. Our results show that variations in synthetic routes have impacts on the nature of Pu associated with both the ferrihydrite precursor and the ferrihydrite recrystallization product (goethite). When a Pu containing solution is added to a ferrihydrite mineral (sorption route), a fraction of the Pu precipitates as PuO_2 nanoparticles and the remaining Pu fraction forms a complex on the mineral surface. After hydrothermal alteration to goethite, the PuO_2-like nanoparticles are preserved while a fraction of Pu is still present as a surface adsorbed species on the goethite mineral surface. There is evidence that this adsorbed species is more weakly bound to goethite than to ferrihydrite, as evidenced by a decrease in the number of Pu-Fe scatters identified in the respective sample. This observation suggests that Pu adsorbed to ferrihydrite may be mobilized during the recrystallization processes. The analysis of the supernatant after hydrothermal alteration of ferrihydrite to goethite showed a small increase in Pu concentration confirming that some Pu re-mobilization occurs during the mineral recrystallization process. However, when ferrihydrite is precipitated directly from a solution containing Fe and Pu (coprecipitation route), no PuO_2-like nanoparticles are observed. Although it is difficult to identify the exact nature of Pu in the sample due to a high degree of disorder, there is evidence that Pu is strongly bound to the ferrihydrite solids through a combination of adsorption and/or coprecipitation as evidenced by the high number of Pu-Fe scatters. A fraction of Pu could coprecipitate with ferrihydrite and/or form a polynuclear inner sphere complex. The EXAFS data show that the Pu binding site changes significantly during ferrihydrite recrystallization to goethite, indicating that Pu is mobilized during hydrothermal alteration. However, only a small fraction of Pu in the highest Pu concentration sample is remobilized to form PuO_2. In the lower concentration goethite samples Pu is strongly sorbed (either coprecipitated and/or adsorbed as inner sphere complex) to the goethite as evidenced by the high number of Pu-Fe scatters, and PuO_2 is not observed. The acid leaching results support this conclusion by showing that less Pu is accessible to leaching in goethite formed via coprecipitation process, compared to the goethite formed via the sorption process. These observations confirm that that the nature of Pu associated with the mineral will affects the leachability of Pu from the solids. In addition, Pu-doped magnetite was synthesized to study in an anaerobic glovebox to study the coprecipitation of magnetite with plutonium. Analysis of the supernatant after 30 days of oxidation experiments showed that less than 1% Pu is released to solution during 30 days oxidation, suggesting that Pu associates strongly to magnetite and is retained upon exposure to oxidative conditions.
- *Thermodynamic database development and international collaboration:* In FY20, we focused on our long-term commitment to engaging our partners in international nuclear waste repository research. This includes participation in the Nuclear Energy Agency Thermochemical Database Project, thermodynamic database collaborations, and surface complexation model international collaborations. Work is in progress to produce a software tool to add new species and to produce enhanced data files for reactive transport codes relevant to the SFWST Generic Disposal System Assessment (GDSA)

efforts. The tool is built around the SUPCRT data base as amended by Chen Zhu and co-workers (SUPCRTBL). The code is meant to be used by someone wanting to add new data to SUPCRT and ensure that it is internally consistent with the existing data. The code will produce a new version of the data file needed to run any of several reactive transport codes. Currently we plan to produce files for PHREEQC, EQ3/6, and GWB. Additional file configurations can be readily added to support the GDSA efforts. Furthermore, our code can readily be modified to use data files other than SUCPRT as the starting database. In particular, this code will be applicable to the modified SUPCRT code under development in the Argillite work package and for use in the US SFWST Generic Disposal System Assessment (GDSA) efforts. A key goal is to facilitate the integration of US SFWST thermodynamic database development with international thermodynamic database compilations (e.g. the NEA-TDB radiochemical thermodynamic data).

- *Understanding smectite-to-illite transformation:* In order to predict how well a bentonite barrier will function over time at repository relevant temperatures for heat generating waste, it is important to understand thermal alteration effects on smectite, a main constituent of bentonite. One type of thermal alteration is the conversion of smectite to illite (illitization) when exposed to elevated temperatures and a sufficient amount of potassium ions, thereby weakening barrier functions. Laboratory studies have tried to reproduce the transformation under a wide variety of conditions. However, the conditions were based on efforts to replicate natural earth processes. To facilitate the conversion of smectite to illite, illitization experiments on less than 2 μm fractions of Na-rich and K-exchanged smectite clay were performed within hydrothermal reaction vessels over one-week, two-week, two-month, and four-month timescales. The clay was exposed to hydrothermal conditions with various liquid to solid ratios at 200°C. Multiple analysis techniques were used to characterize the altered clay and identify extent of conversion, including XRD, XRF, surface area, and morphology changes by SEM; this section reports findings solely provided by XRD. The pore-water chemistry was also analyzed by ICP-OES to detect any dissolved products such as silica content. Results suggest the conversion rate is relatively fast and is dependent not only on the amount of K, but also dissolved silica concentration related to total solid in solution (liquid to solid ratio).

In the next five years, the disposal research will continue to focus on process model development and model implementation in a GDSA framework for different generic reference cases. At the end of the five years, it is anticipated that a GDSA model developed will contain a sufficiently detailed representation of relevant process models and thus can be used for sensitivity analyses and programmatic prioritization.

The crystalline R&D thrust area has a significant focus on opportunities to improve model representations of the most significant processes to repository performance. Buffer erosion is a good example of an instance in which a new mechanistic representation can be developed, building on work that has already been done in Europe. Hydrologic properties of the EDZ represent another opportunity for improved representation. Flow and transport in fractures, including matrix diffusion, are an ongoing focus. Overall, modeling a repository in crystalline rocks involves more issues than other rock types, so there is a continued need for more crystalline R&D activities over the next five years.

Crystalline R&D thrust areas cover a wide range of topics. Primary among these is the continued development of a crystalline media model that can be input to the GDSA PA system framework. In the near-term, i.e. the next two years, model development associated with this activity will be aimed at providing a minimal set of process models and model feeds to the GDSA PA. Modeling of fluid flow and transport in fractured crystalline media will continue to be a thrust area in the next five years. We will

continue to focus on model capability demonstrations using actual field data obtained from international collaborations. Systematic investigations of the potential effects of fracture geometry and distribution on fracture connectivity and hydrologic permeability will continue. Potential implications to site selection and characterization will be explored over the next five years.

The interaction between the crystalline host rock and the EBS has been an important research thrust in the crystalline area and will continue to be so in the coming five years. Engineered buffer materials in the EBS are an important component for waste isolation in a crystalline repository. The performance of various candidate buffer materials under a range of disposal conditions will be investigated over the next five years. The development of a new generation of buffer materials that can be tailored to various disposal environments for effective waste isolation is a significant thrust. Molecular modeling and experimental testing will be used to understand radionuclide interactions with newly developed buffer materials or corrosion products of EBS components. The aim of this modeling is the development of a continuum model used to simulate fluid flow and transport in the EBS as materials degrade. Such a model will be used to evaluate the efficacy of new buffer materials and EBS design options.

International collaborations have been, and will continue to be, a significant aspect of the crystalline research area over the next five years. These activities include continued participation in DECOVALEX as well as other international geologic disposal research programs. Collating and analyzing data from international URL's will be a continued activity in the crystalline area over the next five years.